Journal of Fluids Engineering

Published Bimonthly by ASME

TECHNICAL PAPERS

This journal is printed on acid-free paper, which exceeds the ANSI Z39.48-1992 specification for permanence of paper and library materials. ⊚™
♲ 85% recycled content, including 10% post-consumer fibers.

(Contents continued)

TECHNICAL BRIEFS

Review of Large-Eddy Simulation of Non-Premixed Turbulent Combustion

James J. Riley

e-mail: rileyj@u.washington.edu

Department of Mechanical Engineering,
University of Washington,
Seattle, Washington 98195

Recent developments in the methodology of large-eddy simulation applied to turbulent, reacting flows are reviewed, with specific emphasis on mixture-fraction-based approaches to nonpremixed reactions. Some typical results are presented, and the potential use of the methodology in applications and the future outlook are discussed.
[DOI: 10.1115/1.2169814]

Introduction

With the continuing reliance on fossil fuels as the predominant source for energy, and economic and environmental concerns emphasizing the efficient production of energy with minimal pollutants, the understanding and prediction of turbulent combustion remains a topic of considerable importance in mechanical engineering. And in the past decade, with the continuing increases in the speed, memory and storage of computers, with improvements in numerical methods, and, most importantly, with developments in subgrid-scale modeling, large-eddy simulation (LES) has begun to play a significant role in understanding and predicting turbulent reacting flows.

Early work on large-eddy simulation of turbulent, reacting flows has emphasized non-premixed reactions utilizing both mixture-fraction-based and Monte Carlo approaches. In the latter case, models based upon the filtered density function (FDF) equation (Colucci et al. [1], Jaberi et al. [2], Gicquel et al. [3], James and Jaberi [4]) and upon the linear eddy model (LEM, e.g., Menon and Calhoon [5]) have been developed and tested. In the FDF approach, Monte Carlo methods are introduced to solve for the moments of the modeled FDF equation, while in the LEM approach mechanistic, stochastic models are introduced to model the turbulence advection and mixing processes. Another LES approach has been to employ scale similarity arguments to close the reaction term directly (e.g., DesJardin and Frankel [6]). More recently, work has begun on the more difficult problem of premixed reactions. Several approaches have been employed, including methods to thicken the flame, either with an artificially large diffusivity (e.g., Colin et al. [7]) or larger-scale filtering (Boger et al. [8]), methods to track the flame using a progress-type (*G*) variable (e.g., Chakravarthy and Menon [9], Peters [10]), and also methods using models for flame-wrinkling density (Fureby [11], Knikker et al. [12]).

In this paper, recent developments in the methodology of large-eddy simulation of reacting, turbulent flows will be reviewed, with emphasis on mixture-fraction-based approaches to nonpremixed reactions in single-phase, low Mach number gases. The mixture-fraction-based approaches in large-eddy simulation have, in particular, been developed to the point where they can be used with confidence in both research and applications for certain classes of problems.

In the next section the approach of large-eddy simulation will be reviewed, along with the principal issues in its application to turbulent, reacting flows. In the third section, approaches which rely on the mixture fraction will be presented and, in the final section, some key remaining issues and the outlook for the future will be discussed.

Large-Eddy Simulation

The technique of large-eddy simulation stems from the research of meteorologists in the 1960s (e.g., Smagorinsky [13], Lilly [14], Deardorff [15]). In large-eddy simulation, Reynolds (usually time) averaging is avoided and the three-dimensional, time-dependent, detailed structure of the flow is directly simulated. In meteorological flows, however, as in most technological flows, it is impossible to numerically simulate all of the scales of motion, due to the vast range of length and time scales involved and to the limitations in computer speed and memory. Therefore, in large-eddy simulation, prior to performing the simulations, the governing equations are spatially filtered to remove motions at length (and time) scales not resolvable on the computational mesh. Thus only the "larger eddies" are simulated. For example, consider the velocity field $\mathbf{v}(\mathbf{x},t)$; it can be spatially filtered as

$$\hat{\mathbf{v}}(\mathbf{x},t) = \int G(\mathbf{x} - \mathbf{x}';\hat{\Delta})\mathbf{v}(\mathbf{x}',t)d\mathbf{x}', \qquad (1)$$

where the integral is over the entire computational domain, G is a filter function, usually a top-hat or a Gaussian function, or sometimes a spectral truncation, and $\hat{\Delta}$ is the filtering scale. (Favre, or density-weighted, filtering is often used for large-eddy simulation of reacting flows. For simplicity of presentation in most of this review, however, only non-weighted filtering is considered.)

To understand the effect of this filtering operation, consider filtering the momentum equation for constant density flows:

$$\frac{\partial}{\partial t}\hat{v}_i + \hat{v}_j \frac{\partial}{\partial x_j}\hat{v}_i = -\frac{1}{\rho}\frac{\partial}{\partial x_i}\hat{p} + v\frac{\partial^2}{\partial x_k^2}\hat{v}_i + \frac{1}{\rho}\underbrace{\frac{\partial}{\partial x_k}\hat{\tau}_{ik}}_{sgs}.$$
$$(2)$$

The equation, now for the corresponding filtered quantities, is identical to the momentum equation prior to filtering, except for the addition of the final term on the right-hand side. The quantity $\hat{\tau}_{ik}$, defined as

$$\hat{\tau}_{ik} = -\rho(\widehat{v_i v_k} - \hat{v}_i\hat{v}_k),$$
$$(3)$$

is called the subgrid-scale, or residual, stress tensor, and represents the effects of the subgrid-scale motions (which have been filtered out) on the grid-scale motions (computed in the simulations). This stress tensor requires modeling. Present models estimate the effect of the subgrid scales using information about the motions close to the scale of the computational cutoff. For example, in one modeling approach, the subgrid-scale stress tensor is modeled analogous to the Reynolds stress in mixing length

---

theory [13], with the coefficient chosen by a "dynamic" method (e.g., Germano et al. [16]) which takes into account the behavior of the velocity field at the smaller resolvable length scales.

The approach of LES has distinct advantages and disadvantages when compared to approaches utilizing the Reynolds-averaged Navier Stokes equations (RANS). LES has the disadvantage of being a very large calculation, being three-dimensional and time-dependent, and with as many length scales resolved as possible. It has the advantages, however, that the large-scale motions are treated directly, so that only the small-scale motions require modeling. For turbulent flows the large-scale motions tend to control the overall behavior of the flow, so their direct computation is a distinct advantage. Furthermore, the small, filtered scales of motion contain little energy, so that the computed results are expected to be somewhat insensitive to the model used. Finally, the small scale-motions of a turbulent flow tend to be more universal, especially when compared to the larger-scale motions, so that a proven model should have broader applicability.

The advantage of directly computing the larger-scale motions can be very important for simulating reacting flows, especially if the flows are inherently unsteady, e.g., combustion instabilities, or if motions difficult to model in RANS control the flow, e.g., in bluff-body stabilized flames.

At the present time the approach of LES is very useful as a research tool, and is being used in a limited number of applications. There is some optimism that, as computers continue to develop, and subgrid-scale modeling continues to improve, this approach will prove more and more useful in applications in the future.

In order to understand the potential problems involved in large-eddy simulations of turbulent, reacting flows, consider for simplicity the idealization of a constant density, single-step, Arrhenius, irreversible chemical reaction occurring on a turbulent flow field. Filtering the conservation equation for fuel for this case gives, in nondimensional form,

$$\frac{\partial}{\partial t}\hat{Y}_f + \hat{v}_i \frac{\partial}{\partial x_i}\hat{Y}_f = \frac{1}{\text{Pe}}\frac{\partial^2}{\partial x_i^2}\hat{Y}_f + \widehat{\omega}_f + \frac{\partial}{\partial x_i}\hat{\sigma}_i. \tag{4}$$

Here Y_f is the mass fraction of fuel and Pe is the Peclet number; $\hat{\sigma}_i = -(\widehat{v_i Y_f} - \hat{v}_i \hat{Y}_f)$, representing the flux of $\hat{Y}_f$ due to the subgrid-scale motions, is analogous to the subgrid-scale stresses, and can be treated, e.g., by Smagorinsky's model with a dynamically computed coefficient. The filtered reaction rate term is given by

$$\widehat{\omega}_f = -\text{Da} \cdot \text{filter}\{Y_f Y_o \exp[-E_a/R_u T]\}, \tag{5}$$

where "filter{·}" represents the spatial filtering operation (Eq. (1)), Y_o is the mass fraction of oxidant, T the absolute temperature, R_u the universal gas constant, E_a the activation energy, and Da is the Damköhler number, the latter defined here as an estimate of the ratio of the turbulent time scale to the chemical-reaction time scale. The principal new issue is how to model this term, especially for more complex, temperature-dependent reactions.

For moderate to large Damköhler numbers and also for high activation energies, the flame will be very thin, and the chemical reaction will occur almost entirely at the subgrid scale. This behavior is very different from that of other quantities such as velocity and density, the bulk of whose dynamics is resolvable on the computational mesh, and it appears to have discouraging implications, and indicates that modeling procedures for this term must be very different from those for the flux term $\hat{\sigma}_i$. Of course, any models must be based upon grid-scale quantities. What gives hope that a reasonable model exists is that the overall reaction rate depends on the mixing rate, and the mixing rate depends on the behavior of the larger-scale eddies.

Mixture-Fraction-Based Approach

Consider the problem where the reactive species are nonpremixed, e.g., a fuel jet into air. (Figure 1 shows a slice through a
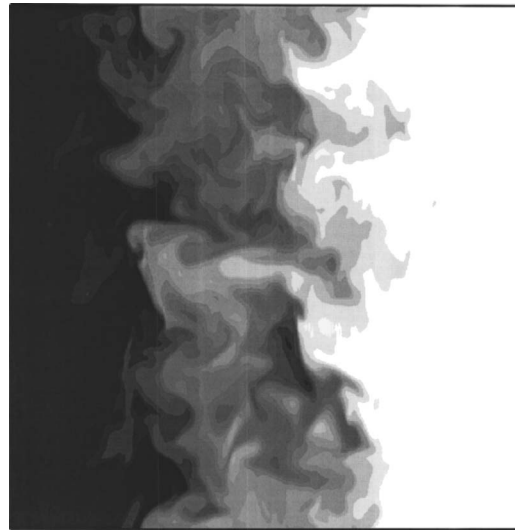
Fig. 1 Slice through the a turbulent region. Nonpremixed turbulent combustion occurs at the interface of the fuel (black) and oxidant (white).

nonpremixed turbulent region, where a reactant (colored black) is diffusing into and reacting with an oxidant (white). The chemical reaction occurs at the interface between the two. The figure was made from direct numerical simulation results employing a 512^3-point computational grid, and reported in de Bruyn Kops et al. [17]. The chemical reaction was a one-step, irreversible, Arrhenius-type, with moderate values for the Damköhler number and activation energy. The simulated velocity field was decaying, homogeneous turbulence with an initial Reynolds number, based upon the Taylor microscale, of about 70.) For the sake of simplicity, we consider the case where a fuel stream of mass fraction Y_{f_J} issues into an oxidant of mass fraction Y_{oE} in a one-step, Arrhenius reaction at low Mach number, although the following arguments can be easily generalized to realistic chemistry [18].

A major assumption in the mixture-fraction-based approaches is that the molecular diffusivities of all chemical species are equal, and furthermore their diffusivities equal the molecular diffusivity of heat. This assumption is justified for certain species, e.g., for atomic and molecular oxygen. Furthermore, for high Reynolds number turbulent flows, it is expected that the overall reaction rates become independent of these diffusivities, a fact that has some experimental, theoretical, and numerical support [19]. It must be realized, however, that the molecular diffusivities of some species are much different from those of others, e.g., the diffusivity of molecular hydrogen is much greater than that of oxygen. In addition, this assumption may break down in regions of gaseous flows where the temperature is high, and hence the viscosity is high and the Reynolds number is lower. Finally, it is important to note that recent theoretical work has suggested methods of relaxing this assumption (e.g., Nilsen and Kosály [20], Nilsen [21], Pitsch [22], Peters [10]).

The concept of a mixture fraction is based upon conserved scalars, examples of which are elementary mass fractions, e.g., those for oxygen and hydrogen, Z_O and Z_H. But, more generally, in considering the conservation equations for the fuel and oxidant, assuming equal diffusivities, the mixture fraction can be defined for this case by [23]

$$Z = \frac{rY_f - Y_o + Y_{oE}}{rY_{f_J} + Y_{oE}}, \tag{6}$$

with the properties that it is conserved, and satisfies the limiting conditions:

$$Z \to \begin{cases} 1 & \text{in the fuel stream} \\ 0 & \text{in the oxidant stream.} \end{cases} \qquad (7)$$

Here r is the mass of oxidant required to react with a unit mass of fuel. An interpretation of Z is that it is the local mass fraction of material originating in the fuel stream, while $(1-Z)$ is the local mass fraction of material originating in the oxidant stream; values of Z between 0 and 1 indicate the amount of mixing that has occurred.

Equilibrium Chemistry. For the case of equilibrium chemistry, the mass fractions of the various chemical species and the temperature can be written as known functions of the mixture fraction, e.g., $Y_f = Y_f^e(Z)$. Define $\hat{p}(Z)$ to be the frequency distribution of Z within a subgrid-scale volume element, where $\hat{p}$ is known as the subgrid-scale pdf [24] or the filtered-density function [1,25]. Then

$$\hat{Y}_f = \int_0^1 Y_f^e(Z)\hat{p}(Z)dZ. \qquad (8)$$

Therefore, if $\hat{p}$ can be determined, then so can $\hat{Y}_f$ and the other filtered mass fractions and filtered temperature.

In analogy with the approach involving the assumed pdf for the Reynolds-averaged equations (see, e.g., Bilger [23]), one model involves assuming a functional form for $\hat{p}$, in particular that of a β-function (Frankel et al. [26]; Cook and Riley [27]). Then $\hat{p}$ can be obtained from the first two filtered moments of Z, i.e., $\hat{Z}$ and the variance squared, or residual, $Z_v^2 = \widehat{Z^2} - \hat{Z}^2$. (Note that care has to be taken in the definition of the variance, since in general $\widehat{\hat{Z}} \neq \hat{Z}$.) The problem then reduces to developing accurate procedures to predict both $\hat{Z}$ and Z_v.

This approach can be readily tested in an a priori fashion using data for Z from either high-resolution direct numerical simulations (DNS) or highly-resolved scalar fields measured in laboratory experiments. (Direct numerical simulations involve solving the governing equations for *all* the dynamically relevant scales of motion, so that no subgrid-scale modeling is required.) Given the values of the mixture fraction, assuming chemical equilibrium, the values of temperature and of the mass fractions for each of the chemical species are also known at each point on the high-resolution grid. These fields can then be filtered to obtain "exact" values for the filtered temperature and species mass fraction fields. Furthermore, the first two moments of Z can be filtered, and used along with the assumed form for $\hat{p}$ to produce models for the filtered fields. This allows one to easily compare the "exact" and modeled fields.

Such a procedure was carried out for constant density flows by Cook and Riley [27], assuming a β-distribution for $\hat{p}$, and using both results from high resolution direct numerical simulations [28] and laboratory data for a jet [29]. In both cases good agreement was obtained when comparing the "exact" to modeled values, validating the estimation of the filtered mass fractions for equilibrium chemistry based upon an assumed form for $\hat{p}$. This testing was extended by Wall et al. [30] to the variable density case, testing β-distribution models for both the subgrid-scale pdf and the density-weighted (Favre) subgrid-scale pdf. The β-distribution model was successful in both cases, although slightly better for the subgrid-scale (non-Favre) pdf.

Several authors have taken advantage of this model for use in large-eddy simulations of chemically-reacting, nonpremixed turbulent shear flows. For example, Jiménez et al. [31] considered a planar, nonpremixed shear layer. Such a flow has considerable intermittency, which is difficult to model with RANS. With the β-distribution assumption for $\hat{p}$, very good agreement was obtained with results from high resolution DNS. Reveillon and Vervisch [32] used a similar approach in studying large-eddy simulations of nonpremixed reactions with heat release. Again,

good agreement was found in comparing modeled results with results from DNS. Branley and Jones [33,34] and also Forkel and Janicka [35] used a similar approach to simulate hydrogen jet diffusion flames, and obtained good agreement with laboratory data for major species. And Pierce and Moin [36] simulated a swirling, confined, coaxial jet including heat release using the same modeling. Again comparisons of simulation results with laboratory data were impressive.

Recently Mellado et al. [37] have relaxed the assumption of a β-function for $\hat{p}$ using a deconvolution procedure with appproximate reconstruction of $\hat{p}$ using additional moments of Z. This approach has the potential to provide overall improvement to mixture-fraction-based approaches.

Quasi-steady Chemistry. The assumption of chemical equilibrium can be relaxed for fast, but finite rate chemistry, i.e., when the Damköhler number is large, but finite. An important value of Z is its stoichiometric value, attained when the fuel and oxidant are in stoichiometric proportions. When the Damköhler number is large, it is expected that the flames are very narrow, and that they occur near the stoichiometric surfaces. Peters [38] took advantage of these facts to develop the flamelet model, wherein the Damköhler number is assumed to be large enough that the flame regions are very "thin." Here thin is taken to mean that the flame thickness δ is much smaller than either of the two local principal radii of curvature R of the flame itself. There is some argument that, in order for this inequality to hold, in addition to the assumption of large Damköhler number, the flame thickness must be small compared to the local Kolmogorov scale [39], although this requirement is in dispute.

At any point in the flow field a local orthogonal coordinate system can be set up, with one unit vector in the direction of the gradient of Z. The equations are transformed into this local system; then, since Z is locally monotonic in the direction of its gradient, Z can be used as an independent variable. Forming the equations for the species mass fractions in this local coordinate system, and neglecting higher order terms in the small parameter δ/R, results in the simplified form of the conservation equation, called the flamelet equation, here written in dimensional form for the fuel mass fraction,

$$\rho \frac{\partial Y_f}{\partial t} = \dot{\omega}_f + \rho \mathcal{D} |\nabla Z|^2 \frac{\partial^2 Y_f}{\partial Z^2}. \qquad (9)$$

Here $\mathcal{D}$ is the molecular diffusivity of fuel. For large Damköhler numbers, which implies that the chemical time scale is much smaller than the turbulence time scale, it is often argued that the reaction is quasi-steady so that the flamelet equation reduces to

$$\dot{\omega}_f = -\rho \frac{1}{2} \chi \frac{\partial^2 Y_f}{\partial Z^2}, \qquad (10)$$

the quasi-steady flamelet equation. Note that this is a simplified form of the conservation equation for the fuel, and can be assumed to hold at each point in the flow. Similar equations can be derived for the other species.

Note that the scalar dissipation rate $\chi = 2\mathcal{D}|\nabla Z|^2$ enters into the theory, carrying information about the local *rate* of scalar mixing. To develop the model further, assumptions are needed regarding χ and its relationship to Z. One approach for χ is to assume that the flow in the vicinity of the diffusion flame is a local counterflow, implying both that δ is less than the Kolmogorov scale and also locally uniform strain [38]. The solution to the quasi-steady flamelet equation can then be written as, e.g.,

$$Y_f = Y_f^{\text{fl}}(Z, \chi). \qquad (11)$$

Therefore, with $\hat{p}(Z, \chi)$ representing the joint frequency distribution of Z and χ in a subgrid-scale volume element, the filtered value of Y_f in this volume element is

$$\hat{Y}_f = \int_0^\infty \int_0^1 Y_f^{\text{fl}}(Z,\chi)\hat{p}(Z,\chi)dZd\chi. \qquad (12)$$

Assumptions are now required to determine $\hat{p}(Z,\chi)$. It is usually assumed that Z and χ are statistically independent inside each volume element; furthermore it can be argued that $\hat{Y}_f$ depends mainly on $\hat{\chi}$, and only weakly on $\chi' = (\widehat{\chi^2} - \hat{\chi}^2)^{1/2}$ [40], which results in

$$\hat{Y}_f = \int_0^1 Y_f^{fl}(Z,\hat{\chi})\hat{p}(Z)dZ. \qquad (13)$$

As in the case for equilibrium chemistry, $\hat{p}$ can be taken to be a β distribution, determined in terms of $\hat{Z}$ and the variance Z_v. Denoting this assumed form as $\hat{p}_a(Z;\hat{Z},Z_v)$, then the model result for $\hat{Y}_f$ for quasi-steady chemistry is

$$\hat{Y}_f = \int_0^1 Y_f^{\text{fl}}(Z,\hat{\chi})\hat{p}_a(Z;\hat{Z},Z_v)dZ = \hat{Y}_f(\hat{Z},Z_v,\hat{\chi}). \qquad (14)$$

These results imply that the filtered mass fractions of the chemical species can be obtained by setting up tables, e.g., for $\hat{Y}_f(\hat{Z},Z_v,\hat{\chi})$, prior to performing an LES. These tables can be constructed by first solving Eq. (10) for an appropriate range of $\hat{\chi}$, and then using the result in Eq. (14) for an appropriate range for $(\hat{Z},Z_v,\hat{\chi})$. Once these tables are set up, then the LES is performed; in it $\hat{Z}$, Z_v and $\hat{\chi}$ would be needed to be computed locally on a pointwise basis; the values for $\hat{Y}_f$ would then be obtained by table look-up. Note that, e.g., one can also determine $\hat{Y}_o$, $\hat{Y}_p$, and $\widehat{\omega}_f$ in a similar manner. For example, the filtered value of the reaction rate for fuel is obtained as

$$\widehat{\omega}_f = \int_0^1 \dot{\omega}_f[Y_f^{fl}(Z,\hat{\chi}), Y_o^{fl}(Z,\hat{\chi}), \dots]\hat{p}_a(Z;\hat{Z},Z_v)dZ, \qquad (15)$$

where, for a given problem, $\dot{\omega}_f(Y_f, Y_o, \dots, T)$ is a known function of the chemical composition and temperature.

Note that, since the chemistry and filtered species concentrations can be tabulated prior to performing the simulations, the method involves very little additional computational overhead compared to simulations for a non-reacting flow, an important attribute of this approach.

This approach can be readily extended to realistic chemistry with exothermicity and strong density variations [18]. The extension involves bringing in the temperature dependence of the various thermodynamically-related quantities, working with the density-weighted (Favre) filter, including filtered thermodynamic state equations, and employing several additional assumptions such as the neglect of the subgrid-scale fluctuations in viscosity. In doing this, the modeling of the subgrid-scale stresses and concentration fluxes, the filtered reaction rates, and the inferred filtered mass fractions and temperature are treated in the same manner as discussed above.

This approach, or variations of it, has been used in several large-eddy simulations of finite-rate, non-premixed chemical reactions. For example, Cook et al. [40], Cook and Riley [18], and de Bruyn Kops et al. [41] have compared predictions of this model with filtered results from direct numerical simulations. It was found that the model works well for moderate to high Damköhler numbers with continuous burning. Jiménez et al. [31] extended their studies to slightly out-of-equilibrium problems. Instead of the counter-flow model for $\hat{\chi}$ mentioned above, they employed a log-normal frequency distribution. Again, good agreement was obtained in comparing model predictions to results from high resolution direct numerical simulations.

More recently, de Bruyn Kops and Riley [42] have applied this
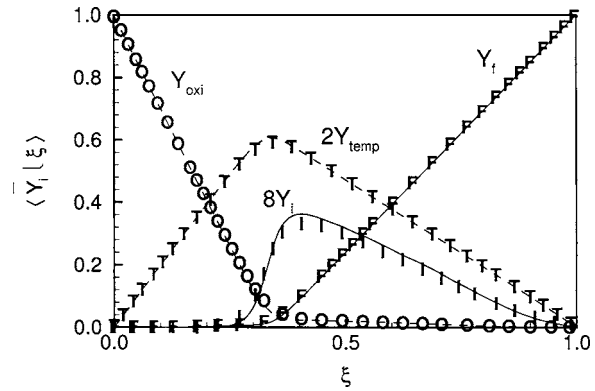
Fig. 2 Filtered mass fraction and scaled temperature for a two-step reaction on a scalar mixing layer. Lines are predictions from a 64^3-point LES, symbols from a 512^3-point DNS. Notation is as in Swaminathan and Bilger [43].

modeling approach to simulate one-step, strongly temperature-dependent reactions, and a two-step methane-oxygen mechanism (Swaminathan and Bilger [43]), both on a scalar mixing layer. The large-eddy simulation results were compared to filtered results from very high resolution direct numerical simulations that had themselves been validated by comparison with laboratory experiments (de Bruyn Kops and Riley [44,45]). Models for Z_v and $\hat{\chi}$ were taken as the best models from a previous study (de Bruyn Kops and Riley [46], see below). The predictions for the mass fractions and temperature were found to be in excellent agreement with the DNS results for moderate to large values of a global Damköhler number. In addition, predictions of the filtered reaction rate were found to be very good when the frequency function for $\hat{\chi}$ is introduced in the computation, as suggested by Jiménez et al. [31]. A typical example of their results is given in Fig. 2, where the filtered mass fraction and scaled temperature for the two-step methane-oxygen mechanism are plotted for a case employing moderate values of the Damköhler number for the two reactions. Lines are predictions from a 64^3-point LES; symbols are from a 512^3-point DNS. Notation is as in Swaminathan and Bilger [43]. The velocity field simulated was decaying, homogeneous turbulence with an initial Reynolds number, based upon the Taylor microscale, of about 70.

Finite-Rate Chemistry. A principal limitation in the quasi-steady flamelet model is its lack of applicability to cases where reactions might be slow, e.g., for free radicals, or where extinction and possible reignition might occur. It is tempting to then treat the time-dependent flamelet equation, Eq. (9), instead of Eq. (10). It must be realized, however, that the computational overhead can then become much greater, as the chemistry in general cannot then be tabulated, and the dynamic equations for species conservation and temperature must be solved, and potentially on higher dimensional computational grids (since Z is also an independent variable).

Pitsch and Steiner [47] have relaxed the assumption of quasi-steadiness, and included the time-derivative term in Eq. (9) in simulating the spatial development of a methane/diffusion flame. The time derivative is interpreted as the time rate of change following the average velocity, conditioned on the stoichiometric value of the mixture fraction. The instantaneous values of the mixture fractions, temperature and scalar dissipation rate are assumed to be independent of the azimuthal θ and radial r coordinates, so that, for example, $Y_f(Z,r,\theta,x,t) = Y_f(Z,x,t)$ in Eq. (9), where x is the axial coordinate. These Z-dependent quantities are analogous to conditional averages discussed below, and there is experimental evidence that, at least in the Reynolds-averaged mean, they are not dependent on r and θ for the jet flame consid-

ered. These assumptions of spatial uniformity greatly simplify the simulations, eliminating the problem of increasing dimensionality mentioned above. The quantity $\chi(Z,x,t)$ is obtained by solving the integral equation,

$$\hat{\chi}(\mathbf{x},t) = \int_0^1 \chi(Z,x,t)\hat{p}(Z,\mathbf{x},t)dZ, \qquad (16)$$

given the local filtered value of χ. In order to solve the integral equation for $\chi(Z,x,t)$, it must also be assumed that $\hat{\chi}$ is uniform over a somewhat large spatial region.

The approach is then to model $\hat{\chi}$ in a manner similar to Girimaji and Zhou [48] (see the next section), solve for $\chi(Z,x,t)$ using (16), and then with $\chi(Z,x,t)$ known to solve the unsteady laminar flamelet equation (Eq. (9)) for $Y_f(Z,x,t)$ and the other species and temperature. The filtered quantities are then obtained from the integral

$$\hat{Y}_f(\mathbf{x},t) = \int_0^1 Y_f(Z,x,t)\hat{p}(Z;\mathbf{x},t)dZ. \qquad (17)$$

Pitsch and Steiner used a reduced form of the GRI 2.11 mechanism (Bowman, C.T., R. K. Hanson, D. F. Davidson, W. C. Gardiner, Jr., V. Lissïanski, G. P. Smith, D. M. Golden, M. Frenlach, E. M. Goldenberg, Gri-mech 2.11, http://www.me.berkeley-edu/gri-mech/) consisting of 29 global reactions to simulate the Sandia flame *D*, a piloted methane/air diffusion flame; they obtained reasonably good agreement with the experimental data.

Bushe and Steiner [49] and Steiner and Bushe [50] employed a variation of the conditional moment closure (CMC) model (Bilger [51], Klimenko [52]) to close the reaction term in the filtered chemical species conservation equations (e.g., Eq. (4)). The CMC model, which produces final equations very similar to those using the flamelet model, but with seemingly different assumptions (Klimenko [53]), deals with averages of quantities, conditioned on the value of the mixture fraction Z. A principal assumption is the neglection of averages of fluctuations about the conditional average; for example, the conditional filtered reaction rate term is modeled as

$$\text{filter}\{\dot{\omega}_f(Y_f,Y_o,\dots)|Z\} = \dot{\omega}_f(\widehat{Y_f|Z},\widehat{Y_o|Z},\dots), \qquad (18)$$

so that the filtered value of $\dot{\omega}_f$ can then be obtained as

$$\hat{\dot{\omega}}_f = \int_0^1 \dot{\omega}_f(\widehat{Y_f|Z},\widehat{Y_o|Z},\dots)\hat{p}(Z)dZ, \qquad (19)$$

similar to Eq. (15) above using the flamelet approach. As with the conditionally filtered value of χ above, the quantities $(\widehat{Y_f|Z})$, etc., are obtained by solving the integral equation

$$\hat{Y}_f = \int_0^1 (\widehat{Y_f|Z})\hat{p}(Z)dZ. \qquad (20)$$

The procedure is therefore to explicitly solve the equations for the filtered species mass fractions and temperature. At each point in time, the filtered reaction rate is needed and can be obtained by first solving the integral equations for the conditionally filtered species mass fractions and temperature, and then utilizing Eq. (19) to obtain the filtered reaction rates. Comparisons of model predictions with filtered results from high resolution direct numerical simulations indicates that the method works well. Furthermore, the authors suggest conditionally filtering on both Z and χ, which may be useful in treating problems with extinction and/or reignition.

Both of these methods appear to have considerable potential for addressing problems with slower chemistry, as long as the chemical reaction mechanisms can be computed efficiently, and either the problem defined has certain symmetries to reduce the dimensionality of the mathematical problem and/or the conditional mo-

ments can be treated in a quasi-homogeneous manner.

Several models have been introduced to treat partial premixing. In addition to the mixture fraction, these models usually employ some type of progress variable in order to indicate the amount of premixing. For example, Pierce and Moin [54] use a mixture fraction and a progress variable, the latter which tracks the global extent of reaction of the local mixture. They apply this approach to a methane-fueled coaxial jet combustor for which laboratory data is available for comparison. Significant premixing occurs in the near field of the combustion zone, resulting in a lifted flame. Good agreement is obtained for model predictions of the experimental data. In another approach, in additional to the mixture fraction and progress variable, Vervisch et al. [55] define a flame indicator $\chi_{F,O} = -D\nabla Y_f \cdot \nabla Y_o$ in order to determine whether the flame is locally premixed or nonpremixed. (It can be shown that $\chi_{F,O} > 0$ in nonpremixed flames, while $\chi_{F,O} < 0$ in premixed flames.) Interesting results for the dynamics of the turbulent flame base were obtained for the case of the lifted flame in a turbulent cold wake.

Recently Mitarai et al. [56] have introduced a quasi-Lagrangian version of the flamelet model, specifically developed to treat problems where extinction and reignition are important. Lagrangian particles are tracked, and their local flamelet equation (Eq. (9)) is solved in time. A simplified model, consistant with overall energy conservation, is used to transfer heat between burning and extinguished flamelets. The model gives good agreement when its predictions are compared with results of direct numerical simulations of nonpremixed reactions which include significant extinction and reignition.

Modeling $\hat{\chi}$ and Z_v

de Bruyn Kops and Riley [46] evaluated several models for $\hat{\chi}$ and Z_v with both a priori and a posteriori comparisons of modeling predictions with results from very high resolution direct numerical simulations of a scalar mixing layer. For the variance Z_v, models were considered which relate Z_v to the resolved gradient of Z, i.e., to $|\nabla\hat{Z}|^2$ (Yoshizawa [57], Mathey and Chollet [58]), and to the variance near the grid-scale cut-off (the test-scale variance) (Cook and Riley [27]). In one form of both models, the coefficient in the models is computed by assuming a form for high wave number spectrum, and fitting this form to the simulation data [59]. It was found that both models worked very well when assumed spectra were used to determine the coefficients.

For the filtered dissipation rate, following Girimaji and Zhou [48] the models were directly related to $|\nabla\hat{Z}|^2$, i.e.,

$$\hat{\chi} = \mathcal{C}|\nabla\hat{Z}|^2,$$

the only difference in the models being the method of computing the coefficient $\mathcal{C}$. In one case the coefficient was related to the energy flux from the grid scales, while in the other cases it was determined by fitting an assumed high wave number spectrum. (Note that for large-eddy simulations, since the equation for $\hat{Z}$ is directly computed, an estimate for $\hat{\chi}$ is immediately available as the flux of $\hat{Z}$ energy from the grid scales to the subgrid scales.) As in the case with Z_v, the models which performed best relied on fitting the assumed form for the spectrum.

Typical results from the study of de Bruyn Kops and Riley are presented in Fig. 3, where the filtered scalar dissipation rate and subgrid-scale variance versus downstream distance are plotted for the case of homogeneous, isotropic, decaying turbulence at an initial Taylor Reynolds number of about 70. The DNS results are obtained using 512^3 grid points; the LES results are from 64^3-point simulations of the same flow. The results from several different models are shown.
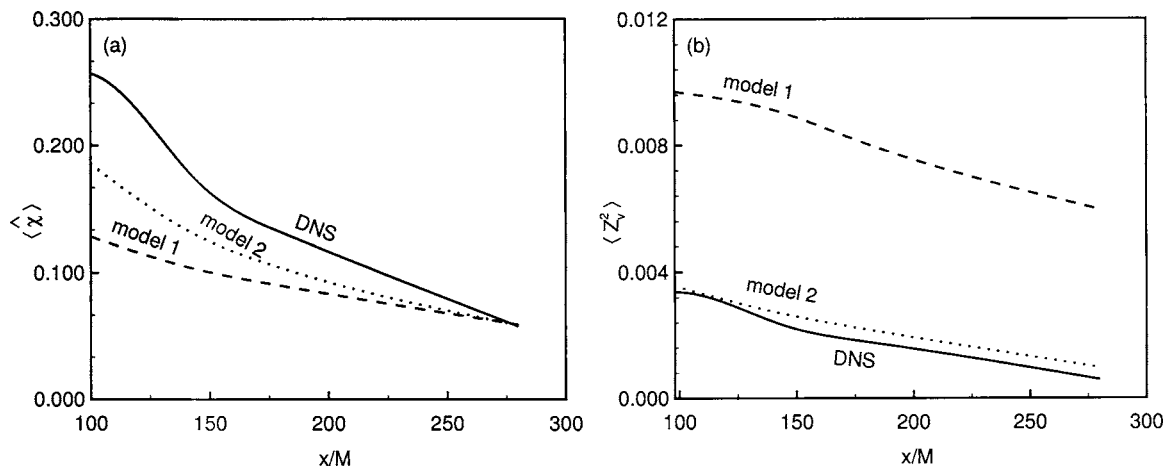
Fig. 3 Filtered dissipation rate and SGS variance versus downstream distance in grid turbulence. The solid lines are from the DNS results obtained with 512^3 grid points; the dashed lines are from LES results from 64^3 simulations of the same flow.

Outlook for the Future

Large-eddy simulation can now confidently be applied to non-premixed problems where continuously-burning, moderate to fast chemistry (moderate to high Damköhler numbers) or equilibrium chemistry can be assumed. Quasi-steady, mixture-fraction-based methods require little additional computational overhead beyond nonreacting LES in this regard. For simulating slower reactions, e.g., for free radicals and for cases with extinction, and cases with reignition, a number of potentially useful methods have been developed. Some employ unsteady versions of the flamelet or CMC equations (e.g., Pitsch and Steiner [47], Bushe and Steiner [49]), while others include the addition of a progress variable to treat partial premixing (e.g., Pierce and Moin [54], Vervisch et al. [55], Koutmos and Mavridis [60]). Monte Carlo methods, based on either a filtered density function equation (Colucci et al. [1], Jaberi et al. [2], Gicquel et al. [3], James and Jaberi [4]) or the mechanistic modeling of turbulent advection and mixing (Menon and Calhoon [5]) have been developed and with considerable potential. The Monte Carlo methods are potentially applicable to a broader range of situations, e.g., slower chemistry and both non-premixed as well as premixed reactions; however, there is considerable additional computational overhead in the Monte Carlo method, and some controversy over the mixing models employed.

Subgrid-scale modeling of premixed and partially-premixed reactions is in several ways more difficult, mainly due to the treatment of the flame itself. Whereas in nonpremixed reactions the quantities of interest are continuous through the flame, in premixed reactions the flame represents an approximate discontinuity in relevant quantities; furthermore the flame can be subject to several instabilities. Even given these difficulties, however, much progress has been made and methods are available to perform LES for these reactions.

Acknowledgment

References

[1] Colucci, P. J., Jaberi, F. A., Givi, P., and Pope, S. B., 1998, "Filtered Density Function for Large Eddy Simulation of Turbulent Reacting Flows," Phys. Fluids, **10**(2), pp. 499–515.
[2] Jaberi, F. A., Colucci, P. J., James, S., Givi, P., and Pope, S. B., 1999, "Filtered Mass Density Function for Large-Eddy Simulation of Turbulent Reacting Flows," J. Fluid Mech., **401**, pp. 85–121.
[3] Gicquel, L. Y. M., Givi, P., Jaberi, F. A., and Pope, S. B., 2002, "Velocity Filtered Density Function for Large Eddy Simulation of Turbulent Flows," Phys. Fluids, **14**(3), pp. 1196–1213.
[4] James, S., and Jaberi, F. A., 2000, "Large Scale Simulations of Two-Dimensional Nonpremixed Methane Jet Flames," Combust. Flame, **123**(4), pp. 465–487.
[5] Menon, S., and Calhoon, W. H., Jr., 1996, "Subgrid Mixing and Molecular Transport Modeling in a Reacting Shear Layer," Proc. Combust. Inst., **26**, pp. 59–66.
[6] DesJardin, P. E., and Frankel, S. H., 1998, "Large Eddy Simulation of a Nonpremixed Reacting Jet: Application and Assessment of Subgrid-Scale Combustion Models," Phys. Fluids, **10**(9), pp. 2298–2314.
[7] Colin, O., Ducros, F., Veynante, D., and Poinsot, T., 2000, "A Thickened Flame Model for Large-Eddy Simulations of Turbulent Premixed Combustion," Phys. Fluids, **12**(7), pp. 1843–1863.
[8] Boger, M., Veynante, D., Boughanem, H., and Trouvé, A., 1998, "Direct Numerical Simulation Analysis of Flame Surface Density Concept for Large Eddy Simulation of Turbulent Premixed Combustion," Proc. Combust. Inst., **27**, pp. 917–924.
[9] Chakravarthy, V. K., and Menon, S., 2001, "Large-Eddy Simulation of Turbulent Premixed Flames in the Flamelet Regime," Combust. Sci. Technol., **162**, pp. 175.
[10] Peters, N., 2000, *Turbulent Combustion*, Cambridge University Press, Cambridge.
[11] Fureby, C., 2000, "Large Eddy Simulation of Combustion Instabilities in a Jet Engine Afterburner," Combust. Sci. Technol., **161**, pp. 213–243.
[12] Knikker, R., Veynante, D., and Meneveau, C., 2002, "A Priori Texting of a Similarity Model for Large Eddy Simulations of Turbulent Premixed Combustion," Proc. Combust. Inst., **29**, pp. 2105–2111 (Part 2).
[13] Smagorinsky, J., 1963, "General Circulation Experiments With the Primitive Equations. 1. The Basic Experiment," Mon. Weather Rev., **91**, pp. 99–164.
[14] Lilly, D. K., 1967, "The Representation of Small-Scale Turbulence in Numerical Simulation Experiments," in *Proceedings of the IBM Scientific Computing Symposium on Environmental Science*, IBM Form No. 320-1951, pp. 195–210.
[15] Deardorff, J. W., 1970, "A Numerical Study of Three-Dimensional Turbulent Channel Flow at Large Reynolds Numbers," J. Fluid Mech., **41**(2), pp. 453–480.
[16] Germano, M., Piomelli, U., Moin, P., and Cabot, W. H., 1991, "A Dynamic Subgrid-Scale Eddy Viscosity Model," Phys. Fluids A, **3**(7), pp. 1760–1765.
[17] de Bruyn Kops, S. M., Riley, J. J., and Kosály, G., 2001, "Direct Numerical Simulation of Reacting Scalar Mixing Layer," Phys. Fluids, **13**(5), pp. 1450–1465.
[18] Cook, A. W., and Riley, J. J., 1998, "Subgrid-Scale Modeling for Turbulent Reacting Flows," Combust. Flame, **112**(4), pp. 593–606.
[19] Kerstein, A. R., 1990, "Linear-Eddy Modeling of Turbulent Transport. 3. Mixing and Differential Molecular-Diffusion in Round Jets," J. Fluid Mech., **216**, pp. 411–435.
[20] Nilsen, V., and Kosaly, G., 1997, "Differentially Diffusing Scalars in Turbulence," Phys. Fluids, **9**(11), pp. 3385–3397.

[21] Nilsen, V., 1998, Ph.D. thesis, University of Washington.
[22] Pitsch, H., 1998, Ph.D. dissertation, RWTH Aachen.
[23] Bilger, R. W., 1980, "Turbulent Flows With Nonpremixed Reactants," in *Turbulent Reacting Flows*, Libby, P. A., and Williams, F. A., eds., Springer-Verlag, Berlin, pp. 65–114.
[24] Gao, F., and O'Brien, E. E., 1993, "A Large-Eddy Simulation Scheme for Turbulent Reacting Flows," Phys. Fluids A, **5**(6), pp. 1282–1284.
[25] Pope, S. B., 2000, *Turbulent Flows*, Cambridge University Press, Cambridge.
[26] Frankel, S. H., Adumitroaie, V., Madnia, C. K., and Givi, P., 1993, in *Engineering Applications of Large Eddy Simulations*, ASME, NY, p. 81.
[27] Cook, A. W., and Riley, J. J., 1994, "A Subgrid Model for Equilibrium Chemistry in Turbulent Flows," Phys. Fluids, **6**(8), pp. 2868–2870.
[28] Mell, W. E., Nilsen, V., Kosály, G., and Riley, J. J., 1994, "Investigation of Closure Models for Nonpremixed Turbulent Reacting Flows," Phys. Fluids, **6**(3), pp. 1331–1356.
[29] Bish, E. S., and Dahm, W. J. A., 1995, "Strained Dissipation and Reaction Layer Analyses of Nonequilibrium Chemistry in Turbulent Reacting Flows," Combust. Flame, **100**(3), pp. 457–464.
[30] Wall, C., Boersma, B. J., and Moin, P., 2000, "An Evaluation of the Assumed β Probability Density Function Subgrid-Scale Model for Large Eddy Simulation of Nonpremixed, Turbulent Combustion With Heat Release," Phys. Fluids, **12**(10), pp. 2522–2529.
[31] Jiménez, J., Liñan, A., Rogers, M. M., and Higuera, F. J., 1997, "A Priori Testing of Subgrid Models for Chemically Reacting Nonpremixed Turbulent Shear Flows," J. Fluid Mech., **349**, pp. 149–171.
[32] Reveillon, J., and Vervisch, L., 1996, "Response of the Dynamic LES Model to Heat Release Induced Effects," Phys. Fluids, **8**(8), pp. 2248–2250.
[33] Branley, N., and Jones, W. P., 1997, "Large Eddy Simulation of a Turbulent Non-Premixed Flame," in *Proceedings of the 11th Symposium on Turbomolecule Shear Flows*, pp. 4.1–4.6, Grenoble.
[34] Branley, N., and Jones, W. P., 2001, "Large Eddy Simulation of a Turbulent NonPremixed Flame," Combust. Flame, **127**(1-2), pp. 1914–1934.
[35] Forkel, H., and Janicka, J., 2000, "Large-Eddy Simulation of a Turbulent Hydrogen Diffusion Flame," Flow, Turbul. Combust., **65**(2), pp. 163–175.
[36] Pierce, C. D., and Moin, P., 1998, "Large-Eddy Simulation of a Confined, Coaxial Jet With Swirl and Heat Release," AIAA paper 98–2892.
[37] Mellado, J. P., Sarkar, S., and Pantano, C., 2003, "Reconstruction Subgrid Models for Nonpremixed Combustion," Phys. Fluids, **15**(11), pp. 3280–3307.
[38] Peters, N., 1984, "Laminar Diffusion Flamelet Models in Non-Premixed Turbulent Combustion," Prog. Energy Combust. Sci., **10**(3), pp. 319–339.
[39] Bilger, R. W., 1988, "The Structure of Turbulent Premixed Flames," Proc. Combust. Inst., **22**, p. 475–466.
[40] Cook, A. W., Riley, J. J., and Kosály, G., 1997, "A Laminar Flamelet Approach to Subgrid-Scale Chemistry in Turbulent Flows," Combust. Flame, **109**(3), pp. 332–341.
[41] de Bruyn Kops, S. M., Riley, J. J., Kosály, G., and Cook, A. W., 1998, "Investigation of Modeling for Non-Premixed Turbulent Combustion," Flow, Turbul. Combust., **60**(1), pp. 105–122.
[42] de Bruyn Kops, S. M., and Riley, J. J., 2003, "Large-Eddy Simulation of a Reacting Scalar Mixing Layer With Arrhenius Chemistry," Comput. Math. Appl., **46**(4), pp. 547–569.
[43] Swaminathan, N., and Bilger, R. W., 1997, "Direct Numerical Simulation of Turbulent Nonpremixed Hydrocarbon Reaction Zones Using a Two-Step Reduced Mechanism," Combust. Sci. Technol., **127**(1-6), pp. 167–196.
[44] de Bruyn Kops, S. M., and Riley, J. J., 1998, "Direct Numerical Simulation of Laboratory Experiments in Isotropic Turbulence," Phys. Fluids, **10**(9), pp. 2125–2127.
[45] de Bruyn Kops, S. M., and Riley, J. J., 2000, "Re-Examining the Thermal Mixing Layer With Numerical Simulations," Phys. Fluids, **12**(1), pp. 185–192.
[46] de Bruyn Kops, S. M., and Riley, J. J., 2001, "Mixing Models for Large-Eddy Simulation of Nonpremixed Turbulent Combustion," ASME J. Fluids Eng., **123**(2), pp. 341–346.
[47] Pitsch, H., and Steiner, H., 2000, "Large-Eddy Simulation of a Turbulent Piloted Methane/Air Diffusion Flame," Phys. Fluids, **12**(10), pp. 2541–2554.
[48] Girimaji, S. S., and Zhou, Y., 1996, "Analysis and Modeling of Subgrid Scalar Mixing Using Numerical Data," Phys. Fluids, **8**(5), pp. 1224–1236.
[49] Bushe, W. K., and Steiner, H., 1999, "Conditional Moment Closure for Large Eddy Simulation of Nonpremixed Turbulent Reacting Flows," Phys. Fluids, **11**(7), pp. 1896–1906.
[50] Steiner, H., and Bushe, W. K., 2001, "Large Eddy Simulation of a Turbulent Reacting Jet With Conditional Source-Term Estimation," Phys. Fluids, **13**(3), pp. 754–769.
[51] Bilger, R. W., 1993, "Conditional Moment Closure for Turbulent Reacting Flows," Phys. Fluids A, **5**(2), pp. 436–444.
[52] Klimenko, A. Yu., 1990, "Multicomponent Diffusion of Various Scalars in Turbulent Flow," Fluid Dyn., **25**, pp. 327–334.
[53] Klimenko, A. Yu., 2001, "On the Relationship Between the Conditional Moment Closure and Unsteady Flamelets," Combust. Theory Modell., **5**(3), pp. 275–294.
[54] Pierce, C. D., and Moin, P., 2004, "Progress-Variable Approach for Large-Eddy Simulation of Non-Premixed Turbulent Combustion," J. Fluid Mech., **504**, pp. 73–97.
[55] Vervisch, L., Hauguel, R., Domingo, P., and Rullaud, M., 2004, "Three Facets of Turbulent Combustion Modelling: DNS of Premixed V-Flame, LES of Lifted Nonpremixed Flame, and RANS of Jet-Flame," J. Turbul., **5**, Art. No. 004.
[56] Mitarai, S., Kosály, G., and Riley, J. J., 2004, "A New Lagrangian Flamelet Model for Local Flame Extinction and Reignition," Combust. Flame, **137**(3), pp. 306–319.
[57] Yoshizawa, A., 1986, "Statistical Theory for Compressible Turbulent Shear Flows, With the Application to Subgrid Modeling," Phys. Fluids, **29**(7), pp. 2152–2164.
[58] Mathey, F., and Chollet, J. P., 1996, "Subgrid Model of Scalar Mixing for Large-Eddy Simulation of Turbulent Flows," *Proceedings of the Second ER-COFTAC Workshop on Direct and Large Eddy Simulations*, Grenoble.
[59] Cook, A. W., 1997, "Determination of the Constant Coefficient in Scale Similarity Models of Turbulence," Phys. Fluids, **9**(5), pp. 1485–1487.
[60] Koutmos, P., and Mavridis, C., 2000, "A Study of Partial Extinction and Reignition Effects in Turbulent Nonpremixed Jet Flames of CH_4 and CO/H_2N_2 With a Two-Scalar Reactedness-Mixture Fraction Presumed PDF Model," Combust. Sci. Technol., **154**, pp. 31–55.

Modeling the Wall Pressure Spectrum in Turbulent Pipe Flows

Peter D. Lysak
Applied Research Laboratory,
Pennsylvania State University,
P.O. Box 30,
State College, PA 16804

An important source of vibration and noise in piping systems is the fluctuating wall pressure produced by the turbulent boundary layer. One approach to calculating the wall pressure fluctuations is to use a stochastic model based on the Poisson pressure equation. If the model is developed in the wave-number domain, the solution to the wave-number-frequency spectrum can be expressed as an integral of the turbulent sources over the boundary layer thickness. Models based on this formulation have been reported in the literature which show good agreement with measured pressure spectra, but they have relied on adjustable "tuning" constants to account for the unknown properties of the turbulent velocity fluctuations. A variation on this approach is presented in this paper, in which only well-known "universal" constants are used to model the turbulent velocity spectrum. The resulting pressure spectrum predictions are shown to be in good agreement with canonical data sets over a wide range of Reynolds numbers.
[DOI: 10.1115/1.2170125]

1 Introduction

Piping systems are subject to flow-induced vibration and noise through the pressure fluctuations resulting from the turbulent boundary layers. Most of the energy in the wall pressure spectrum is contained in wave numbers that convect at speeds comparable to the mean flow, however these wave numbers generally do not produce significant net unsteady forces or noise directly. Rather, the structural excitation and noise generation is produced either by the scattering of the wall pressure at structural discontinuities, or by the excitation from subconvective wave numbers which have wavelengths on the order of the structural and acoustic wavelengths. It is the first of these mechanisms, the scattering of the convective wavelengths, to which the modeling presented in this paper applies. The formulation will be directed toward the prediction of the point frequency spectrum and its cross-stream spatial correlation.

There is a large body of literature concerning the measurement and prediction of the wall pressure point spectrum (see the review by Bull [1] for a survey). Recently, Smol'yakov [2] developed a model which predicts the shape and level of the pressure spectrum accurately over a wide range of Reynolds numbers. However, his model, like other previous models, relied on the use of adjustable constants which were selected to provide the best fit to the available data. The constants were introduced as part of the modeling of the source term of the pressure fluctuations, i.e., the turbulent velocity fluctuations in the boundary layer. An alternative approach is to use an existing model, not designed specifically for the wall pressure sources, to represent the turbulent velocity spectrum. For example, Lysak and Brungart [3] have shown that the von Kármán model can provide accurate predictions of the velocity spectrum given a single point description of the turbulence.

In this paper, a model for the wall pressure spectrum is developed using the von Kármán velocity spectrum to model the source terms. There are no new empirical constants introduced in the formulation; the only numerical constants employed are well-established values used to quantify the boundary layer profile of fully developed pipe flow and the turbulent energy spectrum. Comparisons of the predicted point frequency spectrum with existing data sets show that the model is accurate over a wide range

of Reynolds numbers, particularly at higher frequencies and Reynolds numbers. In addition, the model formulation is extended to predict the transverse spectral correlation length, which is also shown to be in good agreement with existing empirical results.

2 Formulation of the Model

The wall pressure fluctuations underneath a turbulent boundary layer can be described by a stochastic model based on the Poisson pressure equation. Kraichnan [4], followed by Panton and Linebarger [5], Blake [6], and Smol'yakov [2], developed a spectral solution to the Poisson equation in the wave-number domain for pressure sources produced by the interaction of the turbulence with the mean shear. The model presented here follows the spectral approach, and is developed first in terms of the wave-number-frequency spectrum of the wall pressure. From this general result, the point frequency spectrum and its correlation functions can be derived. The final form of the model is expressed as an integral of the turbulent sources over the boundary layer thickness. The turbulent sources are modeled using the von Kármán velocity spectrum, which does not appear to have been used in previous wall pressure modeling.

2.1 Poisson Equation for a Turbulent Shear Flow. The pressure fluctuations in an incompressible flow are governed by a Poisson equation which can be derived from the Navier-Stokes equations and Reynolds decomposition

$$\nabla^2 p = -\rho \frac{\partial^2}{\partial x_i \partial x_j}(2U_i u_j + u_i u_j - \overline{u_i u_j}) \quad (1)$$

The source term consists of contributions from the mean-shear-turbulence interaction and turbulence-turbulence interactions. Direct numerical simulation data for low Reynolds number channel flows [7,8] indicate that both effects may have the same order of magnitude, however the model will be formulated based on the traditional assumption that the turbulence-turbulence terms are negligible in a shear flow. Also, only the streamwise (x_1) component of the mean velocity is significant, and this only varies in the x_2 direction, so the mean-shear-turbulence term becomes

$$\frac{\partial^2}{\partial x_i \partial x_j}(2U_i u_j) = 2\frac{\partial}{\partial x_1}\left(\frac{dU_1}{dx_2}u_2 + U_1\frac{\partial u_j}{\partial x_j}\right) \quad (2)$$

Then, using the continuity equation for the fluctuating velocity, $\partial u_j/\partial x_j=0$, the fluctuating pressure equation reduces to

$$\nabla^2 p = -2\rho \frac{dU_1}{dx_2}\frac{\partial u_2}{\partial x_1} \tag{3}$$

2.2 Spectral Solution of the Poisson Equation. The solution to the Poisson Eq. (3) can be expressed as a volume integral of the source term times a Green's function. Denoting the source term as $q(\mathbf{x},t)$, the solution for free space is given by

$$p(\mathbf{x},t) = \int\int_{-\infty}^{\infty}\int \frac{q(\xi,t)}{4\pi|\mathbf{x}-\xi|}d^3\xi \tag{4}$$

The wall boundary condition $\partial p/\partial x_2 = 0$ can be handled using the method of images. It is assumed that the dominant sources are located close enough to the wall that it can be treated as a flat surface. Then, on the wall the image sources effectively double the pressure, so the wall pressure becomes

$$p_w(x_1,x_3,t) = \int_0^{\infty}\left(\int\int_{-\infty}^{\infty}\frac{q(\xi_1,\xi_2,\xi_3,t)d\xi_1 d\xi_3}{2\pi\sqrt{(x_1-\xi_1)^2+\xi_2^2+(x_3-\xi_3)^2}}\right)d\xi_2 \tag{5}$$

This is the general result used to calculate the instantaneous wall pressure fluctuations for a given source field.

For a stochastic source term such as that produced by turbulent flow, a statistical description of the wall pressure is desired rather than the instantaneous pressure. The wall pressure is typically characterized by a wave-number-frequency spectrum, or equivalently by a point frequency spectrum with streamwise and transverse spectral correlation lengths. In order to derive a model of the wave-number-frequency spectrum, the space-time Fourier transform of the wall pressure is taken,

$$\hat{p}_w(k_1,k_3,\omega) = \frac{1}{(2\pi)^3}\int\int_{-\infty}^{\infty}\int p_w(x_1,x_3,t)e^{-i(k_1x_1+k_3x_3)}e^{-i\omega t}dx_1 dx_3 dt \tag{6}$$

Substituting Eq. (5) into Eq. (6) yields an expression with six integrals, which can be simplified by changing the order of integration so the integration over the x_1-x_3 plane is performed first. Then, using the formula

$$\int\int_{-\infty}^{\infty}\frac{e^{-i(k_1x_1+k_3x_3)}dx_1 dx_3}{2\pi\sqrt{(x_1-\xi_1)^2+\xi_2^2+(x_3-\xi_3)^2}} = \frac{e^{-k\xi_2}}{k}e^{-i(k_1\xi_1+k_3\xi_3)} \tag{7}$$

where $k = \sqrt{k_1^2+k_3^2}$, the Fourier transform of the wall pressure becomes

$$\hat{p}_w(k_1,k_3,\omega) = \int_0^{\infty}\frac{e^{-k\xi_2}}{k}\left[\frac{1}{(2\pi)^3}\int\int_{-\infty}^{\infty}\int q(\xi_1,\xi_2,\xi_3,t)e^{-i(k_1\xi_1+k_3\xi_3)}\right.$$
$$\left.\times e^{-i\omega t}d\xi_1 d\xi_3 dt\right]d\xi_2 \tag{8}$$

Rewriting the result in terms of the Fourier transform of source, and changing variables from ξ_2 to x_2, this reduces to

$$\hat{p}_w(k_1,k_3,\omega) = \int_0^{\infty}\frac{e^{-kx_2}}{k}\hat{q}(k_1,x_2,k_3,\omega)dx_2 \tag{9}$$

The exponential factor shows that the influence of the sources decays with increasing distance from the wall.

The wave-number-frequency spectrum of the wall pressure is defined in terms of the space-time Fourier transform by

$$P(k_1,k_3,\omega) = \frac{E[\hat{p}_w(k_1,k_3,\omega)\hat{p}_w^*(k_1',k_3',\omega')]}{\delta(k_1-k_1')\delta(k_3-k_3')\delta(\omega-\omega')} \tag{10}$$

where E is the expected value operator, δ is the Dirac delta function, and * represents the complex conjugate. It is also useful to define a function representing the correlation between the wave-number-frequency spectra of source layers separated in the wall-normal direction by distance r_2

$$Q(k_1,x_2|r_2,k_3,\omega) = \frac{E[\hat{q}(k_1,x_2,k_3,\omega)\hat{q}^*(k_1',x_2+r_2,k_3',\omega')]}{\delta(k_1-k_1')\delta(k_3-k_3')\delta(\omega-\omega')} \tag{11}$$

Then, substituting Eq. (9) into Eq. (10), letting $x_2'=x_2+r_2$ in the factor $\hat{p}_\omega^*$, changing the order of the integration and the expected value operator, and using Eq. (11) yields

$$P(k_1,k_3,\omega) = \int_0^{\infty}\frac{e^{-2kx_2}}{k}\left(\int_{-x_2}^{\infty}\frac{e^{-kr_2}}{k}Q(k_1,x_2|r_2,k_3,\omega)dr_2\right)dx_2 \tag{12}$$

If it is assumed that Q rapidly decorrelates with increasing r_2, then the limits of integration can be extended from $-\infty$ to ∞ and the exponential decay can be approximated using $e^{-kr_2} \approx 1-kr_2$. With the additional assumption that Q is symmetric about r_2, the $-kr_2$ term cancels upon integration, leaving

$$P(k_1,k_3,\omega) \approx \int_0^{\infty}\frac{e^{-2kx_2}}{k^2}\left(\int_{-\infty}^{\infty}Q(k_1,x_2|r_2,k_3,\omega)dr_2\right)dx_2 \tag{13}$$

It is anticipated that this result will be reasonably accurate even when the symmetry assumption is not strictly valid. A further simplification can be made by expressing the inner integral in terms of the three-dimensional wave-number-frequency spectrum of the source. First, note that the 3D wave-number-frequency spectrum of the source layer at x_2 can be obtained by taking the Fourier transform of Q with respect to r_2

$$\Phi_{qq}(k_1,x_2|k_2,k_3,\omega) = \frac{1}{2\pi}\int_{-\infty}^{\infty}Q(k_1,x_2|r_2,k_3,\omega)e^{-ik_2r_2}dr_2 \tag{14}$$

Then, letting $k_2=0$ shows that the wall pressure wave-number-frequency spectrum can be formulated as

$$P(k_1,k_3,\omega) \approx 2\pi\int_0^{\infty}\frac{e^{-2kx_2}}{k^2}\Phi_{qq}(k_1,x_2|0,k_3,\omega)dx_2 \tag{15}$$

2.3 Turbulent Velocity Model. Returning to the Poisson Eq. (3), the source term for a turbulent shear flow is

$$q = -2\rho\frac{dU_1}{dx_2}\frac{\partial u_2}{\partial x_1} \tag{16}$$

Since the turbulent velocity u_2 is a stochastic variable, it can be characterized by a 3D wave-number-frequency spectrum for each layer above the wall. However, in the turbulence literature, the velocity fluctuations are usually represented by the velocity spectrum tensor $\Phi_{ij}(\mathbf{k})$. The velocity spectrum depends only on the instantaneous velocity field and therefore accounts for only the spatial correlations of the fluctuating velocity, not the temporal correlation. Assuming frozen convection of the turbulence at each position above wall, with local velocity $U_1(x_2)$, the wave-number-frequency spectrum of u_2 becomes

$$\Phi_{22}(k_1,x_2|k_2,k_3)\delta[\omega - U_1(x_2)k_1] \qquad (17)$$

Then, using the differentiation property of the Fourier transform, the wave-number-frequency spectrum of $\partial u_2 / \partial x_1$ is given by

$$k_1^2\Phi_{22}(k_1,x_2|k_2,k_3)\delta[\omega - U_1(x_2)k_1] \qquad (18)$$

Using this result, the wave-number-frequency spectrum of the source equals

$$\Phi_{qq}(k_1,x_2|k_2,k_3,\omega) = 4\rho^2\left(\frac{dU_1}{dx_2}\right)^2 k_1^2\Phi_{22}(k_1,x_2|k_2,k_3)\delta[\omega - U_1(x_2)k_1] \qquad (19)$$

Substituting Eq. (19) into Eq. (15), and dropping the explicit x_2 dependence for clarity, the wall pressure wave-number-frequency spectrum becomes

$$P(k_1,k_3,\omega) \approx 8\pi\rho^2\int_0^\infty\left(\frac{dU_1}{dx_2}\right)^2\Phi_{22}(k_1,0,k_3)\frac{k_1^2}{k^2}$$
$$\times e^{-2kx_2}\delta(\omega - U_1 k_1)dx_2 \qquad (20)$$

This allows the wall pressure spectrum to be computed given the profile of the mean velocity and the turbulent velocity spectrum across the boundary layer.

A model for the velocity spectrum was developed by von Kármán [9]

$$\Phi_{22}(k_1,k_2,k_3) \approx \frac{3}{8\pi}\frac{v^2}{k_e^3}\frac{(k_1/k_e)^2 + (k_3/k_e)^2}{[1 + (k_1/k_e)^2 + (k_2/k_e)^2 + (k_3/k_e)^2]^{17/6}} \qquad (21)$$

where v is the root mean square of the turbulent velocity and k_e represents the wave number of the energy-containing eddies. Although the model was developed for isotropic, homogeneous turbulence, it has been found to be useful in other situations [3]. It is proposed here that the model will provide an accurate representation of the source term for the wall pressure fluctuations provided that v represents the wall-normal component of the turbulent velocity. Also, in order to satisfy the wall boundary condition $\partial p / \partial x_2 = 0$, v should go to zero at the wall.

2.4 Point Frequency Spectrum and Spectral Correlation Lengths. As mentioned earlier, another way to characterize the wall pressure fluctuations is through a point frequency spectrum along with streamwise and transverse spectral correlation lengths. This representation does not add any new information over the wave-number-frequency spectrum, but it is usually easier to interpret since it involves quantities that can be experimentally measured. The point pressure frequency spectrum can be obtained by integrating the wave-number-frequency spectrum over all streamwise and spanwise wave-numbers,

$$\Phi_{pp}(\omega) = \int\!\!\!\int_{-\infty}^\infty P(k_1,k_3,\omega)dk_1 dk_3 \qquad (22)$$

Note that an additional integration over all frequencies returns the mean square pressure

$$\overline{p^2} = \int_{-\infty}^\infty \Phi_{pp}(\omega)d\omega \qquad (23)$$

The calculation of the point frequency spectrum eliminates all the information about the spatial correlation of the pressure. To recover this information, the wave-number integration can be replaced by an inverse Fourier transform, which yields the spatial correlation of the pressure spectrum

$$\Gamma_{pp}(r_1,r_3,\omega) = \int\!\!\!\int_{-\infty}^\infty P(k_1,k_3,\omega)e^{i(k_1 r_1 + k_3 r_3)}dk_1 dk_3 \qquad (24)$$

Often it is only the integrated effect of the spatial correlation function that is of interest. In this case, spectral correlation lengths can be defined,

$$\Lambda_1(\omega) = \frac{\int_0^\infty \Gamma_{pp}(r_1,0,\omega)dr_1}{\Phi_{pp}(\omega)} \qquad (25)$$

and

$$\Lambda_3(\omega) = \frac{\int_0^\infty \Gamma_{pp}(0,r_3,\omega)dr_3}{\Phi_{pp}(\omega)} \qquad (26)$$

where Λ_1 and Λ_3 are the streamwise and transverse spectral correlation lengths, respectively.

The spectral correlation lengths can also be expressed directly in terms of P. Considering Λ_1, the numerator in Eq. (25) can be expanded as

$$\int_0^\infty \Gamma_{pp}(r_1,0,\omega)dr_1 = \frac{1}{2}\int\!\!\!\int_{-\infty}^\infty\!\!\int P(k_1,k_3,\omega)e^{ik_1 r_1}dk_1 dk_3 dr_1 \qquad (27)$$

Then, integrating over r_1 first and noting that

$$\int_{-\infty}^\infty e^{ik_1 r_1}dr_1 = 2\pi\delta(k_1) \qquad (28)$$

the spectral correlation lengths become

$$\Lambda_1(\omega) = \frac{\pi\int_{-\infty}^\infty P(0,k_3,\omega)dk_3}{\Phi_{pp}(\omega)} \qquad (29)$$

and

$$\Lambda_3(\omega) = \frac{\pi\int_{-\infty}^\infty P(k_1,0,\omega)dk_1}{\Phi_{pp}(\omega)} \qquad (30)$$

Finally, explicit formulas for the evaluation of the wall pressure point frequency spectrum and spectral correlation lengths can be derived. Substituting Eq. (21) into Eq. (20) yields

$$P(k_1,k_3,\omega) \approx 3\rho^2\int_0^\infty\left(\frac{dU_1}{dx_2}\right)^2\frac{v^2}{k_e^5}\frac{k_1^2\exp[-2x_2\sqrt{k_1^2 + k_3^2}]}{[1 + (k_1/k_e)^2 + (k_3/k_e)^2]^{17/6}}$$
$$\times\delta(\omega - U_1 k_1)dx_2 \qquad (31)$$

Then, using Eq. (22), and noting that for any function $f(k)$

$$\int_{-\infty}^\infty f(k)\delta(\omega - Uk)dk = \frac{1}{U}f(\omega/U) \qquad (32)$$

the point pressure frequency spectrum becomes

$$\Phi_{pp}(\omega) \approx 3\rho^2\int_0^\infty\left(\frac{dU_1}{dx_2}\right)^2\frac{v^2\omega^2}{U_1^3 k_e^4}I\left(\frac{\omega}{U_1 k_e},k_e x_2\right)dx_2 \qquad (33)$$

where the function

$$I(\xi,\alpha) = \int_{-\infty}^\infty\frac{\exp[-2\alpha\sqrt{\xi^2 + \zeta^2}]}{(1 + \xi^2 + \zeta^2)^{17/6}}d\zeta \qquad (34)$$

is evaluated numerically.

The spectral correlation lengths are evaluated using Eqs. (29) and (30). The streamwise correlation length becomes

$$\Lambda_1 = 0 \tag{35}$$

which is an artifact of the von Kármán model combined with the assumption of frozen convection for each turbulent source layer. In order to make a prediction of Λ_1, the model would need to be modified to include information about the streamwise decay of the turbulence. However, the transverse correlation length can be evaluated using

$$2\Phi_{pp}(\omega)\Lambda_3(\omega) \approx 6\pi\rho^2 \int_0^\infty \left(\frac{dU_1}{dx_2}\right)^2 \frac{v^2\omega^2}{U_1^3 k_e^5} \frac{\exp(-2\omega x_2/U_1)}{[1+(\omega/U_1 k_e)^2]^{17/6}} dx_2 \tag{36}$$

and dividing by $2\Phi_{pp}$. Interestingly, evaluation of the product $2\Phi_{pp}\Lambda_3$, which is important in problems involving the acoustic scattering of the wall pressure at surface discontinuities [10], avoids the necessity of numerically computing the function I.

3 Evaluation of the Boundary Layer Profile

In order to use Eqs. (33) and (36) to determine the frequency spectrum and transverse correlation length of the wall pressure, the profiles of the mean velocity and the turbulence properties must be specified as a function of distance from the wall. In the wall layer of a turbulent boundary layer, these profiles are well-described by universal functions which use fundamental quantities such as the friction velocity and kinematic viscosity as parameters. The outer region of the boundary layer depends on the nature of the flow and the external pressure gradient. For a fully developed pipe flow, the profile of the core region can be approximated by extending the wall layer to the pipe centerline, and modifying the mixing length based on the pipe diameter.

3.1 Mean Velocity. The wall layer consists of a near-wall viscous sublayer and an outer inertial sublayer (also called the logarithmic layer). In the viscous sublayer the viscosity of the fluid is dominant while in the inertial sublayer the mixing action of the turbulence is more important. The shear stress in the wall layer is constant, so the mean velocity is governed by the differential equation

$$(\nu + \nu_t)\frac{dU}{dy} = U_\tau^2 \tag{37}$$

where ν is the kinematic viscosity of the fluid, ν_t is the effective turbulent viscosity, and U_τ is the friction velocity. The turbulent viscosity can be expressed in terms of a mixing length L

$$\nu_t = L^2\frac{dU}{dy} \tag{38}$$

A good model for the mixing length profile is [11]

$$L(y) = \kappa y\left[1 - \exp\left(-\frac{1}{\kappa_w}\frac{U_\tau y}{\nu}\right)\right] \tag{39}$$

where $\kappa \approx 0.4$ is the well-known von Kármán constant and $\kappa_w \approx 25$ is the van Driest damping constant.

Substituting Eq. (38) into Eq. (37) yields

$$L^2\left(\frac{dU}{dy}\right)^2 + \nu\frac{dU}{dy} - U_\tau^2 = 0 \tag{40}$$

This is a quadratic equation which can be solved for the velocity gradient
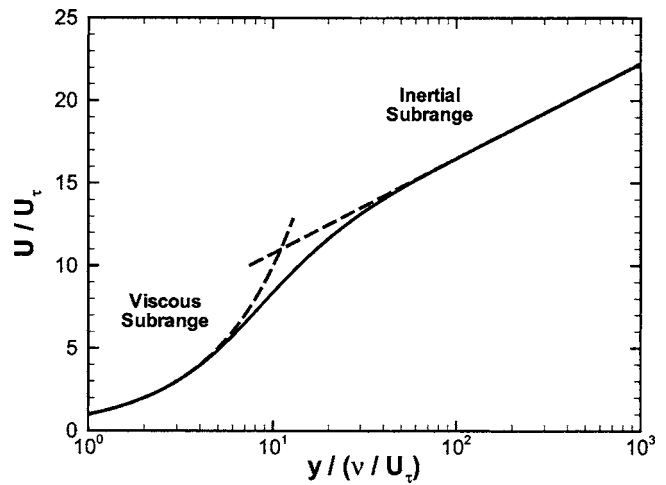
Fig. 1 Mean velocity profile in the wall layer

$$\frac{dU}{dy} = \frac{-\nu + \sqrt{\nu^2 + 4L^2 U_\tau^2}}{2L^2} \tag{41}$$

The mean velocity profile can then be obtained by numerically integrating the velocity gradient

$$U(y) = \int_0^y \frac{dU}{dy}(\eta)d\eta \tag{42}$$

As $y \to 0$, this reduces to the viscous sublayer approximation

$$\frac{U(y)}{U_\tau} \to \frac{U_\tau y}{\nu} \tag{43}$$

and for large y the velocity follows the well-known logarithmic profile of the inertial sublayer

$$\frac{U(y)}{U_\tau} \to \frac{1}{\kappa}\ln\left(\frac{U_\tau y}{\nu}\right) + B \tag{44}$$

where $B \approx 5$. Figure 1 shows the mean velocity profile computed by numerical integration along with the viscous and inertial sublayer asymptotes. For a pipe flow, the wall layer profile is a reasonable approximation all the way to the pipe centerline. This assumption will be more accurate at high Reynolds numbers, where the spatial extent of the inertial sublayer is greater.

3.2 Turbulence. The characteristic velocity and length scale of the turbulence can be obtained from the turbulent viscosity and mixing length. Referring to Eqs. (20) and (21), it is the wall-normal component of the fluctuating velocity that affects the wall pressure. In the wall layer, the rms value of the wall-normal velocity is related to the Reynolds stress [12]

$$v \approx |\overline{uv}|^{1/2} \tag{45}$$

Then, using the turbulent viscosity model

$$\overline{uv} = -\nu_t\frac{dU}{dy} \tag{46}$$

along with Eq. (38), the turbulent velocity profile becomes

$$v(y) = L\frac{dU}{dy} \tag{47}$$

The turbulent velocity is plotted in Fig. 2. It goes to zero at the wall and approaches the friction velocity in the inertial sublayer. For a pipe flow, the turbulent velocity then remains approximately constant through the core region [13]. This behavior is different from an external boundary layer flow, where the turbulent velocity

Fig. 2 Profile of the rms wall-normal velocity

Fig. 3 Mixing length at three different Reynolds numbers $U_\tau D/\nu$ and inertial sublayer asymptote $L = \kappa y$

decays to zero in the outer region.

As discussed in Ref. [3], the characteristic wave number of the energy-containing eddies is related to the turbulent kinetic energy k and dissipation rate ε

$$k_e = 1.9 \frac{\varepsilon}{k^{3/2}} \tag{48}$$

In order to relate this to the mixing length, the k-ε representation of the turbulent viscosity is used

$$\nu_t = C_\mu \frac{k^2}{\varepsilon} \tag{49}$$

where $C_\mu = 0.09$. Then, using Eq. (38) and solving for L yields

$$L = \sqrt{C_\mu \frac{k^2/\varepsilon}{dU/dy}} \tag{50}$$

The velocity gradient can be eliminated from this result by noting that the dissipation rate balances the turbulence production,

$$\varepsilon = C_\mu \frac{k^2}{\varepsilon} \left(\frac{dU}{dy} \right)^2 \tag{51}$$

which gives

$$\frac{dU}{dy} = C_\mu^{-1/2} \frac{\varepsilon}{k} \tag{52}$$

Substituting this result into Eq. (50) allows the mixing length to be expressed in terms of k and ε,

$$L = C_\mu^{3/4} \frac{k^{3/2}}{\varepsilon} \tag{53}$$

Finally, comparison of this result with Eq. (48) shows that

$$k_e(y) = 1.9 \frac{C_\mu^{3/4}}{L} \approx \frac{0.31}{L} \tag{54}$$

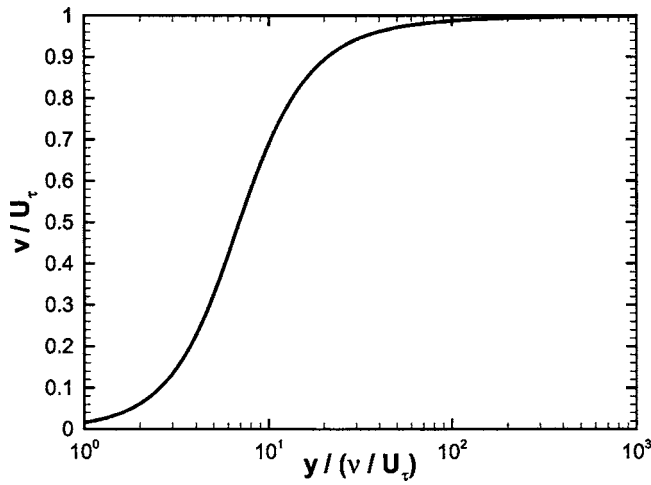**3.3 Mixing Length in the Core Region.** The mixing length given in Eq. (39) grows as κy through the inertial sublayer. In the core region of a pipe flow, the mixing length will be bounded by the size of the pipe. A model for the mixing length valid in the core region is [11]

$$L_0(\eta) = \frac{\kappa_0 D}{2} [1 - 2(1 - \eta)^2 + (1 - \eta)^4] + \frac{\kappa D}{4} (1 - \eta)^2 [1 - (1 - \eta)^2] \tag{55}$$

where $\kappa_0 = 0.14$, $\eta = 2y/D$, and D is the diameter of the pipe. As $y \to 0$, the model reduces to the inertial sublayer profile $L = \kappa y$. For the purpose of computing k_e, the mixing length for the entire boundary layer profile can be expressed by modifying Eq. (39) to be

$$L(y) = L_0 \left(\frac{2y}{D} \right) \left[1 - \exp \left(-\frac{1}{\kappa_w} \frac{U_\tau y}{\nu} \right) \right] \tag{56}$$

Figure 3 shows the mixing length profiles for three different non-dimensional pipe diameters, or Reynolds numbers $U_\tau D/\nu$. The range for each curve extends from the viscous sublayer to the pipe centerline. The extent of the inertial subrange increases with increasing Reynolds number, as does the maximum value of the mixing length.

4 Results

In this section, the results of the model will be presented and compared to experimental data. The wall pressure spectrum and transverse correlation length are calculated using Eqs. (33) and (36), along with the boundary layer profiles given in the previous section. The two parameters ν and k_e characterize the velocity spectrum Φ_{22} at each layer above the wall. Along with the mean velocity gradient, the velocity spectrum constitutes the source term for the wall pressure fluctuations. The empirical constants used to determine the source term are well-established, "universal" constants used in turbulence modeling, and are not specifically tailored for the wall pressure spectrum.

4.1 Frequency Spectrum. Figure 4 shows the calculated point spectra at three different Reynolds numbers $U_\tau D/\nu$. The spectra are normalized using the wall variables U_τ and ν. Also, in order to compare to experimental data, the pressure spectra are shown as one-sided spectra and as a function of cyclic frequency instead of radian frequency. The one-sided spectrum can be calculated from $\Phi_{pp}(\omega)$ using

$$G_{pp}(f) = 4\pi \Phi_{pp}(2\pi f) \tag{57}$$

Note that G_{pp} is defined so that $\overline{p^2} = \int_0^\infty G_{pp}(f) df$.

At higher frequencies, the normalized spectrum is independent of Reynolds number. This universal range consists of a viscous subrange and an inertial subrange. In the viscous subrange, the
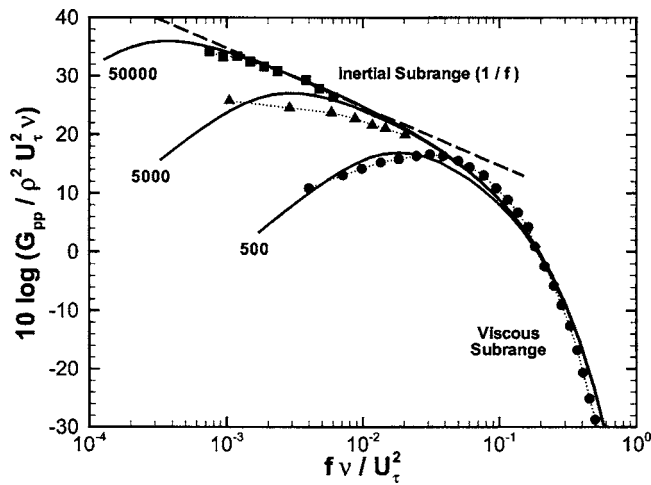
Fig. 4 Point pressure frequency spectra calculated at three different Reynolds numbers $U_\tau D/\nu$, with corresponding experimental data (circles: Lauchle and Daniels [15]; triangles: Bakewell et al. [16]; squares: Carey et al. [17])

Fig. 5 Transverse spectral correlation length calculated at three different Reynolds numbers $U_\tau D/\nu$, along with Corcos empirical model [21,22]

spectrum decays exponentially. The turbulent sources contributing to the viscous subrange are located in the near-wall viscous sublayer, where the small turbulent length scales produce high-frequency pressure fluctuations. The inertial subrange results from sources in the inertial sublayer of the turbulent boundary layer. The frequency extent of the inertial subrange increases with Reynolds number, corresponding to an increased thickness of the inertial sublayer. The turbulent length scales in the inertial sublayer increase linearly with distance from the wall. The spectrum is predicted to roll off at a rate of $1/f$, which is consistent with earlier theoretical modeling by Chase [14].

The peak value of the pressure spectrum depends on Reynolds number when normalized by wall variables. For the lower frequencies, the turbulent sources are located mainly in the core region, where the length scales depend on the pipe diameter. Therefore the magnitude and frequency of the maximum value will depend primarily on the pipe diameter and the bulk velocity. For frequencies below the peak, the spectrum is predicted to rise as f^2 due to the ω^2 factor in Eq. (33). At very low frequencies, the model assumptions of incompressible flow and plane wall geometry are not valid.

In order to validate the model, comparisons were made with existing experimental data from pipe flows. Shown in Fig. 4 are data from Lauchle and Daniels [15], Bakewell et al. [16], and Carey et al. [17]. The latter two datasets have been tabulated and corrected for sensor area by Keith et al. [18]. The wide range of Reynolds numbers represented by these data sets is in part due to the use of different fluids. Lauchle's measurements ($U_\tau D/\nu \approx 570$) were made in glycerin, which permitted very high frequency measurements to be made without spatial averaging effects from the finite transducer size. Bakewell's measurements ($U_\tau D/\nu \approx 10,000$) were in air while Carey's measurements ($U_\tau D/\nu \approx 46,000$) were in water. For these data, the high frequency information has been lost due to spatial averaging by the sensor. The Corcos correction method [19] used by Keith et al. provides an approximation to recover some of the high frequency data, but only data where the correction factor is less than 3 dB have been shown in the plot. In general, measurements of the pressure spectrum over a large frequency range are difficult due to background noise contamination at low frequencies and sensor spatial averaging at high frequencies.

The agreement of the calculated spectra with the experimental data is quite good. In particular, the viscous subrange data from Lauchle's measurements overlays almost perfectly with the
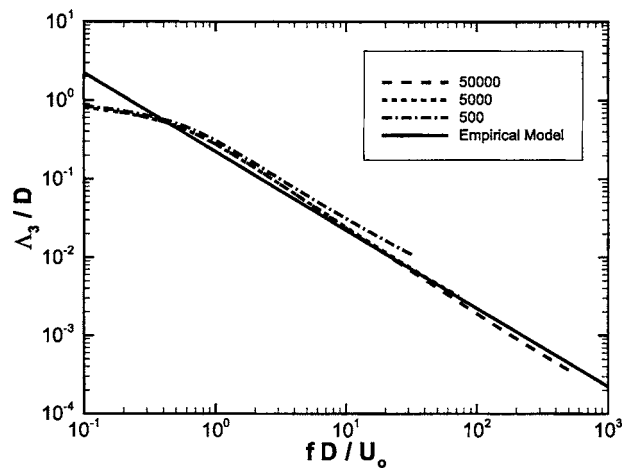
model, and the model appears to be an excellent representation of the inertial subrange data from all three data sets. There is somewhat more variability in the comparisons in the low frequency range, especially with Bakewell's data, where the comparison is best with the model at a lower Reynolds number (5000) than the data (10,000). However, the correct trend is clearly captured by the model, and the predicted peaks of the spectra appears to be accurate. It is likely that a more accurate description of the boundary layer profile in the core region would result in even better agreement in the low frequency range.

There is a larger body of pressure spectra data for flat plate boundary layer flows than for pipe flows. Since the wall layer is independent of the outer flow, the model predictions for the viscous and inertial subranges will also apply to flat plate boundary layers. However, for the outer region, the turbulence profile is different for a flat plate boundary layer. For a pipe flow, the low frequencies are constrained mainly by the limiting effect on the mixing length by the pipe diameter. In an external boundary layer, the mixing length will not be constrained, but the turbulence will decay in the outer region. In principle, the model formulation given by Eq. (33) is equally applicable for a pipe flow or an external boundary layer, provided that the appropriate boundary layer profiles are used. However, it is possible that the relative importance of the turbulence-turbulence interaction terms, which are neglected in this model, may be greater in the outer region of a flat plate boundary layer because the mean velocity gradient becomes very small.

4.2 Transverse Correlation Length. The transverse spectral correlation length is shown in Fig. 5. Unlike the pressure spectrum, there is no viscous subrange for the correlation length. For this reason, it is more appropriate to normalize the correlation length based on the bulk velocity and the pipe diameter, which limits the maximum value. The ratio of the bulk velocity U_0 to the friction velocity can be estimated using the empirical relation [20]

$$\frac{U_0}{U_\tau} = \sqrt{8}\left[2.0\log\left(\sqrt{8}\frac{U_\tau D}{\nu}\right) - 0.8\right] \qquad (58)$$

The correlation length, normalized by U_0 and D, is predicted to be nearly independent of Reynolds number. This is in agreement with similarity hypothesis of Corcos [21]. Also shown in Fig. 5 is a widely used empirical model [22] based on Corcos' formulation

$$\Lambda_3 = 1.4 \frac{U_c}{\omega} \qquad (59)$$

where the convection velocity U_c is taken to be approximately equal to the bulk velocity U_0 for pipe flow. The model results match the empirical relation quite closely. For the low Reynolds number case, there may be a slight loss of accuracy at higher frequencies because the pressure spectrum, which is divided from Eq. (36) to obtain the correlation length, becomes extremely small in the viscous subrange, resulting in a magnification of the error introduced by the numerical integration. At low frequencies, the similarity relation U/ω is unbounded, while the model predicts the correlation length to reach a maximum value approximately equal to the pipe diameter.

5 Conclusion

A model has been presented to predict the wall pressure spectrum in a turbulent boundary layer. The model formulation is based on a spectral solution to the Poisson pressure equation for sources due to mean-shear-turbulence interaction. Modeling of the turbulent velocity spectrum is based on the von Kármán spectrum, with parameters obtained from the turbulent mixing length and Reynolds stress. Since the input to the model comes from the parameters used to describe the turbulent boundary layer, no empirical constants are used other than the well-established universal constants used in modeling the boundary layer and turbulent energy spectrum. The model is relatively simple to implement and executes quickly as it basically involves an integration of the turbulent sources over the boundary layer thickness.

Results of the model have been generated for pipe flows over a wide range of Reynolds numbers. The point pressure frequency spectrum is in excellent agreement with existing measurements and theoretical models. A universal range is predicted with a $1/f$ inertial subrange and an exponentially decaying viscous subrange. The peak of the spectrum depends on the Reynolds number since the largest length scales in the turbulence are limited by the pipe diameter.

The model formulation also includes the transverse spectral correlation length. This is predicted to be nearly Reynolds-number independent and is bounded by the pipe diameter at low frequencies. At higher frequencies, the correlation length decays as $1/f$ and is in good agreement with existing empirical results.

Nomenclature

$$
\begin{aligned}
D &= \text{pipe diameter} \\
E &= \text{expected value} \\
G_{pp} &= \text{one-sided wall pressure frequency spectrum} \\
L &= \text{mixing length} \\
L_0 &= \text{mixing length in core region} \\
P &= \text{wall pressure wave-number-frequency spectrum} \\
Q &= \text{correlation of source layer wave-number-frequency spectra} \\
\mathbf{U} &= \text{mean velocity} \\
U &= \text{mean streamwise velocity, } U=U_1 \\
U_1 &= \text{mean streamwise velocity} \\
U_0 &= \text{pipe bulk velocity} \\
U_\tau &= \text{friction velocity} \\
f &= \text{frequency} \\
\mathbf{k} &= \text{wave number} \\
k &= \text{magnitude of wave number, } k=\sqrt{k_1^2+k_3^2} \\
k &= \text{turbulent kinetic energy} \\
k_e &= \text{wave number of energy-containing eddies} \\
p &= \text{pressure fluctuation} \\
p_w &= \text{wall pressure fluctuation} \\
\hat{p}_w &= \text{space-time Fourier transform of wall pressure fluctuation}
\end{aligned}
$$

$$
\begin{aligned}
q &= \text{source term} \\
\hat{q} &= \text{Fourier transform of source term with respect to } x_1, x_3, t \\
t &= \text{time} \\
x_1 &= \text{streamwise direction} \\
x_2 &= \text{wall-normal direction} \\
x_3 &= \text{transverse direction} \\
\mathbf{u} &= \text{fluctuating velocity} \\
\upsilon &= \text{rms of wall-normal velocity} \\
y &= \text{wall-normal direction, } y=x_2 \\
\Gamma_{pp} &= \text{spatial correlation of wall pressure frequency spectrum} \\
\Lambda_1 &= \text{streamwise spectral correlation length of wall pressure} \\
\Lambda_3 &= \text{transverse spectral correlation length of wall pressure} \\
\Phi_{ij} &= \text{velocity spectrum} \\
\Phi_{pp} &= \text{wall pressure frequency spectrum} \\
\delta &= \text{Dirac delta function} \\
\varepsilon &= \text{turbulent dissipation rate} \\
\kappa &= \text{von Kármán constant} \\
\kappa_w &= \text{van Driest near-wall damping constant} \\
\rho &= \text{fluid density} \\
\nu &= \text{fluid kinematic viscosity} \\
\nu_t &= \text{turbulent eddy viscosity} \\
\omega &= \text{radian frequency}
\end{aligned}
$$

References

[1] Bull, M. K., 1996, "Wall-Pressure Fluctuations Beneath Turbulent Boundary Layers: Some Reflections on Forty Years of Research," J. Sound Vib., **190**, pp. 299–315.

[2] Smol'yakov, A. V., 2000, "Calculation of the Spectra of Pseudosound Wall-Pressure Fluctuations in Turbulent Boundary Layers," Acoust. Phys., **46**, pp. 342–347.

[3] Lysak, P. D., and Brungart, T. A., 2003, "Velocity Spectrum Model for Turbulence Ingestion Noise from Computational-Fluid-Dynamics Calculations," AIAA J., **41**, pp. 1827–1829.

[4] Kraichnan, R. H., 1956, "Pressure Fluctuations in Turbulent Flow over a Flat Plate," J. Acoust. Soc. Am., **28**, pp. 378–390.

[5] Panton, R. L., and Linebarger, J. H., 1974, "Wall Pressure Spectra Calculations for Equilibrium Boundary Layers," J. Fluid Mech., **65**, pp. 261–287.

[6] Blake, W. K., 1986, *Mechanics of Flow-Induced Sound and Vibration*, Academic Press, New York, Chap. 8.

[7] Kim, J., 1989, "On the Structure of Pressure Fluctuations in Simulated Turbulent Channel Flow," J. Fluid Mech., **205**, pp. 421–451.

[8] Chang, P. A., III, Piomell, U., and Blake, W. K., 1999, "Relationship Between Wall Pressure and Velocity-Field Sources," Phys. Fluids, **11**, pp. 3434–3448.

[9] von Kármán, T., 1948, "Progress in the Statistical Theory of Turbulence," Proc. Natl. Acad. Sci. U.S.A., **34**, pp. 530–539.

[10] Amiet, R. K., 1976, "Noise Due to Turbulent Flow Past a Trailing Edge," J. Sound Vib., **47**, pp. 387–393.

[11] Libby, P. A., 1996, *Introduction to Turbulence*, Taylor & Francis, London, Chap. 9.

[12] Mathieu, J., and Scott, J., 2000, *An Introduction to Turbulent Flow*, Cambridge University, Cambridge, England, p. 214.

[13] Laufer, J., 1952, "The Structure of Turbulence in Fully Developed Pipe Flow," National Advisory Committee for Aeronautics Report No. 1174, U.S. Government Printing Office, Washington D.C.

[14] Chase, D. M., 1980, "Modeling the Wavevector-Frequency Spectrum of Turbulent Boundary Layer Wall Pressure," J. Sound Vib., **70**, pp. 29–67.

[15] Lauchle, G. C., and Daniels, M. A., 1987, "Wall-Pressure Fluctuations in Turbulent Pipe Flow," Phys. Fluids, **30**, pp. 3019–3024.

[16] Bakewell, H. P., Jr., Carey, G. F., Libuha, J. J., Schloemer, H. H., and von Winkle, W. A., 1962, "Wall Pressure Correlations in Turbulent Pipe Flow," USL Report No. 559, 1-052-00-00, Naval Underwater Systems Center, New London, CT.

[17] Carey, G. F., Chlupsa, J. E., and Schloemer, H. H., 1967, "Acoustic Turbulent Water-Flow Tunnel," J. Acoust. Soc. Am., **41**, pp. 373–379.

[18] Keith, W. L., Hurdis, D. A., and Abraham, B. M., 1991, "A Comparison of Turbulent Boundary Layer Wall-Pressure Spectra," *ASME Flow Noise Modeling, Measurement, and Control*, NCA-11/FED-130.

[19] Corcos, G. M., 1963, "Resolution of Pressure in Turbulence," J. Acoust. Soc. Am., **35**, pp. 192–199.

[20] White, F. W., 1994, *Fluid Mechanics*, McGraw-Hill, New York, pp. 313–315.

[21] Corcos, G. M., 1964, "The Structure of the Turbulent Pressure Field in Boundary Layer Flows," J. Fluid Mech., **18**, pp. 353–378.

[22] Howe, M. S., 1998, *Acoustics of Fluid-Structure Interactions*, Cambridge University, Cambridge, England, pp. 207–209.

Three-Dimensional Flow of a Newtonian Liquid Through an Annular Space with Axially Varying Eccentricity

Eduarda P. F. de Pina

M. S. Carvalho
Associate Professor

Department of Mechanical Engineering,
Pontifícia Universidade Católica
do Rio de Janeiro (PUC-Rio),
Rua Marquês de São Vicente,
225 Gavea, 22493-900,
Rio de Janeiro, RJ, Brazil
e-mail: msc@mec.puc-rio.br

Flow in annular space occurs in drilling operation of oil and gas wells. The correct prediction of the flow of the drilling mud in the annular space between the well wall and the drill pipe is essential to determine the variation in the mud pressure within the wellbore, the frictional pressure drop, and the efficiency of the transport of the rock drill cuttings. A complete analysis of this situation is extremely complex: the inner cylinder is usually rotating, the wellbore wall will depart significantly from cylindrical, the drill pipe is eccentric, and the eccentricity varies along the well. A complete analysis of this situation would require the solution of the three-dimensional momentum equation and would be computationally expensive and complex. Models available in the literature to study this situation do consider the rotation of the inner cylinder and the non-Newtonian behavior of the drilling fluids, but assume the relative position of the inner with respect to the outer cylinders fixed, i.e., they neglect the variation of the eccentricity along the length of the well, and the flow is considered to be fully developed. This approximation leads to a two-dimensional model to determine the three components of the velocity field in a cross-section of the annulus. The model presented in this work takes into account the variation of the eccentricity along the well; a more appropriate description of the geometric configuration of directional wells. As a consequence, the velocity field varies along the well length and the resulting flow model is three-dimensional. Lubrication theory is used to simplify the governing equations into a two-dimensional differential equation that describes the pressure field. The results show the effect of the variation of the eccentricity on the friction factor, maximum and minimum axial velocity in each cross section, and the presence of azimuthal flow even when the inner cylinder is not rotating.
[DOI: 10.1115/1.2170126]

Keywords: drilling mud flow, eccentric annular space, varying eccentricity, lubrication approximation

1 Introduction

During well drilling operation the drilling mud is pumped from the surface tank through the drilling column, the bits, and then through the annular space between the drill pipe and the wall of the well. The main functions of the mud are to stabilize the well and prevent its wall from collapsing, to transport rock cuttings, to cool the drill bit, and to lubricate the drill pipe. The chemical composition of the muds and the operating conditions are chosen in order to optimize the operation.

Because of the high cost of drilling operations, it is very important to be able to predict the flow behavior through the annular space, the pressure inside the wellbore, the frictional pressure drop of the flow, and the efficiency of the transport of rock drill cutting, as discussed by Lou and Peden [1], Jensen and Sharma [2], and AbdulMajeed [3]. A complete analysis of this situation is extremely complex: the drill pipe usually rotates during operation, the well walls may depart significantly from cylindrical, the muds are colloidal systems that are typically shear thinning exhibiting apparent yield stress, the drill pipe is eccentric, and eccentricity varies along the length of the well. The flow is non-Newtonian

and three dimensional, and the solution of the differential equations that describe the conservation of mass and momentum is complex and computationally expensive.

Several analyses with different simplifications of the real situation are available in the literature. The main goal is usually to determine the frictional pressure loss as a function of flow rate and geometry of the annular space. Even the idealized models are far from simple. Escudier et al. [4] presented an overview of the evolution of the different analysis in this area. The first analysis were limited to Newtonian and non-Newtonian flow inside concentric annulus without rotation of either cylindrical surfaces. The next step was the inclusion of the inner cylinder rotation in the models. Only recently was the axial non-Newtonian flow through an eccentric annulus with inner cylinder rotation analyzed. Examples of such analyses include the work of Siginer and Bakhtiyarov [5], Fang et al. [6], Hussain and Sharif [7], and Escudier et al. [8]. In all these analyses, the flow is assumed to be fully developed and the partial differential equations that describe the velocity components as a function of the radial and azimuthal coordinates are solved numerically. However, in drilling operations, the eccentricity of the drill pipe varies along the length of the well. In some extreme cases in horizontal wells, the inner cylinder may even touch the well wall. The relative position of the inner cylinder center with respect to the outer cylinder center may vary from concentric to fully eccentric along a length of 20 m in
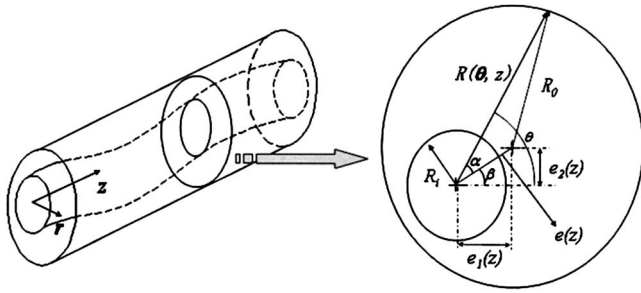

Fig. 1   Configuration of annular space with eccentricity varying along the axial direction

the axial direction. This three-dimensional effect has not yet been analyzed in the literature and may have a strong influence on the pressure drop along the annular space.

To take the variation of the eccentricity along the length of the annular space into account, the three dimensional mass and momentum conservation equations have to be solved. Because of the long length of oil wells, the computational cost to solve the problem would be extremely large. The goal of this work is to analyze this three-dimensional flow with a simplified model. Lubrication theory is used to transform the three-dimensional into a two-dimensional problem. The solution of the flow field becomes much simpler and faster when compared to the complete three-dimensional model. The limitation and accuracy of the lubrication model proposed are tested by comparing the results obtained for a constant eccentricity annulus to those presented by Escudier et al. [8] for fully developed flow in an eccentric annulus. Because the goal is to propose a simplified and accurate model to study the three-dimensional effects, the other complications inherent to this problem are neglected: The flowing liquid is Newtonian and the inner cylinder is stationary. Shear thinning effects and the rotation of the inner cylinder rotation can be included in the model, however if the rotation is above the critical value for the onset of secondary flows (Taylor instability), the lubrication theory is no longer valid.

2   Mathematical Formulation

The geometry of an annular space with the eccentricity of the inner cylinder varying along its the length is sketched in Fig. 1. The radius of the inner and outer cylinders are R_i and R_0, respectively. The coordinate system is attached to the center of the inner cylinder and the position of the center of the outer cylinder is defined through two orthogonal eccentricity functions $e_1(z)$ and $e_2(z)$. The eccentricity in each cross section is $e(z) = \sqrt{e_1^2 + e_2^2}$ and the angle between the direction of the eccentricity and the $\theta = 0$ is $\beta = \arctan(e_2/e_1)$. The radial coordinate of the outer cylinder wall $R(z, \theta)$ is a function of the radius of the inner and outer cylinders, the eccentricity, and the angle of the eccentricity direction

$$R(z, \theta) = e(z)\cos \alpha + \sqrt{R_0^2 - e^2(z)\sin^2 \alpha}$$

where $\alpha = \theta - \beta$, as indicated in Fig. 1. With this geometric description, the drilling column may have any arbitrary configuration inside the well. Without any loss of generality and to simplify the interpretation of the results presented, in this work the eccentricity in one direction was not considered, e.g., $e_2 = 0$, and consequently the center of both cylinders were located on a $z - r$ plane. In this case $\beta = 0$, and the expression for the radial position of the outer cylinder wall reduces to

$$R(z, \theta) = e_1(z)\cos \theta + \sqrt{R_0^2 - e_1^2(z)\sin^2 \theta} \qquad (1)$$

In this work, the function that describes the eccentricity along the length of the annular space $e_1(z)$ is prescribed. In a more sofisti-

cated model, it could be made a function of the dynamics of the rotation of the drill pipe and liquid interaction.

2.1   Governing Equations. The flow in the annular space between the inner and outer cylinders with varying eccentricity is three dimensional. The momentum conservation equations are

$$\rho\left\{ u\frac{\partial u}{\partial z} + v\frac{\partial u}{\partial r} + \frac{w}{r}\frac{\partial u}{\partial \theta} \right\}$$
$$= -\frac{\partial p}{\partial z} + \rho g_z + \mu\left[\frac{\partial^2 u}{\partial z^2} + \frac{1}{r}\frac{\partial}{\partial r}\left(r\frac{\partial u}{\partial r} \right) + \frac{1}{r^2}\frac{\partial^2 u}{\partial \theta^2} \right]$$

$$\rho\left\{ u\frac{\partial v}{\partial z} + v\frac{\partial v}{\partial r} + \frac{w}{r}\frac{\partial v}{\partial \theta} - \frac{w^2}{r} \right\}$$
$$= -\frac{\partial p}{\partial r} + \rho g_r + \mu\left[\frac{\partial^2 v}{\partial z^2} + \frac{\partial}{\partial r}\left(\frac{1}{r}\frac{\partial}{\partial r}(rv) \right) + \frac{1}{r^2}\frac{\partial^2 v}{\partial \theta^2} - \frac{2}{r^2}\frac{\partial w}{\partial \theta} \right]$$
$$\qquad (2)$$

$$\rho\left\{ u\frac{\partial w}{\partial z} + v\frac{\partial w}{\partial r} + \frac{w}{r}\frac{\partial w}{\partial \theta} + \frac{vw}{r} \right\}$$
$$= -\frac{1}{r}\frac{\partial p}{\partial \theta} + \rho g_\theta + \mu\left[\frac{\partial^2 w}{\partial z^2} + \frac{\partial}{\partial r}\left(\frac{1}{r}\frac{\partial}{\partial r}(rw) \right) + \frac{1}{r^2}\frac{\partial^2 w}{\partial \theta^2} + \frac{2}{r^2}\frac{\partial v}{\partial \theta} \right]$$

u, v, and w are the axial, radial, and tangential velocity components. To avoid solving the system of coupled three-dimensional differential equations, dimensional analysis is used to eliminate some of the terms of the equations. The procedure is generally known as lubrication approximation and it is summarized here.

Because the main flow is in the axial direction, the velocity component in the radial direction is much smaller than in the other two directions, i.e., $u, w \gg v$. Moreover, because the oil wells are long and the angle between the inner and outer cylinder walls along the flow direction is small, the variation of the velocity components in the axial and azimuthal directions are much smaller than in the radial direction and consequently the derivatives with respect to the radial direction are much larger than the others

$$\frac{\partial^2 u}{\partial r^2} \gg \frac{\partial^2 u}{\partial z^2}, \frac{\partial^2 u}{\partial \theta^2} \quad \text{and} \quad \frac{\partial^2 w}{\partial r^2} \gg \frac{\partial^2 w}{\partial z^2}, \frac{\partial^2 w}{\partial \theta^2}$$

If the appropriate terms of the Navier-Stokes equation are neglected based on the dimensional analysis and the pressure is modified in order to include hydrostatic effects, the system of differential equations becomes

$$0 = -\frac{\partial p}{\partial z} + \mu\left[\frac{1}{r}\frac{\partial}{\partial r}\left(r\frac{\partial u}{\partial r} \right) \right]$$

$$0 = -\frac{\partial p}{\partial r} \qquad (3)$$

$$0 = -\frac{1}{r}\frac{\partial p}{\partial \theta} + \mu\left[\frac{\partial}{\partial r}\left(\frac{1}{r}\frac{\partial}{\partial r}(rw) \right) \right]$$

The boundary conditions are of zero velocity at the outer and inner cylinder walls (the inner cylinder is stationary). It can be easily observed that in these flows, the pressure is only a function of the axial and azimuthal coordinates: $p = p(z, \theta)$.

The equations of axial and tangential momentum balance can be integrated with the appropriate boundary conditions to yield the velocity profile in the axial and tangential directions. Each velocity component varies with the axial, tangential, and radial directions, as shown in the formulas. The dependence on the axial and tangential coordinates is implicitly defined through the expression for the radial gap, Eq. (1), and the unknown pressure gradient

$$u(z,r,\theta) = \frac{R_i^2}{4\mu}\left(-\frac{\partial p}{\partial z}\right)\left[1 - \left(\frac{r}{R_i}\right)^2 + \frac{(R(z,\theta)/R_i)^2 - 1}{\ln(R(z,\theta)/R_i)}\ln\left(\frac{r}{R_i}\right)\right]$$

(4)

$$w(z,r,\theta) = \frac{R_i^2}{2\mu}\left(\frac{\partial p}{\partial \theta}\right)\left\{\frac{r}{R_i}(\ln r - 1/2) - \frac{R_i}{r}(\ln R_i - 1/2)\right.$$
$$\left. + \left(\frac{r/R_i - R_i/r}{R^2 - R_i^2}\right)[R_i^2(\ln R_i - 1/2) - R^2(\ln R - 1/2)]\right\}$$

(5)

Up to this point, the pressure field $p(z,\theta)$ is still unknown. In order to evaluate it, the integral of the continuity equation is used, as shown below

$$\int_{Ri}^{R}\left\{\frac{1}{r}\frac{\partial w}{\partial \theta} + \frac{\partial u}{\partial z}\right\}dr = 0$$

Each term of the equation can be evaluated as a function of a derivative with respect to the axial and tangential coordinates of the integral along the radial direction of the velocity profiles presented in Eqs. (4) and (5).

$$\int_{Ri}^{R}\frac{\partial u}{\partial z}dr = \frac{\partial}{\partial z}\int_{Ri}^{R}u\,dr - \underbrace{u(R_0)}_{0}\frac{\partial R}{\partial z} + \underbrace{u(R_i)}_{0}\frac{\partial R_i}{\partial z} = \frac{\partial}{\partial z}\int_{Ri}^{R}u(z,r,\theta)dr$$

$$\int_{Ri}^{R}\frac{1}{r}\frac{\partial w}{\partial \theta}dr = \int_{Ri}^{R}\frac{\partial}{\partial \theta}\left[\frac{w}{r}\right]dr = \frac{\partial}{\partial \theta}\int_{Ri}^{R}\frac{w}{r}dr - \frac{1}{r}\underbrace{w(R_0)}_{0}\frac{\partial R}{\partial z}$$
$$+ \frac{1}{r}w(R_i)\underbrace{\frac{\partial R_i}{\partial z}}_{0} = \frac{\partial}{\partial \theta}\int_{Ri}^{R}\frac{w(z,r,\theta)}{r}dr$$

Because the pressure is not a function of the radial coordinate, the pressure gradient terms in the velocity profiles (Eqs. (4) and (5)) can be removed from the integral along the radial coordinate and the integrated continuity equation may be rewritten as

$$\int_{Ri}^{R}\left\{\frac{1}{r}\frac{\partial w}{\partial \theta} + \frac{\partial u}{\partial z}\right\}dr = \frac{\partial}{\partial \theta}\left[\left(\frac{\partial p}{\partial \theta}\right)\int_{Ri}^{R}\frac{f_1(r)}{r}dr\right]$$
$$+ \frac{\partial}{\partial z}\left[\left(\frac{\partial p}{\partial z}\right)\int_{Ri}^{R}f_2(r)dr\right]$$

After evaluating the integrals of the velocity profiles, the integrated continuity equation becomes a differential equation for the pressure field

$$\frac{\partial}{\partial \theta}\left\{F_1(z,\theta)\frac{\partial p}{\partial \theta}\right\} + \frac{\partial}{\partial z}\left\{F_2(z,\theta)\frac{\partial p}{\partial z}\right\} = 0$$

(6)

Where

$$F_1(z,\theta) = \frac{R_i}{2\mu}\left\{\frac{R}{R_i}(\ln R - 3/2) - (\ln R_i - 3/2) + (\ln R_i - 1/2)(R_i/R\right.$$
$$\left. - 1) + \frac{R_i^2(\ln R_i - 1/2) - R^2(\ln R - 1/2)}{R^2 - R_i^2}(R/R_i + R_i/R - 2)\right\}$$

$$F_2(z,\theta) = \left(-\frac{R_i^2}{4\mu}\right)\left\{R - R_i - \frac{R^3 - R_i^3}{3R_i^2}\right.$$
$$\left. + \frac{(R/R_i)^2 - 1}{\ln(R/R_i)}[R_i + R(\ln(R/R_i) - 1)]\right\}$$

The dependence of F_1 and F_2 on the axial and tangential coordinates is through the definition of the radial coordinate of the outer cylinder wall R, given by Eq. (1).

The domain at which Eq. (6) is defined is $0 \leqslant z \leqslant L$ and $0 \leqslant \theta \leqslant 2\pi$, where L is the length of the annular space. The appropriate boundary conditions are fixed pressure at the inlet and outlet of the annular space and periodic conditions

$$p(z=0) = P_{\mathrm{IN}}; \quad p(z=L) = P_{\mathrm{OUT}};$$

$$p(\theta = 0) = p(\theta = 2\pi); \quad \text{and} \quad \frac{\partial p}{\partial \theta}(\theta = 0) = \frac{\partial p}{\partial \theta}(\theta = 2\pi)$$

The variables may be written in dimensionless form as

$$u^* = \frac{u}{\bar{U}}; \quad v^* = \frac{v}{\bar{U}}; \quad w^* = \frac{w}{\bar{U}}; \quad \text{and} \quad p^* = \frac{p}{\dfrac{\mu\bar{U}}{2(R_0 - R_i)}}$$

where $\bar{U}$ is the average axial velocity.

$$\bar{U} = \frac{Q}{A} = \frac{\displaystyle\int_0^{2\pi}\int_{Ri}^{R}u(z=0,r,\theta)r\,dr\,d\theta}{\pi(R^2 - R_i^2)}$$
$$= \frac{1}{\pi(R^2 - R_i^2)}\int_0^{2\pi}\bar{u}(z=0,\theta)d\theta$$

(7)

$\bar{u}(z,\theta)$ is the integral of the axial velocity profile in the radial coordinate

$$\bar{u}(z,\theta) = \frac{R_i^2}{4\mu}\left(-\frac{\partial p}{\partial z}\right)\left\{\frac{R^2 - R_i^2}{2} - \frac{R^4 - R_i^4}{4R_i^2}\right.$$
$$\left. + \frac{\left(\dfrac{R}{R_i}\right)^2 - 1}{4\ln\left(\dfrac{R}{R_i}\right)}\left[R^2\left(2\ln\left(\frac{R}{R_i}\right) - 1\right) + R_i^2\right]\right\}$$

The relevant dimensionless parameters are

- Reynolds Number: $\mathrm{Re} = [\rho\bar{U}2(R_0 - R_i)]/\mu$
- Friction Factor: $f = \Delta p/L\ (R_0 - R_i)/\rho\bar{U}^2$
- Radius ratio: $\kappa = R_i/R_0$
- Eccentricity parameter: $\varepsilon = e^*/(R_0 - R_i)$; where e^* is a characteristic eccentricity
- Dimensionless length: $\Gamma = L/R_0$

3 Solution Method

The differential Eq. (6) was solved by the finite difference method (central difference). A rectangular grid with equally spaced NZ nodes along the axial direction and $N\theta$ nodes along the azimuthal direction was used to discretize the domain, as indicated in Fig. 2. The functions F_1 and F_2 were evaluated at each node position in order to calculate the appropriate derivatives. The resulting algebraic equation for each node (i,j) relates the pressure there $P_{(i,j)}$ with its four neighbors.

$$P_{(i,j)}\left\{-\frac{1}{2\Delta\theta^2}(2F_{1(i,j)} + F_{1(i+1,j)} + F_{1(i-1,j)}) - \frac{1}{2\Delta z^2}(2F_{2(i,j)}\right.$$
$$\left. + F_{2(i,j+1)} + F_{2(i,j-1)})\right\} + P_{(i,j+1)}\left\{\frac{1}{2\Delta z^2}(F_{2(i,j)} + F_{2(i,j+1)})\right\}$$
$$+ P_{(i,j-1)}\left\{\frac{1}{2\Delta z^2}(F_{2(i,j)} + F_{2(i,j-1)})\right\} + P_{(i+1,j)}\left\{\frac{1}{2\Delta\theta^2}(F_{1(i,j)}\right.$$
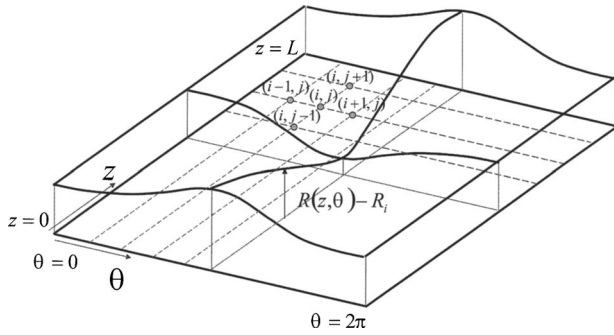
Fig. 2 Domain where the pressure equation is solved. The height of the flow channel varies with the axial and azimuthal coordinates.

$$+ F_{1(i+1,j)} \bigg\} + P_{(i-1,j)} \left\{ \frac{1}{2\Delta\theta^2} (F_{1(i,j)} + F_{1(i-1,j)}) \right\} = 0$$

The resulting system of linear algebraic equation is sparse. The matrix was stored in Compress Sparse Row Format. For the cases presented here, the number of nodes was 4100.

At an imposed pressure difference $\Delta p = P_{in} - P_{out}$ and geometric configuration of the annular space, the pressure field is determined. With the pressure field, the velocity field can be evaluated from Eqs. (4) and (5), and the average axial velocity $\bar{U}$, from Eq. (7). The Reynolds number and friction factor of the flow are then evaluated.

4 Results

4.1 Constant Eccentricity. In order to determine the accuracy of the lubrication approximation, the flow through an eccentric annular space with constant eccentricity along the axial direction was analyzed. In this case, the pressure field can be calculated analytically

$$p(z,\theta) = P_{in} - \frac{z}{L}(P_{in} - P_{out}) \Rightarrow \frac{\partial p}{\partial z} = \frac{P_{out} - P_{in}}{L}; \quad \frac{\partial p}{\partial \theta} = 0$$

The integral of the axial velocity profile in the radial direction $\bar{u}$ is only a function of the tangential coordinate, and the dependence is
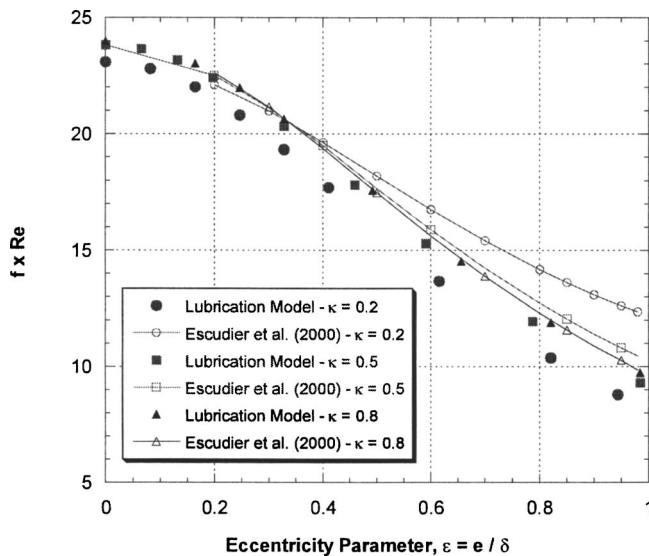
Fig. 3 $f \times \mathrm{Re}$ as a function of eccentricity parameter at $\kappa=0.2$, $\kappa=0.5$, and $\kappa=0.8$ predicted by the lubrication model and the two-dimensional solution presented by Escudier et al. [8]

Fig. 4 Axial velocity $u/\bar{U}$ at eccentricity $\varepsilon = e/(R-R_i)=0$, $\varepsilon =0.33$, and $\varepsilon=0.98$. The radius ratio is $k=0.5$.

defined through the definition of the position of the outer roll $R(\theta)$. The axial average velocity $\bar{U}$ can be evaluated by an integral of $\bar{u}(\theta)$ along the θ coordinate, and the product of the friction factor and Reynolds number $f \times \mathrm{Re}$ is easily calculated. It is presented as a function of the eccentricity in Fig. 3 at $\kappa=0.2$,

Fig. 6 Maximum velocity $u_{max}/\bar{U}$ as a function of the eccentricity parameter

At the higher radius ratio $\kappa=0.8$, the agreement is excellent over the entire range of eccentricity, the relative difference between the prediction of both models is less than 1%. At intermediate values of radius ratio, e.g., $\kappa=0.5$, the agreement is still very good over the entire range of eccentricity. The maximum discrepancy occurs at high eccentricity, and it is less than 10%. At low radius ratio, e.g., $\kappa=0.2$, the agreement is not good. As it is well known, the accuracy of the lubrication model is higher, the smaller the height of the flow channel, which in this case corresponds to the higher radius ratio. When the distance between the two cylinder surfaces is relative large (low eccentricity), the hypothesis that led to the lubrication approximations are not valid. As mentioned before, in oil wells the radius ratio is typically above $\kappa=0.5$, at which the lubrication model predictions are accurate. It is important to notice that the computational time required to evaluate the friction factor predicted by the lubrication model corresponds to the time needed to evaluate a line integral (Eq. (7)), and all the results presented in this section were obtained in less than 5 s, which is orders of magnitude smaller than that of the complete solutions presented by Escudier et al. [8].

The value of $f \times \mathrm{Re}$ falls as eccentricity rises, i.e., at a fixed pressure gradient the flow rate increases as the inner cylinder moves away from the center of the outer cylinder. The variation of the friction factor with eccentricity can be explained by analyzing the axial velocity distribution at three values of eccentricity ($\varepsilon=0$, $\varepsilon=0.33$, and $\varepsilon=0.98$), presented in Fig. 4. The predictions were at radius ratio $\kappa=0.5$. When the two cylinders are concentric, the flow is axisymmetric, as expected. The maximum velocity is
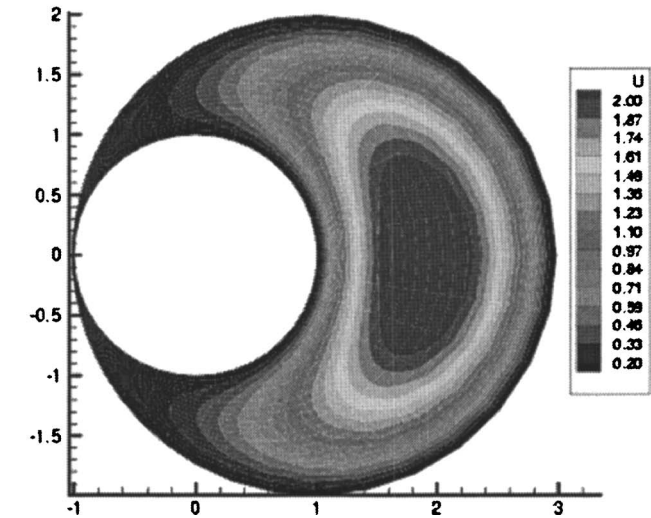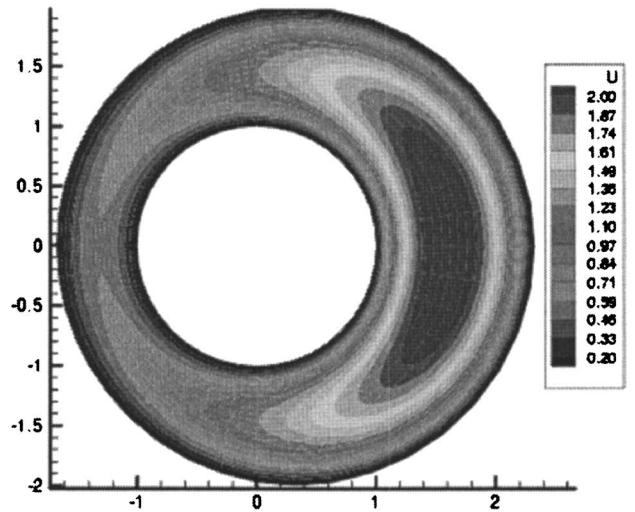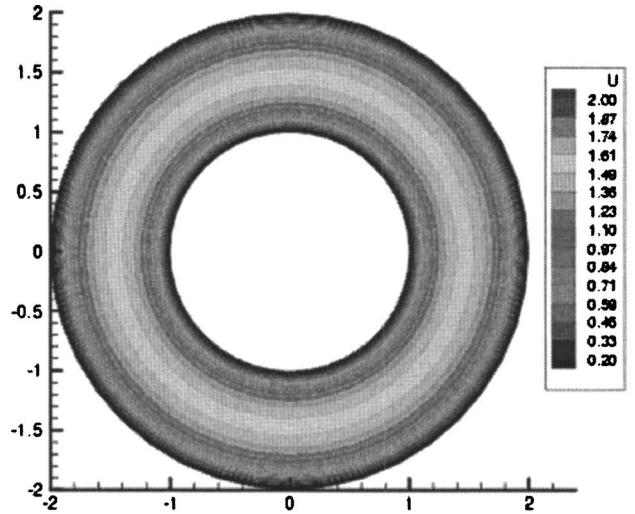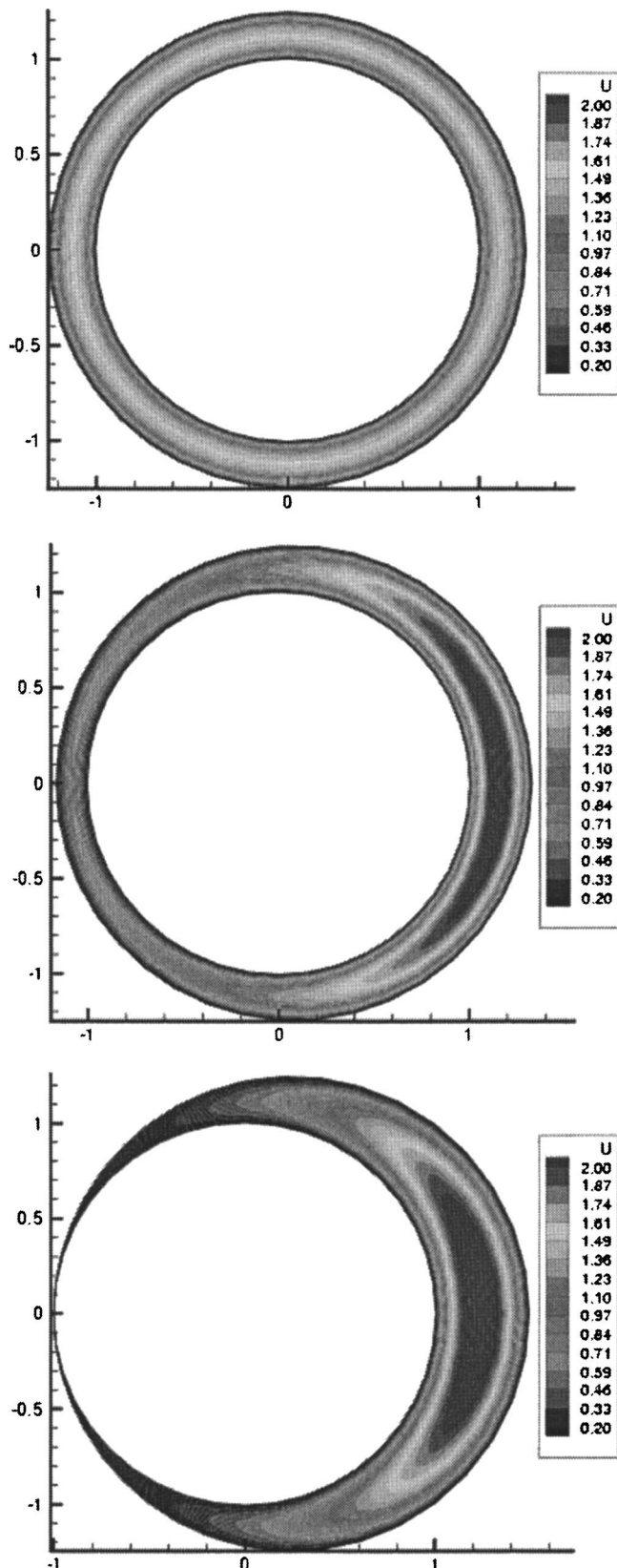

Fig. 5 Axial velocity $u/\bar{U}$ at eccentricity $\varepsilon=e/(R-R_i)=0$, $\varepsilon=0.33$, and $\varepsilon=0.98$. The radius ratio is $k=0.8$.

$\kappa=0.5$, and $\kappa=0.8$. The plot also shows the results presented by Escudier et al. [8], obtained by solving the differential equations that describe the axial component of the velocity field in a cross section of an eccentric annular space using finite volume method.
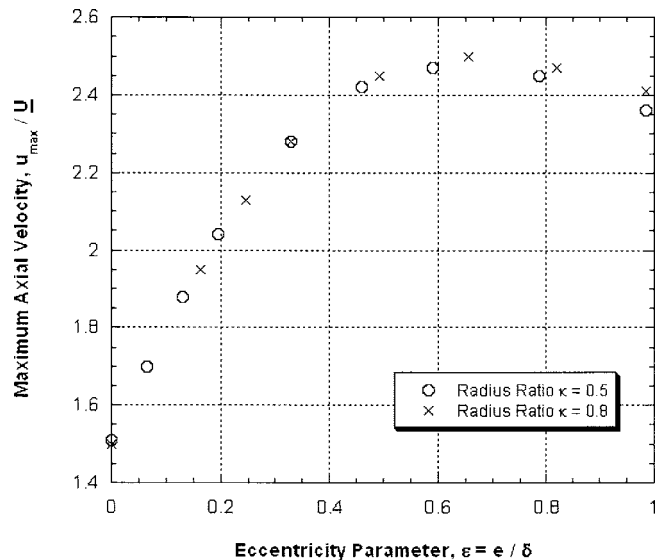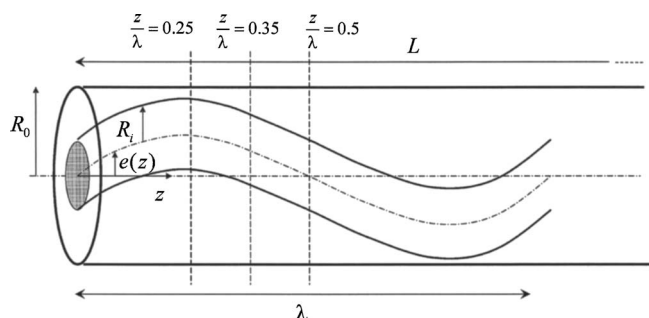

Fig. 7 Sketch of annular space with the position of the center of the inner cylinder described by a sinusoidal function

Fig. 8 (*a*) **Axial and azimuthal velocity fields. The maximum axial velocity is** $u_{max}/\bar{U} = 2.91$. (*b*) **Pressue field. The axial position is** $z/L = 0.25$, **the amplitude of the sinusoidal variation of the eccentricity is** $A/(R_0 - R_i) = 0.98$, **and the wavelength is** $\lambda/R_0 = 164$.

approximately $u_{max} \approx 1.5\bar{U}$. As the inner cylinder moves away from the center, most of the flow occurs in the region of a larger gap between the cylinder surfaces. At $\varepsilon = 0.33$, the maximum velocity is approximately $u_{max} \approx 2.28\bar{U}$, and at $\varepsilon = 0.98$, it is approximately $u_{max} \approx 2.36\bar{U}$. The axial velocity distribution presented in Fig. 4 also agrees well with those reported by Escudier et al. [8]. The behavior at higher radius ratio ($\kappa = 0.8$) is similar, as indicated in Fig. 5. The ratio of the maximum axial velocity to the average velocity as a function of eccentricity is presented in Fig. 6. At low eccentricity it is virtually independent of the radius ratio. It reaches a maximum of $u_{max} \approx 2.5\bar{U}$ at approximately $\varepsilon = 0.65$.

From these results, it is clear that the lubrication model is able to accurately describe the flow in an eccentric annular space at $\kappa > = 0.5$, at a very small computational cost.

4.2 Eccentricity Varying Along the Flow Direction. The effect of the variation of the eccentricity along the length of the well

is analyzed by studying the flow through an annular space in which the variation of the position of the inner cylinder center along the axial direction is described by a sinusoidal function, as sketched in Fig. 7.

$$e_1(z) = A \sin\left(\frac{2\pi z}{\lambda}\right)$$

λ and A are the wavelength and amplitude of the sinusoidal function that describes the eccentricity of the inner cylinder. The cases reported here were obtained at $\kappa = 0.5$, $\Gamma = L/R_0 = 164$, and different values of λ/R_0 and $A/(R_0 - R_i)$. When the amplitude of the variation vanishes, the concentric annulus situation is recovered. In this particular case, the pressure only depends on the axial coordinate and the pressure gradient on the flow direction is constant.

When the amplitude of the sinusoidal variation is different from zero, the gap between the two cylinders is a function of the axial
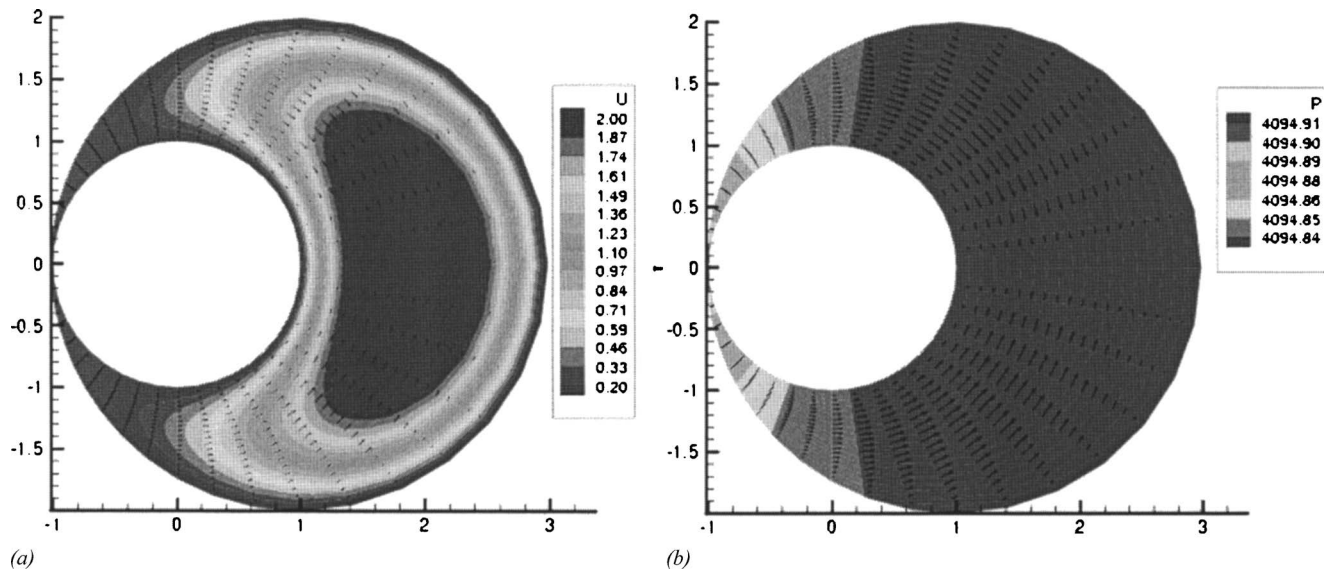

Fig. 9 (*a*) **Axial and azimuthal velocity field. The maximum axial velocity is** $u_{max}/\bar{U} = 2.89$. (*b*) **Pressue field. The axial position is** $z/L = 0.35$, **the amplitude of the sinusoidal variation of the eccentricity is** $A/(R_0 - R_i) = 0.98$, **and the wavelength is** $\lambda/R_0 = 164$.
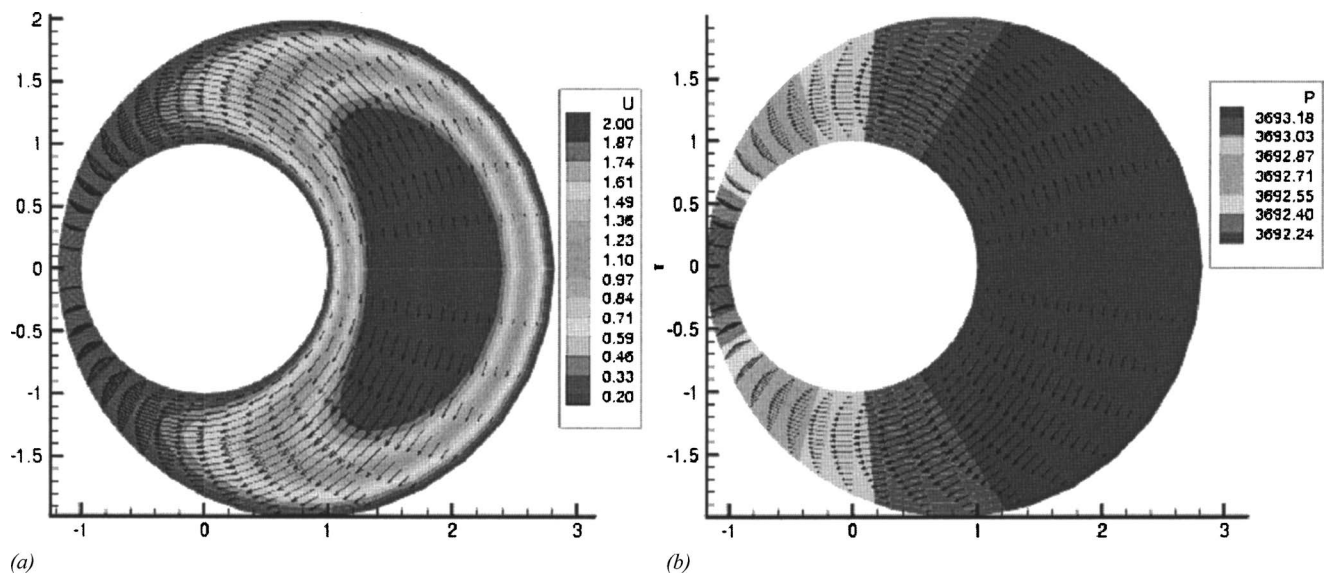
(a)　　　　　　　　　　　　　　　　　　　(b)
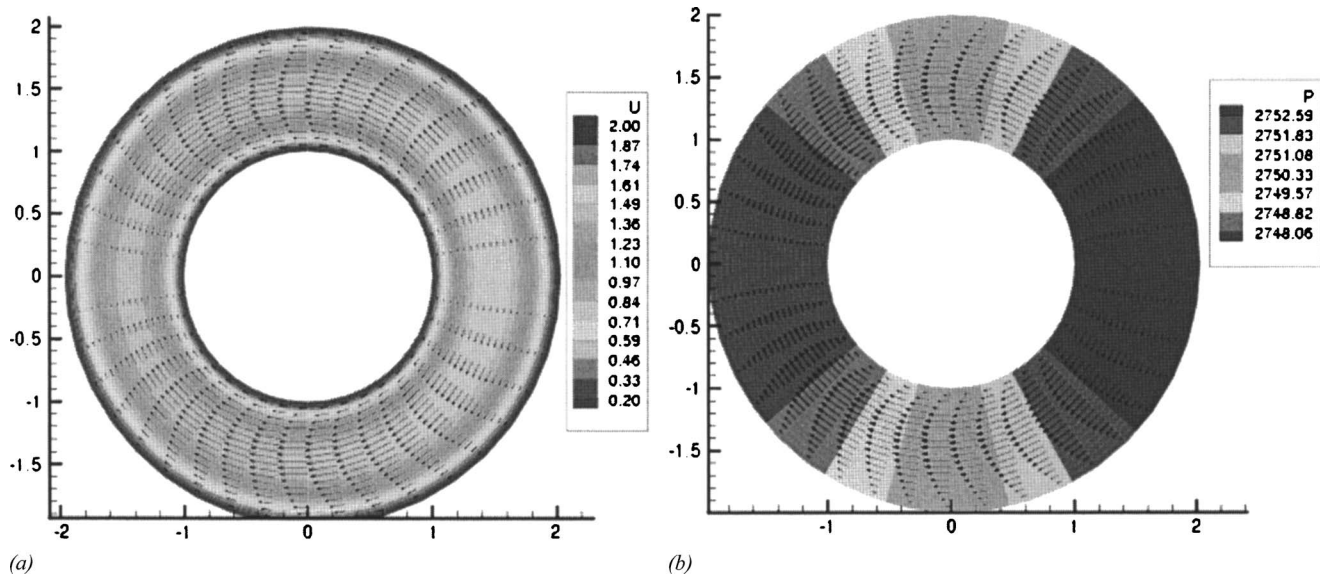
Fig. 10 (*a*) Axial and azimuthal velocity fields. The maximum axial velocity is $u_{max}/\bar{U}=1.6$. (*b*) Pressue field. The axial position is $z/L=0.5$, the amplitude of the sinusoidal variation of the eccentricity is $A/(R_0-R_i)=0.98$, and the wavelength is $\lambda/R_0=164$.

and azimuthal coordinates. The flow is not axisymmetric and there is a pressure gradient in the axial and azimuthal direction. The axial and tangential velocities at different cross sections of the annular space at $A/(R_0-R_i)=0.98$ and $\lambda/R_0=164$ ($L/\lambda=1$) are shown in Figs. 8–10. The cross sections analyzed are marked in Fig. 7. Figure 8 shows the velocity (axial and tangential) and pressure fields at $z/L=0.25$, the cross section at which the minimum distance between the two walls occurs. The local eccentricity is $\varepsilon=0.98$. The maximum axial velocities is approximately $u_{max}=2.91\times\bar{U}$, which is larger than the maximum velocity that occurs at $\varepsilon=0.98$ when the eccentricity is constant along the length of the annular space ($u_{max}=2.36\times\bar{U}$, see Fig. 4($c$)). The pressure on the narrow channel region of the cross section is larger than on the wider region, as indicated in Fig. 8(b), because

of the converging geometry on the axial direction. This pressure gradient in the azimuthal direction is enough to drive liquid from the narrow gap to the wide gap region. At $z/L=0.35$, the azimuthal flow changes direction, as shown in Fig. 9. The higher pressure in the cross section occurs in the wide gap region and drives the flow toward the narrow gap side. This occurs because, at this axial position, the wide gap region is converging and the narrow gap region is diverging in the flow direction. Although the local eccentricity at $z/L=0.5$ is zero, i.e., the cylinders are concentric, the flow is not axisymmetric, i.e., $u=u(z,\theta)$, and there is a tangential flow, as indicated in Fig. 10. Again the variation of the pressure in the cross section is due to the variation of the eccentricity along the axial direction. The maximum axial velocity is approximately $u_{max}=1.6\times\bar{U}$, whereas in a concentric annular
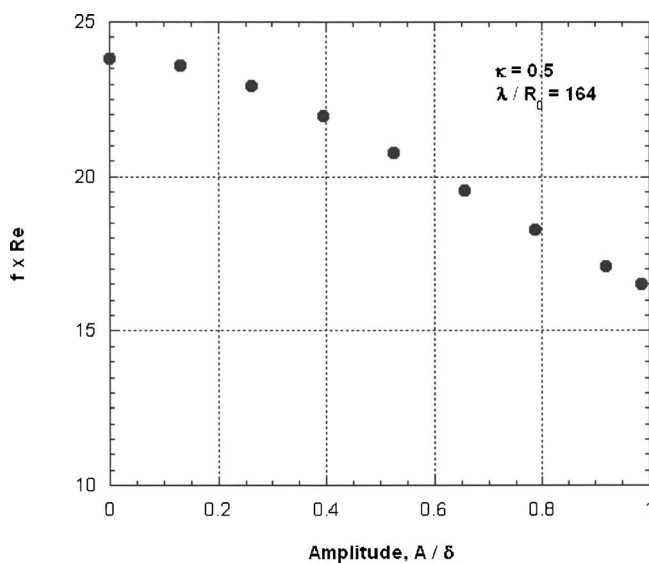
Fig. 11 Friction factor as a function of the amplitude of the sinusoidal variation of the eccentricity along the axial direction
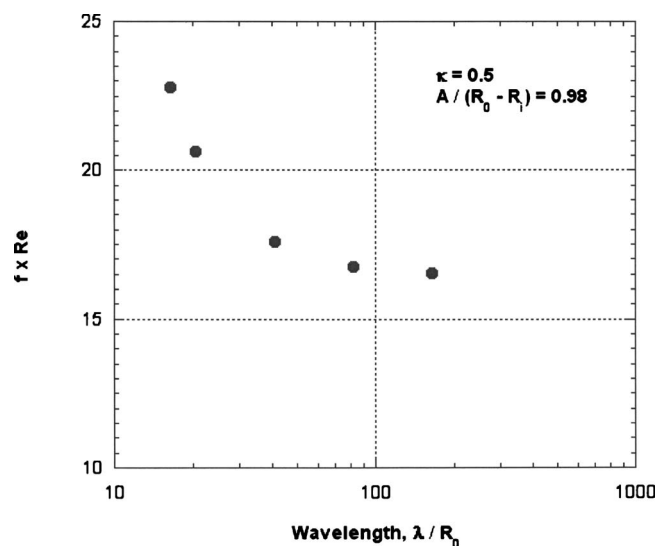
Fig. 12 Friction factor as a function of the wavelength of the sinusoidal variation of the eccentricity along the axial direction
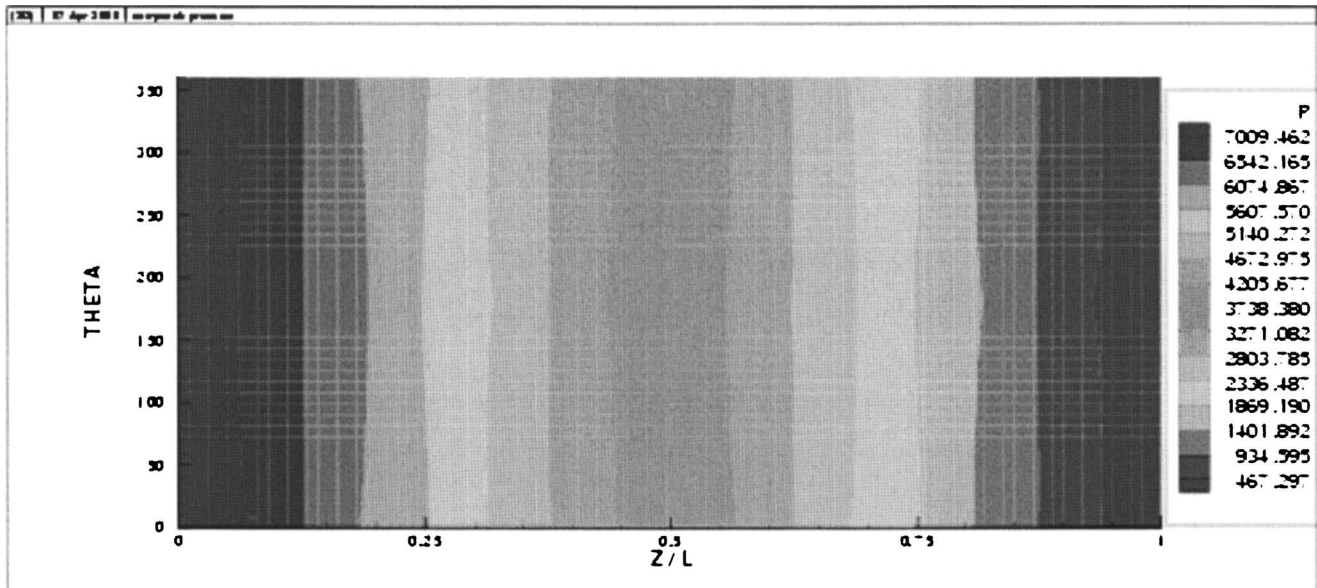
(a)
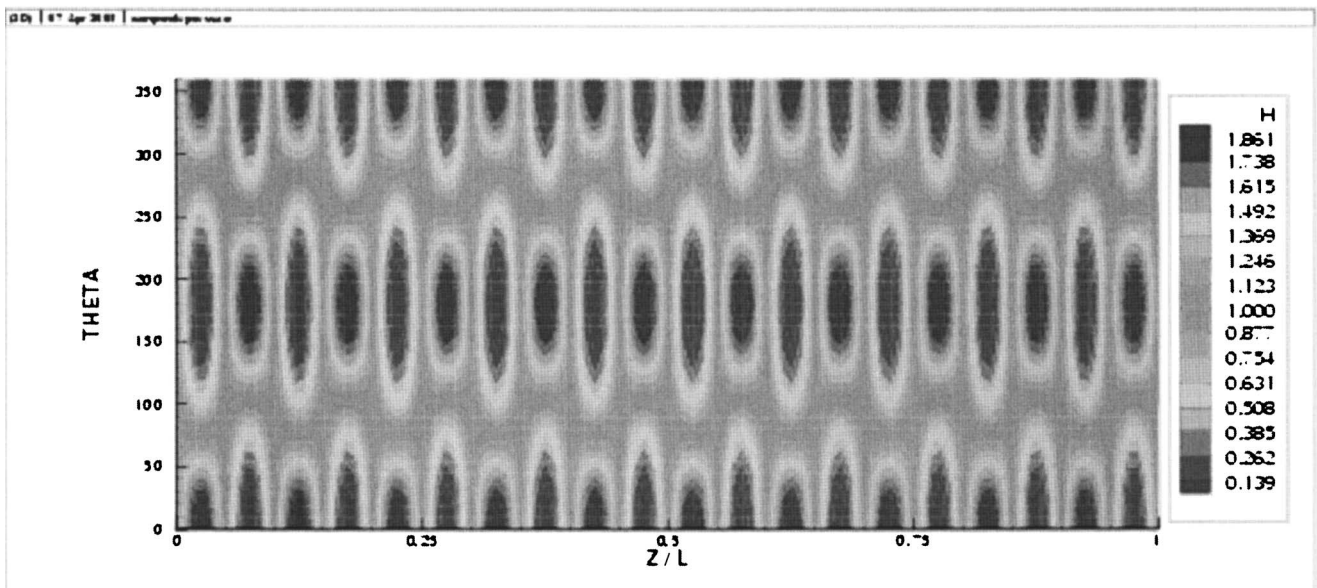
(b)

Fig. 13 Dimensionless pressure in the flow channel (*a*) and dimensionless channel height (*b*), which are a function of the axial and azimuthal coordinate

flow the maximum velocity is approximately $u_{\max} = 1.5 \times \bar{U}$.

The changes on the flow field, presented in the last figures, cause a variation on the pressure drop when compared to a constant eccentricity well. Figure 11 presents the predicted friction factor as a function of the amplitude of the sinusoidal variation of the eccentricity. It decays as the amplitude rises; the formation of wide gap regions decrease the pressure drop. The effect of the wavelength of the sinusoidal variation of the eccentricity λ on the friction factor is shown in Fig. 12. The friction factor rises as the wavelength falls. At low wavelength, the flow channel has many regions of wide and narrow gaps, as shown in Fig. 13, and the secondary azimuthal flow causes the rise on the friction factor.

5 Final Remarks

Lubrication approximation was used to simplify the three-dimensional momentum equation that describes the flow in annu-lar space with eccentricity varying along the axial direction. In the particular case of constant eccentricity annular space, the proposed simple model was able to recover the results of more complex and computationally expensive models available in the literature at radius ratio above $\kappa \geq 0.5$.

The results showed the effect of the variation of the eccentricity along the length of an annular space on the flow pattern and pressure drop. The friction factor of the flow is a strong function of the amplitude and wavelength of the variation of the eccentricity along the length of the well and, therefore, these three-dimensional effects have to be considered in the analysis of the flow between a drilling pipe and the well wall during drilling operation. The use of lubrication approximation greatly reduced the computational cost of the three-dimensional analysis. The model can be extended to include the effect of rotation of the inner cylinder and non-Newtonian behavior of the flow liquid.

Acknowledgment

References

[1] Lou, Y., and Peden, J. M., 1987, "Flow of Drilling Fluids Through Eccentric Annuli," *Proceedings of the 62nd Annual Technical Conference and Exhibition of the Society of Petroleum Engineers*, Society of Petroleum Engineers, Texas, USA, pp. 389–396.

[2] Jensen, T. B., and Sharma, M. P., 1987, "Study of Friction Factor and Equivalent Diameter Correlations for Annular Flow of Non-Newtonian Drilling Fluids," ASME J. Energy Resour. Technol., **109**(4), pp. 200–205.

[3] AbdulMajeed, G. H., 1996, "Frictional Pressure Losses for Annular Flow of Drilling Muds," Polym.-Plast. Technol. Eng., **35**(3), pp. 427–447.

[4] Escudier, M. P., Oliveira, P. J., and Pinho, F. T., 2002, "Fully Developed Laminar Flow of Purely Viscous Non-Newtonian Liquids Through Annuli, Including the Effects of Eccentricity and Inner-Cylinder Rotation," Int. J. Heat Fluid Flow, **23**, pp. 52–73.

[5] Siginer, D. A., and Bakhtiyarov, S. I., 1998, "Flow of Drilling Fluids in Eccentric Annuli," J. Non-Newtonian Fluid Mech., **78**, pp. 119–132.

[6] Fang, P., Manglik, R. M., and Jog, M. A., 1999, "Characteristics of Laminar Viscous Shear-Thinning Fluid Flows in Eccentric Annular Space," J. Non-Newtonian Fluid Mech., **84**(1), pp. 1–18.

[7] Hussain, Q. E., and Sharif, M. A. R., 2000, "Numerical Modeling of Helical Flow of Viscoelastic Fluids in Eccentric Annuli," AIChE J., **46**(10), pp. 1937–1946.

[8] Escudier, M. P., Gouldson, I. W., Oliveira, P. J., and Pinho, F. T., 2000, "Effects of Inner Cylinder Rotation on Laminar Flow of a Newtonian Fluid Through an Eccentric Annulus," Int. J. Heat Fluid Flow, **21**, pp. 92–103.

Large-Eddy Simulation of Transition in a Separation Bubble

Stephen K. Roberts

Metin I. Yaras

Department of Mechanical and
Aerospace Engineering,
Carleton University,
3135 Mackenzie Bldg.,
Ottawa, Ontario, Canada K1S 5B6

In this paper, large-eddy simulation of the transition process in a separation bubble is compared to experimental results. The measurements and simulations are conducted under low freestream turbulence conditions over a flat plate with a streamwise pressure distribution typical of those encountered on the suction side of turbine airfoils. The computational grid is refined to the extent that the simulation qualifies as a "coarse" direct numerical simulation. The simulations are shown to accurately capture the transition process in the separated shear layer. The results of these simulations are used to gain further insight into the breakdown mechanisms in transitioning separation bubbles. [DOI: 10.1115/1.2170123]

Keywords: boundary layer transition, large-eddy simulation, separation bubble

Introduction

The numerous experimental studies on boundary-layer transition performed since the pioneering works of Hall and Hislop [1], Schubauer and Skramstad [2], and Emmons [3] have formed a strong foundation for our current understanding of this flow phenomenon (e.g., Klebanoff et al. [4], Narasimha [5], Stieger and Hodson [6], Hatman and Wang [7], Johnson [8], Solomon et al. [9], Volino and Simon [10], and Roberts and Yaras [11]). The present authors have contributed to these efforts with experiments for combinations of flow Reynolds number, freestream turbulence levels, freestream periodic velocity unsteadiness, streamwise pressure gradients, and surface roughness conditions [11–13]. The majority of experimental studies on boundary-layer transition have been based on single-point measurements using hot-wire anemometry (e.g., [2,7–13]), hot-film anemometry (e.g., Haueisen et al. [14], Zhong et al. [15], Anthony et al. [16]) and laser-doppler velocimetry (e.g., Stieger and Hodson [6], M. Lang et al. [17], Brendel and Mueller [18]). A common shortcoming of such measurement techniques is the absence of information regarding spatial correlation of the flow field. In separation bubbles, the unsteady development of the separated shear layer and the periodic shedding of vertical structures closely interact with the transition and reattachment processes. Thus, availability of time-synchronized information throughout the bubble is crucial to complete our understanding of this flow. Particle-image velocimetry is a relatively recent measurement technique that provides such information (Mills et al. [19], H. Lang et al. [20], Bao and Dallmann [21]), but results with fine temporal resolution are yet to be produced with this technique.

In parallel to experimental efforts, advances in computing power have allowed more refined numerical solutions of the Navier-Stokes equations such that they can be used as numerical wind tunnels. The most refined of such studies, known as direct numerical simulations (DNS), resolve the flow field down to the smallest scale of turbulence. While this technique has been successfully used in studying the transition process in attached (e.g., Rai and Moin [22], Singer and Joslin [23]) and separated (e.g., Alam and Sandham [24], Spalart and Strelets [25], Maucher et al. [26]) boundary layers, the substantial computing requirements, proportional to the third power of flow Reynolds number (Pope [27]), have limited such investigations to simplified computational domains at relatively low flow Reynolds numbers. To circumvent

this limitation, one can resort to large-eddy simulations (LES), where the levels of spatial and temporal discretization of the flow provide adequate resolution for the larger of the turbulence eddies only. This is accomplished by filtering the Navier-Stokes equations, with the spatial computational grid typically serving as the filter. The lack of full resolution of the turbulence spectrum in this technique requires the presence of a subgrid turbulence model. As a minimum, the subgrid model is to provide the correct amount of energy transfer from the resolved scales of turbulence to the unresolved range (forward scatter). In transitional flows, the energy transfer from smaller to larger scales of turbulence (backscatter) has been argued to be important (e.g., Dubois and Bouchon [28]), which adds to the demand from the subgrid turbulence model in these flows.

In typical large-eddy simulations of boundary layers, the scale of the resolved turbulence is of the order of 1000 wall units (Spalart [29]). Due to the substantial effects the subgrid models may have on the development of the transition process, a notable portion of published studies on LES of transitional flows have focused on the evaluation of these models (e.g., Rodi et al. [30], Lesieur and Métais [31]). Despite the considerable progress in this research field, a model that allows the reliable use of LES to explore the physics of transition is yet to be developed. In the interim, many have resorted to resolving as much of the turbulence as possible (e.g., Yang and Voke [32], Ducros et al. [33]), thereby minimizing the effects of the subgrid models on the LES results.

The present study has been undertaken with the objective of providing further insight into the physics of separation-bubble transition, to complement the experimental efforts by the current authors and other research groups (e.g. [6–13]). To minimize any adverse effect of the issues associated with subgrid modeling, the spatial and temporal resolution of the simulations are chosen to be significantly finer than those adopted in many published LES studies on transition flows, with the artificial dissipation inherent in the numerical algorithm providing the dissipation of turbulence energy at the level of unresolved scales. The level of resolution is similar to what is commonly referred to as "Coarse DNS," or "Quasi-DNS" in the published literature (Dubois and Bouchon [28], Spalart [29], Piomelli and Balaras [34]).

Considerable experimental data exists on the time-mean dimensions of transitional separation bubbles, as well as the location of transition onset and rate of transition in these flows [7,11,12,17,18]. Due to the existence in separated shear layers of features associated with both attached boundary layers and free shear layers, the relative roles of the viscous Tollmien-Schlichting instability mechanism and the inviscid Kelvin-Helmholtz type of

Copyright © 2006 by ASME
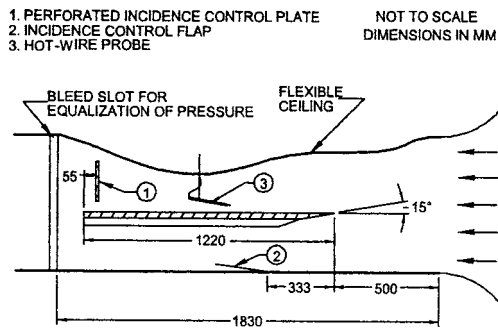
Fig. 1 Schematic of the wind tunnel test section

1. PERFORATED INCIDENCE CONTROL PLATE
2. INCIDENCE CONTROL FLAP
3. HOT-WIRE PROBE

NOT TO SCALE
DIMENSIONS IN MM

Fig. 2 Measured streamwise distribution of the acceleration parameter

instability in the transition of separated shear layers are not completely clear. For example, in their simulations of separation-bubble transition, Yang and Voke [25] and Spalart and Strelets [32] observed the Kelvin-Helmholtz instability mechanism to lead to transition onset. This is in contrast with the extensive hot-wire measurements by the present authors where evidence of significant viscous instability is noted [13]. A number of studies established approximate conditions that appear to dictate the type of instability that is more likely to occur in a given separated shear layer (e.g., Gaster [35], Hammond and Redekopp [36], Allen and Riley [37], Dovgal et al. [38], Rist and Maucher [39]). However, such guidelines do not shed light on possible coexistence of, and interactions between, viscous and inviscid instability mechanisms. The present computational effort has been undertaken to investigate these issues.

Test Case Description

The experiment that forms the basis of comparison for the present simulation was conducted in a wind tunnel facility which is described in detail in previous transition-related publications by the authors (e.g., [13,40]). Briefly, the overall dimensions of the test section are 762 mm, 508 mm, and 1830 mm in width, height, and length, respectively, and it contains a flat test surface upon which two-dimensional streamwise pressure gradients are imposed using a contoured wall forming the ceiling of the test section (Fig. 1). The boundary layer developing over the 1220 mm long test surface is measured with a hot-wire anemometer with a single tungsten sensor of 5 μm diameter and 1.3 mm length. The probe is traversed at multiple streamwise positions along the centerline of the test plate at intervals of 25 mm near and inside the transition zone. Additionally, the boundary layer is traversed in the streamwise direction in 2.0 mm increments, at a distance of 1.25 mm from the test surface, for the purpose of determining the streamwise intermittency distributions and growth rates of instabilities with greater accuracy than is possible using the more sparsely spaced cross-stream traverses.

The measurements were conducted under low freestream turbulence conditions (Tu=0.5%) and for a flow Reynolds number of 350,000, based on the plate length $L=1220$ mm, and a reference velocity U_{ref} of about 4.5 m/s, measured in the freestream, 25 mm downstream from the leading edge of the test surface. For reference, the experiment is documented in Roberts and Yaras [40], and corresponds to the $k_{rms}=0.7$ μm, $Tu_{ref}=0.5\%$, Re_L =350,000 test case with the pressure distribution designated C_{P4}. The streamwise distribution of the acceleration parameter (η $=(\nu/U_e^2)dU_e/dx$) for the test case is shown in Fig. 2.

Numerical Method

Computational Domain and Boundary Conditions. The computational domain is shown schematically in Fig. 3. The inflow boundary is placed 60 mm upstream of the separation location observed in the experiments. The mean velocity and turbu-

lence intensity distributions specified on this boundary correspond to the experimental values, and the turbulence length scale was set to the smallest domain dimension (24 mm). These boundary conditions, along with the perturbations produced by the numerical algorithm, were sufficient to maintain a turbulence intensity during the simulation of 1.2% in the freestream above the separation bubble. This is close to the 1.4% measured in the same region during the experiment, and was sufficient to initiate the transition process without the need to specify transient inflow conditions, or introduce background noise into the computations.
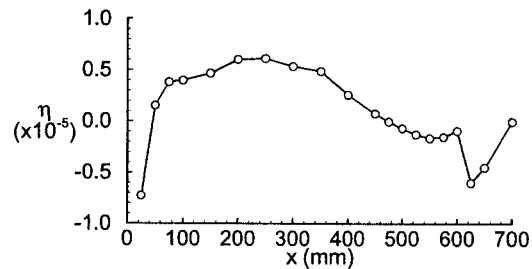
The upper outflow boundary is placed well into the freestream region of the flow field, and the static pressure distribution on this boundary is set to match the experimental values. The streamwise extent of the domain places the rear outflow boundary well downstream of the reattachment region. All flow properties are extrapolated to this boundary from the adjacent set of interior nodes with the restriction that the average static pressure on this boundary be consistent with the pressure specified along the upper outflow boundary.

In the spanwise direction, the domain is bounded by periodic boundaries, and is sized to be approximately four times the measured maximum thickness of the bubble. This spanwise extent is deemed sufficient to allow for natural development of large-scale three-dimensional transient features as the flow transitions to a turbulent state in the separated shear layer.

Solution Method. The large-eddy simulations were performed with the ANSYS-CFX (v. 5.7) commercial (CFD) software. The discretization of spatial derivatives was based on central differencing, and second-order accurate backward Euler integration was used to advance the solution in time. The second-order accuracy of the spatial and temporal discretizations may introduce excessive numerical dissipation, or possibly dispersion, into the solution. The temporal and spatial resolutions described in the next section are relatively fine for large-eddy simulation of the flow in question, and were chosen to help offset any dissipative or dispersive effect of the discretization schemes. Convergence of the solution at each time increment was facilitated through inner iterations based on an algebraic multigrid scheme. Typically, seven inner iterations were found to be sufficient to converge the solution by reducing the L2 norm of the residuals of the filtered continuity and momentum equations by three to four orders of magnitude.

Fig. 3 Schematic of the computational domain

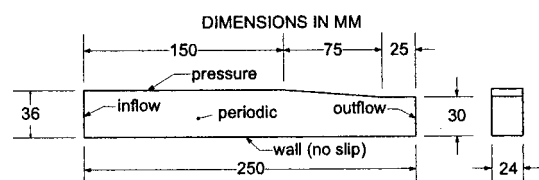**Table 1 Comparison of grids used in LES and DNS studies of transitional and turbulent flows**

Investigators	Method	Δx^+	Δz^+	Δy^+ (1st node)
Current study	LES	36	38	~0.8
Yang and Voke [32]	LES	10–30	9	1
Ducros et al. [33]	LES	44	41	1
ONERA[a]	LES	60	25	2
FLUENT[a]	LES	1100	300	10
CERFACS[a]	LES	1500	100	200
Alam and Sandham [24]	DNS	14–20	~1	~0.5
Rai and Moin [22]	DNS	28	10	1

[a]From the study of Mellen et al. [41].

Computational Grid. The spatial domain was discretized with a structured grid of 176, 52, and 17 nodes in the streamwise, wall-normal, and spanwise directions, respectively. The nodes were evenly spaced in the spanwise and streamwise directions. In the wall-normal direction, the first node was placed to yield a y^+ value of about 1 in the turbulent boundary layer downstream of the separation bubble, and the remaining nodes were distributed with an expansion factor of 1.1. These choices of node counts and distributions yielded reasonably isotropic grid cells in the separated shear layer, with $\Delta x/\Delta y$ and $\Delta z/\Delta y$ varying between 1.2 and 1.8, hence avoiding excessive grid-related distortion of the large-scale turbulence eddies.

In large-eddy simulations, the effect of the subgrid scale turbulence model diminishes as the computational grid is refined, since in the limit all turbulence activity is resolved (DNS). In Table 1, the spatial grid of the present study is compared to published studies on LES and DNS of boundary layer transition [22,24,32,33,41]. The current spatial grid is noted to correspond to a high resolution LES. In DNS, the node spacing of the grid should ideally be smaller than the Kolmogorov length scale, to allow adequate resolution of the smallest energy dissipating eddies. In practice however, accurate DNS has been achieved with node spacing as large as 2–3 times the Kolmogorov scale (e.g., Leonard [42], Yeung and Pope [43]). In the present study, the largest node spacing is approximately 20 times the Kolmogorov scale of the turbulent boundary layer downstream of the separation bubble. It can be argued that with most of the turbulence scales resolved by the computational grid, the specifics of the subgrid scale turbulence model are of lesser importance. The authors have therefore opted to rely on the numerical dissipation of the algorithm to provide the portion of the turbulence energy dissipation that does not occur through the effects of molecular viscosity. The validity of this approach is demonstrated by the favorable comparison of the simulation results with experimental data presented in this paper. It is worth noting that it is not an objective of the present work to evaluate the potential of using algorithm-specific numerical dissipation in LES of boundary-layer transition. Rather, the computational grid was refined as much as the available computing resources permitted, to allow the use of LES as a numerical wind tunnel, without having to seek a precise subgrid scale model.

A time-step size of 0.22 ms was chosen for the simulations, yielding a Courant number ($U\Delta t/\Delta x$) of 1.7 based on the average node spacing and the free stream velocity at the inflow boundary. The chosen time-step size is smaller than the estimated Kolmogorov time scale, and was dictated by the numerical stability of the computations.

Parametric studies confirmed insensitivity of the presented results to refinements in spatial and temporal resolution.

Initial Conditions. The flow field was initialized with a velocity distribution matching that of the inflow boundary, and the pressure distribution specified along the upper outflow boundary was projected to the surface.

The simulation was executed for 12,900 time steps, correspond-ing to 2.84 s of real-time simulation of the flow field. The results beyond the first 2000 time steps were established to be suitable for analysis of the flow field.

Results and Discussion

Time-Averaged Flow Field. The predicted streamwise average velocity ($\bar{U}$) and fluctuating velocity (u'/U_{ref}) in the separation-bubble region are compared to the experimental results in Fig. 4. The streamwise location in this figure is referenced to the point of separation x_s to enable direct comparison of the results. The predicted location of separation is 21 mm downstream of the measured location (4% of the distance between the leading edge and separation location). Fifteen percent variation in the streamwise pressure gradient, which is within the precision of the experimental data, is sufficient to move the separation location by such distances. This factor is judged to be the likely source of discrepancy between the measured and predicted separation points.

As is evident from the path of the time-averaged dividing streamline, the length and thickness of the separation bubble is captured accurately. The time-averaged velocity profiles shown in Fig. 4 are predicted within 15% of the freestream velocity measured in the experiment. Considering the relatively large velocity gradients in the shear layer, these profiles are considered to be in good agreement. The enhanced mass and momentum transfer resulting from transition to a turbulent state in the separated shear layer is key to the reattachment process. It is therefore unlikely to achieve the present level of prediction accuracy for the mean velocity field without capturing the main features of the transition process. This is demonstrated by the contours of u'/U_{ref}, which show similar patterns of turbulence energy in the shear layer, and in the downstream turbulent boundary layer. The discrepancy between the computed and measured fluctuations near the surface beyond $x-x_s=75$ mm is likely a result of rectification errors that occur with single hot-wire measurements in regions of low veloc-
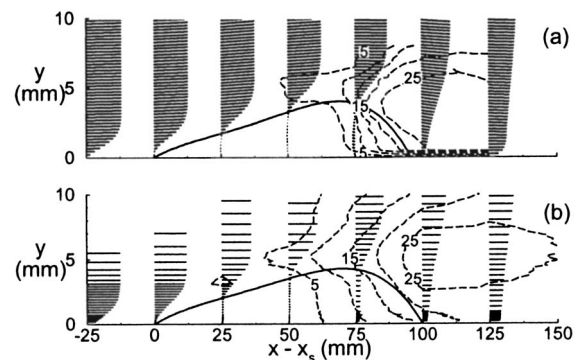

Fig. 4 Time-averaged velocity field in the region of the separation bubble: (a) LES, (b) experimental results (contours show 5% increments of u'/U_{ref})
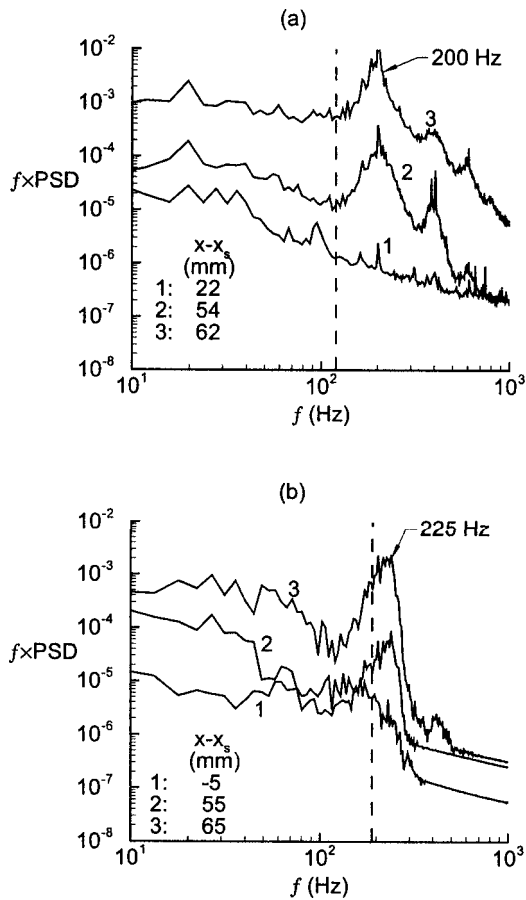
Fig. 5 Power spectra of u'/U_{ref} at various locations in the separation bubble: (a) experimental results, (b) LES
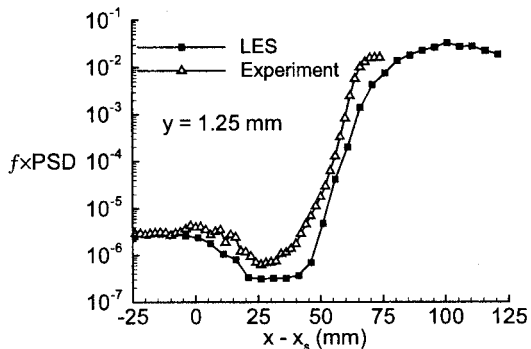

Fig. 6 Growth rates of disturbances at the dominant frequency

Fig. 7 Streamwise velocity contours at midspan during one full cycle of the dominant frequency (the dashed line at $t_0 + T/2$ represents the time-averaged dividing streamline)

ity, and the coarser resolution of the measured profiles.

The Fourier spectra of measured streamwise velocity fluctuations in the separation bubble display a distinct peak at about 200 Hz, starting shortly upstream of the separation location, and growing in amplitude with downstream distance (Fig. 5(a)). The computed spectra given in Fig. 5(b) are noted to agree well with the measured values, although the peak near 200 Hz is not clearly visible until after separation in the experiment. As shown in Fig. 6, the growth rate of disturbances near this frequency is also predicted satisfactorily by the simulation. The agreement between the measured and computed dominant frequency, and the growth rates of disturbances at this frequency, provide further evidence that the main features of the transition process are captured in the

simulation.

The present results are also consistent with the frequency of maximum amplification rate of Tollmien-Schlichting (T-S) waves (f_{MA}), based on a correlation suggested by Walker [44] (Eq. (1)) for attached-flow boundary layer transition, shown by a dashed line in Figs. 5(a) and 5(b). Although f_{MA} is predicted less satisfactorily in the experiment, the uncertainty in Re_{δ^*} in Eq. (1) is greater in this case. While the presence of Tollmien-Schlichting waves in the separated shear layer is clearly evident in these results, this does not prevent breakdown from occurring through the Kelvin-Helmholtz instability in this transition process, as is demonstrated in the next section.

$$f_{\mathrm{MA}} = \frac{3.2 U_e^2}{2\pi\nu \, \mathrm{Re}_{\delta^*}^{3/2}} \tag{1}$$

Transient Flow Development. The temporal variation of the computed streamwise velocity field at midspan of the computational domain is shown in Fig. 7 for one full period ($T=4.4$ ms) of the T-S instability. The highly unsteady nature of the reattachment process is clearly evident from the comparison of the velocity field in the five time planes shown.

The most obvious transient flow pattern is the periodic shedding of a small flow structure (B), containing reverse flow from the main recirculation region (A) of the separation bubble. The most upstream location where this region B breaks from the primary recirculation zone A is $x-x_s=75$ mm. Subsequent to its shedding, this structure convects downstream at approximately half of the local freestream velocity, shown by the dashed line in Fig. 7, and disappears at about $x-x_s=125$ mm. Periodic shedding of this flow structure results in two effective transient reattachment points located at the trailing ends of A and B (Fig. 8). If the one at the downstream end of flow structure B is considered as the reattachment point of the separation bubble, the shedding results in periodic movement of this point by about 30% of the time-averaged bubble length. It is noted that the flow pattern shown in Fig. 8 is very similar to that observed in recent experiments by Stieger et al. [45], which discussed effects of periodic wake impingement on transition in a turbine cascade. The similarity between Fig. 10 of their paper and Fig. 8 of the current work suggests the results of the simulation are also relevant to transition affected by periodic wake impingement, during the quasi-steady
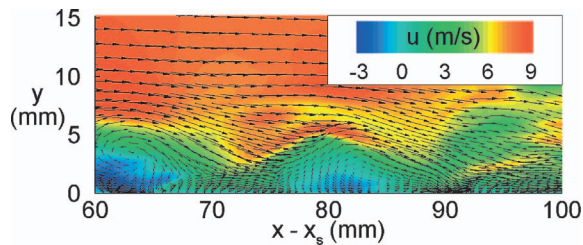
Fig. 8 Magnified view of streamwise velocity contours at mid-span and $t=t_0+3T/4$ showing local reattachment of the flow

Fig. 11 Magnified view of spanwise vorticity at mid-span and $t=t_0$ (the dashed vertical line represents the location of the $x-z$ plane shown in Fig. 12)

period between wake passing events.

At $t=t_0+T$, shedding of the next recirculating flow structure is about to take place (B'), and the state of the bubble is very similar to that at $t=t_0$ (Fig. 7). Thus, the shedding frequency of this structure corresponds to the dominant frequency of the Tollmien-Schlichting waves in the separated shear layer, and in the attached laminar boundary layer. This result is consistent with the wavelength of the wavering developing in the streamlines of the separated shear layer prior to the formation and shedding of structure B (Fig. 9).

The instantaneous spanwise vorticity distribution corresponding to the time planes in Fig. 7 is shown in Fig. 10. Figures 11 and 12 complement Fig. 10 by showing magnified views of the same vorticity field in the $x-y$ and $y-z$ planes, focusing on the region containing the recirculating flow structure B at time t_0. This structure consists of small vortices near the surface, with a concentrated region of vorticity located just above them (Fig. 11). The smaller vortices are most intense in the rear portion of the struc-

ture, and are highly three dimensional, as is evident from Fig. 12.

Based on these results, the periodic shedding taking place at the trailing edge of the separation bubble is summarized schematically in Fig. 13(a). The transient roll up of vorticity in the separated shear layer begins upstream of the location of maximum bubble thickness (1). The resultant vortex grows as it is convected along a path following the time-averaged dividing streamline (2), and is shed at the point of maximum bubble thickness (3). The shedding process is accompanied by entrainment of small three-dimensional vortical structures from within the bubble (4). This flow development is somewhat different from an earlier proposal by Hatman and Wang [7,46] (Fig. 13(b)), in which the shed vortex originates from within the bubble, and the entrained vortices seen near the surface in the current results are replaced by vortices ejected through the separated shear layer under the influence of the shed vortex.

Examination of the velocity fluctuations in the x, y, and z directions suggests that breakdown to turbulence occurs in the lower portion of the shear layer, shortly before the recirculating structure B breaks from the bubble at about $x-x_s=70$ mm. The observed pattern of rollup and breakdown of the separated shear layer is

Fig. 9 Instantaneous streamlines demonstrating shear layer wavering at the T-S wavelength (λ_f)

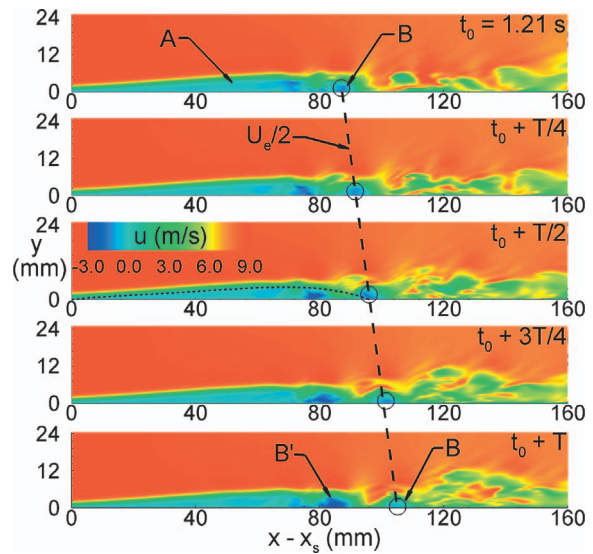Fig. 10 Contours of spanwise vorticity at midspan during one full cycle of the dominant frequency (the dashed line at $t_0+T/2$ represents the time-averaged dividing streamline)

Fig. 12 Spanwise vorticity at $t=t_0$ and $x-x_s=81$ mm (the dashed vertical line represents the location of the $x-y$ plane shown in Fig. 11)
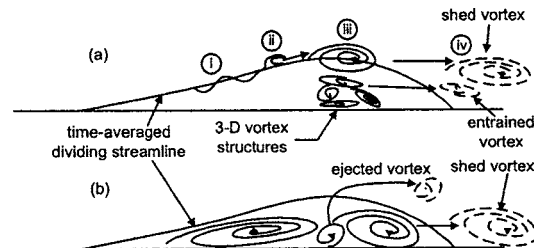
Fig. 13 Schematic representation of the vortex shedding process superimposed on the time-averaged dividing streamline (a) present results; (b) Hatman and Wang [7,46] model

typical of transition driven by Kelvin-Helmholtz (K-H) instability (e.g., Spalart and Strelets [25], Yang and Voke [32], Bernal and Roshko [47], Moser and Rogers [48]). In the present case, the velocity profile just upstream of the transition location is well represented by a hyperbolic tangent function, for which Chandrasekhar [49] calculated the frequency range of K-H instability to correspond to $0 < \kappa d < 1$. For the present case, κd is evaluated to be 0.5, with κ being the wave number of the dominant disturbance frequency ($\kappa = 2\pi/\lambda_f$) and d is a length scale determined by the hyperbolic tangent curve fit to the velocity distribution (about 1/4 of the shear layer thickness). Therefore, the T-S waves, at the very least, appear to provide the initial disturbances for transition to occur through the K-H mechanism. It is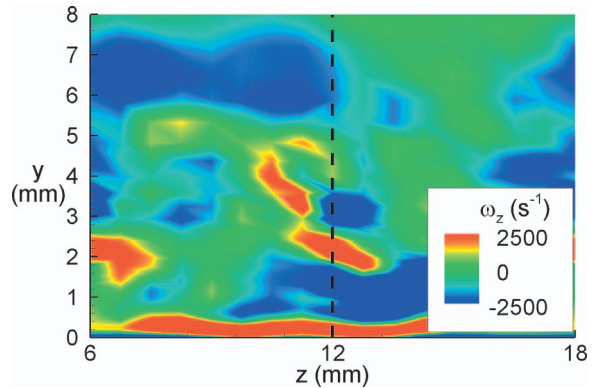 important to note that this interaction between viscous and inviscid modes may not be a general feature of all separation bubbles. Nonetheless, the current simulation demonstrates that transition processes driven by K-H instability may still be significantly affected by T-S waves developing in the laminar boundary layer and in the separated shear layer.

Conclusions

The transition and reattachment of a separated boundary layer has been investigated through large-eddy simulation. Excellent agreement is obtained between experimental hot-wire measurements and the simulation, in terms of the time-averaged length and thickness of the separation bubble and frequency spectra of the velocity fluctuations. The present study complements the hot-wire measurements by identifying certain phenomena that could not be observed experimentally. In this particular case, breakdown to turbulence is shown to take place through the Kelvin-Helmholtz instability. Periodic shedding of vorticity associated with this instability is shown to occur at a frequency that matches the dominant Tollmien-Schlichting frequency in the separated shear layer. Streamwise oscillation of the reattachment location caused by periodic vortex shedding is determined to be a large fraction of the time-averaged bubble length.

Acknowledgment

Nomenclature

d = parameter quantifying the thickness of a hyperbolic tangent shear layer (m)
f = frequency (Hz)
PSD = power spectral density of u'/U_{ref}
Tu = freestream turbulence intensity (%)
T = period of oscillation of the T-S cycle
t = time (s)
t_0 = reference time at the beginning of a T-S cycle
U = local time-averaged velocity magnitude
U_e = time-averaged freestream velocity
U_{ref} = reference velocity measured near the leading edge of the test plate ($U_{\text{ref}}=4.33$ m/s)
u' = streamwise component of fluctuating velocity
x_s = streamwise location of flow separation
x, y, z = streamwise, surface-normal, and spanwise spatial coordinates
Δt = computational time step
$\Delta x, \Delta y, \Delta z$ = streamwise, surface-normal, and spanwise spatial grid dimensions
$\Delta x^+, \Delta y^+, \Delta z^+$ = streamwise, surface-normal, and spanwise spatial grid dimensions expressed in wall units
η = acceleration parameter $\eta=(\nu/U_e^2)dU_e/dx$
κ = wave number corresponding to f_{MA} (m^{-1})
λ_f = wavelength corresponding to f_{MA} (m)
ν = kinematic viscosity

ω_z = spanwise vorticity

Subscript
MA = maximum amplification rate of T-S waves

References

[1] Hall, A. A., and Hislop, G. S., 1938, "Experiments on the Transition of the Laminar Boundary Layer on a Flat Plate," ARC R & M 1843.
[2] Schubauer, G. B., and Skramstad, H. K., 1948, "Laminar Boundary-Layer Oscillations and Transition on a Flat Plate," NACA TN 909.
[3] Emmons, H. W., 1951, "The Laminar-Turbulent Transition in a Boundary Layer-Part 1," J. Aeronautical Sci., **18**, pp. 490–498.
[4] Klebanoff, P. S., Tidstrom, K. D., and Sargent, L. M., 1961, "The Three-dimensional Nature of Boundary-layer Transition," J. Fluid Mech., **12**, pp. 1–42.
[5] Narasimha, R., 1957, "On the Distribution of Intermittency in the Transition Region of a Boundary Layer," J. Aeronautical Sci., **24**, pp. 711–712.
[6] Stieger, R. D., and Hodson, H. P., 2004, "The Transition Mechanism of Highly-Loaded LP Turbine Blades," ASME J. Turbomach., **126**, pp. 536–543.
[7] Hatman, A., and Wang, T., 1999, "A Prediction Model for Separated Flow Transition," ASME J. Turbomach., **121**, pp. 594–602.
[8] Johnson, M. W., 1994, "A Bypass Transition Model for Boundary Layers," ASME J. Turbomach., **116**, pp. 759–764.
[9] Solomon, W. J., Walker, G. J., and Gostelow, J. P., 1996, "Transition Length Prediction for Flows With Rapidly Changing Pressure Gradients," ASME J. Turbomach., **118**, pp. 744–751.
[10] Volino, R. J., and Simon, T. W., 1995, "Bypass Transition in Boundary Layers Including Curvature and Favorable Pressure Gradient Effects," ASME J. Turbomach., **117**, pp. 166–174.
[11] Roberts, S. K., and Yaras, M. I., 2005, "Modeling Transition in Attached and Separated Boundary Layers," ASME J. Turbomach., **127**, pp. 402–411.
[12] Roberts, S. K., and Yaras, M. I., 2003, "Effects of Periodic-Unsteadiness, Freestream Turbulence, and Flow Reynolds Number on Separation-Bubble Transition," ASME Paper No. GT2003-38262.
[13] Roberts, S. K., and Yaras, M. I., 2005, "Boundary Layer Transition Affected by Surface Roughness and Freestream Turbulence," ASME J. Fluids Eng., **127**, pp. 449–457.
[14] Haueisen, V., Henneke, D. K., and Schröder, T., 1997, "Measurements With Surface Mounted Hot Film Sensors on Boundary Layer Transition in Wake Disturbed Flow," AGARD CP-598.
[15] Zhong, S., Kittichaikarn, C., Hodson, H. P., and Ireland, P. T., 2000, "Visualisation of Turbulent Spots under the Influence of Adverse Pressure Gradients," Exp. Fluids, **28**, pp. 385–393.
[16] Anthony, R., Jones, T., and LaGraff, J., 2004, "High Frequency Surface Heat Flux Imaging of Bypass Transition," ASME Paper No. GT2004-54162.
[17] Lang, M., Rist, U., and Wagner, S., 2004, "Investigations on Controlled Transition Development in a Laminar Separation Bubble by Means of LDA and PIV," Exp. Fluids, **36**, pp. 43–52.
[18] Brendel, M., and Mueller, T. J., 1987, "Boundary Layer Measurements on an Airfoil at Low Reynolds Numbers," AIAA Paper No. 87-0495.
[19] Mills, R., Sheridan, J., and Hourigan, K., 2003, "Particle Image Velocimetry and Visualization of Natural and Forced Flow Around Rectangular Cylinders," J. Fluid Mech., **478**, pp. 299–323.
[20] Lang, H., Mørck, T., and Woisetschläger, J., 2002, "Stereoscopic Particle Image Velocimetry in a Transonic Turbine Stage," Exp. Fluids, **32**, pp. 700–709.
[21] Bao, F., and Dallmann, U. C., 2004, "Some Physical Aspects of Separation Bubble on a Rounded Backward-Facing Step," Aerosp. Sci. Technol., **8**, pp. 83–91.
[22] Rai, M. M., and Moin, P., 1993, "Direct Numerical Simulation of Transition and Turbulence in a Spatially Evolving Boundary Layer," J. Comput. Phys., **109**, pp. 169–192.
[23] Singer, B. A., and Joslin, R. D., 1994, "Metamorphosis of a Hairpin Vortex into a Young Turbulent Spot," Phys. Fluids, **6**, pp. 3724–3736.
[24] Alam, M., and Sandham, N. D., 2000, "Direct Numerical Simulation of 'Short' Laminar Separation Bubbles With Turbulent Reattachment," J. Fluid Mech., **410**, pp. 1–28.
[25] Spalart, P. R., and Strelets, M. K., 2000, "Mechanisms of Transition and Heat Transfer in a Separation Bubble," J. Fluid Mech., **403**, pp. 329–349.
[26] Maucher, U., Rist, U., Kloker, M., and Wagner, S., 1999, "DNS of Laminar-Turbulent Transition in Separation-Bubbles," *High Performance Computing in Science and Engineering '99*, E. Krause, and W. Jäger eds., Springer, New York, pp. 279–294.
[27] Pope, S. B., 2000, *Turbulent Flows*, Cambridge University Press, New York.
[28] Dubois, T., and Bouchon, F., 1998, "Subgrid-Scale Models Based on Incremental Unknowns for Large Eddy Simulation," *Center for Turbulence Research Annual Research Briefs*, Stanford, CApp. 221–236.
[29] Spalart, P. R., 2000, "Strategies for Turbulence Modeling and Simulations," Int. J. Heat Fluid Flow, **21**, pp. 252–263.
[30] Rodi, W., and Sheuerer, G., 1985, "Calculation of Laminar-Turbulent Boundary Layer Transition on Turbine Blades," AGARD CP NO. 390.
[31] Lesieur, M., and Métais, O., 1996, "New Trends in Large-Eddy Simulations of Turbulence," Annu. Rev. Fluid Mech., **28**, pp. 45–82.
[32] Yang, Z., and Voke, P. R., 2001, "Large-Eddy Simulation of Boundary-Layer Separation and Transition at a Change of Surface Curvature," J. Fluid Mech., **493**, pp. 305–333.

[33] Ducros, F., Comte, P., and Lesieur, M., 1996, "Large-Eddy Simulation of Transition to Turbulence in a Boundary Layer Developing Spatially Over a Flat Plate," J. Fluid Mech., **326**, pp. 1–36.

[34] Piomelli, U., and Balaras, E., 2002, "Wall-Layer Models for Large Eddy Simulations," Annu. Rev. Fluid Mech., **34**, pp. 349–374.

[35] Gaster, M., 1968, "Growth of Disturbances in Both Space and Time," Phys. Fluids, **11**, pp. 723–727.

[36] Hammond, D. A., and Redekopp, L. G., 1998, "Local and Global Instability Properties of Separation Bubbles," Eur. J. Mech. B/Fluids, **17**, pp. 146–164.

[37] Allen, T., and Riley, N., 1995, "Absolute and Convective Instabilities in Separation Bubbles," Aeronaut. J., **99**, pp. 439–448.

[38] Dovgal, A. V., Kozlov, V. V., and Michalke, A., 1994, "Laminar Boundary Layer Separation: Instability and Associated Phenomena," Prog. Aerosp. Sci., **30**, pp. 61–94.

[39] Rist, U., and Maucher, U., 2002, "Investigations of Time-Growing Instabilities in Laminar Separation Bubbles," Eur. J. Mech. B/Fluids, **21**, pp. 495–509.

[40] Roberts, S. K., and Yaras, M. I., 2005, "Effects of Surface Roughness Geometry on Separation Bubble Transition," ASME Paper No. GT2005-68664, ASME J. Turbomach., (to be published).

[41] Mellen, C. P., Frölich, J., and Rodi, W., 2002, "Lessons From the European LESFOIL Project on LES of Flow around an Airfoil," AIAA Paper No. 2002-0111.

[42] Leonard, A., 1996, "Direct Numerical Simulation of Turbulent Flows," *Simulation and Modeling of Turbulent Flows*, T. Gatski M. Hussaini and J. Lumley, eds., Oxford University Press, New York.

[43] Yeung, P. K., and Pope, S. B., 1989, "Lagrangian Statistics From Direct Numerical Simulations of Isotropic Turbulence," J. Fluid Mech., **207**, pp. 531–586.

[44] Walker, G. J., 1989, "Transitional Flow on Axial Compressor Blading," AIAA J., **27**, pp. 595–602.

[45] Stieger, R. D., Hollis, D., and Hodson, H. P., 2004, "Unsteady Surface Pressures Due to Wake-Induced Transition on a Laminar Separation Bubble on a Low-Pressure Cascade," ASME J. Turbomach., **126**, pp. 544–550.

[46] Hatman, A., and Wang, T., 1998, "Separated-Flow Transition Part 3-Primary Modes and Vortex Dynamics," ASME Paper No. 98-GT-463.

[47] Bernal, L. P., and Roshko, A., 1986, "Streamwise Vortex Structure in Plane Mixing Layers," J. Fluid Mech., **170**, pp. 499–525.

[48] Moser, R. D., and Rogers, M. M., 1993, "Three-Dimensional Evolution of a Plane Mixing Layer: Pairing and Transition to Turbulence," J. Fluid Mech., **247**, pp. 275–320.

[49] Chandrasekhar, S., 1961, *Hydrodynamic and Hydromagnetic Stability*, Clarendon Press, Oxford.

Eric Tromeur
PhD Candidate

Eric Garnier
Doctor
e-mail: garnier@onera.fr

ONERA,
Applied Aerodynamic Department,
BP 72, 29 av. de la division Leclerc,
92322 Châtillon Cedex, France

Pierre Sagaut
Professor
LMM-UPMC/CNRS,
Université Paris VI,
Boite 162, 4 Place Jussieu 75252,
Paris cedex 5, France

Analysis of the Sutton Model for Aero-Optical Properties of Compressible Boundary Layers

In order to assess the capability of the Sutton model to evaluate aero-optical effects in a turbulent boundary layer, large-eddy simulation (LES) evolving spatially and Reynolds averaged Navier-Stokes (RANS) computations are carried out at Mach number equal to 0.9. First aerodynamic fields are proved to compare favorably with theoretical and experimental results. Once validated, the characteristics of the boundary layer allow us to obtain information concerning optical beam degradation. On the one hand, the density field is used to compute phase distortion directly and, on the other hand, by means of the Sutton model. Therefore, LES and RANS simulations allow us to study optical models and the validity of their assumptions. Finally, LES is proved to be considered as a reference tool to evaluate aero-optical effects. [DOI: 10.1115/1.2170128]

1 Introduction

During the last decades, airborne optical devices have been subjected to increasing interest. Indeed, information transmission via optical beam propagation is very useful for detection, reconnaissance, identification, and location through passive techniques such as aerial reconnaissance or active techniques such as for laser target designation. Independently from the application goal, turbulence flow around the airborne system creates perturbations on optical beam transmission due to index-of-refraction fluctuations in the crossing medium [1,2]. These fluctuations are proportional to the local density variations (Gladstone-Dale law). These perturbations limit optical instrument performances of airborne devices.

According to the turbulent flow structure, on the one hand, and the optical beam diameter and its wavelength, on the other hand, optical aberrations undergone by the beam can be of different sorts [3–5]: amplitude wave variation, optical beam deflection, beam-jitter, or even phase distortion (blur of image). Furthermore, all airborne optical devices are surrounded with compressible boundary layer characterized by density variations. Now, the knowledge of the compressible boundary layer structures mainly comes from recent experimental studies [6–8]. These studies have put forward the fact that turbulence is composed of many eddies of different scales. Optical degradation might be different with respect to these more or less coherent structures crossed by the light beam in the inner ($z < 0.2\delta$, where z is the wall-normal distance and δ the boundary layer thickness) and the outer regions of the boundary layer. Near the wall in the inner region, high- and low-velocity streams, called streaks, are due to the existence of streamwise eddies controlled by viscosity effects. On the contrary, in the outer region of the boundary layer ($z > 0.2\delta$), flow structure is entirely controlled by turbulence. The viscous stress is negligible with respect to turbulent stress. The turbulent scales are then given by boundary layer thickness.

These scales are by far higher than the optical beam wavelength and lower than the optical system diameter. Moreover, changes in beam amplitude are known to be negligible across boundary layers [9]. So, wave phase distortion is the main aero-optical aberration undergone by the wave front of the light beam in the process of its propagation in the turbulent medium.

Evaluation of this aberration necessitates the knowledge of density fluctuations ρ' which is accessible only by unsteady simulations (direct numerical simulations (DNS) or large eddy simulation (LES) or by direct measurements. Nevertheless, theoretical developments complemented by experimental measurements have permitted the definition of optical models (such as the Sutton model) which necessitate the knowledge of density fluctuations and density correlation length [10]. Unlike LES, these quantities are not accessible to Reynolds averaged Navier-Stokes (RANS) computations, but approximate models are commonly used [4]. Besides, we can notice that the Sutton model is a very simplified model used for a very complex physics still not well known.

LES is a very usefuly tool for aero-optics because it allows an access to both the direct computation of the wave phase distortion and the indirect computation of this quantity by means of the Sutton model. It is then possible to evaluate (and it is the main purpose of this study) the predictive capacities of this model. Moreover, performing RANS computations, it is also possible to assess the additional hypothesis necessary for the use of the Sutton model with information originating from a RANS computation.

Note that the authors have already tried to assess the Sutton model in a former paper [11]. Nevertheless, the LES of that paper were performed using the temporal approximation assuming periodicity in the streamwise direction. With this methodology, the boundary layer thickens continuously and it is not possible to carry out a temporal averaging process. In the present paper, a recalling method is used to prevent thickening of the boundary layer and the results are believed to be much more reliable.

The LES results are compared with the data acquired experimentally in the T2 trans-sonic wind tunnel of ONERA (center of Toulouse) for both aerodynamic field [12] and optics [13,14] at a Mach number equal to 0.9. The former measurements are performed using hot wire velocimetry whereas Shack-Hartmann sensors are employed for wave-front analysis. To our knowledge, the only available work where aerodynamics and optics data were acquired together in a boundary layer configuration is the in-flight measurements of Gilbert [15]. Nevertheless, such a configuration in not yet affordable for LES and the Mach number of the data presented in this paper is limited to 0.57. From a numerical point of view, the issue of phase distortion through boundary layers has been addressed by Truman [16] via a DNS of an incompressible channel flow at a low Reynolds number. In its simulation, the density is treated as a passive scalar and we can expect our com-

pressible LES to be more realistic. Another important example of numerical computation of phase distortion is the mixing layer LES of Childs [17].

The paper is organized as follows. First, the formalism and the basic equations for a beam propagation are set out before introducing the optical models. In Sec. 3, the filtered equations, the numerical method, and the description of the configuration are detailed. Section 4 presents results for optical beam propagation through a turbulent boundary layer. Comparisons are performed to test the efficiency of the Sutton model on the phase distortion estimation. The general conclusion is presented in Sec. 5.

2 Aero-Optical Formulation

In this section, assumptions and governing equations are summarized for the propagation of electromagnetic waves through a turbulent medium [4]. The theoretical procedure to calculate the phase distortion induced by turbulent fluctuations is also presented.

2.1 Governing Equations. The behavior of an electromagnetic beam propagating through a turbulent medium is governed by Maxwell's equations. Here, the medium is regarded as nonconducting with constant magnetic permeability. Because the time scale for light propagation through a flow field is much smaller than that of turbulent fluctuations, the index of refraction is approximated as being independent of time [9]. Then, the equation which describes the propagation is

$$\nabla^2 \vec{E} - \frac{n^2}{c_0^2} \frac{\partial^2 \vec{E}}{\partial t^2} = 0 \qquad (1)$$

where $\vec{E}$ is the electric field and n is the index of refraction given by $n = c_0/c$, with c the wave speed in the considered medium and c_0 the vacuum wave speed. As for small wavelengths, the field behaves as a plane wave [18], we first model the propagation as a plane wave starting from $z=0$ and propagating to $z=R$. Finally, for monochromatic sinusoidal plane wave of frequency ω, Eq. (1) has an exact solution [18,19]

$$\vec{E}(\vec{r},t) = \vec{E}_0 e^{i[\phi(\vec{k},\vec{r}) - \omega t]} \qquad (2)$$

where $\vec{E}(\vec{r},t)$ is the electric field at a distance $\vec{r}$ for time t given, with $\vec{E}_0$ the electric field amplitude and ω wave pulsation. ϕ is the wave phase at that point in comparison with nonperturbed phase ϕ_0 such as

$$\phi = \phi_0 + \Delta\phi \qquad (3)$$

$\Delta\phi$ is phase variation due to inhomogeneous medium. This variation is named phase distortion.

Finally, wave plane follows optical geometrical laws [20]. In this way, light beam behavior can be fully characterized by means of knowledge of index-of-refraction evolution and phase ϕ in turbulent medium. The index-of-refraction n is linked to wave pulsation ω such as $\omega = k(c/n)$, where k is the wave number of the beam such as $k = 2\pi/\lambda$, with λ the wavelength.

Moreover, the wave phase ϕ is linked with its phase distortion $\Delta\phi$. So, characterizing $\Delta\phi$ enables phase calculation knowing the starting phase ϕ_0.

2.2 Optical Path Difference. In the former section, we have described the propagation of electromagnetic wave characterized by an initial amplitude E_0 of the electric field before entering the turbulent medium. But, if the variation of the refractive index in turbulent medium through which an optical wave propagates is very small, O(10^{-6}), the ray deflection produced by turbulent fluctuations is quite small for a short distance of propagation. Therefore, the wave propagation can be described by the simple approximation of geometrical optics [20]. Moreover, when a monochromatic plane wave passes through a thin layer in which

the refractive index varies, it emerges with nearly unchanged amplitude but with variations of phase (phase distortion) with respect to the original wave front. In this case, one multiplies the exact solution of Eq. (1) by $\exp(i\Delta\phi)$ where $\Delta\phi$ denotes the phase distortion.

$$\Delta\phi(x,y) = k \int_0^L \Delta n(x,y,z)dz \qquad (4)$$

where L is the optical beam propagation distance in perturbed medium. $\Delta n(x,y,z)$ is index-of-refraction perturbation along the optical path from a point S on the aperture where $z_0=0$ to a point P on the focal plane where $z=L$.

Only the knowledge of index of refraction in turbulent medium is therefore necessary and sufficient to characterize the light beam behavior. Considering that optical aberrations are strongly linked to turbulent medium crossed by the light beam, then it seems obvious that index of refraction depends on aerodynamical parameters in such medium. Indeed, the Gladstone-Dale law is used to obtain index-of-refraction variation which is proportional to the local density ρ

$$n(x,y,z) = 1 + G(\lambda)\rho(x,y,z) \qquad (5)$$

with $G(\lambda)$ the Gladstone-Dale constant defined as

$$G(\lambda) = 0.223 \times 10^{-3}\left(1 + \frac{7.52 \times 10^{-15}}{\lambda^2}\right) \text{m}^2/\text{kg} \qquad (6)$$

Finally, the Gladstone-Dale law is used to obtain index-of-refraction variation

$$\Delta n = G(\lambda)\Delta\rho \qquad (7)$$

where $\Delta\rho$ is density variation such as $\Delta\rho = \rho - \rho_0$, with ρ_0 the nonperturbed medium density.

2.3 Optical Models. Theoretical developments complemented by experimental measurements [21] have permitted the definition of a statistical model for evaluation of variance of phase distortion. This variance writes $\sigma_{\phi'}^2 = (\Delta\phi_{\text{rms}})^2$, where $\Delta\phi_{\text{rms}}$ is the root-mean-square phase distortion, is defined as [3]

$$\sigma_{\phi'}^2 = \alpha k^2 \int_0^L \sigma_{n'}^2(z)L_z(z)dz \qquad (8)$$

where $\sigma_{n'}^2$ is the variance of index-of-refraction fluctuations and $L_z(z)$ is the turbulence scale size on density [4] in the wall-normal direction. The α parameter depends on the chosen model for correlation function also named covariance: α is equal to 2 in the case of exponential distribution of the covariance [22] and to $\sqrt{\pi}$ for Gaussian model [23].

If Gladstone-Dale constant is introduced, $\sigma_{n'}^2$ can be linked with the variance of density fluctuations $\sigma_{\rho'}^2$ according to the following equation:

$$\sigma_{n'}^2 = G^2 \sigma_{\rho'}^2 \qquad (9)$$

Then, Eq. (8) is

$$\sigma_{\phi'}^2 = \alpha G^2 k^2 \int_0^L \sigma_{\rho'}^2(z)L_z(z)dz \qquad (10)$$

This equation, thereafter named Sutton model, supposes isotropic flow [10]. Moreover, this one is valid only in the case when turbulence scale size L_z is much smaller than the path length through turbulence, that is to say $L \gg L_z(z)$.

From the statistical Sutton model, the analytical model has been defined [10] to evaluate variance of phase distortion. This model is based on experimental aerodynamical measurements estimating variance of density fluctuations $\sigma_{\rho'}^2$ together with integral scale in
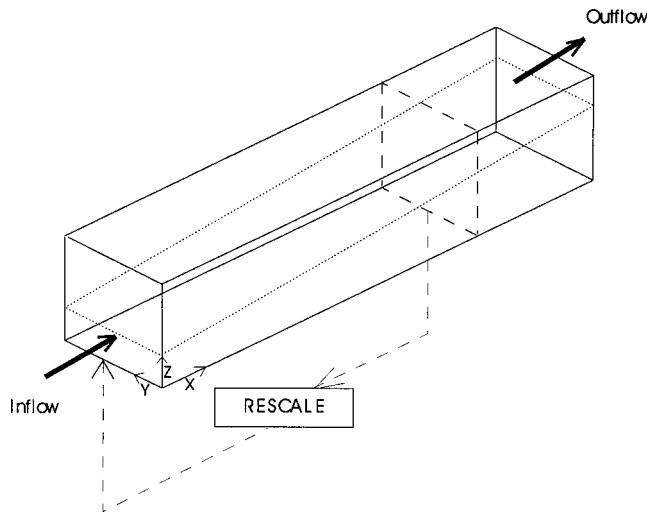
Fig. 1   Generation of inflow turbulent conditions

Fig. 2   Mesh in the (x-z) plane

the wall-normal direction.

Thus, considering that variance of density fluctuations and integral scale are homogeneous ($\sigma^2_{\rho'}(z) = \sigma^2_{\rho'}$ and $L_z(z) = L_z$), evaluation of phase distortion variance—once turbulent boundary layer crossed by light beam—is given by

$$\sigma^2_{\phi'} = \alpha k^2 G^2(\lambda) \delta L_z \sigma^2_{\rho'}, \tag{11}$$

where δ corresponds to the boundary layer thickness. L_z is equal to $L_z = 0.1\delta$ on the basis of flight measurements [21] and $\sigma^2_{\rho'}$ is evaluated as $\sigma^2_{\rho'} = (A|\rho_\omega - \rho_1|)^2$ where A is a scalar which can vary from 0.1 and 0.2 [4], ρ_ω is the wall density and ρ_1 the freestream density.

The variance of density fluctuations $\sigma^2_{\rho'}$ and turbulence scale size L_z are therefore necessary aerodynamical parameters to estimate the variance of phase distortion via these optical models.

3   Mathematical Model

In LES, the large-scale field is computed directly from the solution of the filtered (local-volume averaged) Navier-Stokes equations, and the small scale stresses are modeled. The subgrid-scale (SGS) model then represents the effects of the small scales on the large-scale motions. In this study, the formulation of equations is the one introduced by Vreman et al. [24] and used by Lenormand et al. in LES of compressible plane channel flow [25].

3.1   Numerical Method. In this study, spatially evolving simulation is performed by means of an extension to compressible flows of the rescaling and recycling method (RRM) of Lund et al. [26]. The essential advantage of Lund's method is that it allows a better control on the desired turbulent boundary layer properties at a certain downstream station, such as displacement and momentum thicknesses, and reduces the transient region downstream of inflow required to recover a developed turbulent boundary layer. So, if the target thickness for inflow conditions of the spatial simulation is overshot, the Lund procedure is applied to rescale the boundary layer (Fig. 1). In this paper, we use an adaptation of this RRM introduced by Sagaut et al. [27]: The mean profiles of velocity, temperature, and pressure are fixed and only their fluctuations are rescaled. We can notice that a LES performed in the temporal approximation [11] (periodicity conditions in streamwise and spanwise directions) is used as mean inflow condition for the spatial simulation and the whole turbulent field (replicated in the streamwise and spanwise directions if necessary) is used as initial condition for this simulation.

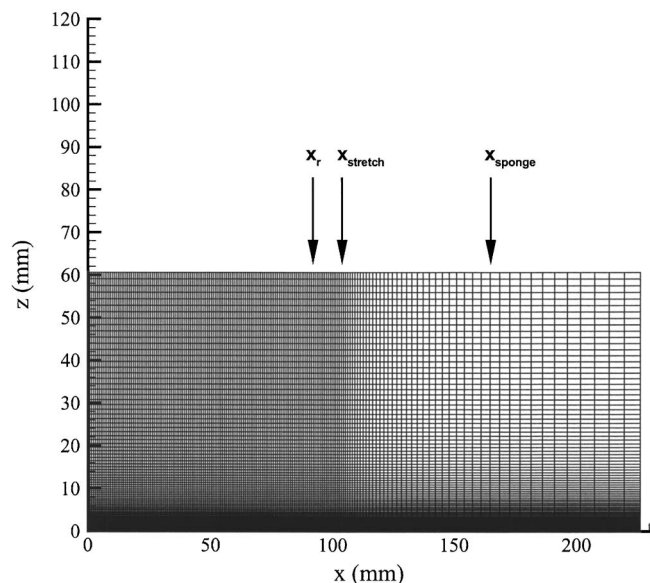Simulations are performed in a Cartesian coordinate system.

The x, y, and z axes are, respectively, oriented along the streamwise, spanwise, and wall-normal directions. The direction of the mean flow is aligned with the x axis and periodicity is imposed in the homogeneous direction y.

Note that uniform grid spacing is used in the spanwise direction and a stretched mesh is used in the wall-normal and streamwise directions. For the latter direction, a preliminary study has been performed in order to fix the stretched zone. The mesh in the (x $-z$) plane is presented in Fig. 2. The longitudinal position of the rescaling abscissa x_r, of the beginning of the stretched zone x_{stretch}, and of the beginning of the sponge zone x_{sponge} are specified in this figure. The latter zone is introduced to damp the reflection of pressure waves.

The time integration is performed by means of a third-order accurate total variation diminishing (TVD) Runge-Kutta method proposed by Shu et al. [28].

Moreover, the convective (implemented using the skew-symmetric form) and viscous terms are, respectively, discretized by means of fourth-order and second-order accurate centered approximations.

The SGS tensor cannot be computed directly, and a SGS model has to be introduced to close the system of filtered equations. In this study, the mixed-scale model [29] has been considered.

Besides, the computation stability is improved by using, on the one hand, a tenth-order filter applied in streamwise direction on variables ($\rho, \rho u, \rho v, \rho w, P$), on the other hand, a nonreflection inflow condition applied above the boundary layer. Temperature and total energy are thereafter obtained.

Concerning boundary conditions, simulation is carried out with a no-slip boundary condition at the wall. Moreover, nonreflection conditions [30] at the top of the computational domain are imposed and provide a satisfactory nonreflecting behavior.

Statistics are collected by averaging in the homogeneous direction y and in time. $\langle \rangle$ denotes such average. The fluctuation variance of a variable ξ is written $\langle \xi'^2 \rangle = \langle \xi^2 \rangle - \langle \xi \rangle^2$ and $\xi_{\text{rms}} = \sqrt{\langle \xi'^2 \rangle}$.

The mesh characteristics of the computation are listed in Table 1. Parameters N_x, N_y, and N_z are, respectively, the number of grid points in the streamwise, spanwise, and wall-normal directions, while Δx^+, Δy^+, and Δz^+ are the grid spacing in viscous wall units such as $z^+ = (u_\tau / \nu_w)z$, where ν_w is the kinematic viscosity. The friction velocity is defined as $u_\tau = [(\mu_w / \rho_w)(\partial \langle u \rangle / \partial z)_w]^{1/2}$ and ρ_w and μ_w are, respectively, the density and the viscosity at the wall. We can notice that one wall unit is equal to 15.5 μm.

Table 1 Mesh characteristics

Δx^+	Δy^+	$\Delta z^+_{(\min)}$	N_x	N_y	N_z
50	18	1	179	95	119

3.2 Flow Configuration. Computations of turbulent boundary layer is performed at a Mach number equal to 0.9 and a Reynolds number equal to 2917 based on the momentum thickness θ such as

$$\mathrm{Re}(\theta) = \frac{\rho_1 u_1 \theta}{\mu(T_w)} \tag{12}$$

where $\mu(T_w)$ is the dynamic viscosity calculated with wall temperature, u_1 is the freestream velocity in the streamwise direction, and θ is defined as

$$\theta = \int_0^\infty \frac{\rho u}{\rho_1 u_1}\left(1 - \frac{\rho u}{\rho_1 u_1}\right) dz \tag{13}$$

Numerical results are compared with hot-wire (HW) velocimetry data obtained by Dussauge et al. [12] at the same Mach number to validate our computations. The other wind tunnel parameters are a stagnation pressure of 2 bars and a stagnation temperature of 300 K. One can notice that the Reynolds number chosen for simulations is 18 times smaller than the experimental one to limit the computational cost. Moreover, we are assuming that Reynolds number is high enough to avoid a strong Reynolds number dependence.

The computational parameters are summarized in Table 2.

The boundary layer thickness remains identical between experiment and LES to keep the same optical path, the Reynolds number reduction has been obtained by a stagnation pressure decrease. The optical data of Refs. [13,14] has been collected in the same wind tunnel and exactly in the same conditions that the aerodynamic data of Ref. [12].

4 Results and Discussion

4.1 Validation. First, a validation of aerodynamic field is performed. Figure 3 shows the Van Driest transformed mean velocity profile. As expected, the behavior in the viscous sublayer ($z^+=5$) is correct. Moreover, the agreement between hot-wire velocimetry (HW) [12] and numerical results is good. Besides, mean velocity profile shows an excellent agreement with theoretical laws in viscous and logarithmic regions.

Furthermore, in order to verify that the computational box is large enough to avoid any correlation of the velocity field, Figs. 4 and 5 show correlations of the streamwise velocity fluctuations R_{uu} versus the spanwise spacing (given in wall units) Δy^+, respectively, close to the wall at $z^+=20$ and in the middle of the boundary layer at $z=0.5\delta$.

Whatever the distance z is, these correlations prove that the domain size is sufficient in the spanwise direction. Indeed, $R_{uu}(y)$ become negligible around $\Delta y^+=100$ at $z^+=20$ (Fig. 4) and for $\Delta y^+>200$ in Fig. 5. We can notice that the correlation length seen in Fig. 4 is in agreement with what is known about velocity correlations in boundary layers [31].

We must now consider the density behavior to estimate the phase distortion. RANS simulations using the Chien $k-\epsilon$ turbulent model are compared with LES profiles. This model enables a

Table 2 Initial computational parameters

Mach	δ (mm)	θ (mm)	Re (δ)	Re (θ)
0.9	20	2.18	29,850	2917
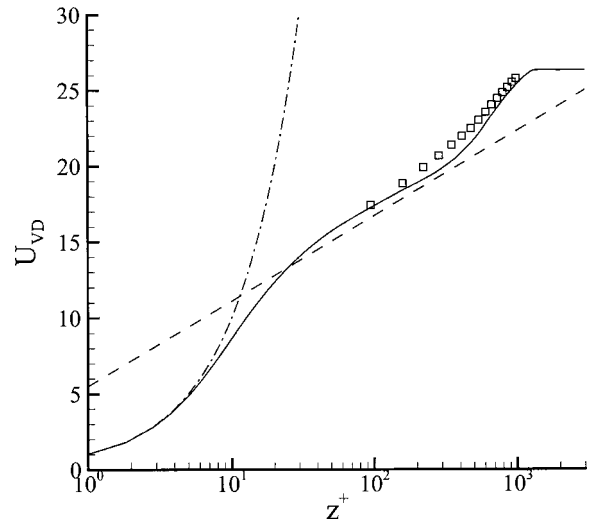
Fig. 3 Van Driest transformed mean velocity profile. LES: —; $u^+=1/0.41 \ln z^+ +5.5$: ----; $u^+=z^+$: ·-·-·-; HW from Ref. [12]: □

treatment of the region close to the wall [32].

Figure 6 shows density mean profiles. The agreement between experimental results obtained by means of hot-wire velocimetry [12] and LES results and RANS computations is very satisfactory. Such agreement enables us to consider the optical results in a positive way. However, optical degradation being linked to density fluctuations $\langle \rho'^2 \rangle$, an agreement on the mean density is not sufficient to be conclusive on the computations validity.

Nevertheless, in RANS calculations, density fluctuation modelings are rare and often need an additional transport equation [33,1,34]. On the contrary, temperature is a more accessible quantity to measurements than density. We must then link temperature and density fluctuations. To do so, Urbin and Knight [35] consider these are no significant pressure fluctuations in the boundary layer. From the state equation, we can write

$$\frac{\rho'}{\langle \rho \rangle} \approx -\frac{T'}{\tilde{T}} \tag{14}$$

where $\tilde{}$ denotes a Favre average.

Then

Fig. 4 Correlation of the streamwise velocity fluctuations $R_{uu}(y)$: $z^+=20$

Fig. 5 Correlation of the streamwise velocity fluctuations $R_{uu}(y)$: $z=0.5\delta$
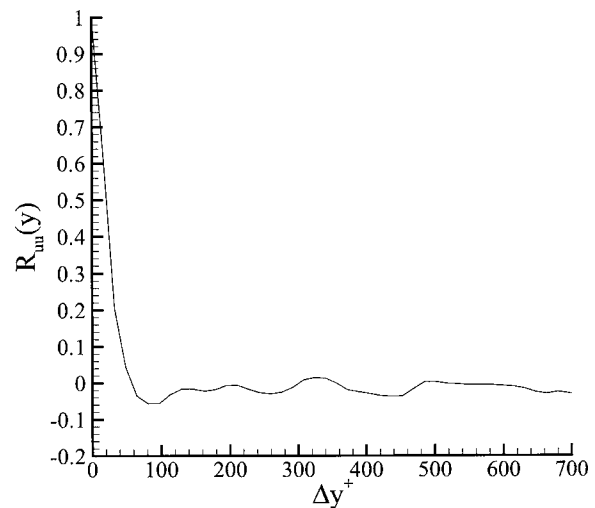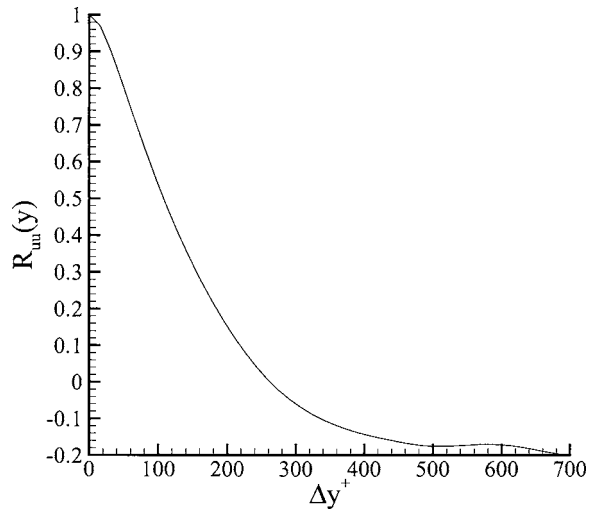

Fig. 7 Autocorrelation of streamwise velocity and temperature fluctuations $R_{u'T'}$

$$\langle \rho'^2 \rangle \approx \left(\frac{\langle \rho \rangle}{\widetilde{T}} \right)^2 \widetilde{T'^2} \qquad (15)$$

Thus, the problem consists of linking temperature fluctuation variance to quantities known in averaged Navier-Stokes equations resolution.

The strong Reynolds analogy (SRA) is generally a strategy used to estimate temperature fluctuations in the boundary layer [36]. One of the SRA relations allows the link of variances of temperature and streamwise velocity fluctuations. This equation leads to a perfect anticorrelation between streamwise velocity and temperature fluctuations such as $R_{u'T'} = -1$ [37].

Although $R_{u'T'}$ experimental value is around −0.9, large eddy simulations show a correlation level close to −0.5 for $0.15 < z/\delta < 0.90$, as represented in Fig. 7. These results are in very good agreement with the ones obtained by Guarini et al. [36] by means of direct numerical simulation where $R_{u'T'} = -0.55$.

Because the strong correlations assumption is not validated between temperature and streamwise velocity fluctuations, Huang et
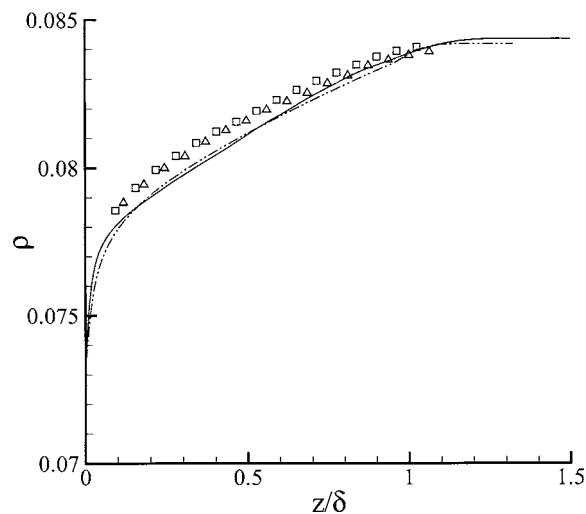
al. [37] suggest an assumption based on mixing length in order to estimate these fluctuations. These are linked to mean quantities gradients by turbulence scales as follows

$$u' = l_u \frac{\partial \widetilde{u}}{\partial z} \quad \text{and} \quad T' = l_T \frac{\partial \widetilde{T}}{\partial z} \qquad (16)$$

where l_u and l_T are, respectively, streamwise velocity and temperature mixing lengths. By multiplying numerator and denominator by $\rho w'$, one can show easily that the ratio l_u/l_T is equal to the turbulent Prandtl number Pr_t.

However, unlike Huang et al. who suppose that these relations (16) are verified on a instantaneous field, Aupoix [38] suggests to use relations for variances calculation such as

$$\widetilde{u'^2} = l_u^2 \left(\frac{\partial \widetilde{u}}{\partial z} \right)^2 \quad \text{and} \quad \widetilde{T'^2} = l_T^2 \left(\frac{\partial \widetilde{T}}{\partial z} \right)^2 \qquad (17)$$

so that the temperature fluctuations can be computed as

$$\widetilde{T'^2} = \frac{\widetilde{u'^2}}{\mathrm{Pr}_t^2} \left(\frac{\partial \langle \widetilde{T} \rangle / \partial z}{\partial \widetilde{u} / \partial z} \right)^2 \qquad (18)$$

Considering the relation (15) and that $\widetilde{u'^2} \approx k_c$ in boundary layers, Aupoix connects density fluctuations to density and streamwise velocity mean value gradients as

$$\langle \rho'^2 \rangle \approx \frac{k_c}{\mathrm{Pr}_t^2} \left(\frac{\partial \langle \rho \rangle / \partial z}{\partial \widetilde{u} / \partial z} \right)^2 \qquad (19)$$

The value of the turbulent Prandtl number is close to 0.9 in boundary layers.

For RANS simulations, density fluctuation profiles are therefore obtained by means of this relation (19).

Figure 8 shows density rms fluctuations $\rho_{\mathrm{rms}} = \sqrt{\langle \rho'^2 \rangle}$. On the one hand, the behavior of these fluctuations is evaluated by means of LES, and on the other hand by means of RANS simulation and hot-wire velocimetry. Although LES profile is similar to experimental profiles, numerical results reveal fluctuations 10% to 20% higher than the ones obtained with hot-wire velocimetry. However, measurement uncertainty is around 10% [12]. Therefore, the agreement of experimental and numerical results is satisfactory.

Besides, the maximum of density fluctuations is located in the region close to the wall. Then, from $z=0.2\delta$ to $z=0.6\delta$, density fluctuations profile is relatively constant both for numerical and experimental cases. So, the optical beam degradation will be nearly uniform in this part of the boundary layer. However, for

Fig. 6 Density mean profiles. LES: —; RANS (Chien): -------; HW (Ma=0,8883) from Ref. [12]: □; HW (Ma=0,8865) from Ref. [12]: △

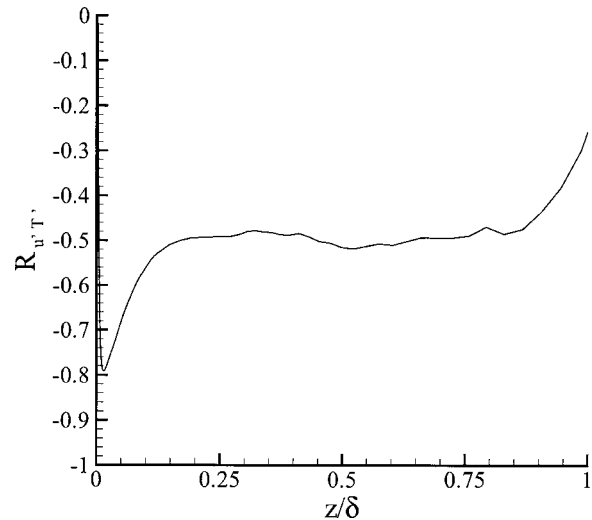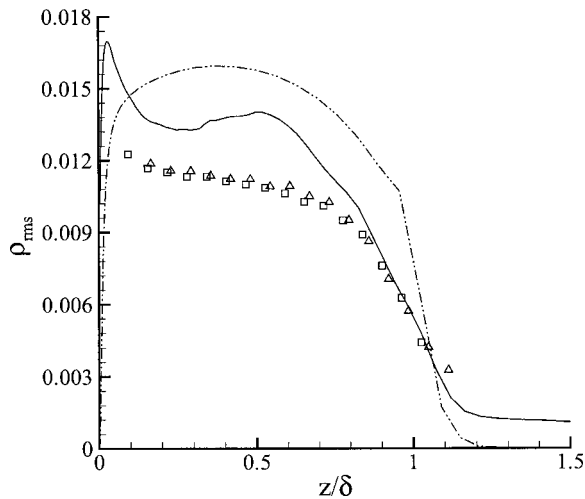Fig. 8 Density fluctuations ρ_{rms}. LES: —; RANS (Chien): -·-·-·; HW (Ma=0,8883) from Ref. [12]: □; HW (Ma=0,8865) from Ref. [12]: △

Fig. 9 Normal turbulent scale size L_z/δ. L_z^{ρ}/δ: —; L_z^{u}/δ: ---; $L_z^{(k-\epsilon)}/\delta$: ---

LES profile, a slight increase in ρ_{rms} can be noticed at $z=0.5\delta$.

Moreover, density fluctuation level obtained via turbulence model are overestimated by about 40% with respect to experimental measurements. Nevertheless, RANS computation are unable to predict a density fluctuations peak next to the wall. This one is due, on the one hand, to the underestimation of turbulent kinetic energy peak and, on the other hand, to the use of the assumption $\widetilde{u'^2} \approx k_c$ that leads to an underestimation of $\widetilde{u'^2}$ close to the wall [38].

4.2 Estimation of Correlation Lengths. Calculating integral scale (also called correlation length) on density L_z^{ρ} in the wall-normal direction is necessary to estimate variance of phase distortion by means of Sutton model. Thus, L_z^{ρ} is obtained via LES such as

$$L_z^{\rho} = \int_{-\infty}^{\infty} R_{\rho'\rho'}(z)dz \qquad (20)$$

where $R_{\rho'\rho'}$ is the density autocorrelation. For a boundary layer flow, the lower bound of integration is $z=0$ and the upper bound is $z=L$ where L is the boundary layer thickness.

Besides, L_z behavior is compared with the one of l length predicted by means of RANS simulation. Most authors [1,39,40] have chosen $l=k_c^{3/2}/\epsilon$ assuming flow equilibrium (ϵ is energy dissipation rate). The choice is questionable in their complex configurations (hypersonic interceptor for the two latter papers). According to the Bradshaw hypothesis, the integral scale of turbulence based on the velocity field can be computed as $l=(2a_1k_c)^{3/2}/\epsilon$, where $a_1=0.15$. This evaluation of the integral length scale was retained because it gives l equal to κz in the logarithmic zone of the boundary layer. In this expression, the von Kármán constant κ is equal to 0.41. Additionally, one must note that this kind of modeling relies on two strong assumptions:

- The first one is to consider that integral scale of velocity fluctuations l is isotropic.
- The second one is to identify density and velocity scales.

Since it is the most important one for the design of the aero-optical model, the validity of the second assumption is checked looking at Fig. 9 which presents the integral scales associated to density (L_z^{ρ}) and velocity (L_z^{u}) obtained via LES and the velocity integral scale evaluated from turbulent variables in the RANS simulation ($L_z^{(k-\epsilon)}=(2a_1k_c)^{3/2}/\epsilon$). Due the turbulent structures in
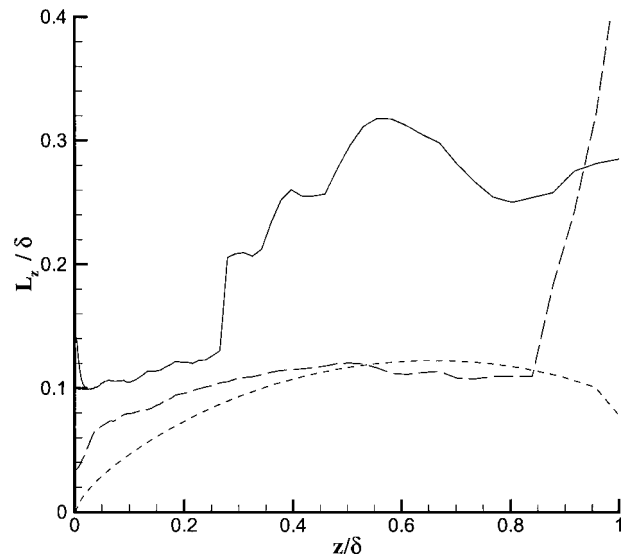
the boundary layer (streaks) which give some coherence to the flow, L_z does not cancel in the near wall vicinity whereas $L_z^{(k-\epsilon)}$ is zero at the wall since the turbulent kinetic energy vanishes. A first observation drawn from LES data is that integral scale of density are much larger than the one of velocity. The second important result is that velocity integral scales predicted by LES and RANS are similar and are in agreement with experimental data coming from flight tests. An important remark is that experimental data are obtained using hot wire anemometry and therefore deal with the integral scale of the physical quantity ρu which is the one really measured by this technique. As a consequence, no direct evaluation of the density integral scale is available and this parameter is evaluated using the assumption discussed in this paragraph. Another important result is that the integral scales are not negligible with respect with the boundary layer thickness in contradiction with one of the assumptions which underlies the Sutton model (10).

4.3 Optical Numerical Results

4.3.1 Characterization of Phase Distortion. In order to put forward the link between index-of-refraction fluctuations $n'=n-\langle n \rangle$ and phase distortion $\Delta \phi$ at the top of the computational domain, spatial evolution of these two quantities is shown in Fig. 10 for a section taken in the middle of the computational domain. $\Delta \phi$ is directly proportional to the integral of index-of-refraction fluctuations across the boundary layer. Gray zones observed at the top of this figure correspond to the fluctuation maximum whereas dark zones are related to the minimum of index-of-refraction fluctuations separated by a dashed line for which $n'=0$. The more important these fluctuations, the stronger the phase distortion.

In this figure, seven stations are considered in order to observe directly the behavior of phase distortion according to the behavior of index-of-refraction fluctuations. For stations 1, 3, 5, 6, and 7, we observe a peak on $\Delta \phi$ which mainly characterize a light beam propagation through a region where $n'>0$. The maximum degradation is obtained at station 4 where $|\Delta \phi|=0.06$ rad.

Moreover, at station 2, index-of-refraction fluctuations are negative for $z<4$ mm and influence then directly $\Delta \phi$ value which decreases around a factor 4 with respect to stations 1 and 3.

Finally, these peaks characterize the degradation phenomenon of the optical beam during its propagation through the boundary layer. This optical degradation depends on structure sizes. With
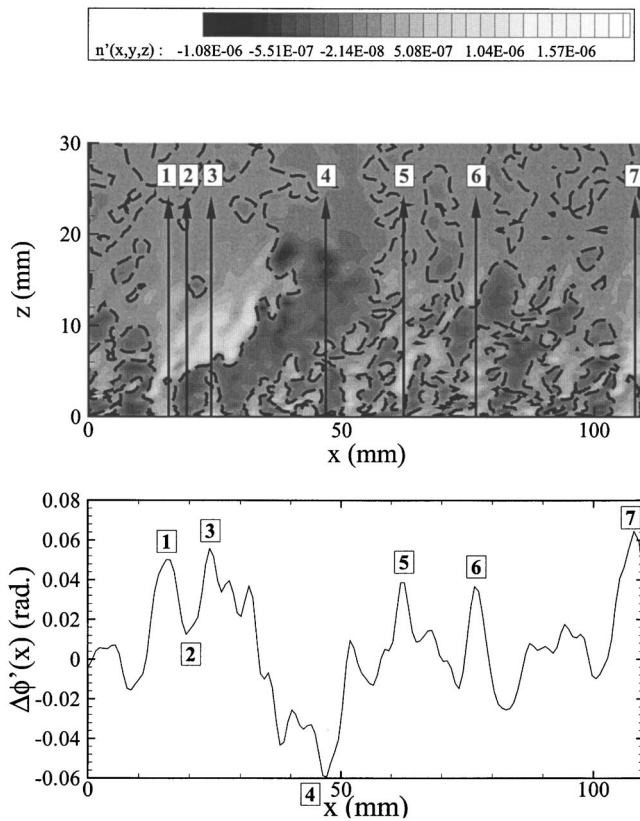
Fig. 10 Spatial evolution of instantaneous index-of-refraction fluctuations n' (top) and phase distortion $\Delta\phi'$ at $z=3\delta$ (bottom). Isovalue $n'=0$: ----.

many small structures, the sign of the distortion alternates rapidly and the total degradation is limited whereas with large structures, significant degradation occurs.

4.3.2 Analysis of the Sutton Model. Unlike RANS simulation which involves approximations to calculate the variance of density fluctuations $\sigma_{\rho'}^2$, and integral scale L_z, LES allows us to obtain directly these two quantities. So, the variance of phase distortion calculated via the Sutton model (Eq. (10)) is estimated either from LES or by means of RANS computation. Moreover, LES allows a direct computation of the phase distortion by means of the equation (4).

The variance evolution of phase distortion $\sigma_{\phi'}^2$ comparing LES results with optical models is shown in Figs. 11 and 12 for, respectively, $\alpha=2$ and $\alpha=\sqrt{\pi}$ (see explanation for these values in Sec. 2.3). In order to assess the validity of the Sutton model, the direct evaluation from LES data is compared with the experimental value and evaluations coming from the Sutton model (10) using the following inputs: (i) the LES velocity integral scale; (ii) the LES density integral scale, and (iii) the RANS velocity integral scale. Values obtained using the empirical model (11) are also reported. The LES and the experimental data do not change in both figures whereas the data computed with Eqs. (10) and (11) change only by 11% (the relative difference between 2 and $\sqrt{\pi}$.

The experimental measurements [13,14] have been carried out by means of 64×64 lenslet high resolution Shack-Hartmann wave-front sensors at a frame rate of 40 Hz. The aerodynamic field is "frozen" by a 1 μs exposure time. The light source is a continuous HeNe Laser ($\lambda=632.8$ nm). The beam crosses the width of the wind tunnel so that the effects of two boundary layers are integrated. It has been verified that the aerodynamic characteristics of these boundary layers are the same. This device gives

Fig. 11 Variance of phase distortion fluctuations: $\alpha=2$. LES (direct computation): —; Eq. (10) with RANS: ---; Eq. (10) with L_z^ρ LES: -------; Eq. (10) with L_z^u LES: ---; The analytical model Eq. (11) (for $A=0,1$): -------; The analytical model Eq. (11) (for $A=0,2$): ⋯⋯⋯; Experience: △

a direct experimental measurement of the phase distortion which can be compared with LES results. The difference between both values is less than the 12% uncertainties due to the Shack-Hartmann device. Thus, these results put forward the need to compute an unsteady simulation in order to avoid the introduction of assumptions to estimate the variance of phase distortion $\sigma_{\phi'}^2$.

It is worth noting that the only value of interest for the designer of an optical device is the integrated value outside the boundary layer and other results analysis is based on this value.

A careful analysis of the plotted results reveals that the direct LES computations and the evaluations performed using the Sutton
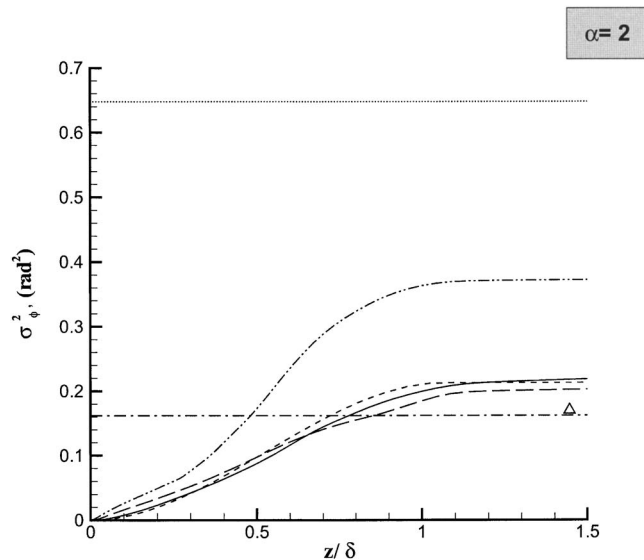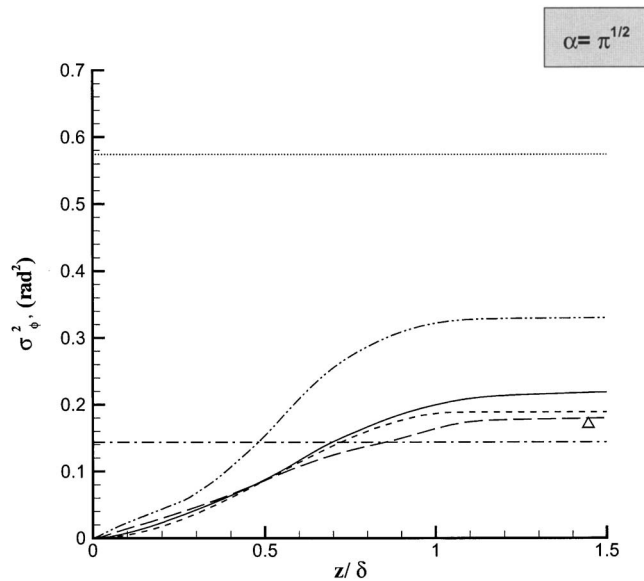

Fig. 12 Variance of phase distortion fluctuations: $\alpha=\sqrt{\pi}$. LES (direct computation): —; Eq. (10) with RANS: -----; Eq. (10) with L_z^ρ LES: -------; Eq. (10) with L_z^u LES: ---; The analytical model Eq. (11) (for $A=0,1$): -------; The analytical model Eq. (11) (for $A=0,2$): ⋯⋯⋯; Experience: △

model with both RANS and LES velocity integral scales are in good agreement with the experimental data. On the contrary, the prediction based on the Sutton model using the density integral scale as an input leads to a much less satisfactory comparison. An important conclusion is therefore that the usual Sutton model is to be used together with the velocity integral scale, despite how it differs from the density integral scale which is the true theoretical quantity to be used. A possible explanation is that the error committed on the evaluation of the integral scale cancels, at least partially, with other errors which originate in the violation of several assumptions which underly the Sutton model. Among them, let us cite the assumptions dealing with the probability density function of the density fluctuations and the scale separation between the integral length and the boundary layer thickness.

5 Conclusion

Spatially evolving LES and RANS computations have been carried out at Mach number equal to 0.9 to assess the capability of the Sutton model to evaluate aero-optical effects. For that purpose, the knowledge of density fluctuations is first necessary. Besides, the study of density field allows us to estimate density correlation lengths needed for the Sutton model computation. LES and RANS simulations show that these lengths are not constant inside the boundary layer. It is shown that the accuracy of the results predicted using the Sutton model based on the velocity integral scale instead of the density integral scale is satisfactory for equilibrium boundary layers. A possible explanation for that is a partial error cancellation.

So, unsteady simulations such as LES are recommended to evaluate directly the aero-optical effects whereas the Sutton model is limiting in accuracy whatever the kind of simulation, especially if boundary layers out of equilibrium are to be investigated.

Acknowledgment

References

[1] Smith, R., Truman, C., and Masson, B., 1990, "Prediction of Optical Phase Degradation Using a Turbulent Transport Equation for the Variance of Index-of-Refraction Fluctuations," AIAA Paper No. 90-0250, *28th Aerospace Sciences Meeting*, January 8–11, Reno, NV.
[2] Clark, R. L., and Farris, R. C., 1987, "A Numerical Method to Predict Aero-Optical Performance in Hypersonic Flight," AIAA Paper No. 87-1396, *19th Fluid Dynamics, Plasma Dynamics and Lasers Conference*, Honolulu, Hawaï, June 8–10.
[3] Sutton, G. W., 1969, "Effects of Turbulent Fluctuations in an Optically Active Fluid Medium," AIAA J., **7**(9), pp. 1737–1743.
[4] Sutton, G. W., 1985, "Aero-Optical Foundations and Applications," AIAA J., **23**(10), pp. 1525–1537.
[5] Jumper, E. J., and Fitzgerald, E. J., 2001, "Recent Advances in Aero-Optics," Prog. Aerosp. Sci., **37**, pp. 299–339.
[6] Robinson, S. K., 1986, "Space-Time Correlation Measurements in a Compressible Boundary Layer," AIAA Paper No. 86-1130.
[7] Smits, A. J., and Dussauge, J.-P., 1996, *Turbulent Shear Layers in Supersonic Flow*, American Institute of Physics, New York.
[8] Spina, E. F., Smits, A. J., and Robinson, S. K., 1994, "The Physics of Supersonic Turbulent Boundary Layers," Annu. Rev. Fluid Mech., **26**, pp. 287–319.
[9] Truman, C. R., and Lee, M. J., 1990, "Effects of Organized Turbulence Structures on the Phase Distortion in a Coherent Optical Beam Propagating Through a Turbulent Shear Flow," Phys. Fluids A, **2**(5), pp. 851–857.
[10] Havener, G., 1992, "Optical Wave Front Variance: A Study on Analytic Models in Use Today," AIAA Paper No. 92-0654, *30th Aerospace Sciences Meeting and Exhibit*, Reno, NV.
[11] Tromeur, E., Garnier, E., Sagaut, P., and Basdevant, C., 2003, "Large Eddy Simulations of Aero-Optical Effects in a Turbulent Boundary Layer," J. Turbul., **4**(5), pp. 1–22.
[12] Dussauge, J.-P., Mucini, S., Mignosi, A., Breil, J. F., and Delrieu, G., 2002, "PRF Effects Aéro-Optiques. Essais Veine Vide et Aulification des Couches Limites Latérales de la Soufflerie T2," Rapport Technique ONERA No. RT 2/06008 DOTA/DMAE.
[13] Deron, R., Tromeur, E., Aupoix, B., and Desse, J. M., 2002, "Rapport d'Activités 2001 du Project de Recherche Fédérateur Effets Aéro-Optiques," No. RT 4/06008 DOTA, ONERA, France.
[14] Rousset-Rouviere, L., Coudrain, C., Deron, R., and Mendez, F., 2003, "Statistical Shack-Hartmann Wavefront Analysis Through Non-Isotropic Turbulence," Optics in Atmospheric Propagation and Adaptive Systems V., Kohnle, A., and Gonglewski, J. D., eds., Proc. SPIE, **4884**, pp. 218–223.
[15] Gilbert, K. G., 1982, "KC-135 Aero-Optical Turbulent Boundary-Layer/Shear-Layer Experiments," *Progress in Astronautics and Aeronautics: Aero-Optical Phenomena*, Gilbert, K. G., and Otten, L. J., eds., Vol. 80, AIAA, NY, pp. 306–324.
[16] Truman, C. R., 1992, "The Influence of Turbulent Structure on Optical Phase Distorsion Through Turbulent Shear Flow," AIAA Paper No. 92-2817.
[17] Childs, R., 1993, "Prediction and Control of Turbulent Aero-Optical Distorsion Using Large Eddy Simulation," AIAA Paper No. 93-2670.
[18] Born, M., and Wolf, E., 1970, *Principles of Optics, Electromagnetic Theory of Propagation, Interference and Diffraction of Light*, Pergamon, 4th ed., Oxford, UK.
[19] Sutton, G. W., 1994, "Effect of Inhomogeneous Turbulence on Imaging Through Turbulent Layers," Appl. Opt., **33**(18), pp. 3972–3976.
[20] Tatarski, V. I., 1961, *Wave Propagation in a Turbulent Medium*, McGraw-Hill, New York.
[21] Rose, W. C., and Johnson, E. A., 1982, "Unsteady Density ena Velocity Measurements in the 6×6 ft Wind Tunnel," *Progress in Astronautics and Aeronautics: Aero-Optical Phenomena*, Gilbert, K. G., and Otten, L. J., eds., Vol. **80**, AIAA, NY, pp. 218–232.
[22] Steinmetz, W. J., 1982, "Optical Degradation Due to a Thin Turbulent Layer," *Progress in Astronautics and Aeronautics Series: Aero-Optical Phenomena*, Gilbert, K. G., and Otten, L. J., eds., Vol. 80, AIAA, NY, pp. 78–100.
[23] Wolters, D.-J., 1973, "Aerodynamic Effects on Airborne Systems," M.D.D. Aircraft Company MDC A 2582.
[24] Vreman, A. W., Geurts, B. J., and Kuerten, J. G. M., 1995, "A Priori Tests of Large Eddy Simulation of the Compressible Plane Mixing Layer," J. Eng. Math., **29**, pp. 299–327.
[25] Lenormand, E., Sagaut, P., and Ta Phuoc, L., 2000, "Large-Eddy Simulation of Compressible Channel Flow at Moderate Reynolds Number," Int. J. Numer. Methods Fluids, **32**, pp. 369–406.
[26] Lund, T. S., Wu, X., and Squires, K. D., 1998, "Generation of Turbulent Inflow Data for Spatially Developing Boundary Layer Simulations," J. Comput. Phys., **140**, pp. 233–258.
[27] Sagaut, P., Garnier, E., Tromeur, E., Larchevêque, L., and Labourasse, E., 2004, "Turbulent Inflow Conditions for LES of Compressible Wall Bounded Flows," AIAA J., **42**(3), pp. 469–477.
[28] Shu, C. W., and Osher, S., 1988, "Efficient Implementation of Essentially Non-Oscillatory Shock-Capturing Schemes I," J. Comput. Phys., **77**, pp. 439–471.
[29] Sagaut, P., 2001, "Large Eddy Simulation for Incompressible Flows: An Introduction," Springer-Verlag, Scientific Computation, pp. 99–101.
[30] Thompson, K. W., 1987, "Time Dependent Boundary Conditions for Hyperbolic Systems," J. Comput. Phys., **68**, pp. 1–24.
[31] Liu, Z., Adrian, R. J., and Hanratty, T. J., 2001, "Large-Scale Modes of Turbulent Channel Flow: Transport Equation Structure," J. Fluid Mech., **448**, pp. 53–80.
[32] Chien, K. Y., 1982, "Prediction of Channel and Boundary Layer Flows with a Low-Reynolds-Number Turbulence Model," AIAA J., **20**(1), pp. 33–38.
[33] Fitzgerald, E. J., 2000, "The Shear Layer Compressibility Mechanism and its Role in Creating Aero-Optical Distortions," PhD. thesis, University of Notre Dame, Notre Dame, Indiana.
[34] Wei, H., and Chen, C. P., 1996, "A Nonequilibrium Algebraic Model for Turbulent Density Fluctuations," Int. J. Heat Mass Transfer, **39**(18), pp. 3989–3991.
[35] Urbin, G., and Knight, D., 2001, "Large-Eddy Simulation of a Supersonic Boundary Layer using an Unstructured Grid," AIAA J., **39**(7), pp. 1288–1295.
[36] Guarini, S. E., Moser, R. D., Shariff, K., and Wray, A., 2000, "Direct Numerical Simulation of a Supersonic Turbulent Boundary Layer at Mach 2.5," J. Fluid Mech., **414**, pp. 1–33.
[37] Huang, P. G., Coleman, G. N., and Bradshaw, P., 1995, "Compressible Turbulent Channel Flows: DNS Results and Modeling," J. Fluid Mech., **305**, pp. 185–218.
[38] Aupoix, B., 2003, "Prévision des Effets Aéro-Optiques en Couche Limite," RT 1/07893 DMAE, Onera, France.
[39] Sutton, G. W., Pond, J. E., Snow, R., and Hwang, Y., 1993, "Hypersonic Interceptor Performance Evaluation Center: Aero-Optics Performance Predictions," AIAA Paper No. 93-2675, *2nd Annual AIAA SDIO Interceptor Technology Conference*, June 6–9, Albuquerque, NM.
[40] Sutton, G. W., and Pond, J. E., 1998, "Aero-Optic and Aerothermal Performance of Externally Cooled Infrared Window at Hypersonic Flight Conditions," *NATO/RTA Symposium of Applied Vehicle Technology Panel on Missile Aerodynamics*, May 11–14.

Effects of Weak Free Stream Nonuniformity on Boundary Layer Transition

Jonathan H. Watmuff

School of Aerospace, Mechanical and
Manufacturing Engineering,
RMIT University,
Melbourne, Australia

Experiments are described in which well-defined weak Free Stream Nonuniformity (FSN) is introduced by placing fine wires upstream of the leading edge of a flat plate. Large amplitude spanwise thickness variations form in the boundary layer as a result of the interaction between the steady laminar wakes from the wires and the leading edge. The centerline of a region of elevated layer thickness is aligned with the centerline of the wake in the freestream and the response is shown to be remarkably sensitive to the spanwise length-scale of the wakes. The region of elevated thickness is equivalent to a long narrow low speed streak in the layer. Elevated Free Stream Turbulence (FST) levels are known to produce randomly forming arrays of long narrow low speed streaks in laminar boundary layers. Therefore the characteristics of the streaks resulting from the FSN are studied in detail in an effort to gain some insight into bypass transition that occurs at elevated FST levels. The shape factors of the profiles in the vicinity of the streak appear to be unaltered from the Blasius value, even though the magnitude of the local thickness variations are as large as 60% of that of the undisturbed layer. Regions of elevated background unsteadiness appear on either side of the streak and it is shown that they are most likely the result of small amplitude spanwise modulation of the layer thickness. The background unsteadiness shares many of the characteristics of Klebanoff modes observed at elevated FST levels. However, the layer remains laminar to the end of the test section ($R_x \approx 1.4 \times 10^6$) and there is no evidence of bursting or other phenomena associated with breakdown to turbulence. A vibrating ribbon apparatus is used to examine interactions between the streak and Tollmien-Schlichting (TS) waves. The deformation of the mean flow introduced by the streak is responsible for substantial phase and amplitude distortion of the waves and the breakdown of the distorted waves is more complex and it occurs at a lower Reynolds number than the breakdown of the K-type secondary instability that is observed when the FSN is not present. [DOI: 10.1115/1.2169813]

Introduction

Watmuff [1] reduced the background unsteadiness, u'/U_1, in a Blasius boundary layer by a *factor* of 30 by improving the flow quality of a small stand-alone wind tunnel. The effectiveness of the improvements was judged by examining contours on spanwise planes derived from hot-wire data. The contours demonstrated a form of boundary layer three-dimensionality in which locally concentrated regions of elevated background unsteadiness appeared to be correlated with small spanwise variations of the layer thickness. The characteristics of the unsteadiness in the concentrated regions were much the same as at other spanwise positions, where the distribution of the unsteadiness levels was more uniform and the Blasius wall distance of the maxima was $\eta = 2.3$. These characteristics have much in common with the Klebanoff modes observed by Klebanoff [2], Kendall [3,4], Matsubara and Alfredson [5] and Westin et al. [6] at elevated FST levels.

The most significant reductions in u'/U_1 were realized after painstaking improvements were made to the uniformity of the porosity of wind tunnel screens. During the course of the flow quality improvements, Watmuff [1] found that even almost immeasurably small FSN variations (e.g., $\Delta U/U_1 \approx 0.05\%$) appeared to be associated with local concentrations of elevated unsteadiness. During the final stages of the flow quality improvements, further improvements to the screen system pro-

duced only a relatively minor reduction in the FST level, but the additional decrease in the FSN led to a threefold reduction of u'/U_1 within the layer.

It is almost certain that the small FSN variations are caused by minor imperfections in the weave of the screen cloth. For example, Watmuff measured the uniformity of the screens by scanning them between a fixed laser and photo detector pair. He found the peak u'/U_1 levels in the layer were reduced by a factor of 1.5 after the same screens were reordered from least to most uniform with x, based on the results of the laser scans.

Insertion of FSN Upstream of the Flat Plate

The extraordinary sensitivity to weak FSN encouraged the author to develop a means of introducing FSN for the purpose of deliberately embedding Klebanoff-modelike features into the boundary layer. The technique consists of stretching a fine wire across the full-width of the test section at a position upstream of the leading edge. The wire is aligned perpendicular to the free stream and to the leading edge.

The motivation for the study was wholly based on the observations made during the painstaking flow quality improvements, i.e., that boundary layer phenomena resulting from FSN may be somehow related to phenomena resulting from elevated FST levels. Consequently, the study might provide some insight into physical processes that occur during bypass transition. The advantage of the technique is that the appearance of the resultant mean flow three-dimensionality and the elevated background unsteadiness in the boundary layer can be easily controlled. By forcing the disturbances to appear at specific spanwise positions of relatively nar-

Table 1 Properties for wires located in test section

| Case	d μm	R_d	C_D	x/d
1T	25.4	17.0	2.17	16,250
2T	25.4	17.0	2.17	7,250
3T	50.8	33.9	1.62	8,125
4T	50.8	33.9	1.62	3,625
5T	101.6	67.9	1.29	1,813

Fig. 1 Spanwise profiles of mean velocity and background unsteadiness for wakes generated by wires located in test section, measured 63.5 mm upstream of leading edge: (*a*) and (*d*) $d=25.4$ μm (case 2*T*); (*b*) and (*e*) $d=50.8$ μm (case 4*T*); (*f*) $d=101.6$ μm (case 5*T*)

row extent, their properties and their interactions with other forms of disturbances, such as TS waves, can be studied in detail.

At the time these experiments were conceived, the author was unaware of the numerical studies by Goldstein and co-workers [7–9] concerning the receptivity to spanwise vorticity in the free-stream. Their work is unique, in the sense that they are the only investigators who have attempted to account for Klebanoff modes as a result of the interaction of free-stream vorticity with the leading edge.

A range of wire diameters, at varying distances from the leading edge has been considered. Kogan et al. [10] also used a wire upstream of the leading edge of a flat plate to generate vortical disturbances which then interacted with the leading edge to introduce disturbances into the boundary layer. However, in their work the Reynolds number based on wire diameter, $R_d=10^5$, leading to unsteady vortex shedding from the wire. At the outset of the present work it was considered essential to introduce only a mean flow disturbance into the free-stream, to avoid additional competing effects that might occur if additional unsteadiness was also introduced, e.g., vortex shedding from the wires could excite extraneous instabilities in the layer. The parameters for wires located in the test section are specified in Table 1, while the effect of weaker FSN produced by wires located upstream of the contraction are specified in Table 2.

Representative mean velocity profiles of the wakes are shown in Figs. 1(*a*)–1(*c*). The profiles were obtained at a position 63.5 mm upstream of the leading edge, which was considered to be far enough upstream to avoid any distortion introduced by deceleration of the flow approaching the leading edge. The velocity defect was measured using a flattened total pressure tube which was connected directly to a sensitive differential pressure transducer and the total pressure from a fixed Pitot-static tube was

Table 2 Properties for wires located upstream of contraction

Case	d μm	R_d	x/d
1U	50.8	6.8	45,000
2U	101.6	13.6	22,500
3U	152.4	20.4	15,000
4U	254.0	33.9	9,000
5U	558.8	74.7	4,091
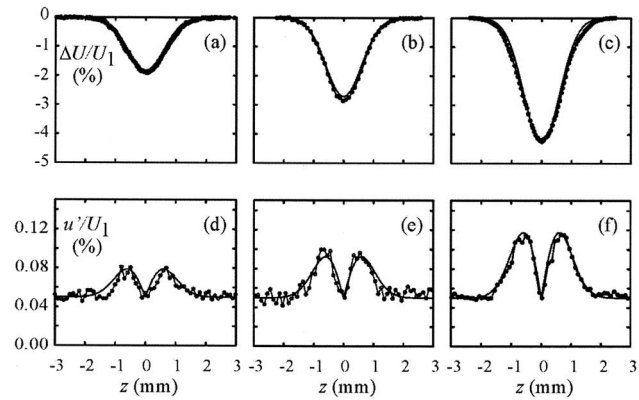
used as the reference pressure. The velocity distribution was calculated by assuming that the total pressure variations are entirely attributable to differences in dynamic pressure.

Linearizing the convective terms in the equations of motion results in a simple diffusion equation, leading to the following expression for the velocity defect of a laminar wake,

$$\frac{U_1 - U}{U_1} = C_D \left(\frac{R_d}{16\pi} \right)^{1/2} \left(\frac{d}{x} \right)^{1/2} \exp \left(-\frac{U_1 z^2}{4\nu x} \right), \tag{1}$$

where x is the streamwise distance from the wire, z is the spanwise distance from the centerline, R_d is the Reynolds number based on wire diameter, d, and free-stream velocity, U_1, and C_D is the drag coefficient. The solid lines in Figs. 1(*a*)–1(*c*) have been calculated from Eq. (1). The agreement of the observations with Eq. (1) is excellent. A similar level of agreement is observed for the wakes generated by wires located further upstream of the leading edge.

Figures 1(*d*)–1(*f*) show u'/U_1 profiles obtained with a normal hot wire. For these measurements, the filament of the wire was aligned parallel to the wire generating the wake. The elevated unsteadiness in the wakes initially caused some concern. However most of the energy content is below 10 Hz and the u'/U_1 maxima coincide with maxima in the spanwise mean velocity gradient. The solid lines have been calculated by assuming that the spanwise location of the wake as a whole, relative to a fixed probe, is given by a Gaussian PDF with standard deviation, $\sigma_z = 15$ μm. Spectral measurements support the contention that the elevated u'/U_1 levels are "fictitious," in the sense that the elevated levels are not the result of eddying motions. Instead, the small standard deviation required to model the background unsteadiness and the low frequency content of the hot-wire signals suggests that mechanical vibration may be responsible for the observations.

The wires located upstream of the contraction are 2.286 m from the leading edge and 150 mm downstream of the last wind tunnel screen. The spanwise mean velocity profiles of wakes generated by these wires are shown in Fig. 2, together with the base flow profile, i.e., without a wire. Profiles of the background unsteadiness were also measured and the distribution is essentially the same as without the presence of the wires.

Properties of Base-Flow Boundary Layer

The spanwise uniformity of the base-flow boundary layer at $x = 1.05$ m, i.e., $R(=R_x^{1/2})=837.5$, is shown in Fig. 3. The displacement thickness, δ_1, is within ±1.5% of the theoretical value, except in the range $0 > z > -10$ mm, where δ_1 increases to be about
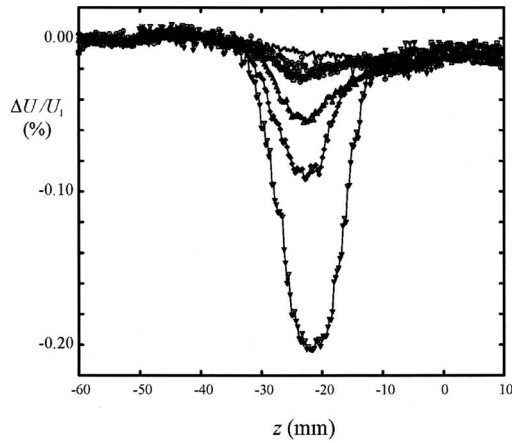
Fig. 2 Spanwise velocity profiles of wakes generated by wires located upstream of contraction, measured 63.5 mm upstream of leading edge: Undisturbed flow; $d=50.8$ μm (case 1U); $d=101.6$ μm (case 2U); $d=152.4$ μm (case 3U); $d=254$ μm (case 4U); and $d=559$ μm (case 5U)

3% larger than the Blasius value. The shape factor, H, is uniform to within $\pm1\%$ and the smaller variations are considered to be random errors introduced by hot-wire calibration drift or by small uncertainties in the wall distance. The contours in Fig. 3(d) demonstrate the low overall background unsteadiness level in the layer, i.e., $u'/U_1 < 0.08\%$. It should be noted that the hot-wire signals are unfiltered and no allowance has been made for electronic noise. The hot-wire anemometers used for this study are described in detail by Watmuff [11]. Great care was taken with the design and layout of the circuit board to minimize noise. For example, the rms output noise level is only about 2 mV when the wire is located inside a container to avoid background draughts. Taking the electronic noise into account it is estimated that the peak background unsteadiness level in the layer, $u'/U_1 < 0.05\%$. The noise would have negligible influence on the phase-averaged measurements since the noise can be considered a random signal and it will be removed by the ensemble averaging process.

Effects of FSN on Boundary Layer

The FSN introduced by the wires leads to a form of three-dimensionality and a pair of locally concentrated regions of el-
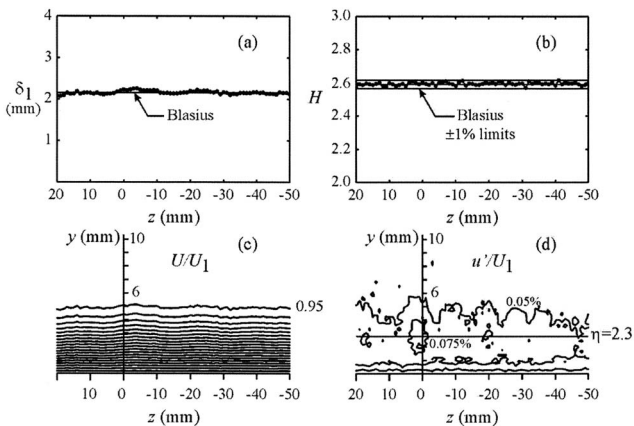

Fig. 3 Spanwise uniformity of base-flow Blasius boundary layer in plane $x=1.05$ m, R $(=R_x^{1/2})=837.5$: (a) displacement thickness, δ_1; (b) shape factor, H; (c) contours of mean velocity, U/U_1; (d) contours of background unsteadiness, u'/U_1
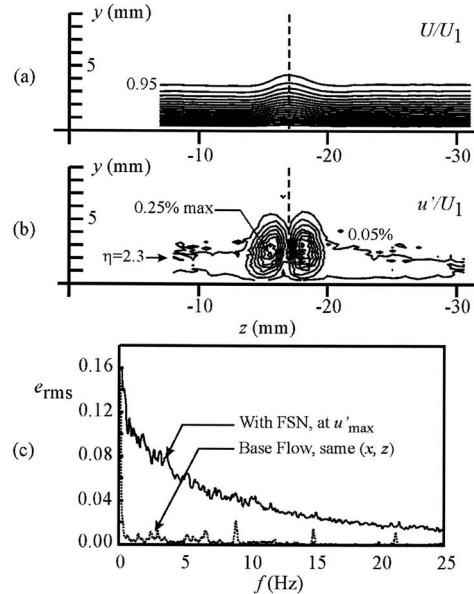

Fig. 4 Effect of low speed streak introduced by FSN. Case 2T, $d=25$ μm wire, spanwise plane at $R=641$ ($x=0.615$ m): (a) contours of mean velocity, U/U_1; (b) contours of background unsteadiness, u'/U_1; (c) power spectra with and without streak

evated background unsteadiness as shown in Figs. 4(a)–4(c). For this case, the FSN is generated by the $d=25$ μm wire (case 2T) and the spanwise plane is located at $R=641$ ($x=0.615$ m). Contours of a similar but weaker form were observed before and at each stage during the flow quality improvements (see Watmuff [1]). The characteristics of u'/U_1 also have much in common with Klebanoff modes appearing at elevated FST levels (Klebanoff [2], Kendall [3,4] and others [5,6]). For example, the two maxima in the background unsteadiness contours are located at the Blasius wall distance of $\eta \approx 2.3$. Furthermore, the elevated background unsteadiness occurs at low frequencies, as shown in Fig. 4(c). The frequency corresponding to branch I of the neutral stability curve at this streamwise position is $f \approx 50$ Hz. It is evident that most of the unsteadiness resulting from the presence of the streak occurs at frequencies much lower than that predicted by classical linear stability theory.

The characteristics of the streaks resulting from the FSN introduced by the wires located in the test section and wires located upstream of the contraction are shown in Figs. 5 and 6, respectively. Both data sets were obtained in the same plane as the results shown in Fig. 3. The velocity defect of wakes generated by wires located upstream of contraction are between one and two orders-of-magnitude smaller than the wakes generated by wires located in the test section, while the width of the distribution is nearly an order-of-magnitude larger. Despite the substantially smaller amplitudes, the increased influence on the boundary layer must be wholly attributed to the increased width of the wakes. The observations suggest that there is a preferred spanwise wavelength for the appearance of mean flow (or slowly varying) disturbances in the boundary layer, and that some mean-flow receptivity mechanism is associated with the FSN at the leading edge.

The spanwise variation of the shape factor, H, in Fig. 5 is within the $\pm1\%$ uncertainty limits of the Blasius value. A slight reduction in shape factor is evident for the largest diameter wire in Fig. 5(c). The insensitivity of H is also evident when the FSN is introduced by wires upstream of the contraction, as shown in Fig. 6. There is only about a 4% reduction in H for the largest diameter wire in Fig. 6(c), despite an approximately 60% increase in the boundary layer thickness. A reduction in H is generally associated with decreased stability of boundary layers, e.g., adverse pressure
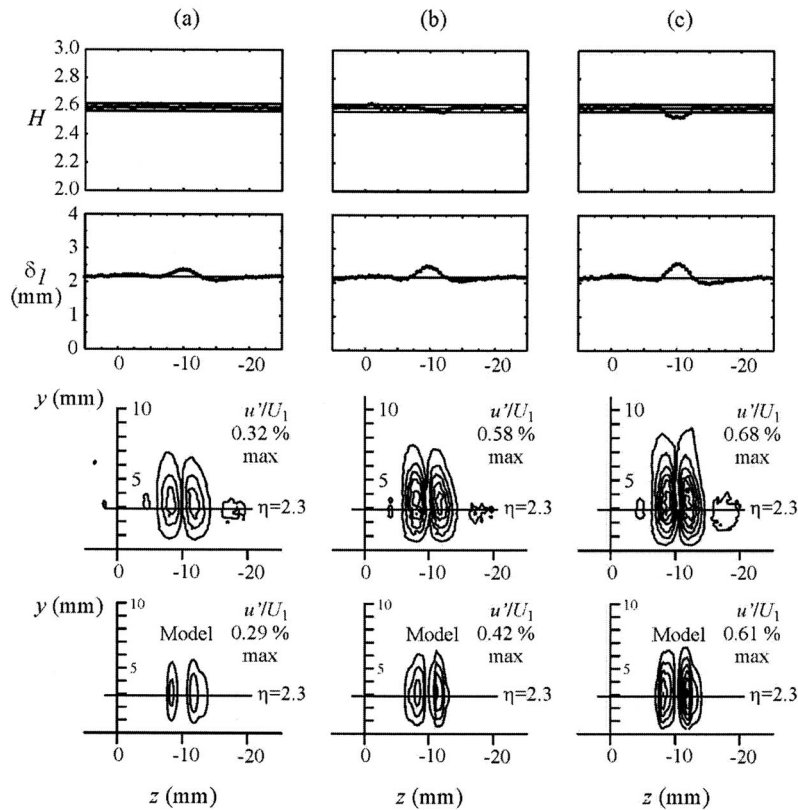
Fig. 5 Characteristics of low speed streaks introduced by FSN generated by wires located in the test section. Measurements in plane at $x = 1.05$ m, $R = 837.5$: (a) $d = 25.4$ μm (case 2T); (b) $d = 50.8$ μm (case 4T); (c) $d = 101.6$ μm (case 5T). Lines $\eta = 2.3$ correspond to the Blasius layer.

gradient. Examination of individual profiles in the vicinity of the H minima does not reveal an inflection point, even close to the test surface.

Klebanoff [2] suggested that the elevated layer unsteadiness at moderate FST levels could be the result of relatively small amplitude modulation of the layer thickness. The Blasius solution can be written, $U/U_1 = f'(\eta) = f'(y/\delta_0)$, where $\delta_0 = (xv/U_1)^{1/2}$ is a measure of the layer thickness. The effect of a small perturbation, δ_P, in thickness can be expressed as a Taylor series, i.e.

$$\frac{U}{U_1} = f'\left(\frac{y}{\delta_0 + \delta_p}\right) = f'(\eta) - \frac{\delta_P}{\delta_0}\eta f''(\eta) + \cdots \quad (2)$$

The difference between U/U_1 resulting from the perturbed thickness and the Blasius solution should be proportional to $\eta f''$, which leads to excellent agreement with Klebanoff's measurements (see Goldstein and Wundrow [9]).

This idea was presumably based on an earlier proposal by Bradshaw [12], which was subject to analytical treatment by Crow [13]. The more general analyses of Goldstein, Leib, and Cowley [7], Goldstein and Lieb [8], and Goldstein and Wundrow [9] incorporate spanwise periodic variation of U_1 and include the effects of bluntness of the leading edge. Goldstein and Leib use the results to accurately predict the form of unsteadiness profiles measured by Klebanoff [2], and Kendall [3,4]. On the basis of the agreement with the measurements, Goldstein and co-workers argue that there is a direct connection between the disturbances resulting from the FSN in their calculations and the Klebanoff modes observed at elevated FST levels.

Evidently the Klebanoff modes are of such a low enough frequency that they can be considered quasisteady and they may be approximated by a steady solution. Nevertheless, it is clear that

the perturbation in layer thickness, δ_P, must vary with time in order for Eq. (2) to account for the observations. Therefore the form of the unsteadiness is an important consideration for establishing a correspondence with the measurements. However, the author is not aware of any considerations that have led to a proposal concerning plausible forms of the δ_P variations.

The spanwise uniformity of the shape factor, H, shown in Figs. 5 and 6 indicates that the complete distribution of streamwise mean-velocity component in a spanwise plane can be determined by specifying the spanwise variation of the displacement thickness. Using this simple empirical model, the velocity at any (y,z) position can be determined by interpolating $\delta_1(z)$ from a spline fit, for example, and then evaluating the local Blasius coordinate, using $\eta(y,z) = 1.7208 y/\delta_1(z)$. The local streamwise velocity $U(y,z)/U_1$ can then be determined for $\eta(y,z)$ from an interpolation of the Blasius solution.

The model described above has been used to explore the effects of small-amplitude modulations of the base flow, in an attempt to provide an explanation for the observations shown in Figs. 5 and 6. A smooth spanwise variation of δ_1 is assumed for the "steady" base flow as shown in Fig. 7(a). The distribution is shown in dimensional form and it has been chosen to approximate the conditions corresponding to the results shown in Figs. 5 and 6, i.e., at the extremities of the span, $\delta_1 = 2.157$ mm, which corresponds with the Blasius value for, $x = 1.05$ m, and the unit Reynolds number, 0.668×10^6 m^{-1}, used in the experiments. The spanwise variation of δ_1 has an overshoot of 12% on the centerline and a small magnitude undershoot is imposed on either side, of approximately -3%, before recovery to the unperturbed Blasius value. These features are also evident in the measurements.
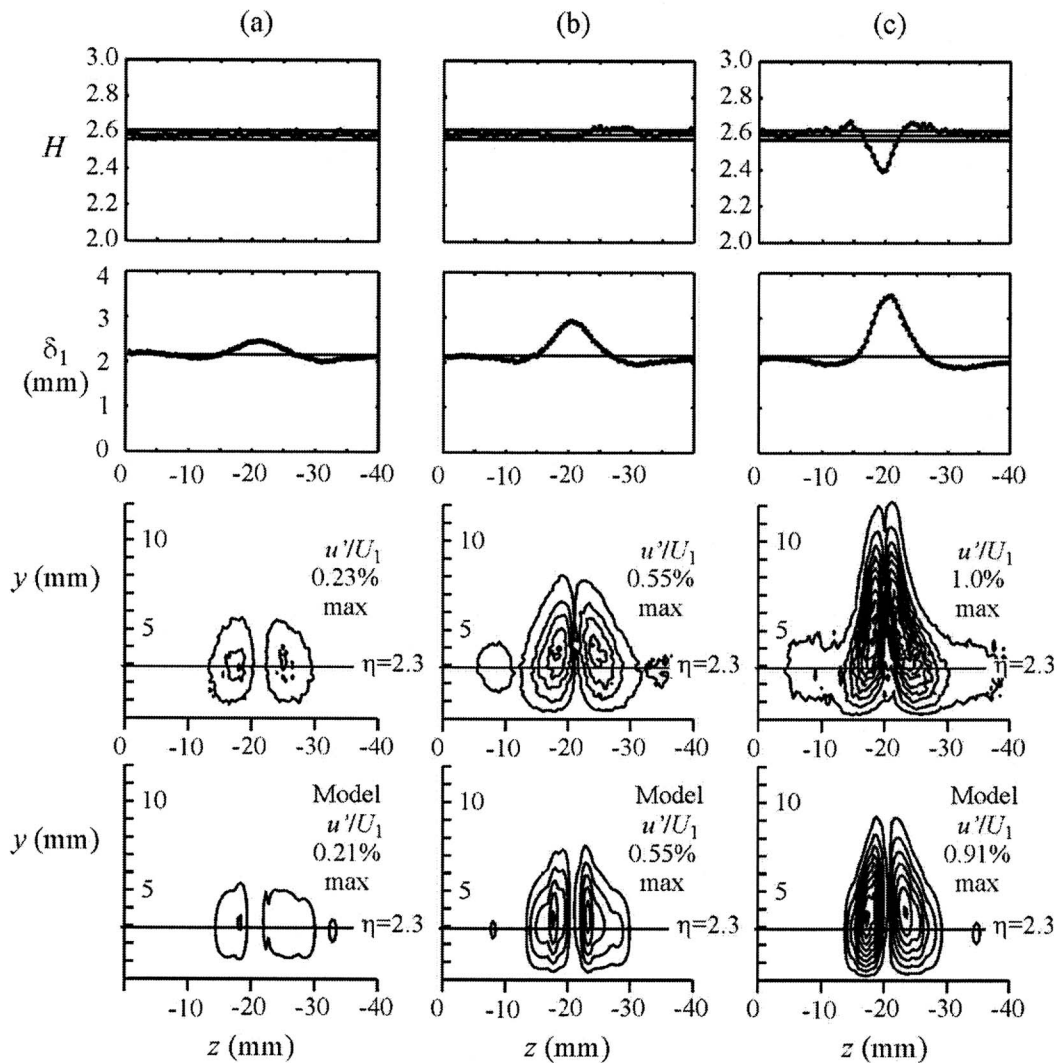
Fig. 6 Characteristics of low speed streaks introduced by FSN generated by wires located upstream of contraction. Measurements in plane $x=1.05$ m, $R=837.5$: (a) $d=50.8$ μm (case 1U); (b) $d=254$ μm (case 4U); and (c) $d=559$ μm (case 5U). Lines $\eta=2.3$ correspond to the Blasius layer.

The mathematical form of the spanwise δ_1 variation is not critical for the model, provided it is smooth. It is convenient to generate the δ_1 distribution by summing two Gaussian distributions; one for the positive and the other for the negative contribution. Contours of the mean flow, U/U_1, and the spanwise derivative, $\partial(U/U_1)/\partial z$ are also shown for the base flow in Fig. 7(a). For the purposes of the modeling, the mean-velocity distribution will be considered to be two-dimensional, i.e., without streamwise derivatives.

For the wakes, the elevated background unsteadiness in the free stream was successfully modeled by applying a Gaussian PDF to the spanwise position of the mean velocity profile. While the variation of δ_1 depends only on the spanwise position, it is clear that gradients of the mean velocity in the layer will exist in both the y- and z-directions. Therefore the effects of varying both the strength and the spanwise position of the δ_1 perturbation are considered. Variations in the strength of the δ_1 perturbation might arise if the FSN was fixed in position but the magnitude of the velocity defect was to vary with time. Variations in the spanwise position of the δ_1 perturbation could arise from corresponding variations in the spanwise position of the FSN with time.

The effect of varying magnitude is modeled by applying a Gaussian PDF to the strength of the δ_1 perturbation, with a stan-

dard deviation given by $\sigma_{\delta_1}/\delta_1=10\%$. The effect of the δ_1 modulation on the mean flow is very small and the contours of U/U_1 in Fig. 7(b) are almost identical to the base flow. The RMS unsteadiness distribution, u'/U_1 in Fig. 7(b), resulting from the δ_1 modulation, shows that the maximum is located on the centerline. Larger values of $\sigma_{\delta_1}/\delta_1$, lead to much the same form of distribution for u'/U_1, i.e., the maximum corresponds with the mean value of the PDF, i.e., the centerline.

The effect of spanwise modulation is modeled by applying a Gaussian PDF to the spanwise position of the δ_1 perturbation. The results for a standard deviation given by, $\sigma_z=200$ μm (approximately 10% δ_1) are shown in Fig. 7(c). Again, the effect of the PDF on the mean flow is very small. The amplitude of σ_z was chosen to generate approximately the same u'/U_1 maximum as for δ_1 perturbation in Fig. 7(b). While the peak u'/U_1 levels may be similar, the distribution in Fig. 7(c) is markedly different. In this case, there are two concentrated regions of elevated amplitude on either side of the centerline, and the magnitude on the centerline is almost zero. The overall similarity between the form and the levels of the u'/U_1 contours in Fig. 7(c) and the experimental observations in Figs. 5 and 6 support the conjecture that the el-
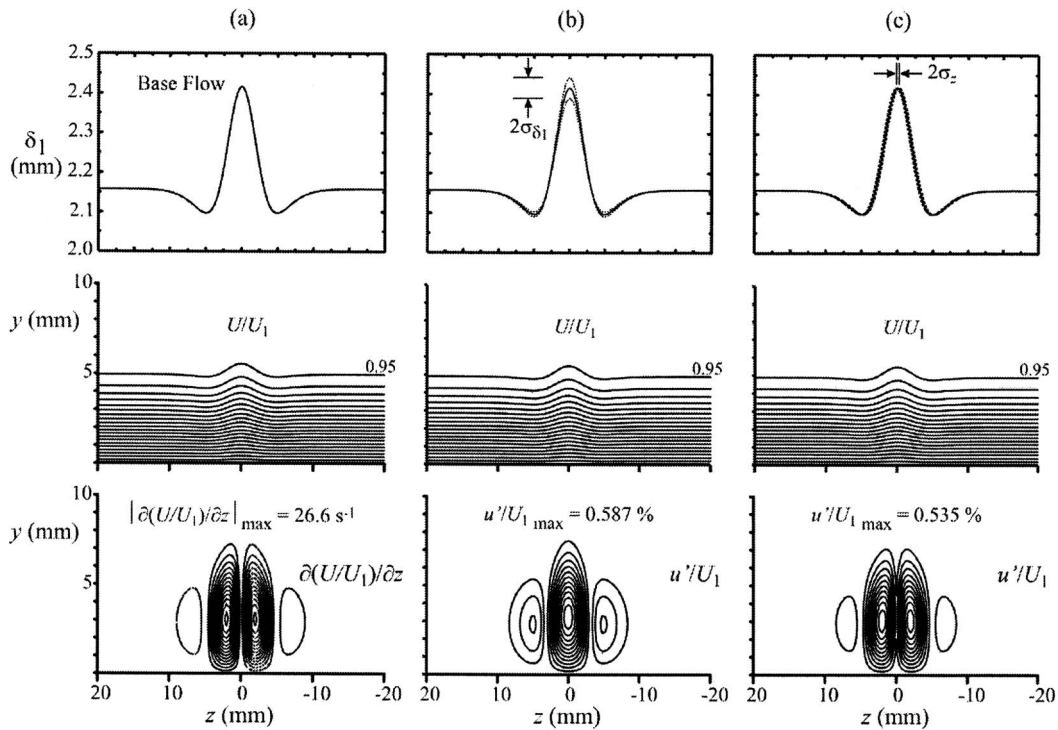
Fig. 7 Modulation of the Blasius boundary layer with spanwise thickness variation but constant shape factor, H: (a) base flow; (b) modulation of magnitude; (c) modulation of spanwise position

evated unsteadiness levels are the result of boundary layer thickness variations in the vicinity of the stationary probe, which arise from small-amplitude low frequency *spanwise modulation* of the boundary layer thickness.

Cubic-spline fits to the observed spanwise δ_1 variations are shown as solid lines in Figs. 5 and 6. Numerical experiments have been conducted to determine the value of σ_z, which produces a modeled u'/U_1 distribution that most closely matches the measurements, where an allowance has been made for the background component without the presence of wires of magnitude u'/U_1 =0.05%. For the spanwise δ_1 variations resulting from wires located in the test section, a value of σ_z=90 μm has been found to closely match the u'/U_1 observations, while for the wires located upstream of the contraction, a value of σ_z=120 μm is required, i.e., about 30% larger. These results are shown in Figs. 5 and 6 and are labeled "Model." The values of σ_z required to reproduce the u'/U_1 levels in the boundary layer is order 4% of the displacement thickness, which is remarkably small.

The σ_z required to reproduce the u'/U_1 levels resulting from wires located in the test section shown in Fig. 5 is about six times larger than that required to reproduce the free-stream u'/U_1 wake profiles shown in Fig. 1. Therefore it is unlikely that the elevated unsteadiness in the boundary layer can be totally accounted for by spanwise oscillations of the mean flow pattern that merely "follow" the instantaneous spanwise position of the wake. The larger amplitude modulation required for the boundary layer simulation may indicate that some unaccounted form of instability mechanism is at play. For example, the mean flow pattern may be the result of a pair of counter-rotating streamwise vortices and the spanwise modulation of the mean flow could be associated with long-wavelength low-frequency small-amplitude spanwise modulation of the strength and/or the position of the vortex pair.

A measure of the integrated effect of the FSN on the development of the boundary-layer mean flow is the growth of δ_1 relative to the Blasius value. Determination of the spanwise δ_1 variations by integration of y-profile measurements, using a grid resolution

corresponding to the results of the six cases shown in Figs. 5 and 6, at 16 streamwise positions, for example, would require accurate mean-flow hot-wire measurements at approximately 2.8×10^5 data points. The measurements would then need to be followed by the painstaking analysis of the 6.8×10^3 individual profiles. Such a task was considered to be too daunting.

An alternative and more approximate method was used to estimate the growth of the δ_1 variations, which only requires the quantity U/U_1 to be determined along a single spanwise profile at fixed wall distance, at each streamwise position, for each case. The Blasius wall distance, $\eta(z)$, is interpolated from each U/U_1 measurement at each data point, by interpolation of the known Blasius solution. The displacement thickness variation is then calculated using, $\delta_1(z)=1.7208 y_p/\eta(z)$, where y_p is the distance of the hot-wire filament from the test surface. The streamwise development of the spanwise variation of δ_1 calculated from the spanwise profiles is shown for all six cases in Fig. 8. The z-coordinate is relative to the peak δ_1 at each streamwise position. A small spanwise shift in the peak δ_1 is evident in the results, corresponding to about 7.5 mm over the streamwise range used for the measurements (1.5 m).

The basis of the method for the determination of the δ_1 variation from the spanwise profiles is the assumption of spanwise uniformity of the shape factor, H, which has not been determined at these positions. Nevertheless, comparison of cursory test results obtained at x=1.05 m indicated that δ_1 estimated from the spanwise profiles, compared surprisingly well with the δ_1 obtained by integration of the mean-velocity profiles shown in Figs. 5 and 6. Overall, the estimated δ_1 estimates were found to be within about ±5% of the values obtained by integration of the mean-velocity profiles.

It is possible that the phenomena responsible for the spanwise thickness variations may exist only in the vicinity of the leading edge. In this case, the elevated thickness relative to the undisturbed layer might be expected to decrease with streamwise dis-
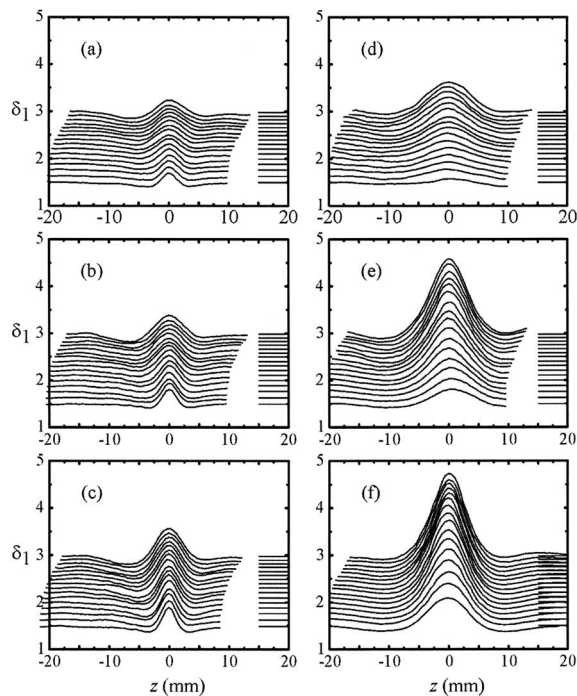
Fig. 8 Streamwise development of the spanwise variation of displacement thickness. Wires located in the test section: (a) d=25.4 μm (case 2T); (b) d=50.8 μm (case 4T); (c) d =101.6 μm (case 5T). Wires located upstream of contraction: (d) d=50.8 μm (case 1U); (e) d=254 μm (case 4U); and (f) d =559 μm (case 5U). Lines shown in range $15<z<20$ indicate corresponding Blasius values, i.e., $\delta_1=1.7208(v_x/U_1)^{1/2}$.

Fig. 9 Development of minimum and maximum of spanwise displacement thickness variation. (a) Wires located in test section: d=25.4 μm (case 2T), d=50.8 μm (case 4T) and d =101.6 μm (case 5T). (b) Wires located upstream of contraction: d=50.8 μm (case 1U), d=254 μm (case 4U), and d =559 μm (case 5U).

tance, owing to viscous diffusion, for example. On the other hand, growth of the spanwise thickness variations with streamwise distance would indicate that the phenomena responsible for the spanwise thickness variations persist in the downstream boundary layer. The development with R of the maximum and minimum δ_1 across the layer is shown in Fig. 9. For all cases with wires located in the test section, Fig. 9(a), the effect of the FSN on the mean flow is such that the growth rates of the δ_1 extrema are much the same as the undisturbed Blasius boundary layer.

This observation still suggests that the phenomena responsible for the spanwise thickness variations is present in the downstream boundary layer, but that some equilibrium condition may be at play to balance a decrease of the thickness extrema with streamwise distance, e.g., owing to viscous diffusion. In contrast, the FSN generated by wires located upstream of the contraction, shown in Fig. 9(b), has a much stronger effect. While the growth rates of the δ_1 minima appear to be much the same as for the undisturbed Blasius boundary layer, it is evident that the growth rates of the δ_1 maxima are much larger. The growth rate for the Cases 1U and 4U appear to be reasonably constant while that for case 5U appears to diminish with R. It is unknown whether the apparent reduction in the growth rate for this case is associated with errors introduced by a significant reduction of the shape factor with R. Evidently, for the FSN generated by the wires located upstream of the contraction, the phenomena responsible for the spanwise thickness variations clearly maintain their presence in the downstream boundary layer.

Another feature of Klebanoff modes generated by elevated FST levels is that the growth of u'/U_1 with streamwise distance appears to be algebraic rather than exponential. Kendall [4] reports that the growth varies as $x^{1/2}$ for FST generated by a turbulence grid. Westin et al. [6] present measurements from their own investigations and by others concerned with elevated FST levels that
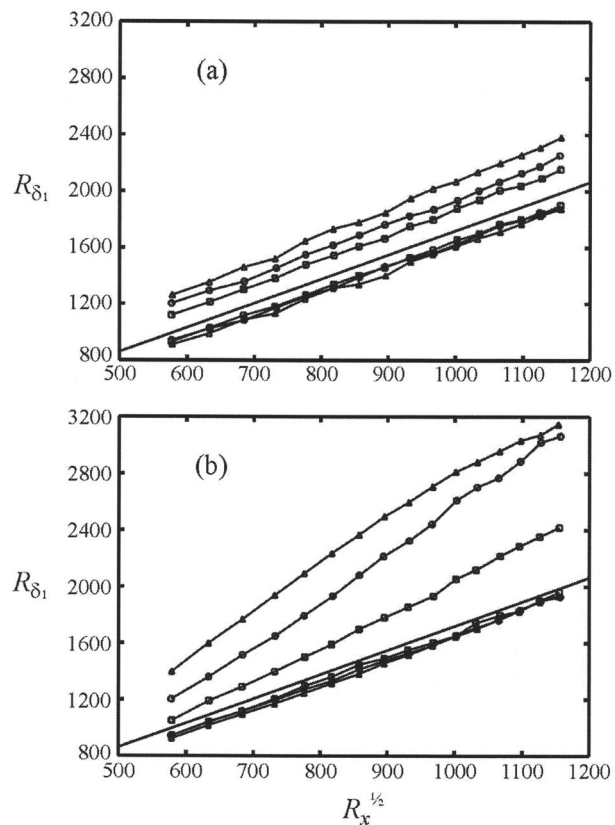
tend to support Kendall's observations. However, the growth rate appears to vary from facility to facility, i.e., there is disagreement concerning the factor of proportionality. Bertolotti and Kendall [14] suggest that one possible reason for the discrepancies is that the Klebanoff modes are associated with the exceedingly low frequency components and that some form of ac-coupling of the hot-wire signal may have been employed. They point out that details concerning the signal processing are often unreported in the literature. Also, the low frequency components require much longer sampling periods than usual for accurate resolution. The author suggests that an alternative explanation for the variance of the factor of proportionally may be that each facility incorporates a different leading edge. Differences in the leading edge geometry combined with the facility dependent FST characteristics are probably a more likely source of the variance in the factor of proportionality.

The growth with Reynolds number of u'/U_1 resulting from FSN introduced by wires in the present work has been determined from hot-wire measurements obtained along a series of spanwise profiles, at a wall distance closely corresponding to the maxima in the background unsteadiness. Separate measurement grids were designed for each case, on the basis of cursory measurements at various streamwise positions. Allowing the wall distance of the measurement grids to grow with $x^{1/2}$ was found to generate grids that pass closely through the locations of the u'/U_1 maxima. The growth of the background unsteadiness in the layer resulting from the FSN introduced by the wires located in the test section is shown in Fig. 10(a) and the growth resulting from FSN introduced by wires located upstream of the contraction is shown in
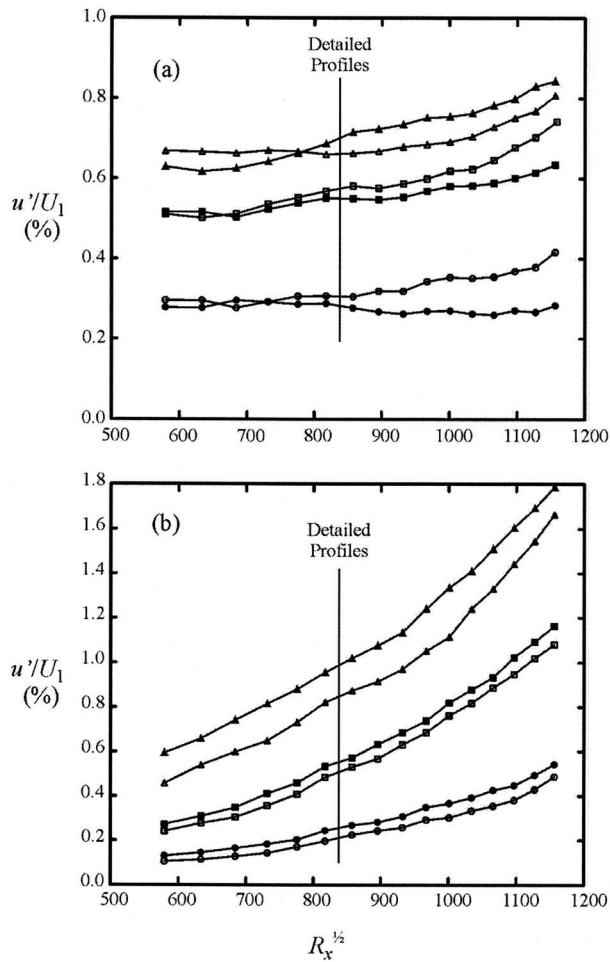
Fig. 10 Growth of peak background disturbance levels. (*a*) Wires located in test section: *d*=25.4 μm (case 2*T*), *d*=50.8 μm (case 4*T*), and *d*=101.6 μm (case 5*T*). (*b*) Wires located upstream of contraction: *d*=50.8 μm (case 1*U*), *d*=254 μm (case 4*U*), and *d*=559 μm (case 5*U*).

Fig. 10(*b*). The growth for both peaks in the background unsteadiness (i.e., at the two spanwise positions) is also shown.

The growth of the peak background unsteadiness levels associated with FSN introduced by the wires located in the test section is weak. For the smallest diameter wire (case 2*T*), the amplitude remains almost constant, with the second peak in the distribution showing a slight decay. For the larger diameter wires, the growth is positive, but still very weak. The growth associated with FSN generated by wires located upstream of the contraction is larger and weakly nonlinear, with an increasing growth rate for larger *R*. The growth rate for the FSN generated by the largest diameter wire is approximately three times larger than that for the smallest diameter wire. The effect on the layer of the FSN originating from wires upstream of the contraction appears to more closely follow the behavior observed for Klebanoff modes at elevated FST levels. Nevertheless the growth does not follow the $x^{1/2}$ variation for FST generated by a turbulence grid that has been confirmed by Matsubara and Alfredson [5] and Westin et al. [6]. Evidently the streak in the present study is stable, presumably because it forms an isolated instance.

Further downstream, at the position where detailed boundary layer measurements have been made, i.e. *x*=1.05 m, the relation given in Eq. (1) indicates that the peak velocity defect is 0.13%, 0.16%, and 0.21% of the freestream velocity for cases 2*T*, 4*T*, and 5*T* respectively, and that the width of the wakes, based on 1% of

the maximum velocity defect, is given by, $\delta_z = \pm 35$ mm. The small magnitude of the velocity defect and the relatively large spanwise extent of the wakes, suggests that the vorticity in the wakes in the outer flow be very small at this location, so that the influence of the FSN on the boundary layer developing downstream of the leading edge is likely to be insignificant.

The stability of the low speed streaks is surprising, considering that they are associated with a local increase of layer thickness that is up to 60% larger than the surrounding flow. Although the use of different wire diameters generates a range of wake strengths, it should be noted that only two spanwise length scales have been considered for the FSN in this paper owing to the experimental difficulty of controlling the spanwise length scale. The sensitivity of the response to the spanwise length-scale has been noted previously and it is likely that there is a spanwise length scale for the FSN that will generate a stronger response of the layer. It is possible that the streak would be unstable for this condition.

Interaction Between Phenomena Resulting from FSN and Tollmien-Schlichting Waves

The boundary layer disturbances resulting from the FSN have always been observed to remain stable, provided that disturbances in the form of Tollmien-Schlichting (TS) waves are not deliberately introduced into the layer. Stability has been observed, even at higher free-stream velocities, such as $U_1 = 15$ ms^{-1}. Only very occasional bursting has been observed at these higher free-stream velocities, and only towards the end test plate, *x*=2.1 m, for U_1 =15 ms^{-1}, where the Reynolds number based on streamwise distance is given by $R_x \approx 2.1 \times 10^6$, i.e., $R \approx 1450$.

Boiko et al. [15] showed that the combination of ribbon generated TS waves and grid generated FST leads to transition at lower Reynolds numbers than when the FST is present alone. However the observations are paradoxical since the growth of the peak wave amplitude appears to be diminished compared to the case where the grid generated FST is not present. A plausible resolution of this paradox is that phase jitter (introduced by cycle-to-cycle variability in the spanwise location of the streaks) results in washout of the phase-averaged wave amplitudes, while the amplitude of discrete waves might actually be larger than without the FST. This scenario is complicated by the additional buffeting associated with the vortical motions in the FST on the fully established layer. Nevertheless, the interactions between streaks and TS waves may help to provide a partial explanation of bypass transition at elevated FST levels.

Following the observations of Boiko et al. [15] the vibrating ribbon technique is used to explore the interactions between TS waves and the phenomena resulting from the FSN. The operating point is given by $F = 2\pi f \nu / U_1^2 = 60 \times 10^{-6}$ and $R=524$, where f is the frequency. The hot-wire signals are averaged on the basis of the phase of the ribbon vibration using 64 phase intervals. It is assumed that each velocity measurement can be described using $U = \bar{U} + u_\phi + u''_\phi$, where $\bar{U}$ is the temporal mean velocity, u_ϕ is the phase-averaged fluctuation about the mean and u''_ϕ is the random fluctuation. For consistency with the transition literature, the term, u, will be used to represent wave amplitude, defined as the RMS of u_ϕ over all phase intervals. The quantity $\overline{u''^2}_\phi$ represents the background unsteadiness at constant phase. The term u'' is defined as the RMS value using all phases.

In the base flow, the growth of RMS wave amplitude, u/U_1, closely follows the predicted growth with *R* obtained using the parabolized stability equations (kindly provided by F. Bertolotti). Extensive spanwise measurements also demonstrate that the waves are highly 2D for $u/U_1 < 1.0\%$. The onset of *K*-type secondary instability occurs for larger u/U_1 (Herbert [16]) followed by the formation of Λ-shaped vortex loops, increased randomness and ultimately the demise to fully turbulent flow.
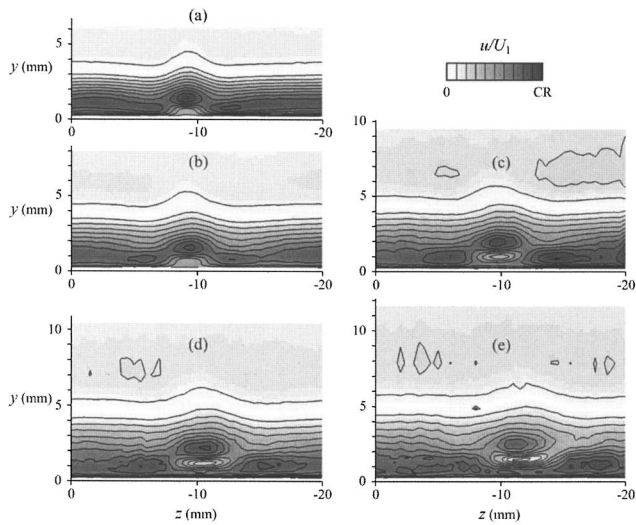
Fig. 11 Interaction of small-amplitude TS waves with disturbance generated by the $d=50.8$ μm wire located in the test section (case $4T$). Contours of rms wave amplitude, u/U_1, in the spanwise plane, with increasing R (streamwise distance). Ribbon amplitude adjusted to ensure $0.1 < u/U_1 < 0.5$%. (a) $R=659.0$, $u_{max}=0.44$%; (b) $R=707.8$, $u_{max}=0.30$%; (c) $R=837.5$, $u_{max}=0.22$%; (d) $R=913.8$, $u_{max}=0.11$%; (e) $R=1017.5$, $u_{max}=0.20$%, (u_{max} defines legend).

Fig. 12 Plan view of pseudo-flow contour surfaces of wave amplitude, u_ϕ/U_1, and contour lines of u_ϕ/U_1 and background unsteadiness u''/U_1 for $R=837.5$. (a) K-type instability in base flow. (b) Same ribbon amplitude, but with FSN, $d=101.5$ μm wire in the test section (case $5T$). Dark surfaces: $u_\phi/U_1=-2.5$%. Light surfaces: $u_\phi/U_1=+2.5$%. Contour lines in plane $y=1.2$ mm. For u_ϕ/U_1, CR$=\pm6.25$%, CI$=0.5$%, black lines are positive and gray lines negative levels. For u''/U_1, CR$=\pm0.60$%, CI$=0.05$%. CR is contour range and CI is the contour increment.

Introduction of the FSN leads to considerable phase and amplitude distortion of the TS waves. However, for small wave amplitudes, e.g., $u/U_1<1.0$%, the distortion is benign in the sense that the streamwise development of contours of u/U_1, in a spanwise plane maintain much the same shape and form. Figure 11 shows contours of rms wave amplitude resulting from interaction of small-amplitude waves with disturbance introduced by the FSN generated by the $d=50.8$ μm wire, case $4T$. The measurements are shown in a series of spanwise planes with increasing R. The largest R, shown Fig. 11(e), is close to branch II. For these measurements, the ribbon amplitude is adjusted to ensure that the rms wave amplitude, $0.1\% < u/U_1 < 0.5\%$ at each streamwise position. The spanwise measurement grid spacing, $\delta_z=0.5$ mm, which is equal to the length of the hot-wire filament. It should be noted that contours of the random background fluctuations appear to be unaffected by the presence of the wave motions. The disturbance from the FSN displaces the wave amplitude contours away from the test surface and this region is also associated with larger wave amplitude.

For larger wave amplitudes the onset of breakdown of organized wave motions occurs at a lower R and is of a more complex form than the K-type instability observed in the base flow. This observation is consistent with recent results of Wu and Luo [17]. Contour surfaces and contour lines of the wave motions u_ϕ/U_1 and random fluctuations u''/U_1 are shown in plan view in Figs. 12(a) and 12(b) for $R=837.5$. The pseudo-flow contour surfaces of u_ϕ/U_1 and the contour lines of u_ϕ/U_1 and u''/U_1 for the base flow are shown in Fig. 12(a). The contours in Fig. 12(b) are for the same ribbon parameters but with the introduction of FSN: corresponding to case $5T$. Note that both u_ϕ/U_1 and u''/U_1 are phase-averaged quantities. The contours have been constructed by using phase as the third (streamwise) coordinate. The spanwise variations of u_ϕ/U_1 in the base flow in Fig. 12(a) demonstrate the onset of K-type instability (Herbert [16]), and it is evident that a small level of randomness is associated with the negative wave amplitudes resulting from cycle-to-cycle variability. The complex distortion of the waves resulting from the FSN is evident in Fig. 12(b). Note that the u''/U_1 levels are larger than for the base flow and that the contours have a well-defined structure.
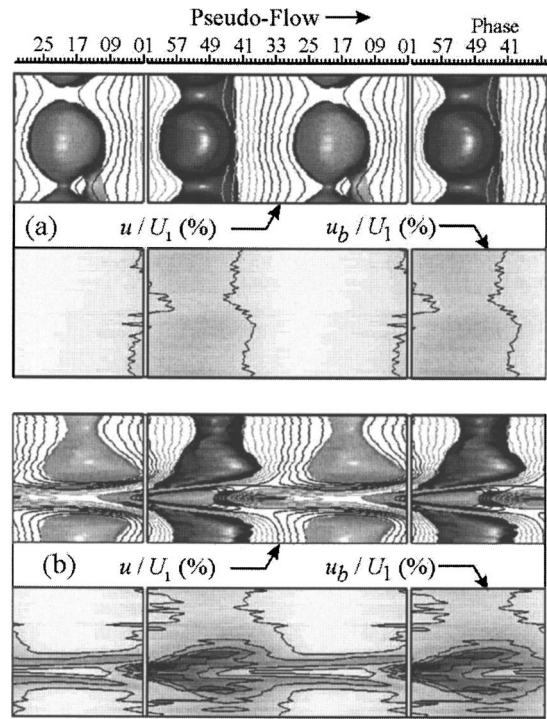
Orthographic views of results corresponding to larger initial wave amplitude are shown in Figs. 13(a) and 13(b). Note that both the u_ϕ/U_1 and u''/U_1 surfaces in Fig. 13(a) clearly show the Λ-shape, which provides additional evidence that the negative waves evolve into vortex loops. With the presence of FSN, the u_ϕ/U_1 surfaces are highly intertwined, and a pair of additional random motions is evident at higher levels.

Part of the reason for complexity is that it is misleading to interpret contours of the perturbations when the mean flow is also subject to considerable distortion at these larger amplitudes. For example, the positive contour surface visible in Fig. 13(a) is misleading since contour surfaces of the total phase-averaged velocity clearly demonstrate that a Λ-shaped deflection is associated with the negative level, as shown for the base-flow in Fig. 14(b). This contour surface corresponds with the total phase-averaged velocity and the contour surface level is given by $(\bar{U}+u_\phi)/U_1=0.4$. However, the complex sinuous motions resulting from the presence of the FSN are still evident in the total phase-averaged velocity contour surface shown in Fig. 14(a).

Concluding Remarks

Narrow low-speed streaks appearing in the boundary layer are shown to be associated with local regions of elevated layer thickness resulting from interaction of FSN with the leading edge. The formation of these streaks is remarkably sensitive to small amplitude FSN. For example, FSN of only 0.2% is responsible for generating a local spanwise boundary layer thickness variation of 60%. The response is also shown to be sensitive to the spanwise length-scale of the FSN, suggesting that there is a preferred span-
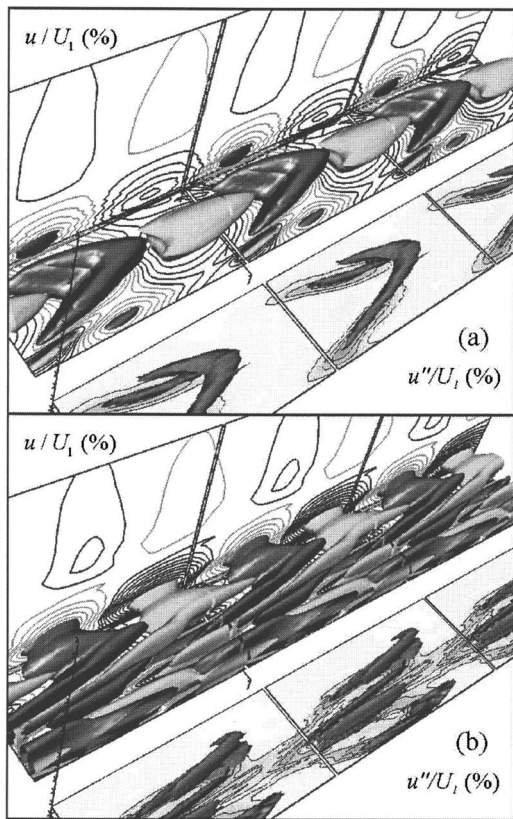
Fig. 13 Pseudoflow contour surfaces and contour lines of wave amplitude, u_ϕ/U_1, and background unsteadiness, u''/U_1, for $R=837.5$. (a) K-type instability in base flow, (b) Same ribbon amplitude, but with FSN, $d=101.5$ μm wire in test section (case 5T). For u_ϕ/U_1, dark surfaces: $u_\phi/U_1=-5.0\%$, light surfaces: $u_\phi/U_1=+5.0\%$, line contours, CR$=\pm19.5\%$, from $\pm0.5\%$, with CI$=1.0\%$ (zero level not shown). For u''/U_1, contour surface; $u''/U_1=+2.0\%$, line contours, CR$=5.0\%$, CI$=0.5\%$. Contour lines shown in the plane $y=0.65$ mm. CR is contour range and CI is contour increment.
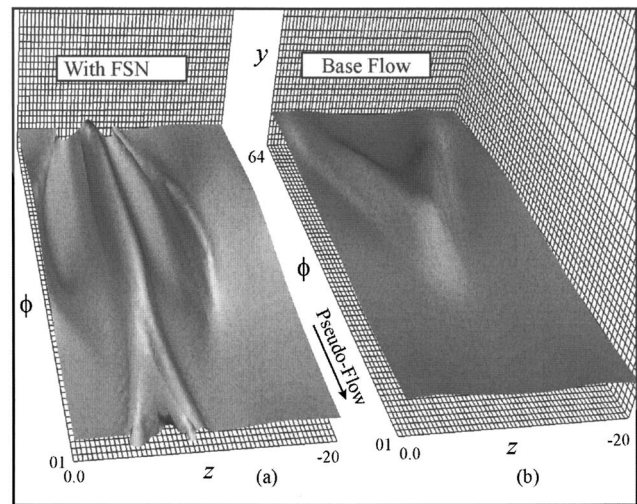

Fig. 14 Pseudoflow visualization of contour surface of the total phase-averaged velocity, $(U+u_\phi)/U_1=0.4$ corresponding to conditions in Fig. 13. (a) FSN, case 5T, showing fine-scale motions, and (b) base flow, with evidence of Λ-shaped loop resulting from K-type instability.

wise wavelength for the appearance of mean flow (or slowly varying) disturbances in the boundary layer. The shape factors of the profiles in the vicinity of the streak appear to be unaltered from the Blasius value. By considering the spanwise distribution of the background unsteadiness observed on either side of the streak it is shown that these regions are most likely the result of small amplitude spanwise modulations of order 2% of the layer thickness. The characteristics of the background unsteadiness share many of the features associated with Klebanoff modes observed at elevated free stream turbulence (FST) levels. However, the layer remains laminar to the end of the test section ($R_x \approx 1.4 \times 10^6$) and there is no evidence of bursting or other phenomena associated with the streak leading to breakdown to turbulence. The stability of the streaks is surprising, but it should be noted that only two spanwise length scales have been considered. It is likely that there is a spanwise length scale for the FSN that will generate an even stronger response of the layer and it is possible that the streak would be unstable in this situation.

Boiko et al. [15] showed that the combination of ribbon generated TS waves and grid generated FST leads to transition at lower Reynolds numbers than when the FST is present alone. Following these observations, a vibrating ribbon apparatus is used to examine interactions between the streak and Tollmien-Schlichting (TS) waves. The deformation of the mean flow introduced by the streak is responsible for substantial phase and amplitude distortion of the waves. However, the wave distortion appears to be only of relatively minor significance until the wave amplitudes reach a level for the onset of secondary instability when the FSN is not present. Nevertheless, the breakdown of the distorted waves is more complex and it occurs at a lower Reynolds number than the breakdown of the K-type secondary instability that is observed when the FSN is not present.

The motivation behind these studies is to gain some insight into transition at elevated FST levels, which has remained a mystery since the thirties. A simplistic proposition is that FST may be viewed as unsteady FSN and that transition at lower R is caused by interactions of a similar nature to those observed in the present study. A better understanding of the dependency on the leading-edge geometry and on the length-scales of the FST might help explain the disparities between controlled experiments noted by Westin et al. [6].

Acknowledgment

Nomenclature

C_D = drag coefficient
F = nondimensional frequency $(=2\pi f\nu/U_1^2)$
H = boundary layer shape factor
R = boundary layer streamwise length-scale $(=\sqrt{R_x})$
R_d = Reynolds number based on diameter
R_x = Reynolds number based on streamwise distance
U = steady streamwise velocity component
U_1 = free-stream velocity component
d = diameter
f = frequency
u_ϕ = phase-averaged streamwise velocity fluctuation
u' = fluctuating streamwise velocity component
u_ϕ = phase-averaged streamwise velocity fluctuation
u''_ϕ = random fluctuating velocity component
$\overline{u''^2}_\phi$ = background unsteadiness at constant phase

x = streamwise coordinate
y = coordinate normal to wall
z = spanwise coordinate
δ_0 = Blasius length scale $(=\sqrt{x\nu/U_1})$
δ_1 = boundary layer displacement thickness
η = Blasius wall distance $(=y\sqrt{U_1/\nu x})$
s = standard deviation
ν = kinematic viscosity

References

[1] Watmuff, J. H., 1998, "Detrimental Effects of Almost Immeasurably Small Free-Stream Nonuniformities Generated by Wind Tunnel Screens," AIAA J., **36**(3), pp. 379–386.
[2] Klebanoff, P. S., 1971, "Effect of Free-Stream Turbulence on a Laminar Boundary Layer," Bull. Am. Phys. Soc., **10**, p. 1323.
[3] Kendall, J. M., 1985, "Experimental Study of Disturbances Produced in a Pre-Transitional Laminar Boundary Layer by Weak Free-Stream Turbulence," AIAA Paper No. 85-1695.
[4] Kendall, J. M., 1990, "Boundary Layer Receptivity to Freestream Turbulence," AIAA Paper No. 90-1504.
[5] Matsubura, M., and Alfredson, P. H., 2001, "Disturbance Growth in Boundary Layers Subjected to Free-Stream Turbulence," J. Fluid Mech., **430**, pp. 149–168.
[6] Westin, K. J. A., Boiko, A. V., Klingmann, B. G. B., Kozlov, V. V., and Alfredsson, P. H., 1994, "Experiments in a Boundary Layer Subject to Free Stream Turbulence. Part 1. Boundary Layer Structure and Receptivity," J. Fluid Mech., **281**, pp. 219–245.
[7] Goldstein, M. E., Leib, S. J., and Cowley, S. J., 1992, "Distortion of a Flat-Plate Boundary Layer by Free-Stream Vorticity Normal to the Plate," J. Fluid Mech., **237**, pp. 231–260.
[8] Goldstein, M. E., and Leib, S. J., 1993, "A Note on the Distortion of a Flat-Plate Boundary Layer by Free-Stream Vorticity Normal to the Plate," J. Fluid Mech., **248**, pp. 531–541.
[9] Goldstein, M. E., and Wundrow, D. W., 1998, "On the Environmental Realizability of Algebraic Growing Disturbances and Their Relation to Klebanoff Modes," Theor. Comput. Fluid Dyn., **10**, pp. 171–186.
[10] Kogan, M. N., Sumilkin, V. G, Ustinov, M. V., and Zhigulev, S. V., 2001, "Response of Boundary Layer Flow to Vortices Normal to the Leading Edge," Eur. J. Mech. B/Fluids, **20**, pp. 813–820.
[11] Watmuff, J. H., 1994, A New High Performance Constant Temperature Hot-wire Anemometer, NASA Contractor Report No. 177645.
[12] Bradshaw, P., 1965, "The Effect of Wind-Tunnel Screens on Nominally Two-Dimensional Boundary Layers," J. Fluid Mech., **22**, pp. 679–687.
[13] Crow, S. C., 1966, "The Spanwise Perturbation of Two-Dimensional Boundary Layers," J. Fluid Mech., **24**, pp. 153–164.
[14] Bertolotti, F. P., and Kendall, J. M., 1997, "Response of the Blasius Boundary Layer to Controlled Free-stream Vortices of Axial Form," AIAA Paper No. 97-2018.
[15] Boiko, A. V., Westin, K. J. A., Klingmann, B. G. B., Kozlov, V. V., and Alfredsson, P. H., 1994, "Experiments in a Boundary Layer Subject to Free Stream Turbulence. Part 2. The Role of TS-Waves in the Transition Process," J. Fluid Mech., **281**, pp. 193–218.
[16] Herbert, T., 1988, "Secondary Instability of Boundary Layers," Annu. Rev. Fluid Mech., **20**, pp. 487–526.
[17] Wu, X., and Luo, J., 2003, "Linear and Nonlinear Instabilities of a Blasius Boundary Layer Perturbed by Streamwise Vortices. Part 1. Steady Streaks," J. Fluid Mech., **483**, pp. 225–248.

Theoretical Analysis on the Secondary Flow in a Rotating Helical Pipe With an Elliptical Cross Section

Yitung Chen[1]

Huajun Chen

Department of Mechanical Engineering,
University of Nevada,
Las Vegas, NV 89154

Jinsuo Zhang

Nuclear Design and Risk Analysis,
Los Alamos National Laboratory,
Los Alamos, NM 87545

Hsuan-Tsung Hsieh

Department of Mechanical Engineering,
University of Nevada,
Las Vegas, NV 89154

In the present study, the flow in a rotating helical pipe with an elliptical cross section is considered. The axes of the elliptical cross section are in arbitrary directions. Using the perturbation method, the Navier-Stokes equations in a rotating helical coordinate system are solved. The combined effects of rotation, torsion, and geometry on the characteristics of secondary flow and fluid particle trajectory are discussed. Some new and interesting conclusions are obtained, such as how the number of secondary flow cells and the secondary flow intensity depends on the ratio of the Corollis force to the centrifugal force. The results show that the increase of torsion has the tendency to transfer the structure of secondary flow into a saddle flow, and that the incline angle α increases or decreases the secondary flow intensity depending on the resultant force between the Corilois force and centrifugal force. [DOI: 10.1115/1.2169818]

Keywords: secondary flow, curved pipe/duct, rotation, Coriolis force

1 Introduction

Flows in rotating pipes are very important in both fundamental scientific and industrial applications. A rotating curved pipe, often used in cooling and transferring systems, is one of the basic elements in rotary machineries such as gas turbines, electric generators, and electric motors. Different from the flow in a stationary curved pipe, the characteristics of the flow in rotating curved pipes are affected by the pressure-driven axial flow, the system rotation, and their interactions. These interactions cause the flow and heat transfer characteristics in a rotating curved pipe to be drastically different from those in a stationary case.

Due to their wide spectrum of applications and richness in physical phenomena, the flows in rotating curved pipes have been studied by many researchers. Ishigaki [1] examined the secondary flow in a rotating circular pipe with small curvatures for both positive and negative rotations and found a six-vortex structure for high Reynolds numbers. Wang and Cheng [2] studied the flow structure in a rotating square duct when the duct wall was either heated or cooled. Zhang et al. [3] considered the flow in a rotating rectangular duct and illustrated the aspect effects on the secondary flow structure. Bifurcation studies on the single liquid flow in rotating curved ducts were carried out by Daskopoulos and Lenhoff [4] for circular pipes and Selmi et al. [5], as well as Selmi and Nandakumar [6] for square ducts. Wang and Cheng [7] experimentally examined the flow stabilities for negative rotation cases. All of the results indicate that the secondary flow in rotating curved pipes is more complex than the secondary flow in stationary curved pipes. Also, the theoretical solutions and experimental relations for the flow in stationary curved pipes are not suitable for that in rotating curved pipes.

To enhance the rate of heat and mass transfer, helical pipes with finite pitches have been used extensively in various industrial applications. Useful characteristics include high rates of heat and mass transfer, good cross-section mixing, and low axial disper-

sion. Previous works on the flow in helical pipes were mainly focused on stationary cases (without system rotation) [8–13].

Although the elliptical pipe is one of the most useful pipes in engineering, only a few studies on the flow have been reported, and most of which are for single parameter elliptical pipe (toroidal or twisted) flows without system rotation. Topakoglu and Ebadian [14,15] and Thomas and Walters [16] obtained the first-order solution of the stream function of the secondary flow in a stationary toroidal elliptical pipe, respectively. Kotorynski [17] gave the perturbation solution of the flow in a stationary twisted elliptical pipe. For the helical pipes, Germano [18] and Zhang and Zhang [19] studied the flow numerically and theoretically, but their works are only limited to the stationary case.

To extend previous solutions to more general cases [20], the fluid flow in the rotating helical pipe with an elliptic cross section, the axes of which are in an arbitrary position with respect to the radius of curvature of the pipe, has been examined in this paper. In terms of tensor analyses, the governing equations in the rotating helical coordinate system are derived and a theoretical analysis has been performed by expanding variables in powers of Dean number. The combined effects of rotation, torsion, and geometry on the secondary flow and fluid particle trajectory are analyzed in detail.

2 Governing Equations

To simplify the problem and make it convenient to solve, various coordinate systems have been used to derive the governing equations in helical pipes, such as Germano [8,18], Wang [9], Liu and Masliyah [11]. Although some differences exist in their results such as the order of the torsion effect, they have successfully deduced the Navier-Stokes equations in a nonorthogonal or orthogonal coordinate system, respectively. Also, Turtle [10] gives an excellent review of both nonorthogonal and orthogonal coordinate systems, showing that the results in the two different coordinate systems are consistent with each other. Bolinder [21] presents a method for deriving the governing equations directly in terms of curvilinear coordinates and physical components. His coordinates have two main advantages: they are suitable for a very wide class
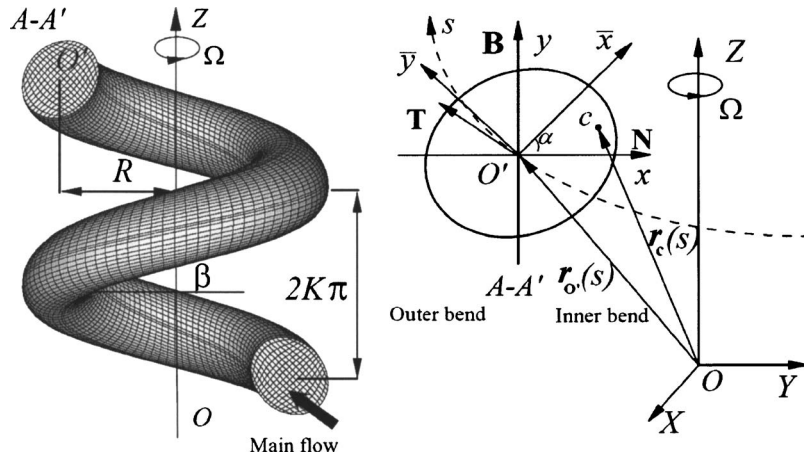

Fig. 1   Rotating helical elliptical pipe and the coordinate system

of pipe shapes, and they are orthogonal. So we will derive the governing equations in the rotating helical coordinate system according to Bolinder [21].

Figure 1 shows the rotating helical pipe of elliptical cross section and the coordinate system used in this work, where the helical pipe of elliptical cross section is rotating around the axis OZ with constant angular velocity Ω, and the axes are in arbitrary position with respect to the radius of curvature of the pipe. The equation for the boundary of the cross section, referred to Cartesian axis $O'\bar{x}$ and $O'\bar{y}$, which are inclined to the $O'x$ and $O'y$ axis as shown in Fig. 1, is taken to be

$$(\bar{x}/a)^2 + (\bar{y}/b)^2 = 1 \tag{1}$$

where a and b are the half axis of the cross section along $\bar{x}$ and $\bar{y}$, respectively.

The centerline of the helical duct is described by the position vector $r_{o'}(s)$ and β, which is the slope of centerline relative to the horizontal plane. R is the radius of curvature radius and $2\pi K$ is the pitch of centerline. Along the centerline, the unit tangent, normal, and binormal vectors are mutually orthogonal and are denoted as T, N, and B, respectively. In the helical coordinate system (x,y,s), (x,y) is defined by the plane of (N,B).

It is assumed that the flow is steady, laminar, and fully developed along the centerline of the helical pipe. In order to render the governing equation dimensionless, we introduce the nondimensional variables as

$$(\hat{x},\hat{s}) = (x,s)/a, \quad \hat{y} = y/b, \quad (\hat{w},\hat{u},\hat{v}) = (w,u,v)/U, \quad \hat{p} = p/(\rho U^2),$$

$$\hat{\Omega} = \Omega a/U, \quad \hat{\kappa} = \kappa a, \quad \hat{\tau} = \tau a, \quad \mathfrak{R} = Ua/v, \quad \lambda = a/b,$$

where u,v,w are velocity components in the (x,y,s) directions, p is the pressure, v is the kinematic viscosity, ρ is the fluid density, U is the reference velocity, and $\mathfrak{R}$ is the Reynolds number. (For simplicity, the superscript "^" is omitted and variables appearing later are all dimensionless.)

In terms of tensor analysis, we can obtain the dimensionless continuity and Navier-Stokes equations as

$$\frac{\partial u}{\partial x} + \lambda \frac{\partial v}{\partial y} + \frac{\tau y}{\lambda M}\frac{\partial w}{\partial x} - \frac{\lambda \tau x}{M}\frac{\partial w}{\partial y} - \frac{\kappa}{M}u = 0 \tag{2}$$

$$u\frac{\partial u}{\partial x} + \lambda v\frac{\partial u}{\partial y} + \frac{w}{M}\left(\frac{\tau y}{\lambda}\frac{\partial u}{\partial x} - \lambda \tau x\frac{\partial u}{\partial y} - \tau v + \kappa w\right)$$

$$= -\frac{\partial P}{\partial x} - 2\Omega(w\cos\beta - v\sin\beta) + \frac{1}{\mathfrak{R}}(\nabla^2\mathbf{V})^{(1)} \tag{3}$$

$$u\frac{\partial v}{\partial x} + \lambda v\frac{\partial v}{\partial y} + \frac{w}{M}\left(\frac{\tau y}{\lambda}\frac{\partial v}{\partial x} - \lambda \tau x\frac{\partial v}{\partial y} + \tau u\right)$$

$$= -\lambda\frac{\partial P}{\partial y} - 2\Omega u\sin\beta + \frac{1}{\mathfrak{R}}(\nabla^2\mathbf{V})^{(2)} \tag{4}$$

$$u\frac{\partial w}{\partial x} + \lambda v\frac{\partial w}{\partial y} + \frac{w}{M}\left(\frac{\tau y}{\lambda}\frac{\partial w}{\partial x} - \lambda \tau x\frac{\partial w}{\partial y} - \kappa u\right)$$

$$= -\frac{1}{M}\left(\frac{\tau y}{\lambda}\frac{\partial P}{\partial x} - \lambda \tau x\frac{\partial P}{\partial y} + \frac{\partial P}{\partial s}\right) + 2\Omega u\cos\beta + \frac{1}{\mathfrak{R}}(\nabla^2\mathbf{V})^{(3)} \tag{5}$$

and

$$(\nabla^2\mathbf{V})^{(1)} = \frac{1}{M^2}\left[\left(M^2 + \frac{\tau^2 y^2}{\lambda^2}\right)\frac{\partial^2 u}{\partial^2 x} + \lambda^2(M^2 + \tau^2 x^2)\frac{\partial^2 u}{\partial^2 y}\right.$$
$$- 2\tau^2 xy\frac{\partial^2 u}{\partial x\,\partial y} + A\frac{\partial u}{\partial x} - \lambda B\frac{\partial u}{\partial y} - \frac{2\tau^2 y}{\lambda}\frac{\partial v}{\partial x} + 2\lambda \tau^2 x\frac{\partial u}{\partial y}$$
$$\left. + \frac{2\kappa\tau y}{\lambda}\frac{\partial w}{\partial x} - 2\lambda\kappa\tau x\frac{\partial w}{\partial y} - (\kappa^2 + \tau^2)u - Cv + Dw\right]$$

$$(\nabla^2\mathbf{V})^{(2)} = \frac{1}{M^2}\left[\left(M^2 + \frac{\tau^2 y^2}{\lambda}\right)\frac{\partial^2 v}{\partial^2 x} + \lambda^2(M^2 + \tau^2 x^2)\frac{\partial^2 v}{\partial^2 y}\right.$$
$$- 2\tau^2 xy\frac{\partial^2 v}{\partial x\,\partial y} + A\frac{\partial v}{\partial x} - \lambda B\frac{\partial v}{\partial y} + \frac{2\tau^2 y}{\lambda}\frac{\partial u}{\partial x} - 2\lambda \tau^2 x\frac{\partial u}{\partial y}$$
$$\left. + \frac{2\kappa\tau y}{\lambda}\frac{\partial w}{\partial x} - 2\lambda\kappa\tau x\frac{\partial w}{\partial y} - Cu - \tau^2 v + \kappa\tau w\right]$$

$$(\nabla^2\mathbf{V})^{(3)} = \frac{1}{M^2}\left[\left(M^2 + \frac{\tau^2 y^2}{\lambda}\right)\frac{\partial^2 w}{\partial^2 x} + \lambda^2(M^2 + \tau^2 x^2)\frac{\partial^2 w}{\partial^2 y}\right.$$
$$- 2\tau^2 xy\frac{\partial^2 w}{\partial x\,\partial y} + A\frac{\partial w}{\partial x} - \lambda B\frac{\partial w}{\partial y} + \frac{2\kappa\tau y}{\lambda}\frac{\partial u}{\partial x} + 2\lambda\kappa\tau x\frac{\partial u}{\partial y}$$
$$\left. - Du + \kappa\tau v - \kappa^2 w\right]$$

where

$$A = \frac{\kappa\tau^2 y^2}{\lambda^2 M} - \tau^2 x - \kappa M, \quad B = \frac{\tau^2 y}{\lambda M},$$

$$C = \frac{\kappa\tau^2 y}{\lambda M}, \quad D = \frac{\kappa^2\tau y}{\lambda M}, \quad M = 1 - \kappa x,$$

$$P = -Gs + p_1(x,y) - \frac{1}{2}\Omega^2\left(\frac{1}{\kappa} - x\right)^2 - \frac{1}{2}\Omega^2\frac{y^2\sin^2\beta}{\lambda^2},$$

and G is the axial pressure gradient which is a positive constant.

Assuming the curvature κ and torsion τ are small, that is, $\kappa = \epsilon \ll 1$ and $\tau = \eta\epsilon \ll 1$. Similar to the work of Dean [22] and Germano [18], we drop higher order terms in κ from Eqs. (2)–(5). This physically corresponds to considering loosely coiled pipes, and following Dean's [22] method, we preserve the centrifugal terms and write

$$\tilde{u} = \Re u, \quad \tilde{v} = \Re v, \quad \tilde{P} = -\tilde{G}s/\Re + \kappa\tilde{p}_1(x,y) \quad (6)$$

where $\tilde{G} = \Re G$. If we assume the reference velocity U is the maximum velocity in a straight elliptical pipe with the same pressure gradient, we have

$$\tilde{G} = 2(1 + \lambda^2) \quad (7)$$

Now, we introduce the Dean number $D = 2\kappa\Re^2$ and rotation number $F = (2\Omega\cos\beta)/\kappa$, where F represents the ratio of the Coriolis force to the centrifugal force. Negative values of F correspond to the case of counter-rotation, while $F = -1$ means that the two forces are of the same magnitude but in the opposite directions. Finally, we obtain the following system:

$$\frac{\partial\tilde{u}}{\partial x} + \lambda\frac{\partial\tilde{v}}{\partial y} + \frac{D\eta}{2\Re}\left(\frac{y}{\lambda}\frac{\partial w}{\partial x} - \lambda x\frac{\partial w}{\partial y}\right) = 0 \quad (8)$$

$$\tilde{u}\frac{\partial\tilde{u}}{\partial x} + \lambda\tilde{v}\frac{\partial\tilde{u}}{\partial y} + \frac{Dw}{2\Re}\left(\frac{\eta y}{\lambda}\frac{\partial\tilde{u}}{\partial x} - \lambda\eta x\frac{\partial\tilde{u}}{\partial y} - \eta\tilde{v} + \Re w\right)$$

$$= -\frac{D}{2}\frac{\partial\tilde{P}}{\partial x} - \frac{DwF}{2} + \nabla^2\tilde{u} \quad (9)$$

$$\tilde{u}\frac{\partial\tilde{v}}{\partial x} + \lambda\tilde{v}\frac{\partial\tilde{v}}{\partial y} + \frac{Dw}{2\Re}\left(\frac{\eta y}{\lambda}\frac{\partial\tilde{v}}{\partial x} - \lambda\eta x\frac{\partial\tilde{v}}{\partial y} + \eta\tilde{u}\right) = -\frac{D}{2}\frac{\partial\tilde{P}}{\partial y} + \nabla^2\tilde{v}$$

$$\quad (10)$$

$$\tilde{u}\frac{\partial w}{\partial x} + \lambda\tilde{v}\frac{\partial w}{\partial y} + \frac{Dw}{2\Re}\left(\frac{\eta y}{\lambda}\frac{\partial w}{\partial x} - \lambda\eta x\frac{\partial w}{\partial y}\right) = 2(1 + \lambda^2) + \nabla^2 w$$

$$\quad (11)$$

where

$$\nabla^2 = \frac{\partial^2}{\partial x^2} + \lambda^2\frac{\partial^2}{\partial y^2}.$$

From the equations above, we see that laminar flow in a rotating helical pipe of elliptical cross section with small curvature and torsion is controlled by four parameters: D (represents the effects of the curvature), F (represents the effects of the rotation), $\eta/\Re$ (represents the effects of the torsion), and λ (represents the effects of the cross section).

Equation (8) automatically satisfies the stream function ψ,

$$\lambda\frac{\partial\psi}{\partial y} = \tilde{u} + \frac{\eta}{2\Re}\frac{1}{\lambda}Dyw, \quad -\frac{\partial\psi}{\partial x} = \tilde{v} - \frac{\eta}{2\Re}Dxw \quad (12)$$

The boundary conditions are

$$\tilde{u} = \tilde{v} = w = 0 \text{ and } \frac{\partial\psi}{\partial x} = \frac{\partial\psi}{\partial y} = 0 \text{ on } Ax^2 + By^2 + 2Cxy = 1$$

$$\quad (13)$$

where $A = \cos^2\alpha + \lambda^2\sin^2\alpha$, $B = (\sin^2\alpha/\lambda^2) + \cos^2\alpha$, $C = ((1/\lambda) - \lambda)\sin\alpha\cos\alpha$, $\lambda = a/b$, and α is the included angle between axis $O'\bar{x}$ and $O'x$.

3 Perturbation Solutions

For small Dean numbers, the axial velocity w and the stream function ψ can be expanded in powers of D as

$$\begin{cases} w = w_0(x,y) + Dw_1(x,y) + D^2w_2(x,y) + \cdots \\ \psi = \psi_0(x,y) + D\psi_1(x,y) + D^2\psi_2(x,y) + \cdots \end{cases} \quad (14)$$

Substituting Eq. (14) into Eqs. (8)–(11) and equating the coefficients of D terms, we obtain the zero-order perturbation equations as

$$\begin{cases} \psi_0 = 0 \\ \nabla^2 w_0 - 2(1 + \lambda^2) = 0 \end{cases} \quad (15)$$

and the first-order perturbation equations as

$$\begin{cases} \nabla^4\psi_1 - \left(w_0 + \frac{1}{2}F\right)\lambda\frac{\partial w_0}{\partial y} + 2\tilde{G}\frac{\eta}{\Re} = 0 \\ \nabla^2 w_1 - \lambda\frac{\partial\psi_1}{\partial y}\frac{\partial w_0}{\partial x} + \lambda\frac{\partial\psi_1}{\partial x}\frac{\partial w_0}{\partial y} = 0 \end{cases} \quad (16)$$

The perturbation equations are solved with the aid of symbolic manipulation on a computer. Considering the boundary conditions (13) and solving the Eqs. (15) and (16), we can obtain the perturbation solutions as

$$w_0 = 1 - Ax^2 - By^2 - 2Cxy, \quad (17a)$$

$$\psi_1 = a_1\frac{\eta}{\Re}w_0^2 + (a_3 x + a_5 y)Fw_0^2 + (a_2 x + a_4 y + a_6 x^2 y + a_7 xy^2 + a_8 x^3 + a_9 y^3)w_0^2, \quad (17b)$$

$$w_1 = w_0(b_1 x + b_2 x^3 + b_3 x^5 + b_4 x^7 + (b_5 + b_6 x^2 + b_7 x^4 + b_8 x^6)y + (b_9 x + b_{10}x^3 + b_{11}x^5)y^2 + (b_{12} + b_{13}x^2 + b_{14}x^4)y^3 + (b_{15}x + b_{16}x^3)y^4 + (b_{17} + b_{18}x^2)y^5 + b_{19}xy^6 + b_{20}y^7) \quad (17c)$$

where a_1 to a_9 are algebraic functions of α, λ and b_1 to b_{20} are algebraic functions of α, λ, F, and $\Re$. We note that these coefficient are complicated, So we have not shown them.

Similar to ψ and w, the secondary flow velocities are given by

$$\tilde{u} = D\tilde{u}_1(x,y) + D^2\tilde{u}_2(x,y) + \cdots, \quad \tilde{v} = D\tilde{v}_1(x,y) + D^2\tilde{v}_2(x,y) + \cdots$$

$$\quad (18)$$

By substituting Eq. (18) into Eq. (12) and collecting terms first order in D, we obtain the perturbation solution of the secondary flow up to the first order

$$\tilde{u}_1 = -\frac{\eta}{\Re}\left(4\lambda w_0 a_1(By + Cx) + \frac{yw_0}{2\lambda}\right) + \lambda F(w_0^2 a_5 - 4w_0(a_3 x + a_5 y)) \times (By + Cx)) - \lambda(4w_0(a_9 y^3 + a_2 x + a_7 xy^2 + a_4 y + a_6 x^2 y + a_8 x^3) \times (By + Cx) - w_0^2(a_4 + a_6 x^2 + 2a_7 xy + 3a_9 y^2)) \quad (19a)$$

$$\tilde{v}_1 = -\frac{\eta}{\Re}\left(\frac{xw_0}{2\lambda} + 4w_0 a_1(Ax + Cy)\right) + F(4w_0(a_3 x + a_5 y)(Ax + Cy) - w_0^2 a_3) + 4w_0((a_9 y^3 + a_2 x + a_7 xy^2 + a_4 y + a_6 x^2 y + a_8 x^3)(Ax + Cy) - w_0(a_2 + 2a_6 xy + a_7 y^2 + 3a_8 x^2)) \quad (19b)$$

Until now, we have obtained the first-order solutions of fluid flow in rotating helical pipe with an elliptic cross section, whose
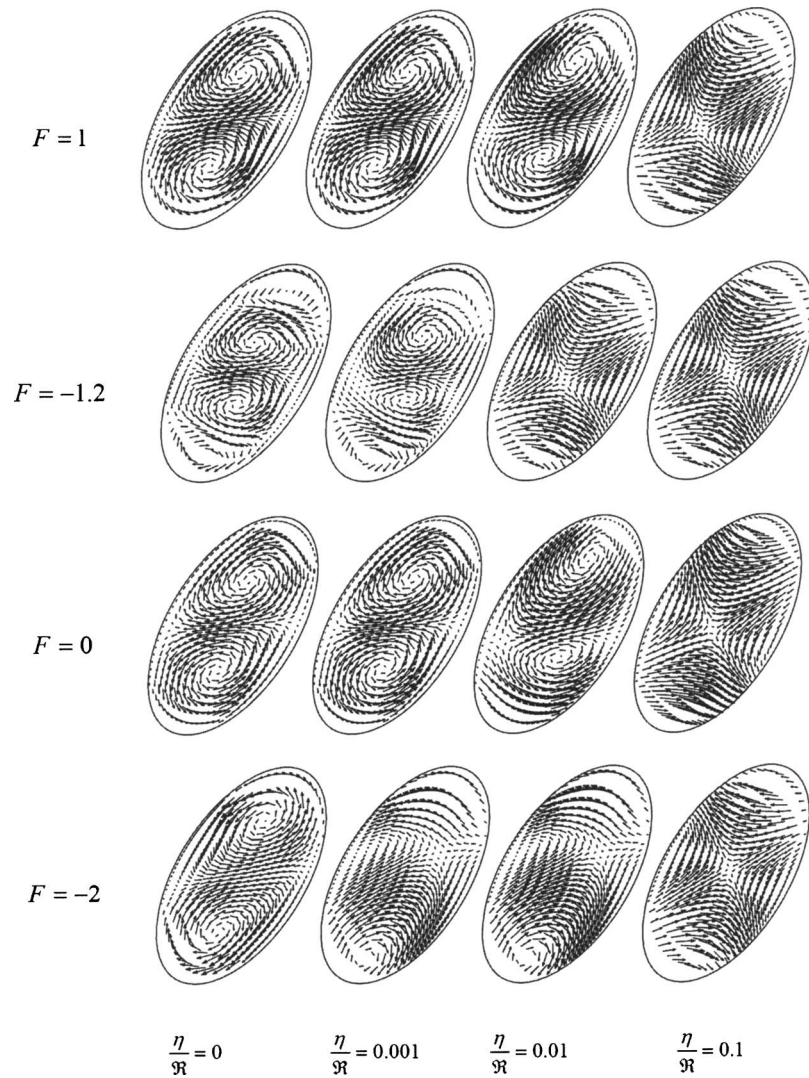
Fig. 2 Vector plots of the secondary flow for $\alpha = \pi/3$ and various values of F and $\eta/\Re$ (the outer bend is to the left)

axis is in an arbitrary position. Equation (17) indicates that to first order, torsion has no effect on the axial velocity. Equation (19) shows that the secondary flow includes three terms: (I) torsion term, (II) rotation term, and (III) curvature term. These terms will generate three kinds of secondary flows that affect one another and make the net secondary flow pattern complicated.

According to the perturbation solutions, we can get the rate of flow through the pipe by

$$Q_h = \int \int_S [1 - Ax^2 - By^2 - 2Cxy + Dw_1 + \cdots]dxdy \quad (20)$$

where S is the area bounded by the curve $Ax^2 + By^2 + 2Cxy = 1$ and w_1 is given by (17c). Then we can get the friction factor ratio between flow in a rotating helical elliptical pipe and stationary straight circular pipe by

$$\frac{f_c}{f_s} = \frac{Q_h}{Q_s} = \frac{2}{\pi} \int \int_S [1 - Ax^2 - By^2 - 2Cxy + Dw_1 + \cdots]dxdy$$

$$(21)$$

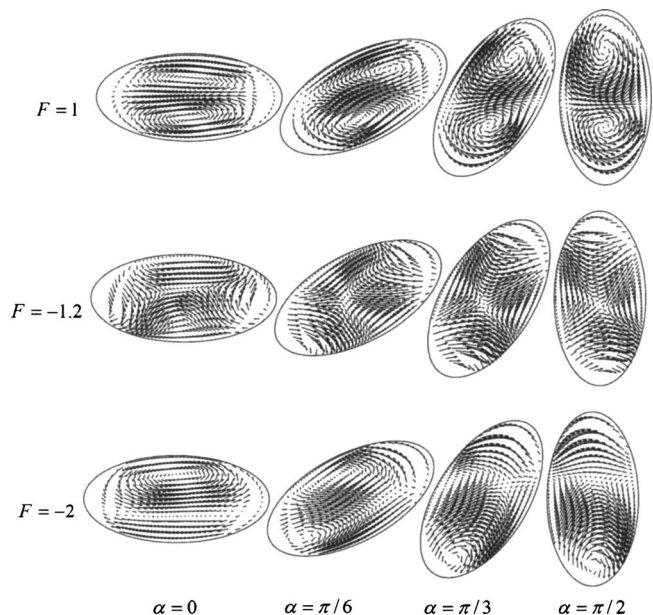where Q_s is the rate of flow in the stationary straight circular pipe with the same axial pressure gradient.

Fig. 3 Vector plots of the secondary flow for $\eta/\Re = 0.01$ and various values of F and α (the outer bend is to the left)
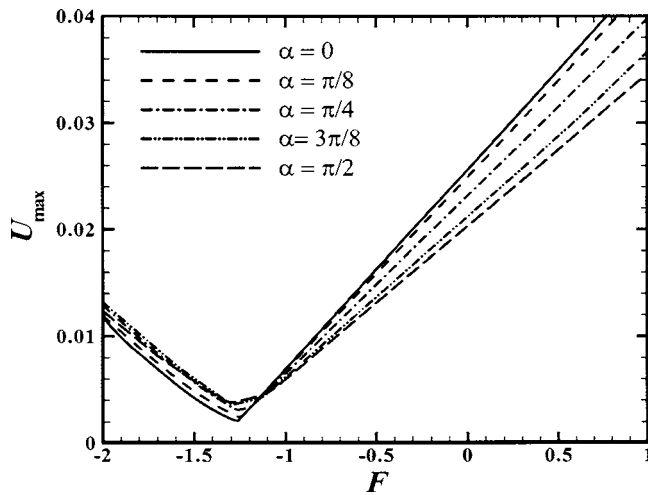
Journal of Fluids Engineering

Fig. 4 Variations of $U_{\max}$ with F for different α ($\eta/\mathfrak{R}=0.001$)

4 Results and Discussion

In the present study, we focus on the characters of the secondary flow. Based on the perturbation solutions, it is found that the structure of the secondary flow depends on the parameters F, $\eta/\mathfrak{R}$, λ, and α. So we will change F, $\eta/\mathfrak{R}$, and α continuously to investigate the combined effects while keeping λ constant ($\lambda=2$).

4.1 Secondary Flow. Figure 2 shows the secondary flow structure for various values of $\eta/\mathfrak{R}$ and F where, the outer bend is to the left-hand side. For co-rotation or non-rotation cases ($F \geq 0$), the Coriolis force has the same direction as that of centrifugal force. Therefore by increasing the system rotation velocity, the secondary flow can be intensified, while the structure remains unchanged.

For the toroidal cases ($\eta/\mathfrak{R}=0$), two asymmetric secondary vortices are found in the cross section when $F=1$ and $F=-2$, while the two cases have the opposite secondary flow directions. This phenomenon can be understood once we recognize that the curvature has the tendency to induce a secondary flow flowing outward along the x-axis, while the counter-rotation has a tendency to induce a secondary flow flowing inward. When $F=-2$, the Coriolis force dominates the secondary flow, which flows inwards along the x axis. When $F=-1.2$, the two types of secondary flows coexist, because the centrifugal force almost equals the Corilis force; while they are in opposite directions. Therefore the net
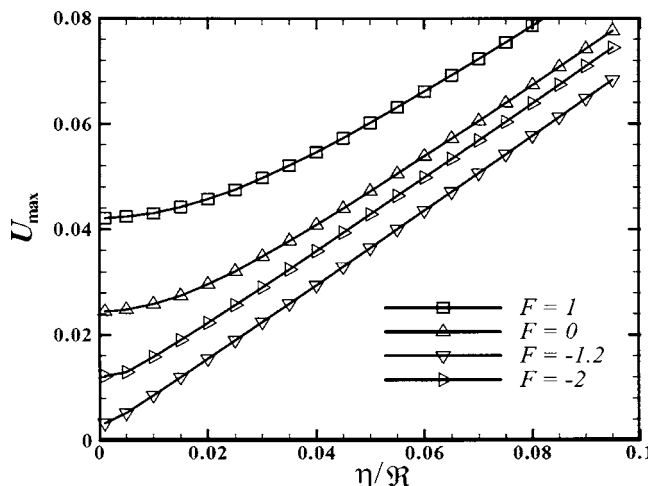
secondary flow appears as a four-cell structure, which has also been reported by Ishigaki [1] when investigating the secondary flow in a rotating curved circular pipe.

For helical cases ($\eta/\mathfrak{R}>0$), the secondary flow structure is much different from that in a toroidal one because of torsion. As $\eta/\mathfrak{R}$ increases, the two-cell or four-cell structure vanishes gradually. When the torsion is sufficiently large, such as $\eta/\mathfrak{R}=0.1$, the secondary flow has a stagnation point which corresponds to a saddle point in phase space. It is also shown that the torsion effect on the secondary flow is most significant when $F=-1.2$. The reason for this is that torsion dominates the secondary flow because the centrifugal force is almost completely balanced by the Coriolis force.

Figure 3 shows variations of secondary flow with α for various values of F. For $F=1$, the two-cell structure almost remains unchanged, except that the centers of the secondary vortices move away from the x-axis gradually with increasing α. When $F=-2$, the structure of the secondary flow changes significantly: the upper cell vanishes gradually while the lower cell is enlarged as α increases. The secondary flow appears as one-cell when $\alpha=\pi/2$. For $F=-1.2$, the secondary flow keeps a saddle point structure as α increases.

According to Ishagaki [1], the secondary flow maximum velocity $U_{\max}=(\sqrt{u^2+v^2})_{\max}$, denotes the secondary flow intensity. The effects of rotation, torsion, and α on the secondary flow intensity are shown in Figs. 4–6. Figure 4 shows that $U_{\max}$ reaches its
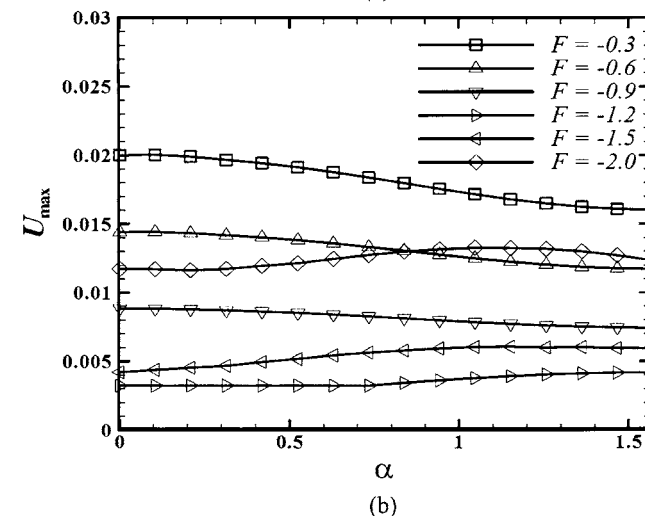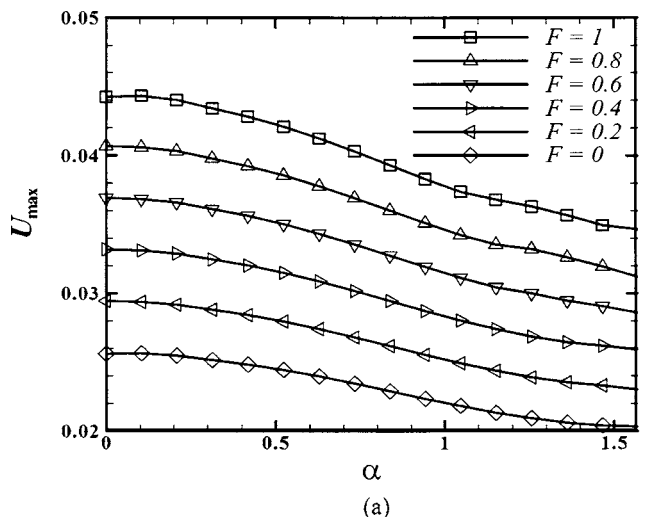

(a)

(b)

Fig. 6 Variations of $U_{\max}$ with α for different F ($\eta/\mathfrak{R}=0.001$)

Fig. 5 Variations of $U_{\max}$ with $\eta/\mathfrak{R}$ for different F ($\alpha=\pi/3$)

$$F = 1$$

Min=-0.0087   Min=-0.0090   Min=-0.0117   Min=-0.0450
Max=0.0087   Max=0.0084   Max=0.0060   Max=0.0000

$$F = -1.2$$

Min=-0.0005   Min=-0.0009   Min=-0.0044   Min=-0.0423
Max=0.0005   Max=0.0002   Max=0.0000   Max=0.0000

$$F = -2$$

Min=-0.0028   Min=-0.0030   Min=-0.0056   Min=-0.0425
Max=0.0028   Max=0.0026   Max=0.0010   Max=0.0000

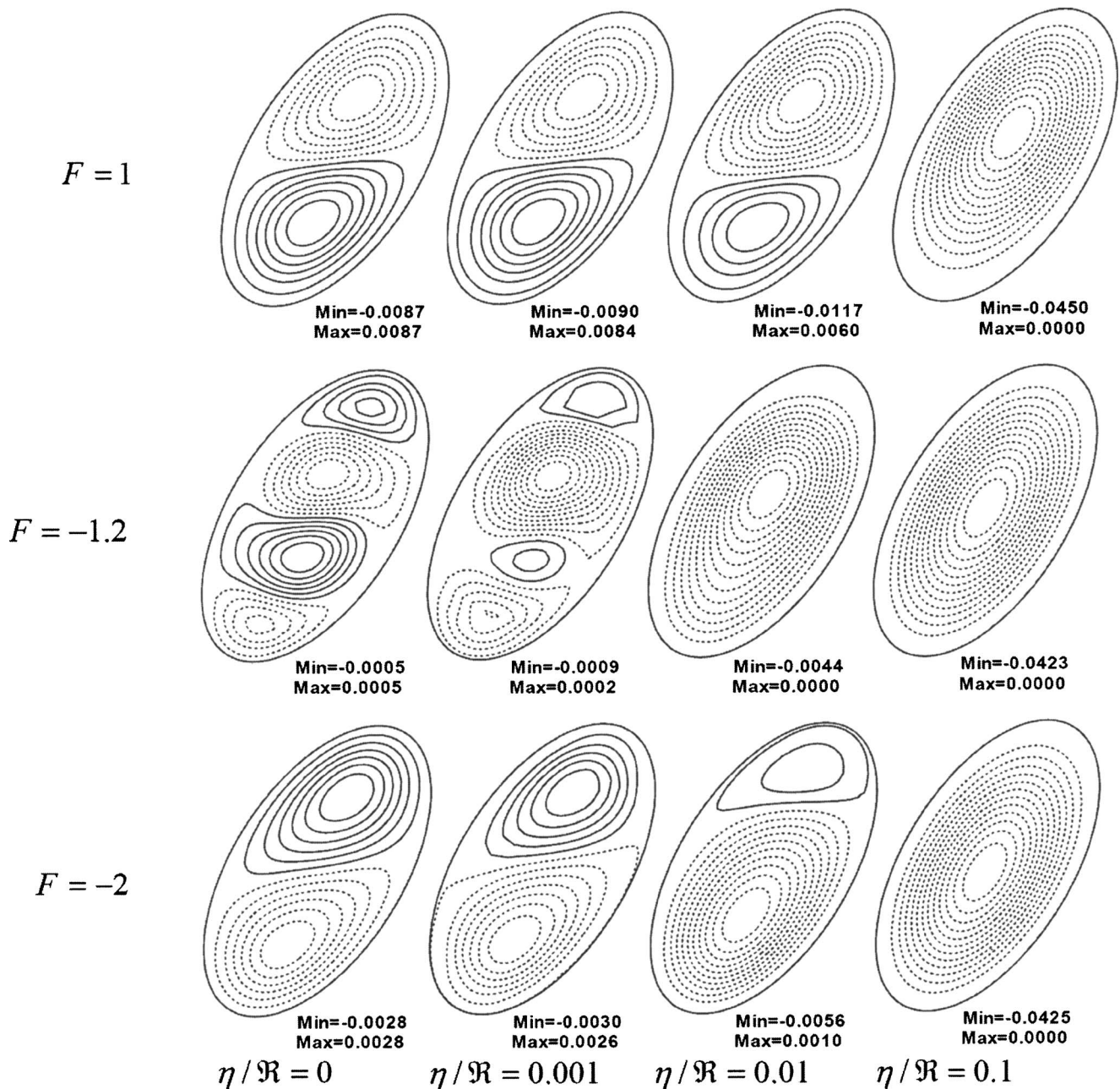$$\eta/\Re = 0 \qquad \eta/\Re = 0.001 \qquad \eta/\Re = 0.01 \qquad \eta/\Re = 0.1$$

Fig. 7   Variations of ψ contours with η/Re for different F ($\alpha = \pi/3$) (right side: outer bend; left side: inner bend)

minimum values for $F \approx -1.2$, which means the secondary flow intensity is weakest when the centrifugal force is almost balanced by the Coriolis force. When $F > -1.2$, U_{max} increases with increasing F, while for $F < -1.2$, U_{max} decreases. Figure 5 shows that increasing torsion can intensify the secondary flow and that U_{max} varies linearly with torsion for $\eta/\Re > 0.03$.

The effect of the incline angle α on the intensity is shown in Fig. 6. For the co-rotation cases [Fig. 6(a)], all of the curves decrease with increasing α, suggesting that the larger α is, the weaker the intensity of the secondary flow will be. Figure 6(b) shows that there evidently exists difference between counter- and co-rotation cases. When $F = -0.3$, $F = -0.6$, and $F = -0.9$, the variations of U_{max} have the same tendency as the co-rotation cases as with increasing α, i.e., the intensity is intensified with α increasing. For the other cases, such as $F = -1.2$, $F = -1.5$, and $F = -2$, U_{max} increases with increasing α, reaching its maximum value at $\alpha \approx 1.0$. All these phenomena indicate that the dependence of the secondary flow intensity on α strongly depends on the resultant force (i.e., the combination of Coriolis force and centrifugal force). When the direction of the resultant force points towards the outer bend, the secondary flow intensity becomes weaker with increasing α while the direction points towards the inner bend, the secondary flow intensity becomes stronger.

4.2 Fluid Particle Trajectory. Based on Eq. (12), the ψ contours do not represent the secondary flow structure truly for a helical pipe because the axial velocity also contributes to the stream function. However, they do show the fluid particle trajectories projected on the (x, y) plane which can be measured experimentally. Therefore it is useful to study the ψ contours for understanding the convection in the cross section of the fluid particles by both secondary flow and axial flow.

Variations of ψ contours with η/Re increasing are shown in Fig. 7 for different values of F (dotted lines represent the clock-
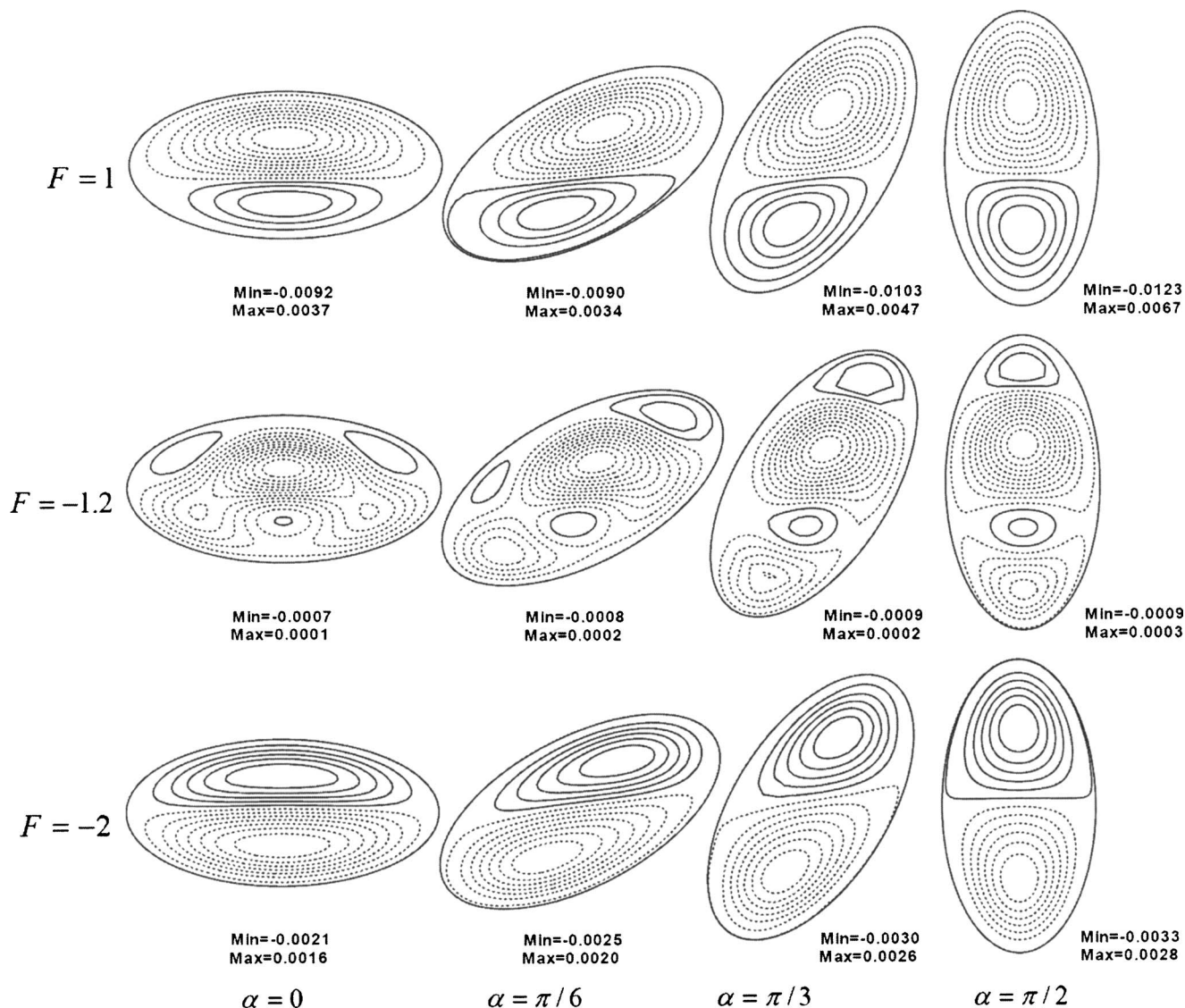
Fig. 8 Variations of ψ contours with α for different F ($\eta/\mathfrak{R}=0.001$) (right side: outer bend; left side: inner bend)

wise rotation or negative stream function regions). For the toroidal case ($\eta/\mathfrak{R}=0$), the axial velocity has no contribution to the stream function and the contours represent the streamlines of the secondary flow and have the same structure with the secondary flow velocity vector plots. Two counter-rotating ψ cells appear in the cases of $F=1$ and $F=-2$ while four ψ cells are found for the case of $F=-1.2$. As $\eta/\mathfrak{R}$ increases, the negative ψ region (clockwise ψ cell) increases; taking up the entire cross section. When $F=-1.2$, the centrifugal force and the Coriolis force balance each other and the twisting force due to torsion plays an important role with respect to ψ contours. As $\eta/\mathfrak{R}$ increases, $|\psi_{\min}|$ increases while $|\psi_{\max}|$ decreases, and $\psi_{\max}-\psi_{\min}$ increases, indicating that the intensity of mass transfer due to flow convection in the cross section by the secondary flow components u and v and the axial flow component w increases with increasing torsion.

Variations of ψ contours with α for different F are shown in Fig. 8. For the cases of $F=1$ and $F=-2$, it seems that increasing α does not change the two-cell structure of ψ contours. For $F=-1.2$ and $\alpha=0$, there are three positive ψ cells and one negative ψ cell. Then as α increases, the positive ψ cell in the lower half domain merges gradually, and the negative ψ cell splits into two cells. Furthermore, we find $\psi_{\max}-\psi_{\min}$ increase slightly as α increases for all of the rotating cases.

5 Conclusion

In the present study, the flow in a rotating helical pipe with an elliptic cross section is theoretically analyzed. The axes of the cross section are in an arbitrary position, and the combined effects of rotation, torsion, and the incline angle on the secondary flow are examined. The major conclusions are summarized.

The number of secondary flow cells and the secondary flow intensity depends strongly on F. When $F\approx-1.2$, a maximum of four secondary cells are found in the cross section at most and the secondary flow intensity becomes weakest. The effects of torsion on the secondary flow are relative to F. For $F\approx-1.2$, torsion has the most influence on the secondary flow structure. As $\eta/\mathfrak{R}$ increases, a stagnation regime will appear in the secondary flow, and the secondary flow intensity increases. The effect of the incline angle α on the secondary flow structure depends on F, and variations of the secondary flow intensity with α depend on the resultant force between the Coriolis force and centrifugal force. The increase of α intensifies the secondary flow when $F<-1.2$, while it weakens the secondary flow for $F>-1.2$. As η/Re increases, the negative ψ region (clockwise rotating ψ cell) increases and finally takes up the entire cross section, and the mass transfer due

to convection by both secondary flow and axial flow in the cross section will be intensified.

References

[1] Ishigaki, H., 1996, "Flow in Rotating Curved Pipes," J. Fluid Mech., **329**, pp. 373–388.

[2] Wang, L. Q., and Cheng, K. C., 1996, "Flow Transition and Combined Free and Forced Convective Heat Transfer in Rotating Curved Channels: The Case of Positive Rotation," Phys. Fluids, **8**, pp. 1153–1573.

[3] Zhang, J. S., Zhang, B. Z., and Jü, J. W., 2001, "Fluid Flow in Rotating Curved Rectangular Duct," Int. J. Heat Fluid Flow, **22**, pp. 583–592.

[4] Daskopoulos, P., and Lenhoff, A. M., 1990, "Flow in Curved Ducts. Part 2. Rotating Ducts," J. Fluid Mech., **217**, pp. 575–593.

[5] Selmi, M., Nandakumar, K., and Finlay, W. H., 1994, "A Bifurcation Study Viscous Flow Through a Rotating Curved Duct," J. Fluid Mech., **262**, pp. 353–375.

[6] Selmi, M., and Nandakumar, K., 1999, "Bifurcation Study of Flow Through Rotating Curved Duct," Phys. Fluids, **11**, pp. 2030–2043.

[7] Wang, L. Q., and Cheng, K. C., 1995, "Flow in Curved Channels with Low Negative Rotation Speeds," Phys. Rev. E, **51**, pp. 1155–1161.

[8] Germano, M., 1982, "On the Effect of Torsion on a Helical Pipe Flow," J. Fluid Mech., **125**, pp. 1–8.

[9] Wang, C. Y., 1981, "On the Low-Reynolds-Number Flow in a Helical Pipe," J. Fluid Mech., **108**, pp. 185–194.

[10] Tuttle, E. R., 1990, "Laminar Flow in Twisted Pipes," J. Fluid Mech., **219**, pp. 545–570.

[11] Liu, S., and Masliyah, J. H., 1993, "Axially Invariant Laminar Flow in Helical Pipes with a Finite Pitch," J. Fluid Mech., **251**, pp. 315–353.

[12] Zabielski, L., and Mestel, A. J., 1998, "Steady Flow in a Helically Symmetric Pipe," J. Fluid Mech., **370**, pp. 297–320.

[13] Zhang, I. S., and Zhang, B. Z., 1999, "Flow in a Helical Pipe," Acta Mech. Sin., **15**(4), pp. 298–312.

[14] Topakoglu, H. C., and Ebadian, M. A., 1985, "On the Steady Laminar Flow of an Incompressible Viscous Fluid in a Curved Pipe of Elliptical Cross Section," J. Fluid Mech., **158**, pp. 329–340.

[15] Topakoglu, H. C., and Ebadian, M. A., 1987, "Viscous Laminar Flow in a Curved Pipe of Elliptical Cross Section," J. Fluid Mech., **184**, pp. 571–580.

[16] Thomas, R. H., and Walters, K., 1965, "On the Flow of an Elastico-Visicous Liquid in a Curved Pipe of Elliptic Cross-Section Under a Pressure Gradient," J. Fluid Mech., **21**, pp. 173–182.

[17] Kotorynski, W. P., 1986, "Steady Laminar Flow Through a Twisted Pipe of Elliptical Cross-Section," Comput. Fluids, **14**, pp. 433–444.

[18] Germano, M., 1989, "The Dean Equations Extended to a Helical Pipe Flow," J. Fluid Mech., **203**, pp. 289–305.

[19] Zhang, J. S., and Zhang, B. Z., 2000, "Laminar Fluid Flow in a Helical Elliptical Pipe," J. Hydrodynam., **12**(2), pp. 62–71.

[20] Zhang, J. S., and Zhang, B. Z., 2003, "Dean Equations Extended to a Rotating Helical Pipe Flow," J. Eng. Mech., **129**(7), pp. 823–829.

[21] Bolinder, C. J., 1996, "Curvilinear Coordinates and Physical Components- An Application to the Problem of Viscous Flow and Heat Transfer in Smoothly Curved Ducts," ASME J. Appl. Mech., **63**, pp. 985–989.

[22] Dean, W. R., 1928, "The Stream-Line Motion of Fluid in a Curved Pipe," Philos. Mag., **7**(5), pp. 673–695.

Prediction of Fluid Inertance in Nonuniform Passageways

D. Nigel Johnston
Department of Mechanical Engineering,
University of Bath,
United Kingdom

The dynamic response, stability, and noise characteristics of fluid components and systems can be strongly influenced by the inertance of the fluid in passageways, which are often of complex geometry. The inertance is a parameter that has often proved to be very difficult to accurately quantify, either theoretically or experimentally. This paper presents a method of numerical calculation of the inertance in a passageway, assuming inviscid, incompressible flow and zero mean flow. The method is simple to apply and can be applied to geometries of arbitrary complexity. Two simple but unorthodox ways of calculating inertance using a computational fluid dynamics and a finite element solid-modeling package are also demonstrated. Results are presented for a simple cylindrical orifice, a simple spool valve, and a conical poppet valve. The effect of the inertance on the response of a poppet valve is demonstrated. [DOI: 10.1115/1.2171713]

Keywords: fluid power, hydraulic, inertance, pressure ripple, fluid-borne noise, stability

1 Introduction

The dynamic behavior of fluid systems can be strongly influenced by the inertance of the fluid in the passageways. The inertance is related to the mass of fluid in a passageway, and results in pressure changes that are proportional to the rate of change of flow rate.

The inertance can have an important effect in many types of fluid system, including hydraulic and pneumatic fluid power, heat engines (e.g., Stirling engines, Stirling coolers, and pulse tube coolers [1]), internal combustion engine air intakes and exhausts, the respiratory system [2] and vocal tract, and musical instruments [3]. Although the focus of this paper is on hydraulic fluid power systems, the methods are applicable to other fields.

In a hydraulic fluid power system, the inertance of the fluid in the pumps, valves, fittings, and other components can have an important effect on the dynamic performance and stability of the system. The inertance also has a significant effect on the fluid-borne noise or pressure ripple characteristics. Fluid-borne noise can be modeled by considering the hydraulic impedance characteristics of the components. The impedance of a component is strongly influenced by the inertance. This is especially true of components that exhibit strong resonances in their impedance spectra, including pumps and motors, accumulators, and some valves.

For simplicity and practicality of computer simulation, reduced-order models of components are often used in which high-frequency dynamic characteristics are neglected and components are modeled as simple inertance, resistance, and capacitance networks. It is often necessary to have accurate models of the inertance of the fluid in the components. This depends on the fluid density, but also depends very strongly on the geometry of the fluid passageway. It can be considered as equivalent to inductance in an electric circuit, where pressure ripple is equivalent to alternating voltage and flow ripple equivalent to alternating current.

Several computer programs have been developed for simulation of fluid-borne noise characteristics of fluid power systems [4–6], and these can be used to aid in the design of hydraulic systems with low pressure ripple. However, for the predictions to be meaningful, detailed knowledge of the impedance characteristics of the hydraulic components is necessary. Johnston and Edge [7] and Edge and Johnston [8] investigated the impedance characteristics

of a range of hydraulic components through experiments and simulation. Their experiments were performed using the "secondary source" method [9], whose test setup is shown schematically in Fig. 1. In this method, the harmonic components of pressure ripple generated by a controllable source (usually a pump, rotary valve, servovalve, or vibrating actuator) are measured at three points in a uniform metal tube. Because the wave propagation characteristics of the fluid in the tube are known quite accurately, it is possible to evaluate the pressure ripple and flow ripple at the point of interest at the inlet port of the component under test. From the ratio of pressure ripple and flow ripple, the entry impedance of the component can be determined. Johnston and Edge [7] and Edge and Johnston [8] found that the impedance of the components could be represented by simple models based on resistance, capacitance, and inertance terms. However, the values of these terms could not easily be predicted and had to be determined by experiment. Lau et al. [10] later developed expressions for the inertance of cylindrical orifices through similar experimental measurements and computational fluid dynamics (CFD) simulation.

Several researchers investigating the dynamic behavior of hydraulic components and systems have found inertance to be an important parameter. For example, Edge and Darling [11] modeled the flow ripple in axial piston pumps. They found that the predicted flow ripple could depend strongly on the inertance in the port plate and, particularly, in the relief grooves, and that pressure oscillations could occur within the cylinder due to resonance associated with the fluid compressibility and inertance. Dickinson et al. [12] and Johnston [13] also included inertance in the valve ports in their models of a vane pump and a reciprocating plunger pump, respectively. The values of inertance used by the above authors may not have been very accurate, as a precise method of calculation was not used. Edge and Johnston [8] found that the natural frequency of an accumulator was dependent on the inertance of the passageway. The value of inertance was difficult to estimate because of the complex geometry.

Equation (1) is a very simple expression for the inertance of a passageway of uniform cross section

$$L = \frac{\rho l}{A} \qquad (1)$$

This is based on the assumption of inviscid flow and neglects "end effects" due to changes in section at the ends of the passageway. Nonetheless, this simple expression is very commonly used. However, the inertance of more complex passageways is much more difficult to accurately quantify, either theoretically or experimen-

Copyright © 2006 by ASME
Transactions of the ASME
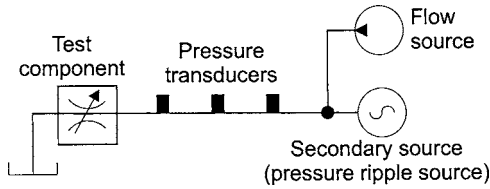
Fig. 1 Simplified hydraulic circuit for "secondary source" test method

Fig. 2 Finite volume cell

tally. This paper presents a method of numerical calculation of the inertance in a fluid passageway. The method is simple to apply and can be applied to geometries of arbitrary complexity.

2 Theory

Neglecting the effects of fluid compressibility, the pressure drop across a component is often considered as the sum of a resistive term and an inertial term [8] as given by Eq. (2). This is a simplification as it assumes that the resistive term can be determined from steady-state considerations [6], and the inertance L is unaffected by viscous effects [14]

$$\Delta p = f(q) + L\frac{\mathrm{d}q}{\mathrm{d}t} \quad (2)$$

where the resistive term $f(q)$ is often represented by the function kq^n, where n is 1 for laminar flow and approaches 2 for turbulent flow.

Linearized impedance analysis is commonly used for noise analysis. The resistive part of Eq. (2) can be linearized for small variations about the mean operating point of the steady-state pressure/flow characteristics [6], and Fourier transforms can be taken, giving

$$\Delta P = RQ + Lj\omega Q \quad (3)$$

This equation neglects wave effects and is valid only for frequency components with wavelengths significantly greater than the dimensions of the component. Hydraulic fluid power components are generally small compared to the wavelengths of the frequencies of interest; thus, this is usually valid (though longitudinal wave effects often need to be considered for tubes and hoses). The assumption that the resistance can be obtained from steady-state considerations may not be valid. For flow through passageways, the resistance increases with frequency [14]. However, for flow through short orifices, the resistance was found by Lau et al. [10] to be relatively independent of frequency.

The inertance term L cannot be evaluated from steady flow measurements and, hence, is more difficult to determine. Inertance is also affected by viscous effects [14] and depends on the nondimensional parameter $\alpha = \bar{l}^2\omega/\nu$. $\bar{l}$ is a characteristic dimension relating to the passageway cross section and, for a circular passageway, $\bar{l} = r$. For large α, the inertance approaches the inviscid value asymptotically and is approximately constant for $\alpha > 10^4$. The inertance increases by $\sim 40\%$ over the inviscid value as $\alpha \rightarrow 0$. Morris and Forster [14] considered flow in microchannels in microfluidic systems, in which low values of α are important. For larger scale fluid systems, the important range of α tends to be much higher and it is often an acceptable compromise between accuracy and complexity to consider the inertance to be constant and to be determined from inviscid considerations. The following analysis assumes inviscid flow.

The flow continuity equation for incompressible flow is

$$\frac{\partial u}{\partial x} + \frac{\partial v}{\partial y} + \frac{\partial w}{\partial z} = 0 \quad (4)$$

Neglecting the effects of viscosity and gravity, we obtain the following equations of motion:
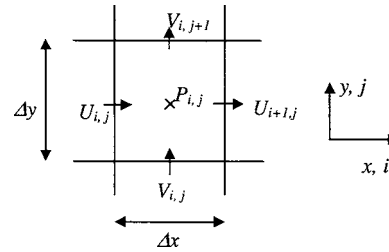
$$\rho\left(\frac{\partial u}{\partial t} + u\frac{\partial u}{\partial x}\right) = -\frac{\partial p}{\partial x}$$

$$\rho\left(\frac{\partial v}{\partial t} + v\frac{\partial v}{\partial y}\right) = -\frac{\partial p}{\partial y} \quad (5)$$

$$\rho\left(\frac{\partial w}{\partial t} + w\frac{\partial w}{\partial z}\right) = -\frac{\partial p}{\partial z}$$

By assuming zero time-averaged flow and the velocities to be small perturbations about zero, we can neglect the second terms in the brackets in Eq. (5) and obtain the simplified equations

$$\rho\frac{u}{\partial t} = -\frac{\partial p}{\partial x}$$

$$\rho\frac{\partial v}{\partial t} = -\frac{\partial p}{\partial y} \quad (6)$$

$$\rho\frac{\partial w}{\partial t} = -\frac{\partial p}{\partial z}$$

Taking Fourier transforms of Eqs. (4) and (6),

$$\frac{\partial U}{\partial x} + \frac{\partial V}{\partial y} + \frac{\partial W}{\partial z} = 0 \quad (7)$$

$$\rho j\omega U = -\frac{\partial P}{\partial x}, \quad \rho j\omega V = -\frac{\partial P}{\partial y}, \quad \rho j\omega W = -\frac{\partial P}{\partial z} \quad (8)$$

Substituting (8) into (7),

$$\frac{\partial^2 P}{\partial x^2} + \frac{\partial^2 P}{\partial y^2} + \frac{\partial^2 P}{\partial z^2} = 0 \quad (9)$$

Equation (9) is a form of Laplace's equation, and a similar equation was developed by Rayleigh [15] for the *velocity potential* for fluid in a passageway. Laplace's equation is applicable to several steady-state physical processes, including gravitation, electromagnetic fields, and temperature distributions in solids. It is inherently a steady-state equation as it does not include time-dependent terms. Although in this paper we are considering dynamically varying flows, we can consider the complex amplitudes U, V, W, and P to be independent of time.

2.2 Simple Finite Volume Numerical Model. Equations (7) and (8) or Eq. (9) can readily be solved numerically using finite difference, finite volume, or finite element techniques. A simple two-dimensional finite volume formulation was used in this case. Consider the rectangular cell shown in Fig. 2, in which variations in the z direction are neglected and the thickness is uniform in the z direction.

Pressure is defined at the cell center, and velocities are defined at the center of faces normal to that velocity. Assuming uniform normal velocities across each face, the continuity equation is

$$U_{i,j}\Delta y + V_{i,j}\Delta x - U_{i+1,j}\Delta y - V_{i,j+1}\Delta x = 0 \quad (10)$$

Equations (8) can be expressed in finite difference form as

$$\rho j \omega U_{i,j} = F_{i,j} \frac{P_{i-1,j} - P_{i,j}}{\Delta x}, \quad \rho j \omega V_{i,j} = G_{i,j} \frac{P_{i,j-1} - P_{i,j}}{\Delta y} \quad (11)$$

where F_{ij} is set to 0 for an impervious boundary and 1 for no boundary between cell $(i-1,j)$ and cell (i,j). Correspondingly G_{ij} is set to 0 for an impervious boundary and 1 for no boundary between cell $(i,j-1)$ and cell (i,j).

Substituting Eq. (11) into Eq. (10) gives

$$F_{i,j} \frac{P_{i-1,j} - P_{i,j}}{\Delta x^2} + G_{i,j} \frac{P_{i,j+1} - P_{i,j}}{\Delta y^2} + F_{i+1,j} \frac{P_{i+1,j} - P_{i,j}}{\Delta x^2}$$

$$+ G_{i+1,j} \frac{P_{i,j+1} - P_{i,j}}{\Delta y^2} = 0 \quad (12)$$

Equation (12) can be used to determine P_{ij} by rearrangement

$$P_{i,j} \left(\frac{F_{i,j}}{\Delta x^2} + \frac{F_{i+1,j}}{\Delta x^2} + \frac{G_{i,j}}{\Delta y^2} + \frac{G_{i,j+1}}{\Delta y^2} \right)$$

$$= \frac{P_{i-1,j}F_{i,j}}{\Delta x^2} + \frac{P_{i+1,j}F_{i+1,j}}{\Delta x^2} + \frac{P_{i,j-1}G_{i,j}}{\Delta y^2} + \frac{P_{i,j+1}G_{i,j+1}}{\Delta y^2} \quad (13)$$

At the inlet and outlet boundaries, the pressure amplitudes in the rows of cells at the boundaries can simply be set to 1 and 0, respectively. The pressures in the internal cells can then be determined by a suitable iterative method, such as successive overrelaxation (for example, [16]).

The normal acceleration $j\omega U$ or $j\omega V$ at the inlet and outlet boundaries can be calculated from Eq. (11). The inertance L can then be found

$$L = \frac{P_{\text{in}} - P_{\text{out}}}{j\omega Q_{\text{in}}} \quad (14)$$

where $j\omega Q_{in}$ is the integral of the normal acceleration over the surface of the inlet boundary.

An equation similar to Eq. (13) can be derived for axisymmetric flow. In this case, F_{ij} and G_{ij} can be used to represent the width of the cell face in the z (circumferential) direction as well as the presence of a no-flow boundary. Assuming uniform cell spacing where x is the axial direction and y is the radius, where $y = (j-1)\Delta y$

$$F_{i,j} = \left(j - \frac{1}{2} \right) \Delta y \quad (15)$$

$$G_{i,j} = (j-1)\Delta y \quad (16)$$

As before, at a no-flow boundary F_{ij} or G_{ij} are set to zero.

2.3 Effect of Mean Flow. The assumption of zero mean flow in Eq. (6) may seem to be a significant limitation and is clearly not the case in many important situations, for example, in a jet passing through an orifice. Lau et al. [10] investigated the impedance of hydraulic orifices with through-flow under noncavitating conditions by measurement and CFD modeling. They estimated the inertance from impedance measurements (for $15 < \alpha < 3000$, approximately) over a range of mean flow rates ($1100 < \text{Re} < 4200$) and found the estimated inertance to be practically independent of the mean flow rate and to correspond quite closely to the theoretical values for cylindrical orifices. CFD predictions with sinusoidally oscillating flow superimposed on a steady flow backed this up. They plotted the real and imaginary parts of the ratio between the pressure ripple and the flow ripple along the centerline of the passageway. The imaginary part is the inertance effect and was practically independent of the mean flow. It followed closely the profile that would be predicted from the full passageway geometry, regardless of the jet and vena contracta geometry. Similarly, the imaginary parts of the pressure-ripple/flow-ripple ratio traversing across the orifice were found to be apparently unaffected by the vena contracta. Peat [17] showed that

mean flow has a negligible effect on wave behavior at a discontinuity in a duct. His analysis assumed a constant mean velocity across the cross section, whereas, in practice, the flow in an abrupt expansion will form a jet in a central core, surrounded by a region of recirculation.

These results suggest that the inertance may be practically independent of the mean flow even when a jet, recirculation, and vena contracta are present, provided that the fluid density does not change appreciably, as, for example, in cavitating flow or high Mach number flow. This indicates that inertance values obtained using the methods described in this paper may be cautiously applied to through-flow conditions.

3 Results

Results are presented here for some common, simple types of hydraulic orifices. In all these cases, the flow was considered to be axisymmetric and, for simplicity, a density and inlet diameter or radius of unity were assumed. Results can readily be scaled to a real diameter and density. It should also be noted that the results are also applicable to flow in the opposite direction for which the same inertance values are obtained. Simulations were performed for a range of grid densities to ensure that numerical errors were $< 1\%$. Between about 20,000 and 2,000,000 uniformly spaced grid points were used in these models, and the predicted inertances were extrapolated toward zero grid spacing to improve the accuracy further.

3.1 Cylindrical Orifice. Cylindrical orifices located axisymmetrically within a uniform tube of larger diameter were considered. A typical contour plot of the pressure amplitudes is shown in Fig. 3. Here the x-axis represents the axis of symmetry. Closely packed contours within the orifice indicate a high pressure gradient in this region, and the contours curve outward in a symmetrical manner from either end of the orifice.

The inertance for a uniform tube is well known, if viscous effects are neglected, to be given by Eq. (1). However, for a tube or orifice of finite length, end effects need to be considered. These end effects relate to the contraction and expansion of the flow streamlines approaching and leaving the ends of the orifice, as shown by the curved contours near the ends of the orifice in Fig. 3. The inertance of such an orifice can be described using an effective length l_e, such that the inertance $L = \rho l_e / A_{\text{orifice}}$, where

$$l_e = l_{\text{orifice}} + k d_{\text{orifice}} \quad (17)$$

Rayleigh [15] determined that the end correction for a circular orifice in an infinite flat plate should lie in the range $\pi/4 < k < 8/3\pi$ ($0.785 < k < 0.849$) and would vary slightly, depending on the length of the orifice.

However, for the common situation where the orifice is located axisymmetrically in a larger diameter tube, this range of values is not necessarily applicable [18]. The method described in Sec. 2 was used to predict the orifice inertance and, hence, the end correction for a range of orifice/tube diameters. The end correction was calculated using

$$L_{\text{orifice}} = \frac{P_{\text{in}} - P_{\text{out}}}{j\omega Q_{\text{in}}} - \frac{\rho l_{\text{tube}}}{A_{\text{tube}}} \quad (18)$$

$$k = \frac{L_{\text{orifice}} A_{\text{orifice}}}{\rho d_{\text{orifice}}} - \frac{l_{\text{orifice}}}{d_{\text{orifice}}} \quad (19)$$

The tube length l_{tube} excludes the length of orifice l_{orifice}. The second term in Eq. (19) is an allowance for the normal inertance of the tube. The tube length l_{tube} in the calculations was at least $2d_{\text{tube}}$; this was found to be sufficient as longer tube lengths were not found to affect the predicted values of k appreciably.

End corrections for a range of ratios of orifice diameter to tube diameter are shown in Fig. 4. Two sets of data points are shown, one for a zero-length orifice (infinitely thin plate) and one for long orifices ($l_{\text{orifice}}/d_{\text{orifice}} > 1$); the end correction was found not to

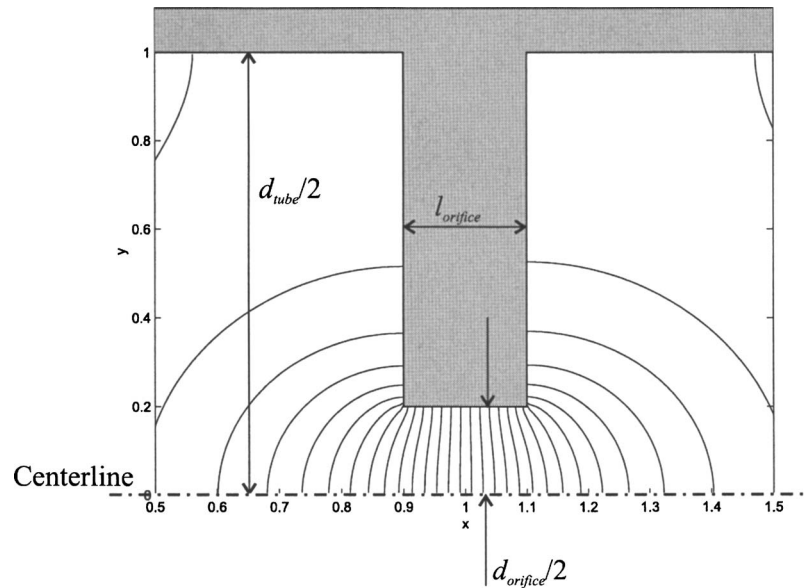**Fig. 3 Cylindrical orifice model: contours of pressure amplitude (only region near orifice shown)**

change appreciably for $l_{orifice}/d_{orifice}$ greater than about 0.5). Third-order polynomials are also shown, which fit the data very closely. These have the equations

Long orifice:
$$k = 0.4581 \left(\frac{d_{orifice}}{d_{tube}} \right)^3 - 0.2564 \left(\frac{d_{orifice}}{d_{tube}} \right)^2$$
$$- 1.0177 \left(\frac{d_{orifice}}{d_{tube}} \right) + 0.8126 \qquad (20)$$

Short orifice:
$$k = 0.4451 \left(\frac{d_{orifice}}{d_{tube}} \right)^3 - 0.1706 \left(\frac{d_{orifice}}{d_{tube}} \right)^2$$
$$- 1.0588 \left(\frac{d_{orifice}}{d_{tube}} \right) + 0.7822 \qquad (21)$$

It can be seen that, for small orifice diameters, the end correction approaches Rayleigh's calculated values. This is expected as Rayleigh considered a hole in an infinite plate, which is equivalent to a vanishingly small hole in a finite plate. The end correction decreases for larger diameters, becoming zero when the orifice diameter is equal to the tube diameter, which would be expected as there is then no streamline contraction. These curves corre-
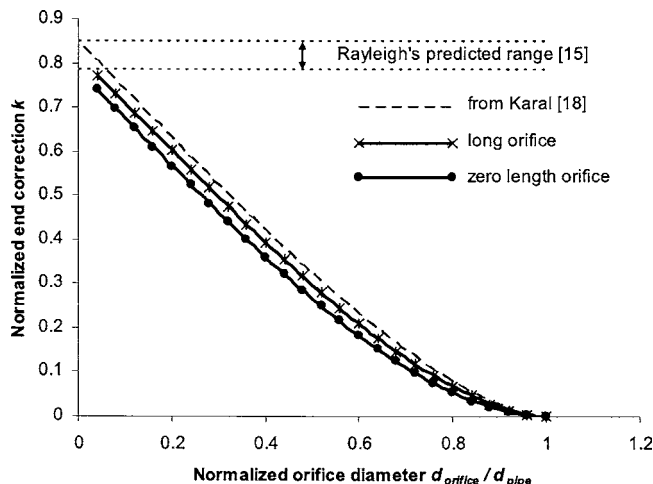

Fig. 4   End correction for cylindrical orifices

spond well with Karal's theoretical curves [18]; the difference is largely due to Karal's assumption of uniform velocity across the orifice diameter. Sahasrabudhe et al. [19] showed that the inertance varies for high frequencies where the wavelength is of a similar order to the diameter. However, for most fluid power hydraulic components, the diameter is much smaller than the wavelengths of interest and a constant inertance can be assumed (these results also neglect variations in inertance due to viscosity [14]).

Note that this end correction is for a double-ended cylindrical orifice; for a single expansion or contraction, the end effect is half of the above values.

3.2 Spool Valve Orifice. Predictions were performed for a simple annular orifice in a spool valve. The model was axisymmetric, and flow travels outward through the annular orifice, though the same inertance is obtained for flow in the opposite direction. The geometry and typical contours of pressure amplitude are shown in Fig. 5. The x-axis represents the axis of symmetry. Flow enters the model axially from the left into an annular chamber with inner diameter $d_{in}/2$ and outer diameter d_{in}. Flow exits axially to the right through a larger annular chamber with inner diameter d_{in} and outer diameter $2d_{in}$. The lengths of the inner and outer chambers l_{in} and l_{out} are defined as the length from the inlet and outlet boundary, respectively, to the edge of the outer annular chamber and are both equal to $d_{in}/2$.

The effective length was calculated using the following equations, in which allowance is made for the inertance of the uniform inlet and outlet passageways in a similar way to that for the cylindrical orifice:

$$L_{orifice} = \frac{P_{in} - P_{out}}{j\omega Q_{in}} - \frac{\rho l_{in}}{A_{in}} - \frac{\rho l_{out}}{A_{out}} \qquad (22)$$

$$l_{eff} = \frac{L_{orifice} A_{orifice}}{\rho} \qquad (23)$$

Predicted effective lengths are shown in Fig. 6 for a range of openings X. In this case, the effective lengths are normalized by dividing by the opening X.

The overall inertance of a spool valve of this geometry can then be determined from Eq. (24), where l_{in} and l_{out} are defined as in Fig. 5, and l_{eff} obtained from Fig. 6.
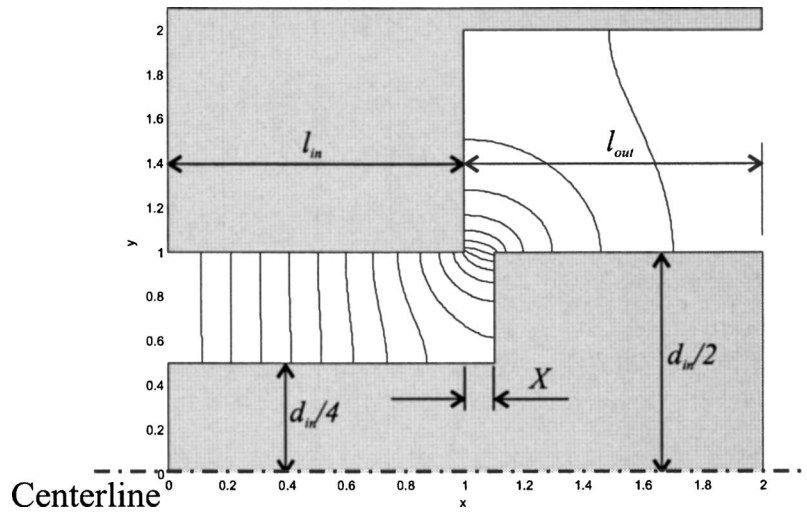
Fig. 5 Spool valve model: contours of pressure amplitude

$$L = \rho\left(\frac{l_{\mathrm{in}}}{A_{\mathrm{in}}} + \frac{l_{\mathrm{out}}}{A_{\mathrm{out}}} + \frac{l_{\mathrm{eff}}}{A_{\mathrm{orifice}}}\right) \qquad (24)$$

Practical spool valves will not be of this exact geometry. However, the effective length should be a good approximation in many cases.

3.3 Poppet Valve. Predictions of inertance were performed for a simple conical poppet valve. A typical contour plot is shown in Fig. 7. The dimensions of the model relative to the inlet diameter d_{in} are listed in Table 1. The left-hand boundary is the inlet and the right-hand boundary the outlet.

The effective length was calculated in the same way as the spool valve, using Eqs. (22) and (23). Results are shown in Fig. 8, in which the effective length is normalized by dividing by the poppet lift X.

The overall inertance can be obtained using Eq. (24). Again, it should be noted that these results are specific to this particular geometry of poppet valve and may not be appropriate for other poppet angles or geometries.

4 Calculation of Inertance Using Commercial Simulation Packages

The numerical method described in Sec. 2 can be applied readily to fairly simple geometries involving straight boundaries and right angles. For more complex geometries, it becomes far more complicated and would be beneficial to use a commercially available modeling package that can handle complex geometries.

It is possible to perform unsteady flow calculations using a CFD package where the flow or pressure is perturbed sinusoidally or with some other wave form [10]. The inertance can be extracted by taking the Fourier transform of the pressure drop and flow rate. However, such dynamic simulations can be very difficult and time consuming to perform.

A novel method is now proposed that is much quicker and simpler, but involves interpreting CFD model results in a slightly unorthodox way. It is possible to configure a CFD model in such a way that, in effect, Laplace's equation is being solved instead of the more complex Navier-Stokes and turbulence equations. This is
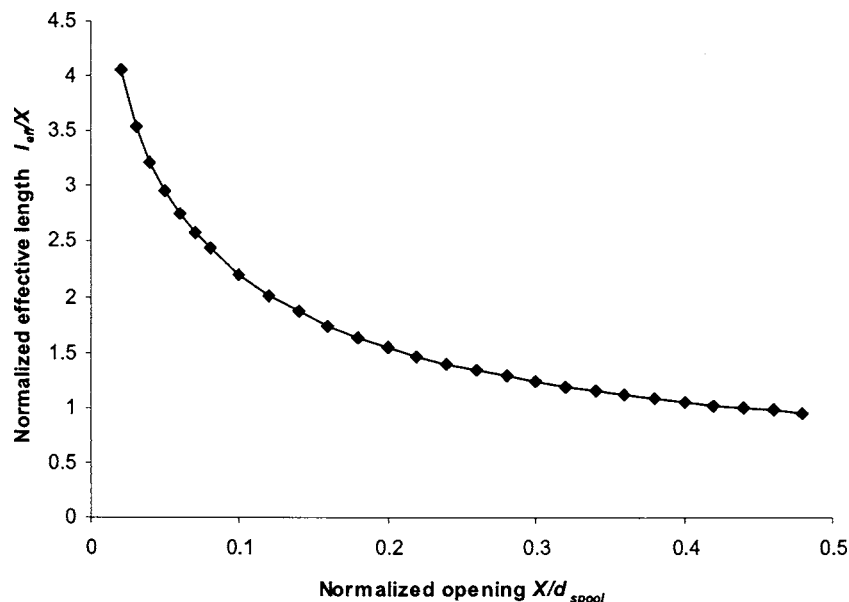

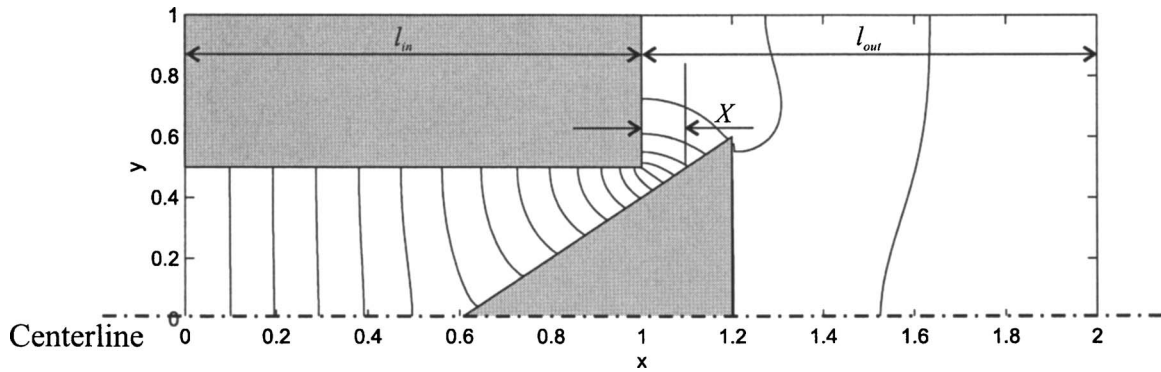**Fig. 6 Effective length for spool valve orifice**

Fig. 7 Poppet valve model: contours of pressure amplitude

done by setting up a model for laminar flow through a porous medium. As will be shown, the resistance to flow through a porous medium is analogous to the inertance in a geometrically similar fluid-filled passageway.

Assuming an isotropic porous medium and provided that the permeability K is sufficiently high that

$$\frac{K\bar{l}}{\rho\bar{v}} \gg 1 \tag{25}$$

where $\bar{l}$ and $\bar{v}$ are a characteristic length and velocity, respectively, inertial effects become negligible [20] and the pressure gradients are given by

$$Ku = -\frac{\partial p}{\partial x}, \quad Kv = -\frac{\partial p}{\partial y}, \quad Kw = -\frac{\partial p}{\partial z} \tag{26}$$

These are of a similar form to Eq. (7). They can be substituted into the continuity equation (4) to give Laplace's equation

Table 1 Dimensions of poppet valve model

Inlet tube length	$1 \times d_{in}$
Poppet outer diameter	$1.2 \times d_{in}$
Poppet face angle	45 deg
Outlet chamber diameter	$2 \times d_{in}$
Outlet chamber length	$1 \times d_{in}$

$$\frac{\partial^2 p}{\partial x^2} + \frac{\partial^2 p}{\partial y^2} + \frac{\partial^2 p}{\partial z^2} = 0 \tag{27}$$

This is similar to Eq. (9), except that it defines the behavior of the steady-state pressure p and not the Fourier transform P. Thus, steady flow in a highly resistive porous medium behaves according to Laplace's equation. CFD calculations can be used to calculate the resistance R of a passageway containing a porous medium for an arbitrary flowrate, where R is the pressure drop divided by the flow rate. The results can then be scaled to calculate the inertance of a geometrically identical "clear" passageway (that is, one without the porous medium), using the equation

$$L = \frac{R\rho}{K} = \frac{p_{in} - p_{out}}{Q}\frac{\rho}{K} \tag{28}$$

This method has the advantage that the capability of commercial CFD codes for generating complex geometries can be made use of, while avoiding the computational difficulties inherent in performing a full dynamic CFD simulation. Indeed, the solution tends to be quicker and more stable than the steady-state solution of flow in a clear passageway because of the linearity and simplicity of Laplace's equation compared to the nonlinearity of the Navier-Stokes equations and turbulence equations.

A simple example of a result using this method is shown in Fig. 9. Here, a square restriction in a square passageway has been modeled. Only a quarter section of the passageway has been modeled; the two faces in full view are symmetry planes. It was found
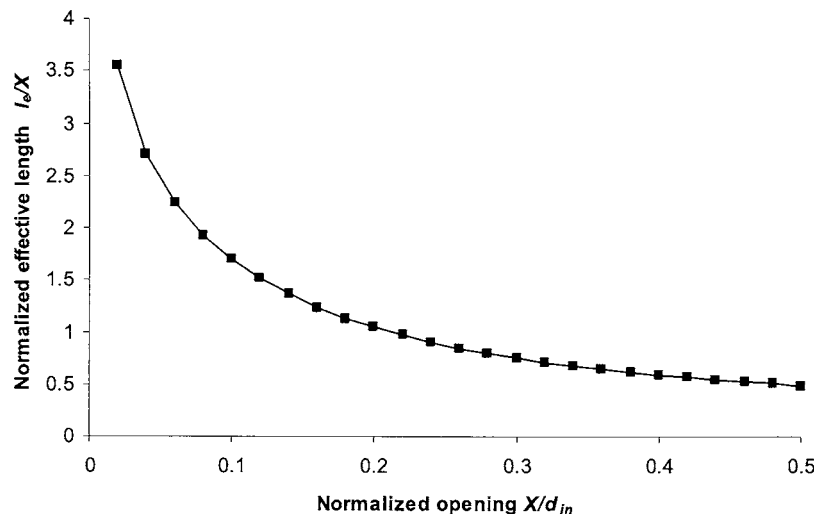

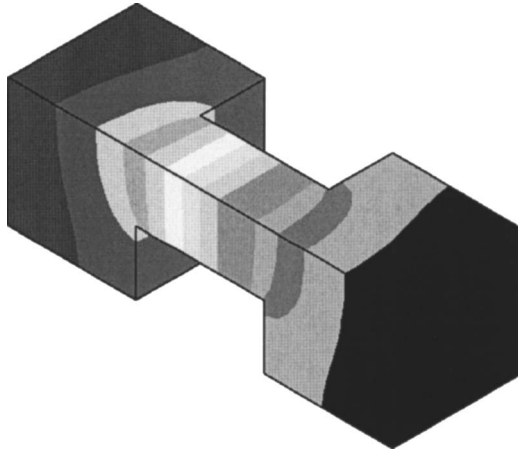**Fig. 8 Effective length for poppet valve**

Fig. 9 Pressure distribution in a square restriction obtained using CFD

that inertance values calculated from CFD results in this way were within 2% of values calculated using the method described in Sec. 2. Differences are likely to be mainly due to discretization errors and related to the grid densities.

It may also be noted that gravitational fields, electromagnetic fields, heat conduction, and electric potential in a resistive solid can all behave according to Laplace's equation under suitable conditions. Therefore, it should also be possible to model inertance using computer packages designed for modeling these other physical phenomena.

For example, a heat transfer modeling package, such as ANSYS®, can be used to model steady-state heat transfer in an isotropic solid of identical geometry to the fluid passageway. Walls of the fluid passageway should be represented by zero heat flux boundaries, and the inlet and outlet of the fluid passageway should be represented by arbitrary prescribed temperatures or heat flux. The equivalent inertance for the identical fluid passageway can then be calculated from Eq. (29), where $\dot{W}$ is the total heat flow through the solid

$$L = \frac{\theta_{\text{in}} - \theta_{\text{out}}}{\dot{W}} \rho k \qquad (29)$$

Results obtained using ANSYS in this way were found to be practically identical to those shown in Sec. 3.

5 Application of Results

These modeling techniques may be useful in many fields in which inertance is important, as described in the Introduction. In hydraulic fluid power applications, they may be useful for modeling of hydraulic system dynamic response, stability, or fluid-borne noise characteristics.

Given the effective length values from Sec. 3, the inertance of that component can readily be calculated using

$$L = \frac{\rho l_{\text{eff}}}{A_{\text{orifice}}} \qquad (30)$$

An example of the importance of inertance in an orifice can be found in the dynamic response of a relief valve. A simplified schematic diagram of the valve considered here is shown in Fig. 10.

The valve, its mathematical model, and the measurement technique that was used were described in detail by Johnston et al. [21]. The mathematical model includes the following effects:

- resistance and inertance in the main orifice and damping orifice
- mass of spool and viscous friction between spool and body

Table 2 Dimensions of approximated damping orifice

Length (mm)	Diameter (mm)	End correction k for method 2
3.3	3.2	$4/(3\pi)$
5.4	1.6	$0.15 + 0.07$
2.4	2.4	0
2.4	1.4	$0.11 + 4/(3\pi)$

- compressibility of fluid in the spring chamber and upstream chamber
- leakage between spool and body (these results were obtained with the spool seals removed, to reduce friction)
- flow forces in orifices

The linearized model equations are given in [21] and are reproduced in the Appendix. The secondary source technique [9] was used to determine the pressure ripple immediately upstream of the valve, and a pressure transducer was located in the wall of the spring chamber. So that the results were not affected by pressure ripple in the downstream line, the valve was operated with a low back pressure so that cavitation occurred downstream of the orifice. This effectively produced a constant pressure region downstream of the valve, decoupling the valve impedance from the impedance of the downstream line.

The damping orifice is approximated to a cylindrical hole with step changes in diameter with dimensions listed in Table 2. The inertance of the damping orifice was estimated using the following three methods:

1. Summing the inertances for each hole section using Eq. (1) and neglecting end effects

$$L_D = \sum \frac{\rho l_i}{A_i} = 5186 \times \rho \text{ kg/m}^4$$

2. As method 1, but including end effects from Eq. (17) and Fig. 4 for each change in orifice diameter. The end corrections k were determined using Fig. 4, based on the ratio of diameters for each change in section. Figure 3 is for a double-sided orifice thus, the values of k were halved to represent each single step change in diameter, and are listed in Table 2.

$$L_D = \sum \frac{\rho(l_i + kd_i)}{A_i} = 6014 \times \rho \text{ kg/m}^4$$

3. Modeling the complete damping orifice using the finite volume method described in Sec. 2, $L_D = 6021 \times \rho \text{ kg/m}^4$

The third method should be the most accurate, in general, as the complete orifice geometry is considered. The first method is oversimplistic and gives a poor estimate. The second method gives a result that is almost identical to the third method and would be quite adequate for this situation.

Figure 11 shows the measured and predicted ratio between the pressure ripple measured in the spring chamber and the inlet pressure ripple, plotted as a function of frequency. The predicted ratio is shown with and without the inclusion of inertance in the damping orifice, calculated using method (3). It can be seen that the inertance has a very strong effect on the results, and good agreement between measurement and prediction is obtained when inertance is included.

Predicted impedance results, with and without the inclusion of inertance in the damping orifice, are shown in Fig. 12. The inertance can be seen to have a very marked effect on the valve impedance, particularly, at frequencies above $\sim$500 Hz. The curve without inertance has one well-damped resonant peak at $\sim$1000 Hz. This is related to the mass of the spool, the spring rate,
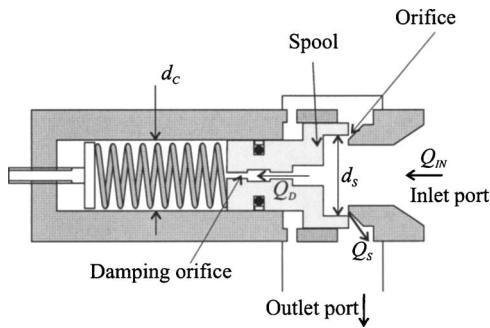
Fig. 10 Simplified schematic diagram of relief valve

the flow forces, and the compressibility of the fluid in the spring chamber. A simple calculation based on the spool mass and spring stiffness alone gives a natural frequency of 390 Hz. The curve with inertance has two peaks, one at 700 Hz and one at 3500 Hz, and a trough at ~2000 Hz. The lower peak relates mainly to the mass of the spool and the spring stiffness, whereas the higher peak relates to the mass of the spool and the compressibility of fluid in the spring chamber, which behaves as a much stiffer spring. At this frequency, the impedance of the damping orifice has become very high so that it is effectively blocked, trapping the fluid in the spring chamber and causing it to act as a liquid spring. The trough at ~2000 Hz corresponds to the peak in the pressure ratio in Fig. 10.

It was shown by Johnston et al. [21] that the inertance in the damping orifice has an important effect on the stability characteristics of the valve and could also have a strong effect on the fluid-borne noise in a circuit incorporating this valve. The inertance in the main orifice was found to have a very small effect in this case.

6 Conclusions

A method has been presented for numerical calculation of the inertance in a hydraulic passageway, which can be applied to geometries of arbitrary complexity. It is based on incompressible, inviscid flow analysis, so the results may be less accurate for very viscous fluids, very small components or very high frequencies. However, it provides a simple means of calculation suitable for a very broad range of applications. Results have been presented for some common hydraulic orifices, these being a simple cylindrical orifice, a simple spool valve, and a conical poppet valve. There is some theoretical, computational, and experimental evidence that mean flow and flow separation have little effect on inertance, so the results presented here are believed to be applicable to situations where there is significant mean flow, such as in flow or pressure control valves. However, further work would be beneficial to establish, fully, the effect of mean flow on inertance.

An unorthodox use of a CFD package and a finite element solid-modeling package has been demonstrated. Resistance to flow in a porous medium behaves in a similar way to inertance in a passageway containing fluid without the porous medium, provided that certain constraints are met. Fluid inertance also behaves in a similar way to heat transfer in a solid. This provides some very convenient ways of obtaining the inertance of complex passageways using readily available software. To the best of the author's knowledge these methods have not been used before.

It is shown that inertance can have a strong effect on component dynamic response. The inertance results presented in this paper may be incorporated into the dynamic simulation of fluid components and systems both in the time domain and frequency domain.
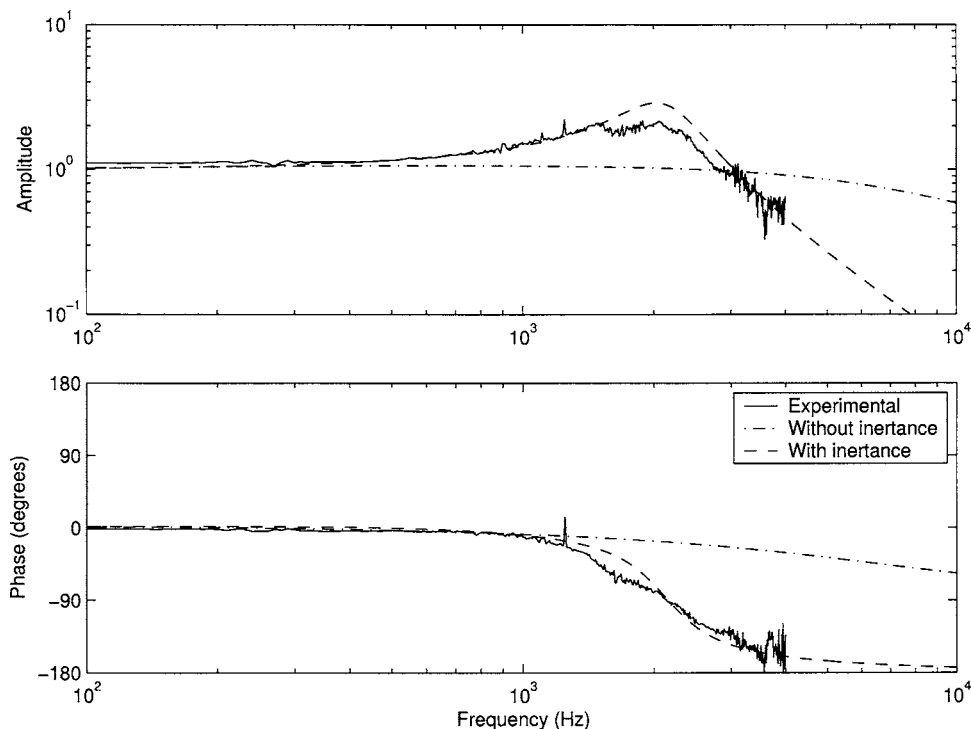
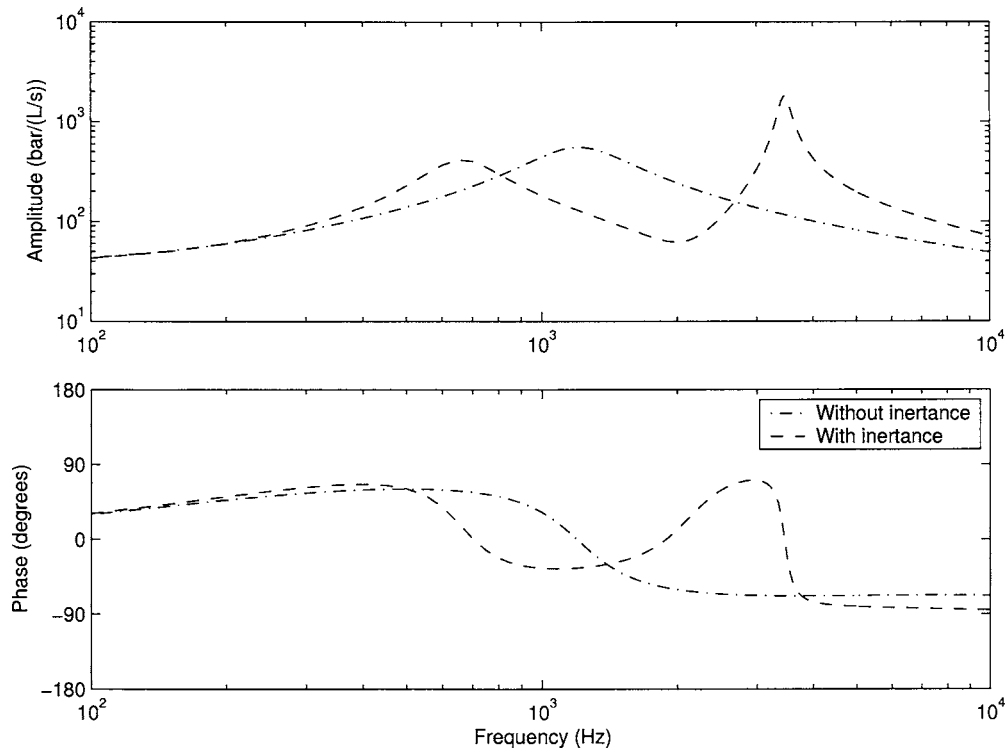**Fig. 11 Measured and predicted pressure ratio in relief valve**

Fig. 12 Predicted impedance of a relief valve

Nomenclature

A = cross-sectional area
B = bulk modulus
d = diameter
F, G = constants
k = thermal conductivity
k = end correction
K = permeability
l = length
L = inertance
$\bar{l}$ = characteristic length
l_e = effective length
P = Fourier transform of pressure
p = pressure
Q = Fourier transform of flowrate
q = flow rate
r = radius
R = resistance
t = time
U, V, W = Fourier transforms of velocity components in x, y, and z, directions respectively
u, v, w = velocity components in x, y, and z directions, respectively
$\bar{v}$ = characteristic velocity
$\dot{W}$ = total heat flow in heat transfer model
X = valve opening
x, y, z = coordinates
α = dimensionless quantity
θ = temperature
ρ = fluid density
ω = frequency

Subscripts

D = damping orifice
i, j = cell indices in x and y directions, respectively
in = inlet

orifice = orifice dimension
out = outlet
tube = tube dimension

Appendix: Linearized, Frequency Domain, Poppet Valve Model

The model is described in more detail in Ref. [21]. The parameter definitions and values are listed in Table 3 and shown in Fig. 10 where appropriate.

The Fourier transformed variables are as follows:

P_C is the pressure ripple in the spring chamber
P_{in} is the inlet flow ripple
Q_D is the flow ripple through the damping orifice
Q_{in} is the inlet flow ripple
Q_S is the flow ripple through the main spool orifice
X is the spool displacement

i. Spool force balance, including flow forces

$$(-m\omega^2 + Cj\omega + k)X = \frac{\pi d_S^2}{4}P_{in} - \frac{\pi d_C^2}{4}P_C$$

$$- \left(2\frac{\rho \bar{q}_S}{C_{CS}\bar{a}_S} \cos\theta \right) Q_S$$

$$+ \left(\frac{\rho \bar{q}_S^2}{C_{CS}\bar{a}_S^2} \frac{\partial a_S}{\partial x} \cos\theta \right) X$$

$$(A1)$$

ii. Flow continuity at the inlet, including compressibility and piston effect due to spool movement

$$\frac{V_{in}}{B_{in}}j\omega P_{in} = Q_{in} - Q_S - Q_D - \frac{\pi d_B^2}{4}j\omega X \qquad (A2)$$

iii. Pressure drop through the damping orifice in the spool

Table 3   Valve parameters

Parameter	Value
Mean orifice area for main spool orifice $\bar{a}_s$	2.83 mm^2
Bulk modulus B_{in}, B_C	14,300 bar
Viscous friction factor C	7.5 Ns/m
Leakage coefficient C_L	1.08×10^{-4} L/s/bar
Main spool flow coefficient asymptotic value C_{QS}	0.75
Damping orifice flow coefficient asymptotic value C_{QD}	0.75
Main spool seat diameter d_s	9.36 mm
Spool diameter in chamber d_C	7.93 mm
Spring stiffness k	74,500 N/m
Effective piston mass (including 1/3 of spring mass) m	12.3 g
Upstream pressure $\bar{p}_{in}$	100 bar
Flowrate $\bar{q}_{in}$, $\bar{q}_s$	17 L/min
Hydraulic resistance of damping orifice R_D	109 bar/(L/s)
Upstream oil volume V_{in}	3.0 cm^3
Oil volume in chamber V_C	2.0 cm^3
Mean value opening $\bar{x}$	0.14 mm
Poppet viscous flow coefficient β	9.9
Poppet seat angle ϕ	42 deg
Viscosity μ	13.9 cP
Effective angle for flow force θ	72 deg
Fluid density ρ	845 kg/m^3

$$P_{in} - P_C = (R_D + L_D j\omega)Q_D \qquad (A3)$$

iv. Pressure drop through the valve, including inertia effects

$$P_{in} = \left[\frac{\rho \bar{q}_S}{(C_{QS}\bar{a}_S)^2} + \frac{\beta \mu \pi d_s}{\bar{a}_S^2} + j\omega \frac{\rho l_S}{\bar{a}_S} \right] Q_S - \left[\left(\frac{\rho \bar{q}_S^2}{C_{QS}^2} \right) \right. $$
$$\left. + 2\beta\mu\pi d_S\bar{q}_S \right) \frac{1}{\bar{a}_S^3}\frac{\partial a_S}{\partial x} + j\omega\frac{\rho l_S \bar{q}_S}{\bar{a}_S^2}\frac{\partial a_S}{\partial x} \right] X \qquad (A4)$$

v. Flow continuity at rear end of spool, including compressibility and piston effect due to spool movement

$$\frac{V_C}{B_C}j\omega P_C = Q_D + \frac{\pi d_C^2}{4}j\omega X - C_L P_C \qquad (A5)$$

The parameters for the valve are listed in Table 3.

Equations (A1)–(A5) were arranged in a matrix form and solved over a range of frequencies to determine P_{in}, P_C, Q_S, Q_D and X for a prescribed inlet flow ripple Q_{in}. The impedance at a particular frequency was then given by P_{in}/Q_{in}.

References

[1] Roach, P. R., and Kashani, A., 1997, "Pulse Tube Coolers With an Inertance Tube: Theory, Modeling and Practice," Cryogenic Engineering Conf., July, Portland, OR, *Advances in Cryogenic Engineering*, Vol. 43B, pp. 1895–1902.

[2] Muramatsu, K., Yukitake, K., Nakamura, M., Matsumoto, I., and Motohiro, Y., 2001, "Monitoring of Nonlinear Respiratory Elastance Using a Multiple Linear Regression Analysis," Eur. Respir. J., **17**(6), pp. 1158–1166.

[3] Wolfe, J., Smith, J., Tann, J., and Fletcher, N. H., 2001, "Acoustic Impedance of Classical and Modern Flutes," J. Sound Vib., **243**, pp. 127–144.

[4] Lecerf, J.-P., 1989, "A Methodology to Describe and Predict Hydraulic Noise in Fluid Power Systems," 2nd Bath International Fluid Power Workshop, Bath, September.

[5] Johnston, D. N., and Edge, K. A., 1989, "Simulation of the Pressure Ripple Characteristics of Hydraulic Circuits," Proc. Inst. Mech. Eng., Part C: J. Mech. Eng. Sci., **203**, pp. 119–127.

[6] Kojima, E., Sinada, M., and Matsui, M., 1992, "Development of a General Purpose Simulation Package for Pulsation in Hydraulic Pipeline Generated by Noise," (in Japanese), Trans Jap. Soc. Mech. Engrs, Ser. B, **58**(546), pp. 356–363.

[7] Johnston, D. N., and Edge, K. A., 1991, "The Impedance Characteristics of Fluid Power Components: Restrictor and Flow Control Valves," Proc. Instn Mech. Engrs, Part I: J. Sys. Control Eng., **205**, pp. 3–10.

[8] Edge, K. A., and Johnston, D. N., 1991, "The Impedance Characteristics of Fluid Power Components: Relief Valves and Accumulators," Proc. Instn Mech. Engrs, Part I: J. Sys. Control Eng., **205**, pp. 11–22.

[9] Johnston, D. N., and Drew, J. E., 1996, "Measurement of Positive Displacement Pump Flow Ripple and Impedance," Proc Instn Mech. Engrs, Part I: J. Sys. Control Eng., **210**, pp. 65–74.

[10] Lau, K. K., Edge, K. A., and Johnston, D. N., 1995, "Impedance Characteristics of Hydraulic Orifices," Proc. Instn Mech. Engrs, Part I: J. Sys. Control Eng., **209**, pp. 241–253.

[11] Edge, K. A., and Darling, J., 1986, "Cylinder Pressure Transients in Oil Hydraulic Pumps With Sliding Plate Valves," Proc. Instn Mech. Engrs, Part B: J. Manage. Eng. Manuf., **200**, pp. 45–54.

[12] Dickinson, A. L., Edge, K. A., and Johnston, D. N., 1993, "Measurement and Prediction of Power Steering Vane Pump Fluidborne Noise," SAE Transactions-Journal of Passenger Cars, **102**(6), pp. 1753–1761.

[13] Johnston, D. N., 1991, "Numerical Modelling of Reciprocating Pumps With Self-Acting Valves," Proc. Instn Mech. Engrs, Part I: J. Sys. Control Eng., **205**, pp. 87–96.

[14] Morris, C. J., and Forster, F. K., 2004, "Oscillatory Flow in Microchannels: Comparison of Exact and Approximate Impedance Models With Experiments," Exp. Fluids, **36**, pp. 928–937.

[15] Rayleigh, J. W. S., 1945, *The Theory of Sound*, Dover, New York, Vol. 2.

[16] Chapra, S. C., and Canale, R. P., *Numerical Methods for Engineers*, McGraw-Hill, New York.

[17] Peat, K. S., 1988, "The Acoustical Impedance at Discontinuities of Ducts in the Presence of a Mean Flow," J. Sound Vib., **127**(1), pp. 123–132.

[18] Karal, F. C., 1953, "The Analogous Acoustical Impedance for Discontinuities and Constrictions of Circular Cross Section," J. Acoust. Soc. Am., **25**, pp. 665–682.

[19] Sahasrabudhe, A. D., Munjal, M. L., and Anantha Ramu, A., 1995, "Analysis of Inertance due to the Higher Order Mode Effects in a Sudden Area Discontinuity," J. Sound Vib., **185**(3), pp. 515–529.

[20] Bird, R. B., 2003, Transport Phenomena, Wiley, New York.

[21] Johnston, D. N., Edge, K. A., and Brunelli, M., 2002, "Impedance and Stability Characteristics of a Relief Valve," Proc. Instn Mech. Engrs, Part I: J. Sys. Control Eng., **216**(I5), pp. 371–382.

Evan M. Griffing
Post-Doctoral Researcher
Department of Chemical and Biomolecular
Engineering,
North Carolina State University,
911 Partners Way,
Raleigh, NC 27695

S. George Bankoff
Professor Emeritus
Department of Chemical and Biological
Engineering,
Northwestern University,
2145 Sheridan Road,
Evanston, IL 60208

Michael J. Miksis
Professor
e-mail: miksis@northwestern.edu
Department of Engineering Sciences and Applied
Mathematics,
Northwestern University,
2145 Sheridan Road,
Evanston, IL 60208

Robert A. Schluter
Professor Emeritus
Department of Physics,
Northwestern University,
2145 Sheridan Road,
Evanston, IL 60208

Electrohydrodynamics of Thin Flowing Films

Thin films of oil flowing down a nearly-vertical plate were subjected to a strong normal electrostatic field. Steady-state height profiles were measured by fluorescence imaging. For electrode potentials less than that required to produce an instability, the two-dimensional response of the interface was <1%. Calculations of the fluid height coupled with the electric field solution were identical to uncoupled calculations for electric fields below the stability threshold. Pressure profiles under the film and three-dimensional effects are also discussed. [DOI: 10.1115/1.2169811]

Introduction

An electrostatic liquid film radiator (ELFR) has been proposed as a very lightweight radiator for rejecting waste heat into space [1,2]. For much larger power capabilities than the International Space Station (>1 MW), the radiator weight becomes a major component of total weight, and can limit the total power capability. Various lightweight schemes have been proposed, such as droplet sprays or moving belts, but in these cases coolant loss over a period of time can occur by evaporation, surface entrainment, and/or droplet collisions. The proposed ELFR consists of a closed hollow membrane, on the inside of which a thin liquid-metal film circulates. The coolant liquid transfers heat to the space surroundings by radiation from the outer shell, which mandates as high a liquid temperature as feasible. A preferred liquid coolant would be lithium, because of its low density, high thermal conductivity, and low vapor pressure. Other alkali metals may also be considered. Each has its own handling and safety problems for experimentation in a laboratory on Earth. Molten salts are therefore also possibilities. Separately, organic liquids of low vapor pressure and dielectric constant would be useful in a smaller ("housekeeping") radiator, which rejects heat from air-conditioning and other housekeeping requirements.

A principal consideration in the design of the ELFR is that the near-Earth atmosphere may contain a large population of micrometeorites. These are overwhelmingly of micron size or less, but may contain larger particles, which could puncture the membrane and possibly cause coolant leakage. Back-up safety measures are therefore indicated. One such feature would be an array of electrodes suspended internally opposite the liquid film, connected to a source of high voltage, such as a small van de Graaf generator. An external leak would be detected by resistivity changes, and the electrode opposite the leak would then be charged to a high voltage. The resulting electric field, exerting a tensile force normal to the liquid surface, may effectively stop the leak. However, of concern in this regard is the possibility of surface waves, which, under the influence of the electric field, might grow in amplitude sufficiently to short out the electrode. Hence an experimental and theoretical investigation of the surface deformations was performed.

Previous work. Kim et al. [3] calculated the linear-stability, steady-state shapes, and time-evolution of a free interface of a thin liquid-metal film flowing down an inclined plate under a finite-length electrode. The coupling of the fluid and the field was included in their linear stability result but not in their study of the evolution of the films. An interesting result was the appearance of a marked thinning, or trough, as the fluid passed under the electrode, followed by a peak as the film left the electrode region. The amplitude of the trough and peak in the profile were shown to increase with electric field and decrease with increased Reynolds number. Two-dimensional disturbances were calculated with a lubrication model for low Reynolds number (Re) and a Kármán-Pohlhausen model for high Re. Both results were compared with a marker-and-cell type computation of the full Navier-Stokes equations, performed with the SOLA algorithm [4], which, however, did not allow for surface tension. Surface tension was also neglected in the steady thin film calculations, and this assumption was shown to be justified by a scaling analysis. The calculated pressure deficiency underneath the fluid was on the order of 1 Pa, which was taken to have a sufficient safety margin for leak stoppage, based on the vapor pressure of liquid lithium at 650 K.
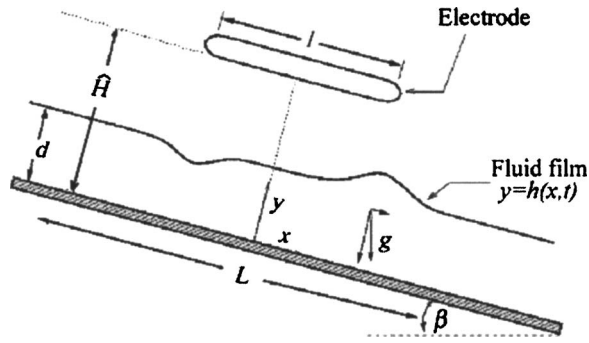
Transactions of the ASME

Fig. 1 Gravity-driven flow on a plate with an inclination of β is subjected to an electric field. The field produces an electrostatic tension at the interface, producing a spatially-varying steady state height profile.

Benjamin [5] and Yih [6] derived the linear stability threshold of a draining film on an inclined plate of infinite length, based on a long wave expansion. They found that the film was unstable when the Reynolds number is greater than a critical value, $Re_c = 5/6 \cot \beta$, and Re is evaluated with the average velocity. This condition is valid in the thin film limit, $\xi = d/L \ll 1$. Kim et al. [3] generalized the analysis for a conductive film to include the effect of an electric field. For a constant potential, ϕ_H, at a height H above the plate, linear stability requires that

$$\mathrm{Re} < 5/6 \cot(\beta) - 10/9 K \frac{H^2(1 - 1/\epsilon_f)^2}{(1/\epsilon_f + H - 1)^3} + \frac{5}{9} \frac{\xi^2}{\mathrm{Ca}} k^2. \qquad (1)$$

González and Castellanos [7,8] performed a weakly nonlinear analysis of a draining liquid-metal film with surface tension acted on by an electric field represented by a constant potential at infinity. In the parameter range where the flow was linearly stable in the absence of the field, but linearly unstable in the presence of the field, a finite-amplitude set of stable traveling waves was found. The problem was modeled on an electrode of infinite length placed at an infinite distance above the plate. Here we consider an electrode of finite length, l, placed at a finite distance above the plate. The present work extends the theoretical model of Kim et al. [3] to include the coupling of the electric field in the numerical solution of the lubrication equation, and experimentally determines height profiles and pressure underneath the flowing films.

Experiment. Before performing verification experiments in space, it would be clearly useful to perform measurements on a liquid-metal film draining on a conductive plate on earth in the laboratory. Mercury, which is much less reactive than lithium, can be substituted for safety reasons. However, the toxicity of mercury, coupled with the difficulty in keeping the circulating mercury surface free from visible contaminants over days of operation, made the procedure unattractive. Experiments were therefore conducted with a vacuum-pump oil (Convoil 20) on a vertical brass plate with a small hole drilled in it. The hole might represent a puncture by a micrometeorite. A coated glass electrode was suspended parallel to the plate. Steady local thickness profiles and pressure underneath the thin flowing film were then measured at various positions along the plate.

Thin Film Model and Numerical Solution

A lubrication model is used to study the gravity-driven flow down an inclined plate. The plate is subject to an electrostatic interfacial pressure produced by a finite electrode, see Fig. 1. The evolution equation for the thickness h was derived in Kim et al. [3],

$$h_t + 3h^2 h_x + 2/3 \bar{C}^{-1} (h_{xxx} h^3)_x + 2/3 \left(1 - \frac{1}{\epsilon_f}\right) \bar{K} [(E_n^2)_x h^3]_x = 0. \qquad (2)$$

Here the dimensionless capillary number is $\bar{C} \xi^3 = \mathrm{Ca}$, while $\bar{K} \xi^{-1} = K$ is a dimensionless number representing the ratio of electric to viscous forces. Both $\bar{C}$ and $\bar{K}$ are assumed to be of order one. The dimensionless film thickness, h, is scaled by the constant upstream fluid depth d, and the spatial coordinate x is scaled by the electrode length l, which is taken to be equal to L. The time t is scaled by L/U_0. Finally, the normal component of the electric field is scaled by F.

Using $\bar{K}$ has the advantage that it depends only on the electric field and physical parameters, rather than on the Reynolds number. It is seen from Eq. (2) that for large Ca the steady-state profile is given by

$$h(t \rightarrow \infty) = \left(1 + 2/3 \left(1 - \frac{1}{\epsilon_f}\right) \bar{K}(E_n^2)_x\right)^{-1/3}.$$

Note that the local height is dependent on the gradient of the normal component of the field. The gradient of the field changes sign from the entrance to exit regions under the electrode, thereby explaining the dip in height (trough) of the film entering the electrode region and the hump on leaving, as shown in Fig. 1. Physically, the changes in fluid depth can be attributed to the pressure gradient in the direction of flow. As the fluid nears the electrode it experiences a drop in pressure, which causes acceleration, and a resulting decrease in height. If the electrode is long enough, the fluid then decelerates until the viscous and gravitational forces again balance, causing the fluid height to return to 1 underneath the electrode. The opposite effect is produced as the fluid leaves the electrode and experiences an increase in pressure.

We determine a steady-state solution to the fluid height [Eq. (2)] both uncoupled and coupled to the potential equation, which provides the electric field. In the uncoupled equations, we solve for the electric field in the absence of a fluid. The electric boundary conditions are $\phi = 1$ at the electrode surface and $\phi = 0$ at the brass plate. For the coupled calculations, we use an electrically conducting fluid ($\epsilon_f = \infty$) in the model; the boundary conditions are $\phi = 1$ at the electrode surface and $\phi = 0$ at the liquid surface.

Solutions of the uncoupled and coupled models become indistinguishable at low ϕ and high H. Physically, the two solutions merge under these conditions, because the deformation of the fluid height, which changes the boundary conditions of the electric problem, is small relative the electrode height. In the experiments presented here, H is large and we expect that the coupling is small. The numerical effect is calculated in order to verify the accuracy of the simplified model; this is discussed in detail in the results section.

The coupling between the fluid height and the electric field is stronger for a conducting fluid than for a dielectric. Therefore, when a numerical comparison of the coupled and uncoupled models for conducting fluids gives nearly identical results, it is safe to apply the uncoupled model for a dielectric fluid. Certainly for stronger fields or lower electrode heights, it would be necessary to solve the more complicated coupled equations for a dielectric fluid.

To facilitate the solution of the external electric field with the thin liquid film in the numerical solution of the lubrication equation, periodic boundary conditions in x were used, instead of a monotonically decreasing field extending to infinity. As expected, our computations implied that as long as the period was large (as done here), these conditions had little effect on the predictions of the model.

An iterative numerical scheme was developed to advance h and ϕ in time. First the evolution equation for h [Eq. (2)] was solved using the method of lines. The equation was discretized in x, and
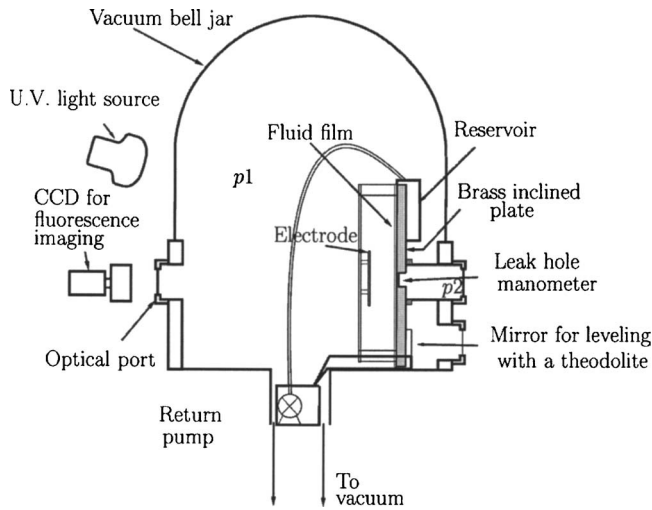
Fig. 2 The experimental apparatus used to measure fluid height and pressure profiles, instability potentials, and leak rates
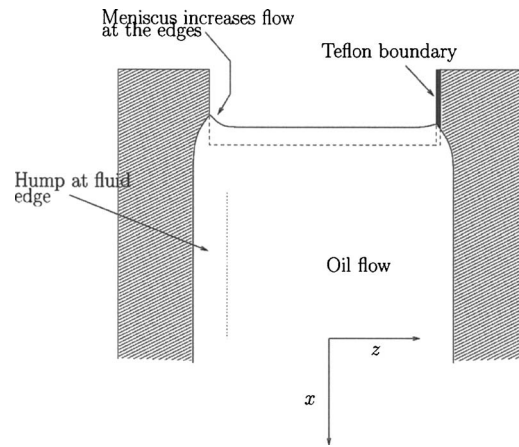

Fig. 3 At the inlet, capillarity produces a meniscus, which causes a greater flow at the edges. This leads to a thicker film and a hump that persists far downstream. A Teflon boundary increased the contact angle, which was shown to decrease the hump size.

the numerical routine LSODE was used to integrate the resulting set of first order ODEs over the first time step. Then the potential equation was solved using the boundary integral numerical method as described by Ramachandran [9] with a periodic Green's functions given by Hocking and Miksis [10]. This procedure was iterated in time. Note that the time step was adjusted such that the maximum change in fluid height remained within a predefined bound.

To obtain steady state solutions we found it convenient to allow the electrode potential to increase from zero to one, such that the transient solution for the fluid depth was smooth. The solution was then marched to steady state while keeping the potential on the electrode equal to one. The computational cost for obtaining a steady state solution depended on the height and potential of the electrode as well as the mesh size required for convergence. More specifically, because of the use of a direct linear equation solver, the operation count for our computational method is of the order of the cube of the number of mesh points.

Experimental Setup. The apparatus (Fig. 2) consisted of an inclined metal plate in a vacuum bell jar with various auxiliary systems. Fluid flowed continuously down the plate, passing in front of an electrode. In experiments on two-dimensional wave formation on an inclined plate, several authors have reported sensitivity to inlet noise and vibrations [11–13]. Therefore, the whole apparatus was suspended by a 2 m cable in order to damp vibrations normal to the interface. The angle of inclination was variable over the range, $80° < \beta < 95°$, and was measured with a theodolite to an accuracy of 10^{-6} rad [14]. This corresponded to a normal component of gravity of -0.85 m/s$^2 < g_n < 1.70$ m/s^2. The electrode was made from coated plate glass, so that the fluorescence imaging method could be used to determine height profiles. The vacuum system prevented gas phase breakdown near the electrode corners, so that high electric fields ($E' > 1.2 \times 10^7$ V/m) could be attained. This is an order of magnitude greater than needed to stop a liquid-metal leak in space.

The physical properties of Convoil 20 were $\rho = 890$ kg/m^3, $\nu = 1.425 \times 10^{-4}$ m^2/s, $\sigma = 3.32 \times 10^{-2}$ N/m, and $\epsilon_f = 2.13$. We should note that experiments determining pressure profiles were also performed with ethanol and gave similar results [14]. For the Convoil 20 experiments, a gear pump fashioned from nylon provided accurately-metered flow with minimal pressure pulses over a range of $0 < Re < 0.25$. Brass and Teflon guides were used to constrain the flow as it passed over a sharp 90 deg edge at the top of the plate. Capillarity at the boundary produced a hump at the

edge of the flow, as shown in Fig. 3. Teflon was used to increase the contact angle and thus decrease the size of the hump. In no case did this edge effect extend more than 5% of the transverse fluid width, so that a central averaged region could be isolated for a two-dimensional measurement.

Reynolds numbers obtained are considerably less than the range $100 < Re < 400$ in design calculations for a lightweight space radiator using liquid lithium as the coolant [2]. Thus, this implies that edge effects in the proposed radiator would be considerably smaller.

The pressure was measured with a manometer, which tapped the vertical plate and used the flowing film as a working fluid, as shown in Fig. 4. The electrode and brass plate are physically
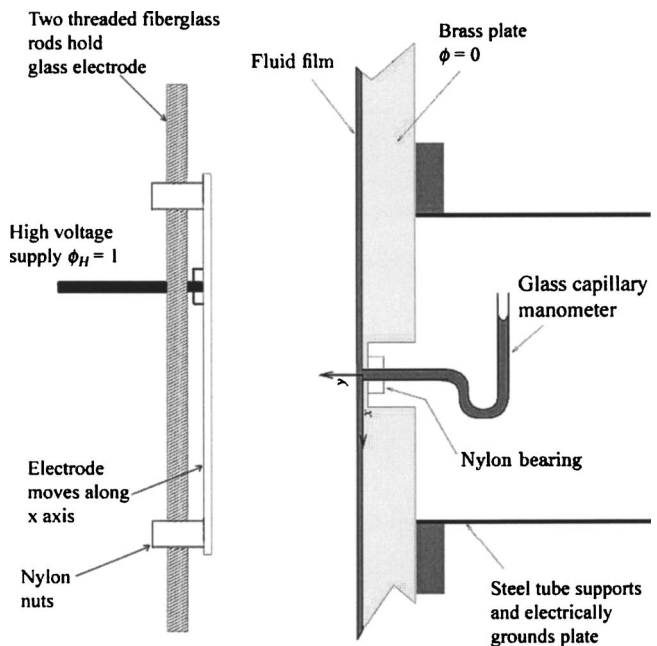

Fig. 4 Cross-sectional view of the fluid manometer, which was connected to the back of the inclined plate. A traveling microscope (not shown) was used to measure the meniscus height. In order to obtain consistent results, a receding contact angle and a new manometer was required for each set of measurements.

connected through 0.15 m of threaded fiberglass rod and a nylon brace. This electrically isolates the two while accurately maintaining relative positioning. The brass plate is supported by a steel tube, which is electrically connected to the power supply ground.

The electrode is electrically connected to the high-voltage power supply positive terminal using a copper tube, which was coated with Glyptal. Metallic paint was applied to ensure a constant potential on the electrode edges. A commercially available antistatic spray, transparent and permanent, was applied to the electrode surface. The electrostatic relaxation time for charge redistribution is estimated to be orders of magnitude shorter than any experimental adjustment time.[1]

A traveling microscope was then used to measure the displacement of the interface with an accuracy of 5.0×10^{-5} m, or 0.392 Pa. The pressure profile, $p(x)$, was obtained by moving the electrode, which was mounted on two threaded rods. While the manometer hole remained fixed, the relative position to the center of the electrode (x) changed.

Height profiles. For the fluid Convoil 20, the height profile of the flowing film was found by use of the fluorescence imaging method due to Liu and Gollub [11] and modified by Johnson et al. [12,13]. The principle of the method is that the brightness of a fluid layer in which a fluor is dissolved and illuminated by ultraviolet light is a function of depth of the fluid (in this case, close to linear).

The quantitative exploitation of the method is given by Johnson et al. [12]. Their procedures were followed as closely as possible. The overall normalization was done during an experimental run by interposing intervals of frame packets (24 at the camera rate of 30/s) between each frame packet that made up an experimental image. These normalization packets were smooth, giving the average luminosity over the field of interest at that moment in the experimental run. The experimental pixel intensities were then divided by the normalization intensities, pixel by pixel. This averaging removed transient structure in the film image and improved accuracy since the normalization image incorporated the entire depth to pixel intensity coefficient at a given time in the experiment.

The dye, 9,10-bis(phenylethynyl)anthracene (BPEA), in the fluid was excited by the incident UV light source. The intensity of the fluorescent response was measured spatially with a linear-response digital camera. Filters on the UV source and the camera lens were used to diminish error due to reflections. The depth of the fluid was obtained from the image intensity by a calibration curve, and showed very small changes in height due to the field for stable electric potentials. However, the signal to noise ratio was low (0.2 for high-frequency noise and 1.0 for low-frequency noise or drift in the signal). There was also the complication of the presence of the electrode.

Using a horizontal plate for calibration with lighting conditions identical to the experiment was not practical, because of the vacuum equipment. The calibration was performed with a vertical falling film and the depth was calculated based on the flow rate. The calculated values of depth should be within 5% of the actual depth, because waves were not observed, and relative error due to thermal noise was estimated to be 0.003. The fluid depth was assumed to be two-dimensional in the central portion of the flow, and parallel profiles were taken by averaging across 52 pixels or 2 cm in the transverse direction. A Gaussian-weighted moving average with a length scale of 21 pixels was then performed in the parallel direction. Transverse profiles were generated in a similar manner, except the spatial variations were on a smaller scale, so that the averaging over x spanned only 8 pixels. Figure 5 shows the oil film, electrode, and areas used to measure the depth pro-
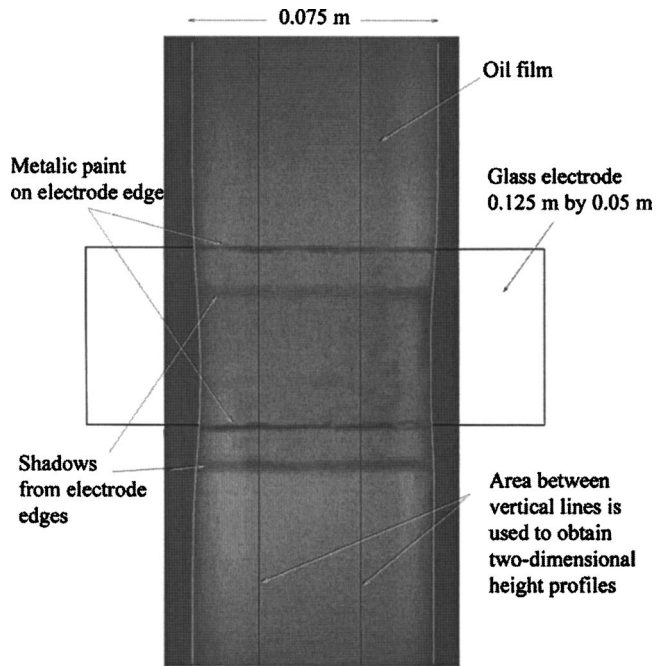

Fig. 5 An image of the oil film flowing down a vertical plate in front of a glass electrode. The image contrast and brightness have been increased to highlight the features. The contact line is outlined with a white line, and the continuation of the electrode past the image edge is drawn in to indicate size. The parameters were ϕ_H=25 kV, $\hat{H}$=0.0237 m, l=0.05 m, and $\bar{K}$=0.0169.

files. The electrode is wider then the fluid width, in order to ensure that the field is two-dimensional over the fluid interface. At the edge of the fluid, the film width contracts by $\sim$0.003 m underneath the electrode, and expands to the original width downstream. This contraction is shown here to be very small relative to the fluid width, and is far from the region of the film used to generate two-dimensional height profiles.

Results

Pressure measurement. Figure 6 compares the experimental pressure profiles for Convoil 20 with the pressure profiles predicted by a calculation of the electrostatic field, uncoupled from the fluid height problem. For this uncoupled calculation, the value of E_n is found on the plate assuming no film is present. The pressure along the plate is equal to $\epsilon_o F^2 E_n^2 / 2\rho U^2$, while that of a dielectric is found by multiplying the pressure for a conductor by $1-1/\epsilon_f$. As expected, it has a maximum value at $x=0$, the center of the electrode. For ethanol, which is a weak electrical conductor, the measured pressure under the film (not shown) is equal to the computed pressure at the interface to within the estimated experimental error (0.5 Pa) [14]. This is consistent with lubrication theory. However, with the dielectric oil the pressure measured by the manometer was almost double the calculated electrostatic pressure for a nonconductive wall (see Fig. 6). In fact, the results of a calculation of the pressure that would be exerted on a conductor match the experimental results well, possibly due to deformation of the field within the thin hole. Field calculations show that, depending on the depth of the narrow cavity in the brass plate, the field within the leak hole can lead to the experimentally-obtained pressure profile, despite the poor conductivity of the oil covering the plate. The deformed electric field lines within the hole enter the metal wall orthogonally. The curvature of the field lines within the hole cause the field to decrease along the axis of the hole. This decrease in the field exerts a local body force on the
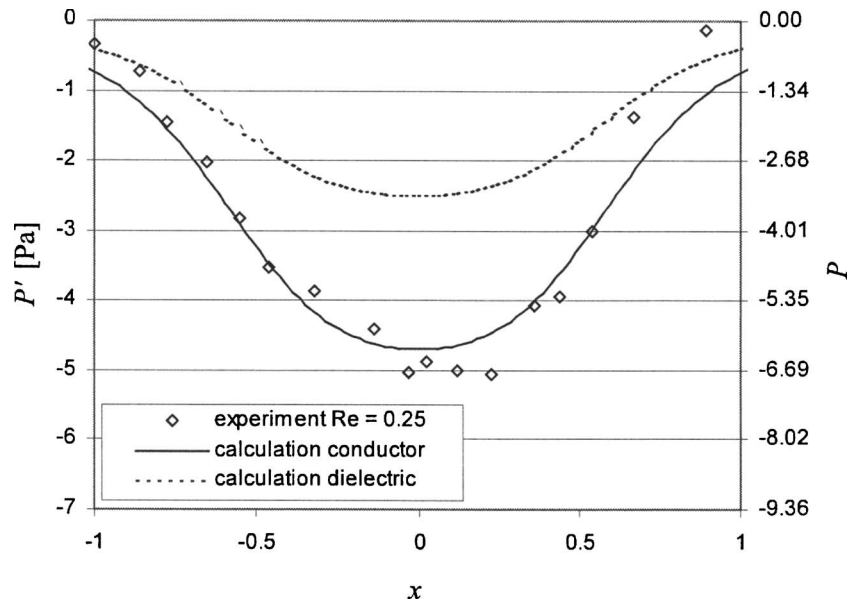
Fig. 6 The experimental pressure profile under a Convoil 20 film for Re=0.25, ϕ_H=25 kV, $\hat{H}$=0.0237 m, and *l*=0.05 m is compared to the pressure exerted by the electric field on the fluid surface. Both dimensional and dimensionless pressures are shown. The *x* axis is dimensionless, to show the position of the electrode which spans the region −0.5<*x*<0.5. The experimental pressure is very close to that which would be exerted on the surface of a conducting film, probably owing to deformation of field lines within the cavity.

fluid, which is in addition to the pressure drop at the interface. A more complete explanation is given by Griffing [14]. The implication for low temperature radiator designs, which incorporate an organic liquid, is that higher pressures might be overcome with the electric field.

Fluid depth measurement. Fluid depth measurements have been made with Convoil 20 oil over a parameter range of (0.07

<Re<0.18), $(0.68 \times 10^{-3} < \bar{K} < 2.44 \times 10^{-2})$, and $(2.2 \times 10^4 < \bar{C} < 3.0 \times 10^4)$. Because of the low signal-to-noise ratio, extensive averaging was used to remove high frequency noise and a polynomial fitting procedure was used to eliminate low frequency noise by assuming a depth profile over some region of the flow. Parallel profiles show the two-dimensional response of the fluid to an electric field, and are compared to the solution of the lubrication equation. Cross-stream profiles are used to develop three-
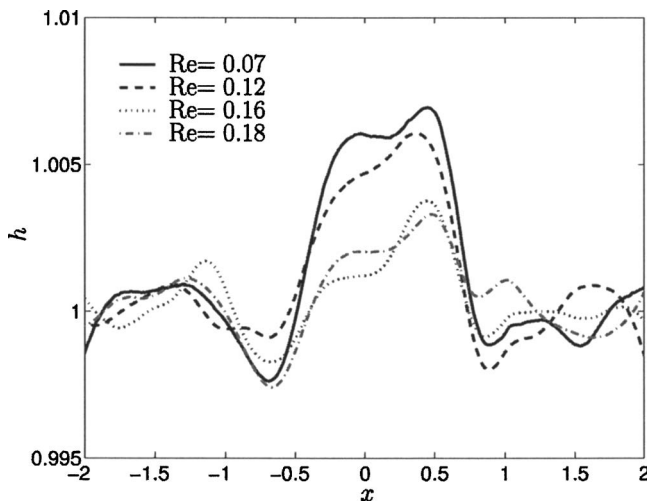

Fig. 7 The experimental height profiles as a function of Reynolds number for $\bar{K}$=1.69×10^{-2}. Both *h* and *x* are dimensionless. The electrode extends from −0.5<*x*<0.5. There is a small decrease in amplitude under the full electrode length as the Reynolds number is increased. This would be expected to be negligible for Re>100, as in ELFR design calculations based on liquid metals, provided that Re<Re$_C$. $\bar{C}$ is specified by Re and the physical properties of oil, and is $\bar{C}$=[2.99×10^4, 2.47×10^4, 2.25×10^4, 2.917×10^4].
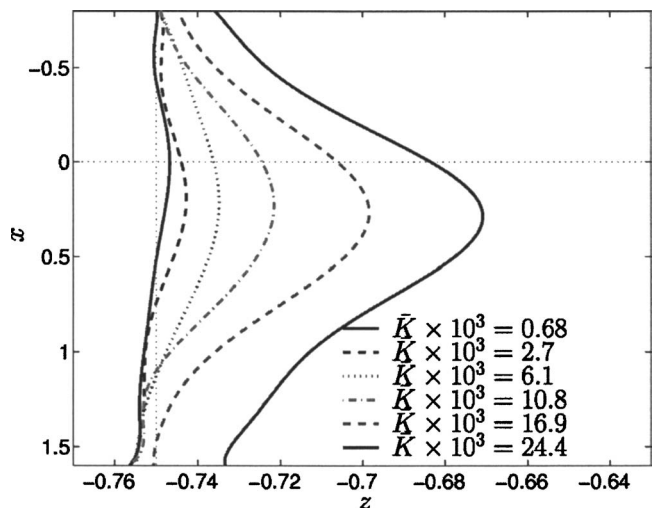

Fig. 8 Contact line at the edge of the oil flow: The electric field causes a contraction in the flow width, which is asymmetric about *x*=0. The flow contraction increases with $\bar{K}$ for the small Reynolds number, Re=0.07 and large capillary number $\bar{C}$ =2.99×10^4. The parameters *x* and *z* are both scaled by 0.05 m. Additional experimental parameters are: $\hat{H}$=0.0237 m, *l* =0.05 m, and ϕ_H=[5,10,15,20,25,30] kV.
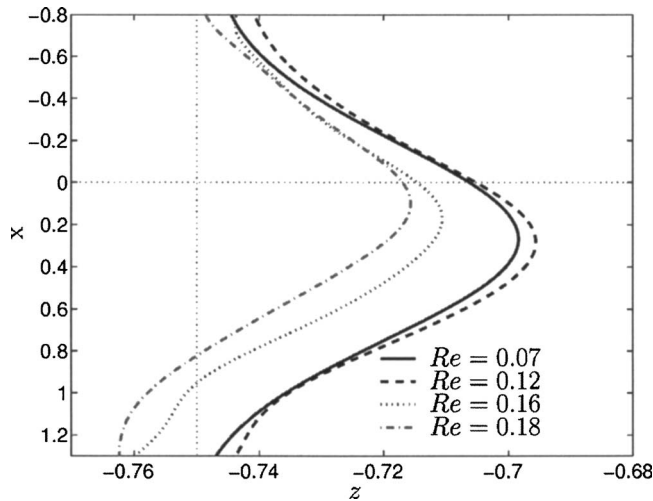
Fig. 9 Contact line at the edge of the oil flow: Increasing the Reynolds number decreases the magnitude of the film contraction for the given electric field F=1055 kV/m, which corresponds to $\bar{K}$=1.69×10⁻². The parameters x and z are both scaled by 0.05 m. Additional experimental parameters are: $\hat{H}$ =0.0237 m, l=0.05 m, ϕ_H=25 kV, and $\bar{C}$=[2.99×10⁴, 2.47×10⁴, 2.25×10⁴, 2.917×10⁴]. If Re is increased by a factor of 1000, as in the proposed ELFR, this effect should be negligible.

dimensional depth plots.

For the parallel profiles, the normalized depth is assumed to be h=1 for $-2 < x < -1$ and $1 < x < 2$. Depth profiles are shown in Fig. 7 for Re=[0.07, 0.12, 0.16, 0.18]. The dimensional fluid depth far from the electrode was 7.6×10^{-4} m, 9.1×10^{-4} m, 1.0 $\times 10^{-3}$ m, and 1.04×10^{-3} m. The error in these plots is estimated to be 4×10^{-7} m or 0.0004 in the dimensionless units that are used in the figures. We based the error on an analysis of both the high frequency and low frequency noises discussed previously. As noted above, each of these curves shows a dip under the leading edge and a peak under the trailing edge of the electrode, similar to calculations by Kim et al. [1] for a conductive fluid.

The contact line (position of the lateral fluid edge) is plotted as a function of electrode potential in Fig. 8, and as a function of Re in Fig. 9. The fluid width contracts as the fluid passes under the electrode. The maximum contraction is located at x=0.2, which is 0.01 m downstream from the center of the electrode. The maximum amplitude of the contraction is 3.3% of the fluid width or 0.0025 m, even at these very low values of Re.

Cross-flow height profiles were obtained in a similar manner as the parallel profiles. In this case, we assumed that the flow over the central region ($-0.3 < z < 0.3$ in dimensionless units) was flat, and fitted this region to a polynomial to correct for low frequency noise. This assumption is more difficult to justify than that used in the parallel case. Therefore, we use a second order polynomial to prevent the filtering of transverse waves. The amplitude of the measured waves along the z axis (Fig. 3) is an order of magnitude larger than that along the parallel axis. Therefore, $h(z=0)$ is assumed to be independent of x, and a second order polynomial fit was defined over $-2 < x < 2$ at z=0. The height profile was then normalized by this curve. The resulting three-dimensional images are shown in Fig. 10.

For low $\bar{K}$, the humps at the fluid edge, which originate at the inlet, propagate downstream with minimal damping. For high $\bar{K}$, peaks form in the humps under the trailing edge of the electrode. The interaction between the fluid and the electric field is complicated by the contact line and is dissimilar to the two-dimensional profiles that form in the center of the flow. These edge effects,

which occupy only a small fraction of the transverse flow dimension, lead to preferred locations for instabilities similar to Taylor cones, which are described in a later paper.

Calculated depth profiles. The computational solution for experimental parameters of Convoil 20 at Re=0.16 and $\bar{K}$=1.69 $\times 10^{-2}$ is shown with the experimental data in Fig. 11. Note that the qualitative comparison between theory and experiment is very good. The only difference is in the small-scale features of the interface. For these parameters (large H, small $\bar{K}$), the fluid deformation (due to the electric field) is small, and the electric field is not significantly altered.

The effect of coupling for a conducting fluid is quantified in Fig. 12, in which the maximum height (of the peak under the trailing edge) is plotted as a function of $\bar{K}$ for several values of H. For low values of $\bar{K}$, the perturbation in fluid height is small and the coupled and uncoupled solutions merge. In the comparison of experiment to our model equations (Fig. 11), the relevant parameters are $\bar{K}$=0.017 and $\hat{H}$=0.0237 m. Figure 12 shows that for electrode heights of $\hat{H}$=0.011 m (the bottom curves), the effect of coupling can be neglected for this value of the electric field number. Uncoupled solutions are shown in Fig. 13 for oil parameters, with surface tensions of 0.2, 3.2, and 32.0 N/m. Increasing the surface tension produces capillary waves trailing the primary peaks. The effect of coupling on the capillary waves is shown in Fig. 14. The coupling of the electric field and the fluid height shortens the wavelength and increases the amplitude of the capillary waves. On increasing the field past some critical value, the solutions did not converge for practical mesh sizes (800 nodes).

Conclusions

To summarize, two-dimensional pressure profiles produced by a finite electrode compared well with calculated electrostatic pressures in the case of a conducting fluid (ethanol [14]). Even for a poorly-conducting low-vapor pressure vacuum pump oil fluid (Convoil 20) deformation of the field lines within the cavity associated with the leak hole used in these experiments caused measured pressures to be nearly equivalent to the conducting case. This result is thought to be caused by the field lines within the leak hole.

The two-dimensional fluid depth profile for Re<0.25 compares favorably with lubrication theory for experimental conditions. The electrode was far from the fluid surface, which essentially decoupled the solutions of the electric field and the fluid height. Both the experiment and the model equations produced a dip in the fluid height under the leading edge of the electrode and a hump under the trailing edge. This profile is physically due to the decrease and increase in pressure, which cause changes in the fluid velocity. Slightly higher fields than those shown in the experimental results caused a short-wave instability, similar to a Taylor cone at the fluid edges.

The effects of coupling the potential equation to the lubrication equation were explored. For large electrode heights (>0.01 m), which are easily attainable in the proposed radiator, coupling had a negligible affect for the experimentally explored electric fields. When surface tension is included, smaller steady state waves precede the dip and hump in the fluid, which characterize the flow. For low electrode heights, the coupled solution is required to adequately describe these smaller waves as well as accurately predict the height of the peak under the trailing edge of the electrode.

The three-dimensional response (transverse to flow) was limited to a small portion of the flow near the contact line. However, it was an order of magnitude greater than that in the parallel direction, due to a hump at the edge of the flowing rivulet caused by nonuniform conditions at the film entrance. The field, which is stronger at the fluid contact line, causes the rivulet to narrow opposite the electrode. The hump height under the electrode in-
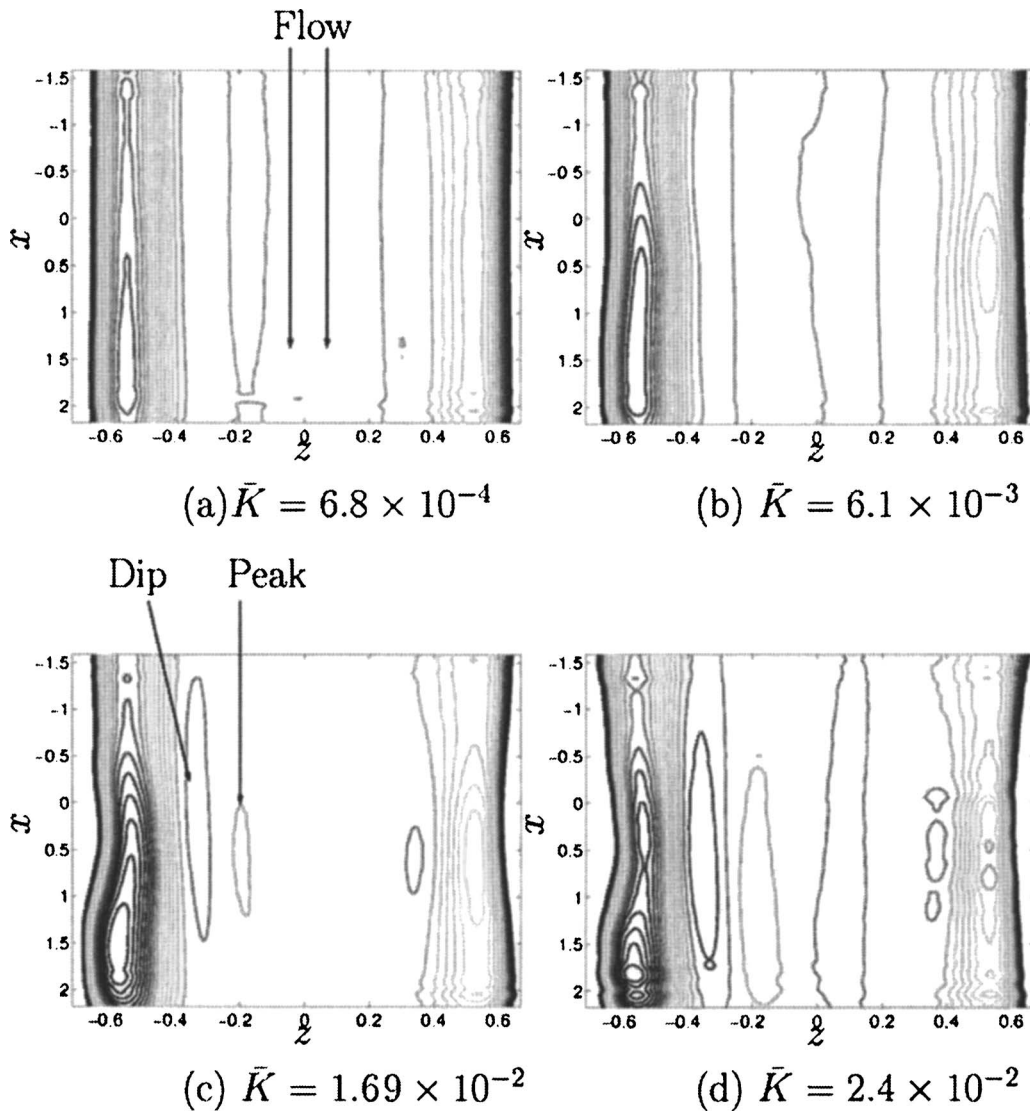
(a) $\bar{K} = 6.8 \times 10^{-4}$

(b) $\bar{K} = 6.1 \times 10^{-3}$

(c) $\bar{K} = 1.69 \times 10^{-2}$

(d) $\bar{K} = 2.4 \times 10^{-2}$

Fig. 10   A dielectric oil flows under a charged electrode, which spans $-0.5 < x < 0.5$. The parameters x and z are both scaled by 0.05 m. For high values of the field, a peak forms under the trailing edge of the electrode, and a transverse instability develops. The change in h between each contour line is 0.017. (*a*) For low values of the electric field, the fluid passes through undisturbed. (*b*)–(*d*) For larger field strength, the hump at the fluid edge increases in height.
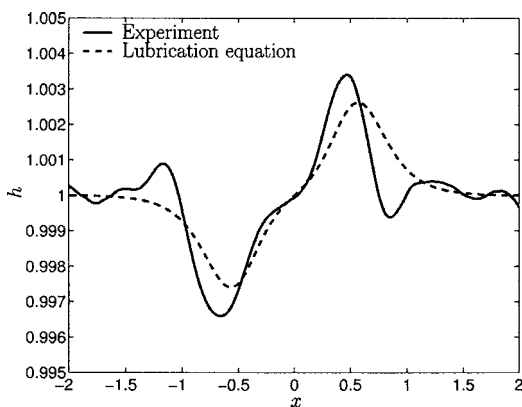
Fig. 11   The experimental height profile at Reynolds number 0.16 is compared to the steady-state solution of the lubrication equation. The x axis is dimensionless, so that the electrode spans from $-0.5 < x < 0.5$. There is a decrease in amplitude of the experimentally-measured standing wave as the Reynolds number is increased. The electric field number is $\bar{K} = 1.69 \times 10^{-2}$.
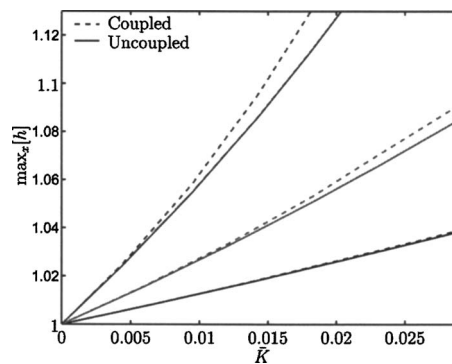
Fig. 12   The maximum height in the peak under the trailing edge of the electrode for coupled and uncoupled solutions. Parameters of the Convoil 20 film were used. The electrode parameters were $l = 0.08$ m, $\hat{H} = 0.00326, 0.00576, 0.01076$ m. The fluid parameters were Re = 0.07, $\bar{C} = 3.0 \times 10^4$.
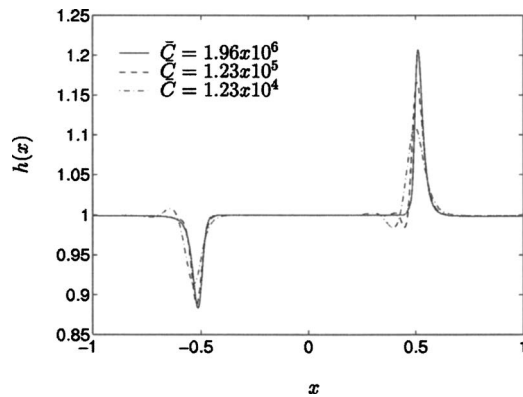
Fig. 13 An uncoupled calculation of the steady-state profile under an electrode of $l=0.08$ m, $\hat{H}=0.00326$ m, and $\phi_H=5$ kV. The physical properties of Convoil 20 are used, except for the dielectric constant; we assume that the fluid is an electrical conductor ($\epsilon_f=\infty$). The flow is specified by Re=0.16, and the electric field number is $\bar{K}=0.038$.
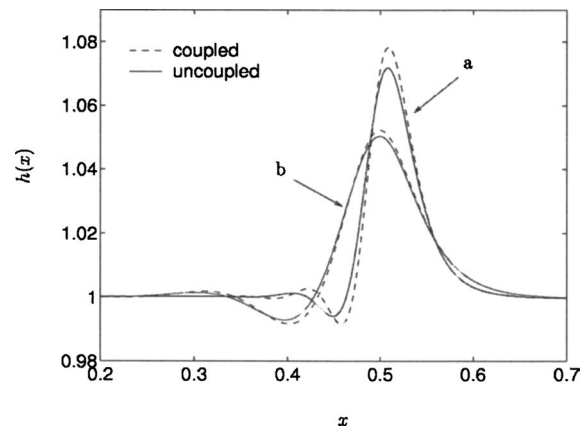

Fig. 14 Coupled and uncoupled calculations of the steady-state profile under an electrode of $l=0.08$ m, $\hat{H}=0.00326$ m, and $\phi_H=3.5$ kV. Physical properties of Convoil 20 are used, except for the surface tension and conductivity; surface tension values of 0.032 N/m (a) and 0.32 N/m (b) were used, and the fluid was assumed to be a conductor ($\epsilon_f=\infty$). The dimensionless parameters were Re=0.16, $\bar{K}=0.0186$, and $\bar{C}=1.23\times10^5$ (a) and $\bar{C}=1.23\times10^4$ (b).

creases with field strength, eventually producing a short-wave instability. The critical field strength is reproducible and is fortunately well above the field strength required to stop a small leak.

Acknowledgment

Nomenclature

β = angle between plate and horizontal axis
ϵ_f = dielectric constant of the fluid
ϵ_0 = permittivity of free space
ξ = d/L
μ = dynamic viscosity
ν = kinematic viscosity
ϕ_H = electric potential at the electrode surface (height $\hat{H}$ above the plate)
ϕ = electric potential (scaled by ϕ_H)
ρ = density
σ = surface tension
$\bar{C}\xi^3$ = Ca=$2\mu U_0/\sigma$=Capillary number
d = undisturbed fluid depth
E_n = normal component of the electric field (scaled by F) along the film interface
F = $\phi_H/\hat{H}$=reference electric field
g_n = normal component of gravity
h = film thickness (scaled by d)
H = $\hat{H}/d$
$\hat{H}$ = height of electrode above the brass plate
k = scaled (on L) wave number
l = electrode length
L = length scale along the plate ($L=l$)
P' = pressure
P = $P'/\rho U_o^2$
U_0 = average fluid velocity in the film
x = spatial coordinate along the plate (scaled by L)

t = time (scaled by L/U_o)
t_f = time to ramp potential for steady state solutions
$\bar{K}\xi^{-1}$ = $K=\epsilon_0 dF^2/4\mu U_0$, or $\bar{K}=3\epsilon_0 F^2/4\rho gL$
Re = $\rho dU_0/\mu$=Reynolds number
Re_C = critical Reynolds number

References

[1] Kim, H., Miksis, M. J., and Bankoff, S. G., 1991, "Lightweight Space Radiator With Leakage Control by Internal Electrostatic Fields," *Proceedings of the Eighth Symposium On Space Nuclear Power Systems*, Albuquerque, NM, CONF-910116, 1280.
[2] Bankoff, S. G., Miksis, M. J., Kim, H., and Gwinner, R., 1994, "Design Considerations for the Rotating Electrostatic Liquid-Film Radiator," Nucl. Eng. Des. **149**, pp. 441–447.
[3] Kim, H., Bankoff, S. G., and Miksis, M. J., 1991, "The Effect of an Electrostatic Field on Film Flow Down an Inclined Plane," Phys. Fluids, **4**(10), pp. 2117–2130.
[4] Hirt, C. W., Nichols, B. D., and Romero, N. C., 1975, "SOLA - A Numerical Solution Algorithm for Transient Fluid Flows," Technical Report, Los Alamos Scientific Laboratory of the University of California, Los Alamos.
[5] Benjamin, T. B., 1957, "Wave Formation in Laminar Flow Down an Inclined Plane," J. Fluid Mech. **2**(6), pp. 554–557.
[6] Yih, C. S., 1963, "Stability of Liquid Flow Down an Inclined Plane," Phys. Fluids **6**, pp. 331.
[7] González, A., and Castellanos, A., 1996, "Nonlinear Electrohydrodynamic Waves on Films Falling Down an Inclined Plane," Phys. Rev. E **53**(4), pp. 3573–3578.
[8] González, A., and Castellanos, A., 1998, "Nonlinear Electrohydrodynamics of Free Surfaces," IEEE Trans. Dielectr. Electr. Insul. **5**(3), pp. 334–343.
[9] Ramachandran, P. A., 1994, *Nonlinear Electrohydrodynamics of Free Surfaces*, Computational Mechanics, Boston.
[10] Hocking, L., and Miksis, M. J., 1993, "Stability of a Ridge of Fluid," J. Fluid Mech. **247**, pp. 157–177.
[11] Liu, J., Paul, J. D., and Gollub, J. P., 1993, "Measurements of the Primary Instabilities of Film Flows," J. Fluid Mech. **250**, pp. 69–101.
[12] Johnson, M. F. G., Schluter, R. A., and Bankoff, S. G., 1997, "Fluorescent Imaging System for Global Measurement of Liquid Film Thickness and Dynamic Contact Angle in Free Surface Flows," Rev. Sci. Instrum. **68**(11), pp. 4097–4102.
[13] Johnson, M. F. G., Schluter, R. A., Bankoff, S. G., and Miksis, M. J., 1999, "Experimental Study of Rivulet Formation on an Inclined Plate by Fluorescent Imaging," J. Fluid Mech. **394**, pp. 339–354.
[14] Griffing, E. M., 2001, "Control of Thin Liquid Films With an Electrostatic Field," Ph.D. thesis, Northwestern University, Evanston, IL.

All-Speed Time-Accurate Underwater Projectile Calculations Using a Preconditioning Algorithm

Michael Dean Neaves
Naval Surface Warfare Center–Panama City,
Integration and Experimentation Branch (HS15),
110 Vernon Avenue,
Panama City, FL 32407
e-mail: michael.neaves@navy.mil

Jack R. Edwards
North Carolina State University,
Mechanical and Aerospace Engineering,
4223 Broughton Hall, Box 7910,
Raleigh, NC 27695
e-mail: jredward@eos.ncsu.edu

An algorithm based on the combination of time-derivative preconditioning strategies with low-diffusion upwinding methods is developed and applied to multiphase, compressible flows characteristic of underwater projectile motion. Multiphase compressible flows are assumed to be in kinematic and thermodynamic equilibrium and are modeled using a homogeneous mixture formulation. Compressibility effects in liquid-phase water are modeled using a temperature-adjusted Tait equation, and gaseous phases (water vapor and air) are treated as an ideal gas. The algorithm is applied to subsonic and supersonic projectiles in water, general multiphase shock tubes, and a high-speed water entry problem. Low-speed solutions are presented and compared to experimental results for validation. Solutions for high-subsonic and transonic projectile flows are compared to experimental imaging results and theoretical results. Results are also presented for several multiphase shock tube calculations. Finally, calculations are presented for a high-speed axisymmetric supercavitating projectile during the important water entry phase of flight. [DOI: 10.1115/1.2169816]

Keywords: compressible multiphase flows, supercavitation, high-speed water entry

Introduction

Supercavitation is a problem of great interest for many naval applications. Supercavitating torpedoes operate in the very low subsonic regimes. Low subsonic to supersonic supercavitating projectiles can be used for underwater mine neutralization and surf zone mine clearance. For many applications, a high-speed water entry is required due to launching/firing projectile above the water surface. The high-speed water entry phase of flight is interesting and challenging due to transition from flight in air to supercavitating flight through water. For the surf zone mine clearance application, projectiles are designed to enter the water vertically, so an axisymmetric approximation is appropriate. The nose shape of a supercavitating projectile is generally governed by lethality and cavity generation concerns with minimizing drag in air being a secondary consideration.

Many approaches exist for calculating low-speed flows in water. Such flows are generally isothermal, allowing one to ignore the decoupled energy equation. A trivial equation of state for water—density equals a constant—is often employed. As speed through water increases beyond the low subsonic regime, these simplifying assumptions break down, as density and temperature begin to vary with pressure. Cavitation also becomes an issue at higher speeds. In order to account for these complexities, one must include the energy equation, a nontrivial equation of state for water, and a model for water vapor formation during cavitation events. Prediction of such flows generally requires the solution of the Navier-Stokes equations governing a multiphase (possibly multicomponent) flow. Algorithms designed for this purpose must have the ability to account for widely-varying time scales and widely differing levels of compressibility and must properly capture discontinuous flow features, such as shock waves and phase interfaces. The development of such algorithms is a subject of

on-going research. The more detailed approaches solve separate systems of transport equations for each phase [1–6]. Most of these approaches either assume that a single pressure characterizes the multiphase flow [1–3] or allow for separate pressures that must equilibrate at a phase interface [4–6]. Formulations that use the first approach are generally not hyperbolic in time. System hyperbolicity is usually restored through the addition of "virtual mass" and other "nonviscous" terms [1,2]. Formulations that use the second approach are generally hyperbolic but require complex fractional-step approaches to restore pressure equilibrium at phase interfaces. Elimination of pressure oscillations at interfaces is a major issue for these techniques [6].

At the other end of the spectrum are homogeneous equilibrium models [7,8]. These approaches enforce thermodynamic equilibrium at all locations in the flow. In regions where two phases can exist, the homogeneous equilibrium model returns a prediction of the bulk density of the two-fluid mixture, from which a volume fraction may be obtained, given saturation-state information. The homogeneous equilibrium model is capable of capturing phase transitions, condensation shocks, and other multiphase flow features, but phase nonequilibrium effects are not handled.

An approach between the preceding two in complexity is the homogeneous mixture model [9,10] where separate continuity equations are solved for each phase, along with equations for the mixture momentum and mixture energy. The model outputs a mass averaged velocity, pressure, and temperature characteristic of the two-fluid mixture, and is thus similar to the homogeneous equilibrium model in that kinematic and thermal equilibrium is assumed. The use of separate continuity equations for each phase allows for a consideration of finite-rate (rather than equilibrium) phase transitions, which may be modeled using nucleation theory or other approaches. Separate equations of state for each phase provide the phasic density as a function of the common pressure and temperature, and as long as these state equations are convex functions, the homogeneous mixture model will generally result in a hyperbolic equation system.

The present work implements a homogeneous mixture model

Copyright © 2006 by ASME

for a compressible, two-phase flow using the combination of a time-derivative preconditioning method [11–13] with a low-diffusion upwinding technique (Edwards' Low Diffusion Flux Splitting Scheme (LDFSS) [14,15]), valid for real fluids at all speeds. The use of time-derivative preconditioning reconciles the varying acoustic speeds present in a compressible, multiphase flow, while the use of low-diffusion upwinding methods provides sharp capturing of grid-aligned discontinuities. Edwards' LDFSS scheme is a member of a popular class of upwinding methods that originated with Liou's Advective Upstream Splitting Method (AUSM) [16,17]. Thus, the extensions presented herein for the homogeneous mixture model should be applicable to other approaches of this type.

An outline of the paper is as follows. First, the governing equations and phase-transition models are described, followed by details of the upwinding approach and equations of state used in this work. Results are then presented for an array of steady and time-dependent flows representative of projectile motion into and within water. Comparisons with experimental data and theoretical results are made for several cases.

Outline of Numerical Procedure

The numerical procedure solves the Navier-Stokes equations governing a homogeneous mixture of fluids using a cell-centered finite-volume method. Inviscid fluxes are discretized using Edwards' LDFSS method [15], while viscous fluxes are discretized using central differences. Turbulence effects are handled using a modified Spalart-Allmaras model [18,19]. The subsections that follow present details of this approach.

Governing Equations. For development, consider the one-dimensional Euler equations for a real fluid with $p = p(\rho, T)$ and $h = h(\rho, T)$

$$\frac{\partial U}{\partial t} + \frac{\partial F}{\partial x} = S \tag{1}$$

where

$$U = \begin{bmatrix} \rho \\ \rho Y_l \\ \rho u \\ \rho H - p \\ \rho Y_a \end{bmatrix}, \quad F = \begin{bmatrix} \rho u \\ \rho Y_l u \\ \rho u^2 + p \\ \rho u H \\ \rho Y_a u \end{bmatrix}, \quad S = \begin{bmatrix} 0 \\ -\dot{m}^+ - \dot{m}^- \\ 0 \\ 0 \\ 0 \end{bmatrix} \tag{2}$$

$$\dot{m}^+ = \frac{C_{\text{prod}} \rho_v \alpha_l^2 (1 - \alpha_l)}{t_\infty} \tag{3}$$

$$\dot{m}^- = \frac{C_{\text{dest}} \rho_v \alpha_l MIN(0, p - p_{\text{sat}})}{\left(\frac{1}{2} \rho_\infty U_\infty^2\right) t_\infty} \tag{4}$$

A global continuity equation is used with liquid-phase water and air species continuity equations. S is a vector of finite-rate source terms used to specify the rate of vapor production and destruction [10]. C_{prod} and C_{dest} are problem dependent. For the present work, $t_\infty = L/U_\infty$, $C_{\text{prod}} = 8 \times 10^1$, and $C_{\text{dest}} = 1 \times 10^4$ unless otherwise stated. H is the total enthalpy, $h + u^2/2$.

Equations of State. Equations of state are required for liquid and gaseous phases to provide closure for the governing equations. Derivatives of various properties with respect to primitive variables are also required for the effective speed of sound, preconditioning matrix, and flux Jacobians used by implicit flow solver. The property derivatives and mixing rules are given in the Appendix.

Liquid Phase. The Tait equation [20] of state for water was formulated for modeling underwater explosions

Table 1 Oldenbourg coefficients

Index	a	b
1	−7.85823	1.99206
2	1.83991	1.10123
3	−11.7811	−0.512506
4	22.6705	−1.75263
5	−15.9393	−45.4485
6	1.77516	-6.75615×10^5

$$p = K_o \left\{ \left(\frac{\rho_l}{\rho_o} \right)^n - 1 \right\} + p_o \tag{5}$$

where p_o and ρ_o are reference values at a reference temperature of T_o(273.15 K). K_o and n are weak functions of temperature and pressure and are assumed constant with values of 3×10^8 Pa and 7, respectively. Saurel et al. proposed modifying the standard Tait equation to include temperature dependence in the modeling of the liquid component of a two-phase mixture [7]. The reference values are simply replaced with saturation values,

$$p = K_o \left\{ \left(\frac{\rho_l}{\rho_{l\text{sat}}(T)} \right)^n - 1 \right\} + p_{\text{sat}}(T) \tag{6}$$

The saturation pressure and density are calculated as functions of temperature using Oldenbourg coefficients [21]

$$\ln\left(\frac{p_{\text{sat}}(T)}{p_c} \right) = \left(\frac{T_c}{T} \right)(a_1\theta + a_2\theta^{1.5} + a_3\theta^3 + a_4\theta^{3.5} + a_5\theta^4 + a_6\theta^{7.5}) \tag{7}$$

$$\frac{\rho_{l\text{sat}}(T)}{\rho_c} = 1 + b_1\theta^{1/3} + b_2\theta^{2/3} + b_3\theta^{5/3} + b_4\theta^{16/3} + b_5\theta^{43/3} + b_6\theta^{110/3} \tag{8}$$

where $\theta = 1 - T/T_c$ and p_c, T_c, and ρ_c are the critical conditions for water (2.264×10^7 Pa, 647.14 K, and 332 kg/m^3). The Oldenbourg coefficients are listed in Table 1.

The enthalpy for the liquid phase at standard pressure is calculated using McBride coefficients [22]. For low-speed liquids, the p/ρ contribution to enthalpy is negligible, but due to the very large pressures generated at higher speeds in water, the pressure term is included in the enthalpy calculation,

$$h_l(T) = h_{\text{McBride}}(T) + \frac{(p - p_{\text{STD}})}{\rho_l} \tag{9}$$

Gaseous Phase. The gaseous phases consist of water vapor and air and are modeled as ideal gases

$$p = \rho_g R T \tag{10}$$

where $R = \hat{R}/\hat{M}$ is universal gas constant divided by the molar mass. The enthalpy for the gaseous phase is calculated with McBride coefficients [22]. Treating the gaseous phase as an ideal gas allows for calculating enthalpy as only a function of temperature.

The equations of state for gas and liquid are easily differentiable with respect to the primitive variables. Note that Saurel et al. version of the Tait equation produces a temperature dependence for the liquid phase.

Effective Speed of Sound. The problem formulation and choice of primitive variables result in the following expression for the effective speed of sound:
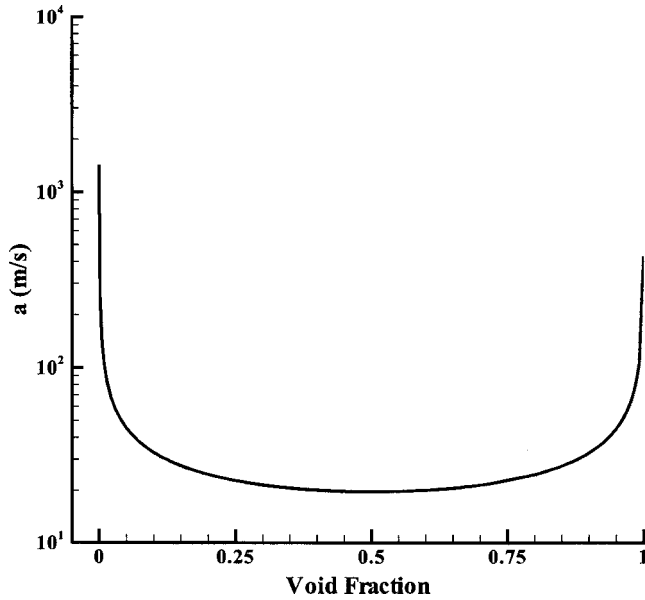
Fig. 1 Effective speed of sound versus void fraction

$$a = \sqrt{\dfrac{\rho \dfrac{\partial h}{\partial T}}{\rho \dfrac{\partial h}{\partial T}\dfrac{\partial \rho}{\partial p} - \rho \dfrac{\partial h}{\partial p}\dfrac{\partial \rho}{\partial T} + \dfrac{\partial \rho}{\partial T}}} \qquad (11)$$

When applied to a quiescent mixture of vapor and liquid at 300 K and one atmosphere, the classic U-shaped effective speed of sound versus void fraction curve is produced, as shown in Fig. 1. The speed of sound of 1430 m/s for a pure liquid is in good agreement with the generally accepted value of slightly less than 1500 m/s. The pure water vapor speed of sound, 429 m/s, agrees with the ideal gas speed of sound for water vapor's molecular weight of 18 at 300 K. A minimum effective speed of sound of 19.7 m/s occurs at a voidage of 0.5. For actual cavities with pressure below the saturation value, the above formulation generally results in a minimum effective speed of sound of around 3 m/s.

Preconditioning Method. The governing equations are preconditioned as follows:

$$P\frac{\partial V}{\partial t} + \frac{\partial F}{\partial x} = S \qquad (12)$$

where P is a preconditioning matrix and V is a suitable list of primitive variables. The choice of primitive variables greatly influences the complexity of the preconditioned system's eigenvalues, the effective speed of sound, and derivatives required to form flux Jacobians. The following primitive variables are chosen:

$$V = [p \quad Y_v \quad u \quad T \quad Y_a]^T \qquad (13)$$

The preconditioning matrix used is that of Weiss and Smith [11]—a variant of the Turkel [12] and Choi/Merkle [13] preconditioners. The preconditioner can be expressed as a rank-one perturbation of the Jacobian matrix $\partial U/\partial V$,

$$P = \frac{\partial U}{\partial V} + \theta u \overset{\triangle\triangle}{v}{}^T \qquad (14)$$

where

$$\overset{\triangle}{u}{}^T = [1 \quad Y_l \quad u \quad H \quad Y_a] \qquad (15)$$

$$\overset{\triangle}{v}{}^T = [1 \quad 0 \quad 0 \quad 0 \quad 0] \qquad (16)$$

$$\theta = \frac{1}{V_{\text{ref}}^2} - \frac{1}{a^2} \qquad (17)$$

$$V_{\text{ref}}^2 = \min(a^2, \max(|\vec{V}|^2, V_\infty^2)) \qquad (18)$$

V_{ref} is a reference velocity designed to prevent adverse behavior in stagnation regions. The quantity a is the effective speed of sound (Eq. (11)) and is a function of density and various thermodynamic derivatives.

The eigenvalues of $P^{-1}(\partial F/\partial V)$ are

$$u, \tfrac{1}{2}\big[(1 + M_{\text{ref}}^2)u \pm \sqrt{u^2(1 - M_{\text{ref}}^2)^2 + 4V_{\text{ref}}^2}\big] \qquad (19)$$

where

$$M_{\text{ref}}^2 = \frac{V_{\text{ref}}^2}{a^2} \qquad (20)$$

LDFSS Flux Splitting. The LDFSS is designed to provide accurate resolution of stationary and moving contact discontinuities while preserving monotonicity of solution and satisfying an entropy condition. Details regarding the original development of LDFSS may be found in Ref. [14]. The development that follows builds upon the real-fluid formulation of LDFSS presented in Ref. [15]. For simplicity, the derivation is for the x direction only.

A key in the extension of LDFSS to operate for arbitrary fluids is the use of a "numerical speed of sound" derived from the acoustic eigenvalues of the preconditioned system and evaluated at a cell interface

$$\tilde{a}_{1/2} = \left[\frac{\sqrt{(1 - M_{\text{ref}}^2)^2 u^2 + 4V_{\text{ref}}^2}}{1 + M_{\text{ref}}^2} \right]_{1/2} \qquad (21)$$

$$M_{\text{ref}}^2 = \frac{V_{\text{ref}}^2}{a^2} \qquad (22)$$

where the "1/2" notation indicates the evaluation of Eq. (21) using cell-averaged velocity and sound speed data, and M_{ref}^2 is a reference Mach number. Different forms for this averaged sound speed can be used. The present work utilizes arithmetic averaging exclusively

$$a_{1/2} = \tfrac{1}{2}(a_L + a_R) \qquad (23)$$

Other quantities needed in the formulation are Mach numbers at left and right states, and van Leer/Liou polynomials in Mach number [16]

$$M_{L,R} = \frac{u_{L,R}}{\tilde{a}_{1/2}} \qquad (24)$$

$$M_{(1)}^\pm = \tfrac{1}{2}(M \pm |M|) \qquad (25)$$

$$M_{(2)}^\pm = \begin{cases} \pm\tfrac{1}{4}(M \pm 1)^2, & |M| < 1 \\ M_{(1)}^\pm & \text{otherwise} \end{cases} \qquad (26)$$

The properties at the left (L) and right (R) states are determined by second-order minmod interpolations.

Given these basic definitions, the inviscid x direction flux **F** can be split into convective and pressure contributions:

$$F = F^c + F^p = u\Phi + p\Psi \qquad (27)$$

where

$$\Phi = \begin{bmatrix} \rho \\ \rho Y_l \\ \rho u \\ \rho H \\ \rho Y_a \end{bmatrix}, \quad \Psi = \begin{bmatrix} 0 \\ 0 \\ 1 \\ 0 \\ 0 \end{bmatrix} \qquad (28)$$

The LDFSS scheme applied to the cell interfaces results in the inviscid flux being split into convective and pressure parts as the sum of left and right components,

$$F_{i+1/2} = F^c_{i+1/2} + F^p_{i+1/2} \qquad (29)$$

$$F^c_{i+1/2} = U^+ \Phi_L + U^- \Phi_R \qquad (30)$$

$$F^p_{i+1/2} = P_{1/2} \Psi_i \qquad (31)$$

where the split velocities $U^\pm$ and the interface pressure $P_{1/2}$ are functions of the Mach number, and are defined as

$$U^+ = \tilde{a}_{1/2} \left[M^+ - M_{1/2} \left(1 - \frac{p_L - p_R}{2 \rho_L V^2_{\mathrm{ref},1/2}} \right) \right] \qquad (32)$$

$$U^- = \tilde{a}_{1/2} \left[M^- + M_{1/2} \left(1 + \frac{p_L - p_R}{2 \rho_R V^2_{\mathrm{ref},1/2}} \right) \right] \qquad (33)$$

$$P_{1/2} = \tfrac{1}{2}(p_L + p_R) + \tfrac{1}{2}(P^+ - P^-)(p_L - p_R) + \rho_{1/2} V^2_{\mathrm{ref},1/2}(P^+ + P^- - 1) \qquad (34)$$

where

$$M^+ = \alpha_L^+ (1 + \beta_L) M_L - \beta_L M^+_{(2),L} \qquad (35)$$

$$M^- = \alpha_R^- (1 + \beta_R) M_R - \beta_R M^-_{(2),R} \qquad (36)$$

In the above equations, $\rho_{1/2}$ is the interface density (determined using an arithmetic average), and $V_{\mathrm{ref},1/2}$ is the interface reference velocity (determined according to Eq. (18)) based on arithmetic averages of the velocity and sound speed). Other quantities used in the preceding definitions are stagnation/sonic-point switching functions:

$$\alpha_{L,R}^\pm = \tfrac{1}{2}[1.0 \pm \mathrm{sign}(1.0, M_{L,R})] \qquad (37)$$

$$\beta_{L,R} = - \max[0.0, 1.0 - \mathrm{int}(|M_{L,R}|)] \qquad (38)$$

an interface Mach number functional

$$M_{1/2} = \tfrac{1}{2}(M^+ - \alpha_L^+ M_L - M^- + \alpha_R^- M_R) \qquad (39)$$

and a van Leer/Liou polynomial of degree 1 used in the pressure splitting

$$P^\pm = \alpha_{L,R}^\pm (1 + \beta_{L,R}) - \frac{\beta_{L,R}}{2}[1.0 \pm M_{L,R}] \qquad (40)$$

Time-Advancement Procedure. A standard alternative to the long turnaround times of explicit flow solvers is to use an implicit flow solver with a less severe Courant, Friedrichs, and Lewy (CFL) [23] stability requirement. Unfortunately, most implicit algorithms are implemented in a nontime-accurate manner for reasons of simplicity in formulation, and as a result, they most often contain approximate factorization and linearization errors. The subiteration techniques of Rai [24] can be used to restore second-order time accuracy while still taking advantage of simplifying approximations to the implicit operator.

The subiteration techniques can be applied to the generic form of a system of partial differential equations. For development, consider the one-dimensional Euler equations as written in Eq. (1) minus the source term and with the addition of a pseudotime term for subiterating

$$\frac{\partial U}{\partial \tau} + \frac{\partial U}{\partial t} + \frac{\partial F}{\partial x} = 0 \qquad (41)$$

Applying preconditioning as defined in Eq. (14) to pseudotime term to aid convergence of subiterations leads to the following:

$$P \frac{\partial V}{\partial \tau} + \frac{\partial U}{\partial t} + \frac{\partial F}{\partial x} = 0 \qquad (42)$$

Discretizing with a first-order finite difference for the pseudo-time derivative and a second-order finite difference for the physical time derivative gives

$$P \left(\frac{V^{p+1} - V^p}{\Delta \tau} \right) + \frac{3U^{p+1} - 4U^n + U^{n-1}}{2\Delta t} + \frac{\partial}{\partial x} F(U^{p+1}) = 0 \quad (43)$$

In this formulation, the pseudotime subiteration index is p, and the physical time step index is n [25]. Linearizing the above results in

$$P \frac{\Delta V}{\Delta \tau} + \frac{3(U^p + M\Delta V) - 4U^n + U^{n-1}}{2\Delta t} + \frac{\partial}{\partial x}\{F(U^p) + A^p \Delta V\} = 0 \qquad (44)$$

where $M = \partial U / \partial V$, and $A^p = \partial F / \partial V$,

$$\left\{ \frac{P}{\Delta \tau} + \frac{3M}{2\Delta t} + \frac{\partial}{\partial x}\{A^p\} \right\} \Delta V = - \frac{3U^p - 4U^n + U^{n-1}}{2\Delta t} - \frac{\partial}{\partial x}\{F(U^p)\} \qquad (45)$$

Equation (45) is approximately factored for multidimensional problems and solved with an Alternating-Direction Implicit (ADI) scheme. Second-order time accuracy is maintained by subiterating in pseudotime with a three-point backward time difference.

Results and Discussion

For all computational results, unless stated otherwise, the flow is assumed turbulent, and a modified Spalart-Allmaras model is used to calculate the eddy viscosity [18,19]. All computational results are axisymmetric, and the freestream temperature is assumed to be 300 K. Results are presented for low-speed cavitation, high-subsonic and transonic supercavitation. Due to the fundamentally unsteady nature of cavity wakes, convergence was limited to approximately three orders of magnitude.

A supersonic convecting liquid sheet and several multiphase shock tube calculations are also presented. A simple convecting liquid sheet was chosen due to problem having an exact solution. A nontrivial problem of interest is a general shock tube problem with any pressure ratio and/or combination of gas and liquid. For the liquid sheet and shock tube problems presented, LDFSS was used without preconditioning. Finally, a water entry calculation is presented for a generic supercavitating projectile.

Steady-State Calculations

Water Flow Over a Hemisphere/Cylinder Geometry. The first test case is water flow over a hemisphere/cylinder geometry with experimental data from Rouse and McNown [26]. The Rouse and McNown data provide surface pressure distributions for various cavitation numbers. Rouse's original data reduction used head differences to calculate cavitation numbers. If the enthalpy is large and elevation changes are small, the cavitation number can be approximated as

$$K = \frac{P_\infty - P_{\mathrm{sat}}}{\frac{1}{2}\rho_\infty U_\infty^2} \qquad (46)$$

The computational grid is 217×85 nodes with clustering at the body surface and shoulder where cavitation onset is expected. Due to a lack of information about test conditions, initial conditions are assumed consistent with capabilities of the Iowa Institute of Hydraulic Research's water tunnel. Freestream temperature and pressure are 300 K and 6557.0 Pa. The cavitation number is varied by changing the freestream velocity.

Figure 2 shows the surface pressure coefficient versus surface distance from the nose for various cavitation numbers ($K=0.2$, 0.3, and 0.4). Near the hemisphere/cylinder transition, the pressure drops below the saturation pressure, and a cavity forms. As the cavitation number drops due to increasing freestream velocity, the shoulder expansion decreases the pressure, and the cavity size grows. The cavity formation mitigates the pressure drop and pro-
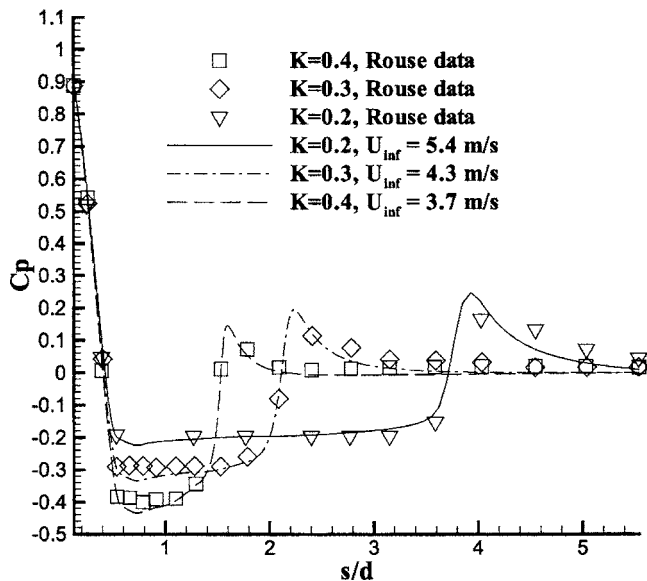
Fig. 2 Surface pressure distributions: *K*=0.2, 0.3, and 0.4

Fig. 4 Cavity thickness of high-subsonic projectile

duces a fairly constant pressure inside the cavity. Pressure recovery downstream ultimately collapses the cavity. Validation is complicated due to experimental data not having an overall error bound. The computational results show good agreement with cavity pressure and cavity size for all cavitation numbers.

High-Subsonic Projectile. A projectile at 970 m/s is considered next for validation in the high-subsonic regime. The projectile has a disk cavitator, a length to base diameter ratio of 12, and three break points along the body. A five block, axisymmetric grid is used with a total of 30,000 grid points. The freestream pressure corresponds to a depth of about 4 m. Test conditions result in a Mach number of 0.68. Imaging and cavity measurements are taken from Hrubes [27]. Figure 3 allows visual comparison of the computed void fractions to a 35-mm shadowgraph. The projectile

is within a well-formed cavity. The experimental projectile appears to be at a slight angle of attack, causing a slight asymmetry of cavity. The calculated cavity appears very similar to the actual cavity. The computed cavity profile is compared to Hrubes' cavity size measurements in Fig. 4. The radial coordinate is stretched for clarity. The cavity edge for the computational results is measured at the 10% void fraction contour. Current computational results are plotted versus photographic data of Hrubes and results from Munzer-Reichardt Theory [28]. The theoretical model is a generalized ellipsoid which is a function of flow and geometric parameters. Although an overall accuracy bound of the experimental measurements is not available, the computational results are in very close agreement with the experimental measurements.

Transonic Projectile. Calculations were performed for a transonic underwater projectile at 1540 m/s. The transonic projectile is similar to the high-subsonic projectile except that the length to base diameter ratio is 10. The experimental depth was about 4 m, and a freestream pressure of approximately 1.5 atm was used. Figure 5 presents contour plots of pressure and density which clearly show the bow shock, cavity, and wake. A logarithmic scale
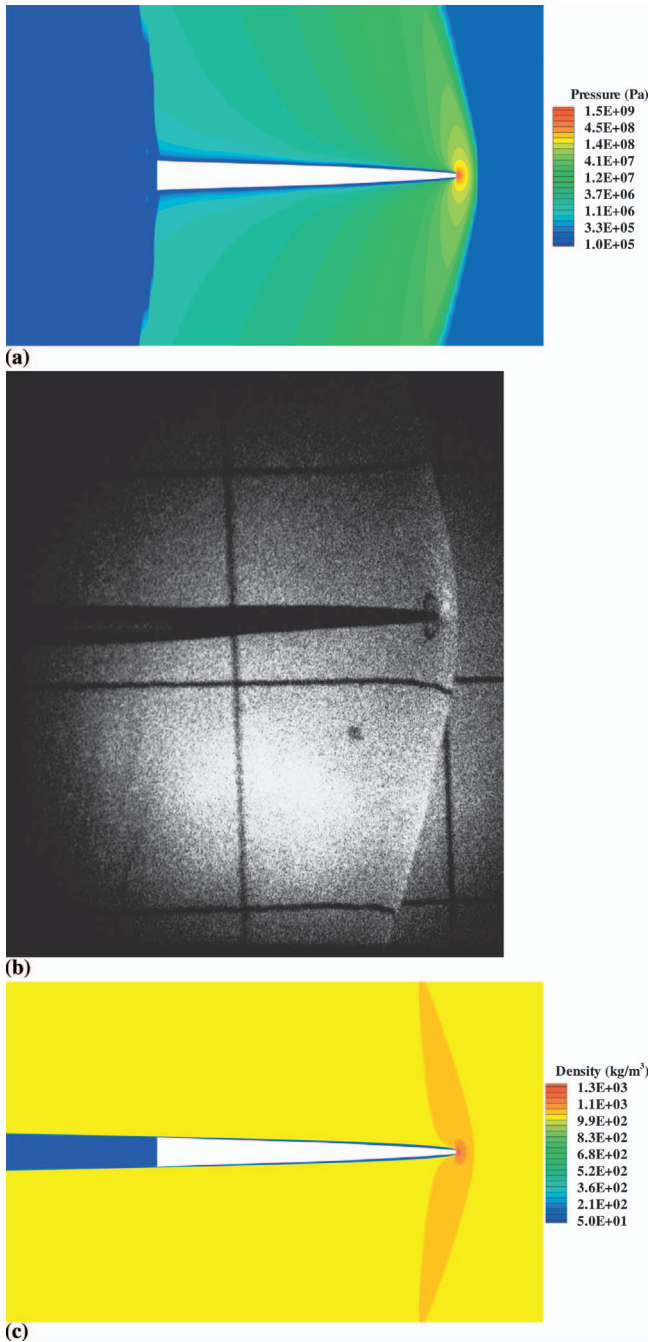

Fig. 3 High-subsonic projectile cavity shadowgraph and computed void fraction contours

288 / Vol. 128, MARCH 2006

(a)

(b)

(c)

Fig. 5 Pressure contours (log scale), density contours, and movie camera image of transonic projectile

is used for pressure contours due to extremely large range of pressures. The freesteam Mach number is 1.07, and as expected for a slightly supersonic freestream Mach number, a detached bow shock stands in front of the disk cavitator. A photograph of the experimental projectile is also shown in Fig. 5. Only the shock wave and the trailing cavity are clear in the photograph. The predicted shock shape and standoff distance compare well with experimental imaging results. The slightly opaque wake cavity can be seen in the photograph and in the density contours. Pressure increases by about 60 times the freestream value across the normal shock and about 9600 times between freestream and the stagnation point. Density at the stagnation point is 1316 kg/m^3. The disk cavitator immediately generates and anchors a stable cavity.

Temperature contours near the cavitator are shown in Fig. 6.

Compression at the stagnation point causes a moderate temperature rise to 323 K. At the stagnation point, the speed of sound reaches a maximum overall value of 3191 m/s. The front region of the cavity is cooled by the liquid to vapor phase transition. Heating occurs at outer boundary of cavity. As cavity continues over projectile, the cavity vapor is gradually heated to a temperature range of 340–360 K. The cavity wake behind the projectile has a core temperate around 450 K. The minimum speed of sound of 1.5 m/s occurs in the cavity interface along the projectile.

Time-Accurate Calculations

Convection of Liquid Sheets. A simple validation problem for a multiphase algorithm is a 1D convecting sheet of liquid surrounded by air. The baseline grid contains 400 points uniformly distributed over 1 m. Initially the liquid sheet begins at 0.2 and ends at 0.4 m. A uniform initial velocity of 1600 m/s results in supersonic conditions in both phases. Pressure and temperature are uniformly initialized to 1 atm and 300 K. A CFL of unity results in a timestep of 6.4×10^{-7} s in air and 4.1×10^{-7} s in water. A significantly smaller fixed global time step of 5×10^{-9} s was chosen to minimize timestep errors during grid convergence studies. The total physical time of calculation was 0.25 ms and required 50,000 time steps. The exact wave moving at 1600 m/s convects 0.4 m during the calculation. Figure 7 shows the calculated density and exact solution after 0.25 ms for various numbers of uniformly spaced grid points. The liquid region is convected from left to right at correct velocity, but contact surfaces with very large density gradients show some dissipation. As expected, the calculated velocity, temperature, and pressure remain invariant.

A grid refinement study was performed to assess the influence of grid spacing on solution error. The grid was repeatedly refined from 400 points to 3200 points by factors by 2. The percent errors for various grids are presented in Fig. 8. Refining the grid produces significant improvement in density interface and error. The magnitude of percent error plotted in Fig. 8 clearly illustrates one of the problems of measuring error near a discontinuity. The density interface is always dissipated and results in a large percentage error on the air-side of density interface for any number of grid points. The log plot of the L_2 norm of the errors and grid spacing shown in Fig. 9 has a slope of 0.75 over the entire range of refinement. Verification of spatial order may exacerbated by all error being generated at the density interface, but the scheme is consistent and calculations are in the asymptotic range.

Multiphase Shock Tubes. Another unsteady multiphase problem is a multiphase shock tube with any combination of liquid, gas, or multiphase mixture. A problem of interest for naval applications is shock propagation in water or across a water-gas interface. The water shock tube is of interest for a wide range of pressure ratios ranging from damaging high-pressure ratios to low-pressure acoustic ratios. All shock tube calculations use 1601 uniformly spaced points with an initial interface at 0.5 m. All shock tube solutions are presented at 0.15 ms, and calculations were performed with a uniform global time step of 10^{-7} s. Unless otherwise stated, initial temperatures are 300 K, and the driving fluid pressure is 10^9 Pa. Only initial states of pure gas or liquid are presented here, but algorithm has no difficulty with phase mixtures.

High-Pressure Water Shock Tube. Figures 10 and 11 present a solution for a water shock tube with an initial pressure ratio of 10^4. The resulting density ratio is 1.233. The effective speed of sound varies from 2752 m/s in driver to 1430 m/s in the driven fluid. A constant global timestep of 10^{-7} s corresponds to a CFL of about 0.3. An expansion and shock wave form in high-pressure and low-pressure regions respectively. Treating the liquid phase as a compressible liquid allows for density variations across the shock, expansion wave, and contact surface. Temperature varies
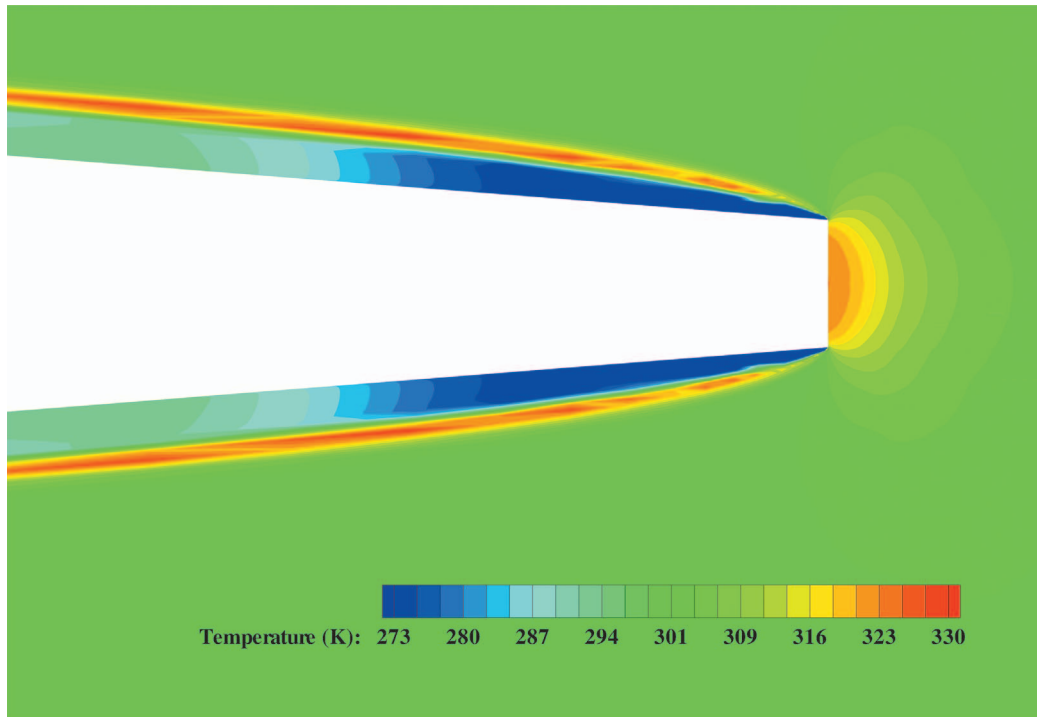
Fig. 6 Temperature contours near cavitator for transonic projectile

from 288 K in expansion wave to 305 K behind shock wave. The moving shock Mach number is about 1.3, and the fluid velocity behind the shock wave is 209.6 m/s. The shock wave is well resolved with minor overshoots. The algorithm appears to capture all features of the high-pressure water shock tube.

Low-Pressure Water Shock Tube. To verify low pressure robustness, a shock tube was calculated with an initial pressure ratio of 1.0001. The initial pressure of the driver fluid is 100010 Pa. The CFL was about 0.25. The calculated pressure and velocity after 0.15 ms are shown in Fig. 12. The extremely low pressure ratio results in calculated density and temperature being constant and a moving shock Mach number of unity. Pressure and velocity at expansion wave and shock are resolved with no oscillations.

Air-Water Shock Tube. The next general shock tube considered is air driving a shock into water. The driver on left is pure air at 10^9 Pa, and the driven fluid is water at 10^5 Pa. The initial density ratio is 11.3 with high-pressure air density being greater than density of water. This calculation demonstrates robustness of algorithm but ignores real-gas effects that could be present in air at such high pressures. The effective speeds of sound in the driver and driven fluids are 347 m/s and 1430 m/s respectively. The time step of 10^{-7} s results in a CFL of 0.37. The solution properties of interest are plotted in Figs. 13 and 14. The strong shock propagating into water can be seen in pressure, velocity, density, and temperature. The moving shock Mach number is about 1.3. The compressibility of water as represented by the Tait equation

Fig. 7 Convecting liquid sheet solution (0.25 ms)

Fig. 8 Convecting liquid sheet percent error (0.25 ms)

290/ Vol. 128, MARCH 2006

Transactions of the ASME

Downloaded 03 Jun 2010 to 171.66.16.155. Redistribution subject to ASME license or copyright; see http://www.asme.org/terms/Terms_Use.cfm

Fig. 9 Order of scheme for convecting liquid sheet calculation
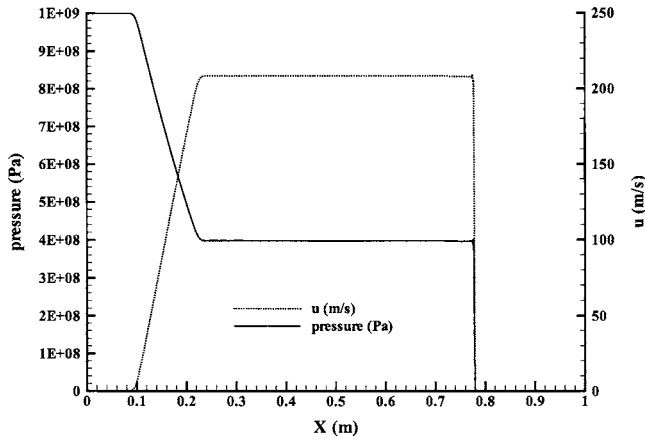
Fig. 10 Pressure and velocity for high-pressure water shock tube (0.15 ms)
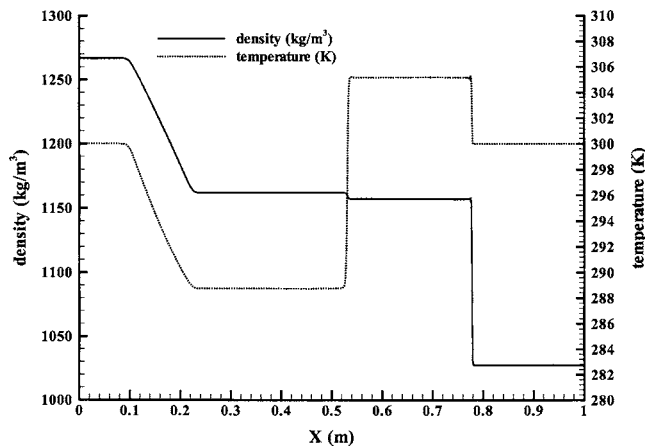

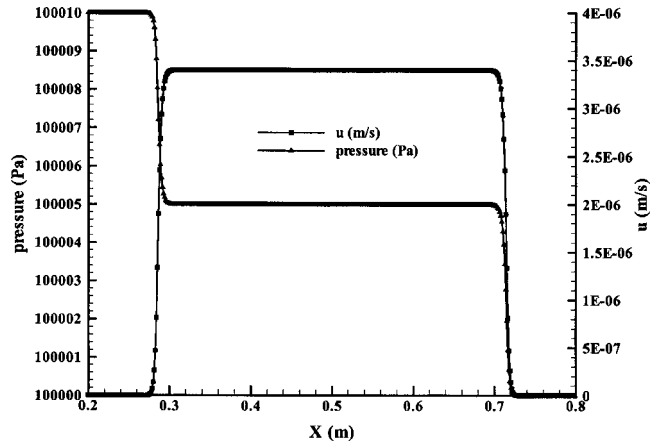**Fig. 11 Density and temperature for high-pressure water shock tube (0.15 ms)**

Fig. 12 Pressure and velocity for low-pressure water shock tube (0.15 ms)

allows for a small density change across the shock wave. A pronounced contact surface results from the wave interactions, as can be seen in the void fraction, density, and temperature plots. The velocity behind the shock is 211 m/s. Due to the slower speed of sound in air, the expansion wave appears slow compared to shock wave traveling in water.

Water-Vapor Shock Tube. The last general shock tube considered is high-pressure water driving a shock into low-pressure water vapor. To provide a valid initial condition for water vapor, the initial temperature was raised to 330 K, and the driven fluid pressure was lowered to 10^4 Pa. Driver fluid pressure is maintained at 10^9 Pa, resulting in a pressure ratio of 10^5. The effective speeds of sound in the driver and driven fluids are 2836 m/s and 450 m/s, respectively. The CFL was 0.46. Calculated properties after 0.15 ms are shown in Figs. 15 and 16. To allow visible plotting of the contact surface and shock wave, pressure and density are plotted on a log scale. A weak shock wave moves into vapor with a moving shock Mach number of 1.77, and an expansion wave travels into water. The widely differing effective speeds of sound allow the expansion to travel much further than the shock wave. The pressure of the water in the expansion behind the contact surface drops dramatically to nearly zero. The attainment of pressure values below the saturation pressure allows a phase change from liquid to vapor according to the rate law (Eq. (4)) which mitigates the pressure drop. Inspection of the void fraction plot shows that vapor is being generated behind original liquid/vapor interface. The very low pressures in a mixture of liquid and vapor result in a minimum effective speed of sound of 10^{-3} m/s. The expansion region has a distinct plateau where the liquid-to-vapor phase change stabilizes pressure at very near the saturation pressure. The expansion pressure plateau is a function of temperature and in general is not at same pressure as the region between the shock and original fluid interface. The liquid-to-vapor phase change results in pressure and velocity not being invariant across the original fluid interface.

Water Entry Calculations. As a final calculation, a time-accurate simulation of a high-speed projectile entering the water is performed [29]. In water, the blunt nose (cavitator) is designed to lower the pressure below saturation value in order to generate the vapor required for a supercavitation mode of travel through water. The axisymmetric 5-block grid shown in Fig. 17 is used with minimum wall spacing of 6.0×10^{-6} m. This grid spacing results in a y^+ value in the range of $1-3$ for all flow conditions encountered. A fixed global time step of 1.0×10^{-5} ms was used for the time-accurate water entry calculation. Freestream pressure and temperature are set to 1 atm and 300 K, respectively. For the water entry calculations, the rate coefficients in Eq. (3) and Eq. (4)
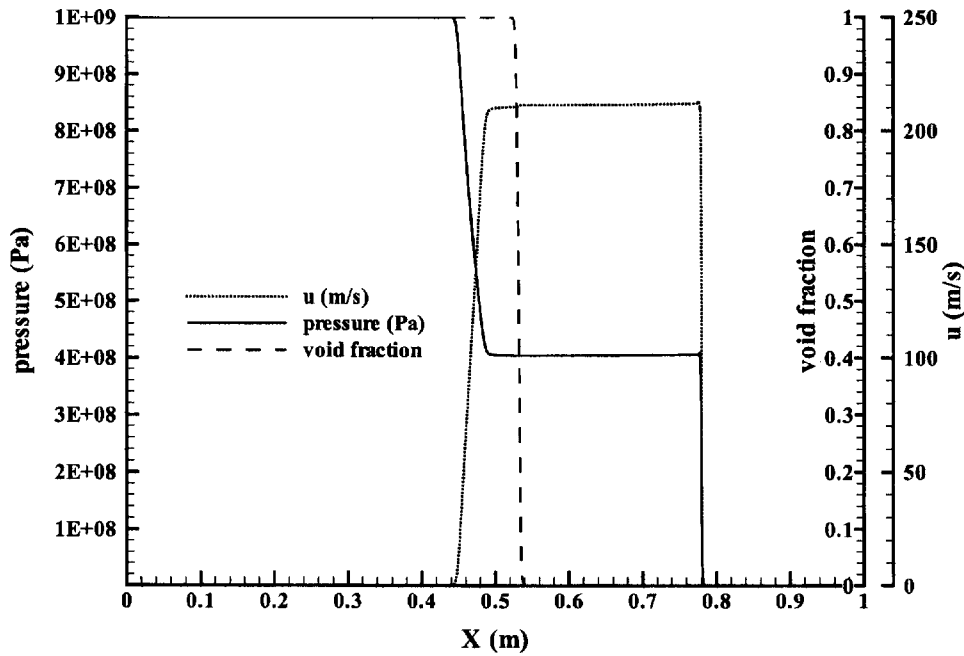
Fig. 13 Pressure, velocity, and void fraction for air-water shock tube (0.15 ms)
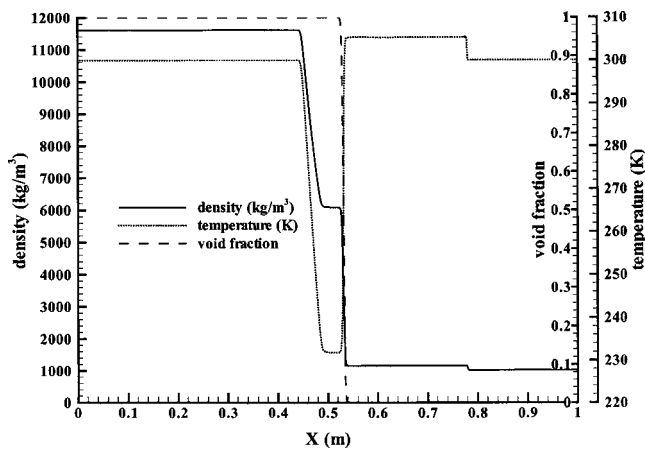
Fig. 14 Density, temperature, and void fraction for air-water shock tube (0.15 ms)
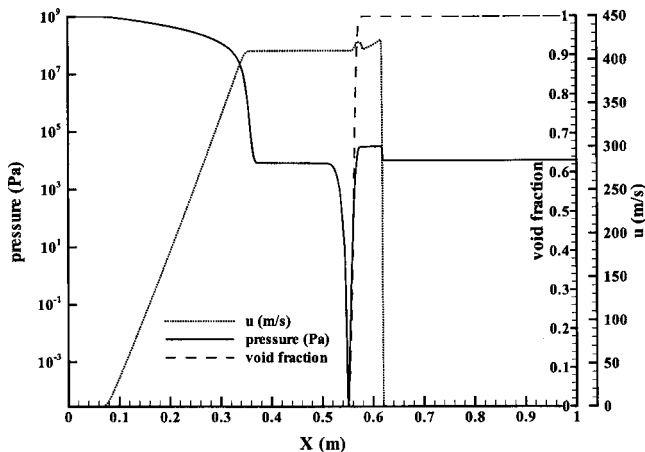
are $C_{prod}=8$ and $C_{dest}=1\times10^7$. The projectile velocity of 420 m/s corresponds to a Mach number of about 1.2 in air and 0.3 in water. The coefficient of drag in air is 0.7938. The pressure and viscous contributions to drag are 6.3708 and 1.5152 N, respectively. In air, viscosity contributes about 19% to overall drag. The steady solution in air is used as an initial condition for the unsteady water entry calculation. The overall coefficient of drag in water is 0.20661 with the pressure component comprising 0.20659 of the total. The viscous contribution to drag in supercavitation mode is several orders of magnitude lower than the pressure contribution. The total drag force in water for the steady supercavitation mode at 420 m/s is 1816 N.

Time-accurate simulations of a high-speed projectile water entry are presented in Figs. 18–20. The steady solution in air was used as initial condition for the unsteady water entry calculation. The water surface was initialized at a distance of 0.05 m from nose of the projectile at a time of 0.0 s.

Figure 18 presents 9 images during the first 0.6 ms of the water entry solution at equal time increments. Water volume fraction contours are plotted with the nonwater contours representing air,

Fig. 15 Pressure, velocity, and void fraction for water-vapor shock tube (0.15 ms)
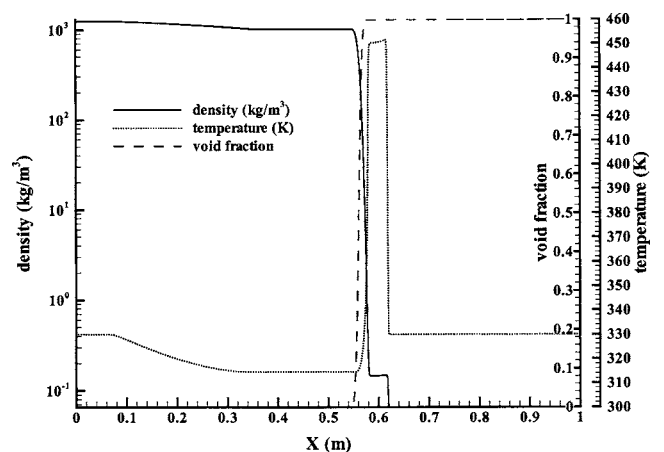
Fig. 16 Density, temperature, and void fraction for water-vapor shock tube (0.15 ms)
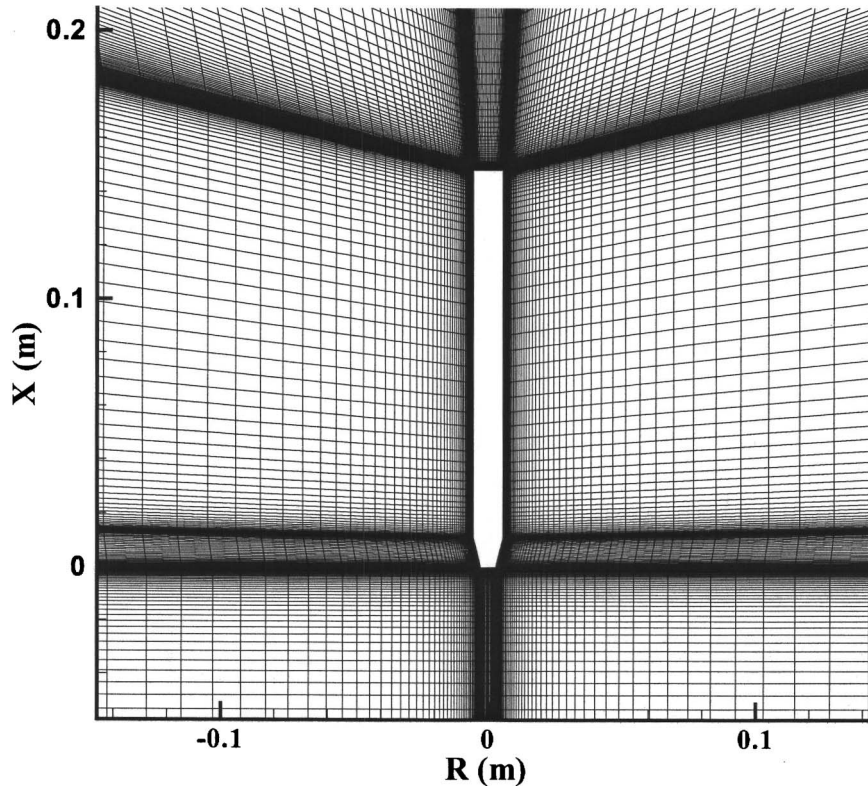
Fig. 17   Grid for generic supercavitating projectile

water vapor, or a combination of the two. In the first two frames, the water level is approaching the nose of the projectile. The algorithm tends to dissipate the moving water-air interface, and while volume fraction displays cavities well, volume fraction contours tend to visually exaggerate the dissipation of the water-air interface. At a time of about 0.15 ms, the nose of the projectile is entering the water. The cavitator is generating vapor, and water is being pushed up and away from the projectile. At 0.225 ms, the projectile is further into the water, and a well-defined cavity appears to be forming. The water rising next to the body is spreading, and the sharp peak is dissipating. Later at time 0.3 ms, the projectile is approximately half into the water and still is encapsulated by a cavity. By 0.45 ms, the projectile is almost completely below the water surface, and the cavity just behind the cavitator appears to be undergoing a transient. A localized cavity collapse sends a disturbance downstream, which is followed by the cavity reforming at cavitator shoulder. The disturbance in the cavity is convected downstream, but the expansion at the nose-to-body transition appears to anchor the cavity by acting as a secondary cavitator. Most of the cavity remains intact during cavity transient. At 0.525 ms, the nose cavity has stabilized and nearly covers the conical nose. By 0.6 ms, the supercavity engulfing the entire body has reformed and is stabilizing. After 0.6 ms, the cavity approaches the steady supercavitation cavity shape.

The projectile is shown at 1.23 ms in Fig. 19. The projectile tip is over three body lengths below the water surface. Vapor volume fraction is plotted on the left of Fig. 19 with air volume fraction on the right. The vapor fraction contours show a vapor supercavity extending from cavitator to well past the projectile. The air vapor fraction contours show significant air entrainment in the wake of the projectile.

Drag versus water level is plotted in Fig. 20. The tip of the projectile is at 0.0, and the base is at about 0.15 m. Total drag is plotted instead of drag coefficients to avoid questionable nondimensionalizations when the projectile passes through water-air interface. Initially the drag is the freestream air value which is very

low compared to drag in water. A large drag rise occurs as the nose of the projectile reaches water level. Several drag spikes occur when the projectile nose penetrates the water surface, as the cavity is being completely formed around the tip of the projectile. As the cavity forms and the projectile transitions to the supercavitation mode, the drag begins to drop. A couple of drag spikes at a water level of about 0.13 m correspond to the cavity collapse transient seen in Fig. 18. During cavity collapse, some of the conical portion of the projectile was wetted with high-pressure water instead of low pressure water vapor. Since almost all drag comes from these high-pressure wetted areas, a temporary cavity breakdown can create significant drag penalties. As the cavity stabilizes and projectile enters supercavitation mode, the drag continues a general downward trend approaching a value of about 1700 N. Air entrainment is probably responsible for the final calculated unsteady drag value of 1700 N differing slightly from steady calculation in water (1816 N).

Conclusions and Future Directions

A low-diffusion upwinding algorithm has been developed for time-accurate calculations of compressible multiphase flows associated with flows ranging from supersonic projectiles in water to multiphase shock tubes. The use of a nontrivial equation of state for water and inclusion of the coupled energy equation allows all-speed calculations for applications where thermal and compressibility effects are significant. Comparisons with experimental data validate the algorithm for low-speed flows. Calculations of cavity size in the high-subsonic regime are validated with experimental measurements. The nature of the transonic experimental data complicates validation, but the computed shock pattern compares favorably to experimental imaging. Calculations demonstrate the ability to solve supersonic flows, multiphase shock tubes, and a water entry problem.

Future work will concentrate on algorithm verification and validation over the entire Mach number regime, extension to three
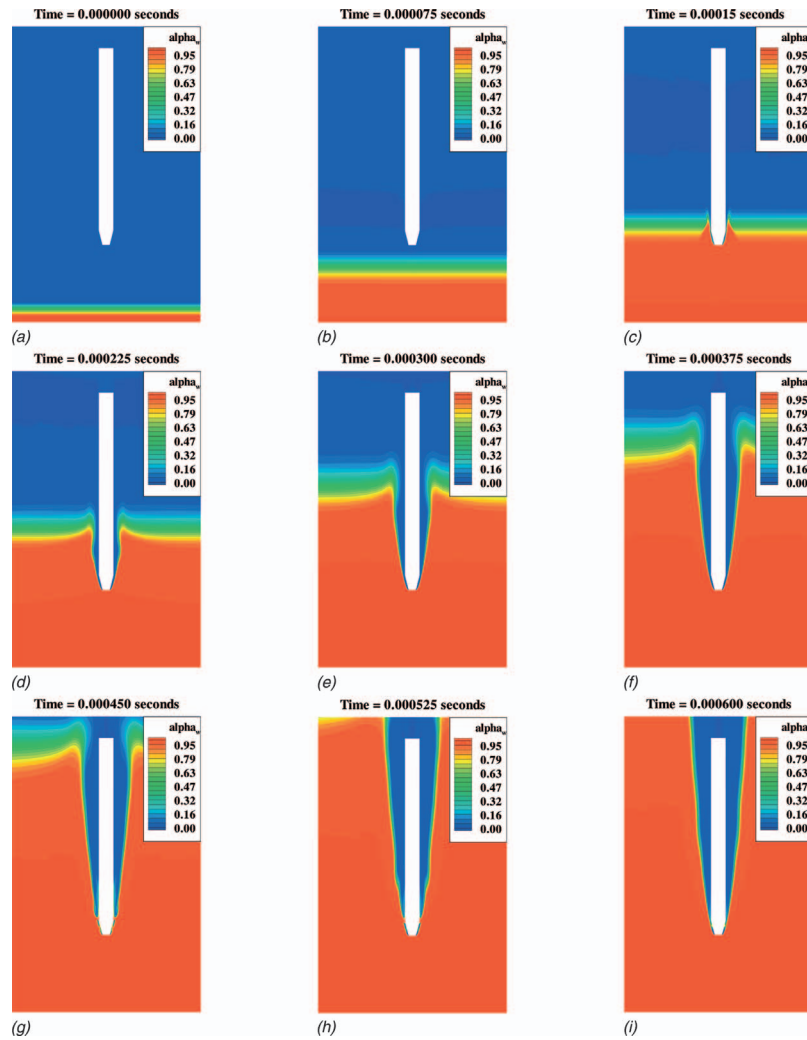
Fig. 18   Supercavitating projectile water entry calculation (water volume fraction contours)
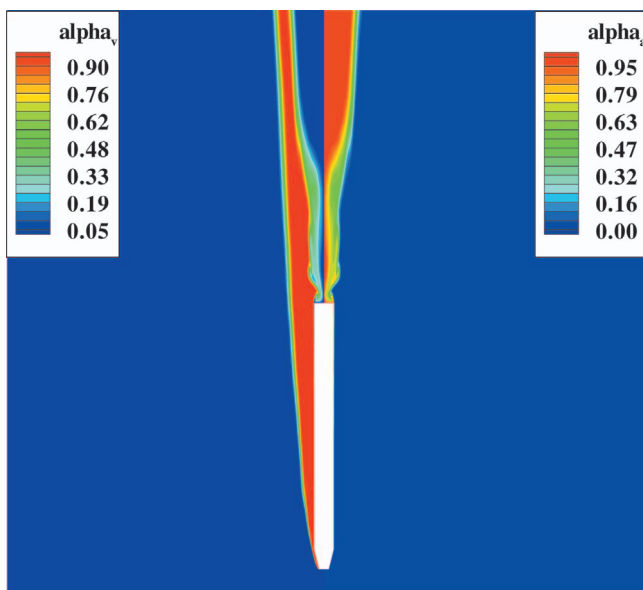

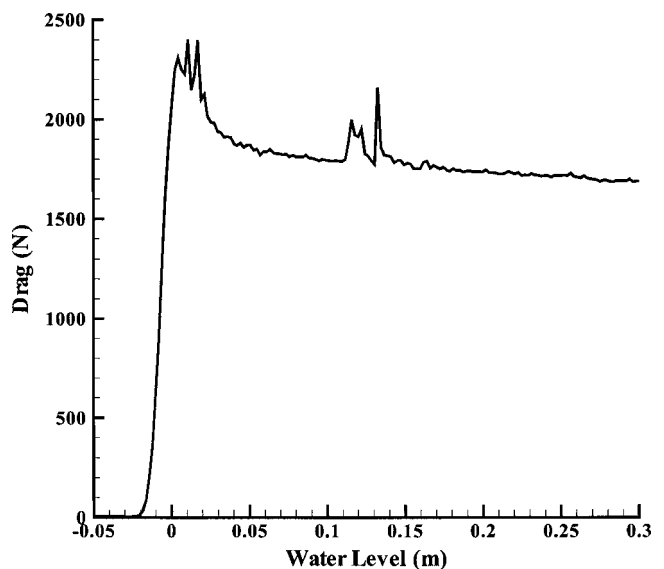Fig. 19   Vapor and air void fractions after water entry (1.23 ms)

Fig. 20   Projectile drag during water entry

dimensions, and better interface tracking. Interface tracking could be improved with dynamic grid adaption, level set methods, or overset grids. Improvement in tracking convected (water-air) and calculated (cavity) interfaces may require a combination of approaches. Viscosity makes a significant contribution to overall drag in air, but is insignificant in water for a supercavitating projectile. For future three-dimensional work, unless viscosity plays an important role in cavity stability, it may be reasonable to ignore viscosity for supercavitating projectiles.

Acknowledgment

Nomenclature

A = flux Jacobian
C = phase change source term coefficients
F = flux vector
H = total enthalpy
K = cavitation number
L = length scale of body
M = Mach number
M = solution variable transformation matrix
P = preconditioning matrix
R = solution residual
S = finite-rate phase change source term vector
T = temperature
U = conserved solution variable vector
V = primitive solution variable vector
Y = mass fraction
a = effective speed of sound
a, b = Oldenbourg coefficients
h = enthalpy
m = rate of phase change
p = pressure
t = time
u, v = velocity components
x, y = space coordinates
α = volume fraction
ρ = density
θ = preconditioning parameter
τ = pseudotime

Subscripts

McBride = McBride value
STD = standard conditions
a = air
c = critical conditions
dest = vapor phase change rate coefficient
g = gaseous phase (vapor and/or air)
l = liquid phase water
o = reference value
prod = liquid phase change rate coefficient
ref = reference quantity
sat = saturation value
∞ = freestream quantity
v = water vapor

Subscripts

p = subiteration index
n = current time level

T = transpose
$+$ = liquid production
$-$ = vapor production

Appendix: Property Derivatives

Property derivatives with respect to the primitive variables are required to calculate the effective speed of sound, the preconditioning matrix, and the flux Jacobians. The derivatives are a function of the individual phase equations of state and the chosen primitive variable vector.

The liquid phase is modeled with a temperature-adjusted Tait equation [7]. The saturated pressure and density derivatives with respect to temperature are easily calculated from the Oldenbourg coefficients [21]. The following parameters are assumed constant: $K_o = 3 \times 10^8$ Pa and $n = 7$.

$$p = K_o \left\{ \left(\frac{\rho_l}{\rho_{lsat}(T)} \right)^n - 1 \right\} + p_{sat}(T) \tag{A1}$$

$$\frac{\partial \rho_l}{\partial P} = \frac{\rho_{lsat}(T)}{n K_o} \left\{ \left(\frac{p - p_{sat}(T)}{K_o} \right) + 1.0 \right\}^{(1/n)-1} \tag{A2}$$

$$\frac{\partial \rho_l}{\partial T} = \frac{-\rho_{lsat}(T)}{n K_o} \left(\frac{\partial p_{sat}(T)}{\partial T} \right) \left\{ \left(\frac{p - p_{sat}(T)}{K_o} \right) + 1.0 \right\}^{(1/n)-1} + \frac{\partial \rho_{sat}(T)}{\partial T} \left\{ \left(\frac{p - p_{sat}(T)}{K_o} \right) + 1.0 \right\}^{1/n} \tag{A3}$$

$$h_l = h_l(T) + \frac{p}{\rho_l} \tag{A4}$$

$$\frac{\partial h_l}{\partial p} = \frac{1}{\rho_l} - \frac{P}{\rho_l^2} \frac{\partial \rho_l}{\partial p} \tag{A5}$$

$$\frac{\partial h_l}{\partial T} = C_p(T) \tag{A6}$$

The gaseous phase (vapor and/or air) is treated as an ideal gas, and the resulting property derivatives are greatly simplified

$$p = \rho_g R T \tag{A7}$$

$$\frac{\partial \rho_g}{\partial p} = \frac{1}{RT} \tag{A8}$$

$$\frac{\partial \rho_g}{\partial T} = \frac{-p}{RT^2} \tag{A9}$$

$$\frac{\partial h_g}{\partial P} = 0 \tag{A10}$$

$$\frac{\partial h_g}{\partial T} = C_p(T) \tag{A11}$$

For an ideal gas, enthalpy is being calculated as only function of temperature using McBride coefficients [22]. Combining the single-phase derivatives and quantities using appropriate mixing rules results in the following [10]:

$$\frac{\partial \rho}{\partial p} = \rho \left(\frac{\alpha_l}{\rho_l} \frac{\partial \rho_l}{\partial p} + \frac{\alpha_v}{\rho_v} \frac{\partial \rho_v}{\partial p} + \frac{\alpha_a}{\rho_a} \frac{\partial \rho_a}{\partial p} \right) \tag{A12}$$

$$\frac{\partial \rho}{\partial T} = \rho \left(\frac{\alpha_l}{\rho_l} \frac{\partial \rho_l}{\partial T} + \frac{\alpha_v}{\rho_v} \frac{\partial \rho_v}{\partial T} + \frac{\alpha_a}{\rho_a} \frac{\partial \rho_a}{\partial T} \right) \tag{A13}$$

$$\frac{\partial h}{\partial p} = Y_l \frac{\partial h_l}{\partial p} + Y_v \frac{\partial h_v}{\partial p} + Y_a \frac{\partial h_a}{\partial p} \tag{A14}$$

$$\frac{\partial h}{\partial T} = Y_l \frac{\partial h_l}{\partial T} + Y_v \frac{\partial h_v}{\partial T} + Y_a \frac{\partial h_a}{\partial T} \tag{A15}$$

$$\frac{\partial \rho}{\partial Y_g} = \rho^2 \left(\frac{1}{\rho_l} - \frac{1}{\rho_g} \right) \tag{A16}$$

$$\frac{\partial h}{\partial Y_g} = h_g - h_l \tag{A17}$$

$$h = Y_l h_l + Y_v h_v + Y_a h_a \tag{A18}$$

References

[1] Ishii, M., 1975, *Thermo-Fluid-Dynamic Theory of Two-Phase Flow*, Eyrolles, Paris.

[2] Stewart, H. B., and Wendroff, B., 1984, "Two-Phase Flow: Models and Methods," J. Comput. Phys., **56**, pp. 363–409.

[3] Tuomi, I., Kumbaro, A., and Paillere, H., 1999, "Approximate Riemann Solvers and Flux Vector Splitting Schemes for Two-Phase Flow," Lecture series 1999-03, von Karman Institute for Fluid Dynamics.

[4] Abgrall, R., and Kami, S., 2001, "Computation of Compressible Multifluids," J. Comput. Phys., **169**, pp. 594–623.

[5] Saurel, R., and Abgrall, R., 1999, "A Multiphase Godunov Method for Compressible Multifluid and Multiphase Flows," J. Comput. Phys., **150**, pp. 425–467.

[6] Abgrall, R., 1996, "How to Prevent Pressure Oscillations in Multicomponent Flow Calculations: A Quasi Conservative Approach," J. Comput. Phys., **125**, pp. 150–160.

[7] Saurel, R., Cocchi, J. P., and Butler, P. B., 1999, "Numerical Study of Cavitation in the Wake of a Hypervelocity Underwater Projectile," J. Propul. Power, **15**(4), pp. 513–522.

[8] Edwards, J. R., Franklin, R. K, and Liou, M.-S., 2000, "Low-Diffusion Flux-Splitting Methods for Real Fluid Flows With Phase Transitions," AIAA J., **38**(9), pp. 1624–l634.

[9] Venkateswaran, S., Lindau, J. W., Kunz, R. F., and Merkle, C. L., 2001, "Preconditioning Algorithms for the Computation of Multi-Phase Mixture Flows," AIAA Paper No. 2001-0279.

[10] Lindau, J. W., Venkateswaran, S., Kunz, R. F., and Merkle, C. L., 2001, "Development of a Fully-Compressible Multi-Phase Reynolds-Averaged Navier-Stokes Model," AIAA Paper No. 2001-2648.

[11] Weiss, J. M., and Smith, W. A., 1994, "Preconditioning Applied to Variable and Constant Density Time-Accurate Flows on Unstructured Meshes," AIAA Paper No. 94-2209.

[12] Turkel, E., 1987, "Preconditioned Methods for Solving the Incompressible and Low Speed Compressible Equations," J. Comput. Phys., **72**, pp. 277–298.

[13] Choi, Y. H., and Merkle, C. L., 1993, "The Application of Preconditioning in Viscous Flows," J. Comput. Phys., **105**, pp. 207–223.

[14] Edwards, J. R., 1997, "A Low-Diffusion Flux-Splitting Scheme for Navier-Stokes Calculations," Comput. Fluids, **26**(6), pp. 635–659.

[15] Edwards, J. R., 2001, "Towards Unified CFD Simulations of Real Fluid Flows," AIAA Paper No. 2001-2524.

[16] Liou, M. S., 1995, "Progress Toward an Improved CFD Method: AUSM+," AIAA Paper No. 1995-1701.

[17] Liou, M. S., 2001, "Ten Years in the Making - AUSM Family," AIAA Paper No. 2001-2521.

[18] Spalart, P. R., and Allmaras, S. R., 1992, "A One-Equation Turbulence Model for Aerodynamic Flows," AIAA Paper No. 92-0439.

[19] Edwards, J. R., and Chandra, S., 1994, "Comparison of Eddy Viscosity - Transport Turbulence Models for Three-Dimensional, Shock-Separated Flowfields," AIAA Paper No. 94-2275.

[20] Cole, R. H., 1948, *Underwater Explosions*, Princeton University Press, Princeton, NJ, pp. 38–39.

[21] Oldenbourg, R., 1989, *Properties of Water and Steam in SI-Units*, Springer-Verlag, Berlin.

[22] McBride, B. J., Gordon, S., and Reno, M. A., 1993, "Coefficients for Calculating Thermodynamic and Transport Properties of Individual Species," NASA Technical Memorandum 4513.

[23] Courant, R., Friedrichs, K. O., and Lewy, H., 1967, "On the Partial Difference Equations of Mathematical Physics," IBM J. Res. Dev., **11**, pp. 215–234.

[24] Rai, M. M., 1987, "Navier-Stokes Simulations of Blade-Vortex Interaction Using High-Order Accurate Upwind Schemes," AIAA Paper No. 87-0543.

[25] Pulliam, T. H., 1993, "Time Accuracy and the Use of Implicit Methods," AIAA Paper No. 93-3360.

[26] Rouse, H., and McNown, J. S., 1948, "Cavitation and Pressure Distribution: Head Forms at Zero Angle of Yaw," State University of Iowa Engineering Bulletin 32, Ames, IA.

[27] Hrubes, J. D., 2001, "High-Speed Imaging of Supercavitating Underwater Projectiles," Exp. Fluids, **30**, pp. 57–64.

[28] Grady, R. J., 1979, Hydroballistics Design Handbook, Vol I, Naval Sea Systems Command, Technical Report No. SEAHAC/79-1, pp. 38–45.

[29] Neaves, M. D., and Edwards, J. R., 2004, "Time-Accurate Calculations of Axisymmetric Water Entry for a Supercavitating Projectile," AIAA Paper No. 2004-2643.

A Multizone Moving Mesh Algorithm for Simulation of Flow Around a Rigid Body With Arbitrary Motion

S. M. Mirsajedi
Ph. D. Candidate
e-mail: m7829904@aut.ac.ir

S. M. H. Karimian
Professor
e-mail: hkarim@aut.ac.ir

M. Mani
Associate Professor
e-mail: mani@aut.ac.ir

Amirkabir University of Technology,
Tehran, Iran, 15875-4413

In this paper, general motion of a two-dimensional body is modeled using a new moving mesh concept. Solution domain is divided into the three zones. The first zone, with a circular boundary, includes the moving body and facilitates the rotational motion of it. The second zone, with a square boundary, includes the first zone and facilitates the translational motion of the body. The third zone is a background grid in which the second zone moves. With this configuration of grids any two-dimensional motion of a body can be modeled with almost no grid insertion or deletion. However, in some stages of motion we merge or split a few number of elements. The discretization method is control-volume based finite-element, and the unsteady form of the Euler equations are solved using AUSM algorithm. To demonstrate the excellent performance of the present method two moving cases including rotational and translational motions are solved. The results show excellent agreement with experimental data or other numerical results.
[DOI: 10.1115/1.2170124]

Keywords: general motion, moving mesh, 2D equations, inviscid flow

1 Introduction

Different problems with unsteady or periodic motion of a rigid body can be found in both nature and industry. Therefore, development of new moving mesh algorithms is greatly needed. The two main components for the solution of flow field around a moving body are flow solver, and the moving grid methodology. In this paper we will focus on the latter one. The simplest method, but not the efficient one, is to regenerate new grid around the body after each step of its motion. However, this would be very time consuming, especially around the complex geometries. It could be also questionable in term of accuracy, since a great deal of interpolation is required.

Because of these difficulties, some researchers perform a grid restructuring in the regions where nonacceptable elements are formed [1,2]. In this method, the displacement of body at each time step should not be larger than the scale of the smallest element in the domain. Even such a local restructuring, which will be repeated for many times, needs deletion and insertion of nodes. To eliminate the number of node deletion/insertion process, Batina [3] introduced the concept of dynamic mesh as a smoothening process, in which the grid points are connected to each other with springs. After each step of body motion, a smoothening process is performed through the balance of spring forces. As a result the rearranged grid points will form more uniform elements than those of previous step. The value of spring factor K is an important factor in this method. There are other references [1,4,5] that have discussed the method of choosing spring factor. For the application of dynamic mesh also see Refs. [6,7].

The smoothening processes such as the one introduced in Ref. [8] are intermediate steps, which can eliminate or decrease the grid regenerations for cases with small motions. To maintain the grid quality [9] of cases with large motions of body, grid restructuring is inevitable. For example, Ref. [8] limits the smoothening

process to a defined layer of grid around the body. This smoothening is continuously applied as the body moves. A grid restructuring is applied in the solution domain only if the grid quality is going to be lost. It is noted that although this restructuring is limited to the mentioned layer, this layer should be redefined after every some time steps of body motion. It is added that redefinition of this layer is also not an easy work. Different criteria have been introduced and discussed for node deletion and insertion in a restructuring process [2,4,8,10].

In cases where large displacements are interested, overset grid has its own application. The most famous method in this category is the Chimera grid [11–13]. It must be noted that special attention should be given to the accuracy of several interpolations that are required in the Chimera grid method. For aerospace applications of Chimera grid, see Ref. [13]. In addition to the above-mentioned methods, hybrid mesh has been also used in moving boundary problems. The flexibility of triangular elements on complex boundaries, and the simple data structure of Cartesian grid have increased the demand of using hybrid triangular-Cartesian meshes [14–20].

In the present method, the number of node deletion/insertion process is minimized to almost nothing. Even in the case of large translational displacements where such a process is normally required, we only merge or split a few number of elements. In this method, solution domain is divided into the three zones. The first zone includes the moving body and its surrounding grid with circular boundary, which is fixed to the body and moves with it. With the circular form of its boundary any rotational motion and oscillation of the body can be simply analyzed; see Fig. 1. The second zone with its square boundary includes the first zone. Due to its rectangular boundary, any translational displacement of the body can be simply modeled by translation of this zone. A similar concept has been used earlier in Ref. [21]. The third zone is a background grid on which the second zone should be moved. We have used unstructured triangular mesh in the first zone, and Cartesian grid in the other zones. However the method has no limitation in using any type of structured and unstructured grids, or a combination of them with different elements in the first zone. This is

Fig. 1 Grid configuration of present method

Fig. 3 First zone after body rotation
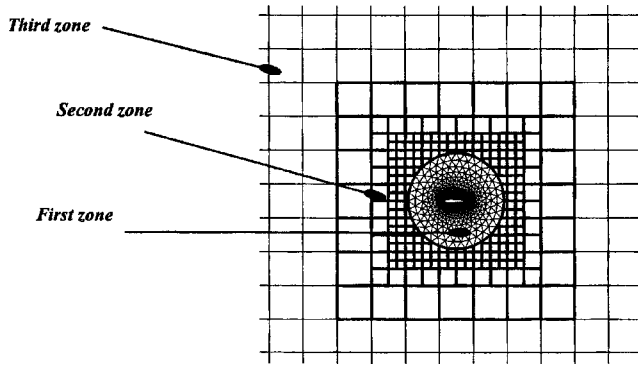
very important since the method allows the user to generate any desired grid around the complex geometries within the first zone.

In the next section, the grid configuration of our methodology will be explained. Then, the solution algorithm and domain discretization will be introduced. Finally the results will be presented to demonstrate excellent performance of our algorithm for translational and rotational/oscillational motions.

2 Grid Configuration

The general motion of a moving body is a combination of translational and rotational motions (including oscillations). In order to simplify the modeling of this general motion, i.e., eliminate any type of grid restructuring or regeneration, and reduce the number of node deletion/insertion process to almost zero, we have divided these two motions throughout the subdivision of solution domain into the three zones.

The first zone, that includes the moving body, has a circular boundary. Within this boundary any type of grid can be generated around the body. As is seen in Fig. 1, in the present method, unstructured triangular grids are used. Depending on the problem, the quality of this grid and the radius of its boundary can be varied. The outer circle in Fig. 2 will be attached to the grids of the second zone, and will not rotate. However, the rest of the grid within the inner circle that is attached to the body will rotate with it, for earlier works in this field see Refs. [8,22]. Therefore, the elements within the inner circle will be rotated, and only the shape of the elements between the two circles (always one set) will be changed. This idea has been used before as shear slip mesh update method (SSMUM) in Refs. [23,24]. Note that SSMUM was only applicable to translational or rotational motions, and not a combination of them, or oblique translation. In Fig. 3, grid configuration around the rotated airfoil is shown. The grid points on each of the two circles (for example n nodes) have been uniformly distributed. After $360/n$ deg of rotation, each node on the inner circle will reach to the location of its next node before this rotation. In this case, with no node deletion or insertion, elements between the

two circles are renumbered with a process shown in Fig. 4. Note that by choosing a larger boundary, even this renumbering occurs far from the higher gradient flow close to the body. The grid of first zone after rotations of 20 deg, 40 deg and 80 deg are shown in Fig. 5.

As is shown in Fig. 1, the second zone with its squared boundary surrounds the first zone. The inner space of the second zone is meshed with Cartesian grid. Due to the rectangular form of this zone's boundary any translational motion of the body can be simply modeled. At the intersection of the Cartesian grid and the
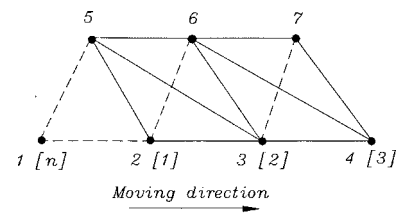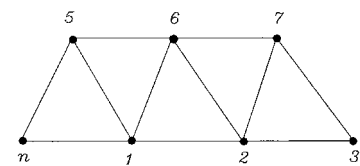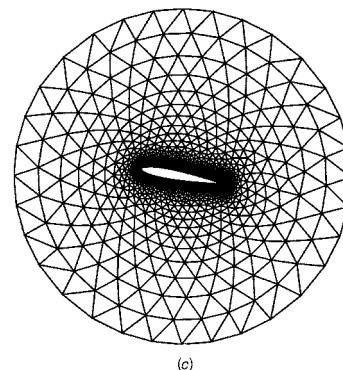

Fig. 4 Renumbering process for $360/n$ deg of rotation. (*a*) Old and new elements. (*b*) New elements after renumbering. (*c*) Whole domain after renumbering.
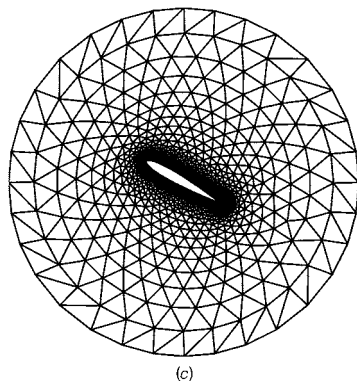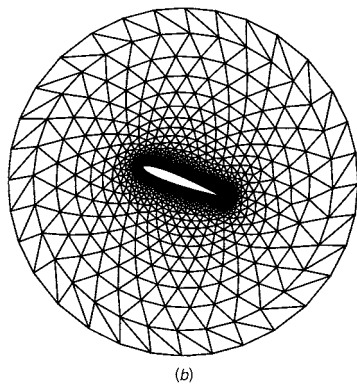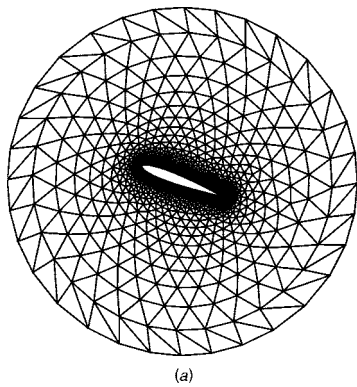

Fig. 2 Unstructured grid within the first zone

(a)

(b)

(c)

Fig. 5   Rotation (*a*) 20 deg, (*b*) 40 deg, and (*c*) 80 deg of airfoil

Fig. 6   Cut cells with hanging nodes at the intersection of first and second zone

boundary of first zone (which does not move), cut cells are formed, which may have hanging nodes as well. This is shown in Fig. 6. With control-volume based finite element discretization method there is no difficulty in handling cut cells with hanging nodes. The Cartesian grid of the second zone in Fig. 1 has three levels. Depending on the problem, the number of grid levels, and the largeness of the squared boundary can be varied, as shown in Figs. 7(*a*) and 7(*b*). The second zone makes its translational motions on a background grid which now will be introduced. In a translational motion, all of the grids within the square boundary will move. As is shown in Figs. 8(*a*) and 8(*b*), grid deformation occurs only within the two sets of elements surrounding the second zone's boundary. Whenever the grid points of the second zone boundary in the front of the body, reach the old location of the next grid points in the front of the body, two sets of elements in the front of the second zone will be merged with each other. Instead the two sets of elements on the rear of the second zone will be split to three sets, as shown in Fig. 8(*c*). Note that after this process we have our uniform background grid and the second zone that have moved a distance equal to *h*. At this stage only a renumbering of elements is required. Since the background grid is

Cartesian, the required interpolation will be very easy. It is noted that during this process the total number of elements and nodes will always remain constant. It should be noted that in this method, there is no limitation for large displacements in any direction.

Some comments should be made here. First, note that there is no need for node deletion/insertion process. We only merge or split a few number of elements in large displacements. Second, note that for a specific displacement, increasing the dimension of background's elements will decrease the number of merging/splitting process. Third, by making the dimension of square boundary larger, the merging/splitting process happens far from the higher gradient regions of flow that mostly occurs close to the body. Fourth, in terms of grid structure, smooth transition of smaller elements of Cartesian grid within the second zone to the larger elements of background grid can be handled by increasing the level of grids in the second zone. Therefore, large elements in the background grid, that will reduce the number of merging/splitting process, will not cause a problem. Fifth, this method in its present form, is not capable of handling rotating bodies that cannot be meshed within a circular boundary, e.g., when the surrounding surface is close to the rotating body.

3   Solution Algorithm

The integral form of the Euler equations for two-dimensional unsteady compressible flow is given below

$$\int_v \frac{\partial W}{\partial t} dv + \oint_S F_n \, ds = 0 \tag{1}$$

where F_n and W are defined as

$$F_n = \begin{pmatrix} \rho(u_n - \omega_n) \\ \rho u(u_n - \omega_n) + Pn_x \\ \rho v(u_n - \omega_n) + Pn_y \\ \rho E(u_n - \omega_n) + Pu_n \end{pmatrix}, \quad W = \begin{pmatrix} \rho \\ \rho u \\ \rho v \\ \rho E \end{pmatrix} \tag{2}$$

and, u_n and ω_n are, respectively, the velocity components of fluid flow and the moving mesh normal to the surface on which F_n is calculated. For more details see Ref. [25].

As is known, ω_n should be calculated based on the geometric conservation laws (GCL). Implementation of GCL eliminates any error that may be produced due to the mesh movement. GCL was first introduced in 1961 [26], and then was implemented in computational fluid dynamics to correctly conserve the physical quantities of fluid flow [27,28]; for more details of GCL see Ref. [29]. Details of the calculation method of ω_n is described in Ref. [30], however for the sake of clarity we shortly introduce it. In Fig. 9, when node numbers 1 and 3 move toward 1′ and 3′, respectively,
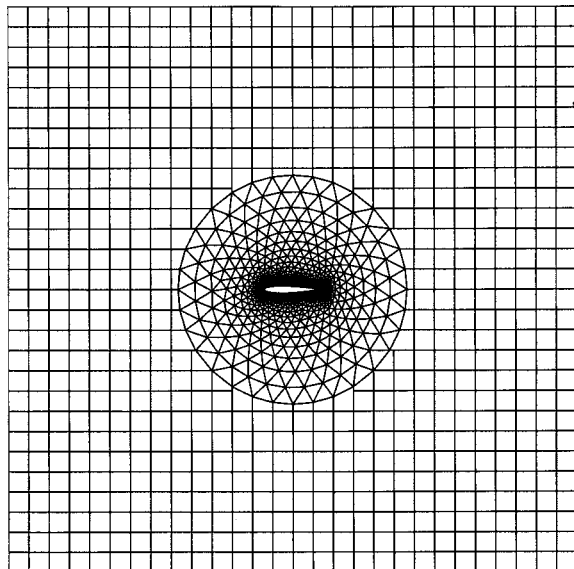
(a)
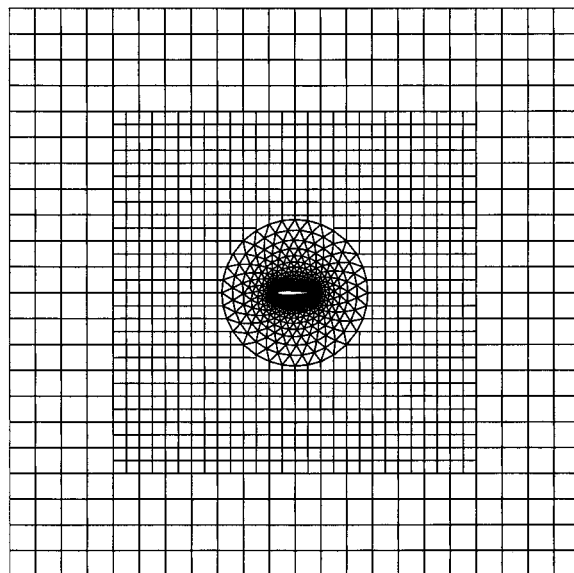
(b)

Fig. 7 (*a*) **Second zone with one grid level,** (*b*) **second zone with larger boundary and two grid level**

subcontrol volume (SCV) of node 2 increases from 'op2qo' to 'o′p′2q′o′'. Therefore, velocities normal to the surfaces *a* and *b*, (i.e. 'op' and 'oq') are calculated as follows

$$(\omega_n)_a = \frac{\Delta V_a}{\Delta t \cdot S_a}, \quad (\omega_n)_b = \frac{\Delta V_b}{\Delta t \cdot S_b} \tag{3}$$

In this way, calculation of ω_n, guarantees the conservation of volume *V* during mesh movement. As stated before, the solution domain includes triangular and Cartesian elements which may have hanging nodes; see Figs. 1 and 6. Using the finite-element method, the conservation equations can be numerically formed on an isolated element, despite its connection with other elements in the solution domain. Since the finite-element method used in this paper is based on control-volume approach, the assembled system of equations represents the discretized form of conservation equations over control volumes formed in the solution domain.

For example, in the first zone with triangular grids, a node is surrounded by a number of elements; see Fig. 10. As seen, each

element is divided into three parts, each of them called a SCV. These SCVs are made by intersecting of triangle medians. SCVs surrounding a node then will form a control volume for that node; the dashed area in Fig. 10. Although in the control-volume based finite-element (CVFE) method conservation equations are held for every control volume, their formation will be effected by an element-by-element assembly of elemental matrix equations. An elemental matrix equation is determined by applying a conservation equation to each of the three SCVs within the element. The finite-element assembly procedure, then, will entail the addition of these SCV equations to the respective control-volume nodal equation. With the CVFE method, elements with hanging nodes, as shown in Fig. 11, can be also handled easily. In this paper left and right values of F_n in the upwind method such as Roe [31], or AUSM [32] are chosen as given in Table 1. For details of CVFE method, see Ref. [33].

After implementation of assembly process over all of the elements, a conservation equation of the following form will be obtained for each node, i.e., node 2 in Fig. 10.

$$\frac{W_2^{n+1} V_2^{n+1} - W_2^n V_2^n}{\Delta t} + \sum_{i=1}^{12} (F_n \cdot \Delta s)_i^n = 0 \tag{4}$$

where *V* is the volume of control volume 2, and Δs is the surface area. In the present paper we have used AUSM to calculate F_n at the control volume subsurfaces.

AUSM proposes to evaluate F_n from two terms, named convective and pressure terms respectively, i.e.,

$$F_{n_{a/b}} = M_{n_{a/b}} \begin{pmatrix} \rho a \\ \rho au \\ \rho av \\ \rho aE \end{pmatrix}_{L/R} + \begin{pmatrix} 0 \\ P_{a/b} n_x \\ P_{a/b} n_y \\ P_{a/b} u_n \end{pmatrix}$$

where

$$(\bullet)_{L/R} = \begin{cases} (\bullet)_L & M_{n_{a/b}} \geqslant 0 \\ (\bullet)_R & M_{n_{a/b}} < 0 \end{cases}$$

For calculation of $M_{n_{a/b}}$ and $P_{a/b}$, we use the following formula:

$$M_{n_{a/b}} = M_{n_L}^+ + M_{n_R}^-, \quad P_{a/b} = P_L^+ + P_R^-$$

where

$$M_n^\pm = \begin{cases} \pm\frac{1}{4}(M_n \pm 1)^2 & |M_n| \leqslant 1 \\ \frac{1}{2}(M_n \pm |M_n|) & |M_n| > 1 \end{cases},$$

$$P^\pm = \begin{cases} \frac{P}{4}(M_n \pm 1)^2 (2 \mp M_n) & |M_n| \leqslant 1 \\ \frac{P}{2}(M_n \pm |M_n|)/M_n & |M_n| > 1 \end{cases}$$

In the next section we will discuss the calculated results.

4   Numerical Results

In this section we first introduce two test cases to demonstrate the correct performance of the present algorithm on moving grids. The first case is defined to demonstrate that the grid motion would not affect the solution. For this purpose, consider a 2D domain with solid boundaries. The fluid is initially stationary with the following parameters, $\rho = 1$ kg/m^3, $P = 1$ bar, and $T = 300$ K. As is shown in Fig. 12, three zones with triangular and Cartesian elements are formed within the solution domain.

With these initial conditions, Euler equations are solved in the domain while the elements oscillate with combined motion of rotation and displacement. After two seconds, with $\Delta t = 1.0$E-6 (s)
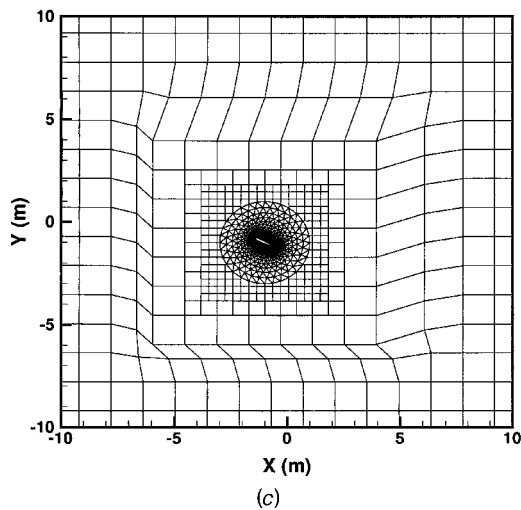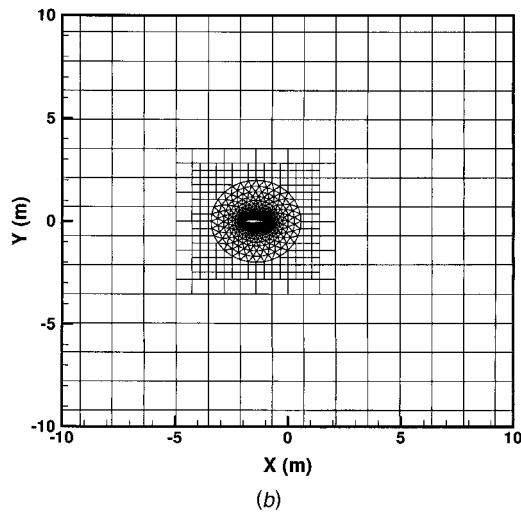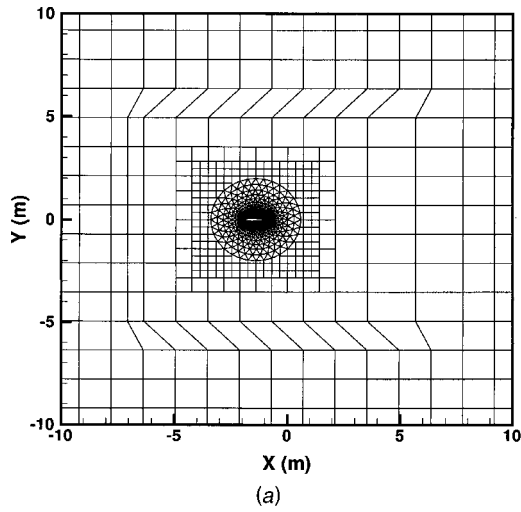
(a)

(b)

(c)

Fig. 8 Second zone motion on the background grid, (*a*) horizontal motion, before renumbering, (*b*) state (*a*) after renumbering, (*c*) oblique motion
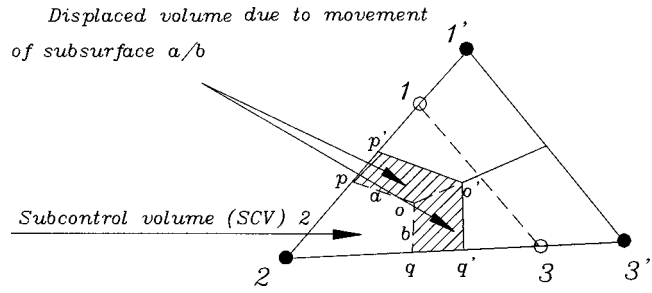

Fig. 9 Simple deformation of an element due to the motion of its two nodes
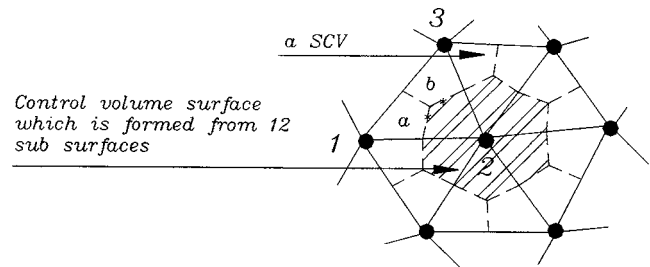

Fig. 10 Formation of a control volume from subcontrol volumes within the surrounding elements

mance of the code in unsteady flow simulation. The unsteady solution of flow with $u=20$ m/s, $T=300$K and $P=1$ bar passing over a circular cylinder is solved with present method (see Fig. 14). After 5 ms and 10 ms, the pressure distribution on the cylinder is plotted in Figs. 15(*a*) and 15(*b*) with title "unsteady flow." It is clear that if the same cylinder starts to move with $u=20$ m/s in a stationary fluid with $P=1$ bar and $T=300°$ K, the same pressure distribution should be obtained after 5 ms and 10 ms. In fact in this case the second zone is moving on the background grid with the speed of 20 m/s. The results obtained from this calculation are plotted in Figs. 15(*a*) and 15(*b*) with the title "moving cylinder."
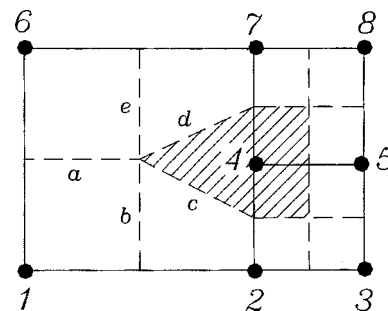
Fig. 11 Formation of a control volume around a hanging node

contours of 1-ρ that is physically expected to remain zero, are plotted in Fig. 13. As is seen, they are almost zero, noting that the machine precision is double. This demonstrates correct implementation of GCL in the code.

The next test case is defined to demonstrate the correct perfor-

Table 1 Left and right nodes when using upwind methods

Figure	Surface	Left	Right
10	a	2	**1**
10	b	3	**2**
11	a	6	**1**
11	b	2	**1**
11	c	4	**2**
11	d	7	**4**
11	**e**	**6**	**7**

Fig. 12 Hybrid empty domain

(*a*)

(*b*)

Fig. 15 Comparison of surface pressure distribution in front of the cylinder computed from unsteady and moving body simulation after (*a*) 5 ms and (*b*) 10 ms
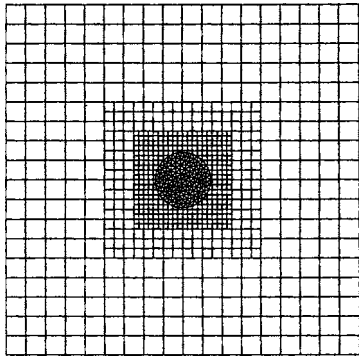
As is seen, both unsteady and moving cylinder results agree with each other, excellently. Now we can conclude that our moving algorithm works correctly.

At this stage, we present the results of our algorithm for two AGARD test cases of CT1 and CT5. In both cases, the airfoil is NACA0012 and oscillates with $\alpha = \alpha_m + \alpha_0 \sin(\omega t)$, where α_m is the mean angle of attack and α_0 its amplitude. The frequency ω is defined throughout the reduced frequency K, that is $K = \omega c / 2 V_\infty$. The time step is $\Delta t = 1.0 \times 10^{-6}$ s and the grid specifications are given in Table 2.

The specifications of our third case are $M_\infty = 0.6$, $\alpha_m = 2.89$ deg, $\alpha_0 = 2.41$ deg, $K = 0.0808$, and $T = 300°$ K. After 0.3 s of oscillations, the C_n-α graph of CT1 case is plotted in Fig. 16. As is seen the calculated results agrees excellently with the experimental results of Ref. [34].

The specifications of our fourth case, i.e.; CT5, are $M_\infty = 0.755$, $\alpha_m = 0.016$ deg, $\alpha_0 = 2.51$ deg, $K = 0.0814$, and $T = 300°$ K. After 0.3 s of oscillations, the C_n-α graph of this case

is plotted in Fig. 17. The present results have the very similar trend of experimental data [34], however two notes should be made. It seems that first, the present results and the experimental data are shifted from each other, and second, the experimental data are more asymmetry than that may happen due to nonzero value of α_m. These two facts can be concluded from the comparison of this experimental data with other numerical results obtained from an inviscid [25,35] or even viscous simulation [7]. We think that α_m may have not been exactly 0.016 in this experiment. Therefore, if α_m is set equal to 0.25, the present algorithm predicts the C_n-α a curve very close to the experiment results as shown in Fig. 18.

5 Conclusion

In this paper, a new multizone moving mesh algorithm is developed to simulate the general motion of a two-dimensional body. Based on the present method, solution domain is divided into the three zones. In the first zone with its circular boundary, the body rotation/oscillation can be easily modeled. By making a Cartesian grid with square boundary around the first zone, called the second zone, the translational motion of the body can be simply simulated. The third zone is a background grid. In this algo-
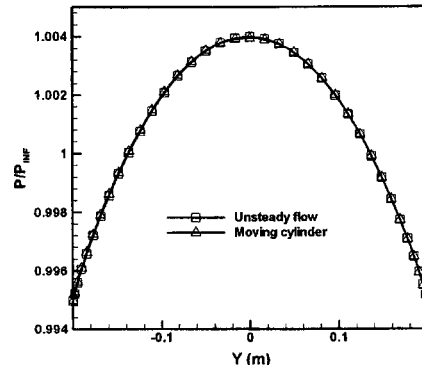

Fig. 13 First test, contours of 1-ρ, after 2 s of grid motion

Fig. 14 Computational grids for motion of cylinder

Table 2 Grid specifications

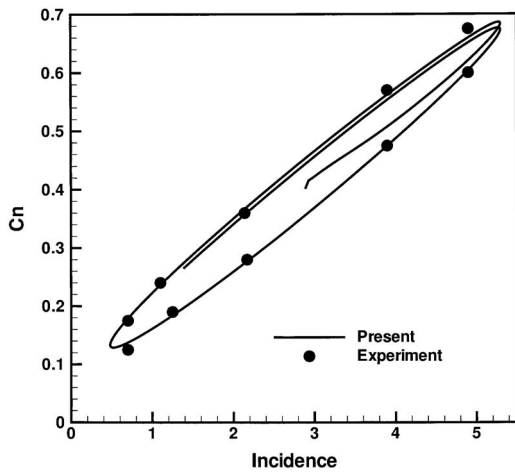|	
Number of nodes on the airfoil	198
Number of nodes on the first zone boundary	64
Number of nodes in the first zone	35,751
Number of grid levels in second zone	3
Number of nodes in the second zone boundary	28
Number of nodes in the second zone	1205
Number of nodes in the background zone	2160

Fig. 16 Comparison of the normal force coefficient loop of CT1 case, present and experimental data [34]
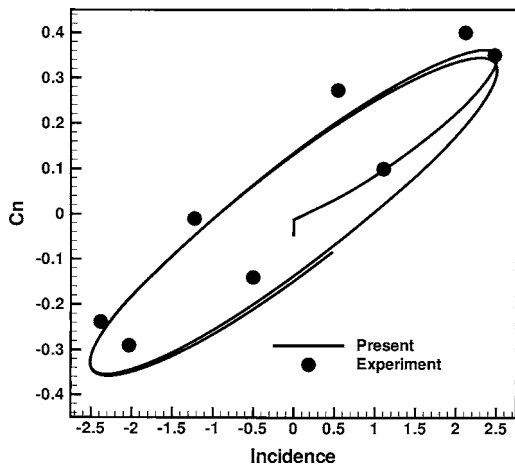

Fig. 17 Comparison of the normal force coefficient loop of CT5 case, Present and experimental data [34]
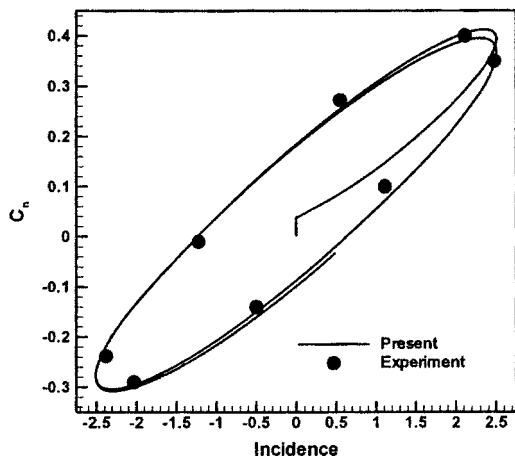

Fig. 18 Comparison of the normal force coefficient loop of CT5 case with Corrected α_m to 0.25, present and experimental data [34]

rithm, the insertion/deletion process of nodes is not needed. Although in some stages of large body displacements, a few elements should be merged or splitted. The computational results have shown excellent agreement with experimental data.

Nomenclature

C_n = coefficient of normal force
E = specific total energy
F = flux vectors in the Euler equations
M = Mach number
n_x = x component of outward normal unit vector
n_y = y component of outward normal unit vector
P = pressure
S = control-volume surface
t = time
u = x component of Cartesian velocity
v = y component of Cartesian velocity
V = control volume
W = vector of conserved variables
α = angle of attack
ρ = density

Subscripts

a, b = denote control surface
n = outward normal vector
L, R = left or right of control surface

Superscripts

n = old time
$n+1$ = present time

References

[1] Goswami, A., and Parpia, I. H., 1991, "Grid Restructuring for Moving Boundaries," AIAA Paper No. 91-1589-CP.
[2] Trepanier, J. Y., Reggio, M., Paraschiviou, M., and Camarero, R., 1992, "Unsteady Euler Solution for Arbitrary Moving Bodies and Boundaries," AIAA Paper No. 92-0051-1992.
[3] Batina, J. T., 1990, "Unsteady Euler Airfoil Solutions Using Unstructured Dynamic Meshes," AIAA J., **28**(8), pp. 1381–1388.
[4] Pirzadeh, S. Z., 1999, "An Adaptive Unstructured Grid Method by Grid Subdivision, Local Remeshing and Grid Movement," 14th AIAA, AIAA Paper No. 99-3255.
[5] Batina, J. T., 1991, "Unsteady Euler Algorithm with Unstructured Dynamic Mesh for Complex Airfoil Aerodynamic Analysis," AIAA J., **29**(3), pp. 327–333.
[6] Tsai, H. M., Wong, A. S. F., Cai, J., Zhu, Y., and Liu, F., 2001, "Unsteady Flow Calculations with a Parallel Multi-block Moving Mesh Algorithm," AIAA J., **39**(6), pp. 1021–1029.
[7] Jahangirian, A., and Hadidoolabi, M., 2004, "An Implicit Solution of the Unsteady Navier-Stokes Equations on Unstructured Moving Grids," *24th International Congress of the Aeronautical Science*, ICAS, Yokohama, Japan.
[8] Hase, J. E., Anderson, D. A., and Parpia, I. H., 1991, "A Delaunay Triangulation Method and Euler Solver for Bodies in Relative Motion," AIAA Paper No. 91-1590-CP.
[9] Zheng, Y., Lewis, R. W., and Gethin, D. T., 1996, "Three-Dimensional Unstructured Mesh Generation Part 1-3," Comput. Methods Appl. Mech. Eng., **134**, pp. 249–310.
[10] Formaggia, L., Peraire, J., and Morgan, K., 1988, "Simulation of a Store Separation Using the Finite Element Method," J. Turbomach., **12**, pp. 175–181.
[11] Steger, J. L., Dougherty, F. C., and Benek, J. A., 1983, *A Chimera Grid Scheme*, in Advances in Grid Generation, American Society of Mechanical Engineers, FED, New York, Vol. 5, pp. 59–69.
[12] Benek, J. A., Buning, P. G., and Steger, J. L., 1985, "A 3-D Chimera Grid Embedding Technique," AIAA Paper No. 85-1523.
[13] Nakahashi, K., Togashi, F., and Sharov, D., 2000, "Intergrid-Boundary Definition Method for Overset Unstructured Grid Approach," AIAA J., **38**(11), pp. 2077–2084.
[14] Kallinderis, Y., Khawaja, A., and Mc-Morris, H., 1996, "Hybrid Prismatic/Tetrahedral Grid Generation for Complex Geometries," AIAA J., **34**, pp. 291–298.
[15] Coirier, W. J., and Jorgenson, P. C. E., 1996, "A Mixed Volume Grid Approach for the Euler and Navier-Stokes Equations," AIAA Paper No. 96-0762.
[16] Karman, S. L., 1995, "SPLITFLOW: A 3D Unstructured Cartesian/Prismatic Grid CFD Code for Complete Geometries," AIAA Paper No. 95-0343.
[17] Zhang, L. P., Zhang, H. X., and Gao, S. C., 1997, "A Cartesian/Unstructured Hybrid Grid Solver and its Applications to 2D/3D Complex Inviscid Flow Fields," *Proceedings of the 7th International Symposium on CFD*, Beijing, China, pp. 347–352.

[18] Zhang, L. P., Yang, Y. J., and Zhang, H. X., 2000, "Numerical Simulations of 3D Inviscid/Viscous Flow Fields on Cartesian/Unstructured/Prismatic Hybrid Grids," *Proceedings of the 4th Asian CFD Conference*, Mianyang, Sichuan, China.

[19] Murman, S., Aftosmis, M., and Berger, M., 2003, "Implicit Approaches for Moving Boundaries in a 3D Cartesian Method," AIAA Paper No. 2003-1119.

[20] Zhang, L. P., and Wang, Z. J., 2004, "A Block LU-SGS Implicit Dual Time-stepping Algorithm for Hybrid Dynamic Meshes," Comput. Fluids, 33, pp. 891–916.

[21] Tezduyar, T. E., Behr, M., Mittal, S., and Liou, J., 1992, "A New Strategy for Finite Element Computations Involving Moving Boundaries and Interfaces—The Deforming-Spatial-Domain/Space-Time Procedure Part II: Computation of Free-Surface Flows, Two-Liquid Flows, and Flows with Drifting Cylinders," Comput. Methods Appl. Mech. Eng., 94, pp. 353–371.

[22] Mittal, S., and Tezduyar, T. E., 1992, "A Finite Element Study of Incompressible Flows Past Oscillating Cylinders and Airfoils," Int. J. Numer. Methods Fluids, 15, pp. 1073–1118.

[23] Behr, M., and Tezduyar, T., 1999, "The Shear-Slip Mesh Update Method," Comput. Methods Appl. Mech. Eng., 174, pp. 261–274.

[24] Behr, M., and Tezduyar, T., 2001, "Shear-Slip Mesh Update in 3D Computation of Complex Flow Problems with Rotating Mechanical Components," Comput. Methods Appl. Mech. Eng., 190, pp. 3189–3200.

[25] Lin, C. Q., and Pahlke, K., 1994, "Numerical Solution of Euler Equations for Aerofoils in Arbitrary Unsteady Motion," Aeronaut. J., June/July, pp. 207–214.

[26] Truilo, J. G., and Trigger, K. R., 1961, "Numerical Solution of the One-Dimensional Hydrodynamic Equations in an Arbitrary Time-Dependent Coordinate System," Univ. of California, Lawrence Radiation Lab. Report UCLR-6522.

[27] Thomas, P. D., and Lombard, C. K., 1978, "The Geometric Conservation Law—A Link Between Finite-Difference and Finite-Volume Methods of Flow Computation on Moving Grids," AIAA Paper No. 78-1208.

[28] Thomas, P. D., and Lombard, C. K., 1979, "Geometric Conservation Laws and its Application to Flow Computation on Moving Grids," AIAA J., 17, pp. 1030–1037.

[29] Zhang, H., Reggio, M., Trepanier, J. Y., and Camarero, R., 1993, "Descrete Form of the GCL for moving Meshes and its Implementation in CFD Schemes," Comput. Fluids, 22(1), pp. 9–23.

[30] Karimian, S. M. H., Amoli, A., and Mazaheri, K., 2002, "Control-Volume Finite-Element Method for the Solution of 2D Euler Equations on Unstructured Moving Grids," Iranian J. Sci. Technol., Trans. B, 26(B3), pp. 465–476.

[31] Roe, P. L., 1981, "Approximate Riemann Solvers, Parameter Vectors, and Difference Schemes," J. Comput. Phys., 43, pp. 357–372.

[32] Liou, M., and Steffen, C. J., 1993, "A New Flux Splitting Scheme," J. Comput. Phys., 107, pp. 23–39.

[33] Karimian, S. M. H., and Schneider, G. E., 1995, "Pressure-Based Control-Volume Finite-Element Method for Flow at All Speeds," AIAA J., 33(11), pp. 1611–1618.

[34] Compendium of Unsteady Aerodynamic Measurements, Report No. AGARD-R-702, 1982.

[35] Gaitonde, A. L., and Fiddes, S. P., 1995, "A Comparison of a Cell-Centre Method and a Cell-Vertex Method for the Solution of Two-dimensional Unsteady Euler Equations on a Moving Grid," Am. Antiq., 209, pp. 203–213.

Aspect Ratio Effects on Turbulent and Transitional Flow in Rectangular Microchannels as Measured With MicroPIV

Hao Li
Graduate Student

Michael G. Olsen[1]
Assistant Professor
e-mail: mgolsen@iastate.edu

Department of Mechanical Engineering,
Iowa State University,
3025 H.M. Black Engineering Building,
Ames, IA 50011

Microscopic particle image velocimetry (microPIV) was used to measure velocities in rectangular microchannels with aspect ratios ranging from 0.97 to 5.69 for $200 < \text{Re} < 3267$. Mean velocity profiles, velocity fluctuations, and Reynolds stresses were determined from the microPIV data. Transition to turbulence was observed at $\text{Re} = 1765 - 2315$ for the five aspect ratios studied, agreeing very well with both recent microscale experiments and macroscale duct flow and indicating no evidence of early transition for any of the aspect ratios studied. The onset of fully turbulent flow was observed at $\text{Re} = 2600 - 3200$. For the fully turbulent flow, the $\langle u' \rangle / u_{\max}$ and $\langle v' \rangle / u_{\max}$ fluctuations at the channel centerline were 6% and 3%–3.5% and generally agreed well with macroscale results. As aspect ratio increased, the $\langle u \rangle / u_{\max}$ and $\langle u' \rangle / u_{\max}$ profiles became flatter, with nearly uniform values extending for some distance from the centerline of the channel. This region of uniform $\langle u \rangle / u_{\max}$ and $\langle u' \rangle / u_{\max}$ became larger with increasing aspect ratio. The Reynolds shear stress for fully turbulent flow also displayed a strong dependence on aspect ratio. For the $W/H = 0.97$ microchannel, $\langle u'v' \rangle / u_{\max}^2$ steadily increased in value moving from the centerline to the wall, but for the higher aspect ratio microchannels, $\langle u'v' \rangle / u_{\max}^2$ remained close to zero in the center region of the microchannel before increasing in value at locations close to the wall, and this region of near zero $\langle u'v' \rangle / u_{\max}^2$ became larger with increasing aspect ratio. This behavior in the Reynolds shear stress is due to the region of uniform velocity and, hence, small mean shear, near the channel centerline of the high aspect ratio microchannels.
[DOI: 10.1115/1.2170122]

1 Introduction

The recent rapid development of microfluidic microelectromechanical systems (MEMS) and their importance in such applications as microscale cooling [1], drug delivery, biotechnical analyses, and telecommunication technologies [2,3] has resulted in a growing interest in understanding flow behavior in microchannels. In microscale cooling applications, microchannels with high aspect ratio are often used because their high surface-area-to-volume ratio makes them more efficient in high heat flux applications than microchannels with square or circular cross sections. However, this important microchannel flow geometry has not received nearly the attention that has been given to circular or square cross-sectional microchannels.

While the body of work on high aspect ratio microchannels is not as large as for square or circular microchannels, there do exist in the literature some interesting results from previous studies. For example, some studies of flow in high aspect ratio microchannels have reported early transition to turbulent flow compared to macroscale flow and found that the transitional Reynolds number in microchannels was dependent on the aspect ratio. Peng and Peterson [4,5] performed single-phase forced convective heat transfer and fluid flow experiments with water flowing through rectangular stainless steel microchannels with heights of 0.2 and 0.3 mm and widths ranging from 0.1 to 0.4 mm. Although the heat transfer experiments showed negligible effect of aspect ratio H/W due to

the small hydraulic radius comparable to the sublayer thickness, the laminar and turbulent flow conditions were still found dependent on the geometric parameters including hydraulic diameter D_h and aspect ratio H/W. Likewise, Mo et al. [6] investigated forced convection of low temperature (80–150 K) nitrogen gas flowing through rectangular channels with consistent width of 20 mm and hydraulic diameters ranging from 0.513 to 1.814 mm, corresponding to aspect ratios of 0.013 to 0.048. The laminar-turbulent transition of Nu showed dependence on channel depth, and an optimum channel aspect ratio for maximizing heat transfer was determined (such behavior was also mentioned in [4]). Pfund et al. [7] detected the turbulent transition by measuring the friction factor and performing flow visualization. The rectangular channels in their study had a constant width of 1 cm and varying mean depths of 521, 263, and 128 μm. Although the transitional Reynolds numbers were much larger than the values of 200–700 which were reported in previous works, they observed transition occurring at Reynolds numbers lower than the critical Reynolds number for macroscale ducts and found transitional Reynolds numbers decreasing with decreasing channel depth.

Although researchers have offered numerous explanations for early transition and deviation from macroscale correlations for friction factor and Nusselt number in microchannel flow (for example, the relatively high surface roughness [8–16], flow compressibility induced by surface friction [17], surface electrostatic charges, axial heat conduction in channel walls [11,12], etc.), these explanations fail to explain why other similar studies with the comparable measurement error and surface roughness have reported good agreement between experimental results and theoretical macroscale predictions and reported negligible aspect ratio effects. For example, Hegab et al. [18,19] examined the effects of

---

Reynolds number, relative roughness, and channel aspect ratio by determining f and Nu from measured temperatures, flow rates, and pressure drops for single-phase R134a flow in aluminum microchannels with hydraulic diameters ranging from approximately 112 to 210 μm and aspect ratios from 1.0 to 1.5. The experimental results indicated the onset of transition from laminar to turbulent flow occurring between Re=2000 and 4000. Wu and Cheng [20] measured the friction factor of deionized water flow in silicon microchannels of trapezoidal cross section with consistent depth and different widths. The experimental data was found to be in good agreement with existing analytical solution for an incompressible, fully developed, laminar flow under-no-slip boundary condition. Also, the transition from laminar to turbulent flow was observed at Re=1500–2000. Baviere et al. [21] experimentally studied friction coefficients as a function of Reynolds number by measuring pressure drop in microchannels with constant width of 25 mm and depths of 100, 200, and 300 μm. Data were collected for Re=0.01–8000. The results showed good agreement between the experimental data and macroscale flow predictions. The transitional Re was found around 2700–3100 for smooth channels, and generally in good agreement with that of macroscale flow.

It is important to note that the previously mentioned experiments were performed using traditional macroscale pressure drop and temperature measurements which can be quite challanging to apply to microscale flows. In these studies, the behavior of the measured friction factors and/or Nusselt numbers with Reynolds number was used as the criterion to determine the presence of laminar, transitional, or fully turbulent flow. The conflicting results of previous research reflects the potential drawbacks of traditional measurement techniques. Recently, researchers have attempted to clarify the sometimes contradictory results on microfluidic flow transition using a relatively new experimental technique—microscopic particle image velocimetry (microPIV) [22–27]. Since its development as a noninvasive measurement technique for microscale flow systems, microPIV has been widely used in researching many different microscale flows [28–31].

MicroPIV has also been used to study transition and turbulence in microchannel flows. Zeighami et al. [32] performed an experimental investigation on transition in a silicon microchannel with dimensions of 150 μm $\times$ 100 μm $\times$ 1 cm. The repeatability of the velocity data and the motion of seed particles perpendicular to the measurement plane were taken as the criteria to distinguish laminar and turbulent flow. Using these criteria, slightly early transition at Re=1200–1600 was suggested. However, in this study, the particle seed density was not sufficient for Reynolds stresses to be measured and or for turbulent structures to be observed. Lee et al. [33] studied flow up to Re=2900 in a rectangular microchannel with an aspect ratio 2.65 and a hydraulic diameter of 380 μm. In this work, the deviation of velocity profiles and a broadening of the microPIV cross-correlation signal peak with turbulence intensity were used to identify transition at Re=2900. Sharp and Adrian [34] performed a detailed set of pressure drop and microPIV experiments on transitional flow in round glass microtubes with diameters between 50 and 247 μm with working fluids of different polarities. In their microPIV experiments, the unsteady fluctuations of the centerline velocity were taken as indicators of the transition to turbulence. In the laminar region, centerline velocity fluctuations of around 1% (due to experimental noise) were observed. However, at higher Reynolds numbers, the centerline velocity fluctuations increased, and the first abrupt increase of the rms value of centerline velocity was taken as the onset of transitional flow. Using this definition, transition was observed between 1800<Re<2200, and thus Sharp and Adrian concluded that the anomalous early transition observed by previous researchers was not occurring. Li et al. [35,36] performed microPIV experiments to study the effect of hydraulic diameter changes in transitional and turbulent flow through square PDMS microchannels with hydraulic diameters ranging from 200 to 640 μm. They were the first researchers to report Reynolds stress data in microchannel

flows. Using the same definition of transition as Sharp and Adrian [34], they found the onset of transition between Re=1800 and 2000, in agreement with macroscale flow results.

In the present work microPIV has been used to obtain instantaneous velocity field data for flow through rectangular channels with approximately consistent hydraulic diameters of 320 μm and a range of aspect ratios from 0.97 to 5.69. The measured streamwise velocity profiles, streamwise and transversal velocity fluctuations, and Reynolds stresses are reported and used to determine both the onset of transition to turbulence and the characteristics of fully developed turbulent flow in microchannels of varying aspect rations. The results are also compared with classical results for macroscale ducts.

2 Microchannel Fabrication

The straight microchannels used in the present experiments were fabricated using PDMS replica molding [37,38]. A brief summary of the fabrication process follows (greater detail of the fabrication process can be found in Li et al. [35,36]. Figure 1 presents the fabrication procedure graphically. The channel molds were made from patterned negative photoresist (SU-8 2100, MicroChem Corp., Newton, MA) on a silicon wafer (100 mm diameter, Montco Silicon Technologies, Inc, Spring City, PA). A coating of the photoresist was spun on the silicon wafer to a uniform thickness, and select regions of the coated wafer were exposed through a transparency film to ultraviolet light. The photoresist was then developed resulting in a mold of the microchannel geometry in relief. Polydimethylsiloxane (PDMS) elastomer (Sylgard(R) 184 Silicon Elastomer Kit, Dow Corning, Midland, MI) was then cast on the molds and baked. Finally, the two halves of the microchannel are plasma treated and bonded to form the complete microchannel.

Microchannels were fabricated with five different aspect ratios and with hydraulic diameters of approximately 320 μm. The different widths were controlled by varying the design drawings of transparencies, and the different depths were controlled by adjusting the amount of photoresist deposited on the wafer, the spinning speed of spin coater, the baking time, and the exposure time to UV light. Accurate determination of dimensions was essential to obtain reliable data. The optical measurement of the dimensions at various positions along the microchannels, accurate to within ± 10 μm, indicated variations in hydraulic diameter over the entire length of the microchannel of between 1.25% to 5%. The final length-averaged dimensions of the five different microchannel geometries are listed in Table 1.

The resulting microchannels were then tested for inner surface roughness using Dektak IIA surface profile measuring system (Veeco Instruments Inc., Santa Barbara, CA). Liner surface profiles were taken of the cast PDMS. These measurements were limited, as the profilometer stylus could only be used on the top and bottom surfaces of the channel. The arithmetic average roughness of the microchannels was calculated by the Dektak IIA software and was determined to be approximately 24 nm. This results in a relative roughness of $\epsilon_s/D_h \approx 0.000074$.

Table 1 Geometric parameters of test microchannels

Channel name	W (μm)	H (μm)	D_h (μm)	Aspect ratio (W/H)
AR1	320	330	325	0.97
AR2	480	230	311	2.09
AR3	640	210	316	3.05
AR4	800	200	320	4.00
AR5	1080	190	323	5.69
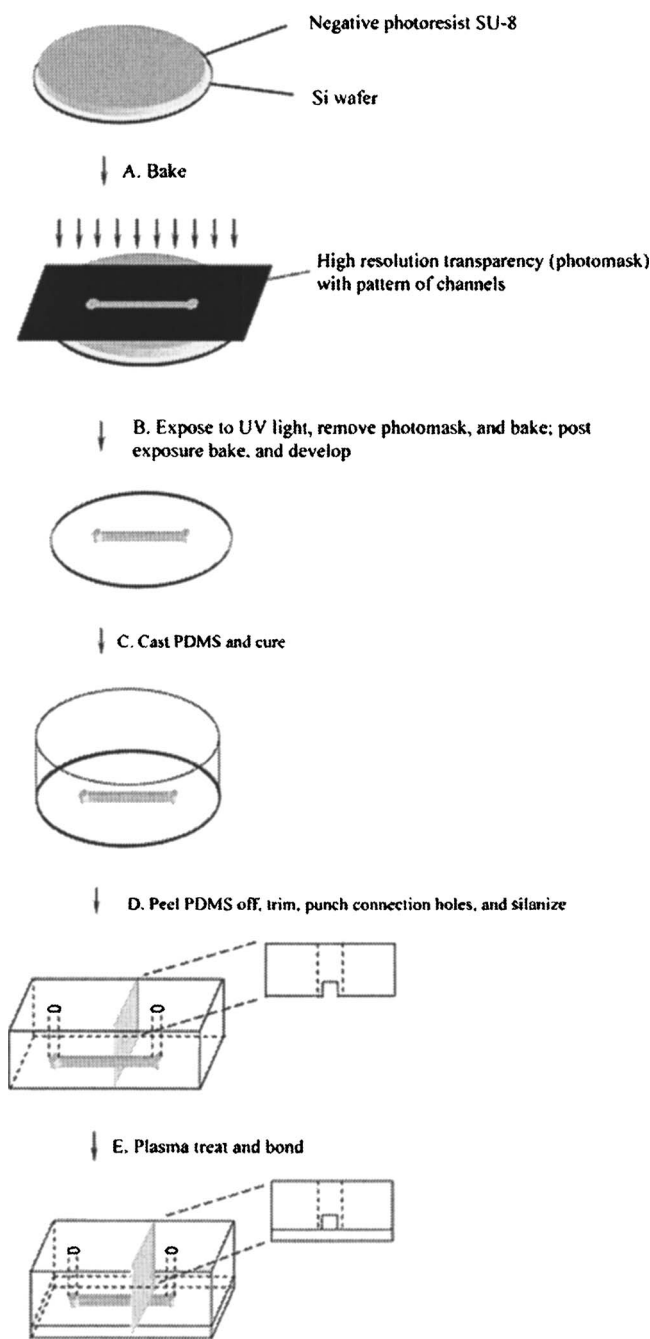
Fig. 1 Summary of the microchannel fabrication technique

Fig. 2 Schematic of experimental setup

3 Experimental Methodology

3.1 Experimental Setup. The experimental system, schematically shown in Fig. 2, consists of two subsystems: (i) the flow delivery system and (ii) the microPIV system. The flow was driven by a micro gear pump and pump head (115 VAC console digital dispensing drive and 0.084 ml/rev suction shoe gear pump head, Cole-Parmer Instrument Co., Vernon Hills, IL) that provides constant flow rates with accuracy of ±0.3%. The working fluid was deionized water. Flow from the gear pump passes through the microchannel, then through a digital flowmeter (0–100 mL/min volumetric water flow meter, Cole-Parmer Instrument Co., Vernon Hills, IL), and finally through a fluid reservoir before returning to the gear pump to begin a second cycle. The flowmeter contained a thermocouple so fluid temperature could be carefully monitored during each run. The purpose of the fluid reservoir was to increase

the thermal mass of the fluid in the system, so that viscous dissipation did not result in any temperature change of the working fluid during the experimental runs.

The microPIV system is shown in the lower portion of Fig. 2. A double pulsed Nd:YAG laser (Continuum, Santa Clara, CA), attenuated to 3 mJ/pulse with a wavelength of 532 nm, was expanded and directed into an aperture in the rear of an inverted biological microscope (Nikon model T-300 Inverted Microscope). The 820 nm diameter fluorescent seed particles (Duke Scientific Co., Palo Alto, CA) were excited by the laser light and emitted light at a peak emission wavelength of 612 nm. The excited light, filtered by a beamsplitter to remove illuminating and background light, was then imaged through the microscope using an objective lens with a magnification of 20× and a numerical aperture of 0.45. A LaVision Flowmaster 3 camera (Lavision Inc., Ypsilanti, MI) was used to capture the PIV image pairs for cross-correlation analysis.

The concentration of the fluorescent particle solution was prepared such that a sufficient number of seed particles fell within the depth of correlation [25,39] of each interrogation region such that erroneous vector measurements were minimized. In the present experiments, the 20×0.45 NA microscope objective yields a depth of correlation of 8.3 μm. Using interrogation windows measuring 28 μm square and overlapping each interrogation region by 50% yielded a vector spacing of 14 μm. Achieving this spatial resolution required a volumetric particle concentration of approximately 0.057%. This volume fraction of seed particles was small enough that any two-phase effects are negligible, and the working fluid could be considered a single-phase fluid.

The experiments were performed at various flow rates corresponding to Reynolds numbers ranging from 200 to 3257. For each set of experiments, sufficient time was allowed to pass after starting the micro gear pump to allow the flow to reach steady state. For smaller flow rates, it took a longer time to reach a steady state compared to higher flow rates. A multi-pass interrogation scheme with decreasingly smaller window sizes was used in the computation of the vector fields to reach the final 32×32 pixel interrogation windows. The only postprocessing performed on the vector fields was the removal of bad vectors. No smoothing of vector fields was performed. The number of velocity fields collected for each Reynolds number ranged from 600 for the lowest, laminar Reynolds numbers to 2000 for the transitional and turbulent Reynolds numbers.

3.2 Measurement Error. There are two sources of measurement errors in the microPIV experiments: errors introduced by

random motion of the seed particles due to Brownian motion, and errors implicit in the interrogation of the PIV images. The significance of Brownian motion in the microPIV measurements can be determined by calculating the Brownian motion parameter [26], defined as

$$\frac{d_e^2}{d_e^2 + 8M^2\beta^2 D\Delta t} \tag{1}$$

where $D = KT/(6\pi\mu d_p)$, β^2 is a constant equal to 3.67, and d_e is the image diameter for a particle in the object plane [40].

$$d_e = \sqrt{M^2 d_p^2 + d_s^2} \tag{2}$$

where $d_s = 2.44(M+1)\lambda f^{\#}$ is the diameter of the diffraction-limited point spread function in the image plane, M is the magnification of the microscopic objective, d_p is the particle diameter, λ is emitted light wavelength from particles, and $f^{\#}$ is focal number of objective.

For values of the Brownian motion parameter close to unity, Brownian motion has a negligible effect on the measured velocity. For the AR5 microchannel at Re=525, the Brownian motion coefficient is equal to 0.9998, indicating that Brownian motion effects are indeed negligible. For the smaller microchannels, or at higher Reynolds numbers in the AR5 microchannel, the Brownian motion effect is even smaller, due to the smaller Δt required for these measurements. Note that the fact that Brownian motion is negligible should not surprising, given the short Δt required for each of the measurements (on the order of 1 μs).

The experimental error due to interrogation of the PIV images can be estimated by assuming that measured particle displacements are accurate to within approximately $\frac{1}{10}$ of a seed particle image diameter [41]. From Eq. (2), $d_e = 38$ μm, yielding an effective particle diameter when projecting back into flow coordinates of 1.9 μm, meaning that the measured particle displacement in the microPIV experiments should be accurate to within 0.19 μm. For the present experiments, the particles travel approximately 8 μm between laser pulses, resulting in an experimental uncertainty of approximately 2.3%.

The relative unimportance of the error due to Brownian motion can also be demonstrated by comparing the particle displacement due to particle diffusion with the uncertainty in determining particle displacement. The distance that a particle is expected to diffuse due to Brownian motion can be found using

$$s = \sqrt{2D\Delta t} \tag{3}$$

For Re=3000 in the AR1 microchannel, the rms particle displacement due to Brownian motion is 0.001 μm, which is only 0.5% of the experimental error. Thus, the effects of Brownian motion can be safely neglected.

The microPIV images were obtained at locations far enough downstream of the microchannel entrance to ensure fully developed flow and avoid any entrance length effects [33]. This was verified by taking measurements at different downstream locations and comparing the mean velocity profiles. In all cases, velocity fields were measured along the microchannel midplane, which was located by finding the maximum velocity peaks in laminar flow.

4 Results and Discussion

The ensemble-averaged streamwise velocity profiles in the different aspect ratio microchannels for various Reynolds numbers are presented in Fig. 3 together with the corresponding fully developed laminar analytical solutions for flow in a rectangular duct [42]. The transverse coordinate has been normalized by $\frac{1}{2}$ of the width of the microchannel, with 0 corresponding to the microchannel centerline and 1 corresponding to the microchannel wall. For the AR1 microchannel ($W/H = 0.97$), the comparison shows good agreement between the measured velocity and the laminar

solution until Re=1535. Deviation from the laminar profile becomes apparent at Re=1885, where the experimental data become flatter than the parabolic laminar solution, with a lower peak value at the centerline and higher velocities close the wall. The measurements were repeated for the AR2, AR3, AR4, and AR5 microchannels ($W/H = 2.09$, 3.05, 4.00 and 5.69, respectively), and these data are shown in Figs. 3(b)–3(e), respectively. For these aspect ratios, the Reynolds numbers at which deviation from the laminar solution is observed range from 1373 to 1837. While some of these results may suggest the onset of early transition, this is not necessarily true, since deviations in the measured mean velocity profile from the analytical laminar solution have been found to occur in both macroscale [43] and microscale [34] channel and duct flows before any other evidence of transition (such as increases in rms velocity fluctuations) is observed. As the Reynolds number is further increased, the measured velocity near the channel centerline deviates further from the laminar prediction and becomes smaller, while the velocity near the channel walls becomes greater, and the measured velocity profiles begin to resemble those of fully turbulent flow.

The changing shape of the mean velocity profiles with increasing Reynolds number is more distinctive in Fig. 4, where the mean velocity profiles are normalized by the centerline velocity. Figure 4 also shows the significant variation of velocity profiles from laminar flow to fully turbulent flow. At low Reynolds number, the velocity profiles are grouped together near the analytical laminar solution. As the Reynolds number increases, the velocity profiles begin to deviate from the laminar solution, and the center region where a uniform velocity exists grows wider. At the highest Reynolds numbers studied, the velocity profiles become grouped again, suggesting that the microchannel flow is reaching a fully turbulent state. It was not possible to achieve the same maximum Reynolds number for all of the geometries investigated due to constraints of the fabrication process. For example, in the AR5 microchannel experiments, efforts were made to reach Reynolds numbers above 2352, however, at higher Reynolds numbers this microchannel catastrophically failed due to the high pressure resulting from the small aspect ratio of this configuration.

In order to quantify and characterize the turbulence in the microchannels, velocity fluctuations and Reynolds shear stresses were calculated from the microPIV data. Figures 5–7 show the dimensionless profiles of $\langle u'\rangle/u_{\max}$, $\langle v'\rangle/u_{\max}$, and $\langle u'v'\rangle/u_{\max}^2$, respectively, for each of the different aspect ratio microchannels as a function of Reynolds number. For all the microchannels, the measured centerline values of $\langle u'\rangle/u_{\max}$ exhibit a band of overlapped fluctuation values around 1.5% at Reynolds numbers lower than Re=1500, as shown in Fig. 5. The measured fluctuations at these low Reynolds numbers are not evidence of turbulence, but are instead due to the measurement uncertainty in the microPIV experiments.

In their microPIV experiments in microtubes, Sharp and Adrian [34] defined transition to turbulence based on a significant increase in the measured centerline streamwise velocity fluctuations. Using this definition for transition in the present experiments, jumps in the streamwise velocity fluctuations are observed at Re =1885, 2315, 1765, 1867, and 1837 for the AR1, AR2, AR3, AR4, and AR5 microchannels, respectively. These measured transitional Reynolds numbers of 1765–2315 for rectangular microchannels agree very well with the transitional Reynolds numbers of 1800–2000 that Sharp and Adrian reported for round microtubes. Since transition in macroscale pipe and duct flows typically occurs at Re=1800–2300, no evidence of early transition was observed in the present study, just as Sharp and Adrian observed no evidence of early transition in their round microtube experiments. Nearly identical transitional Reynolds numbers are obtained if transition is instead defined by a jump in the centerline transverse velocity fluctuations. Using this definition, transition is observed at Re =1885, 2315, 1765, 1867, and 1837 for the AR1, AR2, AR3, AR4, and AR5 microchannels.
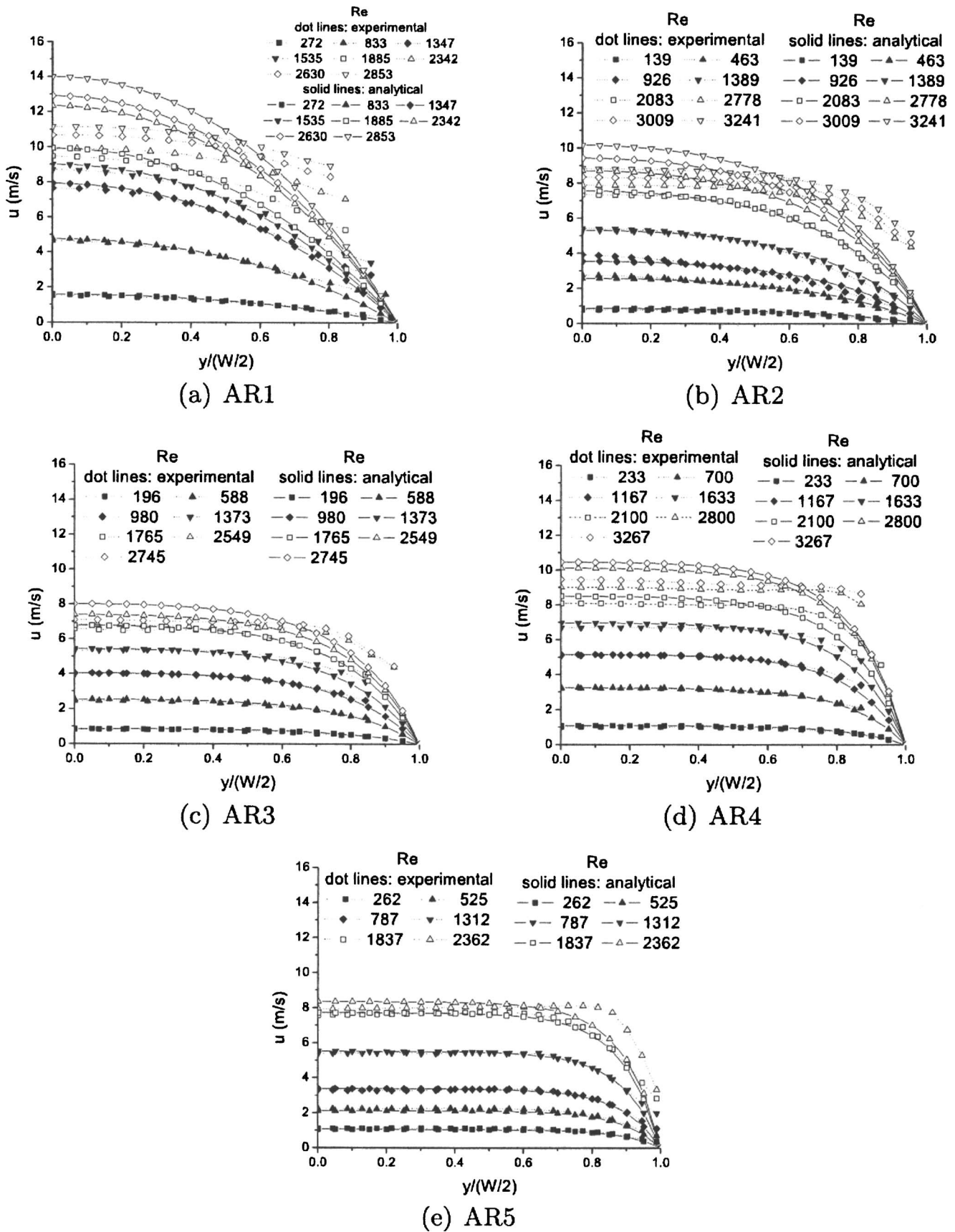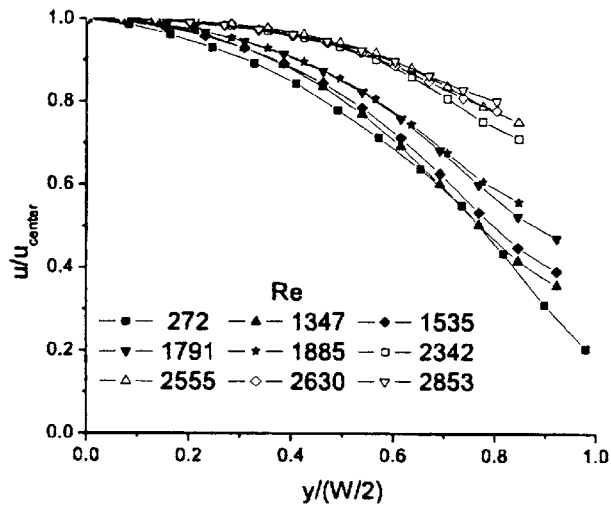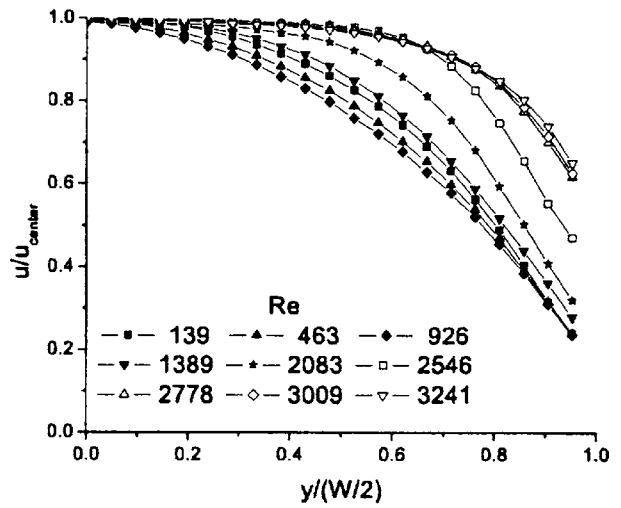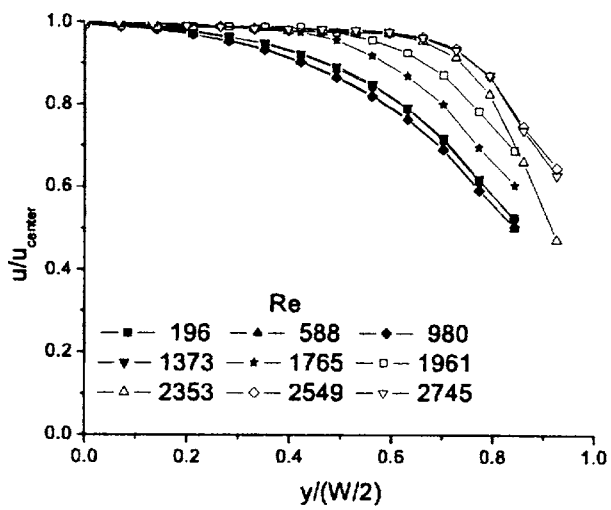
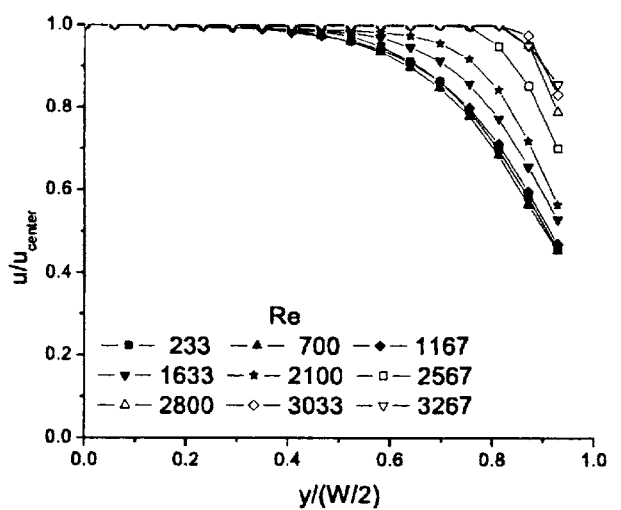Fig. 3   Mean streamwise velocity profiles for five different aspect ratios as measured by microPIV
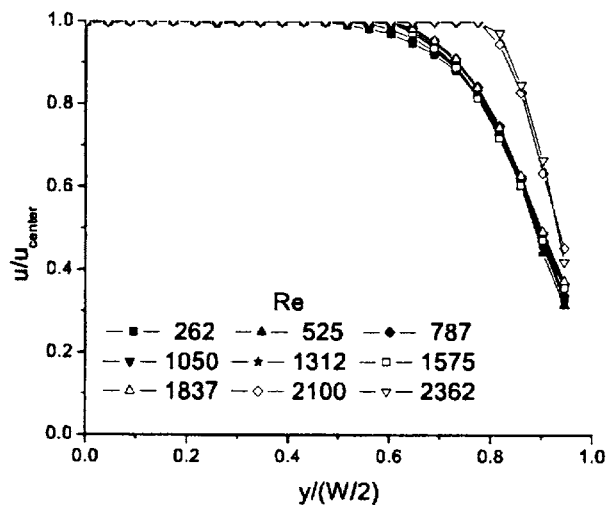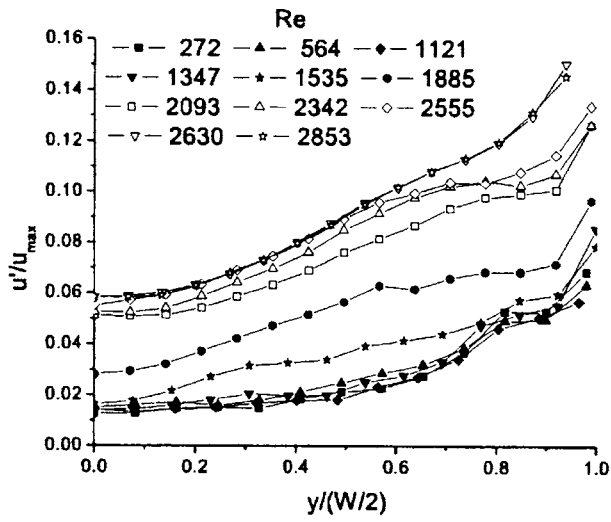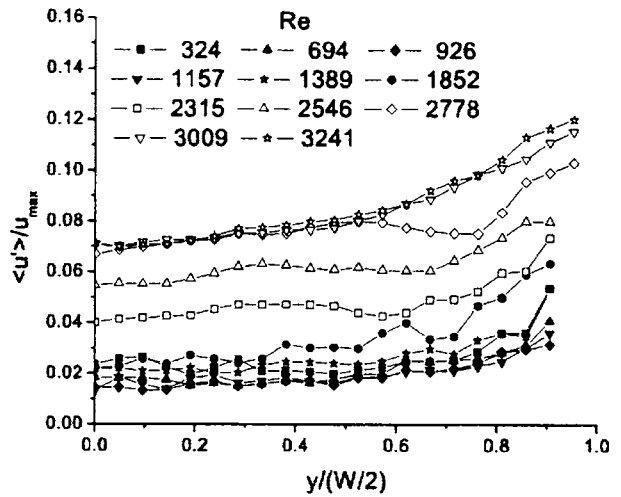
(a) AR1

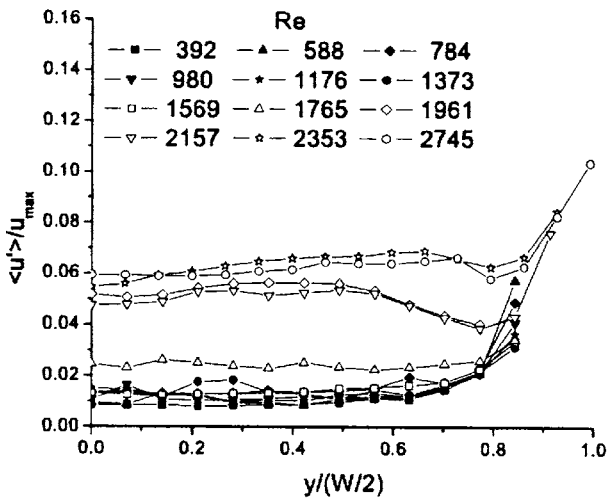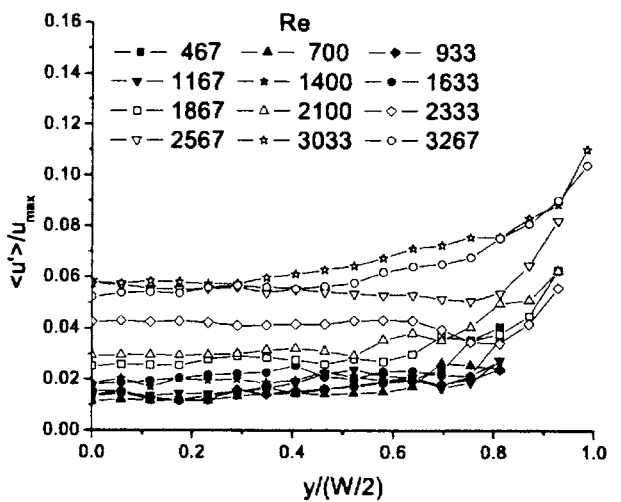(b) AR2

(c) AR3

(d) AR4

(e) AR5

Fig. 4 Normalized streamwise velocity profiles for five different aspect ratios as measured by microPIV
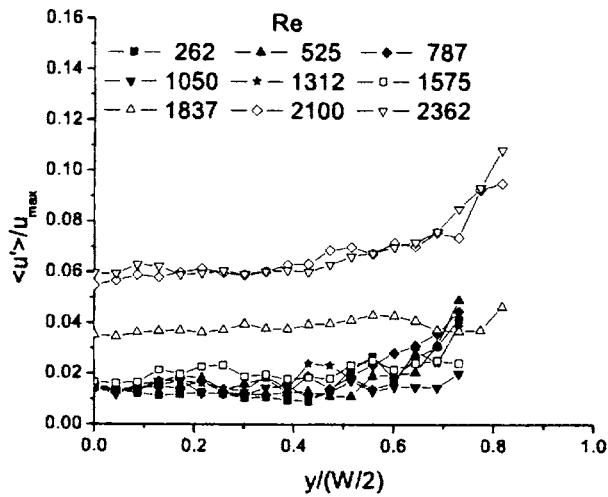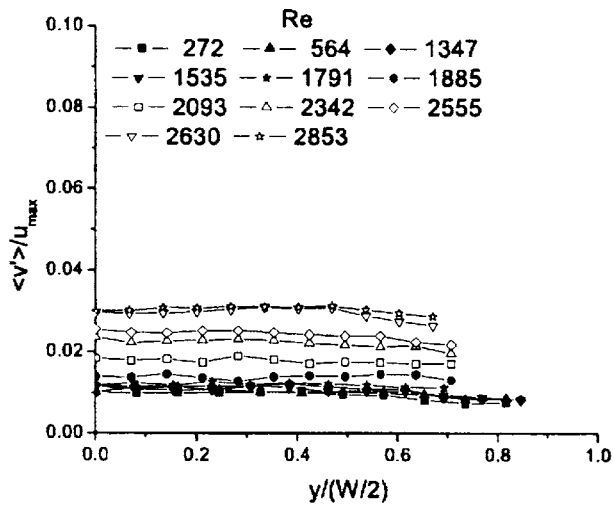
(a) AR1

(b) AR2
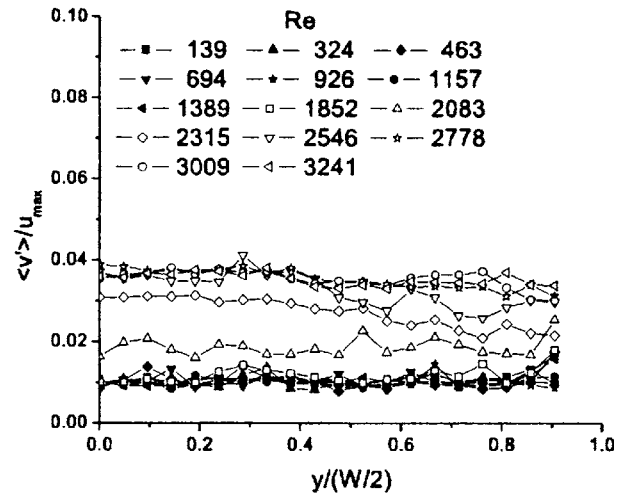

(c) AR3

(d) AR4
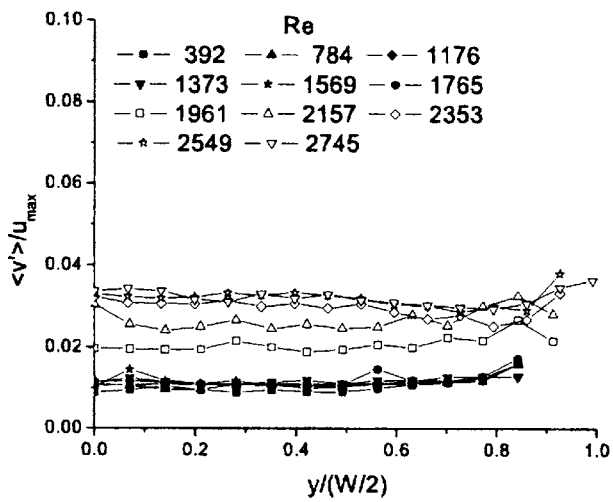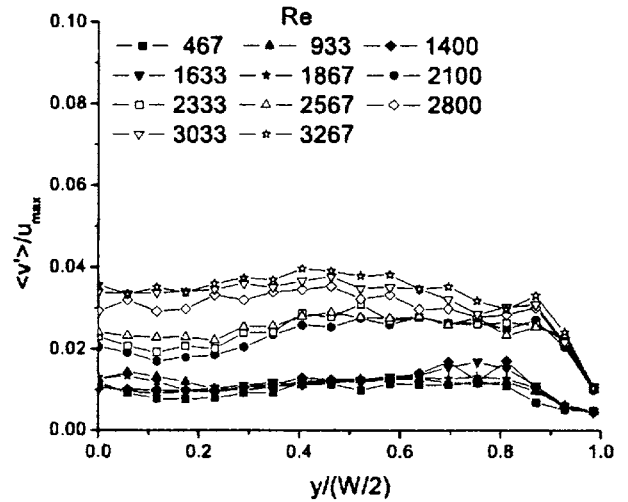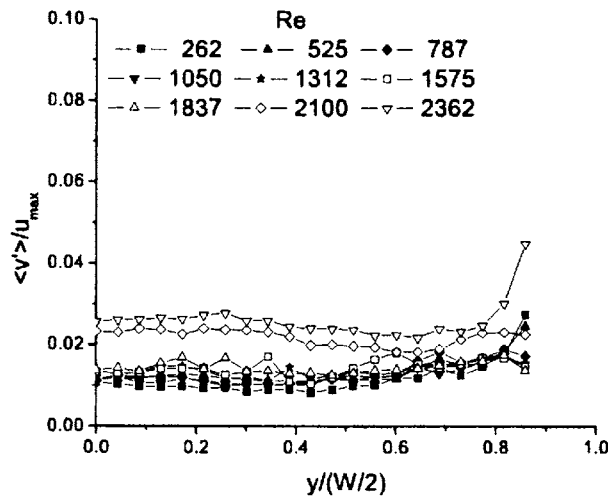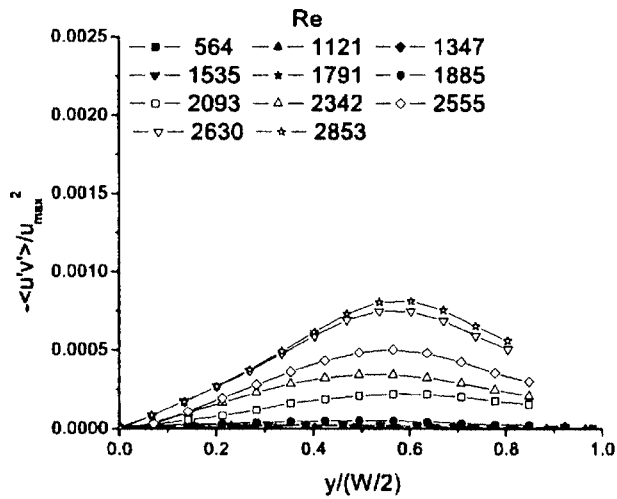

(e) AR5

Fig. 5   Streamwise velocity fluctuation profiles for five different aspect ratios as measured by microPIV

Fig. 6 Transverse velocity fluctuation profiles for five different aspect ratios as measured by microPIV
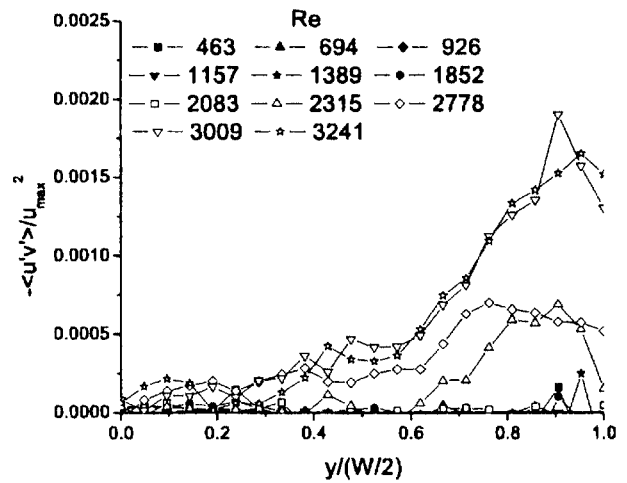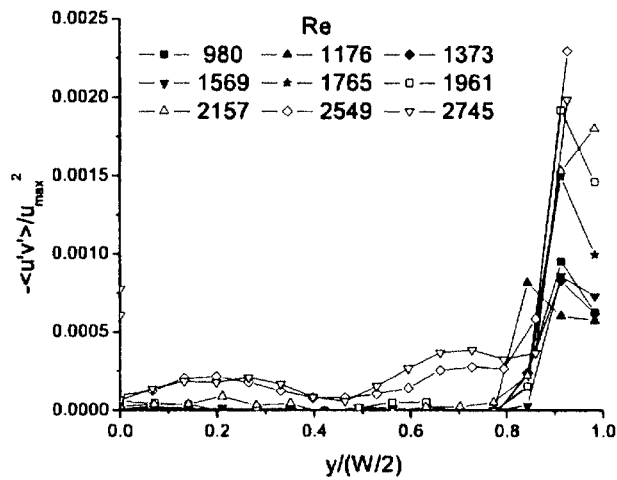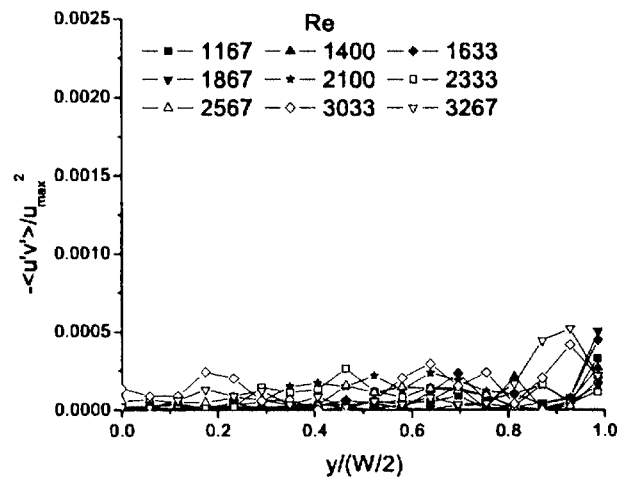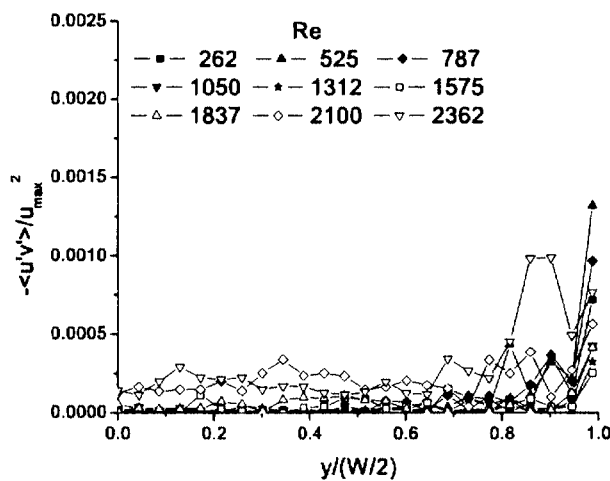
Fig. 7 Reynolds shear stress profiles for five different aspect ratios as measured by microPIV

As the Reynolds number is increased above transition, increases in both the streamwise and transverse velocity fluctuations are observed. Eventually, the fluctuations will no longer appear to increase with increasing Reynolds number, and this behavior, along with the mean velocity profiles approaching that of fully turbulent flow (Fig. 4), is indicative of a fully turbulent state being reached (note that even in fully turbulent duct flow, the mean velocity and velocity fluctuation profiles will continue to show a

weak dependence on Reynolds number, but over the small range of Reynolds numbers investigated in the present study, the fully turbulent results should appear to overlap). Both the $\langle u' \rangle / u_{max}$ and $\langle v' \rangle / u_{max}$ velocity fluctuations consistently overlap for the AR1, AR2, AR3, AR4, and AR5 microchannels at Reynolds numbers somewhere in the range $2400 < \mathrm{Re} < 2700$. Coupling these results with the mean velocity profiles shown in Fig. 4 suggests fully turbulent flow being reached in the approximate range of $2600 < \mathrm{Re} < 3000$.

The measured fully turbulent values for $\langle u' \rangle / u_{max}$ presented in Fig. 5 are slightly higher than classical macroscale results for turbulent square duct flow [44] and high aspect ratio duct flow [45], although the difference is well within the measurement uncertainty of the present experiments. In general, the values for all cases are remarkably consistent, with measured fluctuations of around 6% at the centerline of the microchannel and higher values occurring moving from the centerline to the wall. Note that some of the increase in measured velocity fluctuations close to the walls of the microchannel may be due to an increase in measurement uncertainty near the walls. The measurement uncertainty is higher near the walls because of smaller particle displacements between PIV images due to lower velocities near the walls. For example, if a near-wall location has a velocity that is half of the centerline velocity, the measurement uncertainty is then doubled at the near-wall location.

The measured fully turbulent values of $\langle v' \rangle / u_{max}$ shown in Fig. 6 are also consistent for the various microchannel geometries investigated. For each of the aspect ratios studied, $\langle v' \rangle / u_{max}$ at the centerline is between 3% and 3.5% and shows little variation with transverse location. As with the $\langle u' \rangle / u_{max}$ results, the measured $\langle v' \rangle / u_{max}$ fluctuations for Reynolds numbers in the laminar regime are due to measurement uncertainty and not the presence of turbulent structures.

The effect of aspect ratio on the turbulence characteristics can be observed in Figs. 3–6 by comparing the fully turbulent values of mean velocity and velocity fluctuations for microchannels with different aspect ratios. A close look at the streamwise velocity profiles in Figs. 3(a)–3(e) reveals that as aspect ratio increases, the center region of fully turbulent velocity profiles becomes flatter with a wider uniform distribution of streamwise velocity at the center region. This can be attributed to the diminishing effect that the two side walls in the transverse direction have on the flow relative to the top and bottom walls of the microchannel with increasing aspect ratio. Increasing the aspect ratio to the limiting case of $W/H \rightarrow \infty$, the effect of the side walls would become infinitesimally small, and the flow would approach two-dimensional flow between two infinite parallel plates, in which case the streamwise velocity would be uniform in the transverse direction. The variation of the distribution of fully turbulent velocity fluctuations $\langle u' \rangle / u_{max}$ and $\langle v' \rangle / u_{max}$ in Figs. 5 and 6 also displays a similar aspect ratio effect. The velocity fluctuations become uniform across nearly 80% of the microchannel width as aspect ratio increases and only show variations from the centerline fluctuations close to the side walls. This is because as the aspect ratio increases, the shear stresses induced by the two side walls becomes much smaller than the stresses induced by the top and bottom walls.

The aspect ratio effect is even more pronounced in the data for Reynolds shear stress, $\langle u'v' \rangle / u_{max}^2$, presented in Fig. 7 for the five microchannel geometries studied. In the laminar flow regime, $\langle u'v' \rangle / u_{max}^2$ is very close to zero, as expected, since any Reynolds stress measured for laminar flow is purely an artifact of the measurement uncertainty. As the flow transitions to turbulence, $\langle u'v' \rangle / u_{max}^2$ increases and eventually reaches the fully turbulent value. For the AR1 microchannel, the fully turbulent $\langle u'v' \rangle / u_{max}^2$ is zero at the centerline of the channel (as it must be due to flow symmetry) and steadily increases in value, moving from the cen-

terline to the wall (the shear stress must be zero at the wall due to the no slip condition, but the measurements do not extend close enough to the wall to see this behavior). For the higher aspect ratio microchannels, the Reynolds shear stress is also zero along the centerline of the microchannel, but instead of steadily increasing as one moves towards the wall, $\langle u'v' \rangle / u_{max}^2$ remains close to zero over some distance in the center region of the microchannel before increasing in value at locations close to the wall. This region of near-zero Reynolds shear stress becomes larger with increasing aspect ratio. This behavior in the Reynolds shear stress is due to the region of uniform velocity near the channel centerline in the low aspect ratio microchannels. From Prandtl's mixing length theory, turbulent shear stress is dependent on gradients in the mean velocity field. In regions of nearly uniform mean velocity, the velocity gradients are small and thus the turbulent stresses are close to zero. Since the region of uniform mean velocity near the channel centerline grows with increasing aspect ratio, the region of near zero $\langle u'v' \rangle / u_{max}^2$ also grows. Closer to the walls of the channels, the velocity gradient is strong, thus accounting for the increase in Reynolds shear stress observed in Fig. 7 near the walls.

5 Summary and Conclusions

Microscopic particle image velocimetry was used to measure instantaneous velocity fields in rectangular microchannels with aspect ratios ranging from 0.97 to 5.69 for Reynolds numbers from 200 to 3267. Mean velocity profiles, velocity fluctuations, and Reynolds stresses were determined from the microPIV data. With transition to turbulence defined by an increase in the measured centerline velocity fluctuations, transition was observed at Reynolds numbers ranging from 1765 to 2315 for the five aspect ratios studied. These data agree very well with the recent experiments of Sharp and Adrian [34] in round microtubes and Li and Olsen [35] in square microchannels in which transition was observed for Re between 1800 and 2000. The results are also in agreement with transitional Reynolds numbers for macroscale duct flow, and thus no evidence of early transition was observed for any of the aspect ratios studied. Fully turbulent flow was achieved in all of the microchannels studied except the AR5 microchannel ($W/H = 5.69$), which structurally failed before fully turbulent flow could be achieved. In the other four aspect ratios studied, the onset of fully turbulent flow was observed for Reynolds numbers ranging from 2600 to 3200.

For the fully turbulent flow, the measured $\langle u' \rangle / u_{max}$ and $\langle v' \rangle / u_{max}$ fluctuations at the channel centerline were consistently around 6% and 3–3.5% and generally agreed well with classical macroscale results for turbulent square duct flow [44] and high aspect ratio duct flow [45]. As aspect ratio increased, the measured mean streamwise velocity and streamwise velocity fluctuation profiles became flatter, with nearly uniform values extending for some distance from the centerline of the channel. This region of uniform $\langle u \rangle / u_{max}$ and $\langle u' \rangle / u_{max}$ became larger with increasing aspect ratio.

The Reynolds shear stress for fully turbulent flow also displayed a strong dependence on aspect ratio. In all cases studied, $\langle u'v' \rangle / u_{max}^2$ was zero at the channel centerline, as required by symmetry. For the AR1 microchannel ($W/H = 0.97$) $\langle u'v' \rangle / u_{max}^2$ steadily increased in value moving from the centerline to the wall, but for the higher aspect ratio microchannels, $\langle u'v' \rangle / u_{max}^2$ remained close to zero over some distance in the center region of the microchannel before increasing in value at locations close to the wall, and this region of near zero $\langle u'v' \rangle / u_{max}^2$ became larger with increasing aspect ratio. This behavior in the Reynolds shear stress is due to the region of uniform velocity, and, hence, small mean shear, near the channel centerline of the high aspect ratio microchannels.

Acknowledgment

Nomenclature

Letters

d_e = the image diameter of particle, μm
D = the diffusivity of the seed particles, m^2/s
D_h = the hydraulic diameter of microchannels, μm
d_p = particle diameter, μm
d_s = the diameter of the diffraction-limited point spread function, μm
$f^{\#}$ = focal number
k = Boltzman's constant, 1.3807×10^{-23}, J/K
M = magnification
NA = numerical aperture
Re = Reynolds number
T = temperature, K
u = longitudinal velocity in microchannel, m/s
u' = fluctuation of instantaneous velocity u, m/s
v' = fluctuation of instantaneous transverse velocity, m/s
H = the depth of microchannels, μm
W = width of the microchannel, μm
Δt = time period between two laser pulses, μm
λ = light wavelength, nm
μ = absolute viscosity, kg/(m s)

Symbols

$\langle \; \rangle$ = ensemble averaged value

Subscripts

center = center line value
max = maximum value

References

[1] Tuckerman, D. B., and Pease, R. F., 1981, "High-Performance Heat Sinking for VLSI," IEEE Electron Device Lett., **2**, pp. 126–129.
[2] Henning, A. K., 1998, "Microfluidic MEMS," in *IEEE Aerospace Conference*, p. 4.906, Snowmass, CO, March.
[3] Lipman, J., 1999, "Microfluidics Puts Big Labs on Small Chips," EDN Mag., pp. 79–86, December.
[4] Peng, X. F., and Peterson, G. P., 1996, "Convective Heat Transfer and Fluid Flow Friction for Water Flow in Microchannel Structures," Int. J. Heat Mass Transfer, **39**, pp. 2599–2608.
[5] Peng, X. F., and Peterson, G. P., 1996, "Forced Convection Heat Transfer of Single-Phase Binary Mixtures Through Microchannels," Exp. Therm. Fluid Sci., **12**, pp. 98–104.
[6] Mo, H. L., Zhou, Y. X., Zhu, T. Y., and Guo, T. W., 2004, "Forced Convection of Low Temperature Nitrogen Gas in Rectangular Channels With Small Aspect Ratio," Cryogenics, **44**, pp. 301–307.
[7] Pfund, D., Rector, D., Shekarriz, A., Popescu, A., and Welty, J., 2000, "Pressure Drop Measurements in a Microchannel," Fluid Mech. Transp. Phenom., **46**(8), pp. 1496–1507.
[8] Wu, P. Y., and Little, W. A., 1983, "Measurement of Friction Factor for Flow of Gases in Very Fine Channels Used for Micro-Miniature Joule-Thompson Refrigerators," Cryogenics, **23**, pp. 273–277.
[9] Wu, P. Y., and Little, W. A., 1984, "Measurement of the Heat Transfer Characteristics of Gas Flow in Fine Channel Heat Exchangers Used for Microminiature Refrigerators," Cryogenics, **24**, pp. 415–420.
[10] Qu, W., Mala, G. M., and Li, D., 2000, "Pressure-Driven Water Flows in Trapezoidal Silicon Microchannels," Int. J. Heat Mass Transfer, **43**, pp. 353–364.
[11] Guo, Z. Y., and Li, Z. X., 2003, "Size Effect on Microscale Single-Phase Flow and Heat Transfer," Int. J. Heat Mass Transfer, **46**, pp. 149–159.
[12] Guo, Z. Y., and Li, Z. X., 2003, "Size Effect on Single-Phase Channel Flow and Heat Transfer at Microscale," Int. J. Heat Fluid Flow, **24**, pp. 284–298.
[13] Sabry, M. N., 2000, "Scale Effects on Fluid Flow and Heat Transfer in Microchannels," IEEE Trans. Compon. Packag. Technol., **23**(3), pp. 562–567.
[14] Toh, K. C., Chen, X. Y., and Chai, J. C., 2002, "Numerical Computation of Fluid Flow and Heat Transfer in Microchannels," Int. J. Heat Mass Transfer, **45**, pp. 5133–5141.
[15] Tunc, G., and Bayazitoglu, Y., 2002, "Heat Transfer in Rectangular Microchannels," Int. J. Heat Mass Transfer, **45**, pp. 765–773.
[16] Koo, J., and Kleinstreuer, C., 2003, "Liquid Flow in Microchannels: Experimental Observations and Computational Analyses of Microfluidics Effects," J. Micromech. Microeng., **13**, pp. 568–579.
[17] Chen, C. S., and Kuo, W. J., 2004, "Numerical Study of Compressible Turbulent Flow in Microtubes," Numer. Heat Transfer, Part A, **45**, pp. 85–99.
[18] Hegab, H. E., Bari, A., and Ameel, T., 2002, "Friction and Convection Studies of R-134a in Microchannels Within the Transition and Turbulent Flow Regimes," Exp. Heat Transfer, **15**, pp. 245–259.
[19] Hegab, H. E., Bari, A., and Ameel, T. A., 2001, "Experimental Investigation of Flow and Heat Transfer Characteristics of R-134a in Microchannels," Proc. SPIE, **4560**, pp. 117–125.
[20] Wu, H. Y., and Cheng, P., 2003, "Friction Factors in Smooth Trapezoidal Silicon Microchannels With Different Aspect Ratios," Int. J. Heat Mass Transfer, **46**, pp. 2519–2525.
[21] Baviere, R., Ayela, F., Le Person, S., and Favre-Marinet, M., 2004, "An Experimental Study of Water Flow in Smooth and Rough Rectangular Microchannels," in *Second International Conference on Microchannels and Minichannels (ICMM2004)*, Rochester, New York, June, pp. 221–228.
[22] Santiago, J. G., Wereley, S. T., Meinhart, C. D., Beebe, D. J., and Adrian, R. J., 1998, "A Particle Image Velocimetry System for Microfluidics," Exp. Fluids, **25**, pp. 316–319.
[23] Meinhart, C. D., Wereley, S. T., and Santiago, J. G., 1999, "PIV Measurements of a Microchannel Flow," Exp. Fluids, **27**, pp. 414–419.
[24] Meinhart, C. D., Wereley, S. T., and Gray, M. H. B., 2000, "Volume Illumination for Two-Dimensional Particle Image Velocimetry," Meas. Sci. Technol., **11**(6), pp. 809–814.
[25] Olsen, M. G., and Adrian, R. J., 2000, "Out-of-Focus Effects on Particle Image Visibility and Correlation in Microscopic Particle Image Velocimetry," Exp. Fluids, **29**, pp. S166–S174.
[26] Olsen, M. G., and Adrian, R. J., 2000, "Brownian Motion and Correlation in Particle Image Velocimetry," Opt. Laser Technol., **32**, pp. 621–627.
[27] Devasenathipathy, S., Santiago, J. G., Wereley, S. T., Meinhart, C. D., and Takehara, K., 2003, "Particle Imaging Techniques for Microfabricated Fluidic Systems," Exp. Fluids, **34**, pp. 504–514.
[28] Stone, S. W., Meinhart, C. D., and Wereley, S. T., 2002, "A Microfluidic-Based Nanoscope," Exp. Fluids, **33**, pp. 613–619.
[29] Klank, H., Goranovic, G., Kutter, J. P., Gjelstrup, H., Michelsen, J., and Westergaard, C. H., 2002, "PIV Measurements in a Microfluidic 3d-Sheathing Structure With Three-Dimensional Flow Behaviour," J. Micromech. Microeng., **12**, pp. 862–869.
[30] Kim, M. J., Beskok, A., and Kihm, K. D., 2002, "Electro-Osmosis-Driven Microchannel Flows: A Comparative Study of Microscopic Particle Image Velocimetry Measurements and Numerical Simulations," Exp. Fluids, **33**, pp. 170–180.
[31] Son, S. Y., Kihm, K. D., and Han, J. C., 2002, "PIV Flow Measurements for Heat Transfer Characterization in Two-Pass Square Channels With Smooth and 90° Ribbed Walls," Int. J. Heat Mass Transfer, **45**, pp. 4809–4822.
[32] Zeighami, R., Laser, D., Zhou, P., Asheghi, M., Devasenathipathy, S., Kenny, T., Santiago, J., and Goodson, K., 2000, "Experimental Investigation of Flow Transition in Microchannels Using Micron-Resolution Particle Image Velocimetry," in *Thermomechanical Phenomena in Electronic Systems Proceedings of the Intersociety Conference*, Vol. 2, pp. 148–153.
[33] Lee, S. Y., Wereley, S. T., Gui, L., Qu, W., and Mudawar, I., 2002, "Microchannel Flow Measurement Using Micro Particle Image Velocimetry," in *American Society of Mechanical Engineers, Fluids Engineering Division (Publication) FED*, Vol. 258, pp. 493–500.
[34] Sharp, K. V., and Adrian, R. J., 2004, "Transition From Laminar to Turbulent Flow in Liquid Filled Microtubes," Exp. Fluids, **36**, pp. 741–747.
[35] Li, H., Ewoldt, R., and Olsen, M. G., 2005, "Turbulent and Transitional Velocity Measurements in a Rectangular Microchannel Using Microscopic Particle Image Velocimetry," Exp. Therm. Fluid Sci., **29**, pp. 435–446.
[36] Li, H., and Olsen, M., 2006, "MicroPIV Measurements of Turbulent Flow in Square Microchannels With Hydraulic Diameters From 200 μm to 640 μm," Int. J. Heat Fluid Flow, **27**, pp. 123–134.
[37] Anderson, J. R., Chiu, D. T., Jackman, R. J., Chemiavskaya, O., McDonald, J. C., Wu, H., Whitesides, S. H., and Whitesides, G. M., 2000, "Fabrication of Topologically Complex Three-Dimensional Microfluidic Systems in PDMS by Rapid Prototyping," Anal. Chem., **72**, pp. 3158–3164.
[38] Jo, B. H., Van Lerverghe, L. M., Motsegood, K. M., and Beebe, D. J., 2000, "Three-Dimensional Microchannel Fabrication in Polydimethylsiloxane (PDMS) Elastomer," J. Microelectromech. Syst., **9**, pp. 76–81.
[39] Bourdon, C. J., Olsen, M. G., and Gorby, A. D., 2004, "Validation of Analytical Solution of Depth of Correlation in Microscopic Particle Image Velocimetry," Meas. Sci. Technol., **15**, pp. 318–327.
[40] Adrian, R. J., and Yao, C. S., 1983, "Pulsed Laser Technique Application to Liquid and Gaseous Flows and the Scattering Power of Seed Material," Appl. Opt., **24**, pp. 42–52.
[41] Prasad, A. K., Adrian, R. J., Landreth, C. C., and Offutt, P. W., 1992, "Effect of Resolution on the Speed and Accuracy of Particle Image Velocimetry Interrogation," Exp. Fluids, **13**, pp. 105–116.
[42] White, F. M., 1991, *Viscous Fluid Flow (2nd ed.)*, McGraw-Hill, New York.
[43] Wygnanski, I. J., and Champagne, F. H., 1973, "On Transition in a Pipe; Part 1. The Origin of Puffs and Slugs and the Flow in a Turbulent Slug," J. Fluid Mech., **59**, pp. 281–335.
[44] Schlichting, H., *Boundary-Layer Theory (7th ed.)*, McGraw-Hill, New York.
[45] Tracy, H. J., 1965, "Turbulent Flow in a Three-Dimensional Channel," J. Hydraul. Div., Am. Soc. Civ. Eng., **91**, pp. 9–35.

A Method to Predict Cavitation Inception Using Large-Eddy Simulation and its Application to the Flow Past a Square Cylinder

W. Wienken

Institute of Fluid Mechanics,
Technische Universität Dresden
e-mail: wienken@ism.mw.tu-dresden.de

J. Stiller

Institute for Aerospace Engineering,
Technische Universität Dresden,
D-01062 Dresden, Germany

A. Keller

Technische Universität München,
Versuchsanstalt für Wasserbau und
Wasserwirtschaft,
D-82432 Obernach/Walchensee, Germany

A new method to predict traveling bubble cavitation inception is devised. The crux of the method consists in combining the enhanced predictive capabilities of large-eddy-simulation (LES) for flow computation with a simple but carefully designed stability criterion for the cavitation nuclei. For LES a second-order accurate finite element model based on the Galerkin/least-squares method with Runge-Kutta time integration is applied. The incoming nucleus' spectrum is approximated by a Weibull distribution. Moreover, it is shown that under typical conditions the stability of the nuclei can be evaluated with an algebraic criterion emerging from the Rayleigh-Plesset equation. This criterion can be expressed as modified critical Thoma number and fits well into the LES approach. The method was applied to study cavitation inception in a flow past a square cylinder. A good agreement with experimental results was achieved. Furthermore, the principal advantage over statistical (time-averaged) methods could be clearly demonstrated, even though the spatial resolution and application of the LES were restricted by limited computational resources. As the latter keep on growing, a wider range of applications will become accessible methods for cavitation prediction based on algebraic stability criteria combined with LES. [DOI: 10.1115/1.2170132]

1 Introduction

Cavitation is known for its destructive impact on wetted surfaces, which can lead to fatal failures of hydraulic machinery and hydraulic structures. Therefore, it has to be avoided or at least controlled. This demands that cavitation inception has to be predicted by means of experiments or numerical investigations during the design phase. Due to the rapid development and broader availability of powerful computers and the ability to save costs and time in comparison to experiments numerical methods have become increasingly popular in recent years.

Cavitating flows are characterized by the critical Thoma number, which is defined as

$$\sigma_i = \frac{p - p_v}{\rho u^2 / 2} \tag{1}$$

where p and u denote the freestream pressure and velocity, ρ the density and p_v the vapor pressure. A straightforward method for predicting cavitation inception is to assume that cavitation begins if the local pressure drops down to the vapor pressure. Then, the critical Thoma number is equal to the negative minimum pressure coefficient

$$c_{p,\min} = \frac{p_{\min} - p}{\rho u^2 / 2} = -\sigma_i \tag{2}$$

However, this method is unable to capture real fluid effects which are caused by bubble dynamics, initial nucleus' size, bubble-flow interactions, and pressure fluctuations.

Microbubbles (nuclei) with a radius in the range of micrometers are the origin of cavitation in technical water [1]. In general, the free gas content in the liquid is negligible before cavitation inception

$$\beta_g = \frac{V_{\text{gas}}}{V_{\text{gas+liquid}}} \ll 1 \tag{3}$$

This allows setting up weakly coupled models for the gas and liquid phases. The motion of the liquid phase can be assumed as a single-phase flow that is not affected by the embedded cavitation nuclei. The nuclei itself are considered as independent spherical bubbles which consist of noncondensable gases and vapor. Their dynamics are described by the well-known Rayleigh-Plesset differential equation (11) [2]. Before cavitation incepts, the nuclei are in equilibrium with the surrounding liquid and move with the main flow.

The flow field is determined either by means of experiments or flow calculations. Regarding flow calculations potential methods are widely used for ship propulsors [3]. As they are applicable for inviscid and rotation-free flow, this approach is limited to flows around streamlined bodies without separation and freestream turbulence effects. In contrast, numerical solutions of the Reynolds-averaged Navier-Stokes equations (RANS) include the effects of turbulence by a statistical model. Hsiao and Pauley [4] applied this approach with a k-ε model for the prediction of tip vortex cavitation. While RANS with two-equation models (such as the k-ε or k-ω model) are commonly used in commercial computational fluid dynamics (CFD) codes, a number of conceptual limitations [5] are known. In particular, deficiencies were observed in flows with stagnation, separation, rotation, and secondary motion. Unfortunately, those flows are often afflicted by cavitation. Examples are the flows in barrages, in piston engine cooling channels, or control valves, where complex geometries cause separation and recirculation. More sophisticated turbulence models are Reynolds-stress models or the large-eddy simulation (LES), which gained importance in recent years. In consequence, Lesieur [6] proposed to use LES for the prediction of cavitation inception.

LES is based on the observation that a flow strongly depends on large turbulence structures which are long-living, high-energetic, nonisotropic, and dependent on geometry. In contrast, small scales are short-lived, low-energetic, universal, isotropic, and in statisti-

---

Contributed by the Fluids Engineering Division of ASME for publication in the JOURNAL OF FLUIDS ENGINEERING.

cal average dissipative [7]. In the LES framework, the large scales are computed due to their significance, while the small scales are modeled. In many scientific and technical applications LES proved to be an accurate tool to compute turbulent flow [8]. For the application of LES on flows of engineering interest not all numerical methods are suitable as a wide range of scales must be resolved. The need to resolve high wave-number turbulent fluctuations implies that fine meshes and accurate, unsteady numerical schemes have to be used. Usually, highly accurate finite difference or spectral methods are preferred for LES. Unfortunately, they are restricted to simple geometry and, thus, not applicable for technical flows. More geometric flexibility can be achieved with finite volume or finite element methods on unstructured grids. However, as they are typically less accurate than finite difference or spectral schemes, a larger number of grid points is necessary to achieve the same level of accuracy which demands, in turn, parallelized solvers and powerful computers. In addition, the schemes have to be carefully designed to avoid that numerical dissipation outbalance the subgrid stresses. The overall cost of LES scale with the Reynolds number as $Re^{1.8}$ [9]. As a consequence, LES is considerable more expensive than RANS. However, LES will gain importance in technical applications due to its superior predictive capabilities as the computer performance increases.

Motivated by this perspective, the paper presents an approach to apply LES for the prediction of cavitation inception. As cavitation usually occurs at Reynolds numbers above 100,000, the costs of LES alone are already considerable. Hence, the model for cavitation inception must be tailored in such a way that the total cost is not significantly increased. A direct approach, involving multiple nucleus tracking and simultaneous integration of the associated Raleigh-Plesset equations, is obviously too expensive when combined with unsteady flow computations. Fortunately, under reasonable assumptions a simplified, algebraic criterion for nucleus stability can be derived (Sec. 2). Moreover, the incoming nucleus spectrum remains practically unchanged by fluid motion. Both these ingredients lead to a cost-effective cavitation model which is easily incorporated into the LES framework. The LES model is based on a Galerkin/least-squares finite element (GLS) method which is described in Sec. 3. Employing unstructured tetrahedral grids, it allows for handling geometries of engineering interest. To allow acceptable turnaround times, the computational code is parallelized and run on a multiprocessor system. The overall approach is evaluated in Sec. 4. The method is applied to the flow past a square cylinder which exhibits cavitation inception at a low Reynolds number of 100,000, which is accessible to LES. The results are compared to experiments, as well as to computations based on the Reynolds-averaged Navier-Stokes equations (RANS) in combination with the k-ε and Reynolds stress models.

2 Modeling Cavitation Inception for Traveling Bubble Cavitation

One approach to predict cavitation inception is to track the nucleus' motion by solving ballistic equations and to evaluate their radial oscillation by solving the Rayleigh-Plesset equation. The velocity and pressure of the surrounding fluid are determined from a simultaneous computation of the flow field. This procedure is continued until a stability criteria for the nucleus is violated or the nucleus leaves the flow field. To obtain reliable results, number and size of the nuclei must be consistent with the actual nucleus spectrum. Applications of this approach are given by Kodama et al. [10], Meyer et al. [11], and Hsiao and Pauley [4]. Unfortunately, this approach involves a considerable computational overhead and significant extra cost when applied to unsteady flows. As an alternative, a simplified procedure which is based on an algebraic criterion acting on the nucleus spectrum is derived in the following.

2.1 Nucleus Spectrum. The nucleus spectrum represents the statistical distribution of nuclei sizes in a cavitating flow (see Fig.

4 as an example). If the inflow is homogeneously loaded with nuclei and the drag between the nuclei and the liquid is negligible, only one single spectrum is needed. Drag, in turn, is caused by buoyancy, inertia, pressure gradients, and is affected by friction. In the following, those criteria are discussed to justify this basic assumption.

The effect of buoyancy can be assessed for freely rising gas bubbles. According to Clift and Grace [12] the Reynolds number of the relative bubble motion

$$Re_n = \frac{|u - u_n|R}{\nu} \tag{4}$$

is a function of the Eotvos

$$Eo = 4\frac{g(\rho - \rho_n)R^2}{S} \tag{5}$$

and Morton numbers

$$Mo = \frac{g\eta^4(\rho - \rho_n)}{\rho^2 S^3} \tag{6}$$

Here, R denotes the nucleus radius, respectively, ν the kinetic viscosity, S the surface tension, and g the gravity. For a typical nucleus (subscript: n) in water with a radius $R=50~\mu m$ [1] the Eotvos and Morton numbers are $Eo=1.4\times10^{-3}$ and $Mo=2.7\times10^{-11}$, respectively. The corresponding Reynolds Re_n number tends to zero [12]. This means, drag caused by buoyancy is negligible.

In addition, the effects of inertia can be estimated according to Crowe et al. [13] with the Stokes number

$$St = \frac{\tau_n}{\tau_f} \tag{7}$$

which relates the time scale of nucleus acceleration τ_n with the time scale of flow τ_f. In case of a large Stokes number inertia is dominant and a nucleus reacts slowly on changes in the fluid velocity. Then, significant drag has to be expected. The time scale of nucleus acceleration τ_n can be estimated from a balance of forces. For a cavitation flow with a Reynolds number Re of approximately 10^5 and flow's length scale L in the range of 1 m the relative bubble's motion Reynolds number Re_n is small even for a nucleus at rest ($Re_n=ReR/L<5$). Thus, a creeping flow past the nucleus can be assumed [14], which leads to

$$\frac{d\vec{u}_n}{dt} = \vec{g}\left(1 - \frac{\rho}{\rho_n}\right) + \frac{9}{2}\frac{\nu}{R^2}\frac{\rho}{\rho_n}(\vec{u} - \vec{u}_n) \tag{8}$$

The time scale τ_n is then defined as the time in which a nucleus is accelerated from rest to 95% of the flow velocity. The time scale of flow $\tau_f=L/u_{ref}$ is obtained from the characteristic velocity u_{ref} and the flow's length scale L. This leads after integrating Eq. (8) to

$$St = \frac{2}{3}\frac{\rho_n}{\rho}\left(\frac{R}{L}\right)^2 Re \tag{9}$$

with $Re=Ru_{ref}/\nu$. For a typical nucleus with a radius in micrometer range, a flow's length scale of meters and a Reynolds of $Re=10^6$, the resulting Stokes number is close to $St=10^{-9}$. Computations of Tang et al. [15] show that for low Stokes numbers, such as $St=0,01$, no drag has to be expected, even in a highly nonstationary flow. Furthermore, the effects of pressure gradients in the surrounding of a nucleus are not considered in this work due to the small size of the nuclei.

As friction is based on drag, it only acts if initially drag exits. As far as buoyancy, inertia and pressure gradients do not cause initially drag, the effects of friction can be neglected, too. As a consequence of negligible drag, the initial nucleus' size distribution is not altered by the flow. Assuming, additionally, stable nuclei prior to cavitation inception, the nucleus spectrum measured

at the inlet is valid everywhere.

Different experimental methods to measure the spectrum are compared in Isay [3]. For practical purpose, the measured discrete spectrum can be approximated by the Weibull distribution

$$F(R) = \begin{cases} 0 & \text{for } R = 0 \\ 1 - e^{-(R/\gamma)^\beta} & \text{for } R > 0 \end{cases} \qquad (10)$$

The distribution is tuned with the parameters β and γ to a given discrete spectrum, which, usually, results in a better agreement compared to symmetric or distribution functions with one parameter.

2.2 Stability of Nuclei. The dynamics of an isolated, spherical bubble, surrounded by an uniform pressure, is governed by the Rayleigh-Plesset equation, which is a nonlinear second-order differential equation [2]

$$R\ddot{R} + \frac{3}{2}\dot{R}^2 - \frac{1}{\rho}\left(p_{g,0}\left(\frac{R_0}{R}\right)^{3n} + p_\nu - p(t) - \frac{2S}{R} - 4\eta\frac{\dot{R}}{R} \right) = 0 \qquad (11)$$

The nucleus radius R in Eq. (11) with temporal derivatives $\dot{R}$ and $\ddot{R}$ depends on the fluid properties (surface tension S, density ρ, dynamic viscosity η, and steam pressure p_ν), initial conditions (radius R_0 and partial pressure of the noncondensable gas content of the bubble $p_{g,0} = p_0 + 2S/R_0 - p_\nu$ at the location of the spectrum's measurement), the polytropic constant n and the pressure $p(t)$. The nucleus is in equilibrium for a constant pressure if $\dot{R} = 0$ and $\ddot{R} = 0$, respectively

$$p_{g,0}\left(\frac{R_0}{R_{eq}}\right)^{3n} + p_\nu - p - \frac{2S}{R_{eq}} = 0 \qquad (12)$$

Except for the pressure, all parameters are constant in Eq. (11). Depending on the amplitude and frequency of the pressure oscillations different dynamic reactions of a nucleus can be expected. As Rood [1] and Isay [3] summarize, instantaneous pressure fluctuations caused by turbulence strongly affect cavitation inception. Hence, those oscillations have to be considered in deriving a suitable stability criterion for the nuclei in LES computations. In the following a simple algebraic criterion is derived by comparing the time scales of nucleus oscillation and the turbulent flow.

The eigenfrequency f of a freely oscillating nucleus was derived by Shima [16]

$$f = \frac{1}{2\pi R_0} \sqrt{\frac{3n}{\rho}\left[p + \frac{2S}{R_0}\left(1 + \frac{1}{3n}\right) \right] - \left(\frac{2\eta}{\rho R_0}\right)^2} \qquad (13)$$

For typical cavitation nuclei with radii of 5 μm to 50 μm [1] the resulting frequencies are larger than 20 kHz. On the other hand, in turbulent flow the frequency of pressure and velocity oscillations vary over a wide range. In particular, one can distinguish between

- Oscillations associated with large, coherent structures and
- Turbulent fluctuations in boundary or shear layers

Frequencies of oscillations caused by large, coherent structures are characterized by the Strouhal number $Sr = fL/d$, which is, typically, in the range of 0.1 to 0.2 [14]. Considering engineering flows with length-scales L in the range of meters and velocities u up to 100 m/s, typical frequencies do not exceed 10 Hz.

The unsteady pressure signal of various turbulent boundary and shear layers has been examined experimentally. For example, Farabee and Casarella [17] investigated turbulent boundary layers at $Re_\tau = u_\tau \delta/\nu = 1.169, \ldots, 2.010$ (computed with the wall shear velocity u_τ and the boundary layer thickness δ). The range of measured frequencies covers an interval from 5 Hz to 20 kHz. Scaling analysis revealed the influence of different flow regions, which contribute to certain amplitudes and frequencies. Low fre-

quency contributions originate in the outer boundary layer, medium in the logarithmic region and high in the viscous sublayer. The amplitudes decrease significantly with increasing frequency, e.g., five orders of magnitudes in the range from 3 kHz to 20 kHz. Higher frequencies have to be expected with further decreasing amplitudes which overlap then with nuclei eigenfrequencies. As shown for various cavitating flows, such as hemispherical headforms, cavitation does not incept immediately close to the body surface [1] and, therefore, not in the high-frequency low-amplitude viscous and logarithmic parts of the boundary layer. This indicates that high-frequency pressure waves are not dominant for cavitation inception at their origin, although they prevail in the entire flow field for incompressible flow. In contrast, the pressure in the outer boundary layer is sufficient to cause cavitation inception. However, in this area the flow's time scale is larger than the time scale of nucleus oscillation. Those observations suggest assuming that a nucleus has sufficient time to react on a pressure change with a sequence of equilibrium radii according to Eq. (12). This assumption allows, in turn, to derive an algebraic nucleus stability criterion.

The stability of nuclei in equilibrium is extensively dealt with in literature, e.g., Isay [3] or Brennen [18]. It is reported, that a stable equilibrium radius exists if

$$\left(\frac{3n-1}{3n}\right)\left(\frac{2S}{R_{eq}}\right) > p_\nu - p \qquad (14)$$

Using Eq. (12) the equilibrium radius can be eliminated from Eq. (14) to give

$$(3n-1)p_{g,0}^{1/(1-3n)}\left(\frac{2S}{3nR_0}\right)^{3n/(3n-1)} > p_\nu - p \qquad (15)$$

Since stable oscillations can exist only around a stable equilibrium [18], Eq. (15) represents an algebraic criterion for the stability of a given nucleus.

Apart from the dynamic stability, the effects of diffusion are often considered. Dependent on the gas solution's saturation in the liquid, bubbles grow or shrink. As the time scale of diffusion bubble growth is in the range of minutes [19], the nucleus passes through a low-pressure flow region before a significant nucleus size change caused by diffusion occurs. Hence, diffusion is neglected.

2.3 Computation of Cavitation Inception. Cavitation incepts at the location where the spatial pressure minimum $p_{\min}(t)$ acts. In steady flow $p_{\min}$ is a constant and, thus, the location is fixed. In case of unsteady flow, both the value and location of $p_{\min}(t)$ are a function of time. For a conservative prediction of the critical Thoma number, and to allow an uncoupled computation of the flow, $p_{\min} = \min_{0 \leq t \leq T} p_{\min}(t)$ is used in place of $p_{\min}(t)$.

After rewriting Eq. (1) accordingly, the critical Thoma number is composed of the minimum pressure coefficient and a term, which represents the difference between the minimum and vapor pressure at cavitation inception

$$\sigma_i = \frac{p - p_{\min}}{\rho u^2/2} + \frac{p_{\min} - p_\nu}{\rho u^2/2} = -c_{p,\min} + \frac{p_{\min} - p_\nu}{\rho u^2/2} \qquad (16)$$

The last term can be interpreted as an apparent tensile strength, which is equal to zero for ideal nuclei without surface tension or other effects that delay or promote vaporization. It is determined by using the model for cavitation inception while $c_{p,\min}$ is derived from the computation of the flow field.

At cavitation inception, Keller measured that one out of 180 to 380 nuclei per cubic centemeters are unstable [20]. This finding can be used as well to define cavitation inception: "*Cavitation incepts if P=1% of all nuclei become unstable while being exposed to the lowest pressure in the flow field.*" Employing the Weibull distribution (10), a critical initial radius R_0 with $F(R_0)$

$=P$ in Eq. (17) is determined, which represents the largest stable nucleus size

$$R_0 = \gamma[-\ln(P)]^{1/\beta} \tag{17}$$

Substituting Eq. (17) in Eq. (15) yields the following expression for the apparent tensile strength:

$$p_{\min} - p_\nu = -(3n-1)p_{g,0}^{1/(1-3n)}\left(\frac{2S}{3nR_0}\right)^{3n/(3n-1)} \tag{18}$$

For vanishing surface tension $S=0$, $p_{\min}-p_\nu$ tends to zero and, according to Eq. (16), cavitation incepts when the flow pressure approaches vapor pressure.

To summarize, this approach allows us to predict cavitation inception as a postprocessing to unsteady CFD computations. The first step is to determine the minimum pressure coefficient $c_{p,\min}$ $= \min c_p(\vec{x},t)$. In the second step, the critical Thoma number σ_i is evaluated, by taking into account the tensile strength and the nucleus distribution. A possible disadvantage of this method is the exclusion of further promoting or delaying dynamic effects, such as diffusion [1,3].

3 Computation of the Flow Field with LES

Due to the small free gas content, the influence of the nuclei on the flow field is negligible. Hence, a single-phase flow, which is governed by the Navier-Stokes equations, is considered here.

For LES the Navier-Stokes equations are filtered [21] to give

$$\frac{\partial \mathbf{U}}{\partial t} + \frac{\partial}{\partial x_i}(\mathbf{F}_i + \mathbf{F}_i^{\text{sgs}}) - \frac{\partial}{\partial x_i}(\mathbf{D}_i + \mathbf{D}_i^{\text{sgs}}) = \mathbf{0} \tag{19}$$

The large-scale Eqs. (19) resemble the Navier-Stokes equations except for the subgrid-scale advective flux $\mathbf{F}_i^{\text{sgs}}$ and diffusive flux $\mathbf{D}_i^{\text{sgs}}$, both representing the effect of the filtered subgrid scales. In detail, the terms in Eq. (19) are

$$\mathbf{U} = [\rho \ \rho u_1 \ \rho u_2 \ \rho u_3 \ \rho E]^{\text{T}} \quad \text{resolved conservative variables} \tag{20}$$

$$\mathbf{F}_i = u_i\mathbf{U} + p[0 \ \delta_{i1} \ \delta_{i2} \ \delta_{i3} \ u_i]^{\text{T}} \quad \text{resolved advective flux and} \tag{21}$$

$$\mathbf{D}_i = [0 \ \tau_{i1} \ \tau_{i2} \ \tau_{i3} \ \tau_{ij}u_j - q_i]^{\text{T}} \quad \text{resolved diffusive flux} \tag{22}$$

Here, ρ denotes the density, u the velocity, p the pressure, T the temperature, $E=e+u^2/2$ the specific internal plus kinetic energy, $\tau_{ij} = 2\eta(\dot{\varepsilon}_{ij} - \frac{2}{3}\delta_{ij}\dot{\varepsilon}_{ii})$ the shear stresses with the shear rate $\dot{\varepsilon}_{ij}$ $=(\partial_i u_j + \partial_j u_i)/2$, η the dynamic viscosity, and $q_i = -\lambda \partial_i T$ the heat flux. Following [9], the subgrid-scale advective flux $\mathbf{F}_i^{\text{sgs}}$ is given by

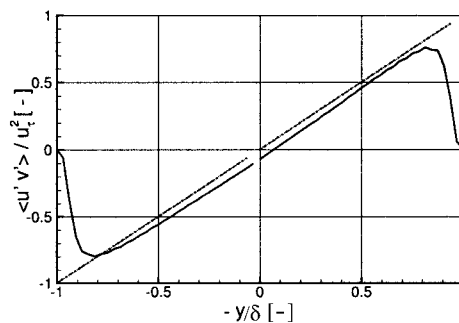$$\mathbf{F}_i^{\text{sgs}} = [0 \ \tau_{1i}^{\text{sgs}} \ \tau_{21i}^{\text{sgs}} \ \tau_{3i}^{\text{sgs}} \ q_i^{\text{sgs}}]^{\text{T}} \tag{23}$$

The subgrid stress τ_{ij}^{sgs} is modeled using the Smagorinsky model [22] including Van Driest wall damping. The subgrid heat flux $q_i^{\text{sgs}} = -\lambda_T \partial_i T$ is computed by using Reynolds similarity [14].
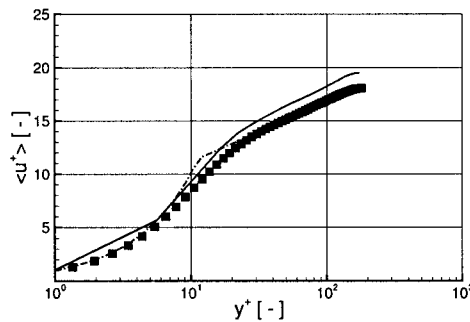
(a) Mean velocity (−: LES; ■: DNS [35] − · −: Logarithmic velocity profile)
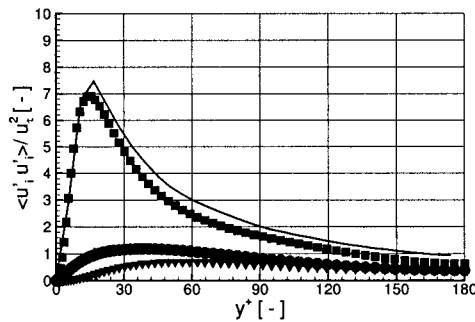
(b) Shear stresses (−: LES; ■,●,▼: DNS [35] comp. 1, 2, 3)

(c) Reynolds-stresses (−: LES; − · −: Theory)

Fig. 1 Turbulent channel flow at Re=180

Furthermore, the subgrid-scale diffusive flux $\mathbf{D}_i^{\text{sgs}}$ is neglected [23]. Though not of particular relevance for the present work, this formulation allows to consider compressibility effects in view of possible applications to cavitation in oil-hydraulic high-pressure devices where compressibility can not be neglected [24].

For spatial discretization the Galerkin/least-squares (GLS) method [25,26] with linear shape functions is applied. In contrast to traditional approaches, the GLS method achieves stability by consistent modifications of test functions rather than adding artificial viscosity. This property is partially lost in low-order (linear) approximations. However, using the residual reconstruction technique proposed in [27], formal second-order accuracy can be retained. Furthermore, the method remains stable even in the incompressible limit if $[p \; \vec{u} \; T]^T$ are chosen as the independent variables [28]. The suitability of piecewise linear GLS methods for LES was first demonstrated by Jansen [29]. The GLS formulation of the large-scale equations reads

$$\int_\Omega [\mathbf{W} \cdot \partial_t \mathbf{U} + \partial_i \mathbf{W}(\mathbf{F}_i + \mathbf{F}_i^{\text{sgs}} - \mathbf{D}_i)]\mathrm{d}V - \int_\Gamma \mathbf{W}(\mathbf{F}_i + \mathbf{F}_i^{\text{sgs}} - \mathbf{D}_i)n_i\mathrm{d}A$$

$$+ \sum_{i=1}^{N_{el}} \int_{\Omega^e} \mathbf{W} \cdot \mathbf{A} \cdot \mathbf{T}[\partial_t \mathbf{U} + \partial_i(\mathbf{F}_i + \mathbf{F}_i^{\text{sgs}}) - \partial_i \mathbf{D}_i] = 0 \qquad (24)$$

The first two integrals constitute the usual Galerkin contributions while the last expression represents the GLS operator. $\mathbf{W}$ is a piecewise linear weight function and $\mathbf{T}$ the stabilization matrix which depends on the local element size and the squares of the advective flux Jacobians $\mathbf{A}$. The spatial discretization results in a time-dependent system of ordinary differential equations which is integrated using an explicit four-stage Runge-Kutta scheme along with a damped Jacobi iteration for resolving the consistent mass matrix.

The numerical model was implemented on top of the grid library MG (multilevel grids) [30,31]. MG provides a light-weight interface for parallel adaptive finite-element solvers on tetrahedral grids. To reduce computational time, the solver is parallelized based on nonoverlapping grid decomposition. In typical production runs, a parallel efficiency of 95% or better is achieved on 120 processors [32].

The solver was carefully verified and proved to be second-order accurate in space and time [33,34]. Furthermore, it was validated for a number of turbulent flows including homogeneous isotropic turbulence, turbulent channel flow, and the Lyn test case, which represents a flow past a square cylinder at Re=21,400 [33,34].

In case of the turbulent plane channel flow at $\text{Re}_\tau=180$ [35], a constant body force drives the flow between two parallel flat plates. The computational domain of dimensions $L_x \times L_y \times L_z = 4\pi\delta \times 2\delta \times \pi\delta$ was discretized using a quasiuniform grid with spacing $\Delta y = L_y/64$, which corresponds $\Delta y^+=5.6$ in wall units. For parallelization, the computational domain was decomposed into 32 partitions. The Smagorinsky model with Van Driest wall damping was applied and the Smagorinsky constant set to 0.1. In Figs. 1(a)–1(c) the mean velocity, the shear stresses and the Reynolds

Table 1   Grid parameters for the computation of the Lyn test case (D: cylinder diameter)

	Computation	
	C–I	C–II
Number of nodes	~268.200	~744.000
Number of elements	1.26 mil.	3.8 mil.
Average element length on body	D/20	D/15
Average element length in wake	D/5	D/7

stresses are compared to the benchmark direct numerical simulation (DNS) by Kim et al. [35]. The mean velocity exceeds the DNS data which can be attributed to the absence of an appropriate wall model. Apart from that, a good agreement between the LES and DNS is achieved.

The Lyn test case represents the flow past an infinite square cylinder at Reynolds Re=21,400. This flow involves a number numerically challenging phenomena, such as separation and the creation of an alternating vortex street. For this case, the impact of the grid resolution close to the body surface and in the wake was examined and the results compared to the data of a workshop [36,37]. For validation purposes, two computations with different resolutions were carried out. The computational parameters are summarized in Table 1. In the first case, C-I, the grid was refined near the body to allow a better resolution of the boundary layers. In case C-II, the resolution was enhanced in the entire wake region, resulting in a significant higher number of grid nodes. In both runs the Smagorinsky model was used with $C_S=0.1$ and Van Driest wall damping.

The characteristic flow parameters are summarized in Table 2 along with corresponding data reviewed in [36,37]. The predicted Strouhal numbers are very close to the experimental value of 1.32 in both cases. The mean drag coefficient $\langle c_w \rangle$ is overestimated by 9.5% when compared to the experiment, but fits well into field of numerical results reported in [36,37]. Too high drag coefficients were generally observed in the workshop [36] for computations without a wall model. Concerning the recirculation length L, the computations produced significantly different results. While C-I reproduced the experimental value with a deviation of less than 5%, L is considerably overestimated in case C-II. The computed fluctuating drag coefficient, as well as the mean and fluctuating lift coefficients fit well in data given in [37] for C-I, whereas larger deviations in latter are observed for C-II.

In summary, a reasonable agreement with the reference data is obtained in case C-I. This result is encouraging, since the employed computational grid is coarser than those used in the workshop [37]. On the other hand, despite of the higher global resolution, the results are clearly less satisfactory in case C-II. This underlines the importance of using a sufficiently fine grid resolution close to walls.

Table 2   Comparison of Lyn test case calculation with experiment and workshop

		Computation			Workshop	
		I	II	Experiment	Minimum value	Maximum value
Strouhal number	Sr	1.31	1.28	1.32	1.30	1.61
Mean resistance coefficient	$\langle c_w \rangle$	2.30	2.28	2.10	2.03	2.79
Fluctuating resistance coefficient	$\langle c_w' \rangle$	0.14	0.11		0.12	0.36
Mean lift coefficient	$\langle c_l \rangle$	−0.12	−0.09		−0.13	0.04
Fluctuating lift coefficient	$\langle c_l' \rangle$	1.07	0.81		1.01	1.68
Recirculation length	L	1.32	2.01	1.38	1.02	1.61

Fig. 2 Cavitation inception

Fig. 4 Computational domain for the LES

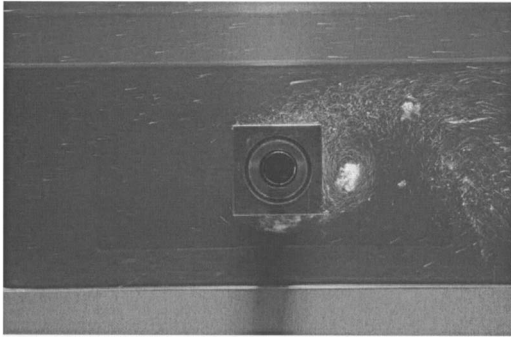## 4 Application to the Flow Past a Square Cylinder

The approach to predict cavitation inception was validated for the flow past a square cylinder. Until cavitation incepts, the flow phenomena are similar to the Lyn test case even though the setup is different regarding the Reynolds number of 100,000, boundary conditions, and dimensions.

4.1 Experiments. Experiments were conducted in a cavitation tunnel at the "Versuchsanstalt für Wasserbau und Wasserwirtschaft," Obernach (Germany). In its test section with a cross-section 0.3×0.3 m the square cylinder (0.04×0.04 m) was centered. Instrumentation included laser Doppler velocity meter, pressure probes, and body force measurement. Additionally, analyzers for the nucleus size distribution and tensile strength were used.

During the experiments the pressure p was lowered for a given velocity u until the first cavitation bubbles and the characteristic noise appeared steadily. No cavitation occurred at velocities smaller than 2.5 m/s, i.e., Re=10^5. The corresponding critical Thoma number is σ_i=5.75. As shown in Fig. 2, cavitation develops in the vortex cores in the wake of the cylinder.

For the prediction of the critical Thoma number the nucleus size distribution was measured and approximated by the Weibull distribution, Fig. 3. The distribution was measured with a "Szintilation" analyzer, which measures the extinction of light and uses it as a scale for the radius.

4.2 Numerical Analysis. The flow past the cylinder was computed with LES and by solving the unsteady Reynolds-averaged Navier-Stokes equations in combination with the k-ε as well as the Reynolds-Stress turbulence model.
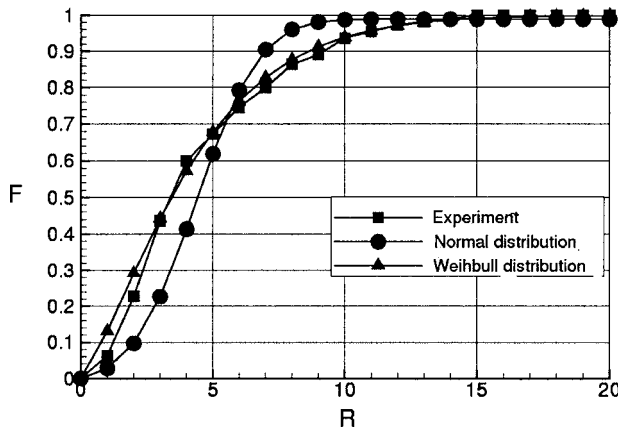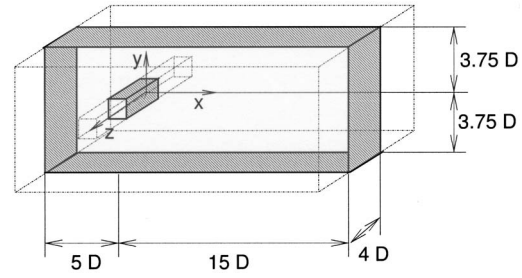
4.2.1 Large-Eddy Simulation. For LES a computational domain of dimensions $L_x \times L_y \times L_z$=20$D \times 7,5D \times 4D$ was chosen, Fig. 4. No-slip conditions were posed at all walls. In contrast to the experiment, however, the spanwise (z) direction was assumed to be periodic. This simplification is supported by experimental observation that cavitation does not incept in the horse-shoe vortex around the body at the side plates. Furthermore a constant laminar flow was assumed at the inlet 5D upstream of the body. Finally, the outlet was modeled using weakly reflecting pressure conditions.

The grid consisted of 4.2×10^6 nodes and was refined close to the body surface. The average element size is $D/25$ near the cylinder and $D/4$ in the far field. The Smagorinsky model was used with C_S=0.1 and the Van Driest damping. No specific wall models were applied. After reaching the developed regime, the statistical properties were obtained by averaging over ten convective time units L_x/u_x. Additionally, results were averaged over the homogeneous spanwise direction. Furthermore, the temporal evolution of $p_{\min}$ was recorded. The computation was run on 64 processors of the SGI O3800 system of the Center of High Performance Computing in Dresden (ZHR) with a total CPU time of approximately 3000 h.

4.2.2 Solutions of the Unsteady Reynolds-Averaged Navier-Stokes Equations in Combination with k-ε Model and RSM. In addition to LES, unsteady RANS computations were conducted with TASCFLOW (Version 2.10). For turbulence modeling, the standard k-ε and Reynolds-Stress models (RSM) [34] with default parameters were employed. The computational grid consisted of 1.97×10^5 nodes and was refined close to the cylinder (Fig. 5). The same boundary conditions as for the LES were used. In total, 1,000 time steps, corresponding to 300 shedding periods, were carried out within one day on a two-processor SGI Octane workstation. The statistical properties were computed by averaging in time and over the homogeneous direction after reaching the developed regime. The temporal evolution of $p_{\min}$ was recorded as well.
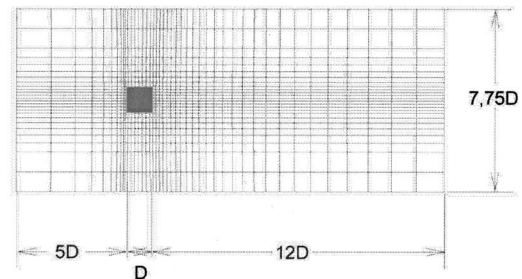

Fig. 3 Nucleus distribution and its approximation by the Weibull and Normal distribution

Fig. 5 Section of the grid used for the unsteady RANS computation (Each fifth gridline is shown)

Table 3 Strouhal number

|	Experiment	LES	RSM	k-ε
Sr	0.143	0.144	0.121	0.121

5 Results

A regular vortex shedding regime developed in all computations independently from the turbulence model. The corresponding Strouhal numbers are listed in Table 3. While the LES shows a good agreement, the k-ε- and Reynolds-Stress models underestimate the Strouhal number. The instantaneous velocity distributions, depicted in Figs. 6(a), 7(a), and 8(a) for the k-ε model, RSM and LES, respectively, demonstrate the formation of a vortex street in all three cases. Although the same grid was used in both RANS simulations, the wake is much less pronounced in the k-ε case. This indicates that too much turbulent energy is dissipated in the k-ε computation. In contrast, the LES (Fig. 8(a)) achieves a significantly finer resolution in the wake and in the lateral recirculation zones, too.

Due to less pronounced vortices in the wake, the lowest pressure is for both RANS computations not, as experimentally found, in the wake but on the body's surface, Figs. 6(b) and 7(b). The pressure coefficients, predicted by LES, in Fig. 8(b) fit well to the measurements and, in contrast to the other computations, the lowest pressure is found correctly in the vortex core. However, the isobar lines in Fig. 8(b) are wrinkled. This indicates that the LES model does not add excessively artificial viscosity and the explicit time integration used here is weakly unstable near the incompressible limit. As a consequence, small-scale pressure oscillations are generated by the steep gradients near the obstacle. These oscillations could be removed by omitting the diffusive flux reconstruction in the GLS formulation, but at the price of losing second-
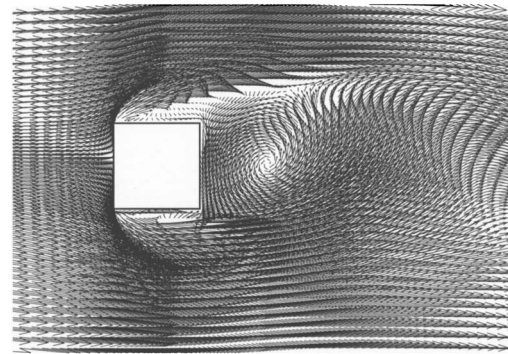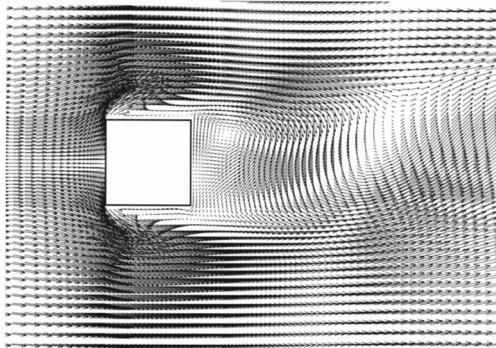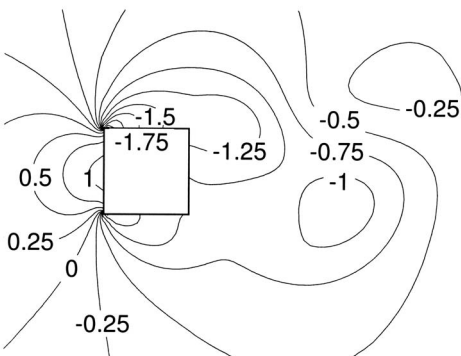

(a) Velocity
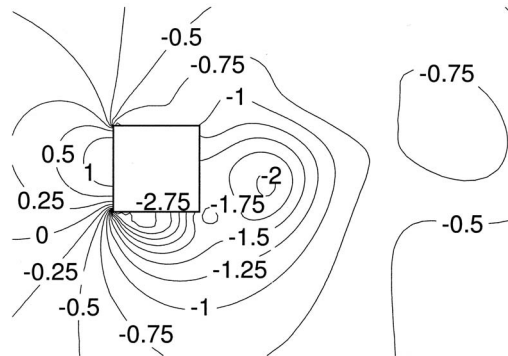
(b) Pressure

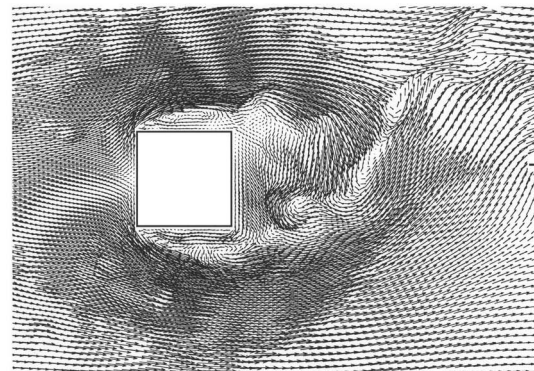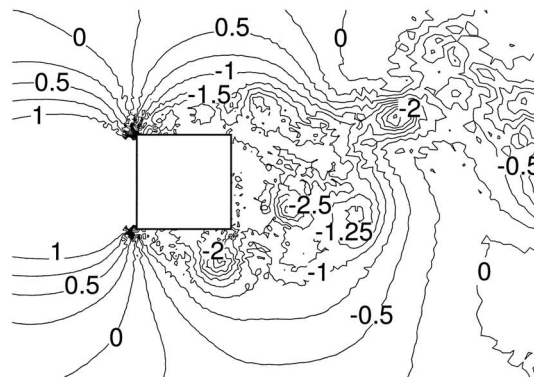**Fig. 7 Velocity and pressure distribution, RSM model**

(a) Velocity

(b) Pressure

Fig. 8 Velocity and pressure distribution, LES

(a) Velocity

(b) Pressure

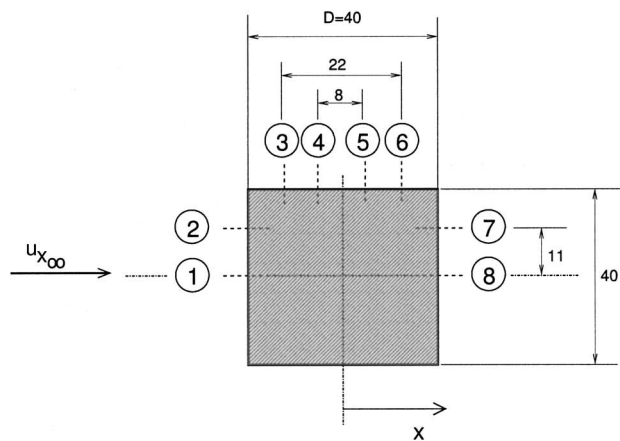**Fig. 6 Velocity and pressure distribution, k-ε model**

(a) Pressure probes

(a) $x = 0$
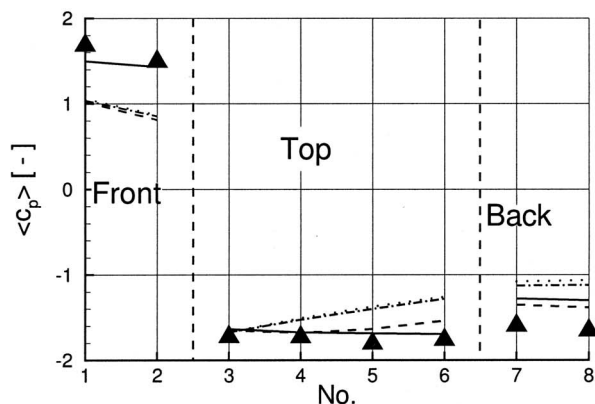
(b) Pressure distribution

(b) $x = D$

Fig. 9 (*a*) **Pressure probes on the cylinder surface** (*b*) **Mean pressure distribution on cylinder surface** (▲; **Experiment;** –: **LES;** − −: **RSM;** − · −: κ-ε)

Fig. 10   Velocity profiles (■; **Experiment;** –: **LES;** ▲ **RSM;** ●: κ-ε)

order accuracy. Report from that, the computed mean pressure coefficients in Fig. 9 agree well with the measurement.
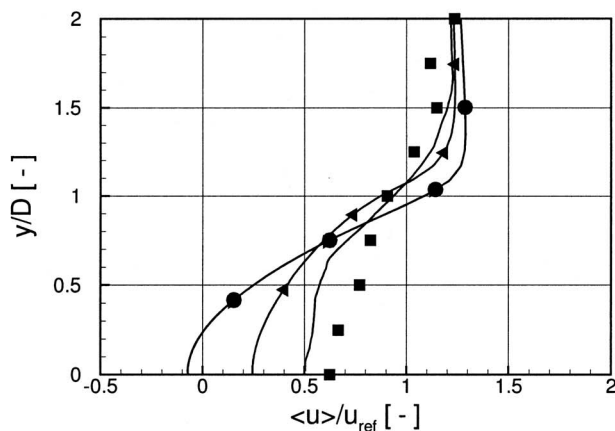
In Fig. 10 the computed time averaged velocity profiles are compared to the experiment. In Fig. 10(*a*) the velocity profile of the section through the body's center (*x*=0) is shown. All computations, especially the LES, resolve well the velocity profile. In the wake, one body diameter downstream from the body's center (*x* =*D*), the extra viscosity of the RSM and, especially, the *k-ε* model inhibit a fast recovery of the velocity in Fig. 10(*b*).

For illustrative purpose, the vortex structures in the wake are visualized in Fig. 11 for the LES and in Fig. 12 for the RSM by isobar surfaces. While in case of the RSM computation one large two-dimensional vortex is visible in Fig. 12, the LES computation resolves a von Karman vortex street. As typical for such a flow at this Reynolds number, the von Karman vortex street is superimposed by secondary instabilities in mean flow direction.

Finally, the critical Thoma number can be computed using Eqs. (16) and (18), Table 4. The prediction by the LES results in a good agreement with the experiment. For the LES, the deviation is with the presented cavitation model 7.7% and without 11.6%. Hence, despite all underlying simplification the cavitation model improves the quality of the prediction. In addition, the location of cavitation inception is correctly captured in the vortex. In contrast, the critical Thoma numbers computed with the unsteady RANS computations exhibit a considerable deviation of more than 41%

and an incorrect location of cavitation inception on the body's surface. As in case of the LES, the cavitation model increases the accuracy of the prediction.

These results indicate that an accurate resolution of the pressure is essential for the correct prediction of cavitation inception. As far as this is provided, suitable cavitation models can ameliorate the accuracy of the critical Thoma number prediction.
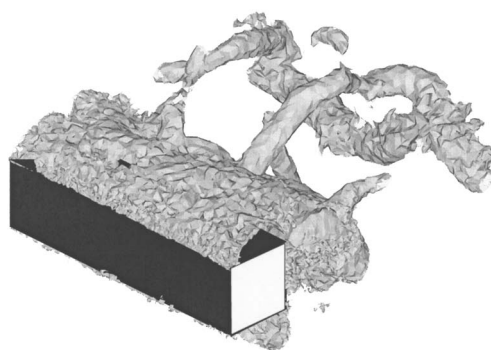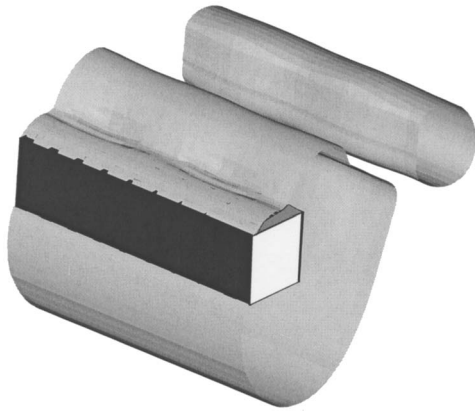

Fig. 11   Isobar surface; LES

Fig. 12 Isobar surface; RSM

6 Conclusion

A new method to predict cavitation inception has been developed for unsteady flows with traveling bubble cavitation. The method combines the enhanced predictive capabilities of large-eddy-simulation (LES) with an algebraic stability criterion for the cavitation nuclei. Despite its simplicity the proposed criterion includes not only the vapor pressure but also effects of tensile strength and nuclei distribution. In particular, the influence of variations in nucleus density and sizes is considered by an approximate nucleus spectrum which remains invariant under typical conditions.

The method was applied to the flow past a square cylinder at the Reynolds number Re=100,000. Both the predicted Thoma number as well as the location of cavitation inception are in good agreement with experimental data. Comparative studies based on a RANS approach with the $k\text{-}\varepsilon$- and Reynolds-stress models resulted in a less favorable agreement. The main reason is that, in contrast to LES, the RANS methods were incapable to capture the large-scale flow structures in the wake of the body correctly and, thus, failed to reproduce the actual position of the pressure minima.

On the other hand, the high computational costs of LES confine its application range to simple configurations. First, the cavitation model must not intervene with the LES solver which lead to the algebraic criterion. Second, the test case should be carefully designed with respect to Reynolds number, geometry, and boundary conditions to avoid unbearable high costs and to ensure a well resolved flow field. Then, the application of LES for the prediction of cavitation inception leads to very encouraging results. As in the given case, a good agreement with experiments can be achieved and principal advantages over statistical (time-averaged) methods obtained. Otherwise, the application of LES for the prediction of cavitation inception should be challenged, especially in environments with limited computer resources.

Acknowledgment

Nomenclature

$\mathbf{A}$ = adjective flux jacobian
$c_{p,\text{min}}$ = minimum pressure coefficient
c_w = drag coefficient
c_L = lift coefficient
D = edge length of square cylinder
$\mathbf{D}_i$ = diffusive flux
e = internal energy
E = total energy
Eo = Eötös number
$\mathbf{F}_i$ = advective flux
g = gravity
L = typical length scale of flow, Recirculation length
Mo = Morton number
n = polytropic constant
p = pressure
P = number of unstable nuclei
q_i = heat flux
R = nucleus radius
Re = Reynolds number
S = surface tension
Sr = Strouhal number
St = Stokes number
t = time
T = temperature
$\mathbf{T}$ = stabilization matrix
u = velocity
$\mathbf{U}$ = conservative variables
$\mathbf{W}$ = piecewise linear weight function

Greek

β = parameter for the Weibull distribution
β_g = free gas content
$\dot{\varepsilon}_{ij}$ = shear rate
γ = parameter for the Weibull distribution
Γ = boundary of solution space
λ = heat conductivity
η = dynamic viscosity
σ_i = critical Thoma number
ρ = density
τ = time scale
τ_{ij} = shear stress
Ω = solution space

Subscripts

eq = equilibrium
f = flow field
g = gas
min = minimum
n = nucleus
ref = reference
sgs = subgrid
v = vapor
0 = initial

Superscripts

+ = boundary layer units

References

[1] Rood, E., 1991, "Review—Mechanism of Cavitation Inception," J. Fluids Eng., **113**, pp. 163–175.
[2] Plesset, M., 1949, "The Dynamics of Cavitation Bubbles," J. Appl. Mech., **16**, pp. 277–287.
[3] Isay, W., 1989, *Kavitation*, Schiffahrts-Verlag Hansa, Hamburg.
[4] Hsiao, C-T., and Pauley, L., 1999, "Study of Tip Vortex Cavitation Inception Using Navier-Stokes Computation and Bubble Dynamic Model," J. Fluids

Eng., **121**, pp. 198–204.

[5] Wilcox, D., 1993, *Turbulence Modeling for CFD*, DCW Industries, La Canada (CA).

[6] Lesieur, M., 1998, "Vorticity and Pressure Distributions in Numerical Simulations of Turbulent Shear Flow," *Proceedings of the Third International Symposium on Cavitation*, Grenoble, France, **1**, pp. 9–18.

[7] Tennekes, H., and Lumley, J., 1972, *A First Course in Turbulence*, MIT Press, Cambridge.

[8] Sagaut, P., 2001, *Large Eddy Simulation for Inkompressible Flows—An Introduction*, Springer-Verlag, Berlin.

[9] Piomelli, U., 1999, "Large-Eddy Simulation: Achievements and Challenges," Prog. Aerosp. Sci., **35**, pp. 335–362.

[10] Kodama, Y., Take, N., Tamiya, S., and Kato, H., 1981, "The Effects of Nuclei on the Inception of Bubble and Sheet Cavitation on Axisymmetric Bodies," J. Fluids Eng., **103**, pp. 557–563.

[11] Meyer, R. S., Billet, M., and Holl, J., 1992, "Freestream Nuclei and Traveling Bubble Cavitation," J. Fluids Eng., **114**(4), pp. 672–679.

[12] Clift, R., and Grace, J., 1978, *Bubbles, Drops and Particles*, Academic Press, New York.

[13] Crowe, C., Troutt, T., and Chung, J., 1995, "Particle Interactions with Vortices," *Fluid Vortices*, S. Green, ed., Kluwer Academic Press, Dordrecht.

[14] Prandtl, L., Oswatitsch, K., and Wieghardt, K., 1989, *Führer durch die Strömungslehre*, 9th edt. Vieweg, Braunschweig.

[15] Tang, L., Wen, F., Yang, Y., Crowe, C., Chung, J., and Troutt, T., 1992, "Self-Organizing Particle Dispersion Mechanism in a Plane Wake," Phys. Fluids A, **4**(10), pp. 2244–2251.

[16] Shima, A., 1970, "The Natural Frequency of a Bubble Oscillating in a Viscous Compressible Liquid," J. Basic Eng., **55**, pp. 555–562.

[17] Farabee, T., and Casarella, M., 1991, "Spectral Features of Wall Pressure Fluctuations Beneath a Turbulent Boundary Layers," Phys. Fluids A, **3**(10), pp. 2410–2420.

[18] Brennen, C. E., 1995, *Cavitation and Bubble Dynamics*, Oxford University Press, New York, Oxford.

[19] Epstein, P., and Plesset, M., 1950, "On the Stability of Gas Bubbles in Liquid-Gas Solutions," J. Chem. Phys., **18**(11), pp. 1505–1509.

[20] Keller, A., 1973, "Experimentelle und Theoretische Untersuchung zum Problem der Modellmäßigen Behandlung von Strömungskavitation," Versuchsanstalt für Wasserbau Oskar von Miller, Obernach/München.

[21] Moin, P., Squires, W., Cabot, W., and Lee, S., 1991, "A Dynamic Subgrid-Scale Model for Compressible Turbulence and Scalar Transport," Phys. Fluids A, **3**(11), pp. 2746–2757.

[22] Smagorinsky, J., 1963, "General Circulation Experiments with the Primitive Equations," Mon. Weather Rev., **91**(3), pp. 99–152.

[23] Vreman, B., Geurts, B., and Kuerten, H., 1995, "Subgrid-modelling in LES of Compressible Flow," Appl. Sci. Res., **54**, pp. 191–203.

[24] Helduser, S., and Rüdiger, F., 2003, "Zwischenbericht zur Sachbeihilfe HE 2715/1-2," Technischer Bericht, Institut für Fluidtechnik, TU Dresden.

[25] Hughes, T., and Mallet, M., 1986, "A New Finite Element Formulation for Computational Fluid Dynamics: III. The Generalized Streamline Operator for Multidimensional Advective-Diffusive Systems," Comput. Methods Appl. Mech. Eng., **58**, pp. 305–328.

[26] Shakib, F., Hughes, T. J. R., and Zdenek, J., 1991, "A New Finite Element Formulation for Computational Fluid Dynamics: X. The compressible Euler and Navier-Stokes Equations," Comput. Methods Appl. Mech. Eng., **89**, pp. 141–219.

[27] Jansen, K., Collis, S. S., Whiting, C., and Shakib, F., 1999, "A Better Consistency Method for Low-Order Stabilized Finite Element Methods," Comput. Methods Appl. Mech. Eng., **174**, pp. 153–170.

[28] Hauke, G., and Hughes, T., 1994, "A Unified Approach to Compressible and Incompressible Flows," Comput. Methods Appl. Mech. Eng., **113**, pp. 389–395.

[29] Jansen, K., 1999, "A Stabilized Finite-Element-Method for Computing Turbulence," Comput. Methods Appl. Mech. Eng., **174**, pp. 299–317.

[30] Stiller, J., Nagel, W., and Fladrich, U., 1999, "Scalability of Parallel Multigrid Adaption," *Multigrid Methods VI*, Dick et al., eds., Springer-Verlag, Berlin, pp. 228–234.

[31] Stiller, J., and Nagel, W. E., 1999, "MG—A Toolbox for Parallel Grid Adaption and Implementing Unstructured Multigrid Solvers," *Parallel Computing, Fundamentals and Applications 2000*, E. H. D'Hollander et al., eds., Imperial College Press, pp. 391–399.

[32] Wienken, W., Stiller, J., and Fladrich, U., 2002, "A Finite-Element Based Navier-Stokes Solver for LES," *Parallel CFD 2002, Parallel Computational Fluid Dynamics-New Frontiers and Multi-Disciplinary Applications*, K. Matsuno, A. Ecer, J. Periaux, N. Satofuka, and P. Fox, eds., Elsevier Publishing Co., pp. 361–368.

[33] Stiller, J., Wienken, W., Fladrich, U., Grundmann, R., and Nagel, W. E., 2004, "Parallel and Adaptive Finite Element Techniques for Flow Simulation," *New Results in Numerical and Experimental Fluid Mechanics IV*, C. Breitsamter et al., eds., Springer-Verlag, pp. 366–373.

[34] Wienken, W., 2002, *Die Large-Eddy-Simulation mittels der Finite-Elemente-Methode zur Bestimmung des Kavitationsbeginns*, VDI-Fortschrittsberichte, Reihe 7 Nr. 453, VDI-Verlag, Düsseldorf.

[35] Kim, J., Moin, M., and Moser, R., 1987, "Turbulence Statistics in Fully Developed Channel Flow at low Reynolds Number," J. Fluid Mech., **177**, pp. 133–166.

[36] Rodi, W., 1998, "Large-Eddy Simulations of the Flow past Bluff Bodies: State-of-the-Art," JSME Int. J., **41**(2), pp. 361–374.

[37] Voke, P., 1997, "Flow Past a Square Cylinder: Test Case LES2," *Direct and Large Eddy Simulation II*, J. Challet, P. Voke, and L. Kouser, eds., Kluwer Academic, Dordrecht.

Angelo Cervone
Project Manager
e-mail: a.cervone@alta-space.com

Cristina Bramanti
Project Engineer

Emilio Rapposelli
Senior Engineer

Alta S.p.A.,
Via Gherardesca 5,
56121 Pisa, Italy

Luca d'Agostino
Professor
Department of Aerospace Engineering,
University of Pisa,
Via G. Caruso,
56100 Pisa, Italy

Thermal Cavitation Experiments on a NACA 0015 Hydrofoil

The present paper illustrates the main results of an experimental campaign conducted in the Thermal Cavitation Tunnel of the Cavitating Pump Rotordynamic Test Facility (CPRTF) at Centrospazio/Alta S.p.A. Experiments were carried out on a NACA 0015 hydrofoil at various incidence angles, cavitation numbers, and freestream temperatures, in order to investigate the characteristics of cavitation instabilities and the impact of thermal cavitation effects. Measured cavity length, surface pressure coefficients, and unsteady pressure spectra are in good agreement with the data available in the open literature and suggest the existence of a strong correlation between the onset of the various forms of cavitation and instabilities, the thermal cavitation effects, and the effects induced by the presence of the walls of the tunnel. Further analytical investigations are planned in order to provide a better interpretation of the above results.
[DOI: 10.1115/1.2169808]

Introduction

Propellant feed turbopumps are a crucial component of all primary rocket propulsion concepts powered by liquid propellant engines because of the severe limitations associated with the design of high power density, dynamically stable machines capable of meeting the extremely demanding suction, pumping and reliability requirements of space transportation systems. In these systems cavitation is the major source of performance degradation of the turbopump and provides the necessary flow excitation and compliance for triggering dangerous rotordynamic and/or fluid mechanic instabilities of the machine or the entire propulsion system (POGO autooscillations). In addition, in cryogenic fluids close to saturation conditions thermodynamic phenomena are known to represent the dominant source of cavitation scaling effects.

As a rough initial approximation, the cavitating behavior of a rotating machine can be related to that of a static cascade of hydrofoils. So, the first step for understanding cavitation instabilities and thermodynamic scaling effects is typically represented by experimentation on test bodies in hydrodynamic tunnels.

Cavitation instabilities on hydrofoils are generated by fluctuations of the cavity length caused by the inherent unsteady nature of the flow and the interaction with the pertinent boundary conditions. Franc [1] distinguishes two classes of instabilities: *system* instabilities, in which the unsteadiness comes from the interaction between the cavitating flow and the rest of the system (inlet and outlet lines, tanks, valves), and *intrinsic* instabilities, whose features, such as frequency content, are independent from the rest of the system.

The most known example of system instability is represented by cavitation surge, sometimes observed in supercavitating hydrofoils (Wade and Acosta [2]) as a result of the extreme sensitivity of long cavities to external pressure fluctuations generated by other components of the circuit.

On the other hand, a typical example of intrinsic instability is the so-called "cloud cavitation." When a sheet cavity on a hydrofoil attains a certain size, it starts a violent periodical oscillation, releasing a cloud cavity downstream at each cycle. Kubota et al. [3], using laser Doppler anemometry with a conditional sampling

technique, showed that the shed cloud consists of a large-scale vortex containing a cluster of many small bubbles. The intrinsic nature of this form of instability has been largely elucidated: experiments carried out in various facilities of different characteristics and hydraulic impedances, or in adjustable configurations of the same facility (Tsujimoto, Watanabe, and Horiguchi [4]), lead to very similar Strouhal numbers for cloud oscillations. Further investigations proved the correlation between cloud cavitation and the re-entrant jet generated at the cavity closure as a result of a critical adverse pressure gradient observed for cavity lengths greater than about 50% of the chord (Callenaere, Franc, and Michel [5]; Kawanami, Kato, Yamaguchi, Tagaya, and Tanimura [6]; Sakoda, Yakushiji, Maeda, and Yamaguchi [7]).

Thermal cavitation effects on hydrofoils have been extensively investigated in the past. Kato et al. [8] observed a temperature depression along the cavity, which becomes more significant when freestream temperature increases. At different freestream temperatures, cavities with comparable lengths were found to have comparable thickness, but could be observed at different cavitation numbers (bigger for higher temperatures). The conclusion drawn by Kato and his collaborators was that the reference length scale of thermodynamic cavitation effect must be the separated layer thickness at the leading edge of the cavity. Tani and Nagashima [9] compared the cavitation behavior of a NACA 0015 hydrofoil in water and in cryogenic fluids, showing the important role of the cavity Mach number, different in the two cases because of the different sound speeds.

Yet, a number of aspects of unsteady flow phenomena in cavitating turbopumps and hydrofoils, including their connection with thermal cavitation effects, are still partially understood and imperfectly predicted by theoretical means alone. Technology progress in this field must therefore heavily rely on detailed experimentation on scaled models. To this purpose Centrospazio/Alta S.p.A. has developed a low-cost instrumented facility, the CPRTF, Cavitating Pump Rotordynamic Test Facility (Rapposelli, Cervone, and d'Agostino [10]). The inlet section of the facility has been recently reconfigured allowing for the installation of a Thermal Cavitation Tunnel, TCT (Rapposelli, Cervone, Bramanti, and d'Agostino [11]), where current experiments have been conducted.
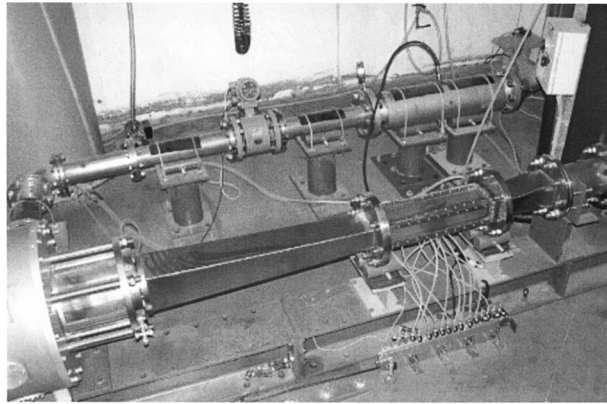
Copyright © 2006 by ASME

Fig. 1 CPRTF with the pump test section (left) and the Thermal Cavitation Tunnel mounted on the suction line

Fig. 3 Pressure coefficient on the suction side of the NACA 0015 hydrofoil in noncavitating conditions for various incidence angles α at room water temperature. CFD simulation at 8 deg incidence angle and room water temperature (solid line). Experimental uncertainty in the evaluation of the pressure coefficient is about 1.5% of the nominal value.

Experimental Apparatus

The CPRTF (Fig. 1) was designed for general experimentation on noncavitating/cavitating turbopumps and test bodies in water under fluid dynamic and thermal cavitation similarity. It has been specifically intended for investigating rotordynamic fluid forces in forced vibration experiments on turbopumps with rotors of adjustable eccentricity and subsynchronous or supersynchronous whirl speeds.

The alternative CPRTF configuration used in the present experimentation is the Thermal Cavitation Tunnel, specifically designed for analyzing 2D or 3D cavitating flows over test bodies. In this configuration the pump is simply used to generate the required mass flow.

The test body, a NACA 0015 hydrofoil with 115 mm chord and 80 mm span length, is mounted on a blind panel on the bottom of the rectangular test section ($120 \times 80 \times 500$ mm). Optical access is allowed through three large Plexiglas windows located on the lateral and top sides of the test section.

Figure 2 shows a schematic of the test section, with the hydrofoil instrumented with 12 pressure taps, 10 on the suction side and 2 on the pressure side. Three taps are located on the bottom panel upstream and 3 downstream of the test section to monitor the inlet/outlet pressure. The incidence angle can be manually adjusted as necessary for the specific experiment.

The tunnel maximum velocity is 8 m/s and the Reynolds number ($\text{Re} = c \cdot V/\nu$) was maintained higher than 5×10^5 in the following tests. The freestream temperature was measured by a digital thermometer mounted inside the water tank. Water was heated by a 5 kW electrical resistance from room conditions to a maximum of 90°C.
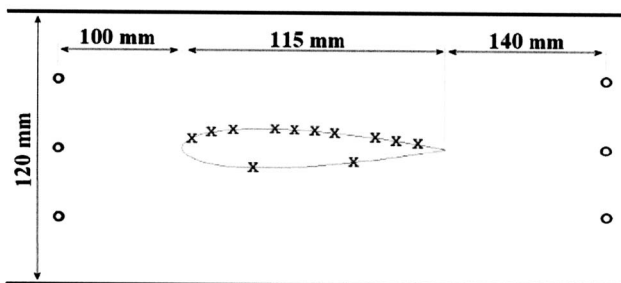

Fig. 2 Schematic of the test section with the NACA 0015 hydrofoil and the locations of the pressure taps on the hydrofoil surface (x), at the section inlet (o) and outlet (o)
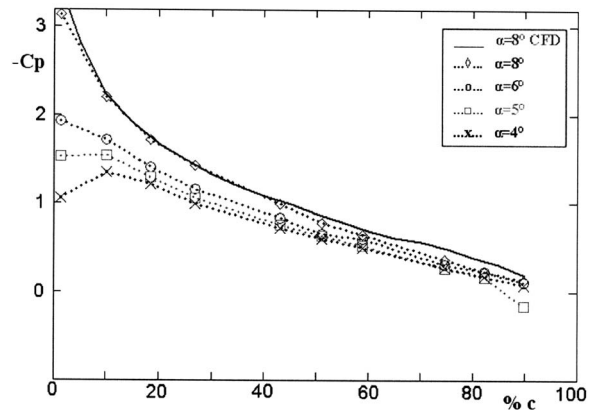
Results and Discussion

Pressure Coefficient. The present experiments have been conducted to analyze the pressure coefficient in noncavitating and inertial/thermal cavitating conditions on the suction side of the NACA 0015 hydrofoil. During these experiments pressure was measured at each pressure tap for constant values of the tunnel velocity, water temperature, incidence angle, and cavitation number,

$$\sigma = (p_{\text{in}} - p_V)/\tfrac{1}{2}\rho V^2.$$

In particular, Fig. 3 shows the pressure coefficient profile in noncavitating conditions for different incidence angles at room water temperature. As expected, the experimental results are different from the surface pressure distribution in unconstrained flow. The lateral constraints to the flow pattern promote "solid blockage" with the increase of the dynamic pressure, the hydrofoil forces and moments at given incidence angle (Kubota, Kato, and Yamaguchi [12]). The absolute value of the pressure coefficient on the suction side of the test body is higher in constrained flows with respect to the unconstrained case: this increase is more significant in test sections where the "solid blockage" effect is more relevant. As a result, different pressure profiles can be measured on the same test body in different test facilities, depending on the position of the lateral constraints (compare, for instance, the data of Fig. 3 with the results obtained by Kjeldsen et al. [13]). In the same way, when the "solid blockage" is more effective, the cavitation inception begins at higher cavitation numbers.

The results have been also compared with a CFD simulation in order to validate the numerical code developed for noncavitating/cavitating flows around 2D or 3D test bodies. The data presented in the figure refer to simulations at 8 deg incidence angle under constrained conditions. Experimental results are in good agreement with the numerical reconstructions.

Figure 4 compares the pressure profiles in cavitating conditions for three different freestream water temperatures at the same cavitation number and incidence angle. At higher temperatures the absorption of the latent heat at the cavity interface increases, reducing the vapor pressure under the unperturbed saturation value. This trend is well reflected in the figure: at 70°C, due to pressure decrement under saturation value, the pressure recovery occurs more upstream than at room temperature.

The experimental uncertainty indicated in the figures has been evaluated taking into account the random oscillations of the acquired data and the precision of the pressure transducers used for the experimentation.
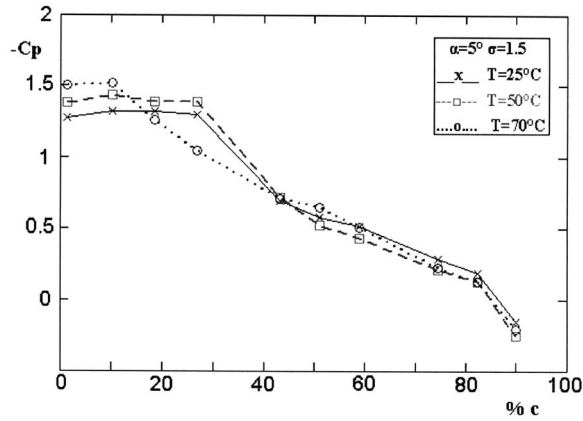
Fig. 4 Influence of thermal cavitation effects on surface pressure distribution on the NACA 0015 hydrofoil at constant angle of attack α and cavitation number σ for several water temperatures T. Experimental uncertainty in the evaluation of the pressure coefficient is about 2% of the nominal value.

Fig. 6 Characteristics of cavity length at 8 deg incidence angle and room water temperature. Experimental uncertainty in the evaluation of the cavity length is about 4% of the chord length.

Cavity Oscillations. A number of experiments were carried out in order to determine the characteristics of the cavity length and oscillations at different incidence angles, cavitation numbers and freestream temperatures. Cavity length for each nominal condition was calculated by taking pictures of the cavitating hydrofoil at a frame rate of 30 fps, during a period of 1 s. The mean cavity length along the span was determined for each picture with a maximum estimated error of 4% of the chord length. As a final result of this process, maximum, minimum and mean value of the 30 cavity lengths were obtained. At the same time, the frequency spectrum of the upstream pressure was measured in each flow condition.

Figure 5 shows the maximum and minimum cavity lengths for various incidence angles at room water temperature. The cavity length and the frequency spectrum of the upstream pressure are shown in Figs. 6 and 7 for the case of 8 deg incidence angle and room water temperature.

Analysis of Figs. 6 and 7 shows that the maximum and minimum cavity lengths provide a good qualitative indication of the cavitation behavior on the hydrofoil at different cavitation numbers. One can recognize three different regimes of cavitation, corresponding to different ranges of values of σ:
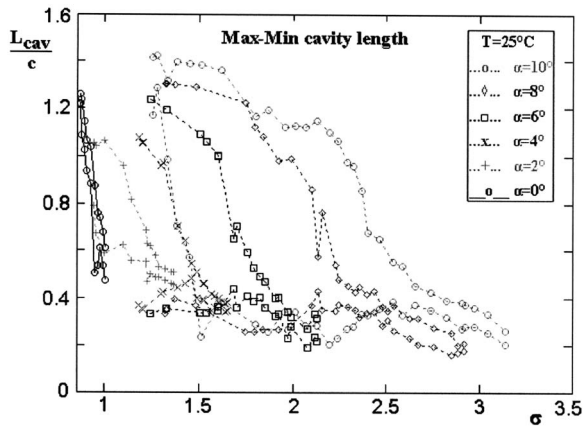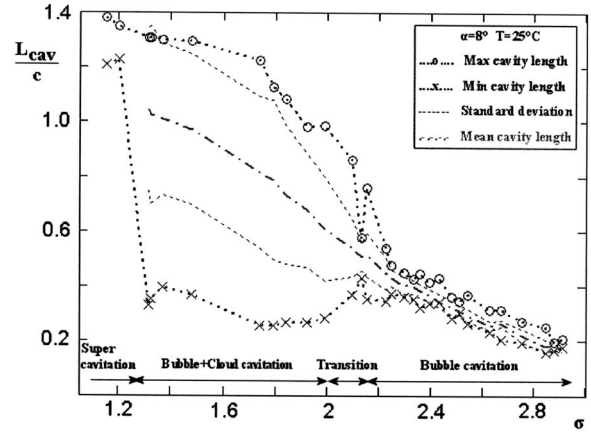
(1) Supercavitation ($\sigma < 1.3$): both minimum and maximum cavity lengths are larger than the chord length. There are practically no cavity oscillations and therefore the frequency spectrum is almost flat.

(2) Bubble+cloud cavitation ($1.3 < \sigma < 2$): the flow pictures show the occurrence of an initial zone of bubbly cavitation, followed by a second zone where the bubbles coalesce and strong cloud cavitation oscillations are observed. The frequency of these oscillations is almost constant at different cavitation numbers with a Strouhal number ($St = f \cdot c / V$) of about 0.2, similar to those obtained by Tsujimoto et al. [4] and Kjeldsen et al. [13]. Other frequencies, multiple of the first, are present in the spectrum. One can speculate that the second frequency might be related to the second, faster re-entrant jet sometimes observed by Sakoda et al. [7]. More likely, since higher frequencies are integer multiples of the fundamental one, they may be the result of the frequency spreading caused by nonlinear effects in the flow field.

(3) Bubble cavitation ($\sigma > 2.1$): after a short transition zone, cloud cavitation disappears. Only the travelling bubble cavitation zone remains, with drastically reduced pressure oscillations (flat frequency spectrum).

Fig. 5 Normalized maximum and minimum lengths of the cavity as function of the cavitation number σ for various incidence angles α at room water temperature. Experimental uncertainty in the evaluation of the cavity length is about 4% of the chord length.
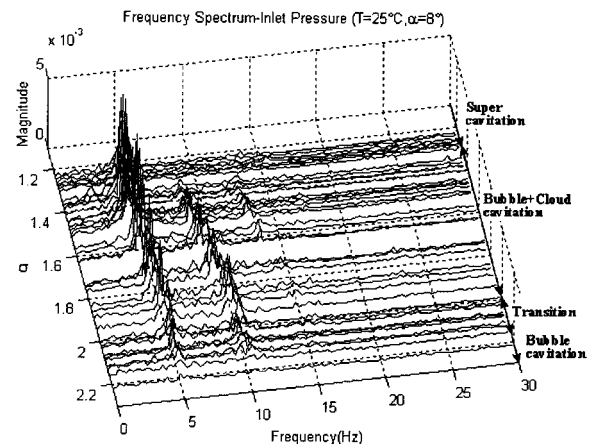

Fig. 7 Frequency spectrum of the upstream pressure at 8 deg incidence angle and room water temperature
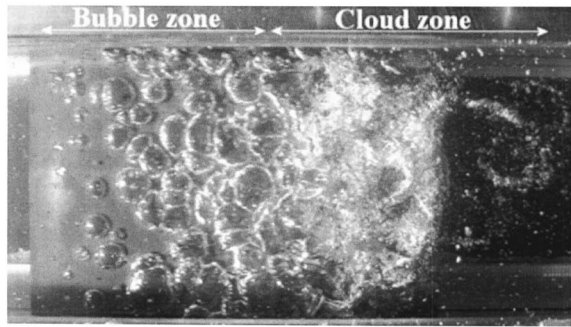
Fig. 8 Typical cavitation appearance in "bubble+cloud" case ($\alpha=4$ deg, $\sigma=1.25$, $T=25°$C)

Fig. 10 Frequency spectrum of the upstream pressure at 8 deg incidence angle and 50°C water temperature

Figure 8 shows the typical aspect of cavitation in "bubble +cloud" case for a particular experimental condition.

Thermal cavitation tests were carried out with a similar procedure for 8 deg incidence angle at two different freestream temperatures (50°C and 70°C). Results are shown in Figs. 9–11.

Figures show that, for higher freestream temperatures, the "bubble+cloud cavitation" zone tends to spread over a wider range of cavitation numbers and to begin at higher values of σ. Similarly, supercavitation also begins at higher cavitation numbers. These findings seem to be in accordance with the results obtained by Kato et al. [8], who compared the temperature depressions in the cavity in water tests at 120°C and 140°C.

At higher freestream temperatures and constant cavitation number, the cavity tends to become thicker and longer, even when there are no oscillations ("bubble cavitation" zone), as shown in Fig. 12.

The above results appear significantly different from the typical data presented in the open literature, where at higher temperatures the cavitation breakdown tends to be shifted towards lower cavitation numbers and the cavity is shorter. A suitable explanation for this apparent disagreement can be given taking into account the influence of the lateral constraints. The observed increase of the cavitation thickness at higher temperatures, when the lateral wall is sufficiently near to the suction side, can promote cavity spreading along the longitudinal direction. This effect is more significant at higher incidence angles, for which the flow is forced to pass through a reduced cross section.

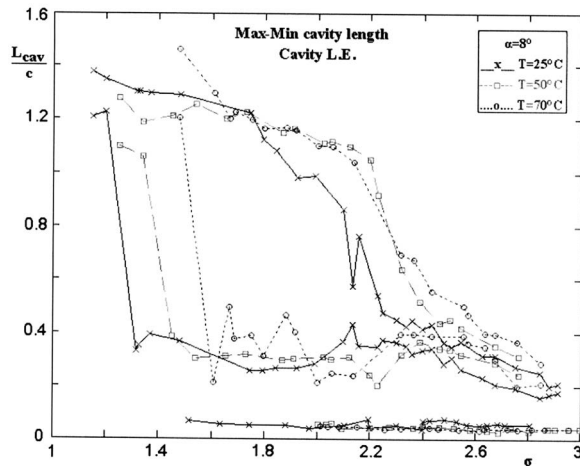The above statement is confirmed by analysis of Figs. 4 and 9.

Fig. 11 Frequency spectrum of the upstream pressure at 8 deg incidence angle and 70°C water temperature

Fig. 9 L.E., maximum and minimum lengths of the cavity for three different water temperatures T at 8 deg incidence angle. Experimental uncertainty in the evaluation of the cavity length is about 4% of the chord length.
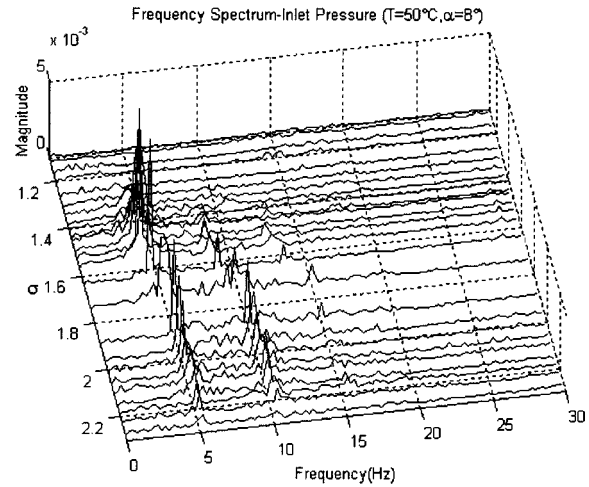

Fig. 12 Cavity thickness for three different water temperatures T at the same incidence angle α and cavitation number σ (α =8 deg, σ=2.5)

Fig. 13 Cavitation appearance at higher freestream temperature (α=8 deg, σ=2, T=70°C)

Fig. 15 Normalized pressure drop caused by the hydrofoil for three different water temperatures T at 8 deg incidence angle. Experimental uncertainty in the evaluation of the pressure drop is about 5% of the nominal value.

At a lower incidence angle (α=5 deg) Fig. 4 shows that the steady part of the cavity tends to become shorter at higher temperature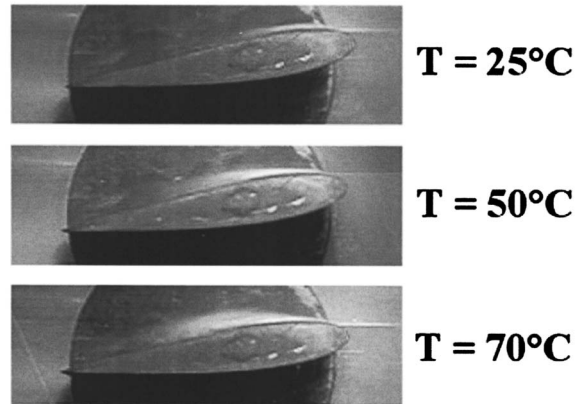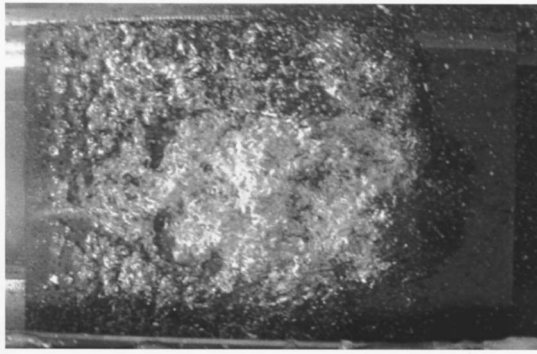s (in accordance with the traditional results), while at a higher incidence angle (α=8 deg) Fig. 9 highlights the outlined opposite behaviour for the maximum cavity length.

Cavitation at higher freestream temperatures looks quite different: bubbles are smaller and tend to coalesce more easily, resulting in a narrower and less defined "bubble zone" compared to the "cloud zone" (Fig. 13).

Thermal Effects on the Pressure Drop. Another set of experiments were conducted in order to determine the pressure drop caused by the hydrofoil at various incidence angles, freestream temperatures, and cavitation numbers. Tests were performed using a differential pressure transducer installed between one of the pressure taps upstream of the test body and the corresponding pressure tap downstream. The pressure drop obtained using this procedure represents therefore a "punctual" value that cannot be directly related to the drag, but should nevertheless exhibit a similar general behavior. Figures 14 and 15 show, respectively, the results obtained for different incidence angles and for the same incidence angle at different freestream temperatures.

The experimental uncertainty indicated in the figures has been evaluated taking into account the random oscillations of the acquired data and the precision of the pressure transducers used for
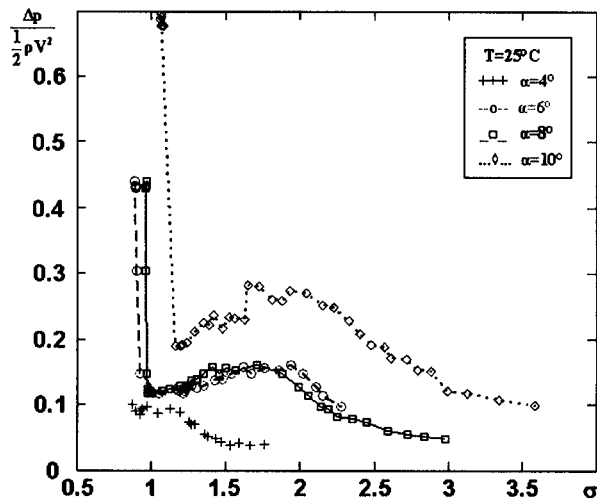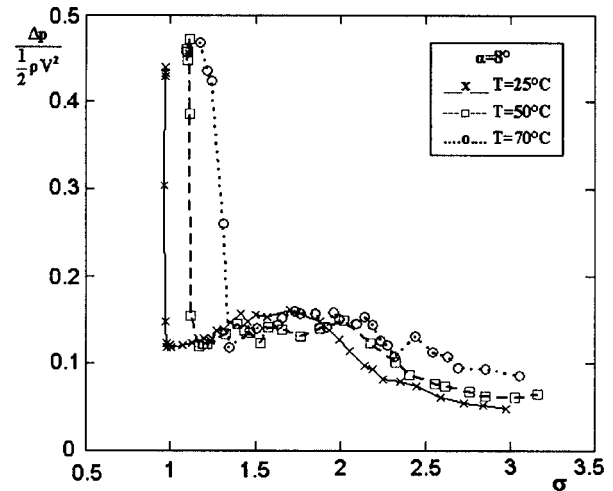
the experimentation.

The figures show a sudden rise of the pressure drop for cavitation numbers slightly smaller than those corresponding to the onset of supercavitation. At higher freestream temperatures this "breakdown" effect occurs at higher cavitation numbers, just like supercavitation and cloud cavitation oscillation.

This behavior, strictly related to the increase of cavity thickness (Fig. 12), is different from that observed on hydrofoils in free flows and in cascades, probably as a result of the more significant "solid blockage" effect (in a free flow there is no solid blockage, in a staggered cascade solid blockage is less effective because the blades overlap only partially).

Conclusions

A number of experiments were carried out on a NACA 0015 hydrofoil in order to investigate the correlation between the onset of the various forms of cavitation and instabilities, the thermal cavitation effects and the wall effects. The main results of the investigation are:

(a) At increasing values of the cavitation number three different cavitation zones develop: supercavitation, bubble+cloud cavitation, and bubble cavitation. Each zone corresponds to a different behaviour of the upstream pressure frequency spectrum.

(b) At higher freestream temperatures, both cloud cavitation oscillation and supercavitation begin at higher cavitation numbers and, for the same cavitation number, cavity tends to become thicker and longer.

(c) The sudden rise of the pressure drop caused by the hydrofoil shifts towards higher cavitation numbers at higher freestream temperatures, as a consequence of the retarded onset of supercavitation.

The last two results could be explained taking into account the interaction between the greater compliance of the cavity and the "solid blockage" effect caused by the tunnel walls, more significant with respect to hydrofoils in free flows and cascades.

Further analytical investigations are planned in order to provide a better interpretation of the above results.

Acknowledgment

Fig. 14 Normalized pressure drop caused by the hydrofoil for various incidence angles α at room water temperature. Experimental uncertainty in the evaluation of the pressure drop is about 5% of the nominal value.

Nomenclature

$$\begin{aligned}
c &= \text{chord length} \\
C_p &= \text{pressure coefficient} \\
f &= \text{frequency} \\
L_{\text{cav}} &= \text{cavity length} \\
p &= \text{pressure} \\
p_{\text{in}} &= \text{hydrofoil upstream pressure} \\
p_V &= \text{vapor pressure} \\
\text{Re} &= \text{Reynolds number} \\
\text{St} &= \text{Strouhal number} \\
T &= \text{freestream temperature} \\
V &= \text{freestream velocity} \\
\alpha &= \text{incidence angle} \\
\nu &= \text{kinematic viscosity} \\
\rho &= \text{density} \\
\sigma &= \text{cavitation number}
\end{aligned}$$

References

[1] Franc, J. P., 2001, "Partial Cavity Instabilities and Re-Entrant Jet," *Proceedings of CAV 2001—International Symposium on Cavitation*, Pasadena, California.

[2] Wade, R. B., and Acosta, A. J., 1966, "Experimental Observations on the Flow Past a Plano-Convex Hydrofoil," J. Basic Eng., **87**, pp. 273–283.

[3] Kubota, A., Kato, H., Yamaguchi, H., and Maeda, M., 1989, "Unsteady Structure Measurement of Cloud Cavitation on a Foil Section Using Conditional Sampling Technique," J. Fluids Eng., **111**, pp. 204–210.

[4] Tsujimoto, Y., Watanabe, S., and Horiguchi, H., 1998, "Linear Analyses of Cavitation Instabilities of Hydrofoils and Cascades," *Proceedings of U.S.–Japan Seminar: Abnormal Flow Phenomena in Turbomachinery*, Osaka, Japan.

[5] Callenaere, M., Franc, J. P., and Michel, J. M., 1998, "Influence of Cavity Thickness and Pressure Gradient on the Unsteady Behaviour of Partial Cavities," *Proceedings of the 3rd International Symposium on Cavitation*, Grenoble, France.

[6] Kawanami, Y., Kato, H., Yamaguchi, H., Tagaya, Y., and Tanimura, M., 1997, "Mechanism and Control of Cloud Cavitation," J. Fluids Eng., **119**, pp. 788–795.

[7] Sakoda, M., Yakushiji, R., Maeda, M., and Yamaguchi, H., 2001, "Mechanism of Cloud Cavitation Generation on a 2-D Hydrofoil," *Proceedings of CAV 2001—Int. Symposium on Cavitation*, Pasadena, California.

[8] Kato, H., Maeda, M., Kamono, H., and Yamaguchi, H., 1996, "Temperature Depression in Cavity," *Proceedings of Fluids Engineering Division Conference*, San Diego, USA.

[9] Tani, N., and Nagashima, T., 2002, "Numerical Analysis Of Cryogenic Cavitating Flow On Hydrofoil—Comparison Between Water and Cryogenic Fluids," *Proceedings of 4th International Conference on Launcher Technology*, Liege, Belgium.

[10] Rapposelli, E., Cervone, A., and d'Agostino, L., 2002, "A New Cavitating Pump Rotordynamic Test Facility," *Proceedings of AIAA Joint Propulsion Conference and Exhibit*, Indianapolis, Indiana.

[11] Rapposelli, E., Cervone, A., Bramanti, C., and d'Agostino, L., 2002, "A New Cavitation Test Facility at Centrospazio," *Proceedings of the 4th International Conference on Launcher Technology*, Liege, Belgium.

[12] Kubota, A., Kato, H., and Yamaguchi, H., 1992, "A New Modelling of Cavitating Flows: A Numerical Study of Unsteady Cavitation on a Hydrofoil Section," J. Fluid Mech., **240**, pp. 59–96.

[13] Kjeldsen, M., Effertz, M., and Arndt, R. E. A., 1998, "Investigation of Unsteady Cavitation Phenomena," *Proceedings of U.S.–Japan Seminar: Abnormal Flow Phenomena in Turbomachinery*, Osaka, Japan.

Exit Flow Field and Performance of Axial Flow Fans

S. C. Yen[1]

Department of Mechanical and Mechatronic
Engineering,
National Taiwan Ocean University,
Keelung, Taiwan 202, ROC

Frank K. T. Lin

Mechanical Industry Research Laboratories,
Industrial Technology Research Institute,
Hsinchu, Taiwan 310, ROC

Flow fields near the exit and the global performance parameters of the various types of axial flow fans are studied with Particle Image Velocimetry and a standard AMCA 210 flow bench. The fans used in this study included the shrouded, shroudless, and winglet-blade types. The velocity vectors, streamlines, vorticity contours, velocity distributions, and performances are presented and discussed. The flow patterns on the radial and axial planes show that a vortex always exists near the exit of the fans at various impeller angles. The experimental results demonstrate that the shrouded fan with winglets has the most stable flow field and the best fan performance. [DOI: 10.1115/1.2169809]

Keywords: axial flow fan, PIV, fan performance, winglet-blade

1 Introduction

The axial flow fan has been widely studied due to its versatile applications. In 1951, Eck [1] defined many geometric parameters and did a serious of systematic analyses. These works improved the capability to evaluate fan performance. The coupled theory of the fan and duct designs for an air moving system were developed by Wallis [2]. Bleier [3] investigated the explanations of these concepts and presented sample calculations to reach the preset requirements in air volume, static pressure, brake horsepower, and efficiency.

Recently, due to the high unsteadiness in the axial flow fan, many researchers have studied the flow field between the blades. The unsteadiness is induced by the velocity fluctuations when the flow passes through the small gaps between the blades. The unsteadiness makes it difficult for the flow field to meet the desired operation conditions. To calibrate the velocity fluctuations, three kinds of velocimetry have usually been used: hot wire anemometers (HW), laser Doppler velocimetry (LDV), and particle image velocimetry (PIV).

The HW method are popularly used. Eduardo et al. [4] produced a series of papers on the rotating stall phenomenon caused by changing the blade pitch of low hub-to-tip ratio fans. They found that tip blockage plays a main role in the inception and disappearance of the rotating stall. Koop and Martinuzzi [5] measured the mean velocity vector and derived the exit angle of an automotive engine cooling fan. They also found the mean flow angle is close to a local minimum of the probability density function of the swirl angle. Sandra et al. [6] investigated how the change of the blade pitch has a major influence on the unsteady operation of the axial flow fan. In their study, they measured the flow field at different radial locations on the inlet and exit planes. They revealed that the highest levels of unsteadiness are located at the hub and shroud regions. Ravindranath and Lakshminarayana [7] studied the wake of a compressor rotor blade. They found that the largest velocity decay appears at the trailing edge of the blade and that the wake width in the trailing edge region varies rapidly.

In the applications of LDV calibrations, Myung and Baek [8] measured a highly forward-swept axial flow fan to probe the leakage flow, leakage vortex, hub vortex, and wake in different operating conditions. The streamwise variation of the velocity in the wake cannot be neglected, especially in turbulent flows. Jang et al. [9] studied the vertical flow field in a propeller fan and evaluated its structure and unsteady behavior with LDV. They found that

three vortex structures are formed near the propeller fan rotor tip: the tip vortex, the leading edge separation vortex, and the tip leakage vortex. They also claimed that the unsteady behavior of the tip and leading edge separation vortices dominates the pressure fluctuations.

The third method is the PIV measurements. Du et al. [10] measured the three-dimensional velocity flow fields of an axial flow fan at the designed flow rates. This measurement shows the existence of a counterclockwise separation vortex near the suction side of the blade. Estevadeordal et al. [11] have studied the axial flow fan at low speed. The instantaneous and time-average velocity were probed at the leading-edge, trailing-edge, and suction and pressure surfaces of the blade by PIV and panel code solution. They demonstrated that the PIV results matched the panel code solution in their design. Lee et al. [12] measured the flow around an isolated axial flow fan. They announced that the strong vortices rotating in the counterclockwise direction are shed from the trailing edges of the blade and that the local maximum values of axial and radial turbulent intensities appear in an alternating manner.

In addition to the flow field analysis, many researchers have focused on output performance, including the fan efficiency and the head, flow, and power coefficients. Shimada et al. [13] carried out experiments to determine the performance and effectiveness of the shroudless and other types of shrouded axial flow with various types of blades. The fan with a fixed shroud and the labyrinth seal prevented the influence of the tip clearance, allowing it to achieve higher fan performance and lower fan noise than the shroudless fan. Oh and Kang [14] used the viscous flow calculation method to study a small fan. They showed dual performance characteristics: radial-type fans move with low flow rates, and axial type fans correspond to high flow rates. They predicted that the head and power coefficients would rise sharply when the flow coefficient is decreased from 0.267 to 0.233, and that the head and power coefficients would rapidly rise at low flow rates. Stinnes and Backstrom [15] presented an experiment involving axial fans in an air-cooled heat exchanger system. They found that fan power consumption is completely independent of off-axis inflow angles up to 45 deg, that the fan pressure rise is independent of off-axis inflow angle, and that the decrement in static pressure rise is equal to the dynamic pressure based on the cross-flow velocity component at the fan inlet. Mizuno and Kikuchi [16] studied the ranges of the cone angle of the diagonal hub and the depth of the fan, and two dimensionless shape parameters were presented and confirmed through experiments. They revealed that a fan with a diagonal flow hub has strong performance and good efficiency and is useful for engine cooling radiator systems.
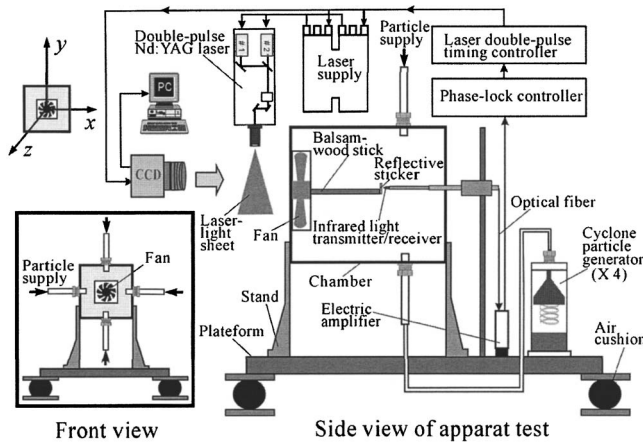
Fig. 1 Experimental setup

For general application, the performances of the fans are defined by the flow rate, the pressure differences, etc. at the exit. In this paper, an experimental study on the shrouded, shroudless, and winglet-blade axial flow fans with various impeller angles are demonstrated. The main goals of this research are: (1) to establish the instantaneous and ensemble average flow fields near the exit of these fans by using PIV measurements, (2) to investigate the flow patterns and the velocity distributions, and (3) to compare the

(a) Shroused Axial Flow Fan
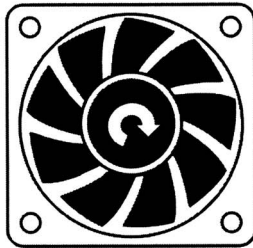
(b) Schemic of Wingleted-Blade
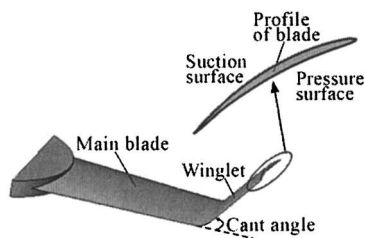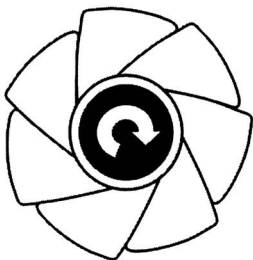
(c) Shroudless Axial Flow Fan

Fig. 2 Outlines and specifications of the fans

global performance parameters with various flow coefficients by using an AMCA wind tunnel test. With these goals achieved, the flow field and performances of the fans can be designed more efficiently.

2 Experimental Arrangements

2.1 Experimental Setup. The experimental apparatus for testing the axial flow fans is presented in Fig. 1. The loading platform is made of $50 \times 30 \times 2$ cm aluminum alloy. Four supporting air cushions are used to eliminate the vibration caused by the rotation of these fans. The chamber size is $30 \times 30 \times 30$ cm. Four aluminum pillars are applied to hold the chamber in a fixed position. The polyamide (PM) particles are seeded into the four particle supply tubes and spread into the chamber by the four cyclone particle generators. The pulse laser is scattered by the plastic particles. The diameters of these particles range from 35 to 70 μm, and the specific weight is 1.03 at 25°C. Ignoring the effect of turbulent diffusion, the relaxation time constant is estimated to be less than 6.25×10^{-5} s, and the Stokes number is at the order of 10^{-6}. Thus, the slip between the flow and particles can be neglected in this experiment. According to Mei's method [17], the seeding particles are estimated to be capable of fluctuating at up to 3 kHz. A piece of Balsam-wood with a reflector is attached to the hub of the fan. A diffusion-scan type Yamatake-Honeywell photoelectric switch is used to detect the fan impeller angle by sensing the reflection signal from the reflector. The photoelectric switch consists of a microdiameter optical fiber infrared light transceiver (model HPF-D018) and a high gain electric amplifier (model HPX-F1). The 0.75 mm diameter transceiver produces a beam of modulated infrared light and receives the target-reflected optical signals. The maximum sensing distance and minimum target sizes are 15 mm and 0.2 mm, respectively. The photoelectric amplifier has a frequency response limit of 20 kHz. Via shunting with a 1.2 kΩ resistor, the output currents are converted into almost square-wave voltage signals. Subsequently, the output voltages are fed into a phase-lock controller in the PIV system.

2.2 Flow Field Measurement. The PIV image acquisition system includes a double-pulse Nd:YAG laser, a CCD camera, and electronic synchronizer consisting of phase-lock and laser double-pulse timing controllers. As shown in Fig. 1, two independently controllable pulse lasers are packed into one casing to generate the consecutive double-pulses. Each laser employs a flash lamp-pumped Nd-YAG rod in a thermally compensated resonator to generate radiation at 1064 nm via an IR head. The maximum pulse rate is 30 double-pulses per second. The maximum pulsing energy is 90 mJ. The pulse width is between 3–5 ns. Jittering is ±0.5 ns. The green light beams, at 532 nm leaving the laser head, are expanded as a 20 deg light sheet through a laser-light sheet generator, which is installed at the exit of the laser-head. The thickness of the laser-light sheet is adjusted to about 0.5 mm. For image grabbing, the particle images are recorded by a Roper Scientific's Megaplus Model ES 1.0 CCD camera with a resolution of 1008×1018 pixels. The pixels are 9 microns square and can be operated continuously or in an external trigger mode. The pixel array is zoomed and mapped to a physical region of approximately 90 mm so that the spatial resolution is about 90 μm/pixel. The external trigger mode is applied in this study by using a timing-controlled trigger signal from the electronic controller. The camera has an output channel data rate of 20 MHz, which gives a maximum frame rate of 30 frames per s. Exposure times of 0.125– 33 ms are possible with the camera's electronic shutter. When operated in frame straddling mode, the maximum framing rate becomes 15 pairs per second. In this study, each image occupies about 2 MB, and 500 image pairs are taken for every operation. The electronic synchronizers consist of a phase-lock signal coordinator and a laser double-pulse timing controller. The phase-lock

Table 1 Fan geometry parameters

Fan	Fan-A	Fan-B	Fan-C
Shroud	Yes	Yes	No
Winglet	No	Yes	No
Diameter (mm)	67	67	90
Number of blades	9	9	7
Rotor speed (rpm) at 12V	4800	3300	2400
Hub-to-tip ratio at rotor inlet	0.88	0.88	0.71
Maximum blade thickness (mm)	1.3	1.3	1.85
Tip clearance (mm)	3	3	NA
Hub inclination (degree)	50	50	30
Chord length at tip(mm)	20	15	40
Chord length at hub(mm)	15.5	10	36.3
Cant angle (degree)	NA	42	NA
Winglet chord length(mm)	NA	15	NA
Winglet span length(mm)	NA	8	NA

Blade profile   suction surface:
$$Z = (1.8 \times 10^3)Y^4 - (2.8 \times 10^5)Y^3 + (1.7 \times 10^7)Y^2 - (4.4 \times 10^8)Y + (4.3 \times 10^9)$$

pressure surface:
$$Z = (1.9 \times 10^3)Y^4 - (3.0 \times 10^5)Y^3 + (1.8 \times 10^7)Y^2 - (4.6 \times 10^8)Y + (4.5 \times 10^9)$$

lead edge arc radius:
$$R_t = (-4.6 \times 10^3)t^2 - (3.6 \times 10^5)t + (-7.1 \times 10^6)$$

signal coordinator receives a series of photoelectric switch signals from an encoder, which is a reflective sticker on the hub of the fan. The encoder has a resolution of 360 pulses/revolution. The output signals of the phase-lock coordinator are fed to the laser double-pulse timing controller according to the settings. The laser double-pulse timing controller bears the output signals for controlling the timing of the lamp flashing and Q-switching of the lasers as well as the shuttering of the camera.

The PIV postprocessing system is composed of an image interrogation and a post interrogation system. Two consecutive image frames are analyzed by using the cross-correlation technique [18]. This technique is embedded in the software VidPIV4, obtained from Optical Flow Systems. It calculates the average displacement of local particle groups in the consecutive images. The in-

terrogation window is set to 32×32 pixels. In order to reduce the velocity bias in the regions of large velocity gradients, the ratio of the displacement of the double-exposed images to the length of the interrogation area is held to be smaller than 1/4, as suggested by Keane and Adrian [19]. Filtering and interpolation are used to identify outliers and then to regenerate the missed values. The global filter finds all the globally inconsistent values, while the local filter finds those that may be globally consistent but are not smoothly consistent with the local variations in vector magnitude and direction. This method of interpolation is based on a weighted mean technique that replaces the values at filtered sites in an iterative manner by replacing those with the greatest number of surrounding valid values first, working toward those that are less favorably positioned, for accurate and reliable interpolation. Adaptive cross correlation, employing smaller interrogation size and smaller grid spacing, is finally applied to the vector field generated from the regular procedure of cross correlation, filtering (global and local), and interpolation to provide higher resolution and accuracy than the first pass. A series of instantaneous vector fields are required to calculate the ensemble averages. By combining a sufficient number of vector fields, the mean velocity field can be obtained. In this study, the mean velocity field of the axial flow fan is obtained by ensemble average of 500 instantaneous image pairs.

2.3 Fan Performance Tests. The shapes and specifications of the axial flow fan are shown in Fig. 2, and the geometry parameters are tabulated in Table 1. The axial flow fan facilities used in this paper are shown schematically in Fig. 3, and they are similar to those used by Chung [20]. The axial flow fan is clamped laterally in the test section of the AMCA 210 flow bench (ANSI/AMCA Standard 210-85, 1985), which serves as a device for measuring the flow rate. The fresh air is drawn into the test section by a suction fan, which is attached to the AMCA 210 flow bench. Three different sizes of metal mesh are set at the upstream and downstream of the nozzles to regulate the flow. By averaging the static pressures measured from the plenum of the AMCA 210, the flow rate can be calculated from the pressure difference. The input power on the fan can be measured by recording the input voltages and currents.
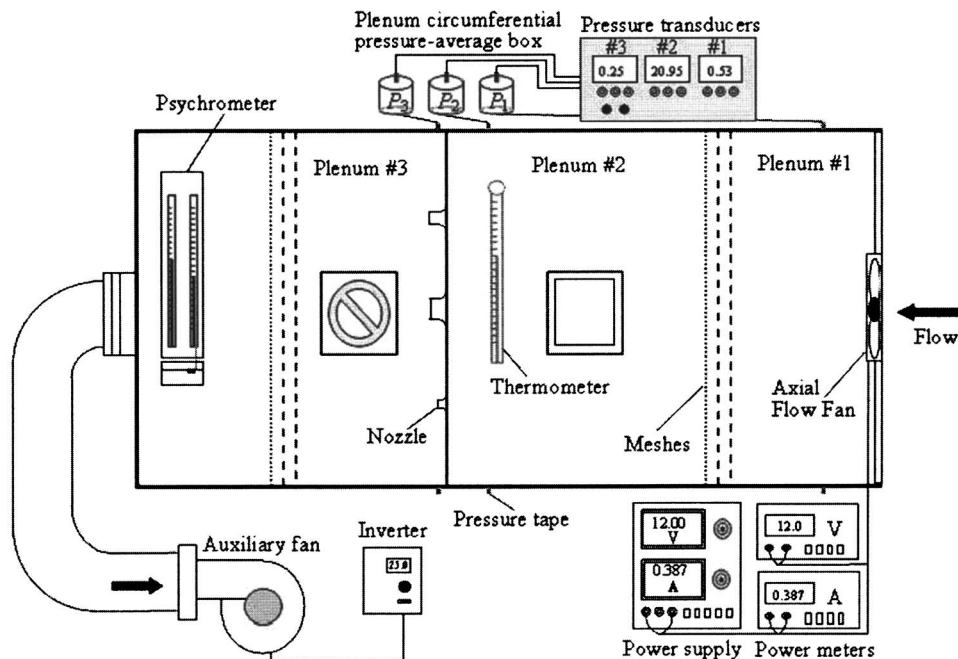

Fig. 3 Schematic of system setup

2.4 Dimensional Analysis in the Fan. Dimensional analysis in the axial flow fan has been studied by many researchers [3,4,21]. Deriving from the Π-products theorem to obtain the dimensionless variables: the head coefficient Ψ, the flow coefficient Φ, the power coefficient Λ, and the fan efficiency η, which are defined as follows:

$$\text{Head coefficient } \Psi = \frac{\Delta P_s}{\rho N^2 D^2} \qquad (1)$$

$$\text{Flow coefficient } \Phi = K\frac{Q}{ND^3} \qquad (2)$$

$$\text{Power coefficient } \Lambda = \frac{\wp}{\rho N^3 D^5} \qquad (3)$$

$$\text{Fan efficiency } \eta = \Psi\Phi/\Lambda \qquad (4)$$

where ΔP_s is the static pressure rise, ρ is the density of the air, N is the rotor speed, D is the fan diameter, Q is the volume flow rate, K is a constant depending on the hub-to-tip ratio [3], and $\wp$ is the fan power.

2.5 Error Analysis. In this paper, the particle images are recorded by a Roper Scientific's Megaplus Model ES 1.0 CCD camera combining the highest resolution (1008×1018 pixels) with the highest frame rate (30 Hz). The current field of view (≈ 9 $\times 9$ cm^2) corresponds to a spatial resolution of 90 microns/pixel. In the velocity interpolation process, the inverse-distance weighting algorithm

$$\tilde{V}_p = \frac{\displaystyle\sum_{k=1}^{N} W_k V_k}{\displaystyle\sum_{k}^{N} W_k}, \qquad (5)$$

is applied for each velocity vector frame. In Eq. (5), $\tilde{V}_p$ is the interpolated velocity at node point p, V_k is the measured velocity, and W_k is the weighting function. The weighting function employed in the present study is $1/r^2$, where r is the distance between the location with measured velocity V_k and the node to be interpolated. According to Davis [22] and Hart [23], the variance σ^2 of an interpolated velocity at node p can be approximated as

$$\sigma^2 = (\tilde{V}_p - V_p)^2 \approx \frac{\displaystyle\sum_{k=1}^{N} W_k \gamma(d_{kp})}{\displaystyle\sum_{k=1}^{N} W_k}, \qquad (6)$$

where the standard variance of $\sigma = \sqrt{\sigma^2}$, and $\gamma(d_{kp})$ is the semi-variance over a distance d_{kp} represented by the separation between

Fig. 4 Flow patterns on radial plane flows of Fan-A, $z/D_{\text{Hub}} = 1.0$, $N = 4800$ rpm, at (*a*) $\theta = 0$ deg; (*b*) $\theta = 10$ deg; (*c*) $\theta = 20$ deg; and (*d*) $\theta = 30$ deg, respectively

Journal of Fluids Engineering

MARCH 2006, Vol. 128 / **335**

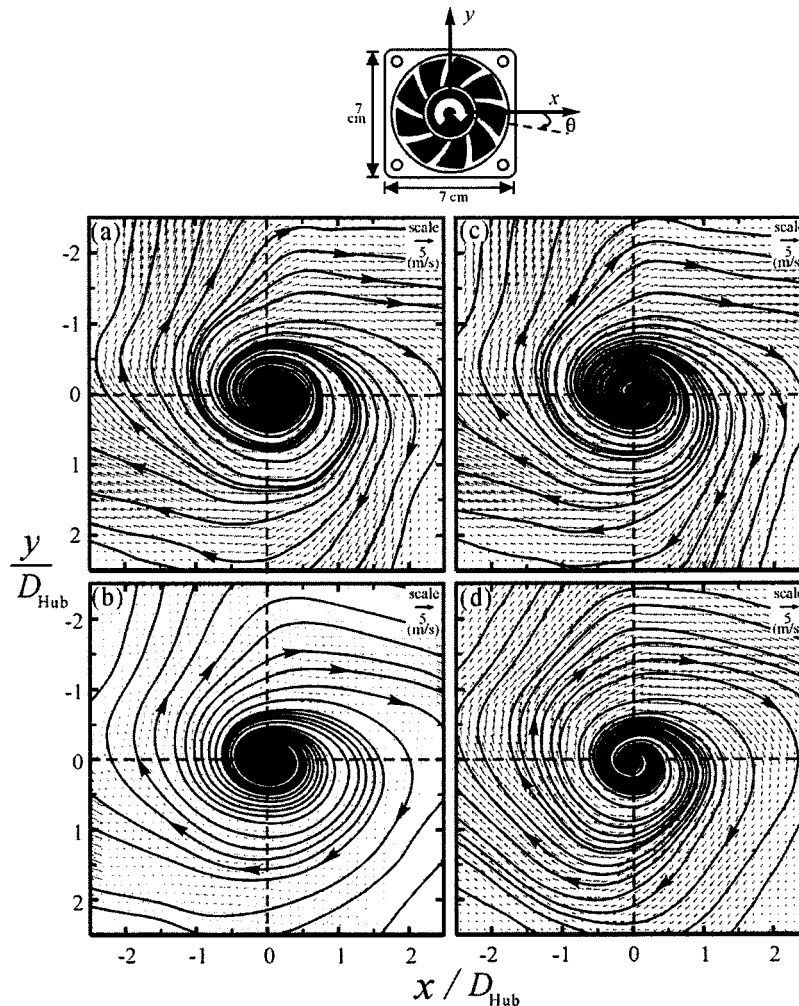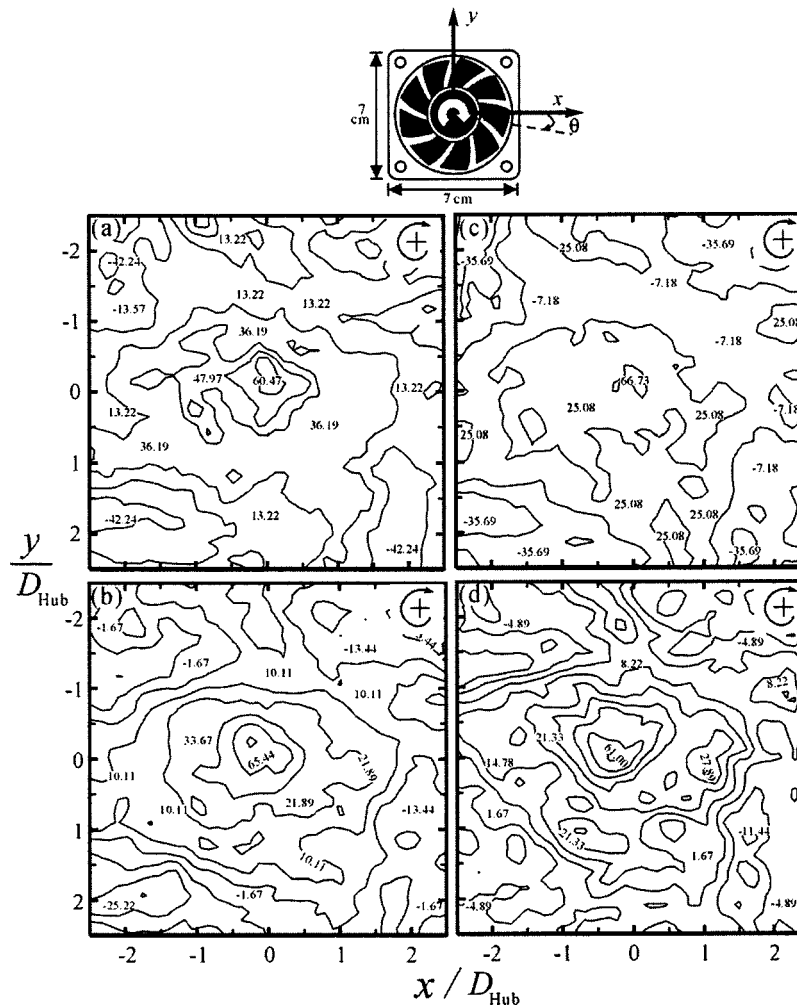**Fig. 5 Vorticity contour on radial plane of Fan-A, $z/D_{\text{Hub}}=1.0$, $N=4800$ rpm, at (*a*) $\theta=0$ deg; (*b*) $\theta=10$ deg; (*c*) $\theta =20$ deg; and (*d*) $\theta=30$ deg, respectively**

the points k and p. The semivariance $\gamma(d_{kp})$ can be estimated as

$$\gamma(d_{kp}) = \frac{\sum (\tilde{V}_p - \tilde{V}_{p+d})^2}{2N}, \qquad (7)$$

which is the sum of the squared differences between measured velocities ($\tilde{V}_p, \tilde{V}_{p+d}$) of pairs of points ($N$ pairs in total) separated by distance d_{kp}. Using this approximation, the ratios between the standard variances and the interpolated velocities (i.e., $\sigma/\tilde{V}_p$) are approximately 10–15%. This estimation of error is in general consistent with the analysis conducted by Spedding and Rignot [24] using the weighting function $W_i=1/r$.

3 Results and Discussion

In an attempt to understand the complex flow phenomena in axial flow fans, the following procedures are implemented: (1) using a PIV measurement system to calibrate the instantaneous and ensemble average flow field in the downstream, (2) discussing the flow field patterns and mean velocity distributions on radial and axial planes, and (3) evaluating the global performance parameters with different flow coefficients regulated in the AMCA 210 wind tunnel.

3.1 Velocity Flow Field

3.1.1 Flows in Radail Planes

3.1.1.1 Velocity vectors and vorticity contour. The PIV-measured velocity vector field and vorticity contour field of Fan-A at $z/D_{\text{Hub}}=1.0$ are shown in Figs. 4 and 5. The streamline patterns are obtained by the shooting method. The vorticity Ω_z can be calculated from the mean velocity data by using the central difference scheme defined as follows:

$$\Omega_z = \frac{\partial V_y}{\partial x} - \frac{\partial V_x}{\partial y} \qquad (8)$$

where V_x and V_y are velocity components measured in x and y directions, respectively. The vortex rotating clockwise is defined positively. Figure 4 shows the flow pattern of Fan-A as impeller angle $\theta=0$, 10, 20, and 30 deg, respectively. A vortex rotating clockwise is observed at the center part of the flow field, and the streamlines are radial-symmetric. Figure 5 shows the vorticity contour field derived from Fig. 4. It also shows that a vortex of $\Omega_z \approx +60$ s^{-1} is located at the flow field center.

3.1.1.2 Velocity distributions. Figures 6(*a*) and 6(*b*) show that the horizontal and vertical velocity distributions along the radial plane in the whole field are similar and symmetric with the hub center. In Fig. 6(*c*) as $\theta=0$, 10, 20, and 30 deg, respectively,
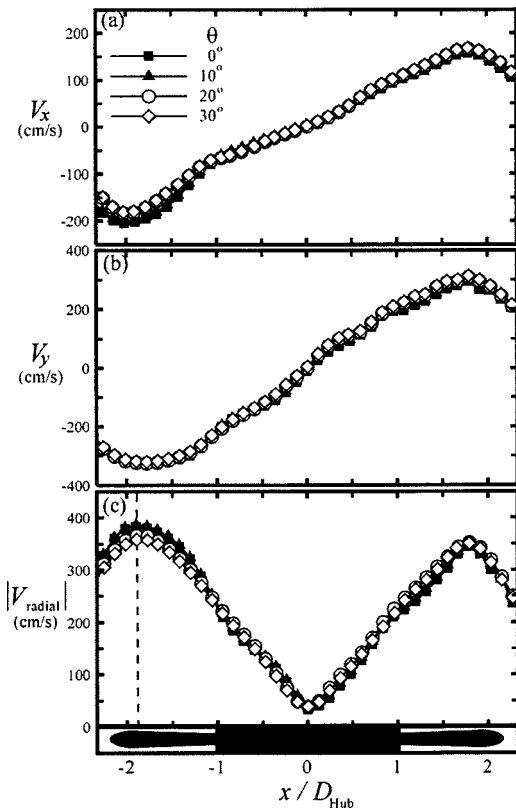
Fig. 6 Velocity profiles of Fan-A on the radial plane, z/D_{Hub} =1.0, N=4800 rpm, for (a) V_x, (b) V_y, and (c) $|V_{radial}|$, respectively
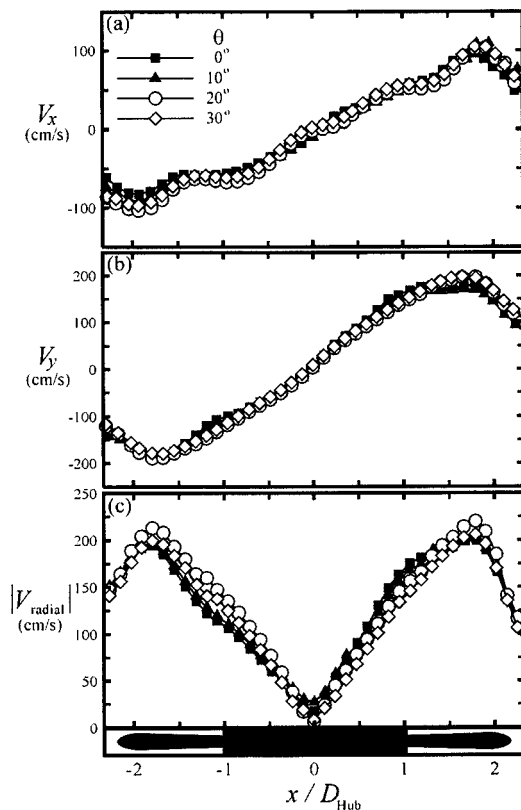

Fig. 7 Velocity profiles of Fan-B on the radial plane, z/D_{Hub} =1.0, N=3300 rpm, for (a) V_x, (b) V_y, and (c) $|V_{radial}|$, respectively
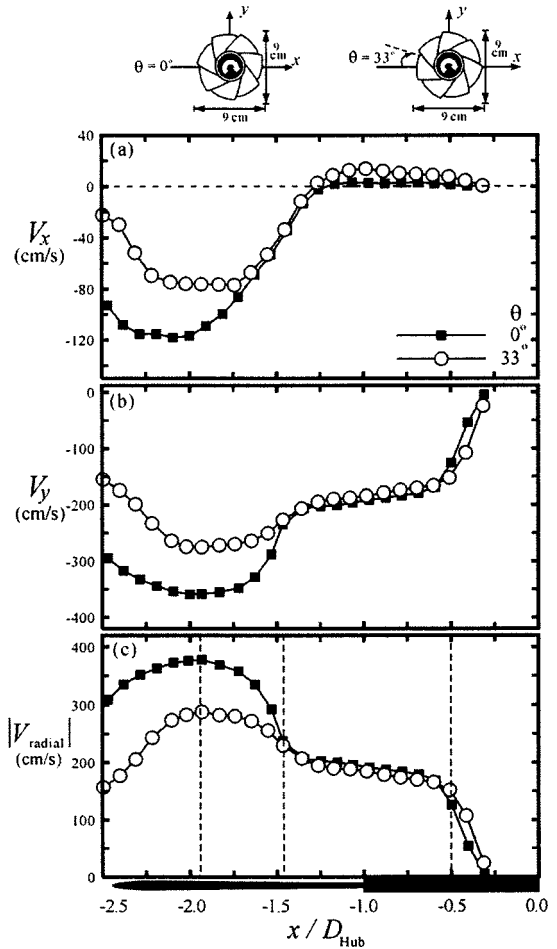

Fig. 8 Velocity profiles of Fan-C on the radial plane, z/D_{Hub} =1.0, N=2400 rpm, for (a) V_x, (b) V_y, and (c) $|V_{radial}|$, respectively

$|V_{radial}|_{min}$ appears at the hub center and $|V_{radial}|_{max} \approx 380$ cm/s at the position of $x/D_{Hub} \approx \pm 1.8$, which is at the position of $2L/3$, where L is the distance measured from the tip of blade to hub center. Figure 7 shows the radial velocity distributions in various impeller angles at $z/D_{Hub}=1.0$ in Fan-B. The velocity curves in Figs. 7(a) and 7(b) are similar to those in Fig. 6. The maximum velocities $V_x \approx |120|$ cm/s and $V_y \approx |210|$ cm/s are both smaller than those in Fan-A. At the origin ($x/D=0$, $z/D=0$), it shows a smaller slope deriving $\Omega_z=35.4$ s^{-1}, smaller than that in Fan-A ($\Omega_z=60.4$ s^{-1}). This conducts a more stable flow field in the exit region. The distribution of the absolute velocity in Fig. 7(c) is similar to that in Fig. 6(c) but $|V_{radial}|_{max} \approx 220$ cm/s is smaller due to the effect of the winglets. It also shows the $|V_{radial}|_{max}$ appearing at $x/D_{Hub} \approx \pm 1.8(2L/3)$. Figure 8 demonstrates the radial velocity distributions with various impeller angles at the normalized z-position, $z/D_{Hub}=1.0$, in Fan-C. As shown in Fig. 8(a), when the normalized position x/D_{Hub} is located between -0.5 and -1.25, the horizontal velocity components are positive and almost fixed. When x/D_{Hub} ranges from -1.25 to -1.94, they decrease. We also observe that the minimum velocity component appears at $x/D_{Hub} \approx -1.94(2L/3)$. The vertical direction velocity component V_y is shown in Fig. 8(b), resembling that in Fig. 8(a). The absolute velocity $|V_{radial}|$ shown in Fig. 8(c) demonstrates three different regions. In the first region, when x/D_{Hub} is in the range between -0.5 and -1.47, the absolute velocity curves do not change significantly. In the second region, the velocity profile increases gradually from the position $x/D_{Hub} \approx -1.47(L/3)$ and then in-
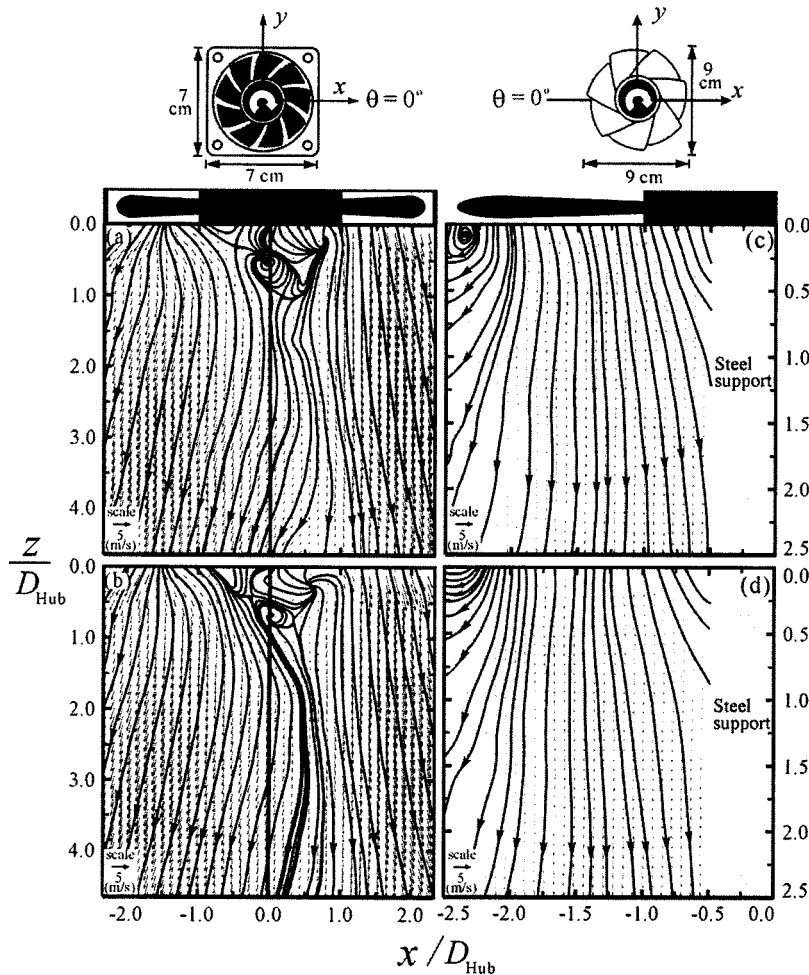
Fig. 9 Flow field patterns on the axial plane: (*a*) Fan-A, $\theta=0$ deg; (*b*) Fan-A, $\theta=20$ deg; (*c*) Fan-C, $\theta=0$ deg; and (d) Fan-C, $\theta=33$ deg

creases sharply from $x/D_{\mathrm{Hub}} \approx -1.94(2L/3)$. In the third region, $x/D_{\mathrm{Hub}} < -1.94$ (near the tip of the blade), the velocity decreases.

3.1.2 Flows in Axial Planes

3.1.2.1 Velocity vectors and streamline. Figure 9 shows the PIV-measured flow field of Fan-A and Fan-C when the impeller angles are changed on the axial plane. In Figs. 9(*a*) and 9(*b*), these two streamline patterns appear similar, and a vortex is formed in the near-hub wake. These vortexes oscillate leftward and rightward before dissipating downstream. This complex flow pattern is analogous to the swirling flow passing through a bluff body presented by Huang and Tsai [25]. Figures 9(*c*) and 9(*d*) show a clockwise vortex appearing at the tip of the blade. This vortex is caused from the pressure difference between the suction and pressure surfaces of the blade. It cannot be observed in the case of shrouded fans. A region with no streamline, shown respectively in Figs. 9(*c*) and 9(*d*) is caused by a steel rod which is used to support Fan-C.

3.1.2.2 Velocity distributions. Figure 10 shows the distributions of the velocity with various impeller angles at $z/D_{\mathrm{Hub}}=1.0$ in Fan-A. The horizontal velocity component in Fig. 10(*a*) is the same as that in Fig. 6(*a*) which is measured on the radial plane. Figures 10(*b*) and 10(*c*) show the asymmetric longitudinal and absolute velocity profiles which are influenced by the oscillation of the vortex when it passes through the hub. Figure 11 presents the distributions of the velocity profiles of Fan-B. The horizontal velocity components in Fig. 11(*a*) are the same as those in Fig.

7(*a*), which are measured on the radial plane. The asymmetric longitudinal and absolute velocities are shown in Figs. 11(*b*) and 11(*c*). The reasons are as mentioned above, but the asymmetricity is lower than that in Fan-A. This is the effect of the winglets, which can increase the lift and reduce the drag. Figure 12 shows the ensemble averaged velocity distributions of Fan-C at $x/D_{\mathrm{Hub}} = -1.75$ and -2.37, respectively. It shows that the velocity is strongly dependent on L, the distance from the tip of the blade to the hub center. We also observe that the flow expands and the velocity decreases at far field according to the absence of the constraining shroud.

3.2 Fan Performance. The AMCA 210 wind tunnel test is used for the fan performance measurements. To confirm that the flow field is steady, the data is not recorded until the test system has operated for about 30 s. Figure 13(*a*) shows the performances of the head coefficient with different volume flow rates. The head coefficient of the static pressure decreases with the increase of the fan flow coefficient for these three kinds of fans. The head coefficients of Fan-B are the largest, followed by those of Fan-A, with those of Fan-C the least. Figure 13(*b*) shows the performance of the power coefficient with different volume flow rates. These curves tend to decrease when the flow coefficient increases. In power consumption, Fan-C consumes the least power, then comes Fan-B, and Fan-A consumes the most power. The reason is that Fan-C has no constraining shroud, so the flow can expand freely. In addition, the winglets in Fan-B can reduce more drag than Fan-A, so it consumes less power.
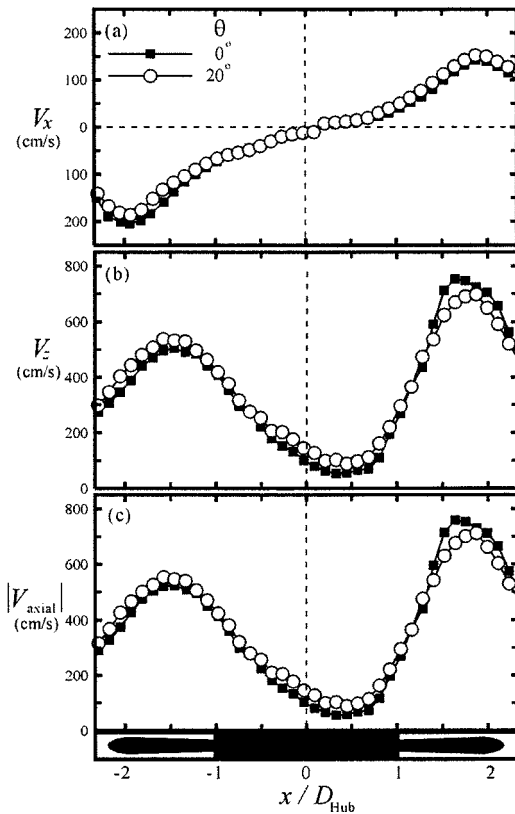
Fig. 10 Velocity profiles of Fan-A on the axial plane, z/D_{Hub} =1.0, N=4800 rpm, for (a) V_x, (b) V_y, and (c) $|V_{axial}|$, respectively
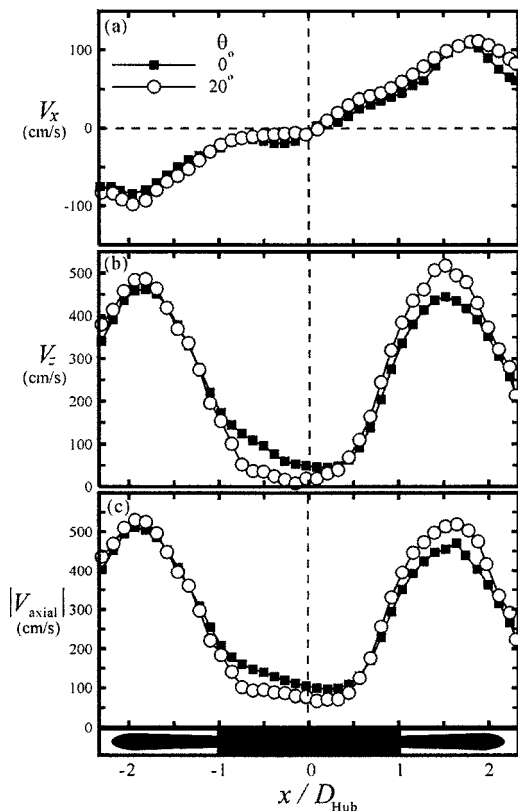

Fig. 11 Velocity profiles of Fan-B on the axial plane, z/D_{Hub} =1.0, N=3300 rpm, for (a) V_x, (b) V_y, and (c) $|V_{axial}|$, respectively
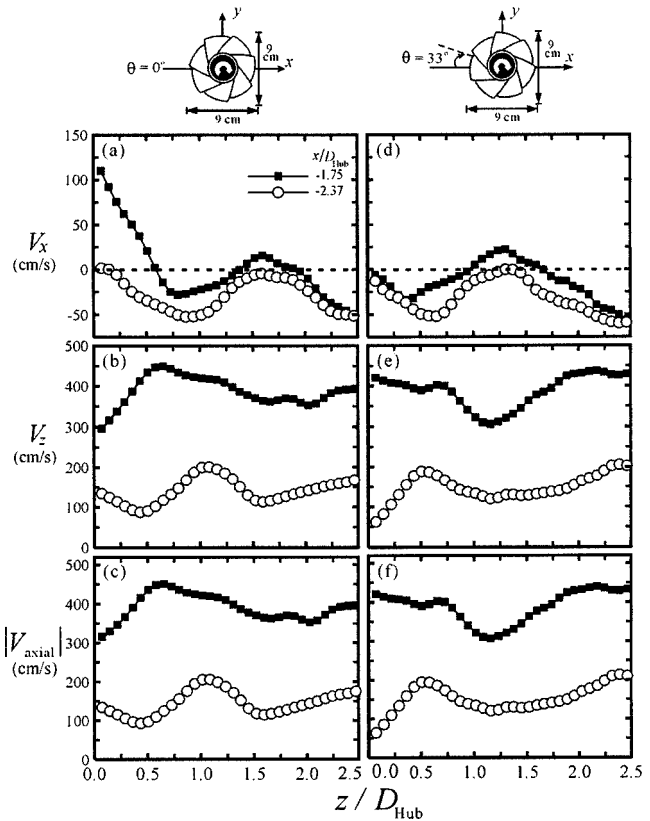

Fig. 12 Velocity profiles of Fan-C on the axial plane, N =2400 rpm at x/D_{Hub}=−1.75(solid rectangles) and x/D_{Hub}= −2.37(circles): (a) V_x, θ=0 deg; (b) V_z, θ=0 deg; (c) $|V_{axial}|$, θ =0 deg; (d) V_x, θ=33 deg; (e) V_z, θ=33 deg; and (f) $|V_{axial}|$, θ =33 deg

3.3 Correlations Between Fan Exit Velocity and Performance. In this paper, we present three different types of fans. The different designs cause different changes in the exit regions of these fans. These variations certainly influence the efficiency of these fans. Derived from Eq. (4), the fan efficiency is calculated and shown in Fig. 14. This figure shows that Fan-B always perform the best efficiency at different flow coefficients. For Fan-B, the maximum efficiency η is 55% as Φ=0.3. The extra 10% efficiency, compared with Fan-A, is due to the winglet effect. In a conventional wing [26], there are two trailing vortices that tend to drag the finite wing, thus inducing a small velocity component in the downward direction at the wing tip. If a winglet of the appropriate design and orientation is fitted to the wing-tip, the tendency of the winglet is to develop from the high pressure region below the wing-tip to the relatively low pressure region on the upper surface [27]. This winglet effect can raise the lift and reduce the drag.

4 Conclusions

The exit flow properties and performances of an axial flow fan at various impeller angles are analyzed. The instantaneous flow fields of the fans are measured with particle image velocimetry. The performance parameters of the fans are obtained by using the AMCA 210 flow bench. The following conclusions are drawn from the results and discussion.

(1) In Fan-A and Fan-B, the outer shrouds constrain the flow field and make the flow fields more stable. The velocity distributions in the x and y directions are almost the same, and the maximum absolute velocity appears at $x/D_{Hub} \approx \pm 1.8(2L/3)$.
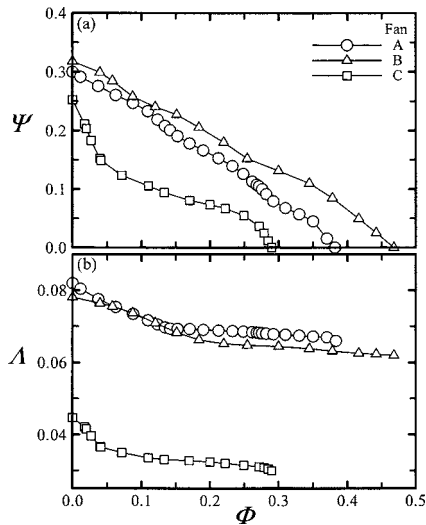
Fig. 13 Total performance of (*a*) head coefficient Ψ and (*b*) power coefficient Λ as a function of flow coefficients Φ
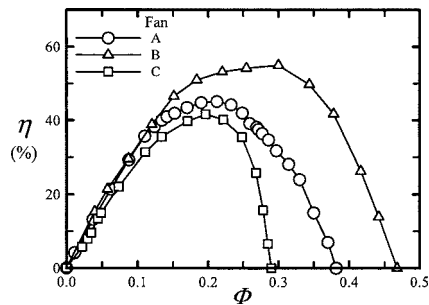

Fig. 14 The fan efficiency η as a function of flow coefficients Φ

(2) In Fan-C, the radial absolute velocity profile increases gradually from $x/D_{Hub} \approx -1.47(L/3)$ and then increases sharply at $x/D_{Hub} \approx -1.94(2L/3)$. On the axial plane, the velocity distributions show that the velocity strongly depends on the position.

(3) Without the constraining shroud, the flow expands and the velocity decreases significantly in the far field. Fan-C demonstrates the worst efficiency despite its large dimensions.

(4) Fan-B shows the most stable flow field and the best fan performance, resulting from the constraining shroud and the winglet-blades, which increase the lift and reduce drag.

Nomenclature

D = fan diameter

D_{Hub} = hub diameter of fans

L = length from the tip of the blade to the hub center

N = rotor speed

P_s = static pressure rise

Q = volume flow rate

R_t = leading edge radius of the blade

t = maximum thickness of the blade

x, y, z = Cartesian coordinates with origin at the center of fans

V_x = horizontal velocity component in x directions (cm/s)

V_y = vertical velocity component in y directions (cm/s)

V_z = longitudinal velocity component in z directions (cm/s)

$|V_{radial}|$ = absolute velocity in radial direction [$\sqrt{V_x^2 + V_y^2}$] (cm/s)

$|V_{axial}|$ = absolute velocity in axial direction [$\sqrt{V_x^2 + V_z^2}$] (cm/s)

θ = impeller angle

ρ = density of the air

Ω = vorticity (1/s)

Ψ = head coefficient, ($=\Delta P_s / \rho N^2 D^2$)

Λ = power coefficient ($=\wp / \rho N^3 D^5$)

Φ = flow coefficient ($=KQ/ND^3$)

η = fan efficiency ($=\Psi\Phi/\Lambda$)

References

[1] Eck, B., 1973, *Fans: Design and Operation of Centrifugal, Axial-Flow and Cross-Flow Fans* (translated and edited by Azad, R. S., and Scott, D. R.), Pergamon, Oxford.

[2] Wallis, R. A., 1983, *Axial Flow Fans and Ducts*, Wiley, New York.

[3] Bleier, F. P., 1998, *Fan Handbook*, McGraw-Hill, New York, pp. 13–117.

[4] Eduardo, B. M., Rafael, B. T., and Carlos, S., 1996, "Hot Wire Measurements During Rotating Stall in a Variable Pitch Axial Flow Fan," ASME Paper No. 96-GT-441.

[5] Koop, G. A., and Martinuzzi, R. J., 2002, "The Measurement of Mean Flow Angles Between an Automotive Fan and Stator," *Proceedings of the 2002 ASME Fluid Engineering Division*, ASME, Canada, FEDSM2002-31431.

[6] Sandra, V. S., Rafael, B. T., Carlos, S. M., and Eduardo, B. M., 2002, "Total Unsteadiness Downstream of an Axial Flow Fan with Variable Pitch Blades," ASME J. Fluids Eng., **124**, pp. 280–283.

[7] Ravindranath, A., and Lakshminarayana, B., 1980, "Mean Velocity and Decay Characteristics of the Near and Far-Wake of a Compressor Rotor Blade of Moderate Loading," ASME J. Eng. Power, **102**, pp. 535–548.

[8] Myung, H. J., and Baek, J. H., 1999, "Mean Velocity Characteristics Behind a Forward Swept Axial-Flow Fan," JSME Int. J., Ser. B, **42**(3), pp. 476–488.

[9] Jang, C. M., Furukawa, M., and Inoue, M., 2001, "Analysis of Vortical Flow Field in a Propeller Fan by LDV Measurements and LES-Part I: Three-Dimensional Vortical Flow Structures," ASME J. Fluids Eng., **123**, pp. 748–754.

[10] Du, Z., Lin, W., Zu, X., and Zhao, Y., 2002, "The Measurement of Three Dimensional Flow Field in an Axial Flow Fan Using PDA," *Proceedings of the 2002 ASME Fluid Engineering Division*, ASME, Canada, FEDSM2002-31098.

[11] Estevadeordal, J., Gogineni, S., Copenhaver, W., Bloch, G., and Brendel, M., 2000, "Flow Field in a Low-Speed Axial Fan: a DPIV Investigation," Exp. Therm. Fluid Sci., **23**, pp. 11–21.

[12] Lee, S. J., Choi, J., and Yoon, J. H., 2003, "Phase-Averaged Velocity Filed Measurements of Flow Around an Isolated Axial-Fan Model," ASME J. Fluids Eng., **125**, pp. 1067–1072.

[13] Shimada, K., Kimura, K., and Watanabe, H., 2003, "A Study of Radiator Cooling Fan with Labyrinth Seal," Society of Automotive Engineers of Japan, **24**, pp. 431–439.

[14] Oh, K. J., and Kang, S. H., 1999, "A Numerical Investigation of the Dual performance Characteristics of a Small Propeller Fan Using Viscous Flow Calculations," Comput. Fluids, **28**, pp. 815–823.

[15] Stinnes, W. H., and von Backstrom, T. W., 2002, "Effect of Cross-Flow on the Performance of Air-Cooled Heat Exchanger Fans," Appl. Therm. Eng., **22**, pp. 1403–1415.

[16] Mizuno, T., and Kikuchi, K., 1990, "Characteristic of Axial Flow Fan with Diagonal Flow Hub," SAE Trans., **99**(6), pp. 49–55.

[17] Mei, R., 1996, "Velocity Fidelity of Flow Tracer Particles," Exp. Fluids, **22**(1), pp. 1–13.

[18] Keane, R. D., and Adrian, R. J., 1992, "Theory of Cross-Correlation Analysis of PIV Images," Appl. Sci. Res., **49**(2), pp. 191–215.

[19] Keane, R. D., and Adrian, R. J., 1990, "Optimization of Particle Image Velocimeters Part I: Double Pulsed Systems," Meas. Sci. Technol., **1**(11), pp. 1202–1215.

[20] Chung, D. L., 2000, "Development of Design Methodology for Cooling System of a Disk Array," Master thesis, National Taiwan University of Science and Technology, Taiwan, pp. 11–13.

[21] Wright, T., 1999, *Fluid Machinery: Performance, Analysis, and Design*, CRC Press, Boca Raton, pp. 41–70.

[22] Davis, J. C., 1986, *Statistics and Data Analysis in Geology*, Wiley, New York, pp. 28–34.

[23] Hart, D. P., 2000, "PIV Error Correction," Exp. Fluids, **29**, pp. 13–22.

[24] Spedding, G. R., and Rignot, E. J., 1993, "Performance Analysis and Application of Grid Interpolation Techniques for Fluid Flows," Exp. Fluids, **15**, pp. 417–430.

[25] Huang, R. F., and Tsai, F. C., 2001, "Observations of Swirling Flows behind Circular Discs," AIAA J., **39**(6), pp. 1106–1112.

[26] Andercon, J. D., 1991, *Fundamentals of Aerodynamics*, McGraw-Hill, New York, pp. 316–317.

[27] Houghton, E. L., and Carpenter, P. W., 1993, *Aerodynamics for Engineering Students*, Edward Arnold, London, pp. 315–317.

Performance and Internal Flow Characteristics of a Very Low Specific Speed Centrifugal Pump

Young-Do Choi[1]
e-mail: ydchoi@mach.me.ynu.ac.jp

Junichi Kurokawa

Jun Matsui

Department of Systems Design,
Division of Systems Research,
Faculty of Engineering,
Yokohama National University,
79-5 Tokiwadai, Hodogaya-ku,
Yokohama 240-8501 Japan

In very low specific speed range ($n_s < 0.25$), the efficiency of the centrifugal pump designed by the conventional method becomes remarkably low. Therefore, positive-displacement pumps have been widely used for long. However, the positive-displacement pumps remain associated with problems such as noise and vibration and they require high manufacturing precision. Since the recently used centrifugal pumps are becoming higher in rotational speed and smaller in size, there appear to be many expectations to develop a new centrifugal pump with high performance in the very low specific speed range. The purpose of this study is to investigate the internal flow characteristics and its influence on the performance of a very low specific speed centrifugal pump. The results show that large reverse flow at the semi-open impeller outlet decreases absolute tangential velocity considerably which in turn decreases the pumping head.
[DOI: 10.1115/1.2169815]

Keywords: centrifugal pump, very low specific speed, semi-open impeller, performance, internal flow

1 Introduction

Recently, a centrifugal pump in the range of very low specific speed, such as $n_s < 0.25$, attracts attention as a substitute for a positive-displacement pump because not only of vibration and noise problems but also due to recent demand towards small size and high rotational speed. However, if the centrifugal pump in the range of very low specific speed is manufactured by a conventional design (e.g., Stepanoff [1]), some serious problems are caused: the impeller passage becomes very narrow ($b_2 < 1$ mm) in order to satisfy the condition of high head and small discharge. It is still difficult to attain high efficiency because the efficiency of a centrifugal pump decreases rapidly with the decrease of specific speed. Rodgers [2] examined experimental data taken in a single-stage partial emission centrifugal compressor as a reference case for very low specific speed turbomachinery. It was reported that the compressor performance at $n_s = 0.15$ was considerably degraded by large windage and recirculation losses, which could be improved by modification of impeller inlet and outlet geometry. Abramian and Howard [3] conducted detailed LDV measurements of flow fields in an impeller passage of a very low specific speed centrifugal pump ($n_s = 0.18$). They used an impeller with eight highly backward swept blades fitted into the passage formed between front and main shrouds (i.e., closed-type impeller). They reported that, in contrast to the usual expectation, flow separation occurred along the blade pressure side at 50% flow rate and the best efficiency point (B.E.P.) was located at 170% of the designed flow rate. The design point of a centrifugal pump is determined by the intersection of the head curves of both an impeller and a volute as pointed out by Worster [4], and usually the B.E.P. coincides with the design point. However, in case of a very low specific speed centrifugal pump, the B.E.P. comes to much higher discharge than the designed. Detailed experimental measurements by Worster [4] and Kurokawa et al. [5] have shown that it is the volute rather than the impeller which determines the best efficiency of low specific speed pump. For the problems caused by

conventional design method in the very low specific speed range, extensive researches have been carried out to clarify the reasons by Kurokawa et al. [5,6]. Low efficiency is mainly caused by large disk friction and the pump efficiency could be raised to about 10% by new design method.

If the design was made according to the conventional procedures (Stepanoff [1]) in the very low specific speed range, the impeller passage height at the outlet would become too narrow to manufacture. This has led to the choice of semi-open-type impellers, the choice that also contributes to the improvement of pump efficiency through the reduction of disk friction loss. In order to decrease the disk friction loss, which is proportional to the fifth power of impeller diameter, the impeller should be as small as possible in radius. Also to replenish the effective head, lowered by the reduction of impeller size, the large outlet angle of impeller blade (i.e., $\beta_2 = 90$ deg) is required. It is worthwhile mentioning that, as suggested by Ohta and Aoki [7] and Minemura et al. [8], the choice of semi-open-type impellers could suppress the performance instability, which is a tendency of positive gradient of head curve, and might appear for impeller blades with large outlet angle. However, little is known about the flow characteristics in the impeller channel of semi-open impeller with large outlet angle.

Since the internal flow of a very low specific speed centrifugal pump gives large influence on the pump performance, a more detailed information is needed for the relation between internal flow and performance characteristics in order to develop high performance centrifugal pump in the range of very low specific speed. The purpose of this study is to investigate the internal flow characteristics and its influence on the performance of a very low specific speed centrifugal pump.

2 Experimental Apparatus and Method

Two kinds of test pumps are adopted for the measurement of the performance and internal flow characteristics. Figure 1 shows the test pump 1 ($n_s = 0.14$) which is used for the measurement of performance characteristics when the tip clearance between suction cover wall and blade tip of semi-open impeller changes. The test pump 1 for tip clearance variation test has a transparent front casing wall which is made of acrylic resin in order to conduct

---
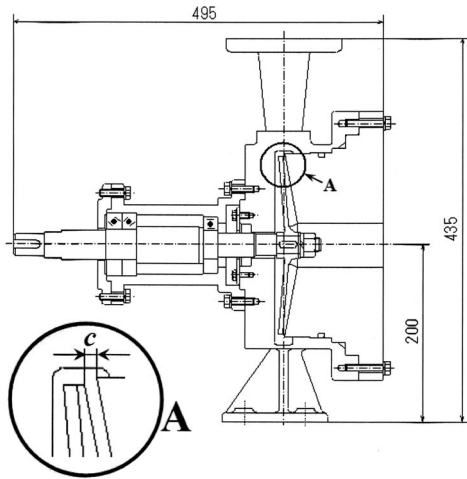
Fig. 1 Schematic view of test pump 1 and tip clearance c

Table 2 Dimensions of test pump 2

Flow rate	$Q_d \, [m^3/s]$	3.75×10^{-4}
Head	$H \, [m]$	1.1
Rotational speed	$n \, [rpm]$	700
Non-dimensional design specific speed	n_s	0.24
Reynolds number	$Re \, [\rho u_2 r_2/\mu]$	2.6×10^5

laser-doppler velocimetry (LDV) measurement and can be displaced in the axial direction for tip clearance adjustment. Five pressure holes are located in the radial direction at the front casing wall to measure the static pressure variation by the change of impeller type and tip clearance ratio. Clear water is used as a working fluid. Table 1 shows detailed dimensions of the test pump 1.

Figure 2 and Table 2 show the schematic view and dimensions of the test pump 2 ($n_s = 0.24$) which is adopted for the internal flow visualization. The test pump 2 has two-dimensional configuration which is located and operated between two pieces of flat plates. The front and side walls of the pump are made of transparent acrylic resin which provides optical access to the flow inside the pump in case of particle image velocimetry (PIV) measurement.

Figure 3 shows the schematic view of test impellers for the test pump 1. Five kinds of test impeller are employed to investigate the influence of tip clearance ratio on the internal flow and performance. The closed impeller A is designed by a conventional method (Stepanoff [1]). The semi-open impellers B and C have same impeller radius but the impeller outlet width is designed differently in order to examine the influence of outlet width variation. In order to insert laser beam for LDV experiment into the area of impeller outlet, at which absolute tangential velocity is measured, the outlet radii of the impellers B and C are cut shorter by 10 mm. The impellers of shortened radii are called impellers B′ or C′, respectively. Tables 3 and 4 show the dimensions of the test impellers for the test pump 1 and the tip clearance ratio in the pump.

Figure 4 shows the schematic view of test impellers for the test pump 2. Two types of the semi-open impeller are tested in order to investigate the internal flow. A large blade outlet angle of $\beta_2 = 90$ deg is chosen and applied to the test impeller D. Also, the semi-open impeller E which has a normal outlet angle of $\beta_2 = 30$ deg is selected to compare the difference of the internal flow and the performance. The outlet width of the test impellers D and E is designed wider than that of a conventional design (Stepanoff [1]) in order to conduct PIV measurement in detail. The main shroud and blades of the test impellers D and E are made of transparent acrylic resin for PIV measurement. Table 5 shows the dimensions of the test impellers for the test pump 2.

In order to measure absolute tangential velocity at the impeller outlet in the test pump 1, LDV measurement is performed. Present

Table 1 Dimensions of test pump 1

Impeller		A, B, C	B', C'
Flow rate	$Q_d \, [m^3/s]$	2.5×10^{-3}	1.25×10^{-3}
Head	$H \, [m]$	55	13.75
Rotational speed	$n \, [rpm]$	3000	1500
Non-dimensional design specific speed	n_s	0.14	
Reynolds number	$Re \, [\rho u_2 r_2/\mu]$	3.2×10^6	1.3×10^6
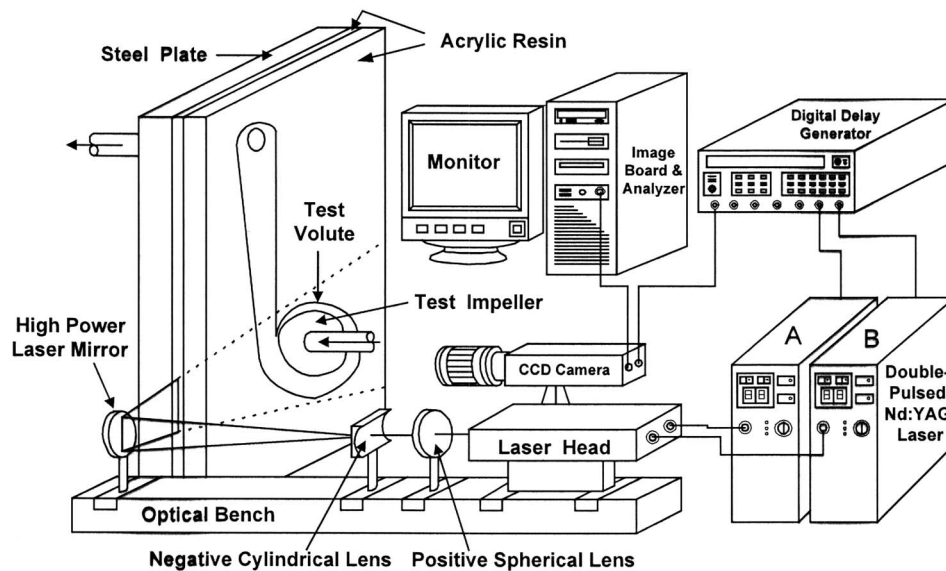
Fig. 2 Test pump 2 and PIV measurement system

Fig. 3   Test impellers for test pump 1
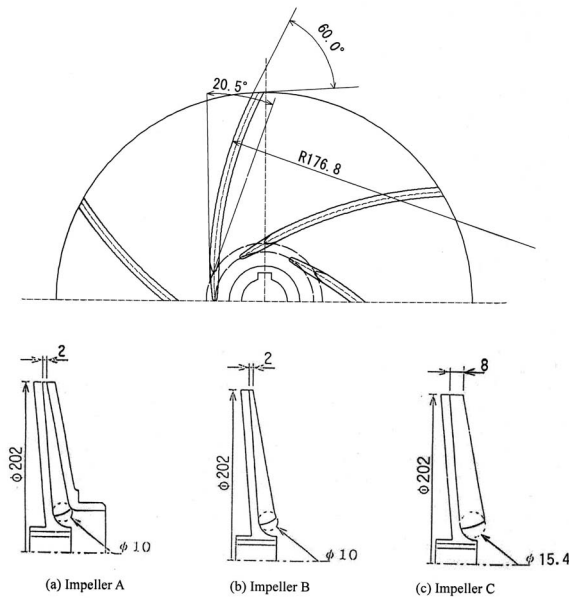

(a) Impeller D

(b) Impeller E

Fig. 4   Test impellers for test pump 2

LDV system comprises of a two-component four-beam fiber optic system in which the wavelengths of the light source are 514.5 nm (green) and 488 nm (blue). Nylon 12 is chosen as a seeding particle (diameter about 4 μm, specific gravity 1.02). For the visualization of the internal flow in the test pump 2, PIV and particle tracking velocimetry (PTV) measurement systems are adopted (Choi et al. [9–11]). Figure 2 shows the schematic view of the two-dimensional PIV measurement system. A laser head and a CCD camera are able to be replaced with a strobe and a high speed camera for the two-dimensional PTV measurement. A double-pulsed Nd:YAG laser sheet (20 mJ) is used as a source of illumination for PIV measurement. Once aligned, the light sheet can be displaced in the direction normal to the impeller main shroud wall using a mirror on the optical bench. The thickness of the light sheet is fixed to 0.5 mm at each plane measured. A strobe illuminates the flow field in front of the suction cover of the test pump 2 for PTV measurement. A CCD camera (resolution 1300 × 1030 pixel, for PIV) and a high speed camera (resolution 512 × 384 pixel, for PTV) take the images of the flow field from the direction perpendicular to a plane of light sheet. The time intervals of the two cameras are set to 100 μs, respectively, in consideration of a maximum fluid velocity at the test impeller outlet. All the triggering pulses for laser emission, camera framing and image grabbling are provided by a digital delay generator for PIV
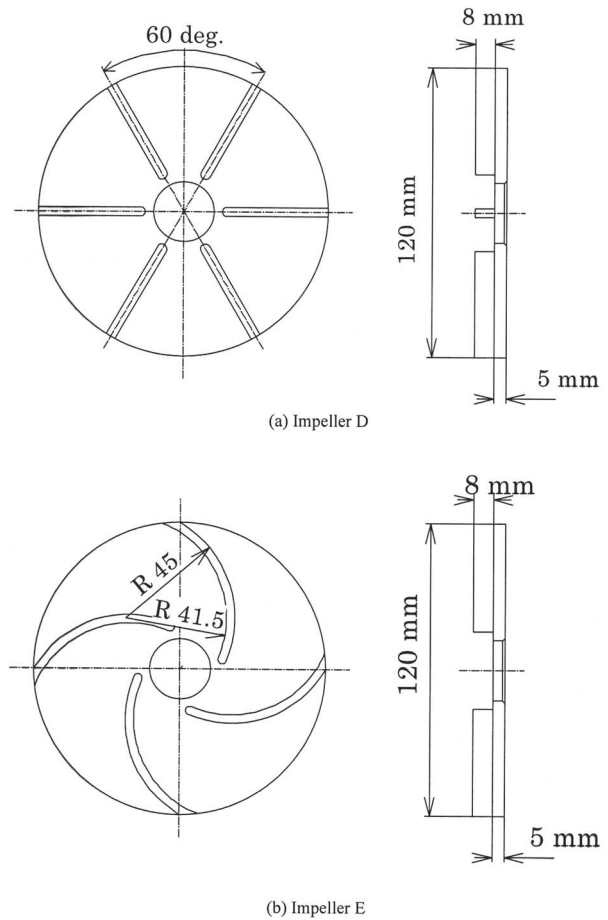
Table 3   Dimensions of test impellers for test pump 1

Test impeller	A	B	C	B'	C'
Type	Closed	Semi-open	Semi-open	Semi-open	Semi-open
Z			6		
t [mm]			4		
b_1 [mm]		10	15.4	10	15.4
b_2 [mm]		2	8	2.25	9
r_2 [mm]		101		91	
β_1 [deg.]		20.5		20.5	
β_2 [deg.]			60		
n_s			0.14		

Table 4   Tip clearance ratio in test pump 1

Test impeller	A	B		C			B'				C'	
b_2 [mm]		2		8			2.25				9	
c [mm]	-	1	2	1	2	4	1.125	2.25	4.5	9	1.125	4.5
c/b_2	-	0.5	1	0.125	0.25	0.5	0.5	1	2	4	0.125	0.5

Table 5 Dimensions of test impellers for test pump 2

Test impeller	D	E
Type	Semi-open	Semi-open
Z	6	4
t	4	3.5
b_1 [mm]	8	
b_2 [mm]	8	
c [mm]	1	
c/b_2	0.125	
r_2 [mm]	60	
β_1 [deg.]	90	22.5
β_2 [deg.]	90	30
n_s	0.24	

measurement, and also a triggering signal captured from the shaft of the test pump 2 is provided to the strobe and the high speed camera for the PTV system. A nylon 12 (diameter about 30 μm, specific gravity 1.02, for PIV) and an ion exchange porous resin (diameter 200–700 μm, specific gravity of 1.02, for PTV) are used as a tracer particle. Clear water is used as a working fluid. In order to receive enough image resolution of the PTV measurement, the internal flow passage of the test pump 2 is divided into four areas, and the divided areas are joined together into one velocity field during the postprocessing procedure. For the PIV measurement, the internal passages of the test impellers D and E are divided into three different viewing locations along the tangential angle (θ) measured from the volute tongue: Area 1(θ=330 deg to 360 deg and 0 deg to 30 deg), area 2(θ=110 deg to 170 deg) and area 3(θ=220 deg to 280 deg). Three separate planes in the direction perpendicular to the impeller axis are measured in areas 1–3: near the suction cover (z/b=0.05, plane 1), middle passage width (z/b=0.5, plane 2) and near the main shroud (z/b=0.95, plane 3). A cross-correlation PIV algorithm (Raffel et al. [12]) and a triple pattern matching PTV algorithm (Nishino and Torii [13]) are used as a particle tracking method.

The uncertainty estimates for each variable in the graphs are based on the method of Abernethy et al. [14]. The total uncertainty (U) of the variables can be found by combining systematic and random errors as $U=[B^2+(tS_{\bar{X}})^2]^{1/2}$, where B is the systematic uncertainty, $S_{\bar{X}}$ is the standard deviation of the mean, and the degree of freedom t is determined to 2 for a 95% confidence level (for a sample size greater than 30). The systematic uncertainty B is estimated based on the calibration data and previous test experience, and the standard deviation of the mean $S_{\bar{X}}$ is computed from the raw test data.

3 Results and Discussions

3.1 Performance Curves for Different Tip Clearance Ratios. Figure 5 shows the performance curves of the test pump 1 with the test impellers A and B, both incorporating the same volute, where the head coefficient (ψ), the power coefficient (ν), the local specific speed (n_{sl}) and the pump efficiency (η) are plotted versus the discharge coefficient (ϕ). The performance curves show that the effective head and the pump efficiency of the closed impeller A are higher than that of the semi-open impeller B. The performance instability, which is characterized by the rising head curve with the increase of discharge, is seen in the range of ϕ <0.04 of the closed impeller A. On the other hand, in the semi-open impeller B, performance instability almost disappears with the increase of tip clearance ratio (c/b_2). Therefore, with appropriate tip clearance ratio, a semi-open impeller can be applied to the countermeasure of performance instability of a closed
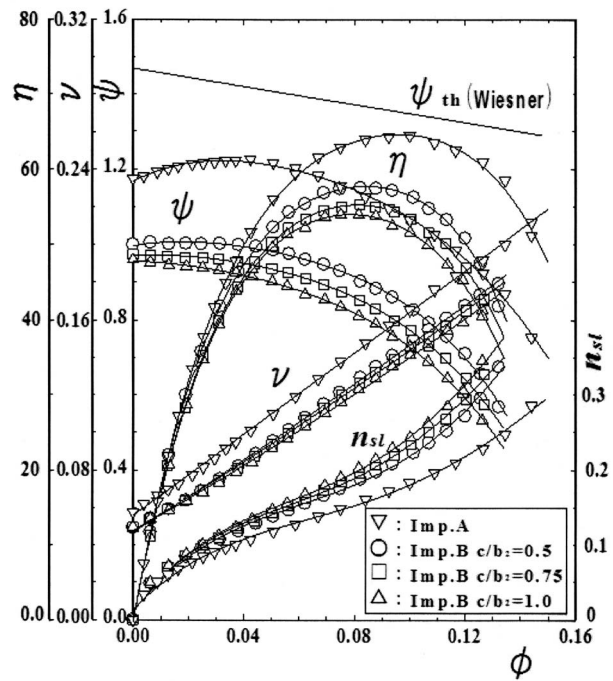

Fig. 5 Performance curves of test pump 1 with change of tip clearance ratio (uncertainty of ϕ= ±1.39%, of ψ= ±1.0%, of ν = ±1.49%, of η= ±2.29%, of n_{sl}= ±1.15%)

impeller.

Figure 6 indicates the best efficiency (η_{max}) and the design point efficiency ($\eta_{D.P.}$) using the semi-open impellers B' and C' with variation of tip clearance ratio. Recall that the best efficiency point (B.E.P.) of a very low specific speed impeller is located in the range of the excessive flow rate and the efficiencies of η_{max} and $\eta_{D.P.}$ locate in the different flow rate range (Abramian and Howard [3]). In spite of the difference of each efficiency defined above, the efficiencies increase simultaneously as the tip clearance ratio decreases. The efficiencies of η_{max} and $\eta_{D.P.}$ of the semi-open impellers B' and C' for the change of tip clearance ratio (c/b_2) can be expressed in a linear curve with gentle gradient and become a constant value in the range of c/b_2>2.

Figure 7 shows the performance curves measured with the semi-open impellers D (β_2=90 deg) and E (β_2=30 deg). As observed from the curves of the head coefficient, the total head achieved by the test impeller D is higher than that of the test
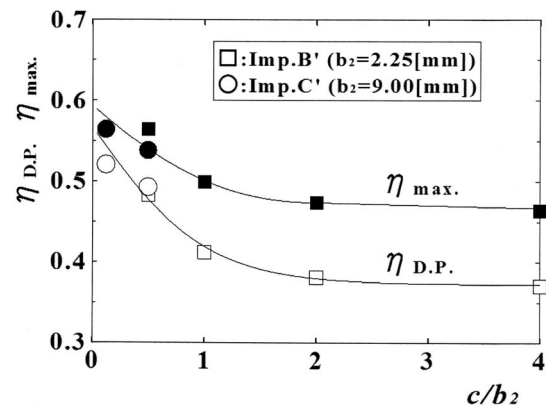

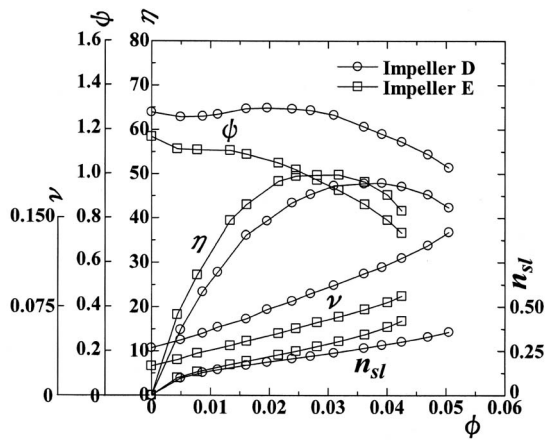**Fig. 6 Effect of tip clearance ratio on efficiency (uncertainty of η_{max}= ±2.29%, of $\eta_{D.P.}$= ±2.29%)**

Fig. 7 Performance curves of test pump 2 (impellers $D(\beta_2 =90 \deg)$ and $E(\beta_2=30 \deg)$) (uncertainty of $\phi=\pm1.41\%$, of $\psi =\pm2.16\%$, of $\nu=\pm1.5\%$, of $\eta=\pm3.18\%$, of $n_{sl}=\pm2.21\%$)

Fig. 8 Absolute tangential velocity at impeller outlet (uncertainty of $v_\theta/r\omega=\pm2.35\%$)

impeller E. However, the best efficiencies for the test impellers D and E (48% versus 50%) are nearly the same in spite of their large difference in blade angle. Note that the test impeller D exhibits a slight performance instability at the low flow rates ($\phi =0.01–0.02$).

3.2 Theoretical Head of the Semi-open Impeller. The theoretical head ψ_{th} of a closed and a semi-open impellers of the same shape has been considered same when the impeller outlet angle is same, and thus the head difference between the theoretical head ψ_{th} and the actual head ψ is the hydraulic loss. From Fig. 5, the head difference $\psi_{th}-\psi$ in the semi-open impeller B is much larger than that in the closed impeller A, even though the pump efficiency difference of the two impellers is not so large. To show this discrepancy more clearly, a detailed examination is discussed below. The pump efficiencies (η) of the test impellers A (closed) and B (semi-open, $c/b_2=1.0$) at the B.E.P. are 65% and 55%, respectively, and the difference of the efficiencies in the impellers is 10%. The efficiency is given as the product of the mechanical efficiency (η_m), the volumetric efficiency (η_v), and the hydraulic efficiency (η_h). Since the difference of the shut-off head, which is mainly dominated by disk friction, is not so large between the closed type and the semi-open-type impellers, the mechanical efficiency of two impellers should not differ so much. Moreover, as there is no leakage in a semi-open-type impeller and small amount of leakage at the B.E.P. in a closed type impeller, the volumetric efficiency of two impellers does not differ so much. It means that the pump efficiency in two impellers should be nearly proportional to the hydraulic efficiency. However, the hydraulic efficiencies ($\eta_h=\psi/\psi_{th}$) of two impellers are 81% and 60% at the B.E.P., respectively and the difference of hydraulic efficiency in two impellers is 21%, which is about twice as much as the efficiency difference.

This discrepancy reveals that the theoretical head of a semi-open impeller should be much lower than that of a closed impeller. Therefore, the conventional idea for the theoretical head ($H_{th}=u_2v_{\theta2}/g$) of a semi-open impeller should be revised to a lower value than that of a closed impeller. In order to clarify the reason of this discrepancy in theoretical head between the closed and semi-open impellers, the impeller internal flow should be examined because the theoretical head (H_{th}) is related closely with absolute tangential velocity ($v_{\theta2}$) at the impeller outlet.

3.3 Absolute Tangential Velocity and Slip Factor. Absolute tangential velocity is measured at the impeller outlet ($r/r_2 =1.02$) of the test pump 1 by use of the LDV system and is mass-averaged in the transverse direction from the suction cover
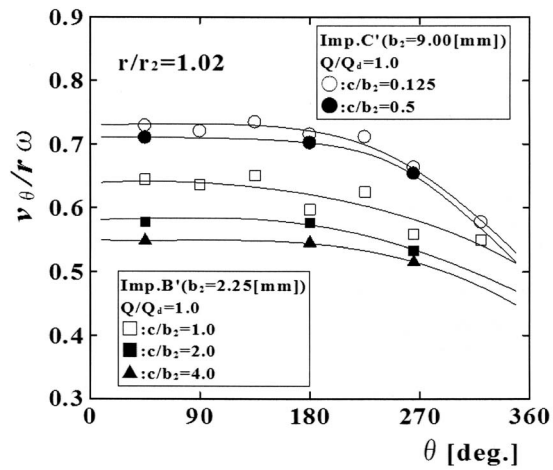
to the main shroud. The measured time-averaged absolute tangential velocity $v_{\theta2}$ at each tangential angle measured from volute tongue (θ) is shown in Fig. 8 with the change of tip clearance ratio. Regardless of the outlet width of the semi-open impellers B′ ($b_2=2.25$ mm) and C′ ($b_2=9$ mm), the absolute tangential velocity at the impeller outlet increases as tip clearance ratio decreases. This result is contradictory to the conventional treatment that the absolute tangential velocity $v_{\theta2}$ at the impeller outlet is same in both impellers B′ and C′, as $H_{th}=u_2v_{\theta2}/g$. Moreover, $v_{\theta2}$ drops rapidly near to the volute angle of about $\theta>270$ deg. This velocity drop in the vicinity of volute tongue at the design flow rate ($Q/Q_d=1.0$) is not in accordance with the usual expectation of constant velocity around the outlet of a normal specific speed impeller (e.g., Kurokawa and Amasaka [15], $n_s=0.45$). This means that the absolute tangential velocity at the impeller outlet is influenced strongly by the volute tongue in the very low specific speed centrifugal pump. To show the dependence of theoretical head upon tip clearance ratio more clearly, slip factor defined as follows is considered:

$$k = (v_{\theta2\infty} - v_{\theta2})/u_2 \qquad (1)$$

where $v_{\theta2\infty}$ and $v_{\theta2}$ are the absolute tangential velocities for case of infinite blade number and the measured tangential velocity averaged around the impeller outlet, respectively. Slip factor of a conventional closed impeller is known to agree well with the value of Wiesner formula (Wiesner [16]) given as

$$k_{\text{Wiesner}} = \sqrt{\sin \beta_2}/Z^{0.7} \qquad (2)$$

However, Fig. 9 shows that the slip factor of the very low specific speed semi-open impellers is larger than that of Wiesner formula and increases with the increase of tip clearance ratio. The inclination of the slip factor becomes flat at the tip clearance ratio of $c/b_2>2$. As tip clearance ratio goes to zero, the slip factor approaches closely to that of a closed impeller. Moreover, an interesting observation is made by comparing the Figs. 6 and 9, that the change of slip factor by tip clearance ratio shows strong relation with the change of pump efficiency by tip clearance ratio. From the relation between slip factor and tip clearance ratio examined here, it is obvious that the absolute tangential velocity ($v_{\theta2}$) is influenced strongly by the tip clearance ratio and hence, theoretical head ($H_{th}=u_2v_{\theta2}/g$) is also strongly dependent on tip clearance ratio. As the values of slip factor and theoretical head are related closely to $v_{\theta2}$, it is necessary to investigate the pump internal flow in detail.
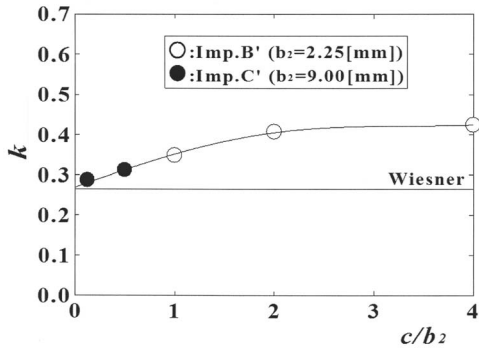
Fig. 9 Change of slip factor by tip clearance ratio (Q/Q_d =1.0) (uncertainty of k= ±2.35%)

3.4 Visualization of Whole Internal Flow Field. In order to investigate the internal flow characteristics of a very low specific speed centrifugal pump, the test pump 2 and the two-dimensional PTV measurement system are adopted. Figure 10 shows phase-averaged velocity vectors measured inside the test pump 2. The impeller passage flow is expressed by relative velocity vectors and the volute passage flow is expressed by absolute velocity vectors. As a strobe is used to illuminate the flow volume of interest, velocity variations across the height of the impeller passage are averaged and expressed by a two-dimensional velocity vector. There exists no velocity vector area in the bottom of the volute passage marked as "out of photographing area" in which no illumination is supplied. The impeller rotates in a clockwise direction. As indicated in Fig. 10(a), the relative flow of the semi-open impeller D shows that through-flow along the confined narrow region of the blade suction side goes out to the impeller outlet but the entire flow direction in the impeller passage deflects toward the blade pressure side from the blade suction side. Moreover, low velocity region is seen in an impeller passage. Leakage flow passing through the tip clearance shows strong tangential directional flow. The whole flow field in the semi-open impeller D is asymmetric to the impeller axis even at the B.E.P. (Q/Q_0=1.0), while the semi-open impeller E is relatively symmetric to the impeller axis as shown in Fig. 10(b). Figure 10(c) shows the velocity vectors of the semi-open impeller D at the partial flow rate of Q/Q_0=0.25. A large passage vortex exists near the blade pressure side of impeller passage in the vicinity of the volute tongue. This passage vortex causes a large increase of relative velocity at the impeller outlet. Therefore, the theoretical head decreases considerably by the decreased absolute tangential velocity at the impeller outlet and thus, there is a strong possibility of the head instability located in the region of the partial flow rate (ϕ=0.01 −0.02).

3.5 Detailed Flow Structure in a Semi-open Impeller Channel. From the visualization of the whole internal flow field in the test pump 2, it has been clarified that the internal flow of a very low specific speed semi-open impeller shows quite different flow pattern as compared with a normal specific speed impeller of a closed type (e.g., Murakami et al. [17], n_s=0.60). However, the influence of tip clearance on impeller channel flow and also on theoretical head is not yet clear. To reveal the tip clearance influence, detailed measurement of the flow structure in the tip clearance as well as in the internal passage of the semi-open impeller D (β_2=90 deg) is carried out using the PIV method.

Figure 11 shows the phase-averaged relative velocity vectors in the semi-open impeller D at the B.E.P. (Q/Q_0=1.0). The relative velocity vectors are measured and visualized in the area 3 (θ =220°~280°) on three different planes parallel to the main shroud wall of the test impeller. Recall that plane 1 is closest to the suction cover (z/b=0.05) while plane 3 is the farthest (z/b

(a)

(b)

(c)
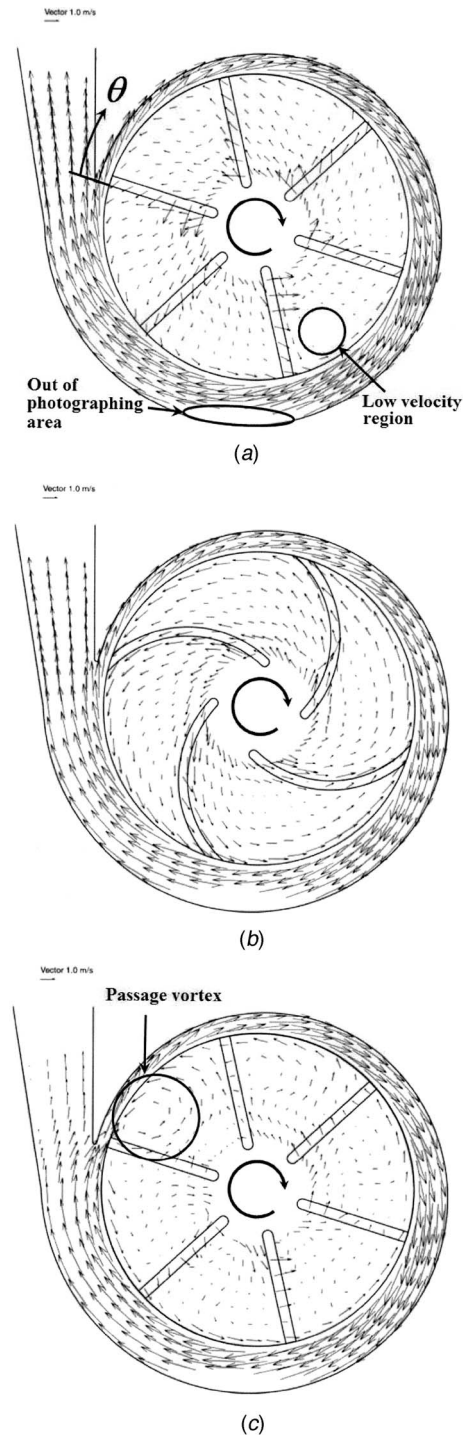
Fig. 10 Phase averaged velocity vectors of test pump 2 (uncertainty of v_θ/u_2= ±3.75%, of v_r/u_2= ±3.75%). (a) Impeller D (Q/Q_0=1.0, PTV). (b) Impeller E (Q/Q_0=1.0, PTV). (c) Impeller D (Q/Q_0=0.25, PTV).

=0.95). A noteworthy feature recognized in these figures is the presence of a strong leakage flow (plane 1) that is traversing the impeller passage through the tip clearance in the direction from the blade pressure side to the blade suction side. As the leakage flow reduces absolute tangential velocity of the fluid, the flow is deflected toward the impeller axis as a result of decrease in centrifugal force. The leakage flow should be interacting with the flow on other planes, thus creating quite complex "secondary

Fig. 11 Phase-averaged relative velocity vectors (impeller D, Q/Q_0=1.0, area 3, PIV) (uncertainty of v_θ/u_2=±3.5%, of v_r/u_2 = ±3.5%). (a) Plane 1 (z/b=0.05). (b) Plane 2 (z/b=0.5). (c) Plane 3 (z/b=0.95).
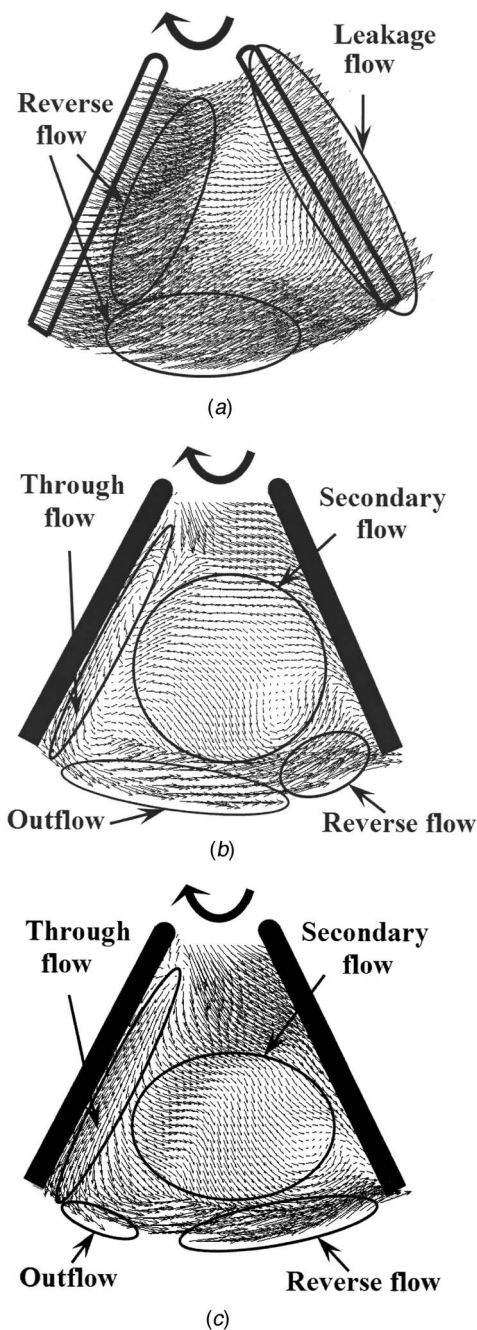
flow" patterns inside the impeller. Moreover, on planes 2 and 3, a narrow strong through-flow along the blade suction side in the impeller passage is observed. At the impeller outlet, the through-flow goes out to the volute passage. As the outward through-flow has high absolute tangential velocity, the flow pattern is responsible for the high head performance of the radial bladed semi-open impeller D. However, in contrast to the flow near to the blade suction side, the flow direction near to the blade pressure side at the impeller outlet is obviously inward marked as "reverse flow" on planes 2 and 3.

The occurrence of reverse flow indicated here on planes 2 and 3 can be explained by considering the origin of those structures.
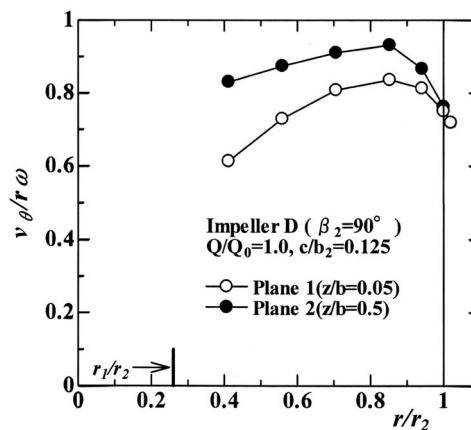

Fig. 12 Absolute tangential velocity ratio (impeller D, Q/Q_0 =1.0, c/b_2=0.125, PIV) (uncertainty of $v_\theta/r\omega$=±3.5%)

When impeller rotates clockwise with angular velocity ω, Coriolis force $-2\rho\omega\times w$ works perpendicular to the angular velocity ω and the relative velocity w. In the radial flow region of impeller passage, Coriolis force acts in the direction from the blade suction side to the blade pressure side. However, strong relative velocity w heads for tangential direction in the vicinity of the impeller outlet, and then strong Coriolis force acts towards impeller center causing reverse flow at the impeller outlet on the blade pressure side.

From the above detailed examination of the flow structure in the very low specific speed semi-open impeller D, two distinctive internal flow structures are clarified as follows: (1) the whole internal flow is dominated by strong leakage flow passing through blade tip clearance in the direction from the blade pressure side to the blade suction side. The leakage flow passing through the tip clearance takes the internal passage flow from the blade suction side to the blade pressure side and thus large secondary flow region locates within the impeller channel. (2) Strong radially inward reverse flow occurs at the impeller outlet on the blade pressure side and radially outward through-flow is confined in a quite narrow region on the blade suction side of the impeller passage.

3.6 Absolute Tangential Velocity Ratio. As the strong reverse flow and the leakage flow within the impeller channel are supposed to give large influence on the impeller outlet flow, the variation of absolute tangential velocity ratio ($v_\theta/r\omega$) in the radial direction of impeller radius is examined in the impeller channel and just behind the impeller outlet (r/r_2=1.02).

Figure 12 shows the variation of $v_\theta/r\omega$ in the tip clearance (plane 1) and middle passage width (plane 2) of the semi-open impeller D (β_2=90 deg). The ratio $v_\theta/r\omega$ on each plane is derived from the averaged absolute tangential velocity in areas 1–3. This shows obvious difference of $v_\theta/r\omega$ between planes 1 and 2. Relatively high $v_\theta/r\omega$ is present in the blade passage (plane 2) and low $v_\theta/r\omega$ in the tip clearance (plane 1). The reason for the velocity difference in the two planes can be found from the presence of strong leakage flow and the reverse flow in the tip clearance as shown in Fig. 11(a). The leakage flow heads for tangential direction, which is opposite to the impeller rotational direction, and thus absolute tangential velocity decreases considerably. Moreover, the reverse flow at the impeller outlet takes the fluid of low absolute tangential velocity at the downstream of impeller exit to the tip clearance, decreases the fluid absolute tangential velocity in the tip clearance (plane 1), and finally mixes with the impeller passage flow which has relatively high absolute tangential velocity. Thus, the ratio $v_\theta/r\omega$ of the mixed internal fluid (plane 2) decreases sharply from inside the impeller outlet (r/r_2=0.85) and the decreased $v_\theta/r\omega$ goes out to the impeller outlet. It should be
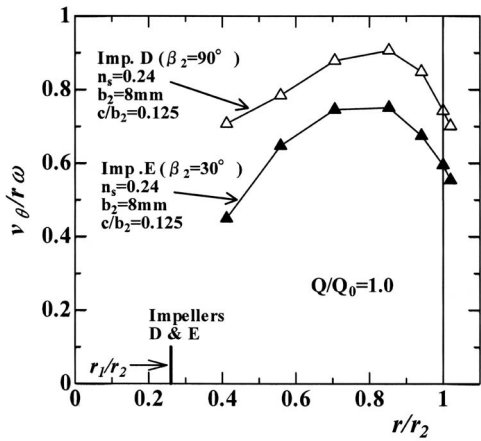
Fig. 13 Change of absolute tangential velocity ratio by blade outlet angle (Impellers D and E, $Q/Q_0=1.0$, PIV) (uncertainty of $v_\theta/r\omega=\pm3.5\%$)

the main reason why even though $v_\theta/r\omega$ in the impeller passage is different at different locations of the planes, the $v_\theta/r\omega$ just behind the impeller outlet becomes almost same regardless of the location of the planes. To examine the influence of the blade outlet angle on the $v_\theta/r\omega$, the semi-open impellers D ($\beta_2=90$ deg) and E ($\beta_2=30$ deg) are compared as shown in Fig. 13. The $v_0/r\omega$ has resulted from averaging of the absolute tangential velocity ratio of all planes and areas measured at the B.E.P. The result indicates that the $v_\theta/r\omega$ of the radial bladed impeller D is relatively higher than that of the backward bladed impeller E. Since the absolute tangential velocity ($v_{\theta2}$) at the impeller outlet contributes to the theoretical head ($H_{th}=u_2v_{\theta2}/g$) of the pump, the higher total head of the test impeller D than that of the test impeller E (Fig. 7) is caused by the high absolute tangential velocity of the test impeller D.

In order to investigate the change of absolute tangential velocity ratio by the tip clearance ratio (c/b_2), semi-open impellers B' and C' are adopted and the result is shown in Fig. 14. The $v_\theta/r\omega$ in the impeller passage is derived from static pressure distribution and the $v_\theta/r\omega$ at the impeller outlet ($r/r_2=1.02$) results from LDV measurement. The radial static pressure distribution on the
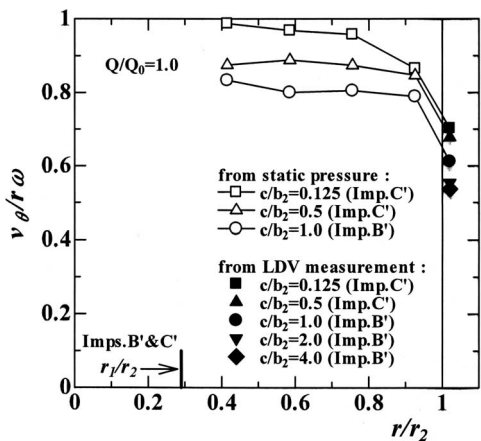

Fig. 14 Change of absolute tangential velocity ratio by tip clearance ratio (impellers B' and C', $Q/Q_0=1.0$) (uncertainty of $v_\theta/r\omega=\pm0.75\%$ and $\pm2.35\%$ static pressure and LDV, respectively)
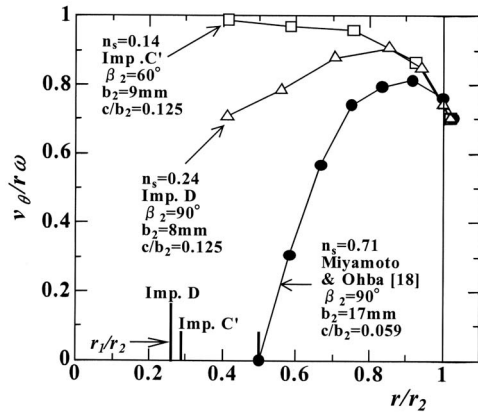
Fig. 15 Change of absolute tangential velocity ratio by specific speed variation ($Q/Q_0=1.0$)

front casing wall is measured and the average tangential velocity v_θ is estimated from the balance between the static pressure gradient and the centrifugal force as follows:

$$dp/dr = \rho v_\theta^2/r$$

$$\therefore v_\theta = \sqrt{r(dp/dr)/\rho} \qquad (3)$$

where dp and dr denote static pressure and radius increments between two measured locations in radial direction. The value of $v_\theta/r\omega$ thus obtained is considered to represent the mean rotational velocity ratio ($z/b_2=0.5$), as the centrifugal force pv_θ^2/r in the boundary layer does not balance with the radial pressure gradient dp/dr. As tip clearance ratio gets closer to $c/b_2=0$ (impeller C', $c/b_2=0.125$), the $v_\theta/r\omega$ becomes almost $v_\theta/r\omega=1.0$ in the impeller passage due to the decrease of tip leakage. This means that the fluid rotates with nearly the same velocity as the impeller rotational speed. However, $v_\theta/r\omega$ decreases sharply in the range of radius ratio of $r/r_2>0.75$ towards the impeller outlet. Moreover, the $v_\theta/r\omega$ decreases with increase of tip clearance ratio in the impeller passage as well as in the impeller outlet, which results due to the increased quantity of reverse flow by the increase of tip clearance ratio as examined by Choi et al. [9]. The reverse flow in tip clearance decreases the absolute tangential velocity $v_{\theta2}$ considerably at the impeller outlet and consequently theoretical head ($H_{th}=u_2v_{\theta2}/g$) decreases significantly.

Figure 15 shows the variation of $v_\theta/r\omega$ against specific speed (n_s) variation. In case of a normal specific speed semi-open impeller (Miyamoto and Ohba [18], $n_s=0.71$), the $v_\theta/r\omega$ increases sharply from the impeller inlet and decreases nearly at the impeller outlet ($r/r_2>0.9$). However, the $v_\theta/r\omega$ of the very low specific speed semi-open impellers C' and D shows quite different inclination. By increase of n_s, $v_\theta/r\omega$ increases largely in the impeller passage. Moreover, the sharp decrease point of the $v_\theta/r\omega$ moves inside the impeller passage by the increase of n_s. The $v_\theta/r\omega$ of the semi-open impeller D ($n_s=0.24$, averaged) indicates that the gradual increment of $v_\theta/r\omega$ changes to steep decrement at the radius ratio of $r/r_2>0.85$. Besides, in case of a very low n_s impeller C' ($n_s=0.14$), the radius ratio of steep decrement point ($r/r_2>0.75$) gets more deviated from that of the normal n_s impeller. Even though the adopted impeller configuration and tip clearance is more or less different, the change of $v_\theta/r\omega$ due to change of n_s shows a good evidence of the influence of reverse flow existing at the impeller outlet.

4 Conclusions

(1) Since there exists a large head difference between a closed and a semi-open impellers in the range of very

low specific speed, theoretical head of a semi-open impeller should be revised by considering the dependence of slip factor on the tip clearance ratio.

(2) Slip factor of a semi-open impeller is affected considerably by the impeller internal flow which is dominated by tip clearance ratio. The slip factor of a semi-open impeller becomes higher than that of Wiesner formula with increase of tip clearance ratio.

(3) The internal flow pattern of a radial bladed semi-open impeller ($\beta_2=90$ deg) is asymmetric to impeller axis even at the best efficiency point. Leakage flow passing through impeller tip clearance in the direction from the blade pressure side to the blade suction side forms a wide tangential direction flow field and generates a strong secondary flow in the impeller passage.

(4) Strong reverse flow enters into semi-open impeller passage through tip clearance near the impeller outlet and mixes with a main stream at the impeller passage. The reverse flow decreases the absolute tangential velocity considerably near the impeller outlet. The absolute tangential velocity at the impeller outlet depends significantly on the tip clearance ratio, which presents considerable influence on the pump performance.

Acknowledgment

Nomenclature

A_2 = impeller outlet area ($=2\pi r_2 b_2$)
b = impeller passage height (mm)
c = tip clearance (mm)
H = effective head (m)
H_{th} = theoretical head (m)
k = slip factor
n = rotational speed (rpm)
n_s = nondimensional specific speed ($=\omega\sqrt{Q_d}/(gH)^{3/4}$)
n_{sl} = nondimensional local specific speed
P = pump power (W)
p = static pressure (Pa)
Q = volume flow rate (m^3/s)
Q_0 = volume flow rate (m^3/s) at the best efficiency point (B.E.P.)
Q_d = designed flow rate (m^3/s)
Re = Reynolds number ($=\rho u_2 r_2/\mu$)
r = radius (mm)
u = tangential velocity of impeller (m/s)
$v_{\theta 2}$ = absolute tangential velocity at the impeller outlet (m/s)
w = relative velocity (m/s)
Z = impeller blade number
z = wall-normal distance from suction cover surface (m)

Greek Symbols

β = blade angle (deg)
η = pump efficiency ($=\rho gQH/P\times 100$)(%)

η_h = hydraulic efficiency
η_m = mechanical efficiency
η_v = volumetric efficiency
θ = tangential angle measured from volute tongue
ν = power coefficient ($=P/(\rho A_2 u_2^3/2)$)
μ = coefficient of viscosity (Pa s)
ρ = density of working fluid (kg/m^3)
ϕ = discharge coefficient ($=Q/A_2 u_2$)
ψ = head coefficient ($=H/(u_2^2/2g)$)
ω = angular velocity of impeller (rad/s)

Subscripts

θ = tangential component of velocity
r = radial component of velocity
2 = quantities at the impeller outlet

References

[1] Stepanoff, A. J., 1957, *Centrifugal and Axial Flow Pumps*, 2nd ed., Wiley, New York, pp. 69–89.
[2] Rodgers, C., 1990, "Experiments With a Low-Specific-Speed Partial Emission Centrifugal Compressor," ASME J. Turbomach., **112**, pp. 30–37.
[3] Abramian, M., and Howard, J. H. G., 1994, "Experimental Investigation of the Steady and Unsteady Relative Flow in a Model Centrifugal Impeller Passage," ASME J. Turbomach., **116**, pp. 269–279.
[4] Worster, R. C., 1963, "The Flow in Volutes and Its Effects on Centrifugal Pump Performance," Proc. Inst. Mech. Eng., **177**(31), pp. 843–871.
[5] Kurokawa, J., Matsumoto, K., Matsui, J., and Kitahora, T., 1998, "Performances of Centrifugal Pumps of Very Low Specific Speed," in *Proceedings of the 19th IAHR Symposium on Hydraulic Machinery and Cavitation*, Singapore, 2, pp. 833–842.
[6] Kurokawa, J., Matsumoto, K., Matsui, J., and Imamura, H., 2000, "Performance Improvement and Peculiar Behavior of Disk Friction and Leakage in Very Low Specific-Speed Pumps," *Proceedings of the 20th IAHR Symposium on Hydraulic Machinery and Systems*, Charlotte, USA, CD-ROM Paper No.3B(PD-02).
[7] Ohta, H., and Aoki, K., 1990, "Study on Centrifugal Pump for High-Viscosity Liquids (Effect of Impeller Blade Number on the Pump Performance)," Trans. Jpn. Soc. Mech. Eng., Ser. B, **56**(644), pp. 1702–1707.
[8] Minemura, K., Kinoshita, K., Ihara, M., and Egashira, K., 1995, "Effects of Design Parameters on Air-Water Two-Phase Flow Performance of a Radial-Flow Pump," Trans. Jpn. Soc. Mech. Eng., Ser. B, **61**(588), pp. 2996–3004.
[9] Choi, Y-D., Kurokawa, J., Matsui, J., and Imamura, H., 2002, "Internal flow characteristics of a centrifugal pump with very low specific speed," in *Proceedings of the 21st IAHR Symposium on Hydraulic Machinery and Systems*, Lausanne, Switzerland, 1, pp. 317–323.
[10] Choi, Y-D., Kurokawa, J., Matsui, J., and Imamura, H., 2002, "An Experimental Study on the Internal Flow Characteristics of a Very Low Specific-Speed Centrifugal Pump," *Proceedings of the 5th JSME-KSME Fluids Engineering Conference*, Nagoya, Japan, CD-ROM Paper No. OS16-3-6.
[11] Choi, Y-D., Nishino, K., Kurokawa, J., and Matsui, J., 2004, "PIV Measurement of Internal Flow Characteristics of Very Low Specific Speed Semi-open Impeller," Exp. Fluids, **37**, pp. 617–630.
[12] Raffel, M., Willert, C., and Kompenhans, J., 1998, *Particle Image Velocimetry—A Practical Guide*, Springer-Verlag, New York, pp. 105–146.
[13] Nishino, K., and Torii, K., 1993, "A Fluid-Dynamically Optimum Particle Tracking Method for 2-D PTV: Triple Pattern Matching Algorithm," in *Proceedings of the 6th International Symposium on Transport Phenomena in Thermal Engineering (ISTP-VI)*, Seoul, Korea, pp. 1411–1416.
[14] Abernethy, R. B., Benedict, R. P., and Dowdell, R. B., 1985, "ASME Measurement Uncertainty," ASME J. Fluids Eng., **107**, pp. 161–164.
[15] Kurokawa, J., and Amasaka, Y., 1983, "A Study on the Internal Flow of Spiral Casing - Part 2: Experimental Determinations of Flow Characteristics in Volutes," Trans. Jpn. Soc. Mech. Eng., Ser. B, **49**(448), pp. 2735–2745.
[16] Wiesner, F. J., 1967, "A Review of Slip Factors for Centrifugal Impellers," ASME J. Eng. Power, **89**, pp. 558–572.
[17] Murakami, M., Kikuyama, K., and Asakura, E., 1980, "Velocity and Pressure Distributions in the Impeller Passages of Centrifugal Pumps," ASME J. Fluids Eng., **102**, pp. 420–426.
[18] Miyamoto, H., and Ohba, H., 1995, "The Effect of Flow Rate on Characteristics in Centrifugal Impellers," JSME Int. J., Ser. B, **38**(1), pp. 25–30.

Alexandre Perrig

François Avellan

Jean-Louis Kueny

Mohamed Farhat

Laboratory for Hydraulic Machines,
Ecole Polytechnique Fédérale de Lausanne
(EPFL),
CH-1015 Lausanne, Switzerland

Etienne Parkinson
VATECH Hydro Ltd.,
Rue des 2 Gares, 6,
CH-1800 Vevey, Switzerland

Flow in a Pelton Turbine Bucket: Numerical and Experimental Investigations

The aim of the paper is to present the results of investigations conducted on the free surface flow in a Pelton turbine model bucket. Unsteady numerical simulations, based on the two-phase homogeneous model, are performed together with wall pressure measurements and flow visualizations. The results obtained allow defining five distinct zones in the bucket from the flow patterns and the pressure signal shapes. The results provided by the numerical simulation are compared for each zone. The flow patterns in the buckets are analyzed from the results. An investigation of the momentum transfer between the water particles and the bucket is performed, showing the regions of the bucket surface that contribute the most to the torque. The study is also conducted for the backside of the bucket, evidencing a probable Coanda interaction between the bucket cutout area and the water jet. [DOI: 10.1115/1.2170120]

Introduction

Performance prediction of hydraulic machines, such as efficiency and dynamic behavior under different operating conditions, is of high interest to manufacturers. The design of Pelton turbines is mainly conducted from know-how and extensive experimental testing. In today's highly competitive market of turbine upgrading and refurbishment, the performance guarantees are often difficult to determine in the short term. An accurate prediction of Pelton machines by numerical simulation would reduce the time required for the design phase.

Few experimental investigations of the flow in Pelton turbines are presented in the literature. Lowy investigated the flow in a fixed bucket and, more particularly, the cutting process of the jet by the bucket cutout [1], whereas Bachman et al. [2] performed flow visualizations around a Pelton runner. Grozev et al. [3] and Kvicinsky et al. [4] performed pressure measurements in nonrotating Pelton buckets in steady state. Water-layer thickness measurements on static buckets were also performed by Kvicinsky et al. [4] and Guilbauld et al. [5].

In recent years, physical models allowing complex free surface flow modeling have been developed and refined. The main models are the volume of fluid (VOF) method and the two-phase homogeneous model. Kvicinsky et al. [6] investigated both models and experimentally validated them in the cases of a jet impinging a flat plate and a nonmoving Pelton turbine bucket [3]. The two-phase homogeneous model appeared to provide the best results in terms of accuracy and computational cost. The first attempts to numerically simulate the flow in a moving Pelton turbine bucket were conducted by Hana [7], Sick et al. [8–10], Janetzky et al. [11], and Mack and Moser [12].

In the present study, extensive experimental and numerical investigations in a rotating Pelton turbine bucket are presented. The transient wall pressure distribution measured on the bucket inner surface of a runner in rotation permits the validation of the physical models by comparing the corresponding numerical results to the measurements. A procedure for advanced instrumentation of reduced-scale turbine models, developed by Kvicinsky et al. [13] and Farhat et al. [14], is applied for the experimental investigations.

At first, the physical models chosen are detailed. These include the two-phase homogeneous model in a rotating frame of reference, the free surface, and surface tension modeling. Then, the numerical setup and the experimental techniques are presented. Finally, the results obtained from both approaches are analyzed, compared, and the momentum transfer in the bucket is discussed.

Two-Phase Homogeneous Model

The flow model used for the numerical simulations is based on the generalized homogeneous multiphase flow model developed by Ishii [15], with the additional sources of momentum for the effects of the Coriolis and centrifugal accelerations in a steady rotating frame of reference. The governing equations are described below

Continuity Equation

$$\frac{\partial \rho_m}{\partial t} + \vec{\nabla} \cdot (\rho_m \vec{W}_m) = 0 \tag{1}$$

where the mixture density ρ_m and the mixture relative flow velocity $\vec{W}_m$ are defined as

$$\rho_m = \sum_{n=1}^{2} \alpha_n \rho_n \text{ and } \vec{W}_m = \frac{\sum_{n=1}^{2} \alpha_n \rho_n \vec{W}_n}{\rho_m} \tag{2}$$

where the volume fraction α_n is given by

$$\alpha_n = \frac{V_n}{\sum_n V_n} \tag{3}$$

Momentum Equation

$$\frac{\partial}{\partial t}(\rho_m \vec{W}_m) + \rho_m (\vec{W}_m \cdot \vec{\nabla}) \vec{W}_m$$

$$= -\vec{\nabla} p_m + \vec{\nabla}(\bar{\bar{\tau}}_m + \bar{\bar{\tau}}_{t_m}) - \rho_m \vec{\omega} \times (\vec{\omega} \times \vec{r}_m) - 2\vec{\omega} \times \vec{W}_m + \vec{f}_m \tag{4}$$

where $\vec{f}_m$ represents any body force.

Diffusion Equation. This drives the mass transfer between each phase by assuming that both phases share the same flow field

$$\frac{\partial \alpha_n \rho_n}{\partial t} + \vec{\nabla} \cdot (\alpha_n \rho_n \vec{W}_m) = \Gamma_n \tag{5}$$

Table 1 Operating conditions for the investigated point

Specific Energy	Discharge	Efficiency	Needle stroke
ψ/ψ_{opt}	ϕ/ϕ_{opt}	η/η_{opt}	s/s_{opt}
1.01	1.03	0.999	1.04

Table 2 Mesh sizes

	Mesh 1 (k)	Mesh 2 (k)	Mesh 3 (k)	Mesh 4 (k)
Number of nodes rotor	70	150	240	608.5
Number of nodes stator	7.5	25	45	76.5
Total number of nodes	77.5	175	285	685

The mixture pressure p_m is written as

$$p_m = \sum_{n=1}^{2} p_n \qquad (6)$$

For keeping the interface as thin as possible, a compressive differencing scheme for the advection of volume fractions and a compressive transient scheme for the volume fraction equations are used according to [16].

The surface-tension model used is based on the continuum surface force model of Brackbill et al. [17]. The surface-tension force is modeled as a volume force concentrated at the interface. The surface-tension force $\vec{F}_{\alpha\beta}$ between a primary fluid α, the liquid phase, and a secondary fluid β, the gaseous phase, is given by

$$\vec{F}_{\alpha\beta} = \vec{f}_{\alpha\beta} \delta_{\alpha\beta} \qquad (7)$$

where

$$\vec{f}_{\alpha\beta} = -\sigma_{\alpha\beta} \kappa_{\alpha\beta} \vec{n}_{\alpha\beta} + \vec{\nabla}_s \sigma_{\alpha\beta} \qquad (8)$$

and

$$\delta_{\alpha\beta} = \begin{cases} 1 & r_{\alpha\beta} \equiv 0 \\ 0 & r_{\alpha\beta} > 0 \end{cases} \qquad (9)$$

The two terms summed on the right-hand side of Eq. (8) reflect the normal and tangential components of the surface tension force. $\delta_{\alpha\beta}$ is called the interface δ function; it is zero away from the interface, thereby ensuring that the surface-tension force is active only near the interface.
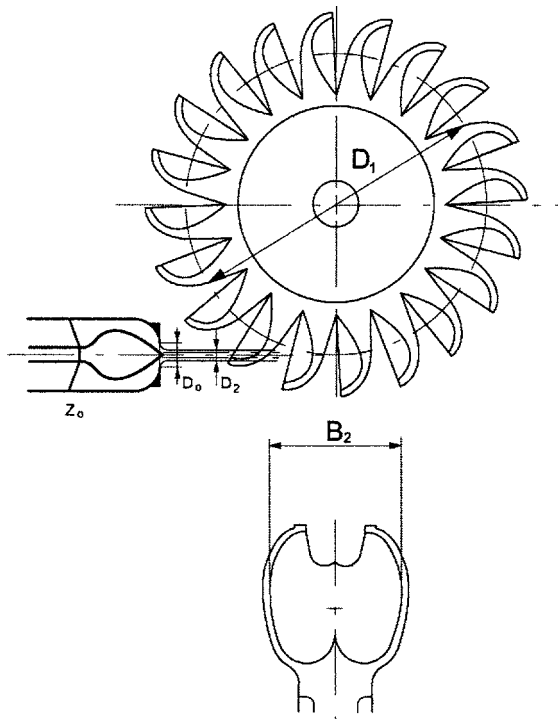

Fig. 1 Single-injector horizontal Pelton turbine

Flow Computation

A single-injector horizontal axis 20-bucket Pelton turbine model of $D_1/B_2 = 3.5$ is investigated (see Fig. 1). For the purpose of the present analysis, a single operating point (see Table 1), close to the best efficiency point, is considered to avoid any off-design driven phenomena.

The numerical simulation of the flow is carried out with the CFX-5® code. The continuity and momentum equations are discretized using a high-resolution upwind scheme with the physical advection terms weighted by a gradient-dependent blend factor, providing a good trade-off between diffusion and dispersion. A second-order backward Euler scheme is used for the transient terms.

The incoming jet is assumed to be ideal, with a constant velocity profile determined from the specific energy and discharge conditions, and the flow relative to the splitter to be symmetrical. The turbulence is taken into account using a $k-\varepsilon$ turbulence model with a standard wall function. No casing is taken into account, and the pressure surrounding the turbine is considered as constant. As far as body forces are concerned, only the surface-tension force acting on the flow is modeled.

The computational domain is divided in two subdomains, i.e., a stator with a dummy injector and a rotor with the runner. By assuming periodic flow, one-quarter of the runner is simulated, i.e., five buckets (Fig. 2). A transient rotor-stator sliding interface is set between the two subdomains. The domains are modeled by an unstructured mesh made of 685 k nodes, i.e., 2.4 million tetrahedral elements.

Quality Check of Numerical Simulation Results

The simulation is run until the rms residuals for the momentum equations reduce below 10^{-5}, and the bucket and runner torques become periodic. The mass flow conservation through the domain is checked as well. In order to check the mesh influence on the solution, four different meshes with an increasing number of elements are tested (see Table 2). Five reference monitoring points, distributed in the bucket inner surface, are selected (see Fig. 4). The rms value of the absolute grid solution error on the calculated
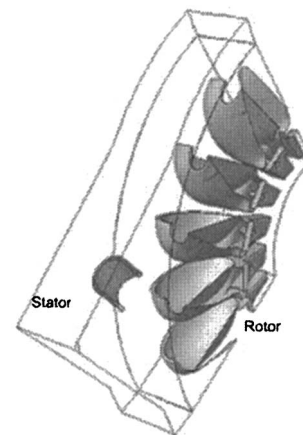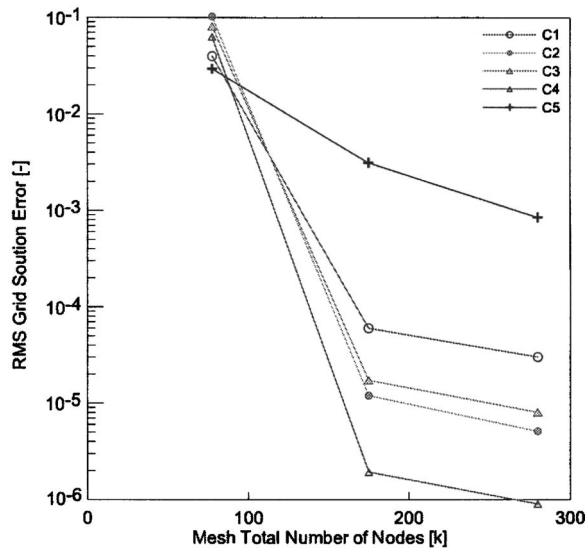

Fig. 2 Computational domain

Fig. 3 Influence of mesh size on solution error for the five pressure taps

Fig. 4 Locations of the five reference pressure taps on the bucket

pressure signal for each monitoring point between the coarse meshes and the finer mesh is determined and plotted in Fig. 3.

$$\text{rms(error)} = \sqrt{\frac{1}{N}\sum_{i=1}^{N}\left(\frac{f_{\text{fine}_i} - f_{ki}}{f_{\text{fine}_i}}\right)^2} \quad (10)$$

where f_{fine_i} is the solution on the finest grid and f_k the solution for coarse grid k. The subscript i refers to the time step, and N is the total number of time steps.

The error decreases with the mesh size increase and remains low from 200 k nodes. It appears that no significant enhancement is to be expected from a further refinement of the mesh.

Pressure Measurement Techniques

The reduced-scale Pelton turbine model is instrumented with an onboard acquisition system developed for measuring the unsteady pressure distribution on the bucket inner surface. Thirty-two miniature piezoresistive pressure transducers of 10 bar range, coated with a silicone compound of the same density as water, are embedded in four buckets.

The onboard electronic for signal conditioning is made of 32 preamplifiers and anti-aliasing filters and is installed in the runner
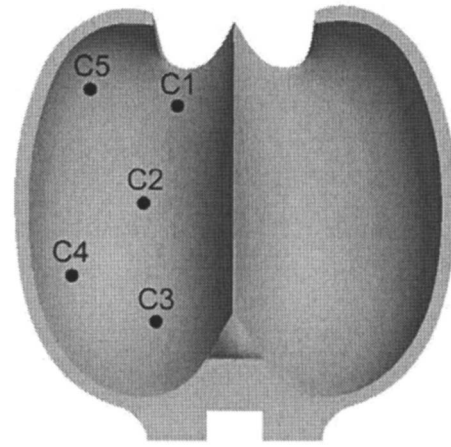
shaft (see Fig. 5). The conditioning electronic equipment connected to eight acquisition boards is located in the turbine shaft. Each board has four channel inputs and 12-bit A/D converters. The maximum sampling frequency is 20 kHz, while the memory storage capability is of 64 k-samples per channel. A host computer is used for monitoring purposes via an ArcNet communication network. External communication and power supply are achieved with a four-channel slip ring. The system is capable of transferring up to 1.5 Mbits/s [14]. The synchronization of the data sampling of active boards is performed through a master-slave scheme, all active modules being synchronously triggered within 5 μs.

The pressure sensor's static calibration is performed by installing the instrumented runner in a pressurized vessel. The measurement error is found to be $<0.5\%$ of the measurement range.

The dynamic calibration of the pressure sensors is carried out in a large vessel with a spark-generated bubble device [14]. The pressure-sensor frequency bandwidth extends up to 25 kHz. A check of the sensors is made with the runner spinning in air to measure the effect of centrifugal load.

Data Reduction

In the following sections, the results are presented over one duty cycle of one bucket, referred as bucket j, assumed to be 90 deg [18]. All discussed data, torque, pressure, discharge, and flow visualization stem from the same bucket.
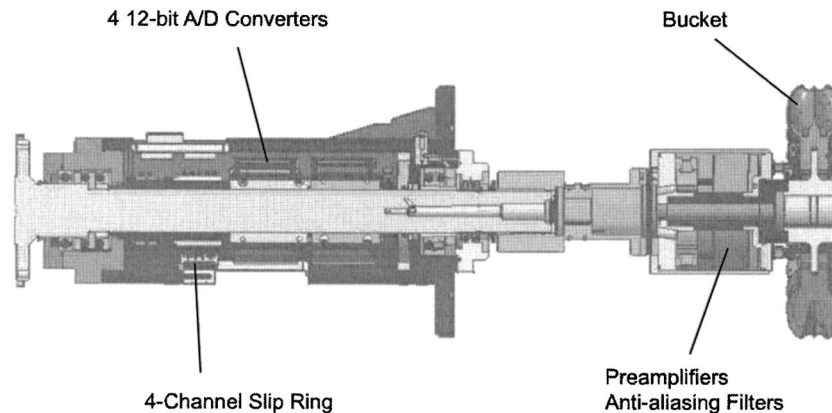

Fig. 5 Instrumentation and data acquisition system installed on the rotating shaft
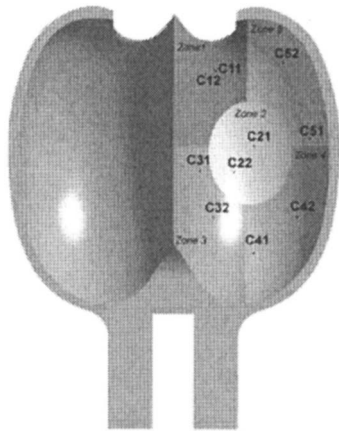
Fig. 6 Definition of the bucket zones with respect to the pressure taps

All the data are presented with respect to the same angular reference. The reference is set as the angular position where bucket j splitter tip is in contact with the jet outer boundary assumed to have remained constant from the injector nozzle. The pressure measurements are phase averaged from 295 runner rotations and synchronized from the tachometric signal.

According to the shape of the phase-averaged transient pressure signals [13,18], the bucket inner surface is divided into five zones of the same surface area, referred as zone 1 through zone 5. Two reference locations for each zone, labeled C11–C52, representative of the local pressure field, are selected for each zone [18] (see Fig. 6).

Numerical Flow Simulation-Measurements Comparison

The results obtained from the measurements and the computations are presented in Fig. 7. The means of comparison are the rise and decay times and slopes, the signal amplitude, the phase shift, and the signal period or duration.

In zone 1, the pressure measurements exhibit either a peak-plateau or a double-peak shape. Rise times are very short, especially in the case of C12. The typical signal for zone 1 can be divided into two portions, ranging, respectively, from 0 deg to 25 deg and from 25 deg to 65 deg duty cycle. In the first portion, the standard deviation remains low, whereas it increases significantly in the second portion, where the second peak, or plateau, is visible. The first portion of the signal is fairly predicted by the simulation in terms of amplitude, with a relative error ranging from 11.5% for C12 to 18% for C11. On the other hand, the signals are well in phase. The rise slope is 35% less in the simulation, and the signal starts earlier. The plateau (see C11) and the second peak (see C12) are barely visible in the numerical flow simulation results, and the calculated period is shorter by 20 deg for C11 and 10 deg for C12.

The pressure signals in zone 2 are in very good accordance between the measurements and the simulation: rise and decay times, signal phases, and signal periods match very well. The predicted amplitude is too high by about 7%. The measured signal exhibits a plateau at maximum amplitude, accounting for 18 deg, i.e., the bucket pitch angle. The measured signal shows a narrow peak of pressure at 12 deg duty cycle. The real amplitude of the peak remains unknown, as its duration is very short, of the order of a few microseconds and the 20 KHz sampling rate too low to capture it adequately. Even if the time step selected for the simulation is three times lower than the experimental sampling rate, the numerical simulation shows a discontinuity for C22. Zone 2 signal accounts for 2/3 of the bucket duty cycle.

In zone 3, the computed amplitudes vary between 7% and 26% below the measured ones. The discontinuity measured by C31 in

the vicinity of 55 deg duty cycle is marked as a change of slope in the simulation, even if the decay slope is underpredicted. For C31, the rise start and the period are in good accordance with the slopes underpredicted, while for C32 the rise and decay slopes are well simulated, but the period is shorter by 6 deg, and the phase shift at signal rise is 2.5 deg.

The numerical flow simulation results for zone 4 underpredict the signal amplitude by more than 15%. For C41, located in the aft region of zone 4, the period is 15 deg shorter than that of the measured signal. The phase shift at signal rise is delayed by 6 deg, while the rise slope is accurately determined. For C42, located closer to the outer edge of the bucket, the period is 8 deg shorter, but the rise is in phase with the measurements.

The signals in zone 5 are well predicted by the numerical flow simulation. Amplitudes for C51 and C52 are very close. Periods are well predicted, but it is remarkable that for C51 the computed signal maximum leads the measurement by 5 deg, while for C52, the maximum of the signal lags them by 6 deg. The differences stated between the numerical flow simulation prediction and the measurements can be explained from the differences between the simulated flow patterns and the real patterns deduced from the available observations and the pressure signals.

Bucket Flow Patterns

The instantaneous bucket discharge functions is computed through a control plane parallel at the tip of bucket j and parallel to the bucket upper edges. Figure 8 shows the instantaneous discharge coefficients entering and leaving the buckets j and $j+1$ during one duty cycle, obtained from the computations. All the angular positions refer to the angular reference defined in the previous section.

The effective discharge coefficient received or released by any bucket can be expressed as

$$\varphi(t) = \frac{4}{\pi B_2^2 U_1} \int_{A_S} \int_0^1 \vec{W}_m \cdot \vec{n} \, dA \, d\alpha \qquad (11)$$

Inflow. Four stages in the bucket duty cycle can be identified from the kinematics and the inflow discharge function. (i) Cut in: From 0 deg to 14 deg, the jet is progressively cut by the bucket. (ii) Full jet: From 14 deg to 32 deg, the full jet feeds the bucket for an angular duration equivalent to the runner pitch [19]. The jet is actually cut by bucket $j+1$ at 18 deg bucket j duty cycle. However, it is not until 32 deg that the disturbed section of the jet reaches the entry plane of bucket j. The decrease of bucket j discharge observed is due to the change in the relative velocities with the radial displacement of the jet section toward the bucket root [20]. (iii) Cut out: From 32 deg to 46 deg the jet section cut by bucket $j+1$ impinges bucket j. (iv) End of inflow: From 32 deg, the jet is completely separated from the injector, but the remaining portion is still catching up on bucket j. The jet section affected by the complete cut reaches bucket j entry plane at 46 deg duty cycle. From a purely kinematics point of view, the jet should separate from bucket $j+1$ backside, keeping its diameter constant, since the particles of the jet are animated by the absolute velocity C, faster than the runner peripheral velocity. The numerical flow simulation results, on the contrary, show a jet of decreasing diameter that stays attached to bucket $j+1$ backside far in the duty cycle. It is remarkable that the end of the feeding process and, more particularly, the behavior of the cut jet, remain unknown, as no usable observations have been performed thus far on the subject.

For the pressure signal and zone flow analysis to follow, it must be emphasized that there is a phase shift between the entry plane and the position of the sensors on the bucket inner surface, which varies from 3 deg in the cutout area (zone 1) to 8 deg at the bottom of the bucket (zones 2 and 3), depending on the estimated
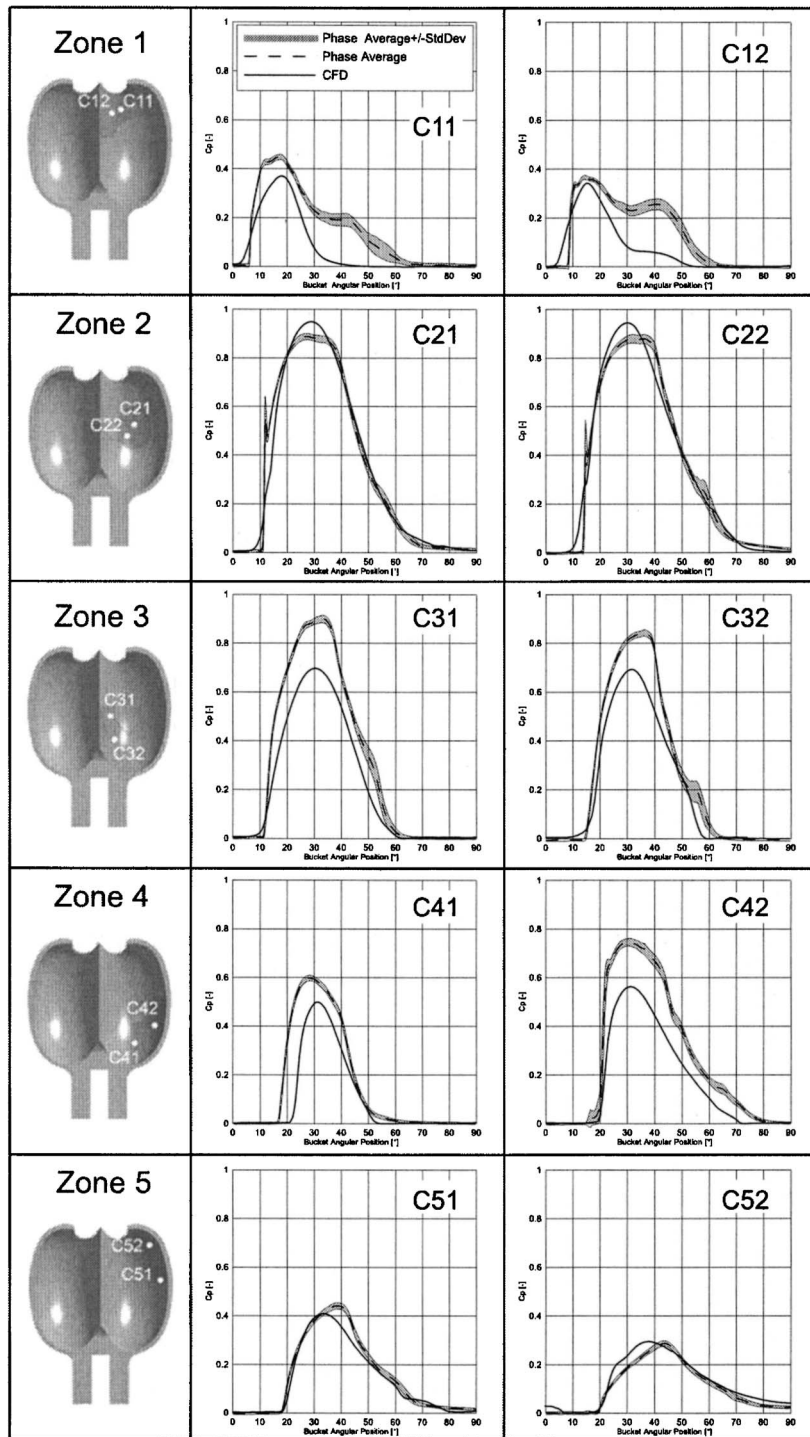
Fig. 7 Comparison of experimental with numerical flow simulation pressure coefficient results

travel time of the water particles from the entry plane. This phase shift has to be taken into account for further analysis.

Outflow. From about 25 deg, the water received at the beginning of the cycle leaves bucket j from the lateral edge, close to its root. The discharge reaches its maximum at the half cycle (45 deg), when the main flow balances from the rear to the outer regions of the bucket. The last drops of water exclusively leave the bucket from the frontal area, near the cutout. The discharge and its radial component decrease never stops, resulting in a line

Fig. 8 Evolution of adjacent bucket discharge functions over the duty cycle

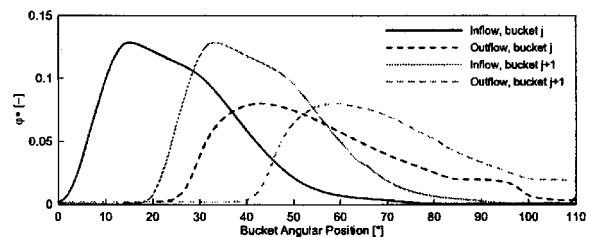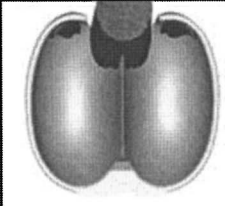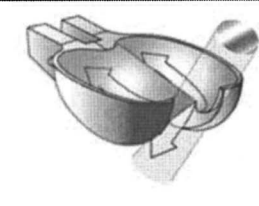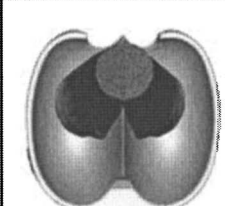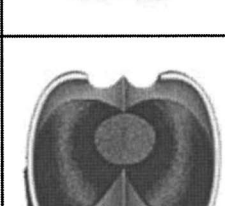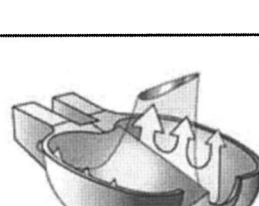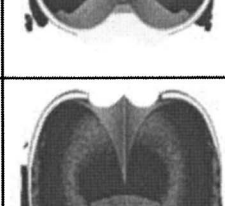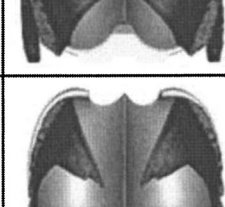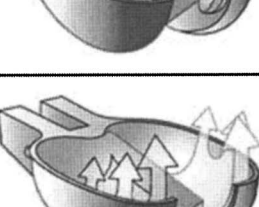| Angular Position	Observations	CFD	Interpretation
0°			
20°			
30°			
45°	N/A		
60°	N/A		

Fig. 9   Evolution of flow pattern along the runner rotation angle

of droplets visible along the entire runner periphery. The evacuation process predicted by the numerical flow simulation is in good accordance with the observations [2].

Flow Analysis

The discussion to follow refers to Fig. 9. The water jet encounters bucket j in zone 1. The first peak of pressure recorded by C11 and C12 sensors is related to the passage of the front of the jet over the sensor. The steep rise slope indicates that the jet interface is sharp, and the small standard deviation confirms the periodicity of the flow. The second peak, or plateau, presents a nonperiodic behavior, as shown by the high standard deviation value. Indeed, three phenomena that are visible from the observations are superposed: (i) As the jet is being cut by bucket $j+1$, after 30 deg, its diameter increases, projecting more water particles on zone 1. (ii) The jet appears to bend toward the bucket j root as the cutting process of bucket $j+1$ starts, modifying its angle of attack relative

to bucket j. (iii) If the flow moves backward in the direction of the bucket root at the beginning of the bucket duty cycle, then it flows toward the cutout, loading zone 1 again in the second half of the duty cycle.

The peak of pressure measured in zone 2 corresponds to the passage of the jet interface over the sensor. It may be related to compressibility effects due to a stagnation point imposed on the flow by the change of bucket surface curvature [13,21]. It is interesting to remark that the area of zone 2 where the peak of pressure is visible often presents erosion damages, even during reduced-scale model testing.

The jet fully feeds bucket j in zone 2 from 20 deg until 38 deg, i.e., the runner pitch. The measured signal remains quasi-steady during the 18 deg pitch period. The flow fills almost the entire bucket helicoidally from zone 2. C21 and C22 account for 5/6 of the bucket duty cycle. The signal shrinks as the feeding process stops. Zone 2 is a focus region that receives water stemming from the whole feeding process. The numerical flow simulation results

for that region are very accurate because the flow received in zone 2 is dominated by inertia effects and is not affected by the jet-bucket interaction.

The short plateau, and a higher-than-average standard deviation at 54 deg duty cycle, visible on the C22 signal may be related with the last section of the cut jet catching up to the bucket, and the transition from jet impact flow to a purely water sheet flow. This would indicate that the feeding process stops earlier than predicted by the numerical simulation.

Zone 3 is where the end of the feeding process occurs. The signal rises are smoother because the front of the jet is not sharp anymore and is preceded by the water sheet already formed in zones 1 and 2. The measured signal for C31 presents a discontinuity at 53 deg duty cycle, followed by a rapid drop of amplitude. This may be related to the last jet section catch-up of the bucket at that instant, as for zone 2. The delay in signal rise may be related to the jet enlargement at the moment of the jet cut stated previously, which is absent in the numerical flow simulation prediction. For C31, the amplitude is underestimated, probably because the flow along the splitter experiences significant shear stresses, for which the standard k-ε turbulence model is probably not valid.

Zone 4 only receives water-sheet flow and is at the beginning of the bucket outflow. The main discrepancies stated in the previous section are the phase shift for C41 and the lack of amplitude of the predicted signals. The predicted sheet of water seems to exhibit a shorter period than the real one, arriving later and leaving the zone earlier. At 15 deg duty cycle, zone 4 is still dry in the numerical flow simulation results, while the measured C41 signal rise indicates that the water sheet already covers zone 4. The predicted water flow trajectory is more laterally deviated than the observed trajectory flowing to the root, bypassing zone 4. The lack of amplitude of the signals is related to the deformation and increase of the diameter stated from the visualizations discussed for zone 1.

From the numerical flow simulation results, the water sheet reaches zone 5 4 deg earlier than zone 4 (see C51 and C52), whereas from the measurements it should be 3 deg late. The accuracy of the prediction is better than in zone 4 because zone 5 is less affected by the deformation and bending of the jet after its encounter with the next bucket.

The main differences that can be stated from the comparison of the experiments and the simulations are as follows: (i) The actual feeding process is faster than predicted by the numerical flow simulation, with more water flowing towards the bucket root, and more water leaving the bucket from zone 4. (ii) The end of the feeding process arises earlier than predicted, between zones 2 and 3, as opposed to the numerical flow simulation, where it arises in zone 3. (iii) The jet enlargement and bending after its encounter with bucket $j+1$ is underestimated in the simulation. (iv) The flow distribution in the bucket: the flow in the buckets balances back and forth, flowing from zone 1 to zone 2 and from zone 2 to zones 3–5 in a counterclockwise pattern [2]. The numerical flow simulation prediction seems to lead the measurements in the first portion of the duty cycle and to lag behind them in the second portion. The jet-cutting process modeling is related to the discrepancies observed. The overall results are accurate enough, however, to draw some conclusions about the power exchange mechanisms involved.

Power Budget

The pressure field does not adequately show where the zones are that contribute the most to the bucket power build up. It is more relevant to investigate the bucket-power history to assess the effective momentum transfer between the flow and the bucket. The critical criteria are as follows: (i) the bucket surface geometry, (ii) the radius of application of the driving force, (iii) the water remaining kinetic energy, and (iv) bucket angle of setting.

The resultant instantaneous power produced by each zone is determined from the projection on the local peripheral direction of the local surface normal pressure of each elementary area A_k that
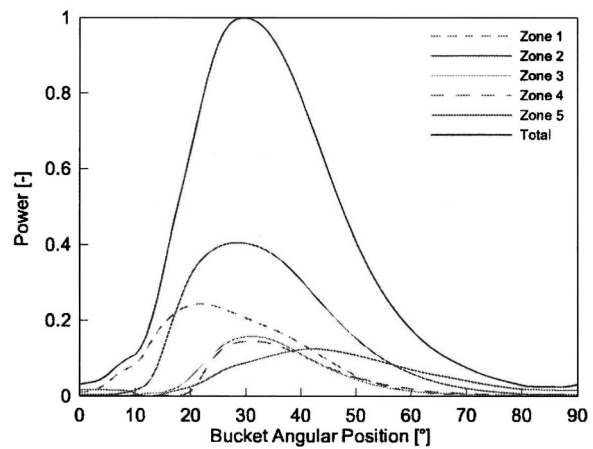

Fig. 10 Contribution of each zone to the total mechanical power exchange as a function of the runner rotation angle. The power is normalized by the total bucket power peak value.

composes zone i, multiplied by the runner angular velocity (see Eq. (12)). The other components of the stress tensor are neglected.

$$P_i = \sum_{k=1}^{m} \vec{t}_{ik} \cdot \vec{\omega} = \left[\sum_{k=1}^{m} \vec{r}_{ik} \left(\int_{A_{ik}} p_{ik}(t) \vec{n}_{ik} dA_{ik} \right) \right] \cdot \vec{\omega} \qquad (12)$$

The pressure field shows the regions that are the most loaded in terms of normal mechanical stress, but does not give real information about the energy transfer in the bucket. The power contribution of the different bucket regions (see Fig. 10) highlights the effective momentum transfer between the flow and the bucket throughout the bucket period. Zones 1 and 2 contribute the most to the bucket power because these two regions experience the direct impingement of the jet at the beginning of the bucket period, when the kinetic energy of the flow is at its maximum. Zone 2 contributions exhibit the longest and tallest pressure signal, lasting more than 2/3 of the bucket period, and accounts for more than 40% of the bucket torque. Zone 2 can be considered as a focal region, which collects all the water particles transiting in the bucket. The flow received in zone 2 during the full jet period is in accordance with the kinematical assumptions made to design the buckets. This explains why the classic design methods permit one to obtain machines of fair efficiency. The maximum power is reached at 30 deg when the contributions of zones 2–4 are at their respective maximums. The first flow particles, which arrived with the highest kinetic energy, are leaving the bucket at that instant. Zones 3 and 4 are far more loaded than zone 5; however, zone 5 surpasses all the other regions in terms of torque contribution duration, accounting for more than 2/3 of the bucket period.

The radius of application of the location, where the momentum change occurs, does not seem to play a significant role in the resulting bucket torque. The most critical point is the jet energy, the surface orientation, and the trajectories of the water particles. Figure 11 shows the torque produced by the inner surfaces of the active buckets of the runner normalized by the mechanical torque measured on the experimental test rig. The mean value of the predicted torque appears to be almost 15% lower than the measured one. This is not consistent with the pressure signals results and the zone power map. This indicates that a significant fraction of the torque is produced by the backside of the bucket.

The torque contribution of the backside of one bucket is reported in Fig. 12. When the bucket first interacts with the jet, a countertorque is visible. During the jet-cutting process, the torque increases and reaches a maximum value at about 12 deg, which is about 7.5% of the torque produced by the whole inner surface of the bucket. This indicates that the backside of the bucket, in the vicinity of the cutout, behaves like the blade of a reaction turbine.
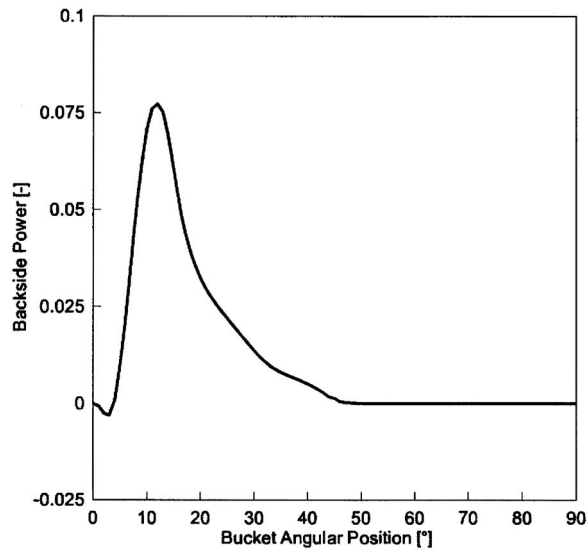
Fig. 11 Contribution to the total mechanical torque of the inner side of a single bucket as a function of the runner rotation angle. The computed values of the torque are normalized by the mean value of the measured torque.

In fact, it had been shown that a lift increase may be obtained when suitably curved convex surfaces are placed near a jet due to the Coanda effect [22–24]. Indeed, attempts were successfully made to develop reaction turbines based on a similar principle, using the deviation of a jet along a curved convex wall to drive the shaft of the machine [22,23]. The assumption of a Coanda interaction is confirmed by the experimental observations of the jet deformation and bendings (see Fig. 9).

Moreover, at some location, the numerical flow simulation results indicate very low pressures that could lead to the onset of cavitation on the machine. Indeed, some Pelton machines do exhibit erosion on the back surface, near the cutout [25,26].

Conclusions

The free surface flow in a Pelton turbine bucket is investigated by using both unsteady numerical simulations, based on the two-phase homogeneous physical model and pressure measurements

carried out in the buckets inner surfaces. The analysis of the results obtained allows identifying five distinct zones in the bucket inner surface. The predicted pressures match the experimental results well, especially in the zones where the flow is dominated by inertia effects and where the flow is not affected by the jet-bucket interaction. From the experiments, the jet appears to be more disturbed during the cut-in process than according to the numerical flow simulation prediction. Moreover, in the zones where the flow undergoes more shear stresses, the prediction for the signal amplitudes is less accurate. This is probably because of the standard k-ε turbulence model.

The computed flow patterns exhibit good agreement with the flow visualizations during the first and last stages of the bucket cycle. Results regarding the cut jet are more difficult to assess since visualizations of this portion of the cycle are not yet available. An analysis of the power transfer in the five bucket regions shows that the outer regions, between D_1 and the cutout, contribute the most to the bucket power. These areas interact early with the jet and, thus, receive water particles with a high momentum. On the other hand, the regions located near the root of the bucket are less productive, in terms of bucket torque contribution, because of the less favorable surface orientation and radius of application.

It appears from the numerical simulation that the bucket backside does contribute to the bucket torque. This is linked with the interaction between the water jet and the bucket cutout profile. The jet appears to adhere to some extent to the bucket back, showing the presence of a Coanda effect. The Coanda effect leads to the creation of a lift force, and from that an angular momentum in the sense of rotation, contributing to the runner torque. The numerical flow simulation results show a contribution of about 7.5%. The accuracy of the prediction is difficult to assess because no experimental pressures are available for the bucket backside. Nevertheless, since the predicted average runner torque is in within 5% with the measured ones, it can be concluded that such a phenomenon exists. From an experimental point of view, the deformation of the jet observed witnesses the Coanda interaction on the bucket backside in the region of the cutout.

Further experiments would require flow visualization and pressure instrumentation of the bucket backside. Moreover, the air flow between adjacent buckets should be thoroughly investigated.
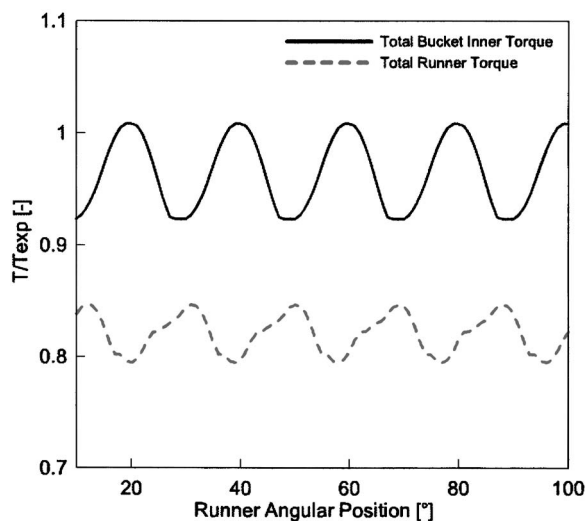
Fig. 12 Bucket backside contribution to the total mechanical power exchange as a function of the runner rotation angle. The power is normalized by the total bucket power peak value.

Nomenclature

A = surface area
α = liquid volume fraction
B_2 = bucket inner width
C_p = pressure coefficient,
$\qquad C_p = p - p_{\mathrm{ref}}/[(1/8)\rho(\omega D_1)^2]$
$\vec{C}$ = absolute flow velocity
D_1 = Pelton diameter
E = specific hydraulic energy
ε = turbulent dissipation rate
η = efficiency
H = head
k = turbulent specific kinetic energy, $k = (1/2)c_i'^2$
κ = free surface mean curvature
n = runner rotation frequency

$\vec{n}$ = normal unit vector
p = static pressure
P = power
Q = discharge
$\vec{r}$ = position vector
$\vec{T}$ = torque
$\vec{U}$ = circumferential velocity
$\vec{W}$ = relative flow velocity
$\vec{\omega}$ = angular rotation speed
φ_{B_2} = discharge coefficient, $\varphi_{B_2} = Q/[z_j(\pi B_2^2/4)U_1]$
ψ = specific energy coefficient, $\psi = 2E/U_1^2$
σ = surface tension
rms = root-mean-square value

Subscripts

m = mixture
n = phase number
1 = zone 1
2 = zone 2
3 = zone 3
4 = zone 4
5 = zone 5
α = liquid phase
β = gas phase
opt = reference to best efficiency point

References

[1] Lowy, R., 1944, "Efficiency analysis of Pelton Wheels," Trans. ASME, **66**, pp. 527–538.

[2] Bachmann, P., Schärer, Ch., Staubli, T., and Vullioud, G., 1990, "Experimental Flow Studies on a 1-Jet Model Turbine Pelton," *Proceedings of 15th IAHR Symposium on Modern Technology in Hydraulic Energy Production*, Sept. 11–14, Belgrade, Yugoslavia, Faculty of Mechanical Engineering, Belgrade, pp. 1–13.

[3] Grozev, G., Obretenov, V., and Trifonov, T., 1988, "Investigation of the Distribution of Pressure Over the Buckets of a Pelton Turbine," *Proceedings of the Conference on Hydraulic Machinery and Flow Measurements*, Sept. 13–15, Ljubljana, Yugoslavia, Turboinštitut, Ljubljana, pp. 119–125.

[4] Kvicinsky, S., Kueny, J.-L., and Avellan, F., 2002, "Numerical and Experimental Analysis of Free Surface Flows in a 3D Non-Rotating Pelton Bucket," *The 9th International Symposium on Transport Phenomena and Dynamic Rotating Machinery*, Feb. 10–14, Honolulu.

[5] Guilbaud, M., Houdeline, J. B., and Philibert, R., 1992, "Study of the Flow in the Various Sections of a Pelton Turbine," *Proceedings of 16th IAHR Symposium on Hydraulic Machinery and Caviation*, Sept. 14–19, São Paulo, Associação Brasileira de Recursos Hídricos, São Paulo, pp. 819–831.

[6] Kvicinsky, S., Longatte, F., Avellan, F., and Kueny, J.-L., 1999, "Free Surface Flows: Experimental Validation of the Volume of Fluid (VOF) Method in the Plane Wall Case," *Proceedings of 3rd ASME/JSME*, San Francisco, ASME, New York, pp. 1–8.

[7] Hana, M., 1998, "A Discussion on Numerical Simulation in Pelton Turbines,"

[8] Sick, M., Keck, H., Parkinson, E., and Vullioud, G., 2000, "New Challenges in Pelton Research," *Hydro 2000 Conference*, Bern, Switzerland.

[9] Parkinson, P., Garcin, H., Bissel, C., Muggli, F., and Braune, A., 2002, "Description of Pelton Flow Patterns With Computational Flow Simulations," *Hydro 2002: Development, Management, Performances*, Nov. 4–7, Kiris, Turkey.

[10] Parkinson, E., Vullioud, G., Geppert, L., and Keck, H., 2002, "Analysis of Pelton Turbine Flow Patterns for Improved Runner-Component Interaction," Int. J. Hydropow. Dams, **1**(5), pp. 100–103.

[11] Janetzky, B., Göde, E., Ruprecht, A., Keck, H., and Schärer, Ch., 1998, "Numerical Simulation of the Flow in a Pelton Bucket," *Proceedings of 19th IAHR Symposium*, Sept. 9–11, Singapore, World Scientific, Singapore, pp. 276–284.

[12] Mack, R., and Moser, W., 2002, "Numerical Investigations of the Flow in a Pelton Turbine," *Proceedings of XXIst IAHR Symposium on Hydraulic Machinery and Systems*, Sept. 9–12, Lausanne, Laboratory for hydraulic machines, Lausanne, pp. 373–378.

[13] Kvicinsky, S., Kueny, J.-L., Avellan, F., and Parkinson, E., 2002, "Experimental and Numerical Analysis of Free Surface Flows in a Rotating Bucket," *Proceedings of XXIst IAHR Symposium on Hydraulic Machinery and Systems*, Sept. 9–12, Lausanne, Laboratory for Hydraulic Machines, Lausanne, pp. 359–364.

[14] Farhat, M., Natal, S., Avellan, F., Paquet, F., Lowys, P., and Couston, M., 2002, "Onboard Measurements and Strain Fluctuations in a Model of Low Head Francis Turbine, Part I: Instrumentation," *Proceedings of the XXIst IAHR Symposium on Hydraulic Machinery and Systems*, Sept. 9–12, Lausanne, Laboratory for hydraulic machines, Lausanne, pp. 865–871.

[15] Ishii, M., 1975, "Thermo-Fluid Dynamic Theory of Two-Phase Flow," *Collection de la Direction des Etudes et Recherches*, EDF, Eyrolles, Paris, pp. 1–248.

[16] Zwart, P. J., Scheuerer, M., and Bogner, M., 2003, "Free Surface Flow Modeling of an Impinging Jet," *ASTAR International Workshop on Advanced Numerical Methods for Multidimensional Simulation of Two-Phase Flow*, Sept. 15–16, GRS Garching, Germany

[17] Brackbill, J. U., Kothe, D. B., and Zemach, C., 1992, "A Continuum Method for Modeling Surface Tension," J. Comput. Phys., **100**, pp. 335–354.

[18] Perrig, A., Farhat, M., Avellan, F., Parkinson, E., Garcin, H., Bissel, C., Valle, M., and Favre, J., 2004, "Numerical Flow Analysis in a Pelton Turbine Bucket," *Proceedings of 22nd IAHR Symposium on Hydraulic Machinery and Systems*, June 29–July 2, Stockholm, Swedpower, Stockholm, pp. A10-3-1–A10-3-14.

[19] Ténot, A., 1930, *Turbines Hydrauliques et Régulateurs Automatiques de Vitesse*, Vols. I & II, Librairie de l'Enseignement Technique, Eyrolles, Paris.

[20] Webster, J., 1971, "Analysis of Jet-Type Impulse Turbines," Water Power, **23**, pp. 287–292.

[21] Johnson, W., and Vickers, G. W., 1973, "Transient Stress Distribution Caused by Water-Jet Impact," J. Mech. Eng. Sci., **15**(4), pp. 302–310.

[22] Wille, R., and Fernholz, H., 1965, "Report on the First European Mechanics Colloquium on the Coanda Effect," J. Fluid Mech., **23**, pp. 801–819.

[23] Teodorescu-Tintea, C., 1967, "On a New Functional Principle in the Theory of Gas Turbines Based on the Coanda Effect: The Turbine Fitted With Depressive Blades," Rev. Roum. Sci. Tech., Ser. Mec. Appl., **12**(1), pp. 85–101.

[24] Fujisawa, N., and Shirai, H., 1987, "Experimental Investigation of the Unsteady Flow Field Around a Savonius Rotor at Maximum Power Performance," Wind Eng., **11**(4), pp. 195–206.

[25] Grein, H., 1990, "Cavitation Pitting and Rain Erosion on Pelton Runners," *Proceedings of 15th IAHR Symposium on Modern Technology in Hydraulic Energy Production*, Sept. 11–14, Belgrade, Yugoslavia, pp. 1–9.

[26] Brivio, R., and Zappi, O., 1995, "La Cavitazione Nelle Turbine Pelton (Parte I)," Energ. Elettr., **72**(2), pp. 45–49.

Numerical Calculation of Pressure Fluctuations in the Volute of a Centrifugal Fan

Rafael Ballesteros-Tajadura
e-mail: rballest@uniovi.es

Sandra Velarde-Suárez

Juan Pablo Hurtado-Cruz

Carlos Santolaria-Morros

Universidad de Oviedo,
Área de Mecánica de Fluidos,
Campus de Gijón,
33271 Gijón. Asturias, Spain

In this work, a numerical model has been applied in order to obtain the wall pressure fluctuations at the volute of an industrial centrifugal fan. The numerical results have been compared to experimental results obtained in the same machine. A three-dimensional numerical simulation of the complete unsteady flow on the whole impeller-volute configuration has been carried out using the computational fluid dynamics code FLUENT®. This code has been employed to calculate the time-dependent pressure both in the impeller and in the volute. In this way, the pressure fluctuations in some locations over the volute wall have been obtained. The power spectra of these fluctuations have been obtained, showing an important peak at the blade passing frequency. The amplitude of this peak presents the highest values near the volute tongue, but the spatial pattern over the volute extension is different depending on the operating conditions. A good agreement has been found between the numerical and the experimental results.
[DOI: 10.1115/1.2170121]

Introduction

Many authors have worked in the measurement of pressure fluctuations in fans as a way to identify sources of aerodynamic noise. A survey of the literature shows examples where surface pressure measurements have been applied successfully in both centrifugal and axial fan noise investigations. In particular, Carolus and Stremel [1] have exposed some of these examples and their own application to a low-pressure axial fan, analyzing the contribution of the inlet turbulence to the generation of noise. Fehse and Neise [2] have investigated the generation of low-frequency noise in centrifugal fans. They found that the broadband components at low frequencies are generated by classical flow separation regions located on the impeller shroud and the blades suction sides. Ohta et al. [3,4] have investigated the tonal noise generation in a low specific speed centrifugal fan. They have shown that the most effective noise source is located closed to the volute tongue, and the extension of the effective source region could be determined by a correlation analysis between the acoustic pressure radiated by the fan and the pressure fluctuation on the volute surface.

In this work, a numerical code has been applied in order to obtain the wall pressure fluctuations at the volute of an industrial centrifugal fan. The study is focused on the fundamental blade passing frequency, analyzing the influence of the flow rate. The numerical results have been compared to experimental results obtained in the same machine (Velarde-Suárez et al. [5]). Those investigations involved acoustic pressure measurements at the fan exit duct and pressure fluctuation measurements on the volute surface (specially in the vicinity of the volute tongue).

The aim of the method described in this paper is to provide a complete description of the flow field within the fan and to evaluate the capabilities of the numerical model to describe the unsteady flow features inside the described fan, which are responsible of the noise generation. Based on the detailed analysis of the pressure fluctuations over the volute wall some features of the fan

noise generation mechanisms are explained, and the zone of effective acoustic radiation has been qualitatively identified.

In a further phase of this research, this methodology of flow description will be used for the prediction of the radiated sound, based on the acoustic analogy (Lighthill [6]). This theory considers the flow field as a superposition of a small amplitude fluctuating sound field and a nonperturbed aerodynamic field that generates the fluctuating field. Thus, it is possible to obtain the noise generation based upon the unsteady incompressible description of the flow acting as a source term of the acoustic pressure field. In this way, the unsteady flow numerical results obtained and presented in this work constitute the basis for a second step in which the sound field will be computed by a numerical solution of an appropriate system of acoustic equations. A similar approach has been presented by Cho and Moon [7] for cross-flow fans.

Description of the Fan and Experimental Procedures

The tested machine is a simple aspirating centrifugal fan driven by an ac 9.2 kW motor rotating at 1500 rpm, with a fluctuation level lower than 0.5% for the whole range of the analyzed flow rates. The shrouded impeller tested has ten backward-curved blades with an outlet diameter of 400 mm. The blades are made of flat sheet metal. The minimum distance between the impeller and the volute tongue is 12.5% of the outlet impeller diameter. The widths of the impeller and volute are, respectively, 130 mm and 248 mm. Figure 1 shows two pictures of the tested fan and Table 1 summarizes the main dimensions of its impeller.

The tests for the aerodynamic and acoustic characterization of the fan have been made in a normalized ducted installation (type B according to ISO 5136 [8]). Figure 2 shows a drawing of this test installation. More details about the installation and measurement procedures have been reported in previous works (Velarde-Suárez et al. [9,10]). After leaving the fan, air flows through a straightener in order to remove the swirl generated by the fan. The measurement instruments were placed at sections A (static pressure) and B (flow rate and sound pressure level). At the end of the facility, an anechoic termination removes undesired noise reflections and the regulation cone permits to modify the fan operating point. The following maximum uncertainties were obtained for the different magnitudes: total pressure: $\pm 1.4\% (\pm 8 \text{ Pa})$, flow rate: $\pm 2\% (\pm 0.03 \text{ m}^3/\text{s})$, shaft power: $\pm 2\% (\pm 40 \text{ W})$.
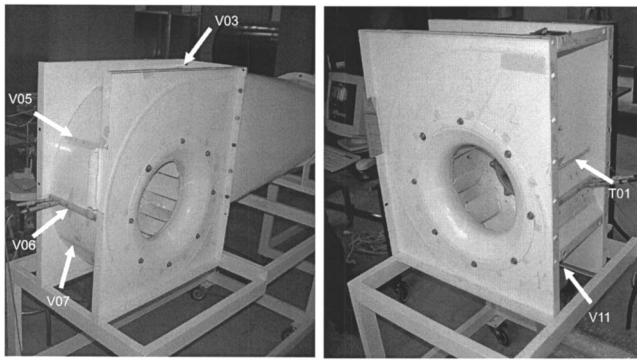
Fig. 1 Tested fan with the location of some measurement points

Table 2 Angular coordinates of the measurement points over the volute

Tongue Points	Angular Position (°)	Volute Points	Angular Position (°)	Volute Points	Angular Position (°)
P01	0	P06	60	P11	210
P02	2	P07	90	P12	240
P03	9	P08	120	P13	270
P04	16	P09	150	P14	300
P05	23	P10	180		

Acoustic pressure measurements at the fan exit duct have been made using a B&K 4189 1/2 in. microphone protected with a nose cone. Additionally, B&K 4138 1/8 in. microphones were flush-mounted on the volute surface, specially in the vicinity of the volute tongue, in order to measure the surface pressure fluctuations. The uncertainty of these two types of microphones has been established by the manufacturer in ±0.2 dB, with a confidence level of 95%. The signals from the microphones were introduced into a personal computer using an analog-to-digital card. The data acquisition frequency was chosen equal to 10 kHz per channel in order to obtain a good resolution. Then, a fast Fourier transform (FFT) algorithm has been used to get the power spectra of the pressure signals obtained both at the fan exit duct and at the volute surface.

The surface pressure fluctuation measurements have been made at five locations (P01 to P05) very close to the volute tongue and at another nine locations (P06 to P14), evenly distributed around the volute. Table 2 summarizes the angular coordinates of the measurement positions over the volute surface. Some of these measurement positions have been marked in Fig. 1. The origin of the angles is placed at the volute tongue. In each angular position, four measurements have been made at the following z/B coordinates: 0.15, 0.30, 0.40, and 0.75. The origin of z coordinates is

placed at the impeller hub and $z/B=0.54$ corresponds to the impeller shroud. Figure 3 shows two sketches of the fan with the location of the measurement points.

Description of the Numerical Simulation Procedure

In parallel with the measurements, numerical simulations of the unsteady flow in the centrifugal fan described above were carried out. In order to verify the capabilities of the numerical model to describe the flow features inside the fan, a two-dimensional numerical simulation of the unsteady flow has been first carried out. A better definition of the flow features was obtained with a complete three-dimensional simulation. All the calculations have been performed with a commercial software package FLUENT®. This code uses the finite volume method and the Navier-Stokes equations are solved on an unstructured grid. The unsteady flow is solved using a sliding mesh technique, which has been successfully applied to turbomachinery flows (González et al. [11]).

The errors in the solution related to the mesh must disappear for an increasingly finer mesh. The total pressure coefficient at the flow rate where the fan exhibits its best efficiency point was used to determine the influence of the mesh size on the solution. The convergence criterion was a maximum residual of 10^{-6}. Figure 4 shows the evolution of the fan total pressure coefficient with the mesh cells in the two-dimensional and in the three-dimensional calculations. According to this figure, the grids with the highest number of mesh cells were considered to be sufficiently reliable to assure mesh independence.

The two-dimensional domain, shown in Fig. 5, is a plane perpendicular to the axis of rotation, and it is supposed to represent the fan in a midblade width plane. Unstructured triangular cells are used to define the open inlet zone, the impeller and the volute (with a total of 160,894 cells), and a refined boundary layer mesh (made of trapezoidal cells) was used around the blades and on the volute wall. Figure 5 shows the unstructured mesh and Fig. 6 shows some details of the refined mesh around the blades and in the volute wall. The minimum cell area is $1.26 \cdot 10^{-10}$ m² and the maximum cell area is $6.79 \cdot 10^{-4}$ m².

Table 1 Impeller dimensions

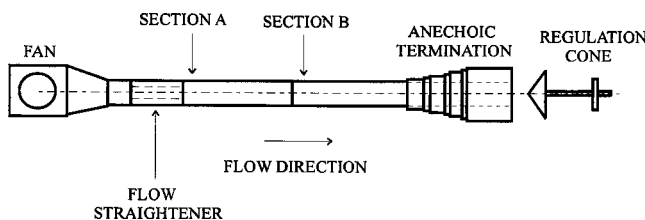|	
Outlet Diameter D_e (mm)	400
Inlet Diameter D_i (mm)	280
Outlet Width (mm)	130
Impeller-Tongue Distance (mm)	50
Impeller-Tongue Distance (% of Outlet Diameter)	12.5 %

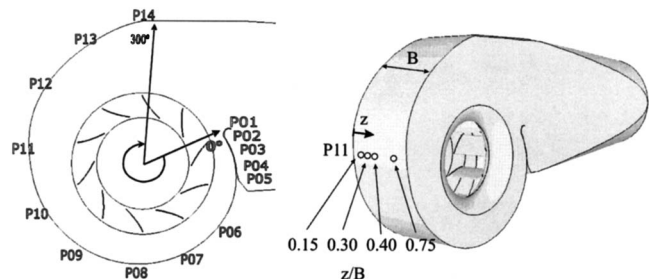**Fig. 2 Sketch of the test installation**

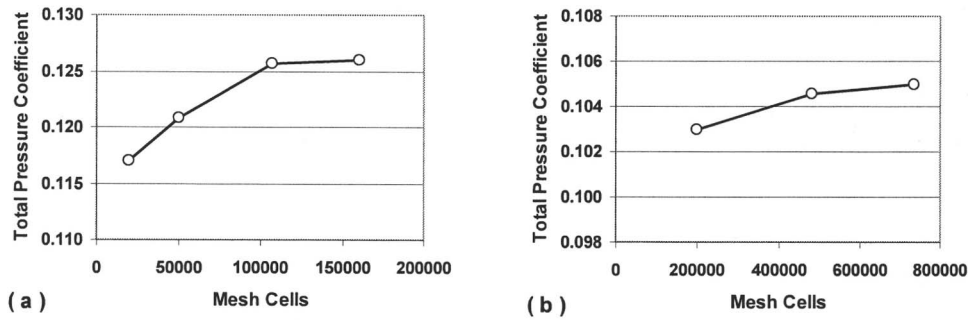**Fig. 3 Sketches of the fan with the measurement points**

Fig. 4 Influence of mesh size on the fan total pressure coefficient. (*a*) Two-dimensional mesh, (*b*) three-dimensional mesh.

For the three-dimensional calculations, unstructured tetrahedral cells are used to define the open inlet zone, the impeller and the volute (with a total of 733,400 cells). The mesh is refined near the tongue and specially in the impeller domain, although for capacity reasons in the three-dimensional simulation the mesh is coarser than in the two-dimensional simulation. Figure 7 shows a general view of the unstructured mesh and Fig. 8 shows some details of the refined mesh in a plane perpendicular to the axis of rotation. The minimum cell volume is $2.21 \cdot 10^{-11}$ m^3 and the maximum cell volume is $6.47 \cdot 10^{-5}$ m^3.

Turbulence is simulated with the standard k-ε model, while the time-dependent term scheme is second order, implicit. The pressure-velocity coupling is performed through the SIMPLEC algorithm. Second order, upwind discretization have been used for convection terms and central difference schemes for diffusion terms.

The modeled boundary conditions are those considered with more physical meaning for turbomachinery flow simulations, that is, total pressure at the domain inlet and a pressure drop proportional to the kinetic energy at the domain outlet. The flow rate is changed by modifying the constant for that pressure drop at the outlet condition, which simulates the closure of a valve.

The walls of the model are stationary with respect to their respective frame of reference, and the nonslip condition is applied. Also, wall functions, based on the logarithmic law (Launder and Spalding [12]), were applied.

The small axial gap (9 mm) between the impeller and the volute rear casing was not modeled. However, the radial gap between the impeller front shroud (5 mm) and the casing was taken into account in the model. Some details of the geometric features of the model are shown in Fig. 9 and the mesh used in the modeled gap is shown in Fig. 10.

The code was run in a cluster of 8 Pentium 4 (2.4 GHz) nodes. The time step used in the unsteady calculation has been set to $1.34 \cdot 10^{-4}$ s in order to get enough time resolution for the dynamic analysis. The impeller grid movement is related with this time step and the rotational speed imposed ($\omega = 157$ rad/s), so a complete revolution is performed each 300 steps (i.e., one blade passage each 30 time steps).
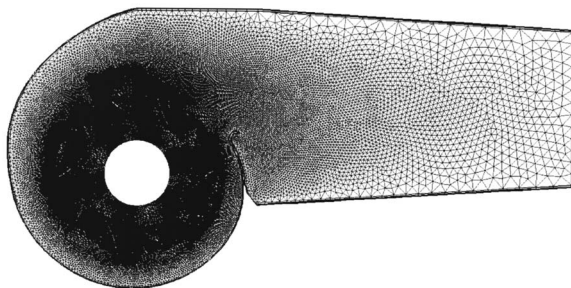
The number of iterations has been adjusted to reduce the residual below an acceptable value in each time step. In particular, the ratio between the sum of the residuals and the sum of the fluxes for a given variable in all the cells is reduced to the value of 10-5 (five orders of magnitude). Initializing the unsteady calculation with the steady solution, over 17 impeller revolutions (approximately 5000 time steps) are necessary to achieve the convergence of the periodic unsteady solution.

Fig. 5 Mesh used in the two-dimensional calculations
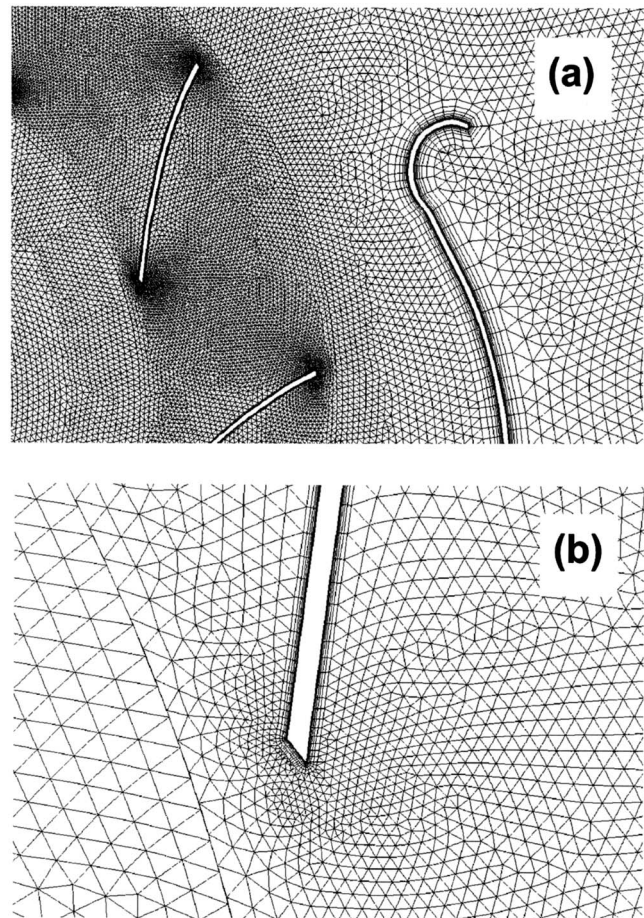
Fig. 6 Details of the mesh used in the two-dimensional calculations. (*a*) Mesh near the volute tongue, (*b*) mesh near the blades leading edge.
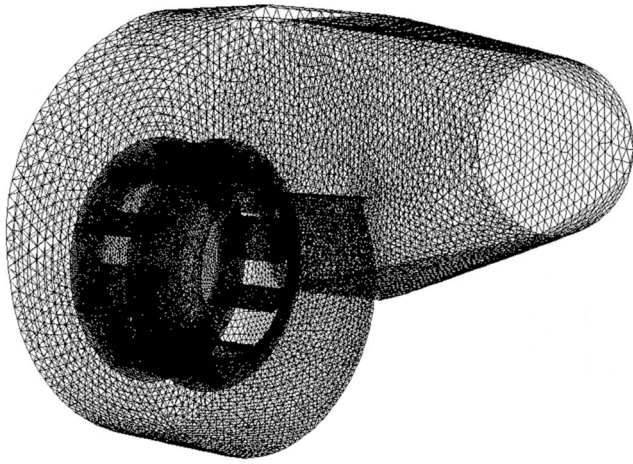
Fig. 7 Sketch of the fan unstructured mesh

Fig. 10 Mesh details around the radial gap between the impeller front shroud and the casing

Results and Discussion

The method described above has been employed to make a comparison for both the numerical and experimental performance curves for the tested fan. The numerical data are obtained after averaging the values of the unsteady calculation. In Fig. 11, the numerical and experimental performance curves for the tested fan are compared. The best efficiency point (BEP) corresponds to a flow rate $Q=0.92$ m^3/s ($\varphi=0.093$), with a total pressure rise P_T $=500$ Pa ($\psi=0.105$). The results obtained in the 2D simulation have been also represented in this figure, in order to illustrate the importance of the 3D effects.

The experimental and 3D-numerical simulated curves agree for flow rates equal and higher than the BEP. At partial load, the matching between 3D-numerical and experimental results is not so high, probably due to the presence of flow separation in the blade channels, which has not been correctly captured by the numerical procedure. The 2D-numerical curve is close to the experimental one only at very high flow rates. As the flow rate is reduced, the difference between this curve and the experimental values is gradually increased, showing the great importance of the three-dimensional effects on the flow and performance.

Fig. 8 Details of the mesh used in the three-dimensional calculations in a plane perpendicular to the axis of rotation
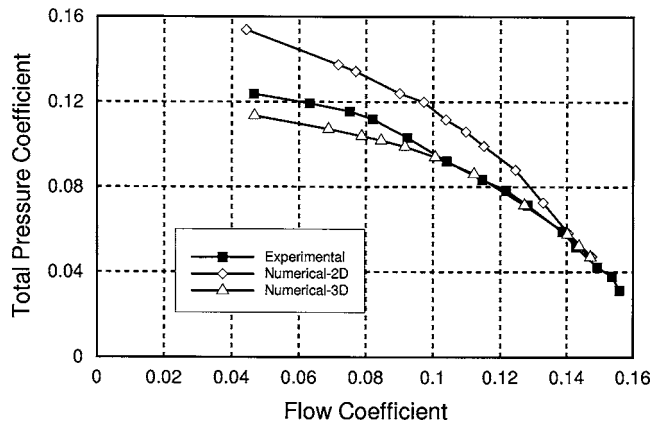
Fig. 11 Comparison between numerical and experimental performance curves

Fig. 9 General view of the geometry of the fan
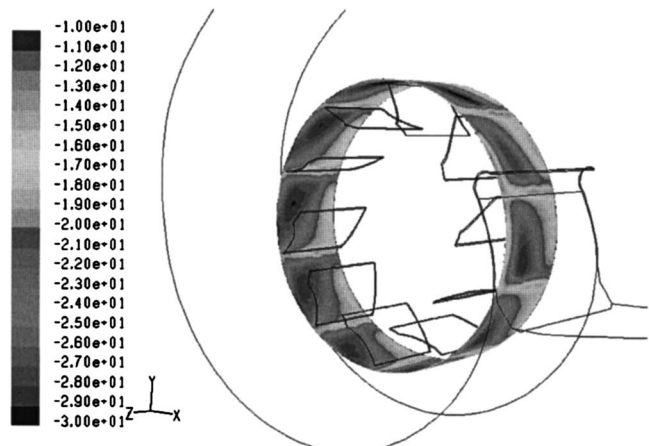
Fig. 12 Contours of relative tangential component of velocity at the impeller outlet (negative values are clockwise)
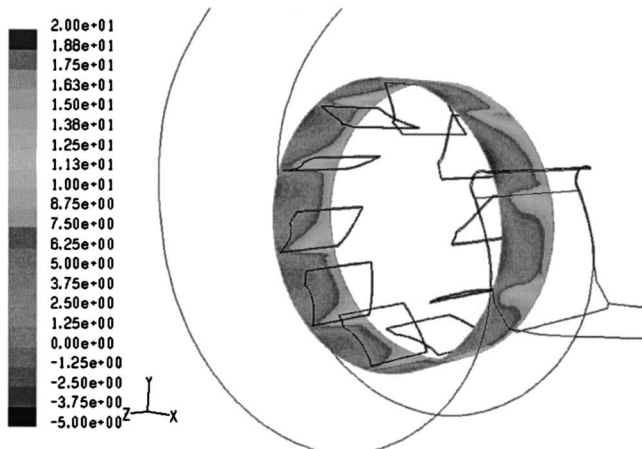
Fig. 13   Contours of radial component of velocity at the impeller outlet

The three-dimensional effects of the flow are illustrated in Figs. 12 and 13. These figures show the 3D-numerical results of the relative tangential component and of the radial component of velocity over a cylindrical surface around the impeller outlet, with the fan operating at the BEP. Both components of velocity exhibit important gradients in the axial direction. In the tangential component, where the negative values are clockwise, the maximum

absolute values correspond to zones into the blades channels located near the impeller shroud whereas the minimum ones appear in the blades wakes and close to the back impeller plate. The case of the radial component is different: zones with very low values (even negatives, with a recirculation pattern) are present near the impeller shroud, whereas the maximum values are concentrated near the hub. This feature indicates that the main fraction of the flow rate passes through the rear middle part of the impeller.

The three-dimensional effects described above cannot be simulated by a 2D-numerical model, and this is the explanation for the deviation found in Fig. 11 between the experimental and 2D results. Furthermo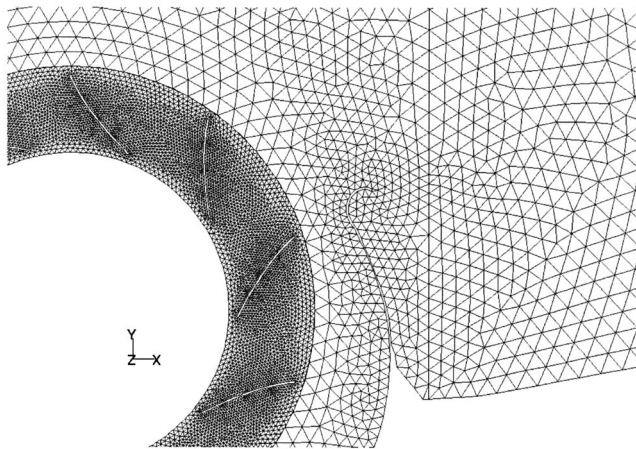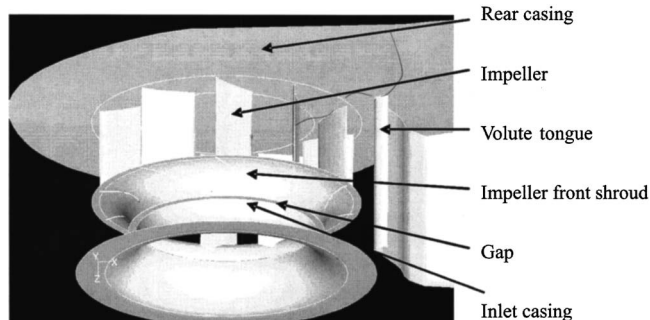re, these three-dimensional effects (particularly the recirculation) become more important when the fan is operating at partial load and hence the difference between the experimental and 2D results increases when the flow rate decreases.

The numerical model described above has been employed to calculate the time-dependent pressure both in the impeller and in the volute. In this way, the pressure fluctuations in some locations over the volute wall have been obtained. The measurement positions detailed in Table 2 have been selected in order to make comparisons between the numerical and experimental results. Figures 14 and 15 show the evolution of pressure fluctuations with time obtained both by 3D-numerical model and experimentally, for two different flow rates: the BEP and $1.35 \times$ BEP. The experimental signals have been phase averaged over one impeller revolution in order to filter the random fluctuations. In these figures, the mean values have omitted and only the fluctuating signal is represented.

In Fig. 14, the results obtained at the position P02 (angular position at 2 deg from the tongue, $z/B = 0.30$) have been repre-
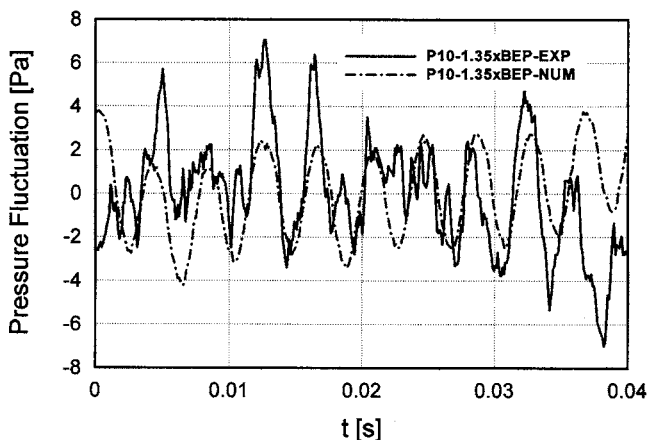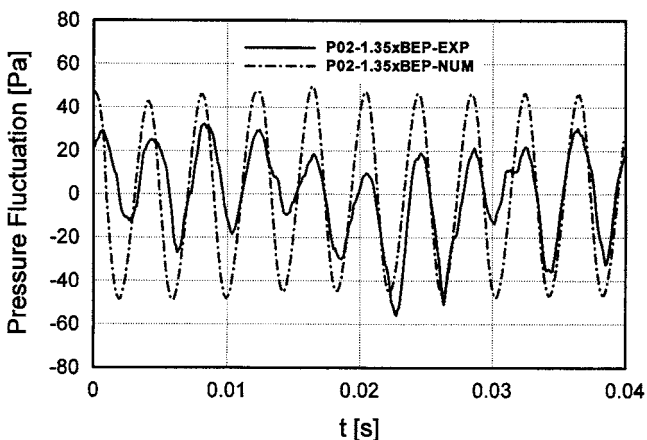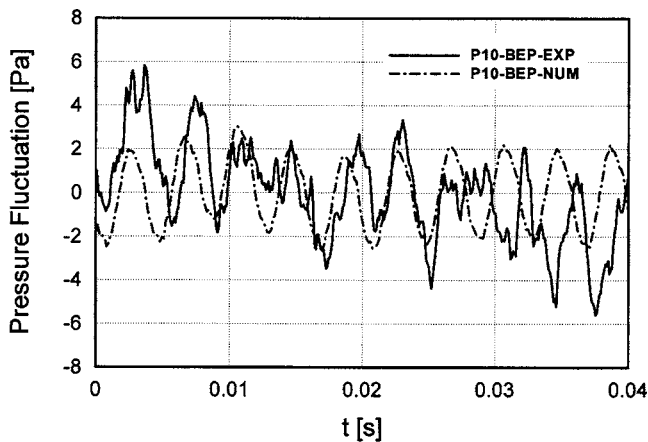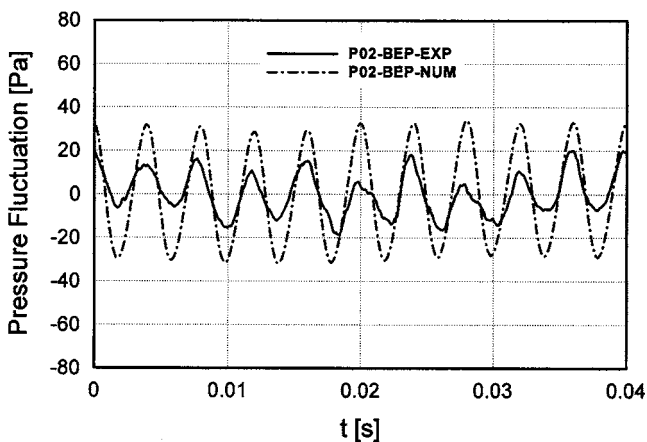
Fig. 14   Evolution of volute pressure fluctuations with time at point P02 (at the tongue, $z/B = 0.30$)

Fig. 15   Evolution of volute pressure fluctuations with time at point P10 (180 deg from the tongue, $z/B = 0.30$)

Journal of Fluids Engineering
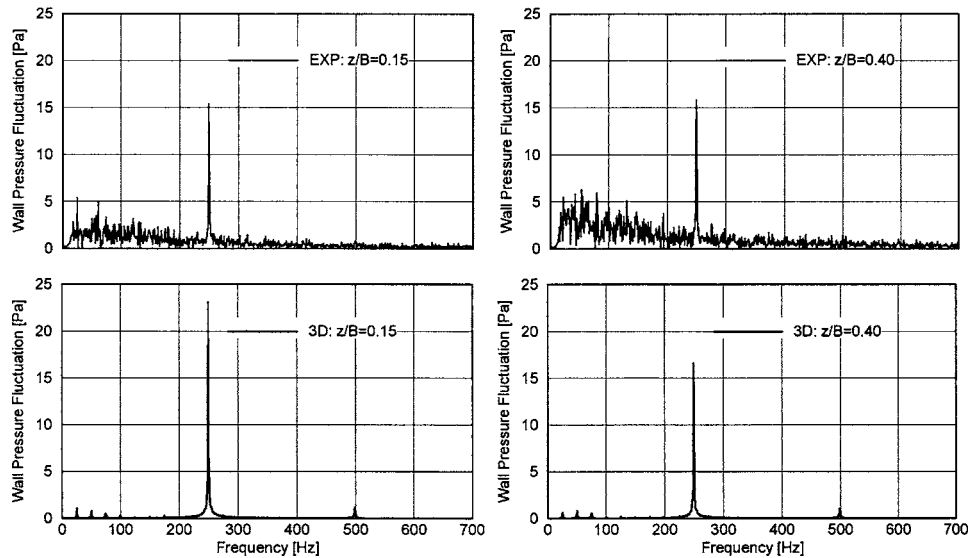
Fig. 16 Power spectra of volute pressure fluctuations in Pa (experimental, upper side; 3D-numerical simulation, bottom side) at the measurement point P02 (at 2 deg from the tongue, z/B=0.15 and z/B=0.40), with the fan operating at the best efficiency point (BEP)
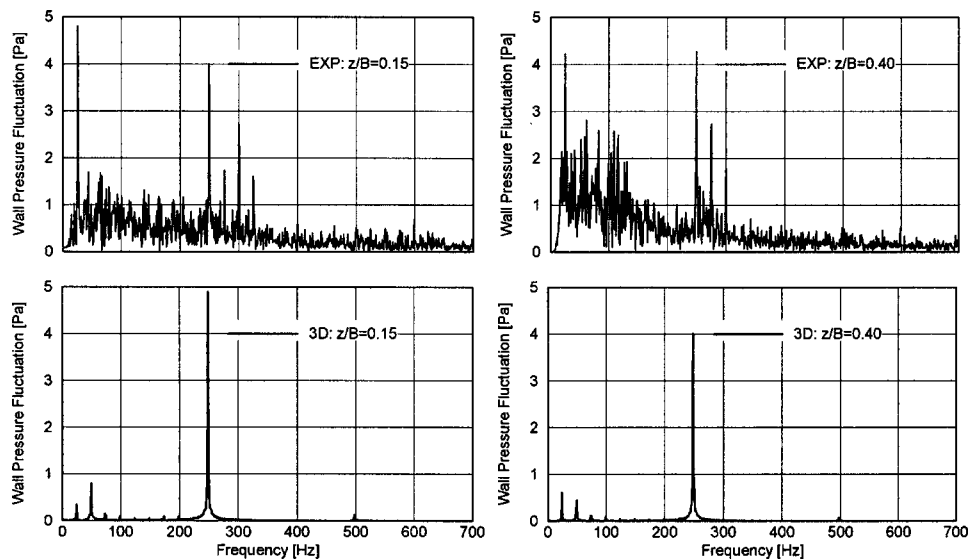
Fig. 17 Power spectra of volute pressure fluctuations in Pa (experimental, upper side; 3D-numerical simulation, bottom side) at the measurement point P06 (at 60 deg from the tongue, z/B=0.15 and z/B=0.40), with the fan operating at the best efficiency point (BEP)

sented. The passing of the ten blades in front of the selected position is clearly observed. The amplitude of the pressure fluctuation increases with the flow rate in this case. The numerical code has reproduced in a reasonable way both the order of magnitude and the temporal pattern of the pressure fluctuations found experimentally.

In Fig. 15, the results obtained at the position P10 (180 deg from the tongue, z/B=0.30) have been represented. The amplitude of the pressure fluctuation at this point diminishes strongly with respect to the precedent case, shown in Fig. 14. The passing of the blades is still clearly observed in the numerical results and the amplitude of the pressure fluctuations is similar to the experimental ones. However, the experimental signals show other sources of pressure fluctuation besides the blades passage, which distorts the clear sinusoidal pattern shown at the tongue. The origin of these distortions will be discussed latter on.

In Figs. 16–18, the power spectra of pressure fluctuations at points P02 (2 deg from the tongue), P06 (60 deg from the tongue) and P10 (180 deg from the tongue), have been represented.

The peak corresponding to the blade passing frequency exhibits high amplitude in the position P02 near the volute tongue, both in the numerical and the experimental signals (Fig. 16) basically due to the interaction between the flow leaving the impeller and the tongue. The numerical and experimental amplitudes coincide in the axial position z/B=0.40, while in the position z/B=0.15 they are slightly different. This disagreement was expected because the position z/B=0.15 is very close to the impeller hub and it is not easy to simulate precisely the small axial gap between the impeller and the volute rear casing.

In the position P06 (60 deg from the tongue), the situation is quite different (Fig. 17). First of all, the amplitudes corresponding
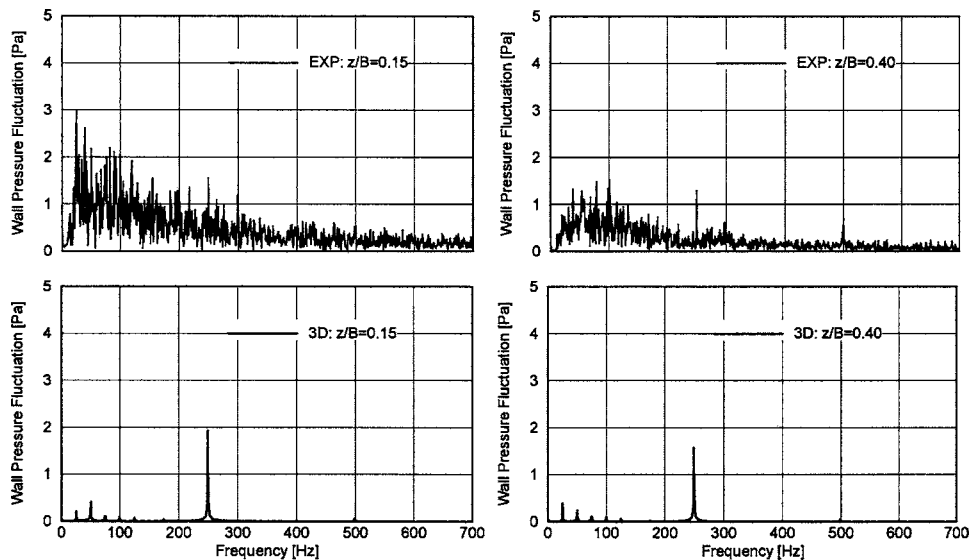
Fig. 18 Power spectra of volute pressure fluctuations in Pa (experimental, upper side; 3D-numerical simulation, bottom side) at the measurement point P10 (at 180 deg from the tongue, z/B=0.15 and z/B=0.40), with the fan operating at the best efficiency point (BEP)

to the blade passing frequency have strongly diminished with respect to the previous case (Fig. 16), although they contribute largely in the spectra, both numerically and experimentally. In this position, the interaction between the impeller and the volute tongue does not appear, besides the radial distance from the impeller to the volute is greater that in the previous case. These two reasons explain the great reduction of the amplitude of the pressure fluctuations with respect to the previous case. Also, the experimental and numerical amplitudes at the blade passing frequency in $z/B=0.40$ are similar, and slightly different in $z/B=0.15$. Second, great peak and broadband amplitudes at low frequencies appear in the experimental spectra. A peak at 25 Hz stands out, corresponding to the impeller rotational frequency. Also, some peaks at 275 Hz, 300 Hz, and 325 Hz appear besides the blade passing frequency at 250 Hz with comparable amplitudes, suggesting the existence of mechanical sources of noise.

In the position P10 (180 deg from the tongue), the amplitude of the pressure fluctuations is lower than in the previous case mentioned (Fig. 18), as a result of the increase of the radial distance between the impeller and the volute wall. The amplitudes at the blade passing frequency are quite similar in the experimental and the numerical spectra. On the other hand, in the experimental spectra important broadband levels at low frequencies appear, specially in the axial position $z/B=0.15$.

In order to clarify the origin of the peaks observed at 275 Hz, 300 Hz, and 325 Hz in the experimental spectra, some vibration signals at the volute front casing were obtained with a 4384 B&K piezoelectric accelerometer, connected to a 2635 B&K amplifier. These signals were then transmitted to a 2133 B&K two-channel narrow-band frequency analyzer. Figure 19 shows the spectra of these vibration signals at six angular positions on the front casing: at 0 deg, 60 deg, 120 deg, 180 deg, 240 deg, and 300 deg from the tongue, i.e., the same angular positions as measurement points P01, P06, P08, P10, P12, and P14. These tests have been carried out in the following operating conditions: with zero flow rate and with $1.70 \times BEP$, the maximum flow rate analyzed in this study.

In these spectra, a noticeable peak at the blade passing frequency is shown, which increases with the flow rate. Therefore, it is shown that the pressure fluctuations generated by the impeller flow generate some casing vibration. Also, important peaks at 275 Hz, 300 Hz, and 325 Hz appear in some cases. In particular, high vibration values at these frequencies have been measured placing the accelerometer in a zone of the front casing located

between 120 deg and 240 deg with respect to the volute tongue. These values do not vary with the flow rate, thus indicating its mechanical origin. Moreover, an impact test demonstrated that the vibration signal at 300 Hz is due to a casing resonance caused by the excitation of a natural frequency.

These results show that components of the signals measured by the microphones at 275 Hz, 300 Hz, and 325 Hz correspond to mechanical vibrations measured by the accelerometers at the fan casing; at these frequencies, the microphones have measured noise due to structural vibrations and not pressure fluctuations generated by the impeller flow. Only the last ones can be correctly simulated by the numerical model and this is the explanation for the differences found in Figs. 17 and 18 between the numerical and experimental results.

In Figs. 20–23, the amplitudes of volute pressure fluctuations at the blade passing frequency have been represented, both 3D numerical and experimental, for four different flow rates: the BEP ($\varphi=0.093$), $0.75 \times BEP$ ($\varphi=0.070$), $1.35 \times BEP$ ($\varphi=0.126$), and $1.70 \times BEP$ ($\varphi=0.158$). The z coordinate has been divided by the volute width B (248 mm). The impeller shroud corresponds to $z/B=0.54$, while $z/B=0$ is the volute rear casing and $z/B=1$ is the volute front casing. On the graph corresponding to $z/B=0.30$, the 2D-numerical pressure fluctuations have been included. This axial position corresponds to the mid-blade width plane.

In all the cases, the maximum values appear concentrated in a small zone very close to the volute tongue, as it was expected. These pressure fluctuations are generated by the interaction between the unsteady flow leaving the impeller and the fixed volute tongue. In the rest of the volute, noticeable amplitudes are also present, due to the jet-wake pattern associated to the continuous blade rotation around the volute. In all the analyzed flow rates, this spatial distribution along the volute is observed, although the values of the amplitudes increase with the flow rate.

The 2D-numerical model reproduces the trend and the order of magnitude of the pressure fluctuations obtained experimentally except in the volute region near the tongue, where there is a great difference between them; this difference increases when the flow rate is above the BEP. As was stated before, this fan exhibits strong three-dimensional effects described above which cannot be simulated by a 2D-numerical model.

The 3D-numerical model can reproduce in a reasonable way the trend and the order of magnitude of the pressure fluctuations ob-

Journal of Fluids Engineering
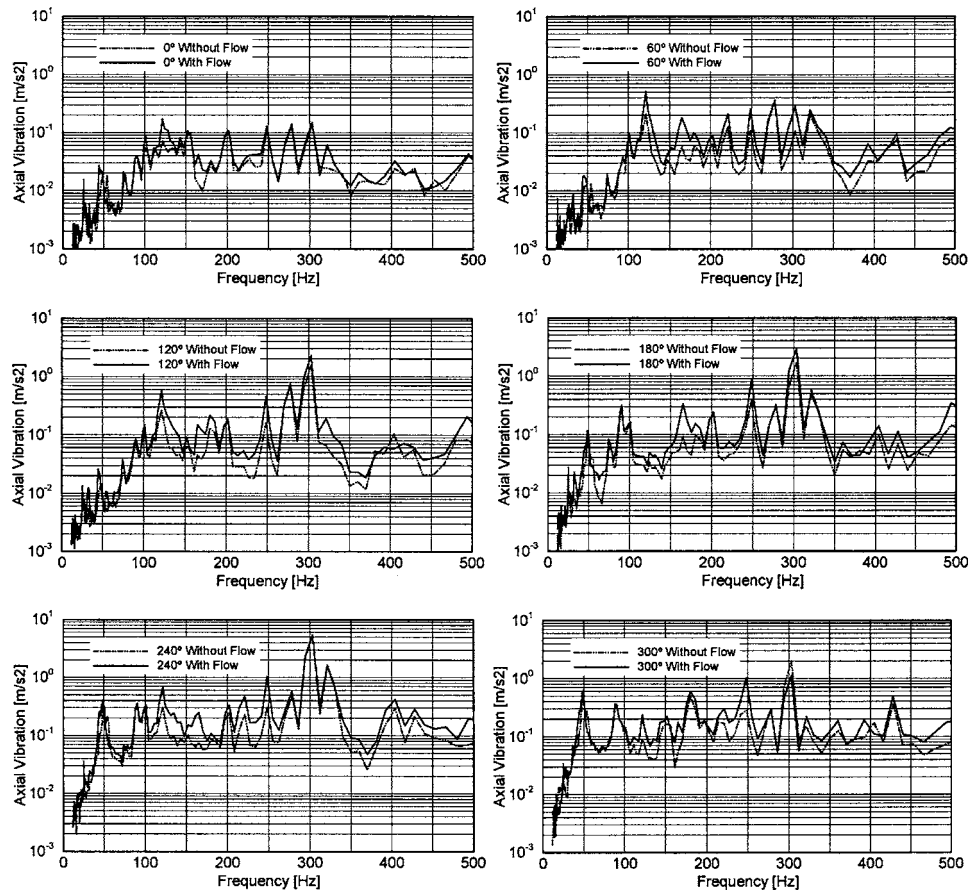
Fig. 19   Power spectra of vibration signals at the volute front casing

Fig. 20   Amplitude (Pa) of volute pressure fluctuation at the blade passing frequency, 2D numerical, 3D numerical and experimental, with the fan operating at 75% of the best efficiency point (0.75×BEP)
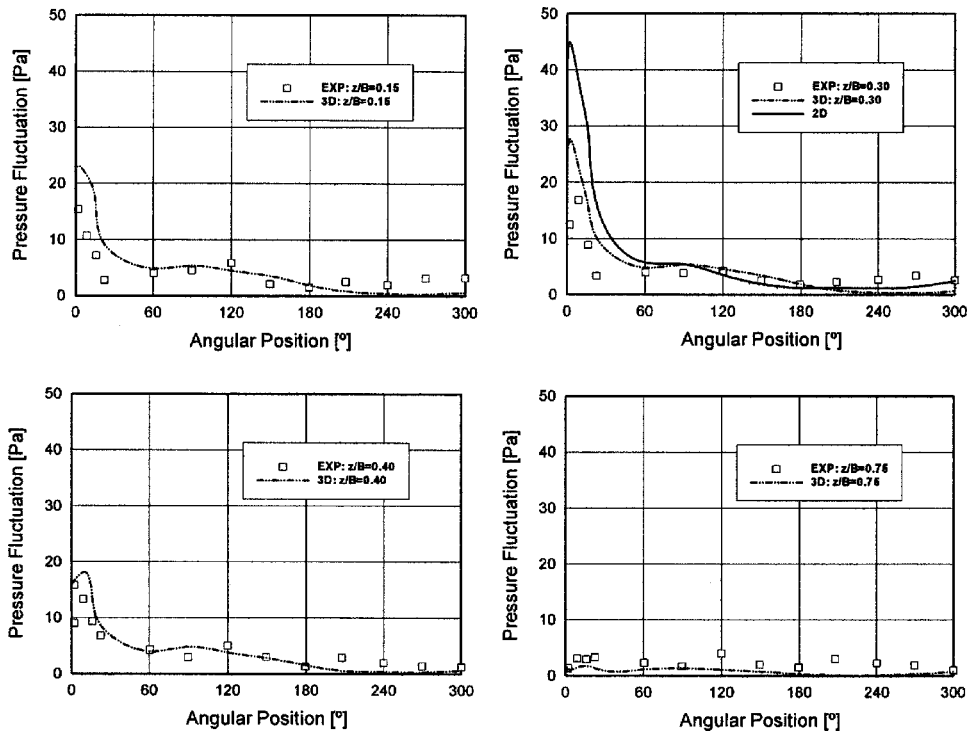
Fig. 21 Amplitude (Pa) of volute pressure fluctuation at the blade passing frequency, 2D numerical, 3D numerical and experimental, with the fan operating at the best efficiency point (BEP)
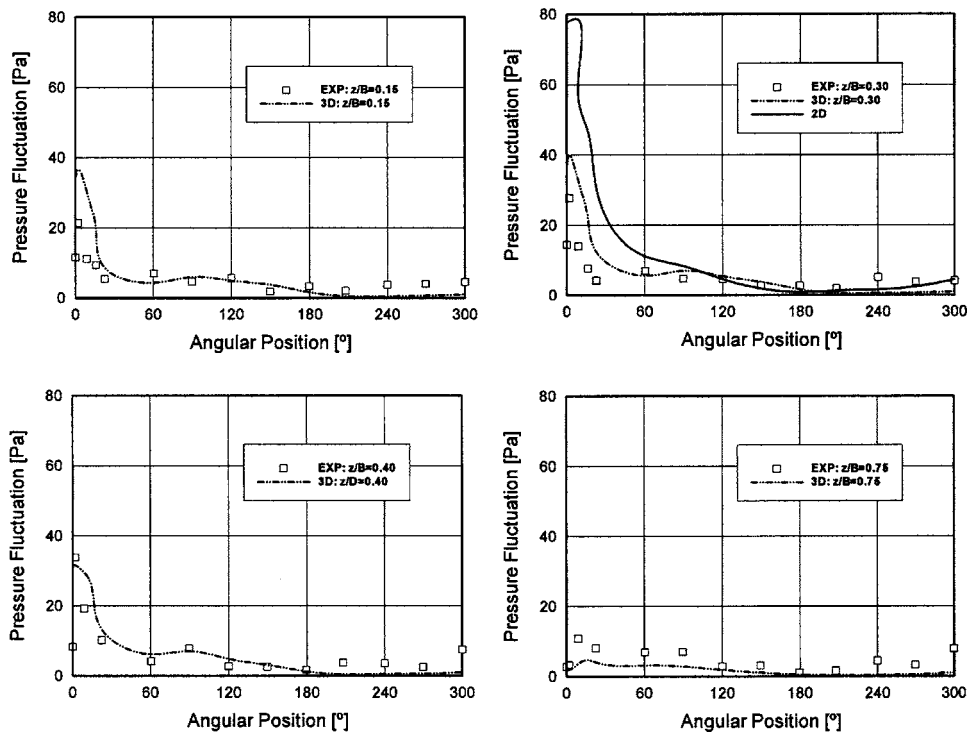
Fig. 22 Amplitude (Pa) of volute pressure fluctuation at the blade passing frequency, 2D numerical, 3D numerical and experimental, with the fan operating at 135% of the best efficiency point ($1.35 \times$ BEP)

tained experimentally. The agreement between experimental and numerical results is especially good in the axial position z/B $=0.40$, in all the analyzed flow rates. As the small axial gap between the impeller and the volute rear casing was not modeled, the 3D-numerical and experimental results corresponding to low

values of z/B are slightly different, specially near the volute tongue. It can also be observed that the agreement between experimental and numerical results improves for flow rates higher than the best efficiency point. This same effect was observed in the comparison of the performance curves shown in Fig. 11. As in
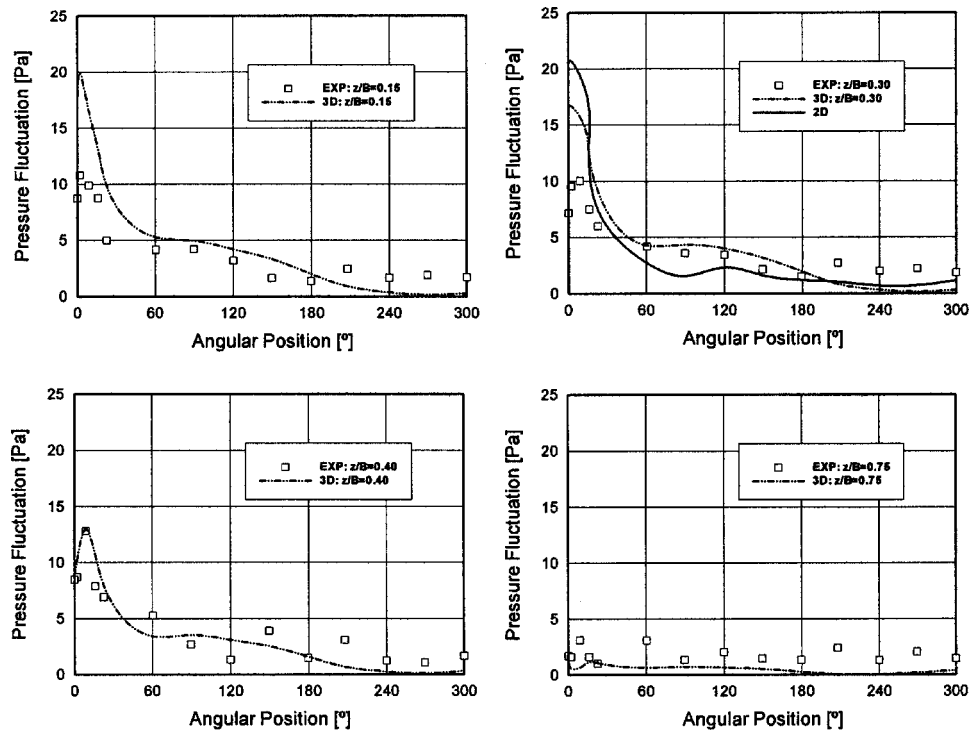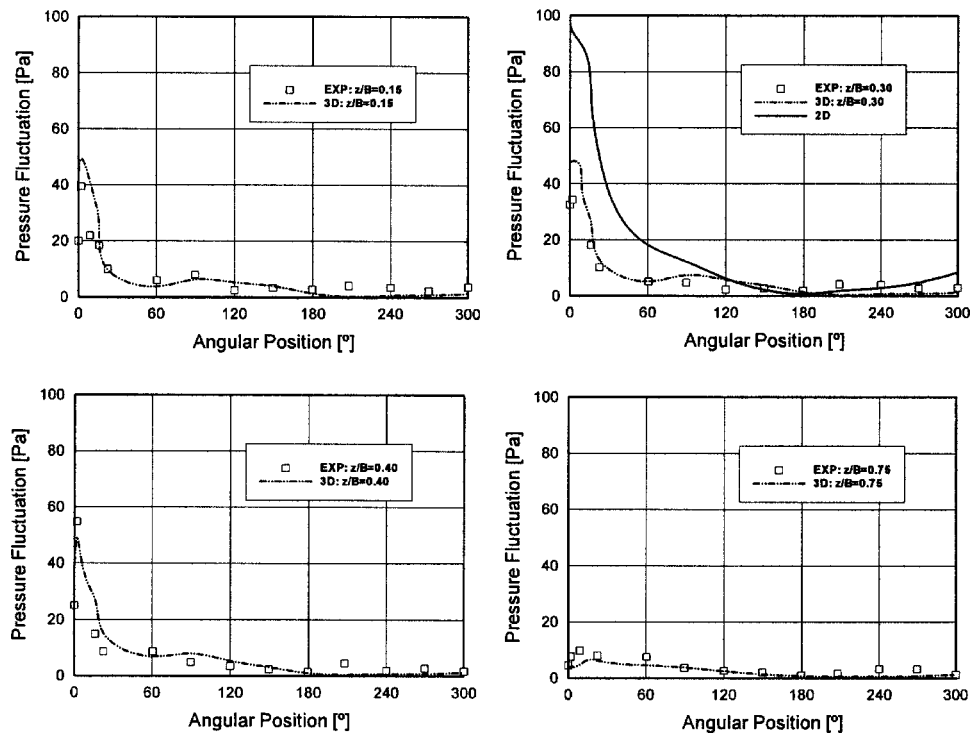
Fig. 23 Amplitude (Pa) of volute pressure fluctuation at the blade passing frequency, 2D numerical, 3D numerical and experimental, with the fan operating at 170% of the best efficiency point (1.70×BEP)

that case, these differences are probably due to the presence of flow separation in the blade channels at partial load, which has not been correctly captured by the numerical procedure.

Another source of discrepancies between the 3D-numerical and the experimental pressure fluctuations can be taken into account: The feasibility that the microphones placed on the volute wall measure noise from distant zones of the flow, i.e., pressure fluctuations of the "acoustic type" which can not be calculated in the three-dimensional simulation. The computation of pressure fluctuations of the "acoustic type" by computational fluid dynamics (CFD) codes which solve the unsteady compressible Navier-Stokes equations exceeds by far the current computational capabilities.

Regardless of the exposed constraints, which would be possibly overcome with a greater computational capability, the presented results permit to conclude that the 3D-numerical methodology developed is a useful tool for the unsteady simulation of the three-dimensional flow in a centrifugal fan. The application of this method to other alternative geometries would permit to establish design criteria for the improvement of the aerodynamic performance of these machines.

On the other hand, the results obtained in the unsteady flow numerical simulation constitute the basis for a second step in which the sound field will be computed by a numerical solution of an appropriate system of acoustic equations, based on the acoustic analogy of Lighthill [6].

Conclusions

A three-dimensional numerical simulation of the unsteady flow in a centrifugal fan has been carried out. The numerical results have been compared to experimental results obtained in the same machine.

The agreement between experimental and numerical performance curves is quite good. The code has also successfully simu-

lated the volute pressure fluctuations due to the aerodynamic field, capturing the main flow phenomena such us the jet-wake effects and the impeller-tongue interaction.

The results obtained in the unsteady flow numerical simulation are encouraging and they constitute the basis for a second step in which the sound field will be computed by a numerical solution of an appropriate system of acoustic equations, based on the acoustic analogy of Lighthill.

Nomenclature

B = volute width
BEP = best efficiency point
D = diameter
P_T = total pressure rise
Q = flow rate
ψ = total pressure coefficient, $\psi = P_T / \rho \omega^2 D^2$
φ = flow coefficient, $\varphi = Q / \omega D^3$
ρ = density
ω = angular velocity

References

[1] Carolus, Th. H., and Stremel, M., 2003, "Blade Surface Pressure Fluctuations and Acoustic Radiation From an Axial Fan Rotor due to Turbulent Inflow," *Proceedings of Second International Symposium on Fan Noise*, Senlis, France, CETIAT-CETIM, France.
[2] Fehse, K. R., and Neise, W., 1999, "Generation Mechanisms of Low-Frequency Centrifugal Fan Noise," AIAA J., **37**, pp. 1173–1179.
[3] Ohta, Y., Outa, E., and Tajima, K., 1996, "Evaluation and Prediction of Blade-Passing Frequency Noise Generated by a Centrifugal Blower," ASME J. Turbomach., **118**, pp. 597–605.
[4] Ohta, Y., Hikichi, M., Outa, E., Tajima, K., and Saito, S., 2000, "Active Can-

cellation of Noise Sources in a Centrifugal Blower," *Proceedings of 9th International Symposium on Unsteady Aerodynamics Aeroacoustics and Aeroelasticity of Turbomachines*, Lyon, France, Presses Universitaires de Grenoble, Grenoble, France, pp. 182–193.

[5] Velarde-Suárez, S., Ballesteros-Tajadura, R., Hurtado-Cruz, J. P., and Santolaria-Morros, C., 2003, "Experimental Determination of the Tonal Noise Sources in a Centrifugal Fan," *Proceedings of the 4th ASME-JSME Joint Fluids Engineering Conference*, Vol. 1643CD, ASME, New York, pp. 1061–1065.

[6] Lighthill, M. J., 1952, "On Sound Generated Aerodynamically. I. General Theory," Proc. R. Soc. London, Ser. A, **211**, pp. 564–587.

[7] Cho, Y., and Moon, Y. J., 2003, "Discrete Noise Prediction of Variable Pitch Cross-Flow Fans by Unsteady Navier-Stokes Computations," ASME J. Fluids Eng., **125**, pp. 543–550.

[8] ISO 5136:1990 and Technical Corrigendum 1:1993, "Determination of Sound Power Radiated Into a Duct by Fans. In-Duct Method."

[9] Velarde-Suárez, S., Santolaria-Morros, C., and Ballesteros-Tajadura, R., 1999, "Experimental Study on the Aeroacoustic Behavior of a Forward-Curved Centrifugal Fan," ASME J. Fluids Eng., **121**, pp. 276–281.

[10] Velarde-Suárez, S., Ballesteros-Tajadura, R., Santolaria-Morros, C., and González-Pérez, J., 2001, "Unsteady Flow Pattern Characteristics Downstream of a Forward-Curved Blades Centrifugal Fan," ASME J. Fluids Eng., **123**, pp. 265–270.

[11] González, J., Fernández, J., Blanco, E., and Santolaria, C., 2002, "Numerical Simulation of the Dynamic Effects Due to Impeller-Volute Interaction in a Centrifugal Pump," ASME J. Fluids Eng., **124**, pp. 348–355.

[12] Launder, B. E., and Spalding, D. B., 1974, "The Numerical Computation of Turbulent Flows," Comput. Methods Appl. Mech. Eng., **3**, pp. 269–289.

Propulsion System Requirements for Long Range, Supersonic Aircraft

Michael J. Brear
e-mail: mjbrear@unimelb.edu.au
Department of Mechanical and Manufacturing
Engineering,
University of Melbourne,
Melbourne, Australia

Jack L. Kerrebrock

Alan H. Epstein

Gas Turbine Laboratory,
Massachusetts Institute of Technology,
Cambridge, MA

This paper discusses the requirements for the propulsion system of supersonic cruise aircraft that are quiet enough to fly over land and operate from civil airports, have trans-pacific range in the order of 11,112 km (6000 nmi), *and payload in the order of* 4545 kg (10,000 lb.). *It is concluded that the resulting requirements for both the fuel consumption and engine thrust/weight ratio for such aircraft will require high compressor exit and turbine inlet temperatures, together with bypass ratios that are significantly higher than typical supersonic-capable engines. Several technologies for improving both the fuel consumption and weight of the propulsion system are suggested. Some of these directly reduce engine weight while others, by improving individual component performance, will enable higher bypass ratios. The latter should therefore also indirectly reduce the bare engine weight. It is emphasized, however, that these specific technologies require considerable further development. While the use of higher bypass ratio is a significant departure from more usual engines designed for supersonic cruise, it is nonetheless considered to be a practical option for an aircraft of this kind.*
[DOI: 10.1115/1.2169810]

Introduction

Long range, supersonic cruise aircraft that are quiet enough to fly over land and operate from civil airports have numerous possible applications. Several aircraft manufacturers are therefore currently investigating concept aircraft of roughly 45,455 kg (100,000 lb) take-off-gross-weight (TOGW). However, regardless of their final application, these aircraft must resolve several fundamental issues in order to be viable, and several of these issues relate to the propulsion system.

Table 1 shows the challenging performance goals required for an aircraft of roughly 100,000 lb. TOGW. Of these, the only fixed requirement concerns the aircraft's sonic boom. The aircraft will not be able to achieve unrestricted, supersonic flight over land unless the peak pressures in the ground signature of the aircraft can be reduced to "acceptable" levels. This is potentially achievable because of the aircraft's small size; in order to achieve the stated boom requirement, the calculations of Bressollette [1] showed that a 100,000 lb. aircraft cruising at $M_{0R}=2$ must have a cruise altitude of approximately $h=18,288$ m (60 kft.).

The performance targets in Table 1 also set challenging goals for the propulsion system. The propulsion system has traditionally been a major problem for several proposed supersonic aircrafts, mainly because of the cruise fuel consumption and the noise at take-off and landing. Once again, the small size of the aircraft may permit certain designs that are not possible for larger aircraft. Specifically, high bypass ratio engines with their lower specific thrust and larger diameter may still be allowable. Indeed, a higher bypass ratio bare engine is expected to be lighter than low bypass engines of the same thrust and in the same engine family. Thus, significant reductions in fuel consumption, noise and engine weight that are enabled by increased bypass ratio may be possible.

This paper is therefore aimed at providing a critical discussion of the required technologies for a 100,000 lb. class, long range, supersonic cruise aircraft in terms of their effects on the thrust specific fuel consumption (TSFC) at cruise. Particular technologies that may significantly reduce engine weight are also discussed. Approximate analyses are performed in order to estimate the performance of the engine during take-off and climb. Using likely aircraft parameters, the limitations placed on the engine by below-cruise flight are then considered.

Methods

The analyses presented for the engine during cruise were performed using the package GASTURB [2]. GASTURB was used to optimize the bypass ratio (BPR) and fan stagnation pressure ratio (π_f) for a given set of input parameters (namely $M_{0R}, h, \pi_C, T_{t4}, \dot{m}_{cool}$, the component efficiencies and pressure recoveries), assuming a fuel with a lower heating value of 43 MJ/kg. The thrust specific fuel consumption (TSFC) was the figure of merit. These calculations found the optimum engine configuration using an "adaptive random search" algorithm that is discussed in greater detail in Kurzke [2]. Some similar, analytical analyses using the theory presented in Oate's [3] were also performed for cases that did not feature turbine film cooling. These agreed closely with the equivalent results obtained using GASTURB.

The engine optimizations also assumed a "mixing efficiency" between the core and bypass streams of 50%. This mixing was assumed to occur at constant area, which in all cases was taken as the area of the inlet capture streamtube. For a given fuel flow rate, the thrust at 50% mixing efficiency lies halfway between those calculated for unmixed and perfectly mixed exhaust streams. A mixing efficiency of 50% is thought to be physically reasonable and different mixing efficiencies made little difference to the conclusions of this paper.

It is also noted that most of the following analyses for the engine at cruise are performed using a cruise Mach number (M_{0R}) of 2, even though the specified goal is 2.4 (Table 1). This is because the sonic boom ground signature requirement at $M_{0R}=2.4$ is expected to be very difficult [1] and flight at $M_{0R}=2.4$ may also preclude the use of composite materials in many parts of the aircraft.

The off-design analyses used a combination of theory presented in Oates [3], Kerrebrock [4], and Seddon and Goldsmith [5]. Consider first a streamtube with its mass flow rate given by

Copyright © 2006 by ASME

Table 1 Aircraft performance goals

Peak sonic boom ground signature	14.4 Pa (0.3 lb./ft.²)
Cruise Mach number (M_{0R})	2.4
Range	11,112 km (6000 nmi)
Cruise lift-to-drag (L/D)	11
TSFC	29.7 g/kN s (1.05 lb/lb h)
Engine thrust/weight ratio	7.5

Table 2 Performance parameters of propulsion system components

Component	Symbol	Current	Best case
Inlet	π_d	0.93	0.97
Compressor	ϵ_c	0.90	0.93
Combustor	π_b	0.98	0.98
Turbine	ϵ_t	0.90	0.93
Nozzle	π_n	0.95	0.97

$$\dot{m} = \rho_t \alpha_t A \frac{\rho}{\rho_t} \frac{a}{a_t} \frac{u}{a} = \frac{A p_t}{\sqrt{T_t}} \sqrt{\frac{\gamma}{R}} \left(1 + \frac{\gamma - 1}{2} M^2\right)^{-[(\gamma+1)/2(\gamma-1)]} M. \quad (1)$$

Equation (1) is then applied to a control volume that extends from the turbine inlet to the nozzle throat. Assuming no stagnation pressure losses from the turbine exit to the nozzle and choking at the turbine inlet and the nozzle throat, continuity of mass requires that

$$\frac{\sqrt{\tau_t}}{\pi_t} = \frac{A_8}{A_4}. \quad (2)$$

Thus, assuming that the turbine efficiency is constant over the flight path and that both the turbine inlet and nozzle throat remain choked, constant turbine stagnation pressure (π_t) and temperature (τ_t) ratios infer that the ratio A_8/A_4 is fixed.

It is shown later that the nozzle throat area (A_8) must vary over the flight path. Equation (2) therefore infers that the turbine inlet area (A_4) must vary in proportion to A_8 if π_t and τ_t are constant. Thus, the following analyses for off-design performance are strictly valid for an engine with variable turbine inlet area. However, the above approximation to an actual, fixed geometry turbine with its associated characteristic map is expected to be of sufficient accuracy for a preliminary study such as this.

Assuming that $\tau_t = \tau_{tR}$, a power balance between the core compressor and turbine gives

$$\tau_{cc} = 1 + (\tau_{ccR} - 1)\frac{\tau_\lambda/\tau_r \tau_f}{(\tau_\lambda/\tau_r \tau_f)_R}, \quad (3)$$

where

$$\tau_\lambda = \frac{C_{Pt}}{C_{Pc}} \frac{T_{t4}}{T_0}, \quad (4)$$

and the turbine inlet stagnation temperature (T_{t4}) was fixed over the flight path. From the definition of the isentropic core compressor efficiency (η_{cc}) assuming a calorifically perfect gas,

$$\pi_{cc} = [1 + \eta_{cc}(\tau_{cc} - 1)]^{\gamma/(\gamma-1)}. \quad (5)$$

Using Eq. (1) and ignoring the massflow added as fuel, mass conservation between (i) the core stream fan face and the (choked) turbine inlet and (ii) the bypass stream fan face and the (choked) nozzle throat leads to

$$BPR = BPR_R \frac{\pi_{ccR}}{\pi_{cc}} \sqrt{\frac{\tau_\lambda/\tau_r \tau_f}{(\tau_\lambda/\tau_r \tau_f)_R}}. \quad (6)$$

A power balance between the fan and the low pressure turbine gives

$$\tau_f = 1 + (\tau_{fR} - 1)\frac{BPR_R + 1}{BPR + 1} \frac{\tau_\lambda/\tau_r}{(\tau_\lambda/\tau_r)_R}. \quad (7)$$

Starting from the initial guess of $\tau_f = \tau_{fR}$, Eqs. (3) and (5)–(7) are then iterated until a converged solution (i.e., set of values for $\tau_f, \tau_{cc}, \pi_{cc}$, BPR) is found for a given flight condition (i.e., value of τ_r). The engine thrust and fuel consumption were then calcu-

lated using usual relations. The nozzle was matched unless stated otherwise and the ICAO standard atmosphere was used in all cases.

The length of the take-off roll (x_T) can be calculated analytically if several, simplifying assumptions are made [4]. If the thrust is assumed constant and equal to its sea-level-static value (F_{SLS}), the change in mass (m) of the aircraft is neglected and the lift coefficient at take-off is given by $C_{LT} = \sqrt{\pi \alpha C_{D0}}$, then x_T can be shown to be

$$x_T = \frac{-a_0^2 m}{\gamma p_0 A_W C_{D0}} \ln\left(1 - \frac{mg}{(F_{SLS} - mg C_f)} \sqrt{\frac{C_{D0}}{\pi \alpha}}\right), \quad (8)$$

and the take-off Mach number (M_{0T}) is

$$M_{0T} = \sqrt{\frac{2mg}{\gamma p_0 A_W C_{LT}}}. \quad (9)$$

The performance of a fixed exit area nozzle was also investigated using theory developed by Zukoski and presented in Kerrebrock [4]. Below cruise, the static pressure (p_s) and Mach number (M_s) at the location of separation within the nozzle is given by

$$M_S = 2\left(\frac{p_0}{p_s} - 1\right). \quad (10)$$

Including the stagnation pressure at the nozzle throat (p_{t8}) from the cycle calculations, it follows that

$$\frac{p_{t8}}{p_0} = \frac{p_s}{P_0}\left[1 + 2(\gamma - 1)\left(\frac{p_0}{p_s} - 1\right)^2\right]^{\gamma/(\gamma-1)}, \quad (11)$$

which is solved iteratively for p_s/p_0. The area at which separation occurs within the nozzle (A_s) is then calculated from mass continuity, and the expressions for the thrust and the TSFC are modified to include the effect of imperfect expansion.

Discussion

Table 2 lists the performance parameters assumed throughout this study. The "current" parameters are the authors' estimate of the current state-of-the-art for supersonic cruise aircraft, whilst the "best case" parameters are estimates of optimal component performance. The "current" inlet pressure recovery is approximately the reported value for both the Concorde external compression [6] and the High Speed Civil Transport (HSCT) mixed compression inlets during cruise [7]. Current compressor and turbine polytropic efficiencies and combustor pressure recovery are typical of modern engines. The current nozzle pressure recovery is thought reasonable for a variable geometry nozzle with leakage [3].

The "best case" inlet pressure recovery is the calculated pressure recovery obtained from a shock-free inlet. This was based on unpublished numerical simulations performed at MIT by Dr. A. Merchant, in which the 3% pressure loss arose from the boundary layers only. The best case, compressor polytropic efficiency is based on experimental results obtained from an aspirated compressor at MIT [8]. The best case, combustor pressure recovery is the same as its equivalent, "current" parameter. The best case, polytropic efficiency of the turbine is an estimate of the best effi-
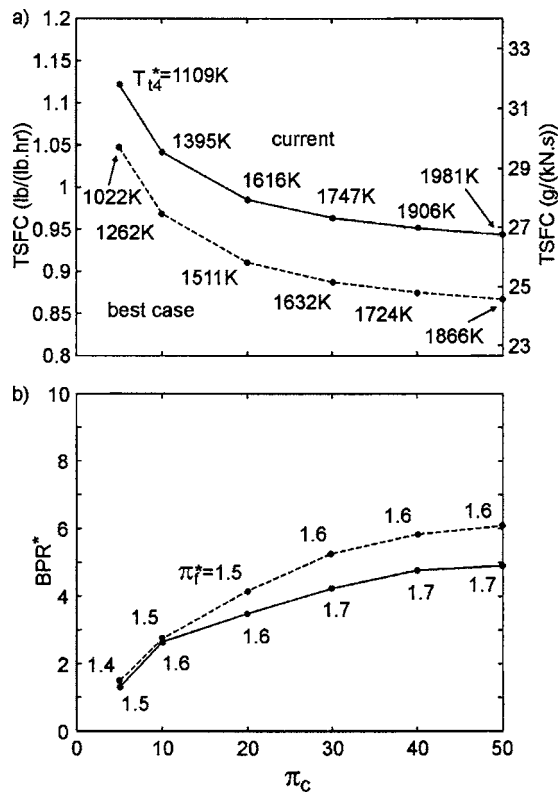
Fig. 1 Effect of π_c on (a) TSFC and (b) respective optimized BPR ($M_{0R}=2$, 50% mixing, T_{t4} and π_f optimized, $h=60$ kft.)
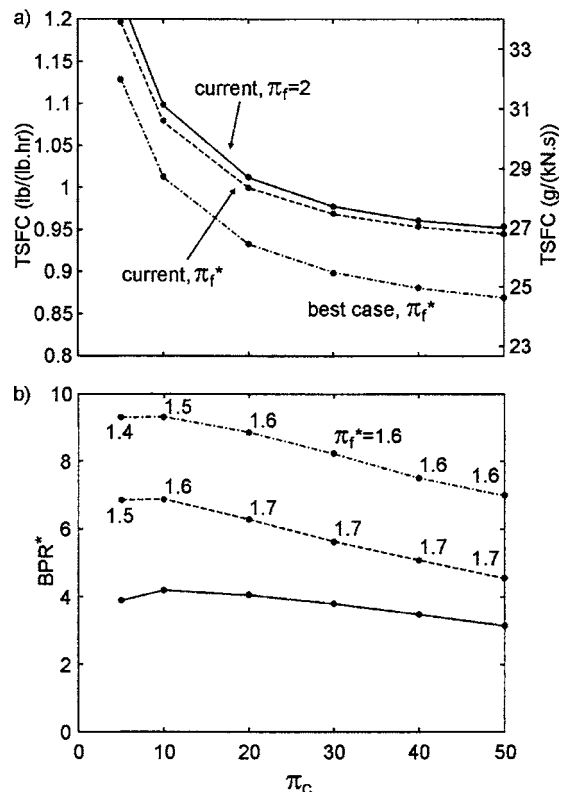

Fig. 2 Effect of π_c on (a) TSFC and (b) respective optimized BPR ($M_{0R}=2$, 50% mixing, $T_{t4}=1940$ K, $h=60$ kft.)

ciency obtainable in the absence of film cooling. The nozzle pressure recovery is an estimate of the pressure recovery resulting from a fixed geometry nozzle, without leakage, operating at matched conditions. It is clear that achieving a "best case," overall engine is an enormous technological challenge, but it serves as a guide as to how improvements in component efficiencies will impact the overall performance and engine configuration.

Overall Compressor Pressure Ratio. Engines designed for supersonic flight are characterized by relatively low compressor pressure ratios. This is due to the combination of the ram compression and the compressor exit stagnation temperature (T_{t3}) material limit enforced on the last stage of the high pressure compressor (HPC) rotor. The T_{t3} limit chosen for later analyses in this paper is $1200\,°F$ (922 K), which limits the overall compressor stagnation pressure ratio ($\pi_c=\pi_{cc}\pi_f$) to be no more than approximately 15 at $M_{0R}=2$.

The core stagnation pressure ratio also infers an optimal turbine inlet stagnation temperature (T_{t4}^*). This arises because the overall efficiency is the product of the thermal and propulsive efficiencies of the engine. An excessively high T_{t4} may result in a high thermal efficiency, but will also cause high core jet velocities and hence a relatively low propulsive efficiency. Too low a value of T_{t4} will result in high propulsive efficiency but relatively low thermal efficiency. Thus, a proper optimization for a given value of π_C necessarily involves T_{t4} as a variable parameter.

Figure 1 shows the variations in the optimal engine configuration with π_C for cruise at $M_{0R}=2$ and $h=60$ kft. Each point along the "current" and "best case" curves represents a different configuration, and the optimal values of T_{t4} and fan stagnation pressure ratio (π_f) are shown alongside each point in Figs. 1(a) and 1(b), respectively. It is clear that an optimum π_C does not occur within the range that is achievable with current materials. Importantly, the sensitivity of the TSFC to variations in π_C around 15 is relatively high, which suggests a large potential thermodynamic

benefit from increasing current material limits. This appears to be less true above roughly $\pi_C=30$. It is also clear that the TSFC goal can be met with turbine inlet temperatures and optimal fan stagnation pressure ratios that are typical of modern, subsonic, civil engines. It is emphasized, however, that these calculations do not include the significant effect of turbine film cooling, which is discussed later in this paper.

Figures 2(a) and 2(b) show the effect of setting T_{t4} at 1940 K. Whilst the TSFC for a given value of π_C is larger than that for the optimized π_C, this becomes less apparent as π_C is increased. Nonetheless, there is a thermodynamic penalty of approximately 2.5% of TSFC if $T_{t4}=1940$ K at $\pi_C=15$. If cycles that feature T_{t4} above T_{t4}^* are to be employed, there must be some other, non-thermodynamic, benefit that arises. A comparison between Fig. 1(b) and 2(b) indirectly suggests a possible means for realizing such a benefit: setting T_{t4} to be greater than T_{t4}^* increases the optimized bypass ratio (BPR*) for the engine. This arises because the added energy present within the core stream is used in part to drive a larger fan rather than to simply increase the core jet velocity. The propulsive efficiency is therefore maximized for the given value of T_{t4}.

Thus, cycles with "above-optimal" T_{t4} will have smaller cores than those with T_{t4}^*. Since the bare engine weight is strongly dependent on the size of the core, it is therefore possible that engines with T_{t4} above the optimum will weigh less than an optimal configuration with the same thrust. This is supported by the extensive correlations of older engine weights compiled by Gerend and Roundhill [9]. They found that increased bypass ratio reduces the engine specific weight (weight per unit total massflow) because "the portion of the total air which must pass through the relatively heavy (in terms of weight per airflow) primary section of the engine decreases." Of course, some design of possible engine configurations is required in order to establish this with current technology and, indeed, whether the penalty in terms of increased
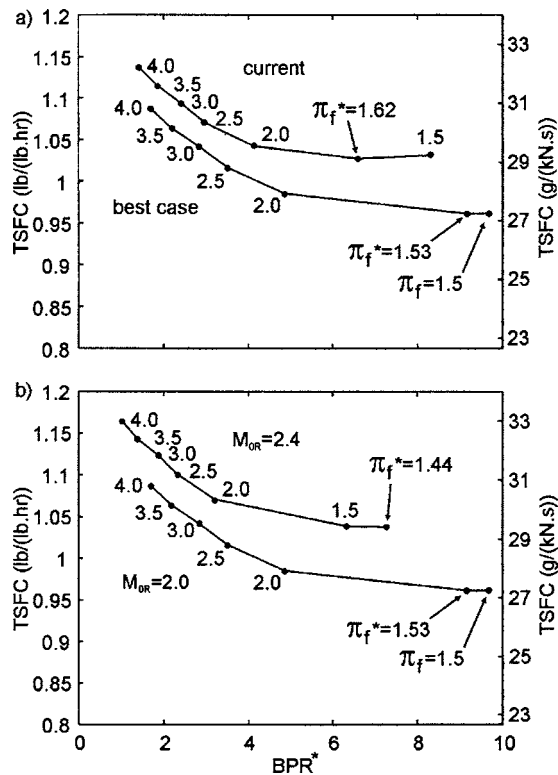
Fig. 3 Variation of TSFC with BPR* for (*a*) differing component efficiencies at $M_{0R}=2$ and, (*b*) differing cruise Mach numbers and "current" component efficiencies (50% mixing, $\pi_c=15$, $T_{t4}=1940$ K, $h=60$ kft.)

TSFC is offset by likely reductions in engine weight. However, given the challenging engine thrust/weight ratio and payload targets (Table 1), it is the authors' view that this possibility is worthy of further consideration.

Bypass Ratio. Figure 3 shows TSFC versus optimized bypass ratio (BPR*) for 50% mixed, "current" and "best case" turbofans with $T_{t4}=1940$ K and $\pi_C=15$. In these calculations, BPR has been optimized at every point along each curve, where each point represents a particular value of π_f. Thus, as π_f approaches a value of 4, BPR* reduces and the engine resembles a typical military engine. Perhaps surprisingly for a supersonic cruise aircraft, BPR* is similar to those of high bypass ratio, subsonic, civil engines at low values of π_f; this is due to the high turbine inlet stagnation temperature (T_{t4}) specified in this instance.

It is nonetheless again clear that large reductions in TSFC can be achieved through the use of higher bypass ratio. Furthermore, substantial benefits in TSFC can be achieved with increased component efficiency, provided that higher bypass ratio cycles are utilized. It is noted in all cases, however, that there is diminishing

TSFC benefit with increased BPR* once π_f falls below 2. The significant further increase in BPR* past this point, and the corresponding increases in engine frontal area is not expected to be practical. As such, most calculations in the paper will use values of π_f close to 2.

Table 3 shows particular, optimized cycles with varying cruise bypass ratios and turbine inlet temperatures (T_{t4}). A "mixing efficiency" of 50% is also assumed for the turbofans. The sea-level-static (SLS) parameters were calculated using the theory from Oates [3] presented earlier. The corrected, fan face massflow rates ($\dot{m}_c$) assume a two engine configuration that produces a total thrust of 9091 lbs. (40,538 N) at $M_{0R}=2$ and $h=60$ kft. (18,288 m). This arises if the aircraft has a mass of 100,000 lbs. (45,454 kg), it meets the L/D target in Table 1 and its engines are sized for cruise. All of the cycles feature a compressor exit stagnation temperature (T_{t3}) less than 1200°F (922 K), which is taken as a material limit. The "best case" and "current" engines listed in Table 3 are optimal cycles for their respective parameters in Table 2 and $\pi_C=15$ (cf. Fig. 1). The "best case" cycle with BPR*=2.7, $\pi_f^*=2.0$, and $T_{t4}=1415$ K at sea-level-static (SLS) has a significantly lower cruise TSFC than the "current" cycle with BPR*=2.4, $\pi_f^*=2.1$, and $T_{t4}^*=1524$ K.

Table 3 also shows the cycle parameters for an "aspirated" configuration. This configuration is discussed in greater detail later in this paper. It is also noted that all the turbofan engines shown in Table 3 feature different bypass ratios at cruise and SLS. This would require variable bypass stream geometry and arises from the modeling requirement that the turbine stagnation temperature and pressure ratios remain constant. One possibility that could achieve this variable geometry would be an unmixed turbofan with separate core and bypass nozzles. However, such complexity should be avoided if possible. Indeed, a constant bypass ratio that forces the turbine to operate over a broader range of conditions is clearly preferable and may be possible. Once again, this requires a degree of detailed engine design, since it requires study of candidate engine performance over the entire working line.

Turbine Air Film Cooling. Turbine air film cooling has a complex effect on the overall cycle performance. Acting against the desired effect of enabling increased turbine inlet temperature, turbine air film cooling also creates entropy by mixing the cooling and core streams, creates pressure losses in the cooling passages and, usually, increases the turbine profile losses because the cooling flow disrupts the core stream flow [4,10]. The first of these three effects is usually the most significant and is the easiest to model [4]. Gasturb does this by considering the cooling and core streams to mix at constant area immediately downstream of the bladerow specified, although it is acknowledged that many, more sophisticated cooling models exist.

Engine performance is particularly sensitive to HP turbine rotor cooling because, unlike HP turbine NGV cooling, it does not contribute to the work output of the HP turbine. Figure 4 shows the effect of typical values [10] of HP turbine rotor cooling mass

Table 3 Selected cycle parameters for $M_{0R}=2$ and $h=60$ kft., assuming 50% mixing efficiency and a two engine configuration

|		BPR	π_f	Core pressure ratio, π_{cc}	Overall pressure ratio, π_c	T_{t3} (K)	T_{t4} (K)	$\dot{m}_c$ (kg/s)	F (lb)	F (N)	D_0 (m)	Cruise TSFC (lb/lb h r)	Cruise TSFC (g/kN s)
Current	cruise	3.1	1.6	9.3	15.0	921	1524	254	4545	20,267	1.51	**1.01**	**28.6**
	SLS	**2.4**	**2.1**	**13.4**	**28.7**	**821**	**1524**	**203**	**21,000**	**93,640**	n/a		
Best case	cruise	3.5	1.5	9.7	15.0	896	1415	299	4545	20,267	1.63	**0.93**	**26.3**
	SLS	**2.7**	**2.0**	**14.4**	**28.8**	**798**	**1415**	**228**	**22,409**	**99,924**	n/a		
Aspirated	cruise	3.7	1.9	7.6	14.5	910	1940	178	4545	20,267	1.26	**1.05**	**29.7**
	SLS	**3.0**	**2.7**	**10.4**	**27.7**	**815**	**1940**	**156**	**20,182**	**89,993**	n/a		
Turbojet	cruise	0	n/a	15.0	15.0	921	1940	54	4545	20,267	0.69	**1.32**	**37.4**
	SLS	**0**	**n/a**	**27.6**	**27.6**	**818**	**1940**	**86**	**21,773**	**97,088**	n/a		
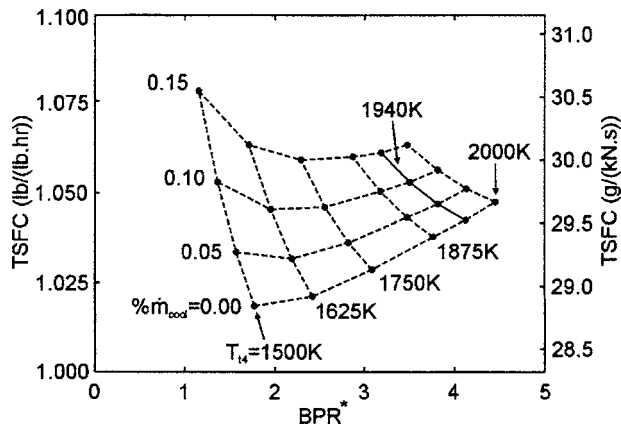
Fig. 4 Effect of % core mass flow used for HP turbine rotor cooling on TSFC for various T_{t4} (M_{0R}=2, 50% mixing "current" technology, π_c=15, π_f=2, h=60 kft.)

Fig. 6 Estimated drag-to-lift (L/D) ratio along a path of constant dynamic pressure (cruise at M_{0R}=2, h=60 kft.)

fraction ($\dot{m}_{\text{cool}}$) on the respective optimized cycles. As expected, increased cooling increases the TSFC for a given T_{t4}. Importantly, the optimized bypass ratio also reduces, which is in keeping with the effect of reduced component efficiencies. Of course, turbine cooling is intended to enable higher thermal efficiency through the use of higher combustor exit temperatures. It is therefore invalid to consider a line of constant T_{t4} and varying $\dot{m}_{\text{cool}}$ for given material and cooling technologies. Rather, a constant blade surface temperature, with both T_{t4} and $\dot{m}_{\text{cool}}$ varying, is correct. Figure 4 nonetheless shows that minimizing $\dot{m}_{\text{cool}}$ maximizes the bypass ratio of the optimized cycle. As mentioned previously, this should also reduce the engine weight in addition to any reductions in TSFC.

Acceleration and Climb. The aircraft is to be optimized for long-range, supersonic cruise and should therefore not be expected to perform over a broad flight envelope. Since the minimization of the structural weight fraction is expected to be a critical design consideration, the aircraft is expected to have a maximum airspeed below cruise that is close to the equivalent airspeed set by its cruise condition, i.e., a path of constant dynamic pressure. Figure 5 shows the normalized thrust for the "aspirated" configuration and an equivalent turbojet (Table 3) along a line with an

Fig. 5 Ratio of thrust to cruise thrust along a path of constant dynamic pressure for the "aspirated configuration" and an equivalent turbojet (cruise at M_{0R}=2, h=60 kft.)

equivalent airspeed equal to that set by cruise at M_{0R}=2 and h=60 kft., with the sea-level-static (SLS) point added. The variation in thrust was calculated using Oates' [3] theory discussed earlier. The balance between the engine thrust and the drag of the aircraft along this flight path will determine the engine sizing.

Engine Sizing. In the absence of a known configuration, the variation in lift-to-drag ratio (L/D) of the aircraft over its climb trajectory must be estimated. Figure 6 shows as a solid line a rough estimate of the L/D variations for an aircraft that meets the target of L/D=11 at cruise. The solid line is based on the dashed line, which is the estimated L/D variation for the Concorde [6,11]. The large increase in drag around M_0=1 (31 kft.) in both cases is due to the appearance of supersonic wave drag.

Figure 7(a) shows the acceleration of the aircraft along a path of constant dynamic pressure, with the engines sized for cruise at M_{0R}=2 and h=60 kft. This assumes that the weight of the aircraft is 100,000 lbs. and utilizes the thrust and L/D variations shown in (Figs. 5 and 6). Assuming that the L/D variations are reasonable, the acceleration for the aspirated configuration is clearly inadequate above M_0=1 (31 kft.) when the engines are sized for cruise. This is also perhaps true for the turbojet, although its greater thrust below cruise (Fig. 5) makes its acceleration acceptable during transonic flight. In both cases, the lack of acceleration between M_0=1 (31 kft.) and cruise is to be expected since it is a common problem for supersonic cruise aircraft. Indeed, the Concorde uses afterburning to overcome the transonic drag rise.

There are several ways to increase the acceleration during transonic climb (Fig. 7(b)). Most obviously, the engines can be oversized for cruise and the resulting weight penalty must be endured. A shallow dive is also a powerful means of increasing the transonic acceleration: as Fig. 7(b) shows, a 1-in-20 ($\sim$3 deg) dive provides a similar acceleration to 50% oversized engines at transonic conditions but, of course, without the associated weight penalty. Given that the weight requirements of the aircraft are very challenging, the use of a shallow dive during transonic acceleration should not be discounted.

Take-off. The large thrust lapse between sea level static and cruise conditions in Fig. 5 suggests that the aircraft could take-off within a short distance. Bressollette [1] found that A_W=222 m^2 and α=2.67 for a boom optimized configuration cruising at M_{0R}=2 and h=60 kft. Taking C_f=0.02, C_{D0}=0.02, and F_{SLS} for a two engine, aspirated configuration in Table 3, the theory presented earlier gives a take-off Mach number (M_{0T}) of 0.26 and the length

Fig. 7 Acceleration along a path of constant dynamic pressure with (*a*) engines sized for cruise (*b*) 50% oversized engine at cruise and aircraft in 1-in-20 (~3 deg) dive ("current" technology, $T_{t4}=1940$ K, cruise at $M_{0R}=2$, $h=60$ kft.)

Fig. 8 Variations in (*a*) inlet areas A_0, A^*, and A_{SS} areas normalized by cruise capture streamtube area (A_{0R}) and (*b*) nozzle areas A_S, A_9, and A_8 normalized by matched exit area at cruise (A_{9R}) along a path of constant dynamic pressure (aspirated configuration, "current" technology, cruise at $M_{0R}=2$, $h=60$ kft.)

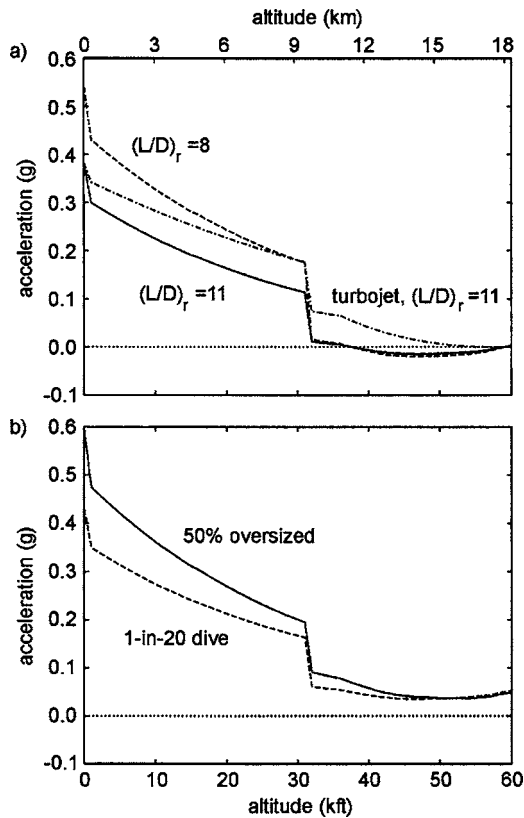of take-off roll (x_T) as 1138 m for the aspirated configuration.

Since the take-off roll under full thrust is relatively short, it seems reasonable to extend it and thus achieve a quieter take-off under part throttle. For example, Oates' [3] theory presented above suggests that if T_{t4} of the aspirated configuration is reduced to 1500 K then $x_T=1479$ m. If, as experiments suggest, the acoustic power for a supersonic jet scales with the third power of the jet velocity [4], the jet sound power level at take-off is then roughly 8 db quieter than that which occurs under full thrust. Of course, this is only a rough estimate, and the engine may not be able to operate at such low throttle settings at take-off.

Inlet Capture Streamtube. A desired inlet pressure recovery of 0.93 or greater at $M_{0R}=2$ does not clearly favor one form of inlet design. For example, the Concorde cruises at $M_{0R}=2$ and has an external compression inlet with a reported pressure recovery of approximately 0.93, whilst the HSCT was designed for cruise at $M_{0R}=2.7$ with a mixed-compression inlet of similar pressure recovery [6,7]. However, given the high bypass ratio engines proposed in this paper, it is expected that the drag of an external compression inlet would be too large. Because of the large frontal area of these engines, the L/D for the airframe could be significantly reduced if external compression is used. As such, an internal or mixed-compression inlet with a high pressure recovery is thought preferable.

Figure 8(*a*) shows normalized areas of the inlet capture streamtube along a path of constant dynamic pressure, once again using Oates' [3] theory presented earlier. The variations in the freestream capture area (A_0) show that a high degree of inlet spillage will occur during flight below cruise conditions. Although not shown in Fig. 8(*a*), A_0 at SLS is infinite and may necessitate the use of an inlet bypass duct during take-off.
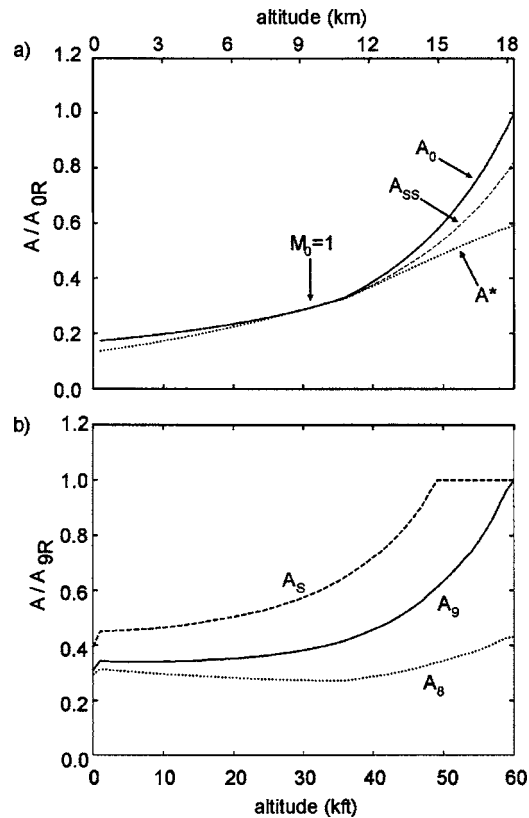
Figure 8(*a*) also shows two other quantities. A^* is the inlet throat area for shock-free inlet flow and indicates that a high degree of variable geometry is required in order to maintain a started isentropic inlet throughout supersonic flight. Furthermore, A_{SS} shows the throat area required along the flight path in order for this shock-free inlet to be self-starting at all conditions. This was calculated by assuming that inlet starting required choked flow at the throat when a normal shock existed at the inlet face [5]. Self-starting therefore places a further requirement on the variable geometry of the inlet, by requiring that the throat is able to open wider during restarting in addition to being able to narrow for flight below cruise conditions. However, if the inlet can be guaranteed not to unstart during cruise, the increased variable geometry required for self-starting could perhaps be avoided by starting the inlet between $M_0=1$ (31 kft.) and $M_0=1.7$ (52 kft.).

Specific Component Technologies: Shock-free Inlets. The "best case" pressure recovery for the inlet was stated in Table 2 to be 0.97. This value is based on unpublished numerical simulations of a shock-free inlet by Dr. A. Merchant of MIT, in which the 3% pressure loss arose from the boundary layers only. In terms of pressure recovery, this type of inlet design is optimal. Nonetheless, the shortcomings of internal compression, shock-free inlets are well known. Most importantly, they are unstable to upstream and downstream disturbances and have no margin for avoiding "unstart." Furthermore, as Fig. 8(*a*) suggests, the degree of variable geometry required to start such an inlet at cruise conditions is considerably larger than, for example, a properly designed mixed-compression inlet. However, the reduction in TSFC achieved through an optimal inlet pressure recovery is significant enough to warrant investigation of this design.

Aspirated Compressor. "Aspirated compressors" employ suction through the blade surface to suppress separation and hence achieve large increases in the stage loading of the compressor and fan. Recent research at MIT has shown that, not including the air bleed, the polytropic efficiency of an aspirated compressor can be as high as 93% [8]. Provided that the amount of bled air is small, as was the case in [8], the thermodynamic penalty for bleeding the air is negligible if this air is used elsewhere in the aircraft. Thus, aspirated compressors offer the potential of very large weight savings in the compressor without significant thermodynamic penalty. For example, the overall compressor pressure ratio (π_C) listed in Table 3 is achievable with a three spool, counter-rotating engine with an aspirated fan and aspirated compressor. The fan consists of one stage, and the compressor has two stages. With "current" component efficiencies, this configuration meets the TSFC target stated in Table 1. Like the best case and current configurations, the diameter of the inlet capture streamtube (D_0) is also thought to be reasonable for an aircraft of this size, despite the configuration's relatively low specific thrust compared to the turbojet. Aspirated compressors are therefore expected to be a particularly attractive option for the aircraft because of the challenging engine weight targets in Table 1.

Nozzle. Engines designed for supersonic cruise usually have variable geometry nozzles. In most cases this is because afterburning requires variability of the nozzle throat area in order to maintain the turbine at a roughly constant pressure ratio. However, variable geometry nozzles commonly leak (leading to a reduction in performance) and they are inevitably heavy and mechanically complex. It is therefore reasonable to investigate the performance of a fixed exit area nozzle during climb, as this may enable significant weight savings and perhaps performance benefits at cruise.

Figure 8(b) shows the variation in the area of fixed and variable exit nozzles along a path of constant dynamic pressure. In order to maintain a matched exhaust stream, the variable exit area (A_9) reduces with reduced altitude. In comparison to this, the fixed exit area nozzle overexpands the exhaust stream when operating below cruise conditions. As the aircraft descends below cruise, this first leads to the formation of a shock-train from the nozzle exit and, later, separation of the exhaust flow within the nozzle itself. This is implied in Fig. 8(b): the horizontal portion of the dashed line A_S just below cruise represents that portion of the flight path during which the shock-train occurs without flow separation within the nozzle. At lower altitudes, the flow separates within the nozzle at area A_S.

The effect of a fixed exhaust area on the specific thrust and TSFC is shown in Fig. 9. While there is a 10–15% increase in the TSFC below cruise, the weight and reliability advantages of a fixed nozzle exit geometry are expected to be substantial. However, the benefits of reduced nozzle weight and reduced leakage, together with the effect on the performance of the turbine need to be quantified. This requires a degree of detailed engine design.

Conclusions

This paper suggested two main requirements of the propulsion system for quiet, long range, supersonic cruise aircraft with a cruise thrust specific fuel consumption (TSFC) of at most 29.7 g/kN s (1.05 lb./lb. h) at a cruise Mach number of 2.0 and an altitude of 18,288 m (60 kft.). These requirements are (i) the use of a high turbine inlet temperature that does not require compressor bleed for cooling the turbine and (ii) the choice of a bypass ratio that is significantly higher than those of typical, supersonic cruise engines. Although only preliminary calculations have been presented, it is intended that an engine with these features will meet the specified fuel consumption targets whilst minimizing the engine weight. Assuming component efficiencies that are currently achievable, analyses presented in this paper suggest that
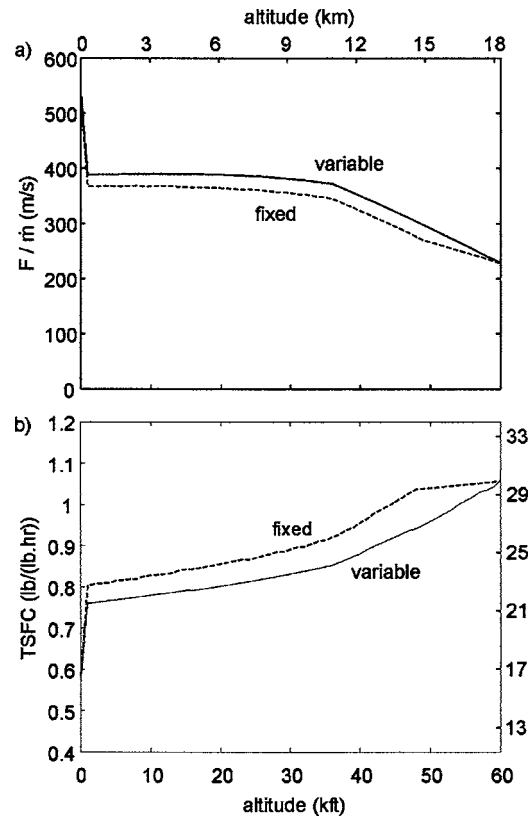
Fig. 9   Variation in (*a*) specific thrust and (*b*) TSFC for variable and fixed area nozzles along a path of constant dynamic pressure (**aspirated configuration, "current" technology, cruise at** M_{0R}=2, *h*=60 kft.)

one possible engine has an overall pressure ratio of 28, a turbine inlet stagnation temperature of 1940 K (3032°F), and a bypass ratio of 3.0 at sea-level-static.

Significant performance benefits can also be achieved through increases in several other component performance parameters. Most importantly, substantial benefits in fuel consumption can be achieved by raising the compressor exit temperature limit and optimizing the turbine inlet temperature accordingly. An "aspirated" compressor and fan, which use suction through the blade surface to achieve large increases in the stage loading, also appear to be ideally suited to this aircraft because of the challenging targets on engine weight.

Internal compression, shock free inlets may also significantly reduce fuel consumption and airframe drag. It is emphasized, however, that this is a very challenging task because of both the required variability in inlet geometry and the difficulty in preventing "inlet unstart."

While preliminary calculations suggest a 10%–15% increase in fuel consumption below cruise, the weight, cruise performance and reliability advantages of a fixed exit nozzle geometry are expected to be substantial. However, the benefits of reduced nozzle weight and reduced leakage, together with the nozzle's effect on the performance of the turbine need to be quantified. This requires a degree of detailed engine design.

Nomenclature

a = sonic velocity (m/s)
A = area (m²)
BPR = bypass ratio
C_{D0} = drag coefficient at zero lift
C_f = rolling friction coefficient
D = drag (N)

F = thrust (N)
h = altitude (kft)
g = gravitational constant (m/s²)
L = lift (N)
M = Mach number
m = aircraft mass (kg)
$\dot{m}_c$ = corrected, fan face massflow rate (kg/s)
$\dot{m}_{cool}$ = % of HPC exit massflow bled through HPT rotor
P = static pressure (Pa)
T = static temperature (K)
TSFC = thrust specific fuel consumption (lb./(lb. h))

Greek Symbols
α = wing aspect ratio
ϵ = polytropic efficiency
π = stagnation pressure ratio
τ = stagnation temperature ratio

Subscripts
b = combustor
c = overall compressor (fan and HPC)
cc = core compressor
d = inlet
e = bare engine
f = fan
n = nozzle
r = ratio of freestream stagnation freesteam static quantity
R = cruise condition
s = nozzle separation
SS = self-starting
t = turbine
t = total (stagnation) quantity
w = wing

Superscripts
* = optimal value
* = choked

Station numbering
0 = freestream
1 = inlet face
2 = fan face
3 = compressor exit
4 = turbine rotor inlet
8 = nozzle throat
9 = nozzle exit

References

[1] Bressollette, A., 2002, "Sonic Boom Considerations in Preliminary Design of Supersonic Aircraft," M. S. thesis, Massachusetts Institute of Technology, Massachusetts.
[2] Kurzke, J., 1998, GASTURB: A Program to Calculate Design and Off-Design Performance of Gas Turbines, User's Manual, Version 8.0, J. Kurzke, Dachau.
[3] Oates, G. C., 1984, Aerothermodynamics of Gas Turbine and Rocket Propulsion, American Institute of Aeronautics and Astronautics (AIAA), New York.
[4] Kerrebrock, J. L., 1996, Aircraft Engines and Gas Turbines, 2nd ed., MIT Press, Cambridge.
[5] Seddon, J., and Goldsmith, E. L., 1985, Intake Aerodynamics, AIAA Education Series, American Institute of Aeronautics and Astronautics (AIAA), New York.
[6] Rech, J., and Leyman, C. S., A Case Study by Aerospatiale and British Aerospace on the Concorde, AIAA Professional Study Series, American Institute of Aeronautics and Astronautics (AIAA), New York.
[7] Wasserbauer, J. F., Meleason, E. T., and Burstadt, P. L., 1996, "Experimental Investigation of the Performance of a Mach-2.7 Two-Dimensional Bifurcated Inlet Duct with 30 Percent Internal Contraction," NASA technical memorandum 106728, National Aeronautics and Space Administration (NASA).
[8] Schuler, B. J., 2000, "Experimental Investigation of an Aspirated Fan Stage," Ph.D. dissertation, Massachusetts Institute of Technology, Cambridge, MA.
[9] Gerend, R. P., and Roundhill, J. P., 1970, "Correlation of Gas Turbine Engine Weights and Dimensions," AIAA Paper No. 70-669.
[10] Young, J. B., and Wilcock, R. C., 2002, "Modelling the Air-Cooled Gas Turbine: Part 1-General Thermodynamics." ASME J. Turbomach., **124**, pp. 207–213.
[11] Squire, L. C., 1981, "Experimental Work on the Aerodynamics of Integrated Slender Wings for Supersonic Flight," Prog. Aerosp. Sci., **20**, pp. 1–96.

Development of a Second Generation In-Flight Icing Simulation Code

Héloïse Beaugendre[1]

François Morency[2]

Wagdi G. Habashi[3]
Director

Computational Fluid Dynamics Laboratory,
Department of Mechanical Engineering,
McGill University,
688 Sherbrooke Street West, 7th Floor,
Montréal, Québec H3A 2S6 Canada

Two-dimensional and quasi-3D in-flight ice accretion simulation codes have been widely used by the aerospace industry for the last two decades as an aid to the certification process. The present paper proposes an efficient numerical method for calculating ice shapes on simple or complex 3D geometries. The resulting ice simulation system, FENSAP-ICE, is built in a modular fashion to successively solve each flow, impingement and accretion via field models based on partial differential equations (PDEs). The FENSAP-ICE system results are compared to other numerical and experimental results on 2D and slightly complex 3D geometries. It is concluded that FENSAP-ICE gives results in agreement with other code calculation results, for the geometries available in the open literature. [DOI: 10.1115/1.2169807]

Introduction

Not all certification conditions can be ice tunnel-tested, flight-tested, tanker-tested or encountered in natural icing testing. The certification process usually consists of a mix of experimental and numerical methods that make it possible to explore, safely, the entire combined aerodynamic and icing envelopes. For more than 50 years now, the aircraft icing community has been using analytical methods to calculate impingement limits and predict ice shapes to be subsequently attached to an aircraft for flight-testing [1]. The decrease in computer calculation cost has led to the rapid development of ice accretion simulation tools in the early 1980s [2]. Usually, such methods are based on either a 2D or quasi-3D inviscid flow code (Panel method) to compute the airflow solution, on Lagrangian particle tracking techniques for droplet impingement calculations, and on a 1D mass and heat transfer balance at the surface to predict ice shapes. The best-known codes using this structure are NASA's LEWICE [3], ONERA [4], TRAJICE2 [5], and Bombardier Aerospace's CANICE [6].

Although code structure has remained mostly the same for nearly 20 years, several improvements have been proposed, making it possible for the most advanced codes to tackle 3D problems [7]. One of the advantages of these pioneering methods is their fast calculation speed, especially on 2D problems. They have, however, known limitations, the most obvious being the inability to handle flow with separation. It is well known that viscous/nonviscous coupling methods are difficult to apply to separated flow, more the norm than the exception for most of the glaze ice accretion cases.

Current computational fluid dynamics technologies can overcome some of the limitations of these fully mature methods, and open new possible uses for in-flight icing prediction tools. Advanced notions such as using computational fluid dynamics to couple aerodynamics and icing, of using computational fluid dynamics to assess the stability and control of iced aircraft or for building a database for an in-flight icing simulator can then be contemplated.

The FENSAP-ICE approach views icing accretion simulation as the interlinking of:

- The computation of the clean and degraded flows via a 3D compressible turbulent Navier-Stokes equations (by any computational fluid dynamics code; here with FENSAP [8]: Finite Element Navier-Stokes Analysis Package);
- The computation of the collection efficiency by a 3D Eulerian method (here with DROP3D [9]);
- The solution of 3D mass balance and heat transfer at surface, using partial differential equations, for prediction of 3D ice accretion shapes (here with ICE3D [10]);
- A conjugate heat transfer problem, in the presence of an anti-icing heat flux across the wing skin (for example, with the use of CHT3D [11]);

all four approaches being partial differential equations (PDE)-based. As shown in Fig. 1, the modules are set in an interactive loop.

This paper first presents a short description of the first three modules. The code results are compared to other 2D and quasi-3D numerical and experimental results from NASA, and are demonstrated for ice accretion on a 3D rotor blade tip.

FENSAP-ICE's Modules Description

Airflow solver. The airflow solver of FENSAP-ICE, FENSAP, can act in an inviscid (Euler) or viscous (Navier-Stokes) mode, as necessitated by the application at hand. For ice accretion simulation, results are extremely sensitive to the turbulent heat fluxes at walls and the Navier-Stokes equations, with appropriate turbulence models, are called for. Currently, a one-equation turbulence model (Spalart-Allmaras [12]), including extension for rough-wall treatment [13], has been implemented and successfully validated [14]. The validation has been done against experimental and numerical results on an attached flow with known equivalent sandgrain roughness value. Glaze ice accretion simulation results depend on the roughness value selected, and an empirical correlation relating roughness to velocity, liquid water content and static temperature, developed for LEWICE, is used [14,15].

The Spalart-Allmaras model offers the possibility to locally trip the flow if the transition point location is known. For ice accretion calculation, the transition location is not known and the flow is assumed to be fully turbulent. Thus, it is expected that numerical results overpredict heat flux near the stagnation point, where the flow should be laminar. But, as ice starts to accrete on an airfoil,
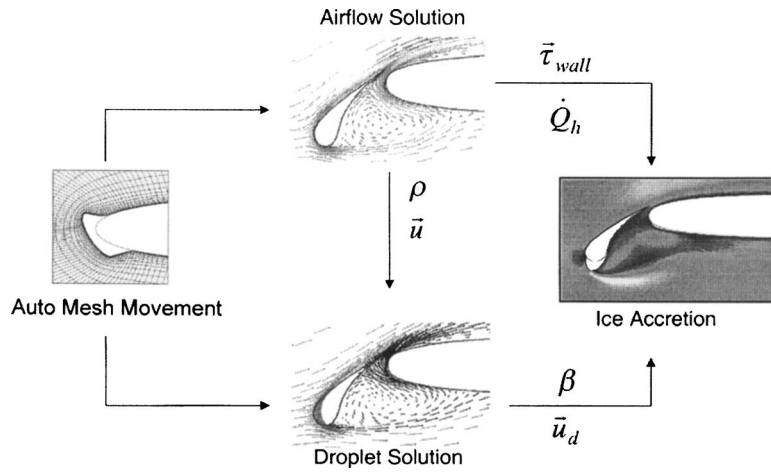

Copyright © 2006 by ASME

Fig. 1 Module interactions within FENSAP-ICE

ice roughness in the stagnation point area causes perturbations in the boundary layer. Transition from laminar to turbulent flow occurs earlier than for a clean airfoil, in the near vicinity of the stagnation point.

Spatial discretization is carried out by finite element method and the nonlinear governing equations are linearized by a Newton method. To advance the solution in time, an implicit Gear scheme is used, along with a generalized minimum residual (GMRES) procedure to iteratively solve the resulting linear equations matrix system. In order to have a nearly optimal mesh for a required number of nodes for a Navier-Stokes calculation, an automatic anisotropic mesh optimization procedure is used [16]. This technology has been shown to yield user-independent and solver-independent results as long as one is not limited in mesh size. When computer memory constrains the problem size, then mesh adaptation provides a rapid way to generate meshes that optimize the prediction of a known scalar physical property of the flow, most often the Mach number.

Gradients needed for heat fluxes at walls are also accurately calculated via a consistent finite volume method postprocessing approach developed by Gresho et al. [17]. This method substantially reduces the numerical error in flux evaluation. Good results will be obtained if the physical models, including heat fluxes and the turbulence model, are appropriate for the problem. It is generally admitted that one- and two-equation turbulence models have difficulties to accurately predict the flow field in a separated region, such as the flow behind an ice horn or ridge, but potential flow methods completely fail in these cases.

Droplet flow solver. The Eulerian droplet impingement model is essentially a two-fluid model consisting of the Euler (inviscid) or Navier-Stokes (viscous turbulent) set of equations for dry air, augmented by the following droplet-specific continuity and momentum equations:

$$\frac{\partial \alpha}{\partial t} + \nabla \cdot (\alpha \mathbf{u}_d) = 0 \tag{1}$$

$$\frac{D\mathbf{u}_d}{Dt} = \frac{C_D \operatorname{Re}_d}{24K}(\mathbf{u}_a - \mathbf{u}_d) + \left(1 - \frac{\rho_a}{\rho_w}\right)\frac{1}{\mathrm{Fr}^2}\mathbf{g} + \frac{\rho_a}{\rho_w}\frac{D_a\mathbf{u}_a}{Dt} \tag{2}$$

where the variables α and $\mathbf{u}_d$ are mean values, respectively, of the nondimensional water volume fraction and droplet velocity over a small fluid element around the location x at time t. The first term on the right-hand side of Eq. (2) represents the drag force on the droplets, while the second and third terms represent, respectively, the buoyancy force from gravity and the forces exerted on an air particle that would have occupied the volume of the droplet [18]. In most cases, the third term is negligible due to the low ratio of

air to water densities.

An empirical correlation is used for the drag coefficient, C_D. The two-fluid model assumes spherical monodispersed droplets, at the median volumetric diameter of the sample size distribution. The spherical droplet approximation is valid for droplet Reynolds numbers below 500. No collision or mixing between the droplets is accounted for, as these are not significant in certification icing situations. The following empirical equation gives the drag coefficient around a sphere, as a function of the Reynolds number:

$$C_D = (24/\operatorname{Re}_d)(1 + 0.15\operatorname{Re}_d^{0.687}) \quad \text{for } \operatorname{Re}_d \leq 1300$$

$$C_D = 0.4 \quad \text{for } \operatorname{Re}_d > 1300 \tag{3}$$

The correlation used goes above $\operatorname{Re}_d = 500$ because during the iterative convergence of the numerical solution, higher droplet Reynolds numbers may occur. The final converged solution, however, should not contain local droplet Reynolds numbers above 500. Otherwise, it means that a different correlation accounting for droplet deformation must be used.

The nondimensional air velocity, $\mathbf{u}_a$, is obtained from the solution of the Navier-Stokes equations. Because of the low liquid water concentration, the effect of the droplets on the airflow is neglected. Airflow can thus be determined before solving Eqs. (1) and (2).

A finite element Galerkin formulation is used to discretize the set of Eqs. (1) and (2), with a streamline upwinding Petrov-Galerkin (SUPG) term added [19].

Ice Accretion Solver

The 3D partial-differential equation-based equilibrium model introduced in Ref. [20] is derived based on the Messinger [1] model. It has been further improved to predict the ice accretion and water runback on the surface [10]. The velocity $\mathbf{u}_f$ of the water in the film is a function of coordinates $\mathbf{x} = (x_1, x_2)$ on the surface and y normal to the surface.

A simplifying assumption consists of taking a linear profile for $\mathbf{u}_f(\mathbf{x}, y)$, with a zero velocity imposed at the wall, i.e.,

$$\mathbf{u}_f(\mathbf{x}, y) = \frac{y}{\mu_w}\boldsymbol{\tau}_{\text{wall}}(\mathbf{x}) \tag{4}$$

where τ_{wall}, the shear stress from the air, is the main driving force for the water film. By selecting a linear velocity profile, body forces such as pressure and gravity are neglected. Except perhaps near stagnation lines, body forces can be shown to have negligible effect on the thin water films that occur in the case of ice accretion [15].

By averaging across the thickness of the film, a mean water film velocity is obtained

$$\overline{\mathbf{u}}_f(\mathbf{x}) = \frac{1}{h_f} \int_0^{h_f} \mathbf{u}_f(\mathbf{x}, y) dy = \frac{h_f}{2\mu_w} \boldsymbol{\tau}_{\text{wall}}(\mathbf{x}) \quad (5)$$

The resulting system of partial differential equations is thus the following mass conservation and energy conservation equations,

$$\rho_w \left[\frac{\partial h_f}{\partial t} + \text{div}(\overline{\mathbf{u}}_f h_f) \right] = U_\infty \text{ LWC } \beta - \dot{m}_{\text{evap}} - \dot{m}_{\text{ice}} \quad (6)$$

where the three terms on the right-hand side correspond to the mass transfer by water droplet impingement (source for the film), the evaporation and the ice accretion (sinks for the film), respectively,

$$\rho_w \left[\begin{array}{c} \dfrac{\partial h_f C_w T}{\partial t} \\ + \text{div}(\overline{\mathbf{u}}_f h_f C_w T) \end{array} \right] = \left[C_w T_{d,\infty} + \frac{\|\mathbf{u}_d\|^2}{2} \right] \times U_\infty \text{ LWC } \beta$$

$$- 0.5(L_{\text{evap}} + L_{\text{subl}})\dot{m}_{\text{evap}}$$
$$+ (L_{\text{fusion}} - C_{\text{ice}}T)\dot{m}_{\text{ice}} + \epsilon\sigma((T_\infty + 273.15)^4$$
$$- (T + 273.15)^4) + \dot{Q}_h \quad (7)$$

where the first three terms on the right-hand side, correspond, respectively to the heat transfer caused by the supercooled water droplets impinging on the surface, and that from evaporation and ice accretion. The last two terms in the equation represent the radiative and convective heat transfer.

The convective heat transfer is obtained from the computational fluid dynamics code, by imposing a constant clean airfoil surface temperature above the free-stream temperature. The heat flux is converted into a heat transfer coefficient, before ice accretion calculations, because the heat transfer coefficient depends only weakly on the surface temperature distribution [21].

The coefficients ρ_w, C_w, C_{ice}, L_{evap}, L_{subl}, L_{fusion} represent physical properties of water, while $T_{d,\infty}$, U_∞, LWC, and T_∞ are airflow and droplet parameters specified by the user. The ambient icing conditions completely determine those values. The temperatures are in Celsius.

The Eulerian droplet module provides local values for the collection efficiency β and the droplet impact velocity $\mathbf{u}_d$. The flow solver provides the local wall shear stress $\boldsymbol{\tau}_{\text{wall}}$ and the convective heat flux $\dot{Q}_h$. The evaporative mass flux is recovered from the convective heat flux using a parametric model [6]. There remain three unknowns: the film thickness h_f, the equilibrium temperature T within the air/water film/ice/wall interface, and the instantaneous mass accumulation of ice $\dot{m}_{\text{ice}}$. Compatibility relations are needed to close the system and one way to write them is the following:

$$h_f \geq 0 \quad (8)$$

$$\dot{m}_{\text{ice}} \geq 0 \quad (9)$$

$$h_f T \geq 0 \quad (10)$$

$$\dot{m}_{\text{ice}} T \leq 0 \quad (11)$$

The discretization of these equations is via finite volume method. The trace of the three-dimensional mesh at the air-structure/ice shape interface is called the surface mesh. From the surface mesh, a dual surface mesh is obtained by connecting the centroids of the surface mesh cells to the mid-edges of the cells. The unknowns are then computed at the center of each cell, corresponding one-to-one to the nodes of the finite element method used for the air and droplet solutions.

After a given ice accretion time, the ice accretion solver returns a wall temperature distribution and the displacements of the sur-

Table 1 Ambient conditions corresponding to 2D test cases

Parameter	Run 403	Run 404	Run 308
T_∞	262.04 K	256.49 K	262.04 K
P_∞	100 kPa	90.76 kPa	90.76 kPa
U_∞	102.8 m s^{-1}	102.8 m s^{-1}	102.8 m s^{-1}
AoA	4 deg	4 deg	4 deg
MVD	20 μm	20 μm	20 μm
LWC	0.55 g/m³	0.55 g/m³	1 g/m³
Re$_\infty$	4.39×10^6	4.14×10^6	4.14×10^6

face nodes. These displacements and temperature distribution can be used to calculate a new airflow solution and start a new calculation cycle. With a Navier-Stokes flow solver, for sufficiently large ice horns, separation may occur. This separation will affect the overall flow field and the local heat transfer coefficient. Although actual turbulence models are not very accurate for separated flows, they still represent a significant improvement on a viscous/nonviscous coupling method. Knowing that first generation codes fail to predict this separation, it can thus be expected that even for 2D glaze ice cases, discrepancies will exist between numerical results.

In the three-dimensional cases, ice accretion results were obtained using only one cycle of calculation (one-shot ice accretion). Thus, the effect of ice accretion on the airflow and droplets fields is neglected. It means losing part of the advantage of using a Navier-Stokes solver. For the actual 3D test cases, this simplification is justified by the rime ice accretion conditions that produce ice shapes with relatively low impact on airflow for the rotor blade tip. This will have to be confirmed in the future by running multiple layer ice accretions.

To do multilayer ice accretions in 3D would take a large amount of computing time. Also, considering that for the nacelle only one-shot ice accretion results are available from the LEWICE code, in this article only one-shot results are shown for 3D calculations.

Two-Dimensional Validations

ICE3D has been compared to numerical solutions obtained with LEWICE, and experimental results obtained in the NASA Glenn Icing Research Tunnel (IRT) [22]. All FENSAP 2D calculations are carried out in a pseudo-3D manner on meshes of one element thickness in the spanwise direction. A consensus [23,24] about the comparison criteria of two icing shapes is difficult to obtain. Indeed, the focus can be on different criteria such as the limit of impact, the ice thickness or the location and angle of a possible horn, etc. As a consequence, the comparisons remain most of the time subjective but conservative enough to satisfy aircraft safety requirements.

Mesh density effects. The effect, on the ice accretion simulation, of mesh density around the leading edge of a NACA 0012 airfoil has been studied with a coarse (90 mesh points on the airfoil), medium (180 mesh points), and fine grid (360 mesh points). The meshes contain, respectively, a total of 23,350, 36,130, and 61,690 nodes. The spacing in the direction normal to the wall is kept the same for the 3 meshes and is equal to 8.4 $\times 10^{-6}$ c, c being the chord of the airfoil. The ambient conditions selected for this test case correspond to the LEWICE Run 403 [22] and are given in Table 1. The accretion time is 7 min. The airflow, impingement and ice accretion solutions on the 3 meshes are compared to each other and compared to LEWICE solutions. For the airflow and impingement solutions the results are plotted against the distance from the stagnation point.

Airflow solution. The turbulence model selected for the simulation is the one-equation Spalart-Allmaras model with an equiva-
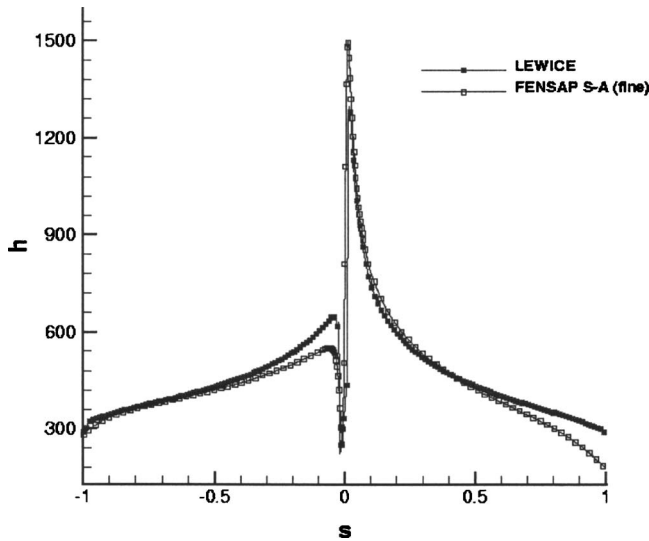
Fig. 2 Convective heat transfer coefficient distribution against the distance from stagnation point

Fig. 4 Run 403 [NASA-CDROM], ice shape comparison between ICE3D (fine grid), LEWICE and experiments

lent sandgrain roughness of 0.55 mm. The grid study shows that the solutions on the medium and fine grids are similar and appear to be mesh-independent, as far as the heat transfer coefficient is concerned.

LEWICE uses an integral method to solve the boundary layer. LEWICE and FENSAP solutions are compared in Fig. 2. The differences between the two curves close to the trailing edge are due to the boundary layer thickness, not taken into account in the LEWICE code. Close to transition points the differences are most probably induced by the turbulence model. The equivalent sandgrain roughness coefficient used for this calculation is the same as in LEWICE. This roughness coefficient is especially calibrated for LEWICE. Although the two turbulence models employed are strongly different, the two solutions agree pretty much and the results are satisfactory.

Impingement solution. The local collection efficiency curves are identical for the three meshes, thus droplet solutions appear to be mesh-independent.

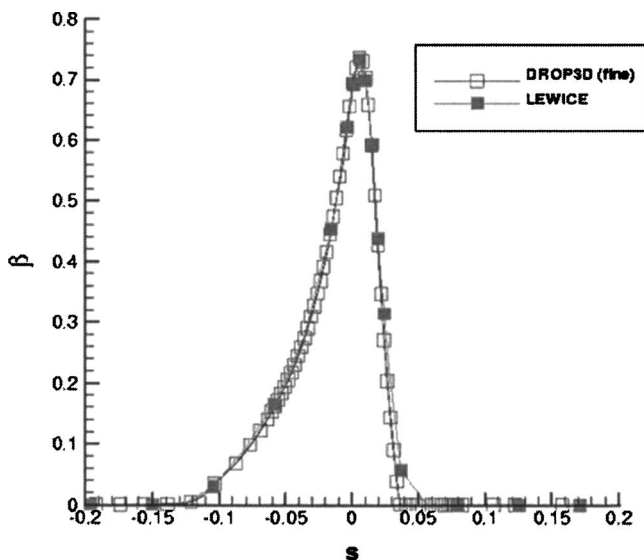The comparison with LEWICE is shown in Fig. 3. The maxi-

Fig. 3 Local collection efficiency distribution against the distance from stagnation point
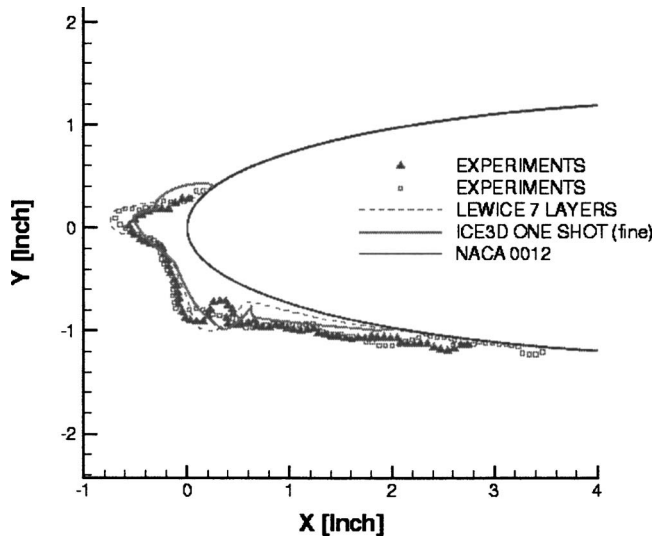
mum collection efficiency predicted by the two codes is identical. The impingement limits are slightly different on the upper part of the airfoil ($s \geq 0$). This is most probably due to a small difference in flow fields. LEWICE solves for a potential flow and the angle of attack is lowered from 4 deg to 3.5 deg to match the overall lift coefficient. For the Navier-Stokes numerical solution, a free stream angle of attack of 4 deg is used.

Ice accretion solution. For the ice accretion module, a one-shot ice accretion simulation is performed on each mesh. The aim is to have larger ice shapes to compare, and also not to mix the effect of mesh density with the effect of airflow solution updates on the solution. Beaugendre [15] has studied this last aspect.

The comparison of ice shapes on the three meshes shows not much difference, and only results on the finer mesh are shown. The mass of ice accreted is the same for the three meshes and is equal to 0.496 kg per unit span.

For this run, two experimental solutions are available and plotted in Fig. 4. The LEWICE numerical solutions obtained with a multistepping approach composed of 7 layers is also available and shown. The one-shot ICE3D shape is acceptable compared to the experimental and numerical solutions, especially if we take into account the fact that the over predicted ice thickness on top of the airfoil will substantially decrease if a multistepping approach were used. Indeed, this part of the airfoil will be in the shadow zone of the bump located between the coordinates: $0 < Y < 0.2$ in.

Validation on Airfoil: NACA 0012. The NACA 0012 airfoil has been used in several test entries. The data from this airfoil represent the highest number of ice shapes that have been created in the icing research tunnel. Through all this section, the ice shapes are plotted in inches.

Run 404. In the first comparison, ice is accreted for 7 min on a NACA 0012 airfoil at 4 deg angle of attack. The ambient icing conditions, which should be close to rime ice accretion are given in Table 1 and correspond to LEWICE Run 404 [22].

Figure 5 shows the final ice shape computed by LEWICE and ICE3D, compared to the experimental ice shape obtained in the IRT. The limits of impact are identical for LEWICE and ICE3D and match the experiments on the suction side of the airfoil, but are underpredicted by both codes on the pressure side of the airfoil. ICE3D's ice shape is thicker and closer to the experimental ice shape than LEWICE on the upper part of the airfoil. This may be due to a larger estimation of the water evaporation by
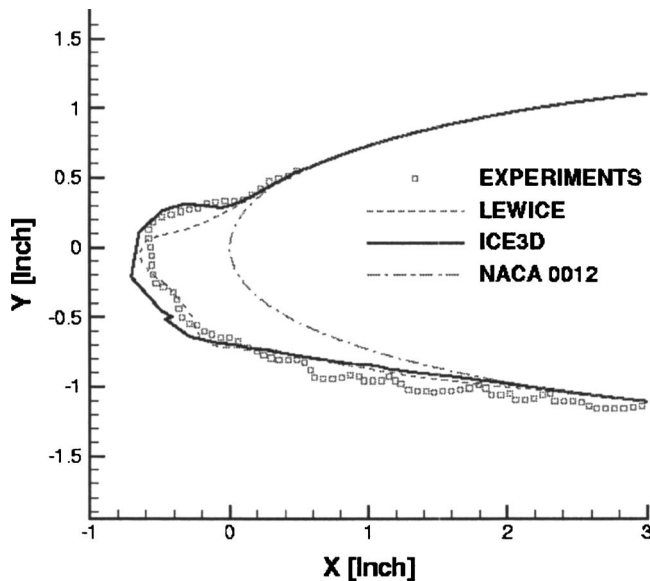
Fig. 5 Run 404 [NASA CD-ROM], ice shape comparison between ICE3D, LEWICE, and experiments

Fig. 7 Run 308 [NASA CD-ROM] comparison between ICE3D, LEWICE and IRT experimental ice shape

LEWICE. ICE3D also predicts a slightly smaller ice thickness on the pressure side, where the LEWICE solution is closer to the measurement.

Run 308. In the second comparison, ice is accreted on a NACA 0012 airfoil at a 4 deg angle of attack for 231 s. The ambient conditions, closer to glaze ice conditions, are summarized in Table 1 and correspond to LEWICE Run 308 [22].

Figure 6 shows the comparison between LEWICE and ICE3D numerical solutions after 47.58 and 95.16 s of accretion. At 47.58 s of accretion, ICE3D and LEWICE solutions are identical: same ice thickness and limits of impact for both codes. After 95.16 s of accretion, LEWICE and ICE3D solutions remain very close to each other, LEWICE predicting a slightly bigger amount of runback than ICE3D. Both codes predict the formation of a horn on the upper part of the NACA 0012 airfoil, with the same
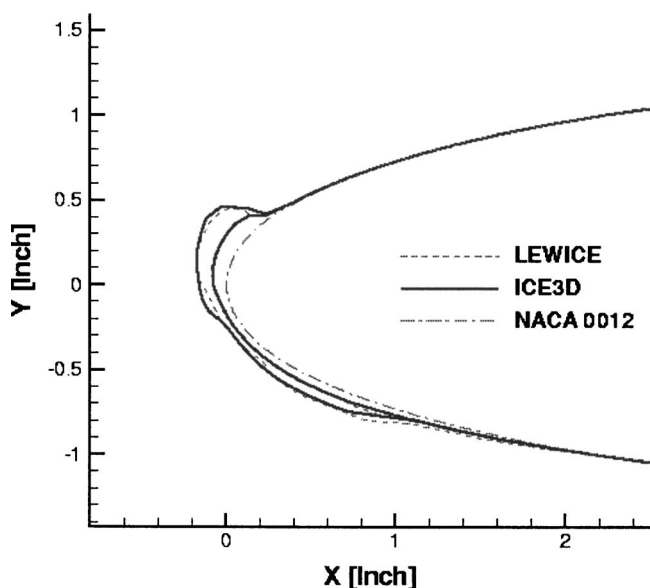
angle and ice thickness.

After 95.16 s of accretion, the horn predicted by ICE3D induces a separation in the flow solution. Contrary to LEWICE, which may be able to predict but not compute separation with only a viscous/inviscid interaction, ICE3D's convective heat transfer coefficient and shear stress decrease suddenly in the separation area. As a consequence, impact may be predicted behind a horn as can be seen in Fig. 7. ICE3D's final ice shape is very close to LEWICE's, but both codes fail to predict the horn's angle of the experimental ice shape. There is still room for improvement in the quality of ice-accretion-shape predictions yielded by current icing codes, as large differences between predicted and experimental ice shapes are often encountered [24] in glaze ice conditions, compounded by the problem of the lack of consistency of ice shapes produced in icing wind tunnels.

3D Helicopter Rotor Blade Tip Results

The first test case considered is a three-dimensional helicopter rotor blade tip. This case was selected because of the availability of experimental and numerical results. Its three-dimensional effects are small, and a quasi-three-dimensional model that accretes ice along the flow streamlines from ONERA calculated a numerical solution [4] to compare to.

This three-dimensional helicopter rotor tip geometry is rather briefly described in paper [4] as follows:

"…from the base to the top along the span, the chord varies from 0.6 to 0.2 m, the leading edge sweep angle starts at 0 and ends at 60 deg. The trailing edge is perpendicular to the flow and is lightly spun so that the incidence angle at the top is 0.74 deg less than at the base. The span is 0.48 m. The rotor blade tip is built from a NACA 13106 airfoil."

Based on this short description, a computer aided design (CAD) of the geometry was produced with the ICEM DDN software. The one-equation Spalart-Allmaras model was used for turbulence modeling and mesh adaptation was carried out with OptiMesh [25], an anisotropic (highly directional and highly stretched) automatic mesh adaptation code. Unfortunately, it turns out that the experimental model does not follow exactly the description given in paper [4].

Airflow solution and mesh adaptation. The conditions for the simulation are shown in Table 2.

To improve the quality of the flow solution, three mesh adap-

Fig. 6 Run 308 [NASA CD-ROM] comparison between ICE3D and LEWICE after 47.58 and 95.16 s of ice accretion

Table 2 Ambient conditions for the helicopter rotor blade tip simulation

Parameter	Value
T_∞	$-30.5\,^\circ$C
P_∞	456 h Pa
Mach	0.52
AoA	9.5 deg
MVD	20 μm
LWC	1 g/m^3
time	91 s

Fig. 9 2D cuts of the convective heat transfer coefficient, in W/m^2 K

tations cycles were carried out with OptiMesh. The OptiMesh algorithm has an a posteriori error estimate based on the Hessian of the solution (hence proportional to the truncation error) and then uses mesh movement, edge refinement, coarsening, and swapping to automatically yield a nearly-optimal adapted grid. These actions are done throughout the numerical solution and the grid edges migrate where the flow phenomena mandate. OptiMesh has proven to asymptotically get to a unique final grid [26], no matter what the initial grid is like and yields results independent of the code used. The initial mesh has 221,800 nodes and 1,118,131 elements, and the final adapted one has 467,705 nodes and 2,546,857 elements.

The grid convergence index method suggested by Roache [27] for unstructured grid refinement based on the number of nodes is used to get an idea of the accuracy of the pressure coefficient distribution on the wing. Accuracy of the Cp distribution at the four stations defined below is conservatively estimated around 4%. Although this error seems large, it was judged acceptable considering that the goal is to predict ice shape using a one-shot ice accretion, thus neglecting effects of the ice growth on the airflow and droplet solutions.

An equivalent sandgrain roughness was used for the icing calculations and it is obtained using an empirical correlation given in [3], and corresponds to 0.269 mm in this case.

To help result discussion, 2D cuts at four different span wise locations are performed. Each cut corresponds to a plane (x,z), and the cuts are referred to as station 1 (location $y=0.09$ m), station 2 (location $y=0.25$ m), station 3 ($y=0.30$ m), and station 4

($y=0.45$ m). The origin of the coordinate system is at the root of the wing at the leading edge. The y-axis is in the spanwise direction, and the x-axis is the curvilinear distance along the surface in the chord wise direction. Positive values for x-axis are above the plane $y=0$, and negative value below. The chord at the root of the wing, namely 0.586 m, scales the curvilinear distance.

As presented in Fig. 8, the finite blade modeled in this article engenders 3D aerodynamic effects; first, with the creation of a local aerodynamic angle of attack different from the free stream and, second, with the creation of a tip vortex at the blade extremity. Due to a negative twist angle, a separation bubble appears in that region. All aerodynamic variables are affected by this flow pattern.

Figure 9 shows the convective heat transfer coefficient for stations 1, 2, 3, and 4. The heat transfer coefficient curves are quite similar along the blade, except close to the tip, station 4, where the vortex induces separation. At this station, the heat transfer coefficient decreases rapidly on the upper side of the wing, before increasing abruptly at the reattachment point. In a separation bubble, heat transfer coefficients are expected to be small.

Collection efficiency distribution. In Fig. 10, the coordinates along the airfoil section corresponding to each station are divided, using the root chord length, to make comparison easier. Keeping in mind that the wing section reduces in size from the root to the
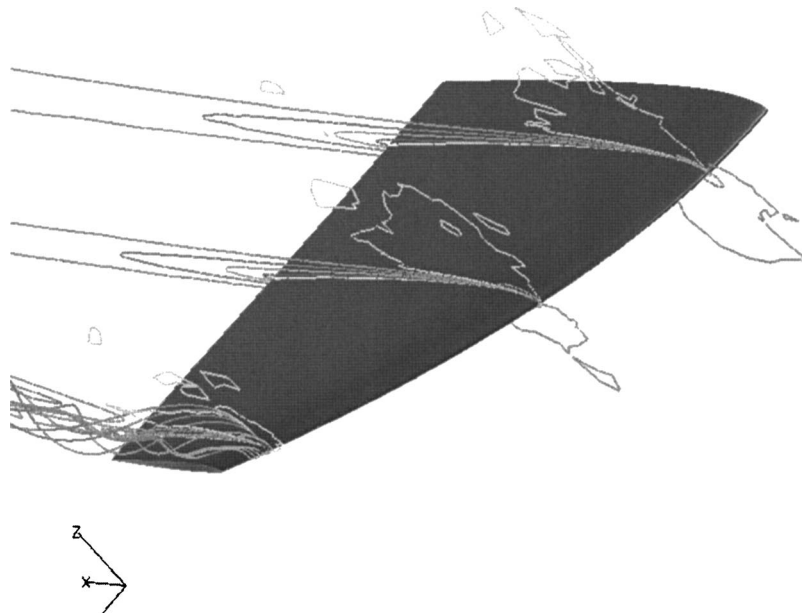
Fig. 8 Turbulent airflow solution, Mach number contours, streamlines at the tip and Cp distribution on the blade

Fig. 10 2D cuts of the collection efficiency for stations 1, 2, 3, and 4 along the curvilinear coordinate

Fig. 12 2D ice cuts along the span wise direction for stations 1, 2, 3, and 4

tip, even if the impingement limits on the lower side are almost constant, they extend further back on the airfoil closer to the tip. On the other hand, the impingement limit on the upper side of the blade decreases from station 1 to station 4. This effect is due to the negative twist angle.

Ice accretion. Once the FENSAP airflow solution and the collection efficiency from DROP3D have been determined, ice accretion can be performed, using ICE3D, on the ada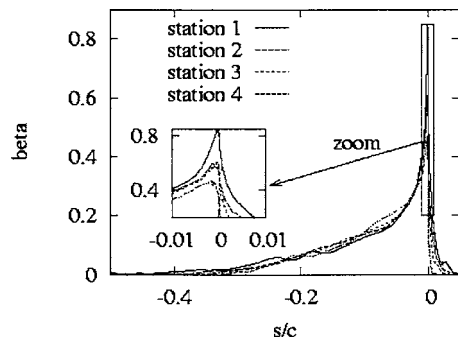pted grid. The 91-s exposure has been simulated in one shot. Figure 11 gives a 3D view of the rime ice accretion at tip.

Two-dimensional cuts of the ice shape corresponding to stations 1, 2, 3, and 4 are plotted in Fig. 12. The global aspect of the ice shape qualitatively agrees with the numerical and experimental results of ONERA [4], keeping in mind that the ONERA results were obtained on a slightly different geometry. The 3D effects are not spectacular, as the geometry does not present strong 3D features and the very cold temperature corresponds to rime ice conditions, making water runback not an important factor. In fact, the ice shape mostly depends on impingement, and this is a good test case to ascertain values calculated by DROP3D.

3D Nonaxisymmetric Nacelle

In this calculation the aim is to predict ice accretion on a 3D nonaxisymmetric Boeing 737-300 [28] nacelle inlet. A complete set of computational and experimental results, made by NASA [29], are available for the airflow solution and the collection efficiency, but not for the ice shapes. Thus, the only thing that one can do is compare ICE3D's predictions to LEWICE's.

The icing calculation process requires three steps: the computation of the airflow, the computation of the droplet solution, and the prediction of the ice shape. Each "step solution" will be compared to the corresponding LEWICE solution and to the experiments, if available.

Two cases were analyzed at a true airspeed of 75 m/s, an inlet mass flow of 10.4 kg/s, a static pressure of 95840 Pa, a droplet Mean Volumetric Diameter of 20.36 μm, and nacelle incidences of 0 deg (run id 092385-1,2,3-737-0 in Ref. [28]) and 15 deg (run id 092385-13,14,15-737-15 in Ref. [28]). 3D rime ice accretion result is shown in Fig. 13 for the 15 deg case.

Tran et al. [30] used OptiMesh and compared Mach number distributions along circumferential cuts, for both incidences. The starting mesh had 108,000 nodes and 624,000 tetrahedra. After two adaptation cycles, the mesh size increased to 152,000 nodes and 824,000 highly anisotropic tetrahedral elements. The calculated Mach number distributions are in good agreement with both experimental and LEWICE results for all circumferential positions, at both incidences. A sample of results, postprocessed to be in the same units of those of Ref. [28], is shown in Figs. 14 and 15.

In order to compute the local catch efficiency β, DROP3D was run for a Langmuir-D droplet distribution. The comparison of local catch efficiency distribution along the same circumferential cuts is presented in the same article [30]. The peak is shown to be within experimental repeatability, estimated to be between 0.20 and 0.25[30]. The results show that, FENSAP-ICE and LEWICE catch efficiency results agree over most of the nacelle. However,

Fig. 11 3D ice shape at blade tip
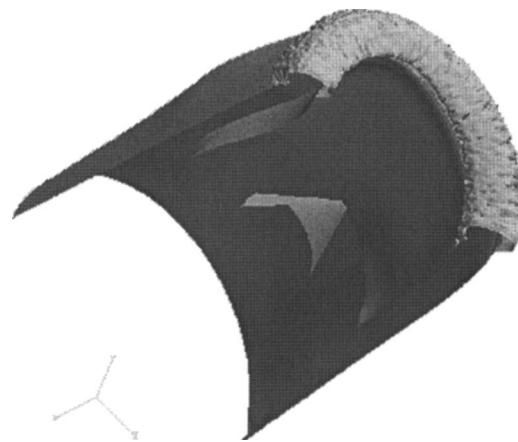
Fig. 13 3D ice accretion on the Boeing 737-300 inlet, rime ice accretion for 15 deg AoA and an inlet mass flow of 10.4 kg/s
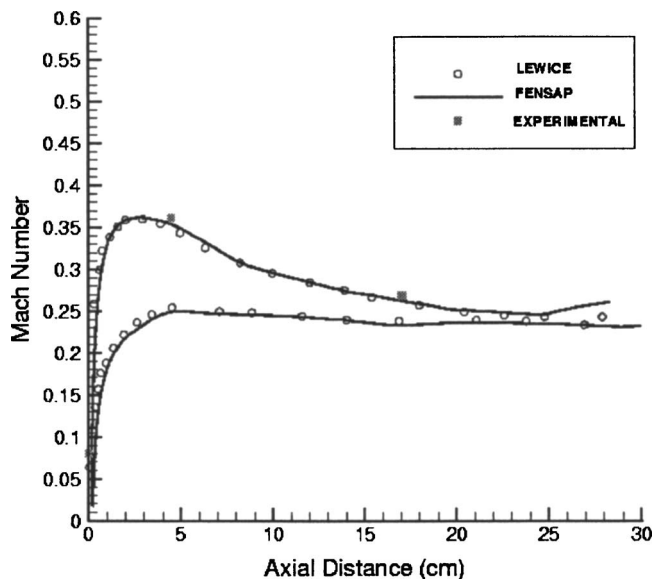
Fig. 14 Mach number distribution for the Boeing 737-300 inlet for 0 deg AoA and an inlet mass flow of 10.4 kg/s, comparison between FENSAP, LEWICE and Experiments, circumferential cut at 45 deg

the impingement limits predicted by FENSAP-ICE are somewhat closer to the experimental values, as it uses a computational fluid dynamics (field) approach that has no difficulties near boundaries. Figures 16 and 17 present selected comparisons between DROP3D, LEWICE, and the experiments.

Two icing conditions were calculated for each incidence of the Boeing 737-300 inlet. The conditions were chosen to represent a rime and a glaze ice situation. The rime conditions are the following: an accretion time of 30 min with a LWC of 0.2 g/m^3 and a static temperature of $-29.9°C$. For the mixed or glaze ice conditions, the time of exposure is still 30 min but the LWC is 0.695 g/m^3 and the static temperature is $-9.3°C$.
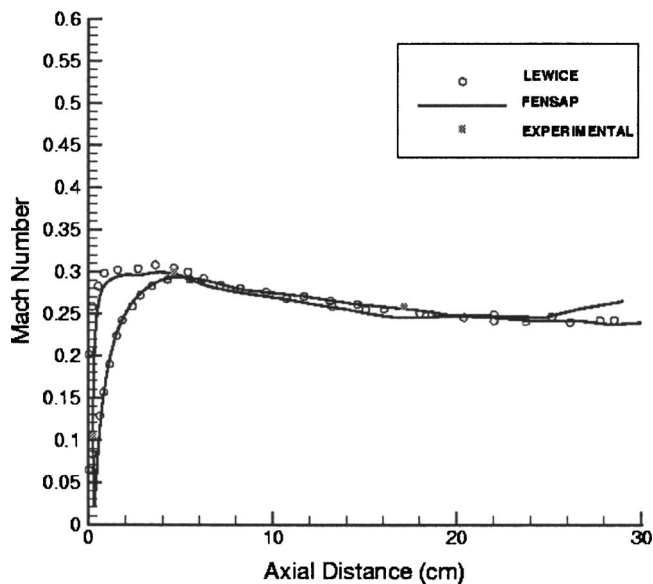
Fig. 15 Mach number distribution for the Boeing 737-300 inlet for 15 deg AoA and an inlet mass flow of 10.4 kg/s, comparison between FENSAP, LEWICE and Experiments, circumferential cut at 45 deg
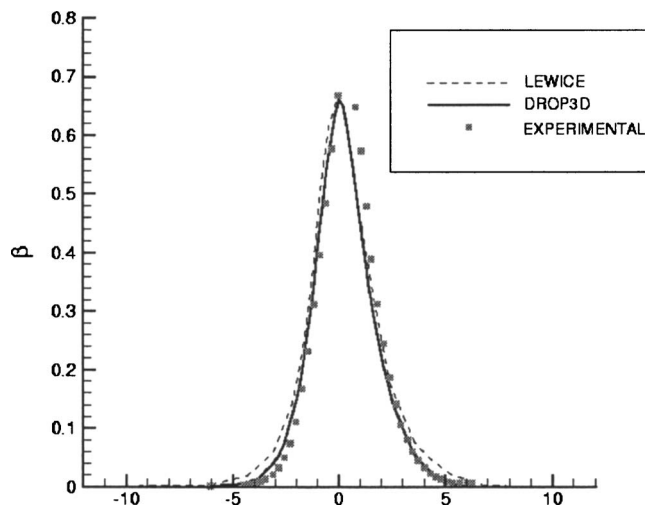
Fig. 16 Local collection efficiency distribution for 0 deg AoA, comparison between DROP3D, LEWICE and Experiments, circumferential cut at 180 deg

In the rime ice case, the comparison between LEWICE and ICE3D is very good for all circumferential positions for both incidences, Figs. 18 and 19.

For the glaze ice condition, the LEWICE and ICE3D predicted ice shapes, Figs. 20 and 21, agree pretty well for all circumferential positions and for both incidences.

Although no experimental data were available, it is comforting that the results obtained by the two codes are in good agreement and look consistent with the conditions for which the shapes were generated and with the airflow and droplet solutions.

Conclusions

A second-generation numerical approach based on partial differential equations has been proposed for calculating all aspects of in-flight icing on complete aircraft. FENSAP-ICE, a code based on the proposed method, has been used to calculate ice shapes on 2D airfoils and 3D aircraft parts. Comparisons against 2D experimental and numerical results available in the literature show that the FENSAP-ICE code gives results as accurate as first generation
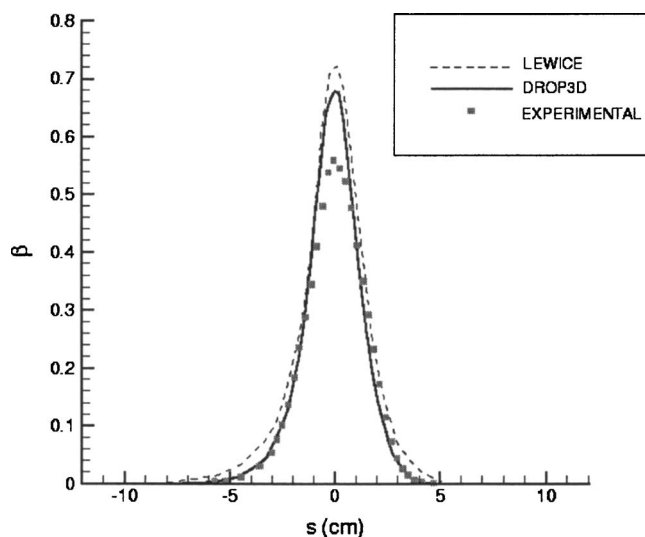
Fig. 17 Local collection efficiency distribution for 15 deg AoA, comparison between DROP3D, LEWICE and Experiments, circumferential cut at 90 deg
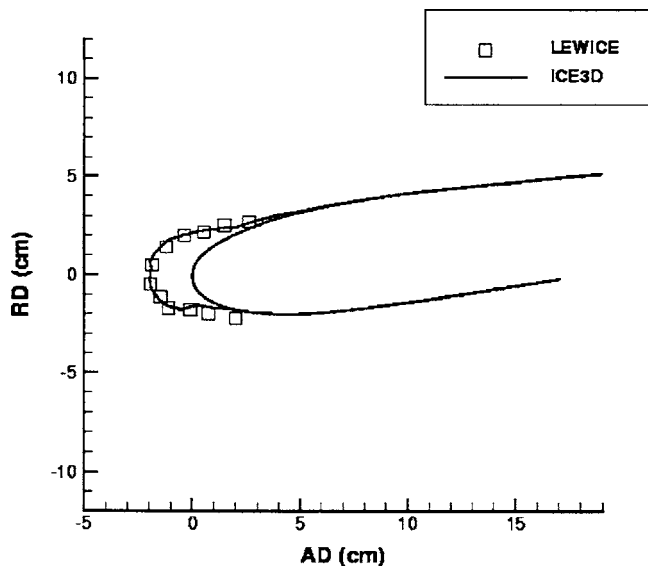
Fig. 18 Rime ice for the Boeing 737-300 inlet for 0 deg AoA, comparison of analytical ice shapes between ICE3D and LEWICE, circumferential cut at 45 deg
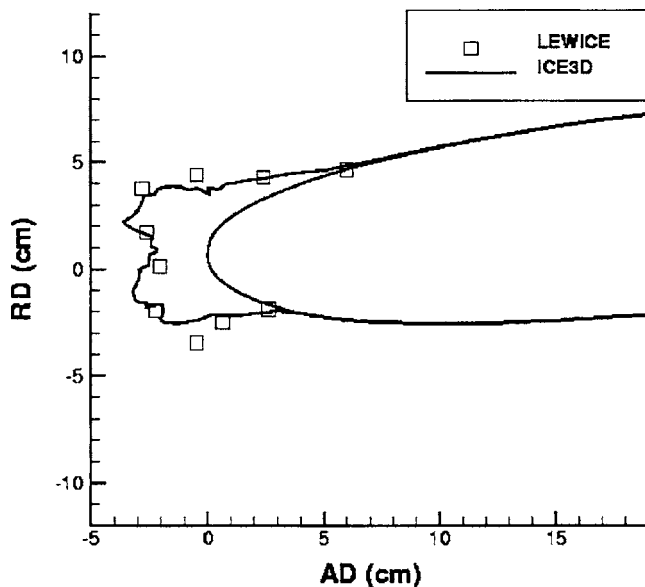
Fig. 20 Glaze ice for the Boeing 737-300 inlet for 0 deg AoA, comparison of analytical ice shapes between ICE3D and LEWICE, circumferential cut at 135 deg

icing codes. Now that the numerical scheme has been shown to work, more tests will have to be carried out in order to test the limits of the physical model used. For example, capability of the turbulence model to predict correctly the separated area behind an ice horn will have to be verified. Also, the effect of the separation area on the growing ice shape is not yet clear. The main strength of the new method compared to first generation icing codes, apart from the 3D ice prediction capability, is the possibility to use advances from other computational fluid dynamic areas where partial differential equations are used.

Apart from the modeling inaccuracies related to the turbulence model on rough surfaces and in separated areas, there are other possible sources of numerical error: mesh related error during solution and error on collection efficiency coefficients due to the lack of updating of the air solution. Using mesh adaptation based on airflow solution and geometry reduces the first error. Tight

coupling between the three modules must be achieved, with thin layers of ice accretion before airflow recalculation, to reduce the second error. Although this article does not show such results, this is currently achieved through the use of an efficient mesh displacement scheme.

Successful 3D calculations around slightly complex geometries have shown the capability of a second-generation computational fluid dynamics-based in-flight icing simulation system. Calculation around a 3D rotor blade tip has shown the capability of the code to calculate the flow field, droplet impingement and ice accretion all on the same mesh. A complete 3D ice accretion prediction on a Boeing 737-300 nacelle, whose flow solution and droplet impingement have already been successfully completed, has also
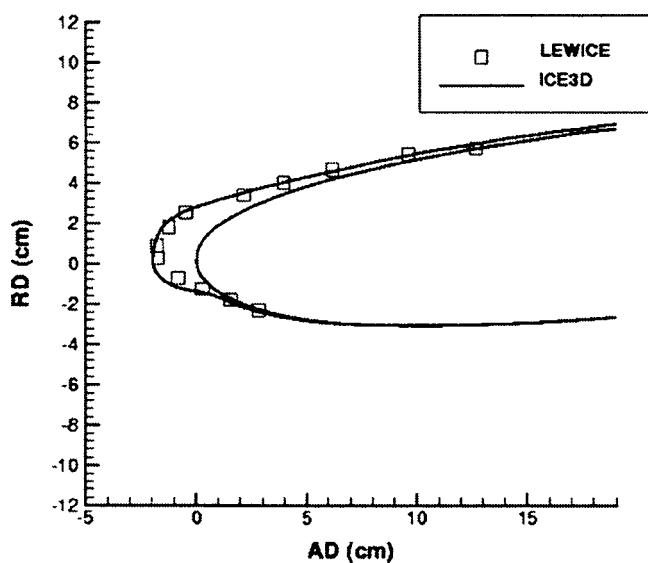
Fig. 19 Rime ice for the Boeing 737-300 inlet for 15 deg AoA, comparison of analytical ice shapes between ICE3D and LEWICE, circumferential cut at 135 deg
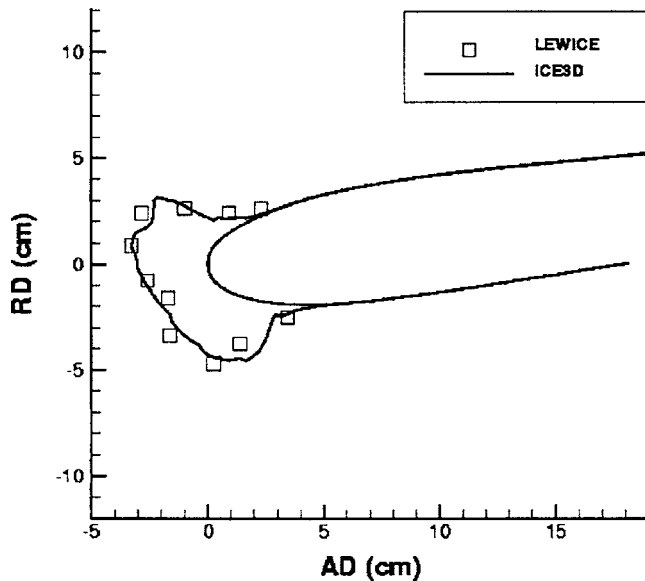
Fig. 21 Glaze ice for the Boeing 737-300 inlet for 15 deg AoA, comparison of analytical ice shapes between ICE3D and LEWICE, circumferential cut at 45 deg

been demonstrated. The code is now being used to tackle even more complex problems such as wing body junctions and high-lift wings.

Nomenclature

Airflow variables

AOA = aerodynamic angle of attack
h = heat transfer coefficient (W/(m^2 K))
L = characteristic length (m)
P_∞ = pressure (Pa)
$\dot{Q}_h$ = convective heat flux (W)
T_∞ = temperature at infinity (K)
$\mathbf{u}_a$ = air velocity (m/s)
U_∞ = velocity at infinity (m/s)
ρ_a = air density (kg/m^3)
μ = laminar dynamic viscosity (N s/m^2)
ν = laminar kinematic viscosity (m^2/s)
τ_{wall} = air wall shear stress tensor (N/m^2)

Droplet variables

d = droplet diameter (m)
Fr = Froude number ($U_\infty/\sqrt{Lg_0}$)
g_0 = magnitude of the gravity vector
g = gravity vector (m/s^2)
K = droplet inertia parameter ($\rho_w d^2 U_\infty/18L\mu_w$)
LWC = liquid water content (g/m^3)
Re_d = droplet Reynolds number ($dU_\infty(\mathbf{u}_a - \mathbf{u}_d)/\nu$)
$\widetilde{T}_{d,\infty}$ = droplets temperature at infinity (°C)
$\mathbf{u}_d$ = droplets velocity (m/s)
α = water volume fraction
β = collection efficiency

Water, ice variables

C_p = pressure coefficient
C_{ice} = specific heat at constant pressure for ice (J/(kg K))
C_w = specific heat at constant pressure for water (J/(kg K))
h_f = film thickness (m)
$\dot{m}_{\text{ice}}$ = instantaneous mass of ice accretion (kg/s)
$\dot{m}_{\text{evap}}$ = instantaneous mass of evaporation (kg/s)
L_{evap} = latent heat of evaporation (J/kg)
L_{fusion} = latent heat of fusion at 0°C (J/kg)
L_{subl} = latent heat of sublimation (J/kg)
T = temperature at wall / air / liquid-water / ice interface (°C)
t = time (s)
$\mathbf{u}_f, \bar{\mathbf{u}}_f$ = film velocity vector and mean film velocity across the thickness (m/s)
ϵ = solid emissivity
σ = Boltzmann constant
μ_w = dynamic viscosity of water (N s/m^2)
ρ_w = water density (kg/m^3)

Geometric variables

s = curvilinear distance from stagnation point
$\mathbf{x} = (x_1, x_2)$ = coordinate along the wall
y = coordinate normal to the wall
X = rotor blade tip chordwise direction
Y = rotor blade tip spanwise direction
Z = normal direction to the plane (X, Y)

References

[1] Messinger, B. L., 1953, "Equilibrium Temperature of an Unheated Icing Surface as a Function of Air Speed," J. Aeronaut. Sci., **20**, pp. 29–42.
[2] MacArthur, C. D., 1983, "Numerical Simulation of Airfoils Ice Accretion," AIAA Paper No. 83-0112.
[3] Ruff, G. A., and Berkowitz, M., 1990, "Users Manual for the NASA Lewis Ice Accretion Prediction Code (LEWICE)," NASA Contractor Report No. 185129.
[4] Hedde, T., and Guffond, D., 1995, "ONERA Three-Dimensional Icing Model," AIAA J., **33**(6), pp. 1038–1045.
[5] Gent, R. W., 1990, "TRAJICE2, A Combined Water Droplet and Ice Accretion Prediction Program for Aerofoil," DRA Technical Report No. TR90054.
[6] Tran, P., Brahimi, M. T., and Paraschivoiu, I., 1994, "Ice Accretion on Aircraft Wings with Thermodynamic Effects," AIAA Paper No. 94-0605.
[7] Bidwell, C., Pinella, D., and Garrison, P., 1999, "Ice Accretion Calculation for a Commercial Transport Using the LEWICE3D, ICEGRID3D and CMARC Programs," AIAA Paper No. 99-0250.
[8] Baruzzi, G. S., Habashi, W. G., Guèvremont, G., and Hafez, M. M., 1995, "A Second Order Finite Element Method for the Solution of the Transonic Euler and Navier-Stokes Equations," Int. J. Numer. Methods Fluids, **20**, pp. 671–693.
[9] Bourgault, Y., Habashi, W. G., Dompierre, J., and Baruzzi, G. S., 1999, "A Finite Element Method Study of Eulerian Droplets Impingement Models," Int. J. Numer. Methods Fluids, **29**, pp. 429–449.
[10] Beaugendre, H., Morency, F., and Habashi, W. G., 2003, "FENSAP-ICE's Three-Dimensional In-flight Ice Accretion Module," J. Aircr., **40**(2), pp. 239–247.
[11] Croce, G., Beaugendre, H., and Habashi, W. G., 2002, "CHT3D: FENSAP-ICE Conjugate Heat Transfer Computations with Droplet Impingement and Runback Effects," AIAA Paper No. 2002-0386.
[12] Spalart, Ph. R., and Allmaras, S. R., 1992, "A One-Equation Turbulence Model for Aerodynamic Flows," AIAA Paper No. 92-0439.
[13] Spalart, P. R., 2000, "Trends in Turbulence Treatments," AIAA Paper No. 2000-2306.
[14] Beaugendre, H., Morency, F., and Habashi, W. G., 2003, "Roughness Implementation in FENSAP-ICE: Model Calibration and Influence on Ice Shapes," J. Aircr., **40**, pp. 1212–1215.
[15] Beaugendre, H., 2003, "A PDE-Based 3D Approach for In-Flight Ice Accretion," Ph.D. dissertation, McGill University, Montreal, QC, Canada.
[16] Habashi, W. G., Dompierre, J., Bourgault, Y., Fortin, M., and Vallet, M. -G., 1998, "Certifiable Computational Fluid Dynamics Through Mesh Optimization," Special Issue on Credible Computational Fluid Dynamics Simulation, AIAA J., **36**(5), pp. 703–711.
[17] Gresho, P. M., Lee, R. L., Sani, R. L., Maslanik, M. K., and Eaton, B. E., 1987, "The Consistent Galerkin FEM for Computing Derived Boundary Quantities in Thermal and/or Fluid Problems," Int. J. Numer. Methods Fluids, **7**, pp. 371–394.
[18] Jackson, R., 2000, *The Dynamics of Fluidized Particles*, Cambridge University Press, Cambridge, Chap. 2.
[19] Hughes, T. J. R., and Brooks, A., 1982, "A Theoretical Framework for Petrov-Galerkin Methods with Discontinuous Weighting Functions: Application to the Streamline-Upwind Procedure," *Finite Element in Fluids*, Gallagher, R. H., Norrie, D. H., Oden, J. T., and Zienckiewicz, O. C., eds., Wiley, New York, Vol. 4, Chap. 3.
[20] Bourgault, Y., Beaugendre, H., and Habashi, W. G., 2000, "Development of a Shallow Water Icing Model in FENSAP-ICE," J. Aircr., **37**, pp. 640–646.
[21] Kays, W. M., and Crawford, B. M., 1993, *Convective Heat and Mass Transfer*, 3rd ed., McGraw-Hill, New York.
[22] Wright, W. B., and Rutkowski, A., 1999, "Validation Results for LEWICE 2.0" and CD-ROM.
[23] SAE Aerospace Recommended Practices, 2003, "Droplet Impingement and Ice Accretion Computer Codes," ARP5903.
[24] Kind, R. J., "Ice Accretion Simulation Evaluation Test," NATO RTO Technical Report No. 38, RTO-TR-038, France, November, 2001.
[25] Lepage, C. Y., Suerich-Gulick, F., and Habashi, W. G., 2002, "Anisotropic 3D Mesh Adaptation on Unstructured Hybrid Meshes," AIAA Paper No. 2002-0859.
[26] Dompierre, J., Vallet, M. -G., Bourgault, Y., Fortin, M., and Habashi, W. G., 2002, "Anisotropic Mesh Adaptation: Towards User-Independent, Mesh-Independent and Solver-Independent CFD Solutions: Part III: Unstructured Meshes," Int. J. Numer. Methods Fluids, **39**, pp. 675–702.
[27] Roache, P. J., 1998, *Verification and Validation in Computational Science and Engineering*, Hermosa, Albuquerque, New Mexico, Chap. 5.
[28] Papadakis, M., Elangonan, R., Freund, G. A., Breer, J. M., Zumwalt, G. W., and Whitmer, L., 1989, "An Experimental Method for Measuring Water Droplet Impingement Efficiency on Two- and Three-Dimensional Bodies," NASA CR-4257, DOT/FAA/CT-87/22.
[29] Bidwell, C. S., 1996, "Collection Efficiency and Ice Accretion Calculations for a Boeing 737-300 Inlet," SAE Paper No. 965570.
[30] Tran, P., Benquet, P., Baruzzi, G., and Habashi, W. G., 2002, "Design of Ice Protection Systems and Icing Certification Through Cost-Effective Use of CFD," AIAA Paper No. 2002-0382.

The Periodical Shear Environment of a Cone-and-Plate Bioreactor

C. A. Chung[1]

C. S. Weng

M. Z. Tu

Department of Mechanical Engineering,
National Central University,
Jhongli 320, Taiwan, R.O.C.

We investigate theoretically the periodic shear environment of a cone-and-plate bioreactor. The imposed frequency is designated to reflect the periodic nature of mammalian cardiac cycles. The working formula obtained for the distribution of shear stresses shall be of substantial interest for applying periodic shear stresses to cell cultures in vitro. [DOI: 10.1115/1.2170127]

Introduction

With rapidly progressing technologies, the future of tissue engineering shall be quite bright. Researchers have discovered that tissue functions may be enhanced through appropriate mechanical stimulation [1,2]. Therefore tissue engineers are keen to find suitable ways to apply pressure forces, stresses, or strains to cell cultures so as to improve the quality of tissue repair. Such a goal may be achieved by the use of bioreactors, devices that are designed to provide certain nutrients and/or required stimuli to enhance the growth of engineered tissues. Focusing on the stimuli of shear stresses, cone-and-plate bioreactors have been used virtually as a standard test apparatus. Such a geometry has been operated under steady conditions for testing the effects of shear forces in vitro, considering, for example, the antiapoptotic gene responses of endothelial cells [3]. It has also been used for checking the interactions between biochemical actions and shear loadings, such as the cross talk between the production of prostacyclin and nitric oxide in smooth muscle cells [4]. Moreover, bioengineers have been trying to extend its usage to apply unsteady shear forces, investigating, for example, the effects of pulsatile shear stresses on the calcium transients in endothelial monolayers [5].

The earliest report on the use of a cone-and-plate geometry may be traced back to Mooney and Ewart [6], who introduced it as a viscometer. The cone-and-plate geometry has the advantage of virtually uniform stress throughout the test region before the onset of secondary flow, which may be induced by increasing the rotation speed. The occurrence of secondary flow makes the stress field difficult to define. Commercial viscometers typically have a small gap angle about 1 deg and a radius of only 2–3 cm so that secondary flow can be reduced for the operation of measuring fluid viscosity. Cox [7] observed secondary flow phenomenon by using a dye-visualization technique. Pelech and Shapiro [8] clearly identified the governing parameter of secondary flow being the Reynolds number, which represents the relative magnitude of the centrifugal force to viscous force. Walters and Waters [9] analyzed the flow using an asymptotic expansion method based on assuming the Reynolds number is small. Cheng [10] measured the torque and found the results agreed well with the previous work. Fewell and Hellums [11] conducted a thorough numerical analysis using a finite difference method. Turian [12] neglecting the wall effects described secondary flow using an expansion method. Heuser and Krause [13] following Turian considered the wall effects assuming the boundary to be a spherical shape adjacent to the air.

As far as the unsteady problem is concerned, a Weissenberg rheogoniometer operates the unsteady cone-and-plate flow [14], for which the cone is oscillating with respect to the plate. Both secondary flow and wall effects are ignored for the unsteady operation because secondary flow or turbulence is regarded as a source of error in rheomeric operations and should be reduced [15]. As for the applications of bioreactors, however, the point is different. A desirable attribute of bioreactors shall be the capability to provide well-defined mechanical stimuli. Primary, secondary, and even turbulent flows occurring in a common device may be all relevant to biometric applications as long as they can be well defined. Sdougos et al. [16] carried out an elaborate analytical and experimental study on the steady-state flow behavior. After that, researchers have adopted their formula to test cellular or gene responses. Chung et al. [17] recently investigated theoretically the oscillatory flow in a cone-and-plate bioreactor. In their analysis, the cone was assumed to rotate in a sinusoidal way with the time average speed equal to zero. The imposed frequency is designated to reflect the mammalian cardiac cycles. As a direct following of their work, this paper extends shear stresses to a periodic state, in which the cone rotates at a steady speed with a sinusoidal oscillation superimposed, so that the shear stress can have nonzero time-mean values. The explicit working formula obtained can be applied to the shear stress distribution in vitro, which shall be of substantial interest to the studies of cellular responses to shear forces.

Problem Formulation

The system considered consists of a rotating cone and a stationary flat plate as shown in Fig. 1, in which the cone rotates at a steady rotational speed with a sinusoidal oscillation superimposed. The dimensional angular speed of the cone is defined as

$$\dot{\theta} = \omega_0 + \Delta\omega \cos(\Omega t^*) \qquad (1)$$

where ω_0 is the average speed, $\Delta\omega$ the amplitude of oscillation, Ω the angular frequency, and t^* the dimensional time. Culture media are aqueous solutions of chemicals and nutrients [18], which are virtually treated as a Newtonian fluid [19]; thus the motion of culture media may be described by the Navier-Stokes (N-S) equations. We nondimensionalize the N-S equations and the boundary conditions with the following scales: The radial coordinate with a reference radius r_0, vertical coordinate with αr_0 (where $\alpha = \tan\theta_0$ is the tangent of the cone angle), both the radial and azimuthal components of velocity with $r_0 \Delta\omega$, the vertical component of velocity with $\alpha r_0 \Delta\omega$, time with Ω^{-1}, pressure with $\rho r_0^2 \Delta\omega^2$ (where ρ is the fluid density). The dimensionless N-S equations in the cylindrical coordinates have the form

$$\frac{1}{r}\frac{\partial}{\partial r}(ru) + \frac{\partial w}{\partial z} = 0 \qquad (2)$$
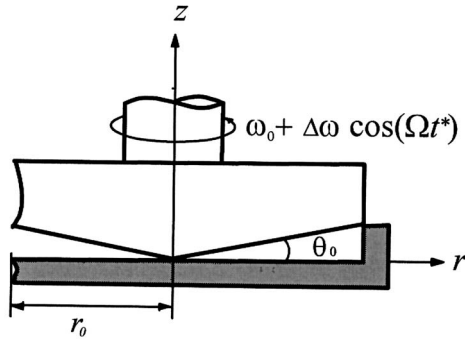
Fig. 1 Schematic diagram of the cone-and-plate bioreactor. The cone rotates in a periodic way with an angular speed defined as $\omega_0 + \Delta\omega \cos(\Omega t^*)$.

$$\delta\frac{\partial u}{\partial t} + \varepsilon\left(u\frac{\partial u}{\partial r} - \frac{v^2}{r} + w\frac{\partial u}{\partial z}\right) = \alpha^2\frac{\partial}{\partial r}\left(\frac{1}{r}\frac{\partial}{\partial r}(ru)\right) + \frac{\partial^2 u}{\partial z^2} - \varepsilon\frac{\partial p}{\partial r}$$

$$(3a)$$

$$\delta\frac{\partial v}{\partial t} + \varepsilon\left(u\frac{\partial v}{\partial r} + \frac{uv}{r} + w\frac{\partial v}{\partial z}\right) = \alpha^2\frac{\partial}{\partial r}\left(\frac{1}{r}\frac{\partial}{\partial r}(rv)\right) + \frac{\partial^2 v}{\partial z^2} \quad (3b)$$

$$\delta\frac{\partial w}{\partial t} + \varepsilon\left(u\frac{\partial w}{\partial r} + w\frac{\partial w}{\partial z}\right) = \alpha^2\frac{1}{r}\frac{\partial}{\partial r}\left(r\frac{\partial w}{\partial r}\right) + \frac{\partial^2 w}{\partial z^2} - \Gamma\frac{\partial p}{\partial z} \quad (3c)$$

Here u, v, and w are the radial, azimuthal, and vertical components of velocity, and t, r, and z are the time, radial, and vertical variables, which are all dimensionless. The assumption of rotational symmetry about the cone axis, i.e., $\partial/\partial\theta = 0$, has been made. The associated boundary conditions are the no-slip conditions on both the cone and plate surfaces and at the device periphery, which, respectively, are

$$z = r, \quad u = w = 0, \quad v = r(\omega + \cos t) \quad (4)$$

$$z = 0, \quad u = v = w = 0 \quad (5)$$

$$r = 1, \quad u = v = w = 0 \quad (6)$$

For the present the reference length r_0 is set to be the rim radius so the device edge is located at $r=1$ as indicated in Eq. (6). The dimensionless parameters appearing in these equations are

$$\delta = \frac{\alpha^2 r_0^2 \Omega}{\nu} \quad (7a)$$

$$\varepsilon = \frac{\alpha^2 r_0^2 \Delta\omega}{\nu} \quad (7b)$$

$$\text{and } \Gamma = \frac{\varepsilon}{\alpha^2} \quad (7c)$$

where ν is the kinematic viscosity of the culture media, δ is the square of the Womersley number representing the ratio of the unsteady inertia force to viscous force, and ε the Reynolds number representing the ratio of the centrifugal force to viscous force.

Primary Flow

As has been shown, most of the biometric applications are concerned with small α, δ, and ε [17], we therefore solved the problem by expanding the flow variables into an asymptotic expansion in the powers of ε

$$\varphi = \varphi_0 + \varepsilon\varphi_1 + \varepsilon^2\varphi_2 + \cdots \quad (8)$$

where $\varphi = u, v, w, p$. Substituting Eq. (8) into Eqs. (2) and (3), and boundary conditions (4)–(6), and collecting coefficients according to the powers of ε, we obtain the perturbation equations for various powers of ε. These equations can be solved order by order. The solution of $O(\varepsilon^0)$ has the form

$$u_0 = w_0 = \partial p_0/\partial z = 0 \quad (9)$$

The remaining nonzero solution is the θ component of velocity v_0. Such a solution reveals the fact that the system can have a simple solution called *primary flow* in the limit of small ε, for which the streamlines are concentric circles and the radial and vertical velocity components are both zero. The azimuthal velocity v_0 is solved using a matched asymptotic expansion method by further expanding the θ-momentunm equation in terms of α. It is too tedious to show all the solution procedures in detail, therefore only solutions are shown in the following.

Considering the gap angle to be small, i.e., $\alpha \ll 1$, v_0 is expressed, using an asymptotic match, as a combination of inner, outer, and matched solutions [20]

$$v_0 = v_{\text{in}} + V_{\text{bl}} - v_{\text{match}} \quad (10)$$

We seek v_{in}, the inner solution in the interior region that is away from the device periphery $r=1$, by further expressing it as a perturbation series in powers of α^2

$$v_{\text{in}} = v_{\text{in}0} + \alpha^2 v_{\text{in}2} + \cdots, \quad \alpha \to 0. \quad (11)$$

The zeroth-order solution $v_{\text{in}0}$ has the form

$$v_{\text{in}0} = z\omega + v_{\text{in}0c}\cos t - v_{\text{in}0s}\sin t, \quad (12)$$

where

$$v_{\text{in}0c} = \frac{r\{\cosh\lambda(z+r)\cos\lambda(z-r) - \cosh\lambda(z-r)\cos\lambda(z+r)\}}{\cosh(2\lambda r) - \cos(2\lambda r)}$$

$$(13a)$$

$$v_{\text{in}0s} = \frac{r\{\sinh\lambda(z+r)\sin\lambda(z-r) - \sinh\lambda(z-r)\sin\lambda(z+r)\}}{\cosh(2\lambda r) - \cos(2\lambda r)}$$

$$(13b)$$

$$\lambda = \sqrt{\delta/2}. \quad (13c)$$

It can be shown that $v_{\text{in}0c} \to z$ and $v_{\text{in}0s} \to 0$ as $\delta \to 0$, reducing to the solution for a quasisteady state. The interior solution (12) cannot satisfy the boundary condition at the device rim $r=1$, indicating that there is a boundary layer adjacent to the periphery. The boundary-layer solution $V_{\text{bl}}(R, z, t)$, where the boundary-layer variable has the form $R = (1-r)/\alpha$, can be expressed as a perturbation series in the powers of α

$$V_{\text{bl}} = V_{\text{bl}0} + \alpha V_{\text{bl}1} + \alpha^2 V_{\text{bl}2} + \cdots \quad (14)$$

We solve the boundary-layer solution of $O(\alpha^0)$ using the method of eigenfunction expansion, which gives

$$v_{\text{bl}0}(r,z,t) = z\omega + \sum_{n=1}^{\infty}\frac{2\omega(-1)^n}{n\pi}e^{-n\pi R}\sin(n\pi z)$$

$$+ \left[z + \sum_{n=1}^{\infty}R_{nr}\sin(n\pi z)\right]\cos(t)$$

$$- \sum_{n=1}^{\infty}R_{ni}\sin(n\pi z)\sin(t) \quad (15)$$

where

Journal of Fluids Engineering

$$R_{nr} = \frac{2(-1)^n}{(n\pi)^4 + \delta^2}\left\{\frac{\delta^2}{n\pi} + n\pi e^{-\lambda_{nr}R}[(n\pi)^2\cos(\lambda_{ni}R) - \delta\sin(\lambda_{ni}R)]\right\}$$

$$(16a)$$

$$R_{ni} = \frac{2(-1)^n n\pi}{(n\pi)^4 + \delta^2}\{\delta - e^{-\lambda_{nr}R}[(n\pi)^2\sin(\lambda_{ni}R) + \delta\cos(\lambda_{ni}R)]\}$$

$$(16b)$$

$$\lambda_{nr} = \Delta_n \cos\theta_n \qquad (16c)$$

$$\lambda_{ni} = \Delta_n \sin\theta_n \qquad (16d)$$

$$\Delta_n = \sqrt[4]{(n\pi)^4 + \delta^2} \qquad (16e)$$

$$\theta_n = \frac{1}{2}\tan^{-1}\left(\frac{\delta}{(n\pi)^2}\right) \qquad (16f)$$

Having had the outer and inner solutions, we can construct the solution of v_0. In Eq. (10), v_{match} is the match solution in the overlap region, i.e., $v_{\text{match}} = v_{\text{in}}(r \to 1) = V_{\text{bl}}(R \to \infty)$. The uniform approximation of v_0 accurate to the leading order has the form

$$v_0 \approx v_{\text{in}0} + V_{\text{bl}0} - v_{\text{in}0}(1,z,t) \qquad (17)$$

where $v_{\text{in}0}(1,z,t)$ is obtained by setting $r=1$ in Eq. (12). Proceeding to higher-order calculations is much more difficult due to the increasing mathematical complexity. Therefore we stop at $O(\alpha^0)$, and perform a numerical simulation solving v_0 using a finite difference method with an alternating direction implicit (ADI) scheme to check the validity of Eq. (17).

We demonstrate in Fig. 2 the primary flow v_0 by showing the contours of the velocity magnitude $|v|$. The parametric values used here are $\alpha=0.05$, $\delta=5$, and $\omega=\omega_0/\Delta\omega=0.5$ corresponding to the case of $\theta_0=3$ deg, $\Omega=200$ rpm, and the reference length is the rim radius of $r_0=1$ cm. Two dimensionless temporal points are presented: (a) $t=\pi/2$ and (b) $t=3\pi/2$. Owing to the nondimensionalization, the cone space has been transformed into a triangle with both the oblique angles equal to 45 deg. It is found that the analytical solution of Eq. (17) and the numerical results are virtually coincident in this figure, indicating that the $O(\alpha^0)$ solution predict quite well provided the cone angle is remaining small. Here the square of the Womersley number is set to be $\delta=5$ to stress the effects of pulsatility. The cone speed is decelerating at $t=\pi/2$ while accelerating at $t=3\pi/2$. The velocity contours in Figs. 2(a) and 2(b) both have the same maximum value of 0.5 located at the rim of the cone but the flow situation is quite different. In the accelerating phase of Fig. 2(b), the majority of fluid has been circulating into the paper, while the fluid in the lower right corner remains flowing out of the paper. The fluid flow always lags the cone motion, and the most pronounced lag happens at the lower rim corner. Therefore the quasistatic estimation predicting a uniform velocity distribution in the radial direction will fail when frequency Ω becomes large. This is revealed more clearly in Fig. 3, in which the shear stress is no longer approximate to a uniform distribution in the radial direction for $\delta=5$. Moreover we see the boundary layer structure adjacent to the device periphery, in which the velocity contours change dramatically to zero. The thickness of the boundary layer as predicted by the theoretical analysis is on the order of α, which is 0.05 in this computational case.

Secondary Flow

We have shown the boundary layer effect is confined in a thin area next to the device periphery. Since cell cultures are placed on the plate not close to the plate edge, we focus on the interior fluid region away from the $r=1$ boundary hereafter to investigate the secondary flow effects. Mathematically, this is done by setting $\alpha=0$ in the equations to ignore the rim effects. On considering the
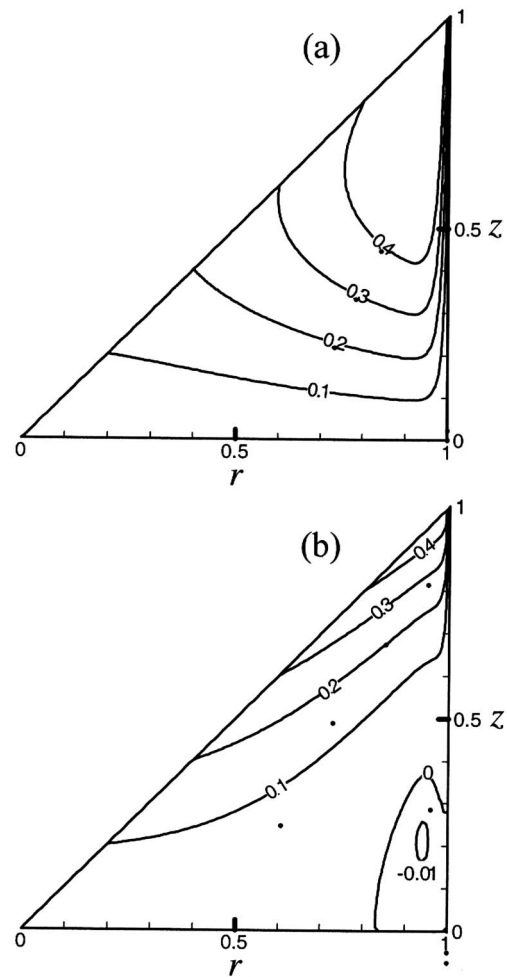
Fig. 2 **The contours of velocity amplitude of primary flow for $\alpha=0.05$, $\delta=5$, and $\omega=\omega_0/\Delta\omega=0.5$. Two temporal points are presented: (a) $t=\pi/2$ and (b) $t=3\pi/2$. The analytical (Eq. (17)) and numerical solutions coincide in the figure.**

value of δ to be practically small, we further expanded the flow variables in the powers of δ. The resulting double series expansions are of the form

$$\varphi = (\varphi_{00} + \delta\varphi_{01} + \delta^2\varphi_{02} + \delta^3\varphi_{03} + \cdots) + \varepsilon(\varphi_{10} + \delta\varphi_{11} + \delta^2\varphi_{12}$$
$$+ \delta^3\varphi_{13} + \cdots) + \varepsilon^2(\varphi_{20} + \delta\varphi_{21} + \cdots) + O(\varepsilon^3) \qquad (18)$$

where $\varphi = u, v, w, p$. Substituting Eq. (18) into Eqs. (2)–(5) and equating the coefficients of like $\varepsilon^m\delta^n$, we obtain the corresponding perturbation equations. We use the symbolic computation tool MATHEMATICA to help solve these perturbation equations order by order. To save space, we present only the results of relevant biometric importance in the following. Since the boundary layer has been ignored, the length scale r_0 can be taken as a local radius by neglecting the effect of periphery; both the Reynolds number and Womersley number can be viewed as a local parameter. Therefore the solution at the dimensionless location $r=1$ can be regarded as a representative of the interior flow field.

The $O(\varepsilon^0\delta^n)$ solutions, which present the primary flow, are exactly the Taylor series expansion of solution (12) about $\delta=0$. By comparing the $O(\varepsilon^0\delta^n)$ solution with the solution given in Eq. (12) that is not an expansion with respect to δ, we found the $O(\varepsilon^0\delta^n)$ solution can have relative error less than 10% provided $\delta<5$. This reveals that the expansions in the powers of δ are likely to have a fast convergence. The $O(\varepsilon\delta^n)$ solution in the

Fig. 3 The primary shear stresses on the plate surface for ω =0.5, α=0.05, and δ=1, 5 respectively, at four sequential instants t=0, $\pi/2$, π, and $3\pi/2$, show that the shear stress is not uniformly distributed in the radial direction when δ becomes large

inner region has the following representative form which appears with time-dependent functions $\cos(2t)$ and $\sin(2t)$:
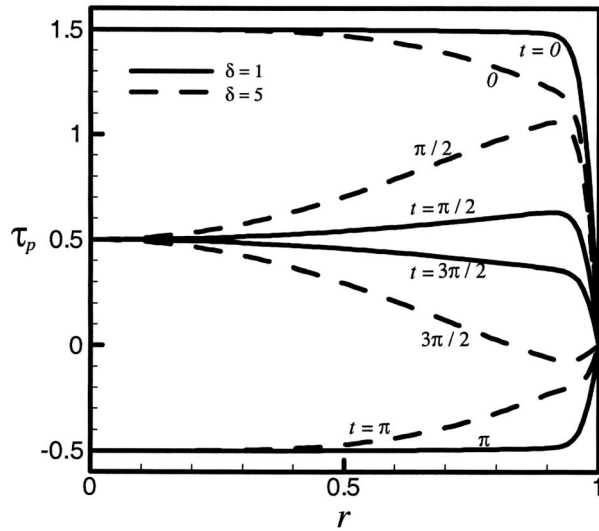
$$u_1|_{r=1} = (1 + 2\omega^2)U_{10} + \delta^2 U_{12} + (4U_{10} + \delta^2 U_{12c})\omega \cos t + (2\delta U_{11s}$$
$$+ \delta^3 U_{13s})\omega \sin t + (U_{10} + \delta^2 U_{12c2})\cos 2t + (\delta U_{11s}$$
$$+ \delta^3 U_{13s2})\sin 2t \tag{19}$$

$$v_1|_{r=1} = 0 \tag{20}$$

$$w_1|_{r=1} = W_{10}(1 + 2\omega^2) + \delta^2 W_{12} + (4W_{10} + \delta^2 W_{12c})\omega \cos t$$
$$+ (2\delta W_{11s} + \delta^3 W_{13s})\omega \sin t + (W_{10} + \delta^2 W_{12c2})\cos 2t$$
$$+ (\delta W_{11s} + \delta^3 W_{13s2})\sin 2t. \tag{21}$$

The flow at this order appears to have only the radial and vertical motion, which is termed *secondary flow*. Obviously, the Reynolds number ε controls the onset of secondary flow, which means that the fluid will be pushed toward the periphery once the centrifugal force becomes large enough. The $O(\varepsilon^2 \delta^n)$ solution provides corrections to all velocity components in three directions, giving the time dependence of $\cos(3t)$ and $\sin(3t)$ to the azimuthal velocity

$$u_2|_{r=1} = U_{20}(1 + 2\omega^2 + 4\omega \cos t + \cos 2t) + \delta(U_{21}\omega \sin t$$
$$+ U_{21s}\sin 2t) \tag{22}$$

$$v_2|_{r=1} = V_{20}(6\omega + 4\omega^3 + 3\cos t + 12\omega^2 \cos t + 6\omega \cos 2t + \cos 3t)$$
$$+ \delta V_{21}(\sin t + 4\omega^2 \sin t + 4\omega \sin 2t + \sin 3t), \tag{23}$$

$$w_2|_{r=1} = W_{20}(1 + 2\omega^2 + 4\omega \cos t + \cos 2t) + \delta(W_{21}\omega \sin t$$
$$+ W_{21s}\sin 2t). \tag{24}$$

Figure 4 shows the feature of the $O(\varepsilon\delta^n)$ solution, i.e., the secondary flow. We display only the first two largest coefficients of velocity in Eqs. (19) and (20). The coefficients of the radial velocity shown in Fig. 4(a) have positive values in the upper region and negative in the lower region, indicating that the fluid near the cone is driven outward by the centrifugal force, and pushed inward near the plate by pressure force, forming a counter clockwise circulation in the r-z plane. Consistent with this circulating flow direction, the fluid in the interior region flows upward
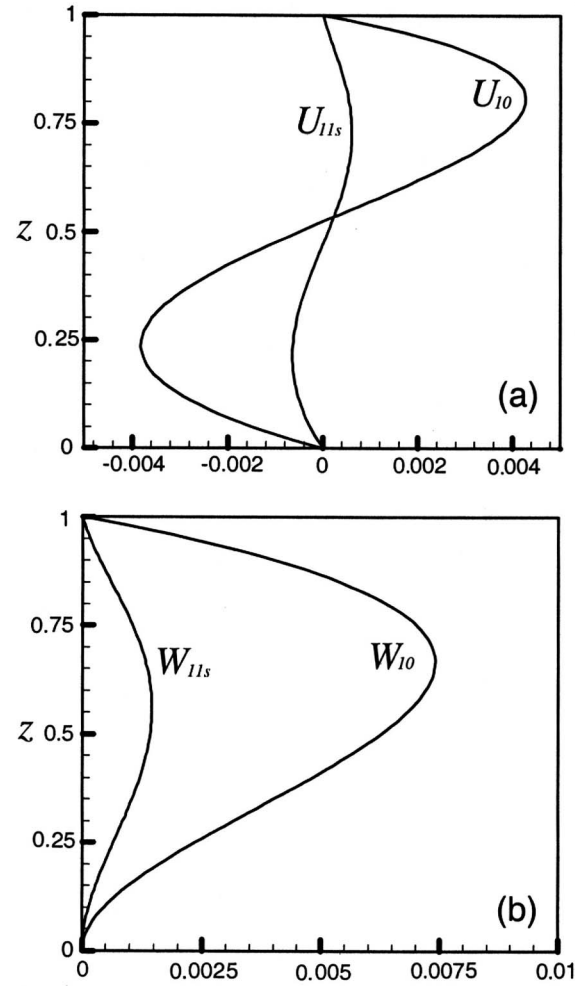
Fig. 4 The coefficients of secondary flow for (a) the radial velocity, and (b) the vertical velocity. Only the first two largest coefficients are shown. The other coefficients in Eqs. (19) and (21) are virtually one order smaller in value.

as displayed in Fig. 4(b) where the vertical velocity coefficients are positive. The velocity coefficients of $O(\varepsilon^2 \delta^n)$ are virtually one order smaller than those of $O(\varepsilon\delta^n)$, indicating the expansion solution will converge also fairly fast with respect to ε. It has been shown in the literature [16] that an expansion solution in the powers of ε could match experimental data till ε=6 (in our notation) if the cone is rotated in a steady state.

Shear Stress on the Plate Surface

The shear stresses on the plate surface are of most biometric interest as the cells are placed on the plate. Based on the azimuthal and radial velocity components we have obtained, the dimensional azimuthal and radial shear stresses acting on the plate surface can be expressed respectively by the two equations

$$\tau_{z\theta}^* = (\mu\Delta\omega/\alpha)\tau_{z\theta} \tag{25}$$

$$\tau_{zr}^* = (\mu\Delta\omega/\alpha)\tau_{zr} \tag{26}$$

where the dimensionless azimuthal stress has the form

$$\tau_{z\theta} = \left.\frac{\partial v}{\partial z}\right|_{z=0,r=1} = \tau_{\theta c0} + \tau_{\theta c1}\cos t + \tau_{\theta s1}\sin t + \omega[\tau_{\theta c2}\cos(2t)$$
$$+ \tau_{\theta s2}\sin(2t)] + \tau_{\theta c3}\cos(3t) + \tau_{\theta s3}\sin(3t) \tag{27}$$

and the dimensionless radial stress has the form

$$\tau_{zr} = \left.\frac{\partial u}{\partial z}\right|_{z=0, r=1} = \tau_{rc0} + \tau_{rc1}\cos(t) + \tau_{rs1}\sin(t) + \tau_{rc2}\cos(2t)$$

$$+ \tau_{rs2}\sin(2t) \qquad (28)$$

The coefficients of the azimuthal shear stress are given by

$$\tau_{\theta c0} = \omega - \varepsilon^2\left(\frac{498\omega + 332\omega^3}{100,800}\right) \qquad (29a)$$

$$\tau_{\theta c1} = 1 - \delta^2\left(\frac{7}{360}\right) - \varepsilon^2\frac{249}{100,800}(1 + 4\omega^2) \qquad (29b)$$

$$\tau_{\theta s1} = \delta\left(\frac{1}{6}\right) - \delta^3\left(\frac{31}{15,120}\right) - \varepsilon^2\delta\frac{289}{567,000}(1 + 4\omega^2) \quad (29c)$$

$$\tau_{\theta c2} = -\varepsilon^2\left(\frac{83}{16,800}\right) \qquad (29d)$$

$$\tau_{\theta s2} = \varepsilon^2\delta\left(\frac{289}{141,750}\right) \qquad (29e)$$

$$\tau_{\theta c3} = \varepsilon^2\left(-\frac{83}{100,800}\right) \qquad (29f)$$

$$\tau_{\theta s3} = \varepsilon^2\delta\left(-\frac{289}{100,800}\right) \qquad (29g)$$

The coefficients of the radial shear stress are

$$\tau_{rc0} = \varepsilon\left(-\frac{1 + 2\omega^2}{30} + \delta^2\frac{1}{4200}\right) + \varepsilon^2\left(\frac{1 + 2\omega^2}{120\Gamma}\right) \qquad (30a)$$

$$\tau_{rc1} = \varepsilon\left(-\frac{4}{30} + \delta^2\frac{23}{21,000}\right) + \varepsilon^2\left(\frac{1}{30\Gamma}\right) \qquad (30b)$$

$$\tau_{rs1} = \varepsilon\left(-\delta\frac{19}{1575} + \delta^3\frac{8263}{436,590,000}\right) - \varepsilon^2\delta\left(\frac{113}{630,00\Gamma}\right)$$

$$(30c)$$

$$\tau_{rc2} = \varepsilon\left(-\frac{1}{30} + \delta^2\frac{3}{3500}\right) + \varepsilon^2\left(\frac{1}{120\Gamma}\right) \qquad (30d)$$

$$\tau_{rs2} = \varepsilon\left(-\delta\frac{19}{3150} + \delta^3\frac{5977}{54,573,750}\right) - \varepsilon^2\left(\delta\frac{97}{126,000\Gamma}\right)$$

$$(30e)$$

To obtain the stress value for a particular location say $r = r_0$, we calculate $\omega = \omega_0/\Delta\omega$, $\delta = \alpha^2 r_0^2\Omega/\nu$, and $\varepsilon = \alpha^2 r_0^2\Delta\omega/\nu$ at $r = r_0$, and substitute them into Eqs. (29) and (30). The working equations for shear distribution are valid in the interior region away from the boundary layer adjacent to the plate edge. By setting $\omega = 0$ for zero mean situations, the equations exactly reduce to Eqs. (35b) and (37b) of [17]. Note that since the cone angle is practically small, the parameter Γ appearing in Eq. (30) has the order of thousands, which makes the expansion solutions converge even faster.

For practical applications, the range of average shear stresses in large arteries is 2–20 dyn/cm^2 with peak values possibly reaching 30–100 dyn/cm^2 at some local regions of disturbed flow [21]. We demonstrate in Fig. 5 the dimensionless shear stresses acting on the plate surface for two cases of $\varepsilon = 1$ and $\varepsilon = 3$, respectively, and with $\omega = 0.5$, $\delta = 1$ fixed. Such parametric values correspond to the real situation of $\alpha = 0.0175$ (the cone angle $\theta_0 = 1$ deg), cells cultured at $r_0 = 1.8$ cm. The rotation amplitude is set to be $\Delta\omega = 100$ rpm and $\Delta\omega = 300$ rpm, respectively. Take $\nu = 0.01$ cm^2/s and $\mu = 0.01$ dyn s/cm^2 then the stress scale $\mu\Delta\omega/\alpha$ is about 6 dyn/cm^2 and 18 dyn/cm^2 for $\varepsilon = 1$ and $\varepsilon = 3$, respectively. The
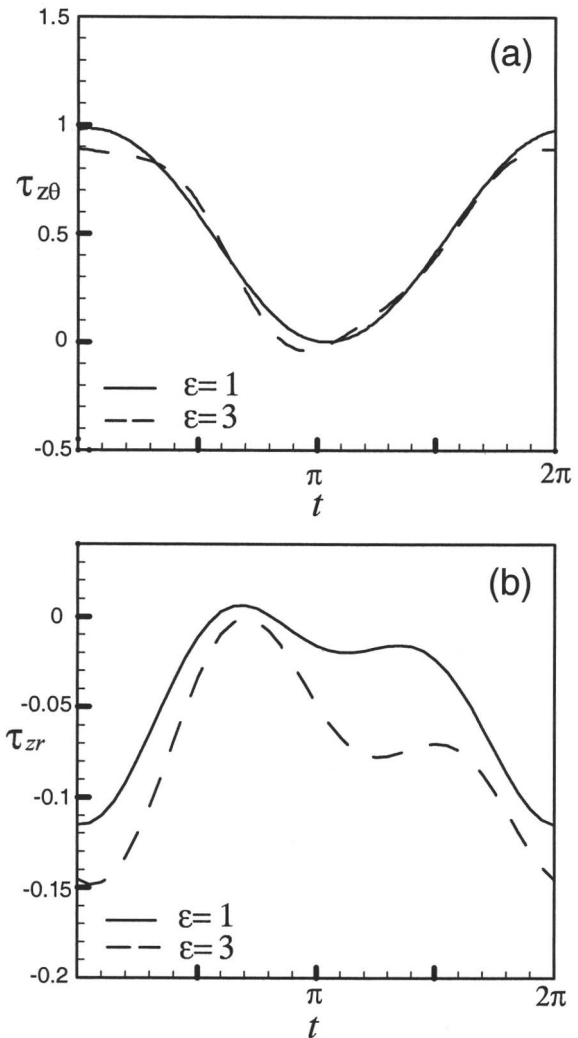
Fig. 5 Dimensionless stresses on the plate surface for $\varepsilon = 1$ (solid lines) and $\varepsilon = 3$ (dashed lines), and $\omega = 0.5$, $\delta = 1$. (a) The primary stress in the azimuthal direction, and (b) the secondary stress in the radial direction.

value of oscillation frequency has been chosen to be $\Omega = 100$ rpm to reflect the cardiovascular cycle scale. In Fig. 5(a), the azimuthal shear at $\varepsilon = 1$ is close to a sinusoidal function of time that can be estimated by a quasisteady approach. As the Reynolds number increases to $\varepsilon = 3$ the shear stress deviates from quasisteady results. The secondary radial shear is displayed in Fig. 5(b). The magnitude of the radial shear is about 10% of the azimuthal stress and the relative magnitude increases with increasing the value of ε.

Conclusions

In this paper, we propose the working equations for subjecting cell cultures to shear stresses in vitro by a cone-and-plate geometry. The periodic shear force is designed to mimic the shear environment induced by the cardiovascular blood flow. The working equations were obtained by expanding the solutions in terms of two parameters: the square of the Womersley number δ and the Reynolds number ε. Though the asymptotic expansions were obtained based on assuming the small values of δ and ε, the resulting solutions are likely to converge well even for δ, $\varepsilon > 1$. We have shown through comparison with primary flow that the expansion solutions in the powers of δ can have relative error less

than 10% provided $\delta < 5$. It was shown by Sdougos et al. [16] that the expansions in the powers of ε for a steady rotation could fit the experimental data well if $\varepsilon < 6$ (in our notation). Because the fitting range of ε in a periodic state is likely to decrease with increasing the average rotational speed, i.e., the parameter ω, we thus conjecture that for the working equations in this paper, the practical ranges of δ and ε should be less than 5. It has also been shown that turbulent transition of steady-state cone-and-plate flow occurred at about $\varepsilon = 48$ [16]. Owing to the effects of oscillation, it is reasonable to speculate that the transitional point for periodic cone-and-plate flow should be lower than $\varepsilon = 48$. The exact transitional state of periodic flow still needs to be determined by experimental investigations. Finally in this paper, the cell thickness has been neglected for developing the macroscopic shear computation. The microscopic departures from a flat boundary due to the presence of endothelial cells will cause a localized perturbation of the macroscopic flow field [22,23]. So far the study of unsteady micro cellular effect is still absent, and shall merit further research efforts in the future.

Acknowledgment

References

[1] Butler, D. L., Goldstein, S. A., and Guilak, F., 2000, "Functional Tissue Engineering: The Role of Biomechanics," J. Biomech. Eng., **122**, pp. 570–575.

[2] Brown, T. D., 2000, "Techniques for Mechanical Stimulation of Cells in vitro: A Review," J. Biomech., **33**, pp. 3–14.

[3] Bartling, B., Tostlebe, H., Darmer, D., Holtz, J., Silber, R.-E., and Morawietz, H., 2000, "Shear Stress-Dependent Expression of Apoptosis-Regulating Genes in Endothelial Cells," Biochem. Biophys. Res. Commun., **278**, pp. 740–746.

[4] Osanai, T., Akutsu, N., Fujita, N., Nakano, T., Takahashi, K., Guan, W., and Okumura, K., 2001, "Cross Talk Between Prostacyclin and Nitric Oxide Under Shear in Smooth Muscle Cell: Role in Monocyte Adhesion," Am. J. Physiol. Heart Circ. Physiol., **281**, pp. H177–H182.

[5] Helmlinger, G., Berk, B. C., and Nerem, R. M., 1995, "Calcium Responses of Endothelial Cell Monolayers Subjected to Pulsatile and Steady Laminar Flow Differ," Am. J. Physiol., **269**, pp. C367–C375.

[6] Mooney, M., and Ewart, R. H., 1934, "The Conicylindrical Viscometer," Physics (N.Y.), **5**, pp. 350–354.

[7] Cox, D. B., 1962, "Radial Flow in the Cone-Plate Viscometer," Nature (London), **193**, p. 670.

[8] Pelech, I., and Shapiro, A. H., 1964, "Flexible Disk Rotating on a Gas Film Next to a Wall," ASME J. Appl. Mech., **31**(57), pp. 7–584.

[9] Walters, K., and Waters, N. D., 1966, "Polymer Systems, Deformation and Flow," *Proc. Brit. Soc. Rheol.*, R. E. Wetton and R. W. Whorlow eds., Macmillan, pp. 211–235.

[10] Cheng, D. C.-H., 1968, "The Effect of Secondary Flow on the Viscosity Measurement Using a Cone-and-Plate Viscometers," Chem. Eng. Sci., **23**, pp. 895–899.

[11] Fewell, M. E., and Hellum, J. D., 1977, "The Secondary Flow of Newtonian Fluids in Cone-and-Plate Viscometers," Trans. Soc. Rheol., **21**, pp. 535–565.

[12] Turian, R. M., 1972, "Perturbation Solution of the Steady Newtonian Flow in the Cone and Plate and Parallel Plate Systems," Ind. Eng. Chem. Fundam., **11**, pp. 361–368.

[13] Heuser, G., and Krause, E., 1979, "The Flow Field of Newtonian Fluids in Cone and Plate Viscometers With Small Gap Angles," Rheol. Acta, **18**, pp. 531–564.

[14] Drasler, W. J., Smith, II C. M., and Keller, K. H., 1987, "Viscoelasticity of Packed Erythrocyte Suspensions Subjected to Low Amplitude Oscillatory Deformation," Biophys. J., **52**, pp. 357–365.

[15] Turian, R. M., 1977, "Oscillatory Motion in the Cone and Plate Perturbation Analysis of Secondary Flow Effects," Ind. Eng. Chem. Fundam., **16**, pp. 348–356.

[16] Sdougos, H. P., Bussolari, S. R., and Dewey, C. F., 1984, "Secondary Flow and Turbulence in a Cone-and-Plate Device," J. Fluid Mech., **138**, pp. 379–404.

[17] Chung, C. A., Tzou, M. R., and Ho, R. W., 2005, "Oscillatory Flow in a Cone-and-Plate Bioreactor," ASME J. Biomech. Eng., **127**, pp. 601–610.

[18] Freshney, R. I., 2000, *Culture of Animal Cells: A Manual of Basic Technique*, 4th ed., Wiley, New York, Chap. 8.

[19] Bussolari, S. R., Dewey, C. F., and Gimbrone, M. A., 1982, "An Aparatus for Subjecting Living Cells to Fluid Shear Stress," Rev. Sci. Instrum., **53**, pp. 1851–1854.

[20] Bender, C. M., and Orszag, S. A., 1999, *Advanced Mathematical Methods for Scientists and Engineers*, Springer, New York, pp. 419–430.

[21] Giddens, D. P., Zarins, C. K., and Glagov, S., 1993, "The Role of Fluid Mechanics in the Localization and Detection of Atherosclerosis," J. Biomech. Eng., **115**, pp. 588–594.

[22] Barbee, K. A., Mundel, T., Lal, R., and Davies, P. F., 1995, "Subcellular Distribution of Shear Stress at the Surface of Flow-aligned and Nonaligned Endothelial Monolayers," Am. J. Physiol., **268**, pp. H1765–H1772.

[23] Yamaguchi, T., Yamamoto, Y., and Liu, H., 2000, "Computational Mechanical Model Studies on the Spontaneous Emergent Morphogenesis of the Cultured Endothelial Cells," J. Biomech., **33**, pp. 115–126.

Optimization of Plasma Spray Processing Parameters for Deposition of Nanostructured Powders for Coating Formation

I. Ahmed
Mechanical Engineering,
Wichita State University
e-mail: ikram.ahmed@wichita.edu

T. L. Bergman
Mechanical Engineering,
The University of Connecticut
e-mail: tberg@engr.uconn.edu

When nanostructured powder particles are used for thermal spray coatings, the retention of the original nanostructure that is engineered into the raw stock is a principal objective, along with production of some molten material in order to adhere the sprayed material to the surface being coated. Therefore, in contrast with spraying conventional powders, complete melting of the nanostructured raw stock is to be avoided. In this study, the melting and resolidification of sprayed material is correlated to a spray processing parameter that has been introduced in the literature by some of the spray processing practitioners. Using computer modeling, processing of zirconia agglomerates with plasma spraying has been simulated. Transition regions for the phase change response of the sprayed material to the thermal processing conditions are identified. The retained nanostructure content and liquid fraction of the sprayed material are correlated to particle diameters, injection velocities, as well as this thermal spray processing parameter. Finally, a novel method to produce desired coatings composed of partially molten material using a bimodal particle size distribution of the sprayed powder is suggested.
[DOI: 10.1115/1.2170131]

Keywords: nanostructured materials, plasma spray, melting and resolidification

Introduction

In thermal spray coating, $10-100~\mu$m diameter powder particles (of ceramics, metallic carbides, or metal mixtures, referred to as precursors) are introduced into a high temperature flame [1,2]. The particles are heated and directed toward the surface being coated (referred to as the substrate), where they are deposited as splats, and eventually form the coating. In high velocity oxygen-fuel flames, temperatures (with stoichiometric combustion) barely reach above the melting point of some of the ceramics used in such coatings (e.g., 2970 K for zirconia), and therefore particle adhesion to the substrate is aided by the conversion of kinetic energies into the enthalpy of melting upon impact (an alternative explanation for particle adhesion, especially when supersonic detonation guns are used, is given in terms of superplastic deformation upon impact). In plasma sprays, gases are heated and ionized by dc arcs or radio frequency inductors inside a torch, which are then discharged through a nozzle. Here the temperatures are much higher than precursor melting points and somewhat easier to control, but the velocities are much lower (~ 300 m/s), and therefore coating adhesion is attained by full or partial melting of the powder particles prior to impact. A significant modification of the conventional plasma spray process has been achieved through the use of *agglomerations* of ~ 100 nm particles to the larger, conventional size range—referred to as nanostructured particles in the relevant literature. Such agglomeration is necessary to avoid "slip," or the non-continuum interaction between the flame and the individual nanosized particles (high Knudsen number effect). Plasma spray coating using nanostructured powder precursors therefore presents a unique thermal manufacturing problem where the objective may be to retain as much of the material in its original, unsintered state as possible (by preserving the "nanosized" entities), and yet maximize the

deposition efficiency (by providing good adhesion, or sufficient molten material). Since the properties of coatings deposited with such powders are strongly dependent on both (1) good adhesion and (2) the amount of nanostructure retained, it is critical that the processing conditions be tailored in a manner to ensure optimal partial melting of the sprayed material. Additional background information regarding thermal plasma spraying of nanostructured material is available elsewhere [3,4].

The important processing conditions in plasma spraying include arc power and nozzle size, gas flow rate and gas composition, powder particle size and feed rate, carrier gas flow rate (for introducing precursor powders into the flame), the location, size, and orientation of the precursor injector, and the torch-to-substrate standoff distance. Further complicating matters is the fact that natural and random variations such as unavoidable fluctuations in the plasma arc, turbulent mixing of the ambient air and the plasma jet, size distributions of the sprayed powder, as well as small variations in their injection velocities can all contribute to the thermal response of the particles and, in turn, the quality of the coating. Specification of the appropriate combination of thermal processing parameters is therefore a complex problem that has been traditionally solved using trial-and-error approaches, although the situation has been significantly improving over recent years due to significant strides made in the areas of measurement and diagnostics, online control, as well as computer simulation [5].

Coating characterization and experimental diagnostics of the plasma spraying operation suggest that the number of processing parameters might be reduced to a few parameters for characterizing and controlling the spraying process. One such parameter has been labeled the critical plasma spraying parameter, or CPSP [6,7]. Based on coating microstructure and properties, this parameter was originally defined simply as the torch power divided by the primary gas flow rate (the torch power input did not take into account torch efficiency). It was observed that CPSP could be an indicator of limited (partial) melting of the powder and retained

Copyright © 2006 by ASME

nanostructure in the coatings [7]. Further experimental observations of plasma temperatures using spectroscopic measurements for various torch powers and gas flow rates showed that a somewhat modified form of CPSP, hereafter referred to as CPSP* $= (\eta_{torch}P_{torch})^{1/4}/Q_{Ar}$ provided the best possible correlation between plasma torch operating conditions and temperature measurements close to the torch exit [6]. Therefore, this parameter is not a dimensionless, universally applicable parameter such as can be deduced in simpler fluid dynamics and heat transfer problems. However, it is recognized as a measure of the "energy density," or the thermal energy content, of the plasma jet. Being based on only three variables (torch power input, torch efficiency, and primary gas flow rate), this parameter may provide a means for reproducing the same "processing conditions" for a wide range of spraying applications as well as spraying hardware. Therefore, by incorporating a number of individual parameters (dc arc voltage and current, primary gas flow rate, or the total gas flow rate and the ratio of primary and secondary gases, as well as torch inner geometry, the latter via torch efficiency, or cooling rate), this single parameter may afford control over coating processes. In the case of nanostructured coatings, especially, the coating characteristics seem to be largely dependent on the ratio of molten to unmolten material in the sprayed powder [7], and the correlation between this ratio and CPSP* is attempted here using computational modeling and simulation.

Recent computer simulations of the thermal spraying process have made it possible to analyze powder heating and acceleration phenomena in plasma sprays to an extent impracticable using other means such as traditional online diagnostics or coating characterization. In such simulations, the degree of particle melting, vaporization, as well as resolidification can be tracked as the powder is injected into (and thereafter propelled by) the plasma flame to the substrate to be coated [8]. By computationally varying the spraying conditions, therefore, the effect of these conditions on the particle state prior to deposition can be predicted in an inexpensive manner, as material and equipment usage can be avoided. However, it is important to realize that such simulations are limited in their applicability by the assumptions made in conjunction with the computational scheme. For example, a 2D axisymmetric calculation will not correctly model the 3D effects of radial powder injection, especially when a high enough powder feed rate is involved that significantly modifies the plasma jet characteristics. A number of recent computational studies therefore have taken this factor into account in order to study particle deposition patterns on the substrate [9,10]; the effect of carrier gas and primary gas flow rates [11], as well as multiple injection ports for powders [12]. Very few of the plasma spray simulations reported in the current literature include plasma chemistry as well as the full 3D effects [13]. In general, 3D calculations cannot include the plasma chemical reactions because of the prohibitive costs involved, in terms of both CPU time and memory requirements.

Here, we study a fully 3D model of a thermal plasma spray system with external, radial injection of nanostructured agglomerates. The states of the sprayed powder particles are tracked as these particles are injected at a fixed location near the plasma torch exit, and the final states are recorded at a fixed stand-off distance. These data are recorded for five different particle sizes, two different plasma gas compositions (argon to hydrogen ratio), three powder injection velocities, and three torch powers levels expected to cover the practicable range. Using the definition of CPSP* provided above [6], its role in determining the outcome of a plasma spray process is analyzed and discussed in terms of the ratio of molten and unmolten material in the agglomerates. The computer simulations presented below may provide further insight into the basic phenomena involved in thermal spraying processes. These insights may also be helpful in controlling a complex process where very few parameters can be manipulated completely independently without affecting the others.
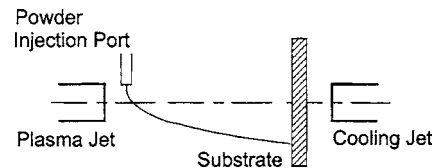

Fig. 1 A schematic representation of the plasma spray system modeled here: the nozzle diameter is 8 mm; the standoff distance (between the nozzle exit and the substrate) is 100 mm, and the disc shaped substrate has a diameter of 50 mm and a thickness of 3 mm. The powder injector diameter is 2 mm, and it is positioned radially inward at a distance of 5 mm from the nozzle exit as well as from the jet axis.

Melting and Resolidification Phenomena

The Physical Problem. The physical phenomena modeled here include a plasma stream issuing into standard atmospheric conditions, entraining the ambient air, which together forms a jet to be used to process the powdered material. The plasma is assumed to be a mixture of argon and hydrogen gases at specified temperatures and volumetric compositions at the nozzle exit. The geometric configuration, which is typical of atmospheric plasma sprays with external powder injection, is shown in Fig. 1. As also shown in Fig. 1, the powder material is injected radially (at 90 deg with the jet axis) near the nozzle exit by means of a carrier gas (argon at standard conditions). The fluid flow modeling takes into account the presence of a stationary, disc shaped substrate onto which the sprayed powder is directed for deposition, and the axis of the substrate coincides with that of the plasma jet for a simplified geometry. A fixed powder feed rate of 6 kg/h was used in these calculations although the usual range for powder feed rate is 3–6 kg/h [1]. The high feed rate was used in conjunction with a previous study that was performed to demonstrate the need for 3D computational fluid dynamics (CFD) simulations for "loaded sprays" (see below) [9]. The details of the splat deposition process are not included in these simulations, but the impingement of the plasma-air mixture on the substrate is reported since it is considered to be a significant fluid dynamics phenomenon. A summary of the processing conditions used for predicting the particle states is provided in Table 1. Plasma torch exit temperatures and velocities, which are used as input parameters for the modeling (see below), are based on the first law of thermodynamics (and a fixed torch efficiency of 70%), with enthalpy values obtained from the compilations by Boulos et al. [14]. Experimental verification of especially the plasma torch exit velocities is difficult, if not impossible. The plasma exit temperatures appear to be reasonably close to measured temperatures [6], although a number of factors can lead to significant differences (the temperatures in Table 1 appear to be underestimated at lower power levels). These factors include assumptions of local thermal equilibrium, torch efficiency, as well as other assumptions inherent in the estimation of experimental uncertainties [6].

Modeling and Computer Simulation. The plasma jet (i.e., its velocity and temperature fields) was calculated using a finite volume method based commercial software [15] for computational fluid dynamics (CFD). The well-known SIMPLE scheme [15] was used along with second-order differencing schemes (upwind for the convective terms and central differencing for the diffusive terms) in the conservation equations for momentum, energy, and the gaseous species. The gaseous phase was modeled as an ideal gas mixture of argon, hydrogen, and air at local thermodynamic equilibrium. This implies that the transport and thermodynamic properties of the gas (or plasma) phase components are taken to be those calculated at equilibrium conditions (at the local temperature and 1 atm) [14]. The mixture properties were calculated by the CFD code following Wilke's formula [16]. Plasma chemistry (species dissociation, ionization, or recombination) was not

Table 1 Summary of processing parameters used in the predictions

Particle diameter, D_p (μm) (total flow-rate: 6 kg/h)			30, 40, 50, 60, 70			
Carrier gas injection velocity, V_{inj} (m/s) (argon at 1 atm and 295 K)			5, 15, 30			
Primary gas content (Ar %, Vol.)			80.0		86.3	
Total gas (Ar and H_2) flow rates, volumetric (ft^3/h and litre/min at 1 atm and 295 K) as well as corresponding mass flow rates	Q (SCFH)	100	100	100	93.0	96.0	91.0
	(L/min)	(47.2)	(47.2)	(47.2)	(43.9)	(45.3)	(42.9)
	$\dot{m}$ (gm/s)	1.04	1.04	1.04	1.03	1.06	1.01
Plasma torch power input, P_{torch} (kW)		13.5	27	39.3	11.4	27.7	48.1
Power delivered to plasma (kW), $\eta_{torch}=0.7$		9.46	19.0	27.5	8.00	19.4	33.7
CPSP$^*=(\eta_{torch}P_{torch})^{1/4}/Q_{Ar}\times1000$(W$^{1/4}$/SCFH)		122	146	160	118	143	172
Average plasma torch exit velocity (m/s)		380	590	650	360	560	620
Average plasma torch exit temperature (K)		7350	11,450	12,750	8000	12,000	14,000

considered. To account for the radial injection of particles into the plasma jet, the physical system was considered to be fully three dimensional and elliptic in behavior. The plasma jet (and the entrained ambient air) impinging onto the substrate along with the injected powder particles (and the carrier gas) were all calculated as a steady-state problem, using the k-ε turbulence modeling scheme. These calculations were carried out in a structured grid with increased mesh densities near the plasma exit and axis (with uniform variation in the angular direction). Grid independence studies were made with the finest two grids being 20 (axial) $\times$ 24 (radial) $\times$ 32 (angular) and $40\times24\times32$, respectively. The maximum difference in the local temperatures being of the order of 6%, the former grid was used for all subsequent calculations. The calculations were performed on 300 MHz workstations, and it would take in the order of a week to obtain the fully converged calculations including fluid-particle interactions (see below). For all CFD calculations as well as particle state predictions described below, convergence was assumed when the maximum relative difference in any variable ϕ between two consecutive iterations, $(\phi^{n+1}-\phi^n)/\phi^n$, decreased to less than 10^{-6}.

Empirical correlations were used for predicting particle drag force (Stokes law) and surface heating (Ranz-Marshall correlations) induced by local plasma velocity and temperature conditions, and these included corrections for variable fluid phase transport properties (due to nonuniform temperature) in the boundary layer and noncontinuum effects (for high Knudsen number) [8]. The effects of particle vaporization were not considered since the pertinent temperatures ($\sim$4100 K) were never reached in the simulations performed for the present study.

The agglomerated powder particles are treated as spherical entities driven by the gaseous phase while being subjected to heating (or cooling, depending on the relative temperature of the surrounding gas). The internal heat transfer (including melting and resolidification) processes were assumed to be one dimensional. The complexities of heat transfer in the (porous) agglomerates (with possible sintering below melting point) were neglected because of the lack of a simple model as well as of the necessary data that could be incorporated in the current CFD scheme. Heat transfer and solid-liquid phase change phenomena internal to the particles were therefore calculated using a conventional enthalpy method developed previously [17,18] and linked with the CFD code [19]. Powder material properties were based on those for zirconia stabilized with 7% yttria by weight [20,21].

Note that the results presented here are for "loaded" spray jets. That is, the plasma flow solution is coupled with the multiple particle trajectories calculated. This coupling is due to the fluid-particle interaction, or the cooling as well as deceleration of the jet by the presence of the initially room temperature particles that are injected at a low velocity relative to that of the jet exit. The coupling phenomena were modeled numerically by employing a two-

step iterative scheme. Specifically, a steady-state plasma flow field was first calculated without the particles. Next, particles were injected and tracked in a Lagrangian manner. A number of particles were injected into the plasma jet at specified velocities ($=V_{inj}$) and thereafter tracked to obtain the results for an ensemble with a specific particle size. The influence of turbulent velocity fluctuations on each individual trajectory was taken into account in a Monte Carlo scheme, and therefore every trajectory (as well as every particle's heating history) is unique. However, the net effect from one particle size and injection velocity on the plasma flow field was obtained from a number of particle trajectory simulations. The thermal energy and momentum exchanges between the particles and the fluid phase were recorded and the plasma flow field was updated through the appropriate source functions in the conservation equations for (gas phase) momentum and energy. These two calculation steps (for particle ensembles and the plasma flow field, respectively) were alternated for an adequate number of iterations to obtain a converged solution for the coupled plasma-particle flow field. The final particle trajectory and thermal history was obtained from this plasma flow field for each particle size. It may be noted that such a coupled solution is critical when 3D calculations are performed, especially with radial injection of powders and a high powder flow rate. The number of trajectories ($\sim$300) used for each particle size and injection velocity was deemed to be sufficient by comparing the average evolutions (the degree of melting and resolidification as a function of distance from the injection point) obtained from a much larger ensemble ($\sim$1000) with the maximum (relative) differences in particle states being less than 1%.

Definition of Particle States. The particle states used for the current analysis are defined in terms of two quantities as found at the substrate (for all the results presented in this paper, the substrate is placed at a fixed $L_{stdf}=100$ mm): The first is the fraction of material never molten in a particle (f_{RN}) during the spraying process. For nanostructured agglomerates, this fraction will be indicative of the *maximum* retained nanostructured material in a particle (assuming all molten material will undergo recrystallization due to melting). The second is the instantaneous liquid fraction in a particle (f_L). Initially, when a particle is gaining thermal energy from the surrounding plasma, and a solid-liquid melt front is moving inward within the particle, the relation between the two quantities is described by the simple relation

$$f_L = 1 - f_{RN} \tag{1}$$

When the heated particles are outside of the plasma jet core they begin to cool, and resolidification can ensue at the surface of the particle leading to a second solid-liquid melt front that propagates inward. As indicated earlier, the resolidified material near the sur-
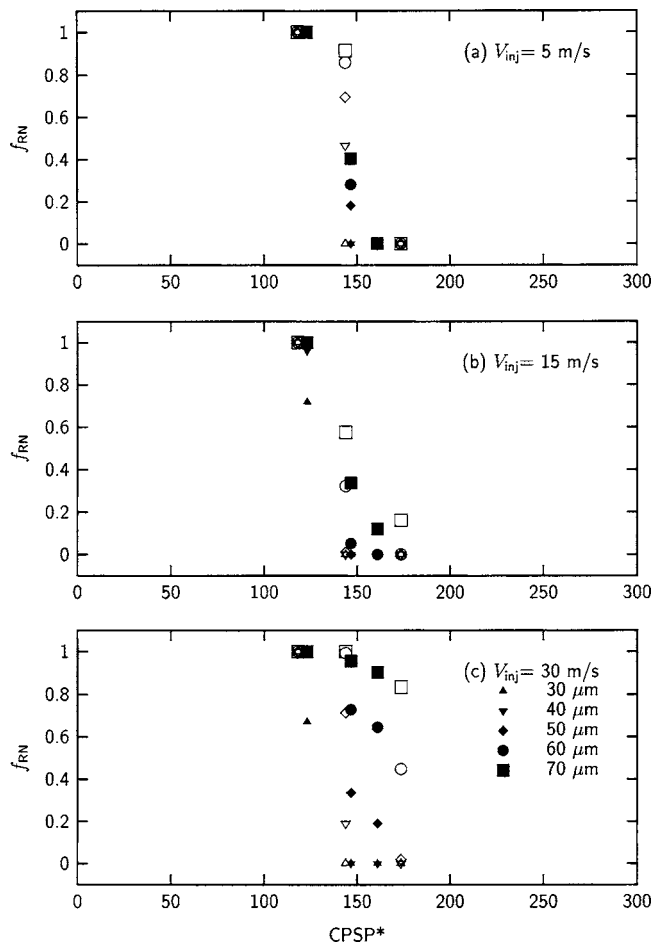
Fig. 2 Retained nanostructure in particles sprayed with three injection velocities and two plasma gas compositions: solid symbols: 80% argon, open symbols: 86.3% argon

face is *not* nanostructured, and the instantaneous liquid fraction in each particle is given by the inequality

$$f_L < 1 - f_{RN} \qquad (2)$$

where the degree of inequality represents the amount of sintered, i.e., non-nanostructured material. Therefore, Eq. (2) also describes the reduction in the molten material that provides an adhesion mechanism during splat deposition. It may be noted that f_L (or f_{RN}) depends on the particle's thermal history mentioned above, and variations in this quantity can result from turbulent mixing of air entrained into the plasma jet as well as from statistical variations in powder injection velocity and angle [22]. The latter (statistical) variations have not been considered here.

Predictions. Predictions were obtained for plasma sprays operated with two plasma gas compositions and three power levels. This leads to three CPSP* values at each composition, ranging from 120 to 170 for a total of six spraying conditions. The f_{RN} values as detected at $L_{stdf}=100$ mm for each of the five particle sizes (30–70 μm) are presented in Fig. 2.

A strong dependence on CPSP* can be observed at the lower V_{inj} (=5 m/s), with the indication of a narrow transition CPSP* in Fig. 2(a). Below this transitional value of CPSP* ($\sim$148), the particles are fully solid and unmolten, and hence retain all their nanostructure. At the highest CPSP*, particles of all sizes undergo complete melting, leading to no retained nanostructure. At or near the transition CPSP*, the larger particles retain more of the nanostructure as expected. In general, particles sprayed with a lower

H_2 content (rendering the plasma mixture to be less conductive) also retain more of the nanostructure. Note that the behavior shown in Fig. 2(a) is undesirable from the processing point of view. The results indicate that a particular solid-liquid state, characterized by the presence of *both* retained nanostructure and some liquid phase material, may not be easily attained by adjusting thermal processing conditions only.

At $V_{inj}=15$ m/s (Fig. 2(b)), the sharp dependence of f_{RN} upon CPSP* is smeared, although the complete absence of any molten material at the lower CPSP* as well as the complete melting of the material at the higher CPSP* is still clear. At $V_{inj}=30$ m/s (Fig. 2(c)), a large scatter in the data indicates further widening of the transitional CPSP* region, although in general the larger particles retain most of their unmolten state at every CPSP*. The scatter may be explained by the higher initial momentum and thermal mass of the large particles. A particle with a higher initial momentum (injected radially into the plasma jet) can pass through the diameter of the jet fast enough to emerge relatively unaffected. A very small fraction of its total volume, if any, might be molten even if it passes through the hottest part of the jet. Nevertheless, different particle sizes travel through different parts of the jet, resulting in different lengths of time as well as temperatures of exposure, leading to very different heating histories. It is also noted that a higher value of V_{inj} requires higher carrier gas flow rates, leading to increased turbulent mixing and dilution of the plasma jet near the powder injection port. This may also be partially responsible for a higher f_{RN} at higher V_{inj} in particles larger than 40 μm at any CPSP*, as becomes evident when Figs. 2(a)–2(c) are compared.

For f_L as a function of CPSP* in different particle sizes sprayed at $V_{inj}=5$ m/s, as seen in Fig. 3(a), the distribution is nearly a mirror image of that found in Fig. 2(a). An exact mirror image would imply the validity of Eq. (1); however, the particles (of all sizes) sprayed with CPSP* $\sim$150 have undergone some re-solidification. Likewise, the f_L distribution at higher V_{inj} show nearly opposite distributions (with $f_L=1-f_{RN}$). Any deviation from the mirror image distribution implies the appearance of re-solidified material near the particle surface (Eq. (2)). At $V_{inj}=30$ m/s, Fig. 3(c), it is clear that mostly the smaller particles (30–50 μm) retain any molten material. As for the 50–60 μm particles, since resolidification begins at the particle surfaces, it is uncertain whether the trapped molten material will be available as the necessary adhesive, unless the thin shell of resolidified material breaks upon impact, exposing the liquid parts to the substrate.

In order to explore the correlation between retained nanostructure and molten material in particles of different sizes, the two quantities (f_{RN} and f_L) have been plotted against each other in Fig. 4. No differentiation is made regarding plasma composition. At any injection velocity, for the particles that retain both some nanostructured and some molten material (i.e., $f_L, f_{RN}>0$), significant deviations from the ideal conditions described by Eq. (1) are observed. At the lowest injection velocity, ($V_{inj}=5$ m/s, Fig. 4(a)), only a few particles ($D_p=40-70$ μm) are off either axis. At the intermediate injection velocity, ($V_{inj}=15$ m/s, Fig. 4(b)), only the larger particles ($D_p=60-70$ μm) particles are found off either axis (i.e., in a state with both some retained nanostructure and some molten, liquid material at $L_{stdf}=100$ mm). At the highest V_{inj} (=30 m/s) a banded distribution appears, due mostly to the smaller particles partially resolidified after having undergone partial melting, Fig. 4(c). In addition, the largest particles ($D_p=70$ μm), which were only partially molten, are completely resolidified as those reach the substrate. Note that in Fig. 4 the vertical distance between any data point and the straight line (Eq. (1)) represents the fraction of resolidified material, or the loss in nanostructure (as well as in "adhesive" material).

The data presented in Fig. 4 have been regrouped into three levels of CPSP*—low, transition, and high (Fig. 5). The symbol scheme for different particle sizes is the same as in Fig. 4, but
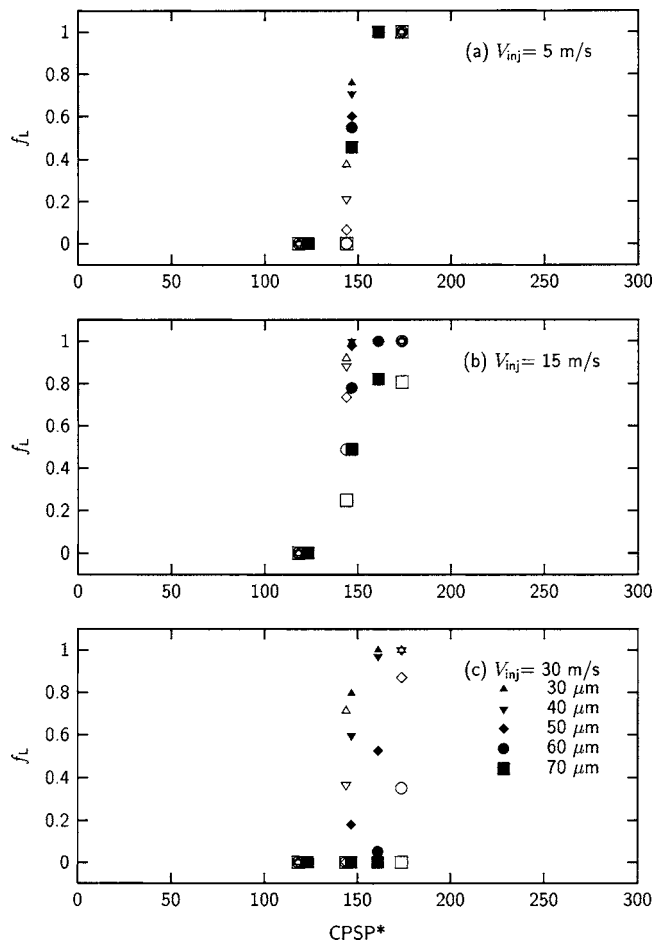
Fig. 3 Instantaneous liquid fraction for the particles presented in Fig. 2, at a standoff distance of 100 mm
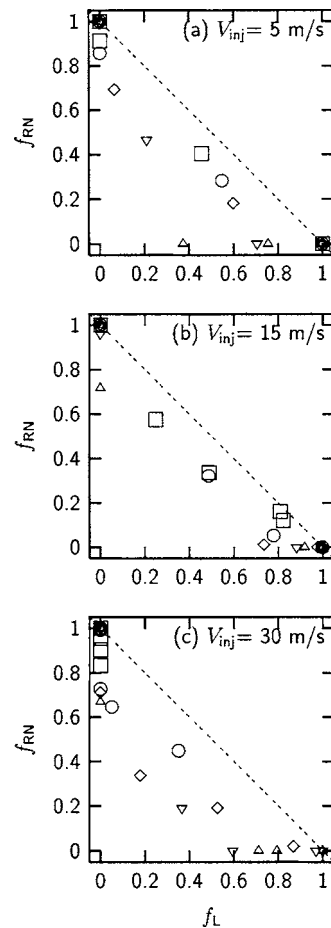

Fig. 4 Retained nanostructure versus molten material fraction correlation as a function of injection velocity. Symbols represent different particle sizes as before (Fig. 2(c)), but no differentiation is made regarding plasma composition. The dashed line represents Eq. (1).

with larger symbols representing a higher V_{inj}. The role of CPSP* in producing f_L, $f_{RN} > 0$ is further elucidated here. At the lower CPSP*, all but three particle sizes are found to have never been molten in the process, and the three partially molten particles arrive at the substrate fully resolidified. The largest number of particles in states of f_L, $f_{RN} > 0$ are found at the transition CPSP* identified earlier ($\sim$150; Fig. 5(b)). Here the scatter in the data is also the maximum, although a banded distribution can be discerned. In addition, a number of smaller particles ($D_p = 30$–50 μm) are found to have undergone complete melting followed by partial resolidification, while some of the larger particles are found to have undergone partial melting followed by complete resolidification ($D_p = 50$–70 μm). At the highest CPSP*, most of the smaller particles are found to have lost some or all their nanostructure, and are delivered at the substrate in a completely molten state ($f_L = 1$). Only the larger particles (50–70 μm) retain some of their nanostructure (with no molten material), and a few of those in the intermediate size range ($D_p = 50$–60 μm) can be found in states of f_L, $f_{RN} > 0$.

Optimization of Processing Parameters

Processing Parameters. Irrespective of what f_{RN}-f_L ratio of the sprayed material may be desired in the final coating to be produced with nanostructured precursors, ideally the two quantities should be related by Eq. (1), once the correct CPSP* (as well as L_{stdf}) has been determined for a particular D_p. Nevertheless, as has been observed, this ideal situation may not be achievable in a batch of powder that has a wide range of sizes (and hence the less

than 100% deposition efficiency in all plasma spray processes, whether the powder is nanostructured or not). In light of the results presented above, it can be stated that within a narrow CPSP* window, some control over a limited range of nonzero f_{RN}-f_L values may be possible with certain V_{inj} and D_p.

The fact that particle size can be chosen as a processing parameter determining the final coating characteristics, in spite of the variations inherent in and caused by the plasma jet production and the particle injection processes, has been demonstrated experimentally by depositing coatings with monosized powders [23]. There, it was found that the degree of melting may be a function of particle size only, and further that for an optimum particle size, many properties of the coating (which are apparently dependent on the degree of melting) are also the least sensitive to variations other processing conditions examined (such as plasma gas composition and nozzle size). This processing parameter (D_p) may be even more critical in the context of precursors with nanostructured agglomerates. One such instance may be where the plasma torch (nozzle) size, torch power, and stand-off distance are fixed by physical and geometrical constraints (for example, in case of coating internal surfaces of small diameter cylinders, L_{stdf} can be as small as 30 mm, and the torch powers levels as low as 5 kW). In such cases, an appropriate D_p and V_{inj} may need to be determined for the CPSP* and L_{stdf} allowable, instead of working out an optimum CPSP* suitable for powders with a given D_p distribution used in general applications.
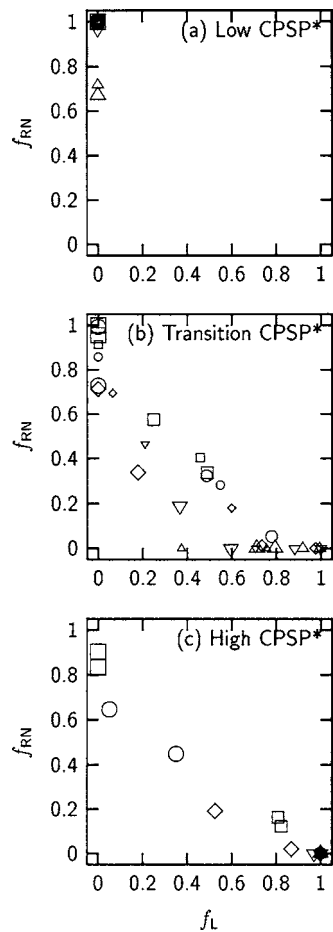
Fig. 5 Retained nanostructure versus molten material fraction correlation as a function of CPSP* levels. The relative size of each symbol represents the injection velocity (5 m/s, 15 m/s, and 30 m/s) of the particle of particular size; see Fig. 2(c) for a legend for particle sizes).

Fig. 6 Aggregate retained nanostructure (top) and liquid fraction (bottom) in a powder batch consisting of equal numbers of 30 μm and 70 μm agglomerates sprayed with the same three injection velocities and various CPSP* values as in Fig. 5

Predictions for Particle Ensembles. The preceding results suggest that it may be possible to control the amount of molten and nanostructured material delivered at the substrate by tailoring the size distribution of the powder. This fine-tuning process may be carried out at a known transition CPSP* and V_{inj} (determined for a specific spray system hardware) that is found to yield a considerably wide range of nonzero f_{RN} and f_L for certain particle sizes.

If the size distribution of the injected powder is given in number densities, the amount of molten material at a certain L_{stdf} can be calculated by integrating, over the relevant size range, the mass-weighted product of f_L, and the number density at each particle size. If the number as well as size of all the particles is known (as in the present modeling study), the following expressions may be used for calculating the pertinent aggregate fractions in a batch of powder:

Aggregate instantaneous molten material

$$F_L = \sum f_{L,i} m_i \qquad (3)$$

Aggregate retained nanostructure

$$F_{RN} = \sum f_{RN,i} m_i \qquad (4)$$

Here, m_i is the mass-fraction of the i-th particle with respect to the total mass of a sample. With a slight modification, the above could also be used to a good approximation for a powder batch with bimodal size distributions and very narrow spreads at each of the
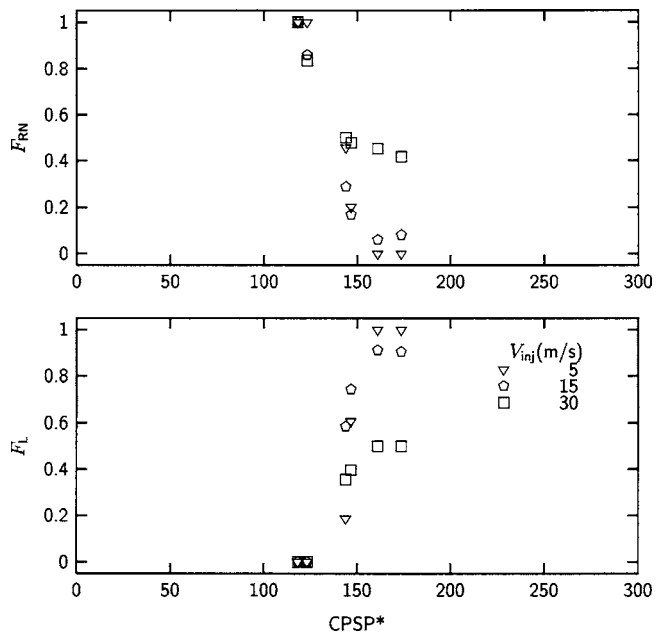
nominal particle sizes, with m_i representing the mass fraction of the i-th size group.

To repeat, it may be highly desirable to provide material that is partially molten, and partially unmolten, to the surface to be coated. Achieving such a condition may be possible by manipulating the size distribution of the sprayed powder. Here a sample calculation, for illustrating the utility of modeling and simulation as a process design tool, is presented for a hypothetical batch of powder with an equal amount of 30 μm and 70 μm particles based on predictions for f_{RN} and f_L already presented above. The aggregate retained nanostructure (F_{RN}) and aggregate molten fraction (F_L) of this batch of powder are presented in Fig. 6, all other processing conditions being the same as those used for the previously discussed results.

As evident in Fig. 6, a sharp transitional CPSP* no longer exists. The undesirable effects of spraying at extreme values of CPSP* and low V_{inj} cannot be avoided, however (no molten material at all, or all molten material and no nanostructure). Nevertheless, at the intermediate CPSP* values, a reasonably consistent correlation between retained nanostructure and molten fraction (in the aggregate sense) is observed. The data points also spread over a wider range of F_L (or F_{RN}, alternatively) for the three V_{inj} studied, implying the possibility of improved control over the F_{RN}-F_L ratio by varying quantities of the two particle sizes. It may be noted that using this approach, other ratios of F_{RN}-F_L may also be obtained for powder batches with a possibly different size distribution.

When the two aggregate quantities (F_{RN} and F_L) for the above particular batch are compared against each other, a more desirable trend similar to Eq. (1) emerges as seen in Fig. 7(a). Nevertheless, this trend again implies the existence of a narrow transition regime of CPSP*. Furthermore, V_{inj} does not appear to be a very useful processing parameter for controlling the F_{RN}-F_L ratio. The only practical way to control this ratio within the range where F_{RN}, $F_L > 0$ may be through altering the proportions of the two particle sizes in a batch.

In order to further investigate the influence of powder size distribution on the phase change behavior of the sprayed material, a second powder batch with a continuously varying distribution of
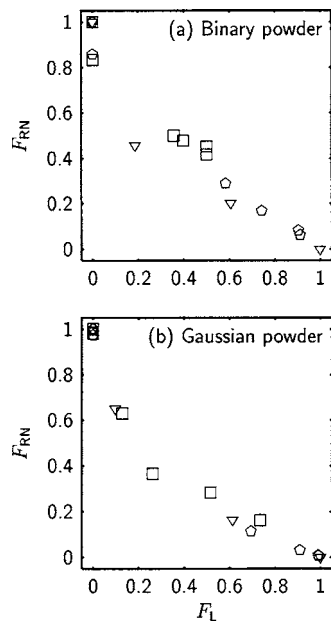
Fig. 7 Aggregate retained nanostructure versus liquid fraction correlations. (*a*) For the powder batch presented in Fig. 6 (with a binary distribution, with 30 μm and 70 μm particles only). (*b*) For a batch of powder with a Gaussian mass distribution for particles sizes 30 μm through 70 μm with a mean diameter of 50 μm and a standard deviation of 10 μm. See the legend of Fig. 6 for particle injection velocity (V_{inj}) information.

particles sizes was analyzed (Gaussian, with a mean size of 50 μm and a standard deviation of 10 μm). In order to retain a reasonable amount of nanostructure in the powder (arbitrarily selected as $0.3 < F_{RN} < 0.7$), it is necessary to control CPSP* within 2.1%, 7.0%, and 7.8% of the operating point (with V_{inj}=5 m/s, 15 m/s, and 30 m/s, respectively) when the Gaussian distribution is used. In contrast, if the bimodal distribution consisting of 30 μm and 70 μm particles is used, the same range of retained nanostructure $(0.3 < F_{RN} < 0.7)$ corresponds to CPSP* ranges of 3.2%, 10.2%, and 25%. Clearly, the use of the bimodal size distribution offers enhanced controllability of F_{RN}. Furthermore, if one assumes that CPSP* may be controlled to within 2% due to the inherent variations in system operation, the Gaussian powder must be used only in conjunction with a high V_{inj}. On the other hand, use of the bimodal feedstock leads to significantly enhanced control over F_{RN}, regardless of V_{inj}.

This influence of the powder size distribution on resulting powder state is further illustrated in Fig. 7(*b*), where F_{RN} versus F_L data are presented for the Gaussian powder. If, for example, an optimum range of processing conditions is defined with $0.3 < F_{RN} < 0.7$ *and* $0.7 > F_L > 0.3$, the binary powder appears to provide the desired powder state for five individual operating conditions, in contrast to only one operating condition for the Gaussian powder.

It is noted here that the F_{RN} and F_L values of Figs. 6 and 7 were calculated using f_{RN} and f_L values predicted for two particle sizes in a spray loaded with 6 kg/h of a powder batch consisting of equal mass fractions each of five particle sizes. The F_{RN}-F_L correlation will change to a minor degree if the relevant quantities are recalculated in a spray consisting of only 30 μm and 70 μm particles. It is also noted that single-port radial injection systems may not be practicable when combining two different sized particles, as their deposition footprints will not coincide, and further adjustments (in injection velocity and/or direction) may be necessary by, for example, including multiple injection ports.

Conclusions

Results from computer modeling and simulation have been used to analyze and predict particle states of nanostructured materials sprayed with plasma sprays. It has been shown that when partially molten powder is to be deposited, the window of operating conditions can be rather narrow. However, within the range of operating conditions studied, it may be still possible to control and optimize coating characteristics by controlling powder size distribution. Using different powder sizes in combination to generate desired coating characteristics may require further modification of injection hardware (injection angle, for example), but these aspects of process control will need further simulation and experimentation [12]. In any case, it appears that the working parameter CPSP*, initially introduced by experimentalists for relating coating properties to processing parameters, is a reasonable indicator of the state of the sprayed material for a given spray system configuration.

Nomenclature

D_p = powder particle diameter, μm
f_L = instantaneous fraction of molten material in an individual particle
f_{RN} = fraction of material never molten in a particle during spraying
F_L = aggregate fraction of molten material in a powder batch
F_{RN} = aggregate fraction of material never molten in a batch
Kn = Knudsen number, the ratio of molecular *mean free path* to powder particle diameter
L_{stdf} = stand-off distance between torch and substrate, mm
P_{torch} = torch power input, volt $\times$ ampere (W); actual power delivered to the plasma is obtained by multiplying W by torch efficiency
Q = gas flow rate, standard cubic feet per hour
V_{inj} = carrier gas injection velocity, m/s

References

[1] Pawlowski, L., 1995, *The Science and Engineering of Thermal Spray Coatings*, Wiley, New York.
[2] Heimann, R. B., 1996, *Plasma-Spray Coating: Principles and Applications*, Wiley, New York.
[3] Shaw, L. L., Goberman, D., Ren, R., Gell, M., Jiang, S., Wang, Y., Xiao, T. D., and Strutt, P. R., 2000, "The Dependency of Microstructure and Properties of Nanostructured Coatings on Plasma Spray Conditions," Surf. Coat. Technol., **130**(1), pp. 1–8.
[4] Jordan, E. H., Gell, M., Sohn, Y. H., Goberman, D., Shaw, L., Jiang, S., Wang, M., Xiao, T. D., Wang, Y., and Strutt, P., 2001, "Fabrication and Evaluation of Plasma Sprayed Nanostructured Alumina-Titania Coatings With Superior Properties," Mater. Sci. Eng., A, **301**(1), pp. 80–89.
[5] Fauchais, P., Vardelle, A., and Dussoubs, B., 2001, "Quo Vadis Thermal Spraying?" J. Therm. Spray Technol., **10**(1), pp. 44–66.
[6] Semenov, S., and Cetegen, B., 2001, "Spectroscopic Temperature Measurements in Direct Current Arc Plasma Jets Used in Thermal Spray Processing of Materials," J. Therm. Spray Technol., **10**(2), pp. 326–336.
[7] Gell, M., Jordan, E. H., Sohn, Y. H., Goberman, D., Shaw, L., and Xiao, T. D., 2001, "Development and Implementation of Plasma Sprayed Nanostructured Ceramic Coatings," Surf. Coat. Technol., **146–147**, pp. 48–54.
[8] Wan, Y.-P., Prasad, V., Wang, G.-X., Sampath, S., and Fincke, J., 1999, "Modeling of a Powder Particle Heating, Melting, Resolidification, and Evaporation in Plasma Spraying Processes," ASME J. Heat Transfer, **121**, pp. 691–699.
[9] Ahmed, I., and Bergman, T. L., 2001, "Simulation of Thermal Plasma Spraying of Partially Molten Ceramics: Effect of Carrier Gas on Particle Deposition and Phase Change Phenomena," ASME J. Heat Transfer, **123**(1), pp. 188–196.
[10] Ramesh, K., Ng, H. W., and Yu, S. C. M., 2003, "Influence of Process Parameters on the Deposition Footprint in Plasma-spray Coating," J. Therm. Spray Technol., **12**(3), pp. 377–392.
[11] Ramesh, K., Yu, S. C. M., Ng, H. W., and Berndt, C. C., 2003, "Computational Study and Experimental Comparison of the In-Flight Particle Behavior for an External Injection Plasma Spray Process," J. Therm. Spray Technol., **12**(4), pp. 508–522.
[12] Dussoubs, B., Vardelle, A., Mariaux, G., Themelis, N. J., and Fauchais, P., 2001, "Modeling of Plasma Spraying of Two Powders," J. Therm. Spray Tech-

nol., **10**(1), pp. 105–110.

[13] Bandyopadhyay, R., and Nylen, P., 2003, "A Computational Fluid Dynamic Analysis of Gas and Particle Flow in Flame Spraying," J. Therm. Spray Technol., **12**(4), pp. 492–503.

[14] Boulos, M., Fauchais, P., and Pfender, E., 1994, *Thermal Plasmas*, Vol. 1, Plenum Press, New York.

[15] *FLUENT 4.4 User's Guide and Update Manual*, 1995-2002, Fluent, Inc., 10 Cavendish Court, Lebanon, New Hampshire.

[16] Bird, R. B., Stewart, E. W., and Lightfoot, E. N., *Transport Phenomena*, Wiley, New York, 1960.

[17] Ahmed, I., and Bergman, T. L., 2002, "An Engineering Model for Solid-Liquid Phase Change Within Sprayed Ceramic Coatings of Non-Uniform Thickness," Numer. Heat Transfer, Part A, **41**, pp. 113–129.

[18] Crank, J., 1984, *Free and Moving Boundary Problems*, Clarendon Press, Oxford, UK.

[19] Ahmed, I., and Bergman, T. L., 2000, "Three-Dimensional Simulation of Thermal Plasma Spraying of Partially Molten Ceramic Agglomerates," J. Therm. Spray Technol., **9**(2), pp. 215–224.

[20] Hasselman, D. P. H., Johnson, L. F., Bensten, L. D., Syed, R., Lee, H. L., and Swain, M. V., 1987, "Thermal Diffusivity and Conductivity of Dense Polycrystalline ZrO2 Ceramics: A Survey," Am. Ceram. Soc. Bull., **66**, pp. 799–806.

[21] Ganz, B., Koch, R., Krebs, W., and Wittig, S., 1998, "Spectral Emissivity Measurements of Thermal Barrier Coatings," *Proceedings of the 7th AIAA/ASME Joint Thermophysics and Heat Transfer Conference*, Part 1 (of 4), Armaly, B. F., Howell, J. R., Kaminski, D. A., Phinney, L., Thynell, S. T., Chan, S. H., Yang, J. C., Gore, J., Ezekoye, D., Gill, W., and Zhou, C. Q., eds., ASME, New York, HTD 357-1, pp. 291–296.

[22] Williamson, R. L., Fincke, J. R., and Chang, C. H., 2002, "Numerical Study of the Relative Importance of Turbulence, Particle Size and Density, and Injection Parameters on Particle Behavior during Thermal Plasma Spraying," J. Therm. Spray Technol., **11**, pp. 107–108.

[23] Erickson, L. C., Troczynski, T., Hawthorne, H. M., Tai, H., and Ross, D., 1999, "Alumina Coatings by Plasma Spraying of Monosize Sapphire Particles," J. Therm. Spray Technol., **8**, pp. 421–426.

Technical Briefs

Power Assessment of Flowing Compressed Air

Maolin Cai

Kenji Kawashima

Toshiharu Kagawa
e-mail: caiml@k-k.pi.titech.ac.jp

Precision and Intelligence Laboratory,
Tokyo Institute of Technology,
4259 Nagatsuta-cho, Midori-ku, Yokohama,
Kanagawa Prefecture, 226-8503 Japan

This study proposes a new concept for quantifying the energy of flowing compressed air, called air power. Air power is defined as the work-producing potential of compressed air, and its definition and general equation are presented. The properties of air power are also discussed. Air power is comprised of two components, transmission power and expansion power, while air temperature and kinetic energy can generally be neglected.
[DOI: 10.1115/1.2170129]

1 Introduction

The demands of industrialization have increasingly required the use of compressed air in factories and workshops since the 1960s. Compared with oil or electric systems, compressed air systems are cleaner, cheaper, and easier to maintain. However, compressed air systems can be expensive to operate [1]. The cost for producing 0.6 MPa to 0.9 MPa compressed air in Japan averages around U.S. \$0.02–0.03 per cubic meter, with the compressor's electricity responsible for 80% to 90% of the cost. In fact, compressed air systems typically consume 10% to 20% of the total electricity in manufacturing factories, reaching 40 billion kilowatt hour per year in Japan.

A significant portion of the energy consumed by compressed air systems is wasted due to improper settings and operation, as well as air leaks and inappropriate equipment. Addressing these concerns typically saves about 30%. Therefore, improving the efficiency of compressed air systems and reducing air consumption is essential for minimizing energy costs.

Air volume or flow rate is typically used to represent air consumption because there is no standard method for determining the power consumed by compressed air flow. This paper proposes a

new concept, called air power, to represent this power. In hydraulics, fluid power is calculated by multiplying the gauge pressure and the fluid's volumetric flow rate. This method, however, cannot be applied to air because it assumes incompressibility. The electric power applied to a compressor, which is the energy source for the air power, is not proportional to its pressure output for a given flow rate. Therefore, the role of air pressure must be studied. Using only the flow rate does not specify the power lost in the supply pipes or supplied to the actuators, which are considered extremely important for streamlining energy consumption. Therefore, air power must be sufficiently defined and quantified.

This paper introduces a typical compressed air system and discusses the cyclic state change for air and energy conversion. Air power is defined as a property of compressed air and uses energy, a thermodynamics concept, to derive a general equation [2]. Then, properties of air power including composition, temperature considerations, kinetic energy, and power loss factors are discussed.

2 Air Power Proposal

2.1 Energy Conversion in Compressed Air Systems. Figure 1 shows a typical compressed air system. The system contains a compressor, an air dryer, and filter used to remove steam and contaminants, an accumulation vessel, a regulator used to stabilize the downstream pressure, a pipe network, and terminal equipment such as pneumatic cylinders and motors, etc.

The compressor's electric motor converts the electric power into torque that sucks air in from the atmosphere and compresses it. Once the air is output from the compressor, it is cleaned and regulated, and then supplied to the terminal equipment through pipes. Finally, the compressed air is released back into the atmosphere after actuating the terminal equipment. The energy flow in this process is schematically illustrated in Fig. 2. From this figure it is clear that the air power is generated from the compressor's mechanical power. The air power is then converted back into mechanical power to operate the terminal equipment.

According to thermodynamics, the energy of flowing air is determined by enthalpy, provided that kinetic and gravity potential energy are negligible [3]. However, enthalpy cannot be used to represent air power because air enthalpy does not change when air is compressed isothermally. Therefore, air power should be investigated in terms of the energy conversion for the state change of air.

For simplicity, two ideal processes are discussed. These two processes experience no losses. In the first process, compressed air is produced in a simple piston-type compressor. The other process involves a pneumatic cylinder consuming compressed air. These two processes are depicted in Fig. 3.

2.2 Ideal Production of Compressed Air. It is well known that air compression requires the least amount of work in an isothermal process. Assuming that there is no friction or air leak, the ideal process is described as follows.

1. Suck: Pull the piston from Position A to B to suck air from the atmosphere in a quasi-static process.

Fig. 1 A typical compressed air system

Fig. 3 Ideal production and ideal consumption of compressed air
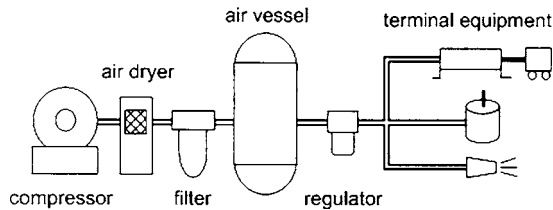
2. Compress: Close Valve 1 and push the piston from Position B to C to compress the air quasistatically until the air pressure reaches p_s. This process is considered an isothermal process.

3. Supply: Open Valve 1 and close Valve 2. Then push the piston from Position C to A to completely expel the compressed air under constant pressure p_s. The compressed air is supplied to the cylinder on the right.

Using the equation $p_a V_a = p_s V_s$ for isothermal compression, the required mechanical work for producing compressed air of pressure p_s and volume V_s is

$$W_i' = W_{i1}' + W_{i2}' + W_{i3}'$$

$$= 0 + \int_{V_a}^{V_s} (p - p_a)(-dV) + (p_s - p_a)V_s = p_s V_s \ln \frac{p_s}{p_a} \quad (1)$$

2.3 Ideal Consumption of Compressed Air. The actuator most often used in compressed air systems is a pneumatic cylinder. Assuming that there is no friction or air leak, the ideal scenario for performing the maximum level of mechanical work is described as follows.

1. Supply: This step is identical to Step 3 in Sec. 2.2. The piston is pushed from Position A to C at a constant pressure of P_s in a quasistatic process.

2. Expand: Close Valve 1 and expand the supplied air quasistatically until it reaches the atmospheric state. During this process, the piston is pushed from Position C to B. The air state change is considered isothermal.

3. Return: Open Valve 2 and pull back the piston from Position B to A in a quasistatic process.

The work done in these steps can be calculated by Eq. (2). This equation also represents the work-producing potential of compressed air at a pressure p_s and a volume V_s.

$$W_o' = W_{o1}' + W_{o2}' + W_{o3}'$$

$$= (p_s - p_a)V_s + \int_{V_s}^{V_a} (p - p_a)dV + 0 = p_s V_s \ln \frac{p_s}{p_a} \quad (2)$$

It can be seen that air state changes for ideal consumption are the opposite of those for ideal production. The state changes for a unit mass of air is depicted by the P-V diagram in Fig. 4. The area ABCA represents the mechanical work calculated by Eqs. (1) and (2).

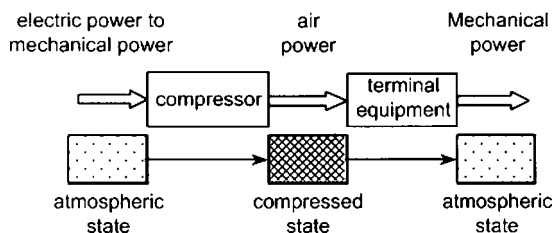From this figure it is evident that the energy produced is com-
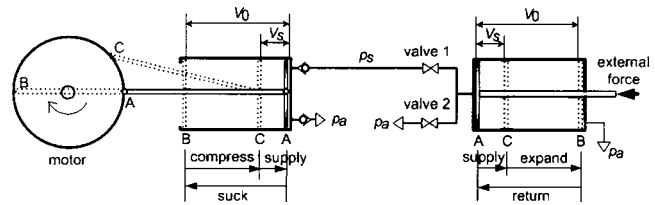
pletely consumed without any loss. In addition, it is clear that the compressed air is used to transmit the energy. The transmitted amount of air can be determined from its pressure and volume, which will be employed by the proposed air power calculation.

2.4 Definition of Air Power. A quasistatic process is sometimes referred to as a reversible process [3]. In thermodynamics, an isothermal process is also considered a reversible process. Therefore, it can be said that $p_s V_s \ln(p_s/p_a)$ represents the mechanical work exchanged in a reversible process. In actual processes, however, losses due to friction are inevitable. Therefore, the following relationship is more realistic:

$$W_i \geqslant p_s V_s \ln \frac{p_s}{p_a} \geqslant W_o \quad (3)$$

Observing the energy flow depicted in Fig. 2, Eq. (3) suggests that air power should be represented by $p_s V_s \ln(p_s/p_a)$. To verify this assertion, a thermodynamics term called energy is used to derive a general conclusion. Energy represents the work-producing potential that can be extracted from a substance. In this study, this output potential of compressed air is its available energy. Therefore, the available energy per unit mass of air can be expressed by Eq. (4) [3].

$$e = (h - h_a) - T_a(s - s_a) \quad (4)$$

It can be easily proven that e is related to the mechanical work done in the production and consumption of compressed air as follows [4]:

$$W_i \geqslant m \cdot e \geqslant W_o \quad (5)$$

In this equation, the quantities are equal if they refer to reversible processes. When the air temperature is T_∞ Eq. (4) can be expanded to [4]

$$e = (h - h_a) - T_a(s - s_a)|_{T=T_a} = \frac{pV}{m} \ln \frac{p}{p_a} \quad (6)$$

Equation (3) can be obtained by combining Eqs. (5) and (6).

Therefore, the available energy represents the air power energy, so air power can be defined as the flux of the available energy that
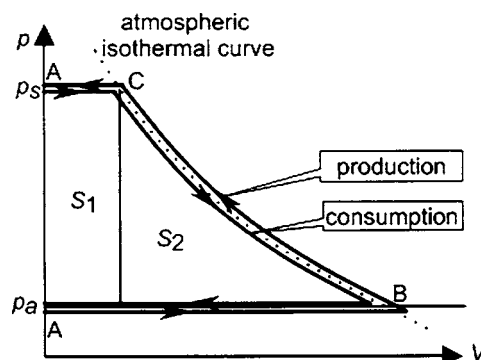

Fig. 2 Energy flow and air state change

Fig. 4 P-V diagram of ideal production and consumption
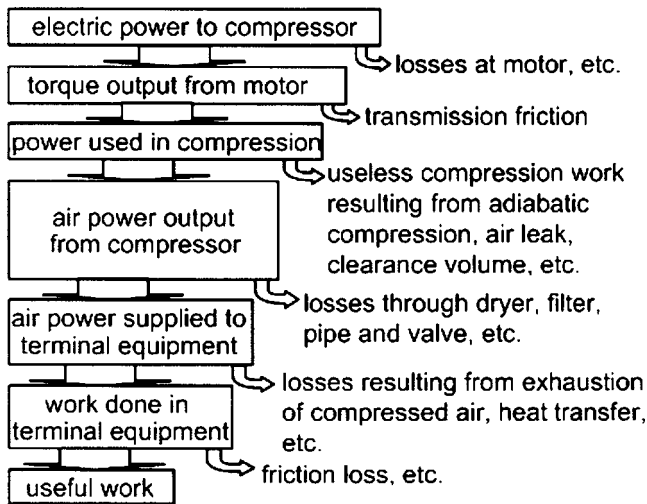
Fig. 5 Energy flow in compressed air systems

Fig. 6 Temperature influence on air power

can be extracted from flowing air as it undergoes a reversible process from a given state to the atmospheric state. This definition of air power is expressed as

$$P = G[(h - h_a) - T_a(s - s_a)] \tag{7}$$

Figure 5 shows the position of air power in compressed air systems using this definition.

Because h and s are both functions of air pressure and temperature, air power can be calculated as follows by expanding Eq. (7) [3]:

$$P = GRT_a\left[\ln\frac{p}{p_a} + \frac{\kappa}{\kappa - 1}\left(\frac{T}{T_a} - 1 - \ln\frac{T}{T_a}\right)\right] \tag{8}$$

Generally, compressed air flows at atmospheric temperature in pipes. According to Boyle-Charles Law, $GRT_a = pQ = p_aQ_a$ at atmospheric temperature, where Q and Q_a are the volumetric flow rate at a compressed state and at atmospheric state, respectively. Substituting this equation and $T = T_a$ into Eq. (8), air power at atmospheric temperature can be reduced to

$$P = GRT_a\ln\frac{p}{p_a} = pQ\ln\frac{p}{p_a} = p_aQ_a\ln\frac{p}{p_a} \tag{9}$$

Therefore, air power is proportional to flow rate. Table 1 provides examples of air power under various pressures at a flow rate of 1000 l/min. This table reveals that the unit of air power is kilowatt which is as the same as for electric power. This will facilitate the management of air energy consumption in factories.

This definition of air power will make it easy to determine energy losses due to pressure losses and air leaks, and will enable the investigation of internal energy distributions in current compressed air systems.

3 Properties of Air Power

3.1 Temperature Influence on Air Power. Equation (8) indicates that air power is also a function of air temperature. Figure 6 shows the relationship between air power and air temperature at
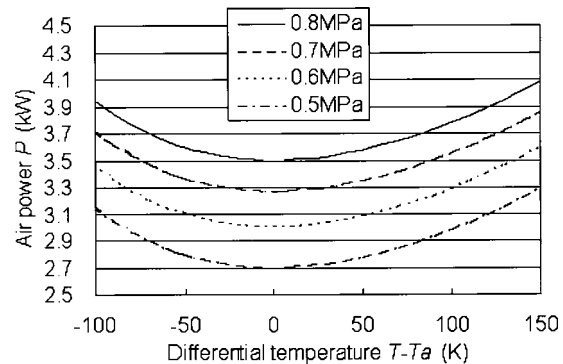
Table 1 A calculation example of air power

Flow rate	1000 l/min(ANR)			
Absolute pressure (MPa)	0.4	0.6	0.8	1.0
Air power (kW)	2.32	3.00	3.49	3.87

a volumetric flow rate of 1000 l/min ($G = 1.2$ kg/min). The figure reveals that air power reaches a minimum when the air temperature is equal to atmospheric temperature. The higher the differential air temperature, the larger the air power. This characteristic can be explained by the thermodynamic properties of available energy.

Available energy is a relative potential that only exists when the air's state differs from the standard surroundings. Therefore, the greater the difference between air states, the larger the available energy.

Figure 6 indicates that the air power increases about 15% when the temperature difference is 100 K. The typical air temperature output from compressors is approximately 10 K to 50 K higher than atmospheric temperature. This will increase the air power by several percent. However, the temperature will return to atmospheric temperature as the air travels to the terminal equipment through the cooler, dryer, vessel, and pipe. In other words, the increased power due to the temperature rise will be lost during transmission. Therefore, air temperature should be neglected when calculating air power. Equation (9) can be employed for air power calculations.

3.2 Composition of Air Power. It can be seen from the previous discussion on ideal processes that the air power equation should be composed of two parts. The first part represents the transmission power, which addresses the power required to push the air downstream. The second part represents the expansion power, which addresses the available work due to air expansion. P_t and P_e are used to represent these two parts, respectively, and can be calculated using the following equations.

$$P = P_t + P_e \tag{10}$$

$$P_t = (p - p_a)Q = p_aQ_a\left(1 - \frac{p_a}{p}\right) \tag{11}$$

$$P_e = pQ\ln\frac{p}{p_a} - (p - p_a)Q = p_aQ_a\left(\ln\frac{p}{p_a} + \frac{p_a}{p} - 1\right) \tag{12}$$

In P-V diagram shown in Fig. 4, P_t and P_e are equal to the areas of S_1 and S_2, respectively.

Figure 7 displays a representative example using Eqs. (11) and (12). This figure indicates that the transmission power and expansion power are identical when the air pressure is equal to 0.52 MPa. The higher the air pressure, the larger the ratio of expansion power. Because the air supply pressure in factories ranges between 0.6 MPa and 1.0 MPa, the expansion power is typically larger than the transmission power for compressed air systems.

As shown in Eq. (11), transmission power for air is calculated using the same expression as hydraulic power. However, flowing air contains not only transmission power, but also expansion power. Even when the upstream supply is shut off, compressed air can still perform work by expanding, unlike liquids. This is the

Fig. 7   Composition of air power

Fig. 8   Ratio of kinetic energy in air power
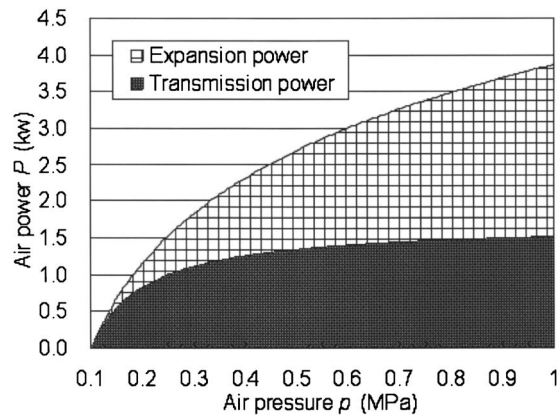
significant difference in the power transmission between compressible and incompressible fluids. Therefore, both transmission power and expansion power must be considered when analyzing the power of flowing air.

3.3   Kinetic Energy in Air Power. Although kinetic energy is not included in Eq. (7), it can be also be converted into mechanical work. According to the exact definition of air power, the kinetic energy of the flowing air should also be included in the air power calculation. The kinetic energy of flowing air can be determined by the following equation:

$$P_k = \frac{d}{dt}\left(\frac{1}{2}mv^2\right) = \frac{8(p_a Q_a)^3}{RT(p\pi d^2)^2} \qquad (13)$$

In this equation, m is the mass of the air, v is the average air velocity, and d is diameter of the pipe.

Figure 8 displays the ratio of P_k in air power. Kinetic energy accounts for less than 5% of the available energy when the average velocity is below 100 m/s at pressures above 0.3 MPa. Therefore, kinetic energy can be neglected for air transmission pipes in factories, where the average air velocity rarely exceeds 100 m/s. However, when analyzing the internal energy distribution in pneumatic components, kinetic energy should be considered because the air flows at high velocities when it passes through narrow openings.

3.4   Factors Causing Power Loss. Because air power is a type of energy, factors attributing to the loss of energy must be included in the air power calculation. Theoretically, energy loss occurs in irreversible processes [3]. Therefore, any irreversible process in compressed air systems will reduce the air power. In compressed air systems, there are two primary classes of irreversible processes.

The first class is mechanical irreversible processes, which are caused by both internal and external friction. External friction generally refers to the friction generated between the interior pipe wall and the flowing air. This friction is primarily responsible for the pressure loss in pipes. Internal friction exists in various forms, including viscous friction, vortex, and disorder flow. These power losses are converted to heat.

The second class is thermal irreversible processes. These include the heat transfer between air and its external surroundings and air mixture. Air temperature changes when air is compressed and expanded, and these changes are lost due to heat transfer. Most of the heat transfer in air compression systems occurs in the after-cooler and refrigeration dryer directly after compression. Air mixture generally refers to air charge. For example, introducing 1 dm³ of compressed air at a pressure of 0.6 MPa to a 10 dm³ capacity tank with an initial pressure of 0.3 MPa results in an
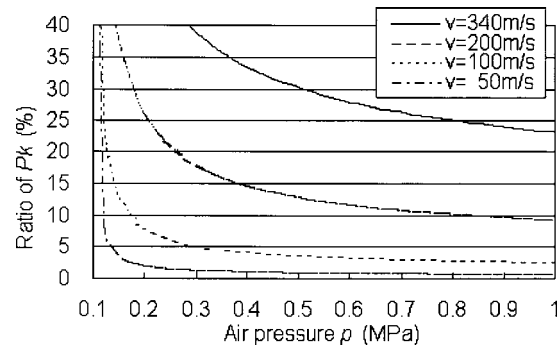
energy loss of 359 J.

All of these factors should be reduced or eliminated to realize energy savings in compressed air systems.

4   Conclusion

Air power was defined and a general equation for calculating air power was derived after investigating the energy flow in compressed air systems and the work-producing potential of compressed air.

Air power can be broken into two parts: transmission power and expansion power, with expansion power usually the larger of the two. This is the significant difference between the power transmission of compressible and incompressible fluids. Temperature and kinetic energy can generally be neglected when calculating air power. However, irreversible processes such as friction, heat transfer, and air mixture will cause air power loss and must be considered.

Nomenclature

e = available energy of a unit mass of air (J/kg)
G = mass flow rate (kg/s)
h = enthalpy of a unit mass of air (J/kg)
p = absolute air pressure (Pa)
P = air power (Pa)
Q = volumetric flow rate (m³/s)
R = gas constant (J/(kg K))
s = entropy of a unit mass of air (J/(K kg))
T = temperature (K)
V = volume (m³)
W = mechanical work (J)
κ = specific heat ratio

Subscripts

a = atmosphere
e = expansion power
k = kinetic energy
i = production of compressed air
o = consumption of compressed air
s = air supply
t = transmission power

Superscripts

$'$ = ideal reversible process

References

[1] Energy Efficiency Office, 1994, "Compressing Air Costs," Good Practice Guide No. 126, United Kingdom.
[2] Rant, Z., 1956, Exergie, ein neues Wort für "Technische Arbeitsfähigkeit," Forsch. Ing.-Wes., 22, S.36/37 (in German).
[3] Li, Kam W., 1995, *Applied Thermodynamics: Availability Method and Energy Conversion*, Taylor & Francis, London.
[4] Cai, M., and Kagawa, T., 2001, "Energy Consumption Assessment of Pneumatic Actuating Systems Including Compressor," *Proceedings of International Conference on Compressors and Their Systems*, London, United Kingdom, IMechE, London, United Kingdom, pp. 381–390.

On the Convergence of Higher Order Upwind Differencing Schemes for Tridiagonal Iterative Solution of the Advection-Diffusion Equation

Sandip Mazumder
Member, ASME
Department of Mechanical Engineering,
The Ohio State University,
Columbus, OH 43202
e-mail: mazumder.2@osu.edu

1 Introduction

In order to reduce numerical diffusion associated with first-order upwind differencing schemes (UDS), higher order upwind differencing schemes are often employed in computational fluid dynamics (CFD) calculations. The two most popular higher order UDS are the second-order UDS [1] and the quadratic upwind interpolation for convective kinematics (QUICK) scheme [2].

It is well known that the use of either of the aforementioned two schemes results in a system of equations that may not converge when using an iterative solution method [3]. Even for the one-dimensional advection-diffusion equation, since the stencil extends beyond three nodes, a single tridiagonal matrix inversion is not sufficient, and iterations are necessary to solve the resulting system of algebraic equations. Thus, one-dimensional calculations are sufficient for extracting meaningful information pertaining to the stability of these schemes in the context of iterative solution.

In this Technical Brief, the convergence characteristics of tridiagonal iterative solution of the equations resulting from use of the second-order UDS and the QUICK scheme are investigated using discrete Fourier analysis. It is found that the chosen iterative method diverges at intermediate Peclet numbers for both schemes. Since these findings are not intuitive, prior to drawing firm conclusions, numerical experiments were performed to verify these findings. The numerical experiments show that the stability and convergence characteristics of both schemes agree perfectly with the results predicted by the discrete Fourier analysis. It is also shown that introduction of a small amount of diagonal dominance through the use of so-called inertial damping factors makes both schemes unconditionally stable. Once again, the convergence characteristics of the modified equations are examined by both methods, and the results are in perfect agreement with each other, lending credibility to the final results and conclusions.

2 Analysis and Results

The equation governing the conservation of physical quantities encountered in fluid flow, heat transfer, and mass transfer is the generalized advection-diffusion transport equation, written as [4]

$$\frac{\partial}{\partial t}(\rho\phi) + \nabla \cdot (\rho \mathbf{U}\phi) = \nabla \cdot (\Gamma_\phi \nabla \phi) + \dot{S}_\phi \qquad (1)$$

where ρ is the density, ϕ is the conserved scalar (or vector component) in question, $\mathbf{U}$ is mass-averaged bulk fluid velocity vector, Γ_ϕ is the diffusion coefficient of ϕ, and $\dot{S}_\phi$ is the production rate of ϕ. At steady state, and under the assumption of one-dimensional transport and no sources, Eq. (1) reduces to

$$\frac{d}{dx}\left(\rho u\phi - \Gamma_\phi \frac{d\phi}{dx}\right) = 0 \qquad (2)$$

where u is the component of the fluid velocity in the x direction. Under the assumption of constant flow speed, constant density, and constant diffusion coefficient, Eq. (2) may be written in non-dimensional form as

$$\frac{d}{dx^*}\left(\text{Pe}_L\phi - \frac{d\phi}{dx^*}\right) = 0 \qquad (3)$$

where the Peclet number based on the total length is defined as $\text{Pe}_L = \rho u L/\Gamma_\phi$, L being the total length of the domain. The nondimensional length is denoted by $x^* = x/L$.

The finite-volume method guarantees conservation and is, arguably, the most popular method for numerical solution of conservation equations encountered in fluid dynamics. Upon finite-volume integration of Eq. (3) on a one-dimensional uniform mesh, the following flux balance equation is obtained

$$\left(\text{Pe}_L\phi_e - \frac{d\phi}{dx^*}\bigg|_e\right) - \left(\text{Pe}_L\phi_w - \frac{d\phi}{dx^*}\bigg|_w\right) = 0 \qquad (4)$$

where the subscripts "e" and "w" carry their usual meanings. The diffusion flux is usually treated using central differencing, while a variety of schemes are available to treat the advection flux. Two higher order upwind difference schemes, namely, the second-order UDS and the QUICK schemes, are considered here. In what follows, the analysis is presented for the QUICK scheme. The analysis for the second-order UDS follows the same procedure.

Using central differencing for diffusion and the QUICK scheme for advection, Eq. (4) may be written in terms of the nodal values as

$$\text{Pe}_L\left[\frac{3}{8}\phi_O + \frac{3}{8}\phi_E - \frac{7}{8}\phi_W + \frac{1}{8}\phi_{WW}\right] - \frac{1}{\delta}[\phi_E - 2\phi_O + \phi_W] = 0 \qquad (5)$$

where the subscripts "O," "E," "W," and "WW" carry their usual meanings, and $\delta = \Delta x/L$ is the nondimensional size of each control volume. Upon examination of Eq. (5) it is clear that the resulting coefficient matrix will have four bands even for this one-dimensional problem, and the final solution cannot be obtained by a single tridiagonal matrix (TDMA) inversion. TDMA inversion may be still used within an iterative procedure in which the contribution of the WW node is treated explicitly (at previous iteration), while the contributions of all the other nodes are treated implicitly (at current iteration), resulting in the following equation:

$$\phi_O^{k+1} + A_E\phi_E^{k+1} + A_W\phi_W^{k+1} = -A_{WW}\phi_{WW}^k \qquad (6)$$

where the superscript "k" represents an iteration index. The normalized (by the central diagonal) link coefficients A_W, A_E, etc., can be easily inferred from Eq. (5). Subtracting Eq. (6) from a similar equation for the exact numerical solution, obtained using the same discretization scheme, an equation for the error can be formulated [5]

$$\varepsilon_O^{k+1} = A_E\varepsilon_E^{k+1} + A_W\varepsilon_W^{k+1} = -A_{WW}\varepsilon_{WW}^k \qquad (7)$$

Following standard procedures of convergence analysis [5,6], the error can be written as a summation of a finite number of Fourier modes

$$\varepsilon_j^k = \sum_{m=0}^{M-1} C_m^k \exp(ij\theta_m) \qquad (8)$$

where ε_j^k denotes the error at the jth node and kth iteration, and C_m^k is the amplitude of the mth Fourier mode at the kth iteration. The total number of control volumes (or cells) in the domain is $M-1$, and is also equal to the maximum number of Fourier modes than can be resolved by the mesh. It is well known that the largest
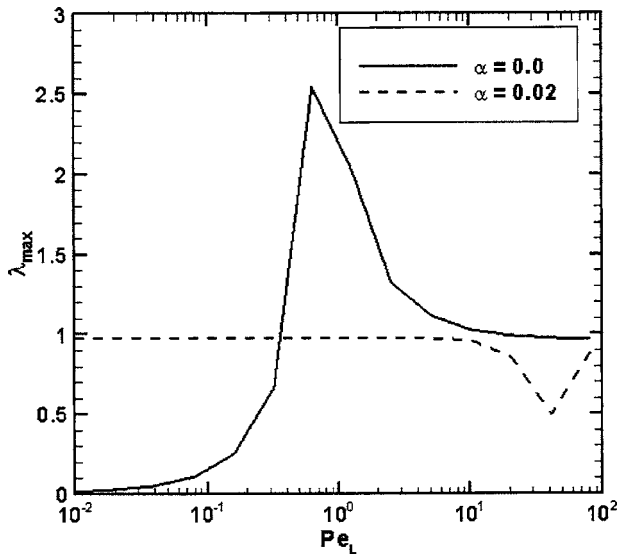
Fig. 1 Spectral radius for iterative TDMA solution of the one-dimensional advection-diffusion equation using the QUICK scheme with 100 cells
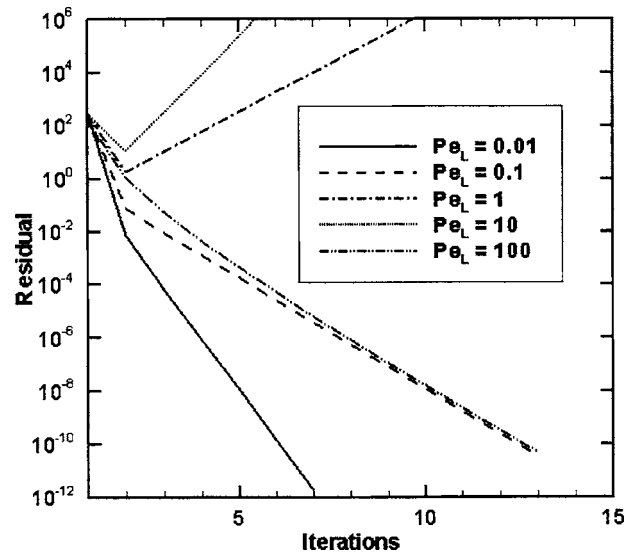

Fig. 2 Convergence of the one-dimensional advection-diffusion equation solved using the finite-volume method with the QUICK scheme for advection and central difference for diffusion

eigenvalue of the iteration matrix corresponds to the smallest frequency [5,6], i.e., the smallest value of θ_m, denoted by $\theta = \pi/(M-1)$. Thus, analysis of all the modes shown in Eq. (8) is unnecessary. In realization of this fact, the subscript "m" is dropped in the analysis that follows with the understanding that the mode under consideration corresponds to the smallest frequency. Substitution of the relevant smallest frequency mode of Eq. (8) into Eq. (7) yields

$$C^{k+1}(1 + A_E e^{i\theta} + A_W e^{-i\theta}) = -C^k A_{WW} e^{-2i\theta} \quad (9)$$

where C^{k+1} is the amplitude of the error at the $(k+1)$th iteration, and C^k is the amplitude of the error at the kth iteration. The ratio of these two amplitudes represents the eigenvalue λ of the iteration matrix, and in this case, is given by

$$\lambda = \frac{C^{k+1}}{C^k} = \frac{-A_{WW} e^{-2i\theta}}{(1 + A_E e^{i\theta} + A_W e^{-i\theta})} \quad (10)$$

The spectral radius of the iteration matrix λ_{max} is given by

$$\lambda_{max} = \sqrt{\lambda\lambda^*} \quad (11)$$

where λ^* is the complex conjugate of λ. For the errors to damp out and the iterative scheme to converge, the spectral radius must be less than unity.

Figure 1 shows ($\alpha=0$ curve) the spectral radius of the QUICK scheme calculated using Eqs. (10) and (11). For these calculations 100 cells were considered. It is clear that the iterative solution method will diverge at intermediate Peclet numbers ranging between approximately 0.4 and 20, and will converge at small and large Peclet numbers. In order to validate this finding, Eq. (6) was solved using the iterative procedure discussed earlier. Dirichlet boundary conditions ($\phi(0)=0$ and $\phi(L)=1$) were used to prevent generation of additional instabilities at the boundaries. An initial guess $\phi=0$ was used everywhere. Figure 2 shows the residuals for various Peclet numbers. It is seen that the convergence behavior agrees perfectly with the predictions of the discrete Fourier analysis. For Peclet numbers equal to 1 and 10 (which are both within the range 0.4–20), the scheme diverges, and converges for all other cases, exactly as predicted by Fourier analysis. The spectral radii predicted by discrete Fourier analysis and the residuals for the second-order UDS are shown in Figs. 3 and 4, respectively. The behavior is similar to that of the QUICK scheme with slight

differences in the range of Peclet numbers for which divergence occurs. Once again, the numerical experiments agree well with the results of the convergence analysis, as expected.

The convergence of the iterative solution method applied to both schemes can be enhanced by introducing additional diagonal dominance through the use of the so-called inertial damping factor. This is done by adding $\alpha\phi_O^{k+1}$ to the left-hand side of Eq. (6) and $\alpha\phi_O^k$ to the right-hand side of the same equation, based upon the realization that upon convergence these two terms will cancel each other. Here, α is the so-called inertial damping factor and is a user-prescribed real number that can assume any value. $\alpha=0$ represents the case already discussed. Following the same procedure outlined earlier for the QUICK scheme, the eigenvalue corresponding to the Fourier mode with the smallest frequency is derived as
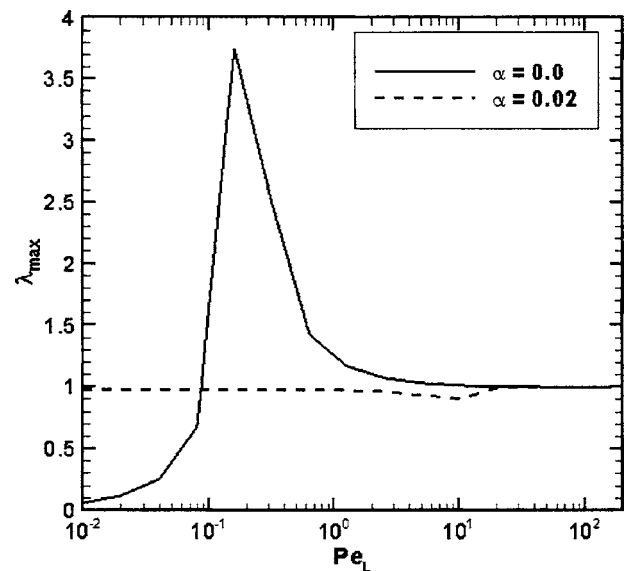

Fig. 3 Spectral radius for iterative TDMA solution of the one-dimensional advection-diffusion equation using the second order upwind differencing scheme with 100 cells
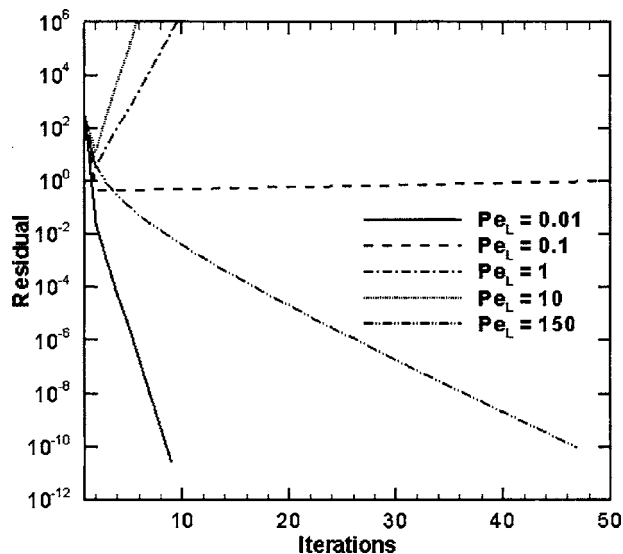
Fig. 4 Convergence of the one-dimensional advection-diffusion equation solved using the finite-volume method with the second-order upwind difference scheme for advection and central difference for diffusion

Fig. 6 Convergence of the one-dimensional advection-diffusion equation solved using the finite-volume method with the second-order upwind difference scheme for advection and central difference for diffusion, and an inertial damping factor α equal to 0.02

$$\lambda = \frac{C^{k+1}}{C^k} = \frac{-A_{WW}e^{-2i\theta}}{(1 + \alpha + A_E e^{i\theta} + A_W e^{-i\theta})} \qquad (12)$$

Figure 1 shows the spectral radius of the iteration matrix for a small value of α equal to 0.02 for the QUICK scheme. Dramatically different behavior is observed when compared to the $\alpha=0$ case. The first important finding is that the spectral radius is less than unity irrespective of the Peclet number. The second important finding is that if inertial damping is used (i.e., $\alpha>0.02$), for small Peclet numbers, the spectral radius increases from a value very close to zero to a value that is very close to unity, implying that the convergence is expected to deteriorate for small Peclet numbers. Once again, to validate the predictions of the discrete Fourier analysis, numerical experiments were performed. The residuals for the $\alpha=0.02$ case are shown in Figs. 5 and 6 for the QUICK

and the second-order UDS, respectively. As predicted by the discrete Fourier analysis, all cases converge, and the convergence for small Peclet numbers is significantly slower than the case without inertial damping. The conclusion to be drawn from these results is that while positive inertial damping (which is equivalent to using under relaxation) is desirable for intermediate to large Peclet numbers, it should not be used for pure diffusion (Laplace or Poisson) equations. It can be shown easily that the use of successive over-relaxation, as commonly employed for diffusion equations, is equivalent to using a negative inertial damping factor, in which case, the convergence actually improves over the case where no inertial damping is used.

3 Summary and Conclusions

Discrete Fourier analysis of the errors associated with tridiagonal iterative solution of the one-dimensional advection-diffusion equation using higher order UDS has been performed in order to gain a quantitative understanding of the convergence of the iterative method. Results of the analysis show that both the chosen iterative method will not converge for either the second-order UDS or the QUICK scheme at intermediate Peclet numbers and will converge at small and large Peclet numbers for both schemes. The results of the discrete Fourier analysis were confirmed by actually solving the one-dimensional advection diffusion equation at various Peclet numbers. The spectral radii of the iteration matrices can be dramatically altered by adding a small amount of diagonal dominance, which makes both schemes converge at all Peclet numbers. It is also shown that such a modification slows down the convergence of small Peclet number cases, and is, therefore, not recommended for Laplace or Poisson equations. Since tridiagonal line sweeps are commonly used for iterative solution of the multidimensional advection-diffusion equation on structured meshes, the findings of this one-dimensional analysis apply directly to multidimensional problems where line-by-line sweeps are used.
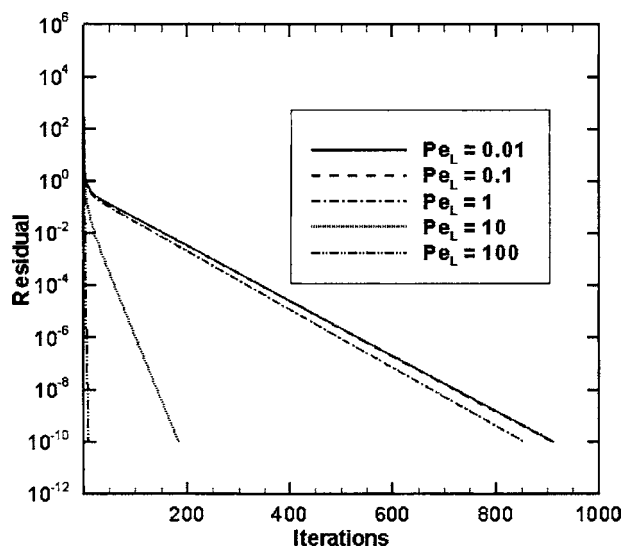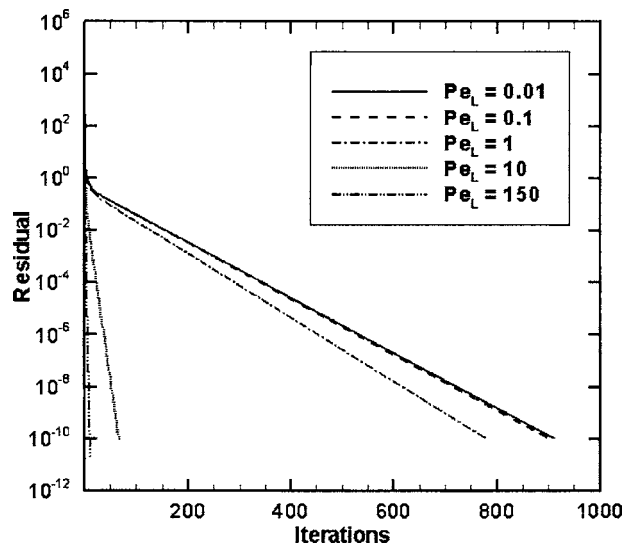

Fig. 5 Convergence of the one-dimensional advection-diffusion equation solved using the finite-volume method with the QUICK scheme for advection and central difference for diffusion, and an inertial damping factor α equal to 0.02

Nomenclature

C^k = amplitude of error at kth iteration
i = $\sqrt{-1}$
k = iteration index

M = number of nodes
Pe_L = Peclet number based on the total length L
$\dot{S}_\phi$ = production rate of scalar ϕ
$\mathbf{U}$ = fluid velocity vector (m/s)
x = space variable (m)

Greek

α = inertial damping factor
δ = nondimensional grid spacing
ε^k = error between exact numerical solution and solution at kth iteration
λ = eigenvalue of iteration matrix
λ_{max} = spectral radius of iteration matrix
ϕ = general scalar
ρ = mixture density (kg/m^3)

θ = angular frequency (rad)
Γ_ϕ = diffusion coefficient (m^2/s)

References

[1] Shyy, W., Thakur, S., and Wright, J., 1992, "Second-Order Upwind and Central Difference Schemes for Recirculating Flow Computation," AIAA J., **30**, pp. 923–932.
[2] Leonard, B. P., 1979, "A Stable and Accurate Convective Modelling Procedure Based on Quadratic Interpolation," Comput. Methods Appl. Mech. Eng., **19**, pp. 59–98.
[3] Alves, M. A., Oliveira, P. J., and Pinho, F. T., 2003, "A Convergent and Universally Bounded Interpolation Scheme for the Treatment of Advection," Int. J. Numer. Methods Fluids, **41**, pp. 47–75.
[4] Kuo, K. K., 1986, *Principles of Combustion*, Wiley, New York.
[5] Hirsch, C., 1990, *Numerical Computation of Internal and External Flows*, Vols. 1 and 2, Wiley, New York.
[6] Wesseling, P., 2004, *An Introduction to Multi-Grid Methods*, R. T. Edwards Inc., Philadelphia, PA.